

**Low-Energy Ballistic Lunar Transfers**

by

**Jeffrey S. Parker**

B.A., Physics / Astronomy, Whitman College, 2001

M.S., Aerospace Engineering Sciences, University of  
Colorado, 2003

A thesis submitted to the  
Faculty of the Graduate School of the  
University of Colorado in partial fulfillment  
of the requirements for the degree of  
Doctor of Philosophy  
Department of Aerospace Engineering Sciences  
2007

This thesis entitled:  
Low-Energy Ballistic Lunar Transfers  
written by Jeffrey S. Parker  
has been approved for the Department of Aerospace Engineering Sciences

---

George Born

---

Prof. Steve Nerem

---

Prof. Elizabeth Bradley

---

Dr. Eric Leuliette

---

Dr. Rodney Anderson

Date \_\_\_\_\_

The final copy of this thesis has been examined by the signatories, and we find that both the content and the form meet acceptable presentation standards of scholarly work in the above mentioned discipline.

Parker, Jeffrey S. (Ph.D., Aerospace Engineering Sciences)

Low-Energy Ballistic Lunar Transfers

Thesis directed by Prof. George Born

A systematic method is developed that uses dynamical systems theory to model, analyze, and construct low-energy ballistic lunar transfers (BLTs). It has been found that low-energy BLTs may be produced by intersecting the stable manifold of an unstable Earth-Moon three-body orbit with the Earth. A spacecraft following such a trajectory is only required to perform a single maneuver, namely, the Trans-Lunar Injection maneuver, in order to complete the transfer. After the Trans-Lunar Injection maneuver, the spacecraft follows an entirely ballistic trajectory that asymptotically approaches and arrives at the target lunar three-body orbit. Because these orbit transfers require no orbit insertion maneuver at the three-body orbit, the transfers may be used to send spacecraft 25 – 40% more massive than spacecraft sent to the same orbits via conventional, direct transfers. From the targeted three-body orbits, the spacecraft may transfer to nearly any region within the Earth-Moon system, including any location on the surface of the Moon. The systematic methods developed in this research allow low-energy BLTs to be characterized by six parameters. It has been found that BLTs exist in families, where a family of BLTs consists of transfers whose parameters vary in a continuous fashion from one end of the family to the other. The families are easily identified and studied using a BLT State Space Map (BLT Map). The present research studies BLT Maps and has surveyed a wide variety of BLTs that exist in the observed families. It has been found that many types of BLTs may be constructed between 185-km low Earth parking orbits and lunar three-body orbits that require less than 3.27 km/s and fewer than 120 days of transfer time. Under certain conditions, BLTs may be constructed that require less than 3.2 km/s and fewer than 100 days of transfer time.

It has been found that BLTs may implement LEO parking orbits with nearly any combination of altitude and inclination; they may depart from their LEO parking orbits nearly any day of each month; and they may target a variety of different classes of unstable Earth-Moon three-body orbits. Finally, studies are provided that address how low-energy transfers impact the design of spacecraft systems and how BLT Maps may be implemented as pragmatic tools in the design of practical lunar missions.

## **Dedication**

To my family, for their overwhelming support, encouragement, and love.

Jen Marson Parker, my wonderful wife

My parents Rick and Bonnie Parker

My brother Morgan and my sister Becky

All of my crazy cousins, aunts, uncles, and grandparents

## Acknowledgements

It is a pleasure to thank so many people who have made this thesis possible. First and foremost I would like to express gratitude to my advisor, George Born, for all of his incredible support and patience, which has lifted me through many challenges that we have faced during this research. I would like to express my deepest appreciation to Rodney Anderson, who first introduced me to my research and has supported me ever since. He was there to guide me up the Flatirons during my first visit to Boulder and he was there to gracefully scrutinize my dissertation in its final form. It is a pleasure to thank Steve Nerem and Eric Leuliette for all of their help, kindness, and guidance as I struggled to identify the focus for my research. Their patience opened up the opportunity for me to begin this research, and I owe them a debt of gratitude because this research has been an impetus for inspiration to me. I would also like to thank Liz Bradley for her sage advice and for being available for me during difficult and complicated times. I genuinely appreciate her support.

It has been a pleasure working with the people at the Colorado Center for Astrodynamics Research. I have enjoyed tackling many dynamical systems problems with Rodney, Keric, and Kate. I also wish to thank Bob Leben for making CCAR a warm and fuzzy place. Finally, I have enjoyed sharing this experience with all of my numerous office-mates over the years; in particular, I would like to express special thanks to Brian Powell for all of his help and support.

All of this work has been performed through generous support by a National

Defense Science and Engineering Graduate (NDSEG) Fellowship sponsored by the Deputy Under Secretary of Defense for Science and Technology and the Office of Naval Research; and by a NASA Graduate Student Researchers Program (GSRP) Fellowship by the National Aeronautics and Space Administration through the Jet Propulsion Laboratory. I am indebted to these programs for their support and generosity.

Finally, I would like to express sincere gratitude to my friends and family who have supported me throughout this work. Somehow Jen Marson found me charming enough during these stressful years to marry me and I love her all the more for that. I am constantly amazed at the unending support and patience that my family has shown to me.

To each of the above, I extend my deepest appreciation.

## Contents

### Chapter

<b>1</b>	<b>Introduction</b>	<b>1</b>
1.1	Ballistic Lunar Transfers (BLTs) . . . . .	3
1.2	BLT Maps . . . . .	6
1.3	Dissertation Organization . . . . .	8
1.4	History / Literature Review . . . . .	9
1.4.1	Classical Work in the Three-Body Problem . . . . .	10
1.4.2	Modern Work in Dynamical Systems . . . . .	11
1.4.3	Astronomical Observations of Three-Body Dynamics . . . . .	12
1.4.4	A Brief History of Periodic Orbits . . . . .	13
1.4.5	A Brief History of Orbital Transfers . . . . .	14
1.4.6	A Brief History of Orbital Captures . . . . .	15
1.4.7	A Brief History of Lunar Transfers . . . . .	16
1.4.8	A Brief History of Control, Station-Keeping, and Rendezvous in Three-Body Orbits . . . . .	18
1.4.9	A Brief History of Theoretical Mission Designs . . . . .	19
1.4.10	A Brief History of Real Mission Designs . . . . .	20
1.5	Contributions of this Dissertation . . . . .	24
<b>2</b>	<b>Models</b>	<b>25</b>
2.1	Introduction . . . . .	25

2.2	The Two-Body Problem . . . . .	26
2.3	The Three-Body Problem (TBP) . . . . .	28
2.3.1	Circular Restricted Three-Body Problem (CRTBP) . . . . .	32
2.4	The Four-Body Problem . . . . .	41
2.4.1	Bicircular Model . . . . .	43
2.4.2	Patched Three-Body Model . . . . .	45
2.5	The Full Solar System . . . . .	49
2.5.1	JPL Ephemeris Model . . . . .	49
2.6	Discussion . . . . .	51
<b>3</b>	<b>Methodology</b> . . . . .	<b>53</b>
3.1	Introduction . . . . .	53
3.2	Dynamical Systems Theory . . . . .	54
3.3	Solutions to the CRTBP . . . . .	55
3.3.1	Fixed-Point Solutions: Five Lagrange Points . . . . .	55
3.3.2	Sample Periodic and Quasiperiodic Orbit Solutions . . . . .	56
3.3.3	Orbit Parameters . . . . .	61
3.4	The State Transition and Monodromy Matrices . . . . .	61
3.5	Differential Correction . . . . .	63
3.5.1	Single-Shooting Differential Correction . . . . .	64
3.5.2	Multiple-Shooting Differential Correction . . . . .	65
3.6	Constructing Periodic Orbits . . . . .	71
3.6.1	Periodic Orbits in the CRTBP . . . . .	72
3.6.2	Single-Shooting Method for Constructing Simple Periodic Symmetric Orbits in the CRTBP . . . . .	73
3.6.3	Differentially-Correcting Orbits into the JPL Ephemeris Model . .	76
3.7	The Continuation Method . . . . .	80

3.8	Stability . . . . .	81
3.8.1	Eigenvalues of an Orbit's Monodromy Matrix . . . . .	82
3.8.2	The Stability Index . . . . .	85
3.8.3	The Perturbation Doubling Time . . . . .	86
3.9	Invariant Manifolds . . . . .	88
3.9.1	Invariant Manifolds of the Unstable Lagrange Points . . . . .	89
3.9.2	Invariant Manifolds of Unstable Periodic Orbits . . . . .	94
3.9.3	Invariant Manifolds of Unstable Quasiperiodic Orbits . . . . .	98
3.10	Orbit Transfers . . . . .	99
3.10.1	Surface to Orbit Transfers . . . . .	99
3.10.2	Orbit Transfers and Chains . . . . .	106
3.11	Becoming Captured or Temporarily Captured . . . . .	112
3.12	Discussion . . . . .	118
<b>4</b>	<b>Direct Ballistic Lunar Transfers</b>	<b>119</b>
4.1	Introduction . . . . .	119
4.2	Direct Transfers to Low Lunar Orbits . . . . .	121
4.3	Direct Transfers to Lunar Halo Orbits . . . . .	127
4.3.1	Constructing Direct Lunar Halo Transfers . . . . .	127
4.3.2	Surveying Direct Lunar Halo Orbit Transfers . . . . .	136
4.3.3	Discussion of Results . . . . .	153
4.4	Conclusions . . . . .	157
<b>5</b>	<b>Low-Energy Ballistic Lunar Transfers</b>	<b>161</b>
5.1	Introduction . . . . .	161
5.2	Background . . . . .	163
5.3	The Mission Segments of a BLT . . . . .	167
5.3.1	The LEO Parking Orbit . . . . .	167

5.3.2	The Outbound Trajectory . . . . .	168
5.3.3	Lunar Encounter . . . . .	169
5.3.4	Available Options from the Lunar Three-Body Orbit . . . . .	170
5.3.5	Example Transfer from the Lunar Three-Body Orbit . . . . .	171
5.4	Modeling and Analyzing a Ballistic Lunar Transfer . . . . .	173
5.4.1	Earth Staging Orbits . . . . .	175
5.4.2	Lunar Staging Orbits . . . . .	178
5.4.3	An Example Modeled BLT . . . . .	180
5.4.4	Discussion . . . . .	182
5.5	Energy Analysis of a BLT . . . . .	183
5.6	Constructing a BLT in the Patched Three-Body Model . . . . .	189
5.6.1	Parameters . . . . .	190
5.6.2	Producing the BLT . . . . .	194
5.7	Constructing a BLT in the JPL Ephemeris Model . . . . .	197
5.7.1	Building a BLT in the JPL Ephemeris Model . . . . .	197
5.7.2	Converting a BLT from the Patched Three-Body Model Directly into the JPL Ephemeris Model . . . . .	200
5.7.3	Discussion . . . . .	206
5.8	Comparison Between Different Models . . . . .	207
5.8.1	Comparing the Patched Three-Body BLT with the Nominal JPL Ephemeris BLT . . . . .	207
5.8.2	Comparing the Patched Three-Body BLT with Several JPL Ephemeris BLTs . . . . .	215
5.8.3	Summary of Comparison . . . . .	218
5.9	Comparison with Conventional Transfers . . . . .	218
5.10	Conclusions . . . . .	219

<b>6 Families of Ballistic Lunar Transfers</b>	222
6.1 Introduction . . . . .	222
6.2 BLT State Space Maps . . . . .	223
6.2.1 Parameterization . . . . .	224
6.2.2 Slight Perturbations . . . . .	225
6.2.3 Example Full BLT Maps . . . . .	228
6.2.4 Extracting Families . . . . .	237
6.3 A Survey of Families of BLTs . . . . .	242
6.3.1 Families of Exterior BLTs . . . . .	242
6.3.2 Comparing Symmetric Families on Either Side of the BLT Map .	251
6.3.3 Families of Interior BLTs . . . . .	254
6.3.4 Fractal Patterns Observed in the Interior BLT Map . . . . .	259
6.3.5 Discussion . . . . .	260
6.4 Evolving BLT Maps . . . . .	261
6.4.1 Varying the Transfer Duration . . . . .	262
6.4.2 Varying the Lunar L <sub>2</sub> Orbit's Jacobi Constant . . . . .	264
6.5 BLT Maps for Different Lunar Orbit Families . . . . .	267
6.5.1 Low-Energy Transfers to a Lunar L <sub>1</sub> Halo Orbit . . . . .	267
6.5.2 Low-Energy Transfers to a Distant Prograde Orbit . . . . .	273
6.5.3 Discussion . . . . .	276
6.6 Validating BLT Maps in the JPL Ephemeris Model . . . . .	278
6.7 Summary and Conclusions . . . . .	285
<b>7 Applications to Practical Mission Design</b>	288
7.1 Spacecraft Systems Considerations . . . . .	289
7.1.1 Increased Payload Mass . . . . .	291
7.1.2 Navigation Considerations . . . . .	301

7.1.3	Station-Keeping Costs . . . . .	306
7.1.4	Communication System . . . . .	308
7.1.5	Power System . . . . .	310
7.1.6	Thermal System . . . . .	311
7.1.7	Attitude Determination and Control System . . . . .	311
7.1.8	Mission Operations . . . . .	312
7.2	Applying BLT Maps to Practical Mission Design . . . . .	314
7.2.1	Departure Opportunities . . . . .	314
7.2.2	Departure Opportunities from a Particular Inclination . . . . .	320
7.2.3	Identifying Rendezvous Trajectories . . . . .	323
7.2.4	Identifying Desirable BLTs . . . . .	325
7.3	Applications to Mission Designs . . . . .	330
7.4	Discussion . . . . .	333
<b>8</b>	<b>Summary and Conclusions</b>	<b>335</b>
8.1	Contributions to the Field . . . . .	335
8.2	A Summary of Dynamical Systems Techniques Applied to the Construction of Orbit Transfers . . . . .	336
8.2.1	Parameterization . . . . .	336
8.2.2	Direct Lunar Halo Orbit Transfers . . . . .	337
8.2.3	Low-Energy Ballistic Lunar Transfers . . . . .	338
8.2.4	BLT Maps . . . . .	339
8.2.5	Applications of BLT Maps to Practical Lunar Missions . . . . .	339
8.3	Conclusions . . . . .	340
8.4	Future Work . . . . .	340

<b>Bibliography</b>	343
---------------------	-----

## Appendix

<b>A Planar Simple Periodic Symmetric Orbits</b>	358
A.1 Class 1: Orbits Centered about $L_3$ . . . . .	365
A.2 Class 2: Orbits Centered about $M_1$ . . . . .	368
A.2.1 Prograde Orbits about $M_1$ . . . . .	368
A.2.2 Retrograde Orbits about $M_1$ . . . . .	369
A.3 Class 3: Orbits Centered about $M_1+M_2$ . . . . .	370
A.3.1 Prograde Orbits about $M_1+M_2$ . . . . .	370
A.3.2 Retrograde Orbits about $M_1+M_2$ . . . . .	373
A.4 Class 4: Orbits Centered about $L_1$ . . . . .	376
A.5 Class 5: Orbits Centered about $M_2$ . . . . .	377
A.5.1 Prograde Orbits about $M_2$ . . . . .	377
A.5.2 Retrograde Orbits about $M_2$ . . . . .	379
A.6 Class 6: Orbits Centered about $L_2$ . . . . .	380
A.7 Discussion . . . . .	381
<b>B Three-Dimensional Simple Periodic Symmetric Orbits</b>	382
B.1 Class 1: Orbits Centered about $L_3$ . . . . .	388
B.2 Class 2: Orbits Centered about $M_1$ . . . . .	391
B.2.1 Prograde Orbits about $M_1$ . . . . .	391
B.2.2 Retrograde Orbits about $M_1$ . . . . .	391
B.3 Class 3: Orbits Centered about $M_1+M_2$ . . . . .	395
B.3.1 Prograde Orbits about $M_1+M_2$ . . . . .	395
B.3.2 Retrograde Orbits about $M_1+M_2$ . . . . .	395
B.4 Class 4: Orbits Centered about $L_1$ . . . . .	397

B.5	Class 5: Orbits Centered about $M_2$	401
B.5.1	Prograde Orbits about $M_2$	401
B.5.2	Retrograde Orbits about $M_2$	401
B.6	Class 6: Orbits Centered about $L_2$	404
B.7	Class M1: Miscellaneous Orbits Centered about $M_1$	404
B.7.1	Prograde Class M1 Orbits	406
B.7.2	Retrograde Class M1 Orbits	409
B.8	Class M2: Miscellaneous Orbits Centered about $M_2$	410
B.9	Discussion	411
C	Analytical Expressions for the Lagrange Points	412
C.1	Introduction	412
C.2	Setting Up the System	412
C.3	Triangular Points	415
C.4	Collinear Points	415
C.4.1	Case 132: Identifying the $L_1$ point	416
C.4.2	Case 123: Identifying the $L_2$ point	417
C.4.3	Case 312: Identifying the $L_3$ point	418
C.5	Algorithms	419
C.5.1	Numerical Determination of $L_1$	420
C.5.2	Numerical Determination of $L_2$	420
C.5.3	Numerical Determination of $L_3$	421
D	Conversions Between Reference Frames	422
D.1	Introduction	422
D.2	Standard Synodic to Inertial	423
D.3	Inertial to Standard Synodic	424
D.4	Earth-Moon to Sun-Earth	425

D.5 Sun-Earth to Earth-Moon . . . . .	426
D.6 Standard Synodic to JPL Ephemeris . . . . .	427
D.7 JPL Ephemeris to Standard Synodic . . . . .	430
<b>E Computational Considerations</b>	<b>433</b>
E.1 Introduction . . . . .	433
E.2 Development . . . . .	433
E.3 Numerical Integration . . . . .	434
E.4 Producing BLTs in the Patched Three-Body Model . . . . .	438
E.5 Producing BLTs in the JPL Ephemeris Model . . . . .	439
E.6 Producing BLT Maps . . . . .	439

## Tables

### **Table**

2.1 A summary of the degrees of freedom and integrals of motion in two-body and three-body systems. . . . .	32
2.2 The parameters of the Earth-Moon and Sun-Earth/Moon three-body systems (Vallado, 1997). . . . .	34
3.1 The locations of the five Lagrange points in the Sun-Earth and Earth-Moon circular three-body systems. . . . .	56
3.2 A summary of the resulting motion of a particle in a periodic orbit, whose state is perturbed along the eigenvector corresponding to a given eigenvalue. . . . .	83
3.3 A summary of several categories of orbit transfers in the CRTBP. . . . .	107
4.1 A summary of the costs associated with departing the 185-km circular LEO parking orbit at various values of $\theta$ , transferring directly to a 100-km circular lunar orbit. . . . .	124
4.2 The transfer durations of many historical missions that have implemented direct lunar transfers. . . . .	126
5.1 A summary of the six parameters used to produce BLTs in the Patched Three-Body model. . . . .	194

5.2 A comparison of certain parameters of the LEO parking orbit and departure conditions for the BLTs produced in the Patched Three-Body and JPL Ephemeris models. . . . .	210
5.3 The injection $\Delta V$ magnitudes of the JPL Ephemeris BLTs converted from the nominal Patched Three-Body BLT for the optimal reference Julian Date in several consecutive months. . . . .	217
6.1 The parameters used to produce the results shown in Figures 6.1 and 6.2. . . . .	226
6.2 The parameters used to produce the results shown in Section 6.2.3. . . . .	229
6.3 The parameters used to produce the BLT Maps presented in this chapter. . . . .	261
6.4 The parameters used to produce the exterior JPL Ephemeris BLT Map shown in Figure 6.45. . . . .	280
6.5 The parameters used to produce the three extended exterior JPL Ephemeris BLT Maps shown in Figures 6.47 – 6.49. . . . .	282
7.1 A summary of ballistic transfer options for a transfer between a circular 185-km LEO parking orbit and a lunar $L_2$ Halo orbit with Jacobi constant of 3.05. . . . .	290
7.2 A summary of trajectory segments that may be used to transfer a spacecraft from a circular 185-km LEO parking orbit to a 100-km circular lunar orbit (LLO) or to the $100 \times 8000$ km frozen orbit, in addition to those segments presented in Table 7.1. . . . .	291
7.3 The maximum mass that several launch vehicles can place into a LEO parking orbit. . . . .	292
7.4 A summary of the two stages of a fictitious spacecraft propulsion system that will be used to transfer the spacecraft from the Earth to the Moon. . . . .	293

7.5 A summary of the final payload mass for a two-stage spacecraft system using various ballistic transfer options for a transfer between a circular 185-km LEO parking orbit and a lunar L <sub>2</sub> Halo orbit with Jacobi constant of 3.05. . . . .	296
7.6 A summary of a similar scenario as in Table 7.5, but in this case the Trans-Lunar Injection ΔV is performed by the launch vehicle and thus not considered in the spacecraft system trade study. . . . .	297
7.7 A summary of the mission itineraries for Scenarios B and C. . . . .	298
7.8 A summary of the final payload mass for a two-stage spacecraft system using various ballistic transfer options for a transfer between a circular 185-km LEO parking orbit and a circular 100-km lunar orbit. . . . .	298
7.9 A summary of the final payload mass for a two-stage spacecraft system using various ballistic transfer options for a transfer between a circular 185-km LEO parking orbit and a 100 × 8000 km frozen lunar orbit. . . . .	298
7.10 A summary of the simplified Scenario B, where the launch vehicle performs the Trans-Lunar Injection maneuver and the spacecraft's only trade is its orbit-insertion maneuver. . . . .	299
7.11 A summary of the simplified Scenario C, where the launch vehicle performs the Trans-Lunar Injection maneuver and the spacecraft's only trade is its orbit-insertion maneuver. . . . .	299
7.12 Statistics for the maximum apogee distance of the BLTs that have been identified in this dissertation between a 185-km LEO parking orbit and the lunar L <sub>2</sub> Halo orbit with a Jacobi constant of 3.05. . . . .	309
7.13 A summary of the relative free space loss penalty of several types of lunar transfers compared with a direct transfer between the Earth and a low lunar orbit about the Moon. . . . .	310

A.1	Classification of symmetric periodic orbits in the PCRTBP based on their orthogonal $x$ -axis crossings. . . . .	360
A.2	A summary of the families of simple periodic symmetric orbits presented in this study. . . . .	360
B.1	A summary of the families of simple periodic symmetric three-dimensional orbits presented in this study. . . . .	384
E.1	The overhead computational costs for each of the four propagation methods tested. . . . .	436
E.2	The average computation time required by each of the four propagation methods for each of the six sample trajectories shown in Figure E.1. . . .	438
E.3	The parameters used to produce the BLT Maps shown in Section 6.2.3 and in Figure E.2. . . . .	441

## Figures

### Figure

1.1 An example ballistic lunar transfer, viewed in the Sun-Earth rotating frame. . . . .	4
1.2 The same BLT shown in Figure 1.1 now viewed in the Earth-centered inertial frame. . . . .	4
1.3 The same BLT shown in Figures 1.1 and 1.2 now viewed in the Earth-Moon rotating frame. . . . .	5
<b>1.4 A BLT Map.</b> . . . . .	7
1.5 The trajectory of ISEE-3 / ICE (GSFC, 2007a). . . . .	21
1.6 The transfer trajectory of SOHO (NASA, 2007a). . . . .	22
1.7 The transfer trajectory of WMAP (GSFC, 2007b). . . . .	22
1.8 The trajectory that the Genesis spacecraft followed (JPL, 2007). . . . .	23
2.1 A trajectory about the Earth that is perturbed by the Moon. . . . .	30
2.2 A dramatic example of third-body interactions. . . . .	30
2.3 The zero-velocity curves for the circular restricted three-body system with Earth-Moon masses. . . . .	37
2.4 A three-dimensional view of the zero-velocity surface, reversed about the z-axis to mimic the potential of the CRTBP system. . . . .	37
2.5 Example trajectories of particles with Jacobi constants equal to approximately 3.12 and 3.19 in the Earth-Moon system. . . . .	39

2.6	The forbidden region in the Earth-Moon system for five values of the Jacobi constant. . . . .	39
2.7	The Earth, Moon, and five Lagrange points in the rotating coordinate system of the CRTBP. . . . .	41
2.8	The locations of the collinear Lagrange points as functions of the mass parameter $\mu$ . . . . .	42
2.9	The locations of the collinear Lagrange points in the Jovian and Saturnian three-body systems. . . . .	42
2.10	A plot depicting the relative proximity of the five Earth-Moon Lagrange points and the two nearby Sun-Earth Lagrange points. . . . .	43
3.1	The locations of the five Lagrange points in the Earth-Moon CRTBP. . . .	56
3.2	A portion of the family of Halo orbits about $L_2$ in the Earth-Moon system. . . . .	59
3.3	A sample of Lissajous curves representing Lissajous orbits in the Earth-Moon system. . . . .	60
3.4	A portion of the family of Lyapunov orbits about $L_2$ in the Earth-Moon system. . . . .	60
3.5	The two orbits shown demonstrate how the parameter $\tau$ moves from 0 to 1 about an orbit. . . . .	62
3.6	The single-shooting differential-correction routine. . . . .	65
3.7	An exaggerated demonstration of the implementation of the multiple-shooting differential corrector used to convert a Halo orbit from the CRTBP into the JPL Ephemeris. . . . .	70
3.8	A comparison between a Halo orbit produced in the CRTBP and a quasi-Halo orbit produced in the JPL Ephemeris model of the real solar system. . . . .	77
3.9	A single $L_2$ Halo orbit in the Earth-Moon CRTBP is differentially-corrected into the JPL Ephemeris model. . . . .	78

3.10 An example of the process of differentially-correcting and pruning a Halo orbit from the Earth-Moon CRTBP into the JPL Ephemeris model . . . . .	79
3.11 A plot of the initial conditions of the family of Lyapunov orbits about the Earth-Moon L <sub>2</sub> point (LL <sub>2</sub> ). . . . .	81
3.12 Plots of the orbits in the family of LL <sub>2</sub> Lyapunov orbits corresponding to those initial conditions shown in Figure 3.11. . . . .	81
3.13 A dynamical saddle point, such as that of the unstable Lagrange points in the CRTBP. . . . .	91
3.14 The stable and unstable invariant manifolds of the first Lagrange point of the Earth-Moon three-body system. . . . .	92
3.15 The stable and unstable invariant manifolds of the second Lagrange point of the Earth-Moon three-body system. . . . .	93
3.16 The stable and unstable invariant manifolds of the third Lagrange point of the Earth-Moon three-body system. . . . .	93
3.17 The stable and unstable manifolds of a Lyapunov orbit about the Earth-Moon L <sub>2</sub> point. . . . .	97
3.18 The stable manifold of a resonant lunar flyby orbit. . . . .	97
3.19 Example Halo orbits in the family of Northern Halo orbits about the Sun-Earth L <sub>2</sub> point. . . . .	100
3.20 An example unstable Halo orbit about the Sun-Earth L <sub>2</sub> point and its stable invariant manifold. . . . .	101
3.21 The perigee altitude and ecliptic inclination of the trajectories in the stable manifold shown in Figure 3.20 as functions of $\tau$ . . . . .	102
3.22 The stable manifold of a Sun-Earth L <sub>2</sub> Halo orbit propagated for successively longer amounts of time. . . . .	104
3.23 The altitude of closest approach of each trajectory in the stable manifolds shown in Figure 3.22 with respect to the Earth. . . . .	105

3.24 A plot of several families of three-body orbits in the Earth-Moon CRTBP, where the orbits' Jacobi constant values are plotted as a function of their initial $x$ -values. . . . .	108
3.25 The intersection of the unstable manifold of a Lyapunov orbit about the Earth-Moon $L_1$ point and the stable manifold of a Lyapunov orbit about the Earth-Moon $L_2$ point. . . . .	109
3.26 Two example free transfers between the orbits shown in Figure 3.25. . .	109
3.27 Free transfers between a Lyapunov orbit about $LL_1$ , a Distant Prograde Orbit about the Moon, and a Lyapunov orbit about $LL_2$ , where each orbit and every trajectory shown have the same Jacobi constant, $C = 3.13443929.110$	110
3.28 A complex periodic orbit that consists of two revolutions about the $L_1$ Lyapunov orbit, followed by one revolution about the Distant Prograde Orbit, before it repeats itself. . . . .	111
3.29 Several example complex periodic orbits that exist in the same family as the orbit shown in Figure 3.28. . . . .	112
3.30 A survey of six example three-body orbits near the Moon. . . . .	116
3.31 An example of a trajectory that a spacecraft may follow to transfer from an unstable orbit that is not always classified as a temporarily captured orbit to a trajectory that is generally accepted to be temporarily captured.	117
4.1 The definition of the angle $\theta$ when describing direct lunar transfers. . . .	122
4.2 A summary of four different lunar transfers that each depart from the same LEO orbit at an angle, $\theta$ , of $125^\circ$ . . . . .	123
4.3 Five example direct transfers to 100-km prograde lunar orbits, shown in the rotating frame and inertial frame. . . . .	125
4.4 Two perspectives of an example scenario that may be used to transfer a spacecraft from a 185-km LEO parking orbit to a lunar $L_1$ Halo orbit. . .	128

4.5 Example trajectories that implement the <b>perigee-point</b> scheme to directly transfer from LEO to a lunar L <sub>1</sub> Halo orbit. . . . .	130
4.6 Plots of the maneuver requirements to transfer onto a lunar L <sub>1</sub> Halo orbit using the perigee-point scheme. . . . .	131
4.7 Example trajectories that implement the <b>open-point</b> scheme to directly transfer from LEO to a specific manifold of a specific lunar L <sub>1</sub> Halo orbit. . . . .	133
4.8 Plots of the maneuver requirements to transfer onto a specific manifold of a specific lunar L <sub>1</sub> Halo orbit using the open-point scheme. . . . .	133
4.9 Plots of the distance between the spacecraft and the two massive bodies for each $\Delta t_m$ -point along the Manifold segment. . . . .	134
4.10 Plots summarizing the required maneuvers and the total maneuver cost associated with the least expensive open-point lunar transfer for each trajectory on the stable manifold of a single lunar L <sub>1</sub> Halo orbit. . . . .	135
4.11 The total $\Delta V$ cost of many transfers to the exterior stable manifold of each orbit in the family of lunar L <sub>1</sub> Halo orbits, including a Pareto front of optimal solutions. . . . .	138
4.12 Several example transfers between 185-km LEO parking orbits and the exterior stable manifold of lunar L <sub>1</sub> Halo orbits. . . . .	139
4.13 The two transfer maneuver magnitudes that combine to produce the total $\Delta V$ cost of the transfers shown in Figures 4.11 and 4.12. . . . .	141
4.14 The total $\Delta V$ cost of many transfers to the interior stable manifold of each orbit in the family of lunar L <sub>1</sub> Halo orbits. . . . .	142
4.15 Several example transfers between 185-km LEO parking orbits and the interior stable manifold of lunar L <sub>1</sub> Halo orbits. . . . .	143
4.16 The two transfer maneuver magnitudes that combine to produce the total $\Delta V$ cost of the transfers shown in Figures 4.14 and 4.15. . . . .	145

4.17 The total $\Delta V$ cost of many transfers to the exterior stable manifold of each orbit in the family of lunar L <sub>2</sub> Halo orbits, including a Pareto front of optimal solutions. . . . .	146
4.18 Several example transfers between 185-km LEO parking orbits and the exterior stable manifold of lunar L <sub>2</sub> Halo orbits. . . . .	147
4.19 The two transfer maneuver magnitudes that combine to produce the total $\Delta V$ cost of the transfers shown in Figures 4.17 and 4.18. . . . .	148
4.20 The total $\Delta V$ cost of many transfers to the interior stable manifold of each orbit in the family of lunar L <sub>2</sub> Halo orbits. . . . .	150
4.21 Several example transfers between 185-km LEO parking orbits and the interior stable manifold of lunar L <sub>2</sub> Halo orbits. . . . .	151
4.22 The two transfer maneuver magnitudes that combine to produce the total $\Delta V$ cost of the transfers shown in Figures 4.20 and 4.21. . . . .	153
4.23 The total $\Delta V$ cost of many transfers to lunar L <sub>1</sub> Halo orbits using either interior or exterior transfers. . . . .	154
4.24 The total $\Delta V$ cost of many transfers to lunar L <sub>2</sub> Halo orbits using either interior or exterior transfers. . . . .	154
4.25 The Jacobi constant of each lunar Halo orbit as a function of the Halo orbits' $x_0$ -values. . . . .	155
4.26 The total $\Delta V$ cost of direct lunar Halo orbit transfers as a function of the Halo orbits' Jacobi constant values. . . . .	156
4.27 A summary of the minimum amount of total $\Delta V$ required to reach any Halo orbit using the fastest optimized transfers (approximately 5 days) as well as an envelope of longer low- $\Delta V$ transfers (1 – 2 months). . . . .	159
4.28 A summary of the minimum amount of total $\Delta V$ required to reach Halo orbits with a given Jacobi constant. . . . .	159

5.1	Two example low-energy ballistic lunar transfers. . . . .	167
5.2	An example lunar Halo staging orbit and its unstable manifold. . . . .	172
5.3	One particular trajectory that a spacecraft may take to depart the lunar Halo staging orbit. . . . .	172
5.4	The radii and inclination combinations that may be obtained at per- ilune of the unstable manifolds of several Northern Halo orbits about the Earth-Moon L <sub>2</sub> point. . . . .	173
5.5	Four perspectives of the family of Northern Halo orbits about the Sun- Earth L <sub>2</sub> point. . . . .	176
5.6	Two perspectives of an example Northern Halo orbit about the Sun- Earth L <sub>2</sub> point, shown with the interior half of its stable manifold. . . . .	177
5.7	Two perspectives of the same Northern EL <sub>2</sub> Halo orbit shown in Fig- ure 5.6, this time shown with the interior half of its unstable manifold. One can see that the unstable manifold intersects the Moon's orbit. . . .	177
5.8	Two perspectives of an example Northern Halo orbit about the Earth- Moon L <sub>2</sub> point, shown with the exterior half of its stable manifold. . . .	179
5.9	Two perspectives of the first portion of the example BLT, modeled using the stable manifold of a Halo orbit about the Sun-Earth L <sub>2</sub> point. The spacecraft's outbound motion shadows the Halo orbit's stable manifold.	180
5.10	Two perspectives of the second portion of the example BLT, modeled using the unstable manifold of a Halo orbit about the Sun-Earth L <sub>2</sub> point.	181
5.11	Two perspectives of the third portion of the example BLT, modeled using the stable manifold of a Halo orbit about the Earth-Moon L <sub>2</sub> point. . . .	182
5.12	A top-down perspective of the example BLT, shown with all three man- ifolds that are used to model it. . . . .	183
5.13	The magnitude of the radius vector of the spacecraft with respect to both the Earth and the Moon as the spacecraft traverses the example BLT. . .	184

5.14 The two-body specific energy of a spacecraft with respect to the Earth over time as it traverses an example BLT. . . . .	185
5.15 Four two-body orbital elements of the spacecraft with respect to the Earth as the spacecraft traverses the example BLT. . . . .	186
5.16 The two-body specific energy of a spacecraft with respect to the Moon over time as it traverses an example BLT. . . . .	187
5.17 The evolution of the spacecraft's Jacobi constant with respect to the Sun-Earth three-body system as the spacecraft traverses the example BLT. . .	188
5.18 The evolution of the spacecraft's Jacobi constant with respect to the Earth-Moon three-body system as the spacecraft traverses the example BLT. .	188
5.19 The definition of $\theta$ , the Sun-Earth-Moon angle. . . . .	191
5.20 The two orbits shown demonstrate how the parameter $\tau$ moves from 0 to 1 about an orbit. . . . .	192
5.21 An example stable invariant manifold with the Interior and Exterior halves identified. . . . .	193
5.22 The Patched Three-Body BLT converted into the JPL reference frame using four different reference Julian Dates. . . . .	201
5.23 The minimum gap distance that exists in each month for 86 consecutive months when patching the Earth-Moon BLT segments with the Sun-Earth BLT segments. . . . .	202
5.24 Several iterations in the process of differentially correcting the Patched Three-Body BLT into the JPL Ephemeris model, shown in the Sun-Earth synodic reference frame. . . . .	204
5.25 Several iterations in the process of differentially correcting the Patched Three-Body BLT into the JPL Ephemeris model, shown in the Earth-Moon synodic reference frame. . . . .	204

5.26 A plot comparing the general characteristics of the Patched Three-Body BLT and the JPL Ephemeris BLT. . . . .	208
5.27 A comparison of the departure trajectories of the Patched Three-Body BLT and JPL Ephemeris BLT. . . . .	209
5.28 A comparison of the distances between the spacecraft and the Earth and Moon during each of the two compared trajectories. . . . .	211
5.29 A comparison of the two-body specific energy of a spacecraft with respect to the Earth as a spacecraft traverses both the Patched Three-Body BLT and the JPL Ephemeris BLT. . . . .	212
5.30 A comparison of the two-body specific energy of a spacecraft with respect to the Moon as a spacecraft traverses both the Patched Three-Body BLT and the JPL Ephemeris BLT. . . . .	212
5.31 A comparison of a spacecraft's Jacobi constant with respect to the Sun-Earth three-body system as a spacecraft traverses both the Patched Three-Body BLT and the JPL Ephemeris BLT. . . . .	214
5.32 A comparison of a spacecraft's Jacobi constant with respect to the Earth-Moon three-body system as a spacecraft traverses both the Patched Three-Body BLT and the JPL Ephemeris BLT. . . . .	214
5.33 The trajectories of several BLTs produced in the JPL Ephemeris model using the Conversion method for several different reference Julian Dates.	216
5.34 The LEO departure segments of the BLTs shown in Figure 5.33. . . . .	216
6.1 Two plots showing the BLT state space near the nominal BLT. . . . .	226
6.2 Four plots displaying the performance parameters of families that may be extracted from the plots shown in Figure 6.1 . . . . .	228
6.3 An example exterior BLT Map. . . . .	230

6.4	The same plot shown in Figure 6.3 with example trajectories shown, indicating the variety of BLT families that exist. . . . .	231
6.5	An example interior BLT Map. . . . .	233
6.6	The same plot shown in Figure 6.5 with example trajectories shown, indicating the variety of BLT families that exist. . . . .	234
6.7	An example interior ballistic lunar transfer that is particularly complicated, demonstrating the sensitivity of such BLTs to their initial conditions. . . . .	236
6.8	The same interior BLT shown in Figure 6.7 plotted in the Earth-Moon synodic reference frame at three different scales. . . . .	237
6.9	The same interior BLT shown in Figures 6.7 and 6.8 plotted in three dimensions in the Earth-Moon synodic reference frame. . . . .	237
6.10	The BLT Map shown in Figure 6.3 with a contour superimposed, indicating all available ballistic lunar transfers that depart the Earth from 185-km LEO parking orbits. . . . .	238
6.11	The families of BLTs that depart the Earth from 185-km LEO parking orbits, encountering the lunar Halo orbit from the exterior (left) and interior (right). . . . .	242
6.12	The numerically-converged $(\theta, \tau)$ -combinations, which yield BLTs that depart from LEO altitudes within 0.1 meters of the desired 185 kilometers. . . . .	243
6.13	Several example trajectories in Family A of exterior BLTs. Also shown are four plots that indicate how four parameters vary as functions of $\theta$ for this family. . . . .	245
6.14	Several example trajectories in Family B of exterior BLTs, with the same four parametric plots presented for this family as shown in Figure 6.13. . .	245
6.15	Several example trajectories in Family C of exterior BLTs, with the same four parametric plots presented for this family as shown in Figure 6.13. . .	246

6.16 Several example trajectories in Family D of exterior BLTs, with the same four parametric plots presented for this family as shown in Figure 6.13. . .	247
6.17 Several example trajectories in Family E of exterior BLTs, with the same four parametric plots presented for this family as shown in Figure 6.13. . .	247
6.18 Six plots comparing approximately 50 families of exterior BLTs. . . . .	249
6.19 The same six plots presented in Figure 6.18 but for approximately 50 new families. . . . .	250
6.20 A plot of two BLTs that are nearly symmetric, where the two BLTs are labeled according to which half of the exterior BLT Map they exist in. . .	252
6.21 Four parametric plots comparing parameters of the families of the two BLTs shown in Figure 6.20. . . . .	253
6.22 A parametric plot comparing the transfer duration with the $\Delta V$ cost of the families of the two BLTs shown in Figure 6.20. . . . .	254
6.23 The numerically-converged $(\theta, \tau)$ -combinations, which yield interior BLTs that depart from LEO altitudes within 0.1 meters of the desired 185 kilometers. A huge number of families of interior BLTs appear to exist. . . .	255
6.24 A survey of the $\Delta V$ cost as a function of $\theta$ for the interior BLTs displayed in Figure 6.23. . . . .	256
6.25 A survey of the transfer duration as a function of $\theta$ for the interior BLTs displayed in Figure 6.23. . . . .	256
6.26 A parametric plot comparing the transfer duration with the $\Delta V$ cost of all of the interior BLTs surveyed in Figures 6.23 – 6.25. . . . .	256
6.27 The locations of the two example families of BLTs in their respective BLT Maps. . . . .	257
6.28 The example “Family A” of exterior BLTs along with four parametric plots showing the family’s performance parameters. . . . .	258

6.29 An example family of interior BLTs whose transfer characteristics compare very closely with the family of exterior BLTs shown in Figure 6.28. . .	258
6.30 An example chaotic region within the interior BLT Map explored to very fine detail. . . . .	259
6.31 A succession of exterior BLT Maps with propagation times between 93.6 days and 759.9 days. . . . .	263
6.32 A succession of interior BLT Maps with propagation times between 93.6 days and 759.9 days. . . . .	263
6.33 A succession of exterior BLT maps, produced by varying the Jacobi constant of the target L <sub>2</sub> Halo orbit. . . . .	265
6.34 A succession of interior BLT Maps using the same parameters as Figure 6.33, but for interior BLTs. . . . .	266
6.35 An example interior BLT to a lunar L <sub>1</sub> Halo orbit, shown in the Sun-Earth synodic reference frame. . . . .	268
6.36 The same BLT presented in Figure 6.35, but now shown in the Earth-Moon synodic reference frame. . . . .	268
6.37 An example exterior BLT to a lunar L <sub>1</sub> Halo orbit, shown in the Sun-Earth synodic reference frame. . . . .	270
6.38 The same BLT presented in Figure 6.37, but now shown in the Earth-Moon synodic reference frame. . . . .	270
6.39 The interior BLT Map for low-energy transfers to the example lunar L <sub>1</sub> Halo orbit. . . . .	271
6.40 The exterior BLT Map for low-energy transfers to the example lunar L <sub>1</sub> Halo orbit. . . . .	272
6.41 An example BLT to a distant prograde orbit, shown in the Sun-Earth synodic reference frame. . . . .	274

6.42 The same BLT presented in Figure 6.41, but now shown in the Earth-Moon synodic reference frame. . . . .	274
6.43 The exterior BLT Map for low-energy transfers to the example distant prograde orbit about the Moon. . . . .	276
6.44 The interior BLT Map for low-energy transfers to the example distant prograde orbit about the Moon. . . . .	277
6.45 The exterior BLT Map produced in the JPL Ephemeris model of the solar system. . . . .	280
6.46 A direct comparison between the Patched Three-Body and JPL Ephemeris exterior BLT Maps targeting the L <sub>2</sub> three-body orbit with a nominal Jacobi constant of 3.05. . . . .	281
6.47 The exterior JPL Ephemeris BLT Map shown in Figure 6.45 continued over three months' worth of JD <sub>0</sub> -values. . . . .	282
6.48 The exterior JPL Ephemeris BLT Map with an initial Jacobi constant of 3.10 continued over three months' worth of JD <sub>0</sub> -values. . . . .	283
6.49 The exterior JPL Ephemeris BLT Map with an initial Jacobi constant of 3.15 continued over three months' worth of JD <sub>0</sub> -values. . . . .	283
6.50 The same exterior JPL Ephemeris BLT Map shown in Figure 6.45, but now with 12 example exterior BLTs around its perimeter. . . . .	285
 7.1 Two views of a lunar L <sub>2</sub> Halo orbit, colored according to the value of $\lambda_{max}$ : the red regions are more unstable than the blue regions, but all regions of the Halo orbit are unstable. . . . .	303
7.2 A comparison of three parameters of the Halo orbit shown in Figure 7.1. . . . .	303
7.3 Two views of an example interior BLT to a lunar L <sub>2</sub> Halo orbit, colored according to the value of $\lambda_{max}$ . . . . .	305
7.4 A comparison of three parameters of the BLT shown in Figure 7.3. . . . .	305

7.5	The example BLT Map used to demonstrate a departure opportunity analysis. . . . .	315
7.6	The Trans-Lunar Injection $\Delta V$ value of each exterior BLT in Figure 7.5 as a function of the BLT's corresponding Trans-Lunar Injection $\theta$ -value, $\theta_{TLI}$ . . . . .	317
7.7	The Trans-Lunar Injection ecliptic inclination value of each exterior BLT in Figure 7.5 as a function of the BLT's corresponding Trans-Lunar Injection $\theta$ -value, $\theta_{TLI}$ . . . . .	317
7.8	The transfer duration of each exterior BLT in Figure 7.5 as a function of the BLT's corresponding Trans-Lunar Injection $\theta$ -value, $\theta_{TLI}$ . . . . .	318
7.9	The Trans-Lunar Injection $\Delta V$ value of each exterior BLT in Figure 7.5 as a function of the BLT's corresponding Trans-Lunar Injection $\theta$ -value, $\theta_{TLI}$ . The value of $\theta_{TLI}$ has been wrapped into the range $[0^\circ, 360^\circ]$ . . . . .	319
7.10	The Trans-Lunar Injection ecliptic inclination value of each exterior BLT in Figure 7.5 as a function of the BLT's corresponding Trans-Lunar Injection $\theta$ -value, $\theta_{TLI}$ . The value of $\theta_{TLI}$ has been wrapped into the range $[0^\circ, 360^\circ]$ . . . . .	319
7.11	The transfer duration of each exterior BLT in Figure 7.5 as a function of the BLT's corresponding Trans-Lunar Injection $\theta$ -value, $\theta_{TLI}$ . The value of $\theta_{TLI}$ has been wrapped into the range $[0^\circ, 360^\circ]$ . . . . .	320
7.12	The transfer duration and Trans-Lunar Injection $\Delta V$ departure options for each BLT that departs from a 185-km LEO parking orbit with an ecliptic inclination of $20^\circ \pm 1^\circ$ . . . . .	321
7.13	The transfer duration and Trans-Lunar Injection $\Delta V$ departure options for each BLT that departs from a 185-km LEO parking orbit with an ecliptic inclination of $25^\circ \pm 1^\circ$ . . . . .	322

7.14 The transfer duration and Trans-Lunar Injection $\Delta V$ departure options for each BLT that departs from a 185-km LEO parking orbit with an ecliptic inclination of $30^\circ \pm 1^\circ$ . . . . .	322
7.15 The exterior BLT Map shown in Figure 7.5 with a rendezvous trajectory superimposed. . . . .	324
7.16 The exterior BLT Map and the superimposed rendezvous trajectory from Figure 7.15 with several example BLTs that a spacecraft may follow to successfully rendezvous with the target object prior to the target epoch. . . . .	325
7.17 Plots of the secular perturbation of the right-ascension of the ascending node, $\dot{\Omega}$ , for orbits that have inclination values between $0^\circ$ and $90^\circ$ and apogee altitudes between 100 km and 8000 km. The perigee altitude of each orbit has been set to 185 km. . . . .	329
7.18 Plots of the secular perturbation of the argument of perigee, $\dot{\omega}$ , for orbits that have inclination values between $0^\circ$ and $90^\circ$ and apogee altitudes between 100 km and 8000 km. The perigee altitude of each orbit has been set to 185 km. . . . .	329
A.1 A portion of the family of Lyapunov orbits about $L_2$ in the Earth-Moon system. . . . .	359
A.2 A plot of $x_0$ vs. $\dot{y}_0$ for the families of periodic orbits presented in this study. . . . .	362
A.3 A plot of $x_0$ vs. $\dot{y}_0$ for the families of periodic orbits on the far side of $L_3$ . . . . .	362
A.4 A plot of $x_0$ vs. $\dot{y}_0$ for the families of periodic orbits between $L_3$ and the Earth. . . . .	363
A.5 A plot of $x_0$ vs. $\dot{y}_0$ for the families of periodic orbits between the Earth and the Moon. . . . .	363
A.6 A plot of $x_0$ vs. $\dot{y}_0$ for the families of periodic orbits between the Moon and $L_2$ . . . . .	364

A.7 A plot of $x_0$ vs. $C$ for the families of periodic orbits presented in this study.	364
A.8 A plot of $x_0$ vs. $P$ , the orbital period, for the families of periodic orbits presented in this study. . . . .	365
A.9 Three plots describing the family of Lyapunov orbits centered about $L_3$ . . . . .	366
A.10 Horseshoe-shaped orbits with varying numbers of upper and lower loops. . . . .	367
A.11 Four plots describing the prograde Class 2 family centered about the Earth. . . . .	368
A.12 Three plots describing the family of retrograde orbits centered about the Earth. . . . .	369
A.13 A few characteristic orbits in the families that make periodic lunar flybys as well as $n$ loops in the vicinity of $L_4$ / $L_5$ . . . . .	370
A.14 Three curves showing how the orbital period depends on the initial condition of the orbit for orbits in three families of prograde Class 3 orbits. These orbits are all unstable and in resonance with the Moon. . . . .	371
A.15 Characteristic plots of four resonant prograde lunar flyby orbits. . . . .	372
A.16 Four plots describing the retrograde Class 3 family centered about the Earth+Moon. . . . .	373
A.17 Four plots describing the second retrograde Class 3 family centered about the Earth+Moon. . . . .	374
A.18 Four plots describing the third retrograde Class 3 family centered about the Earth+Moon. . . . .	375
A.19 Three plots describing the family of Lyapunov orbits centered about $L_1$ . . . . .	376
A.20 Four plots describing the first prograde Class 5 family centered about the Moon. . . . .	377
A.21 Four plots describing the second prograde Class 5 family centered about the Moon. . . . .	378
A.22 Three plots describing the family of retrograde orbits centered about the Moon. . . . .	379

A.23 Three plots describing the family of Lyapunov orbits centered about L <sub>2</sub> .	380
B.1 Plots of $x_0$ vs. $z_0$ and $x_0$ vs. $\dot{y}_0$ for the families of three-dimensional periodic orbits presented in this study.	385
B.2 Plots of $x_0$ vs. $z_0$ and $x_0$ vs. $\dot{y}_0$ for the families of three-dimensional periodic orbits on the far side of L <sub>3</sub> .	385
B.3 Plots of $x_0$ vs. $z_0$ and $x_0$ vs. $\dot{y}_0$ for the families of three-dimensional periodic orbits between L <sub>3</sub> and the Earth.	386
B.4 Plots of $x_0$ vs. $z_0$ and $x_0$ vs. $\dot{y}_0$ for the families of three-dimensional periodic orbits between the Earth and the Moon.	386
B.5 Plots of $x_0$ vs. $z_0$ and $x_0$ vs. $\dot{y}_0$ for the families of three-dimensional periodic orbits between the Moon and L <sub>2</sub> .	387
B.6 Plots of $x_0$ vs. $C$ and $x_0$ vs. $P$ , the orbital period, for the families of three-dimensional periodic orbits presented in this study.	387
B.7 Four perspectives of the family of Halo orbits centered about L <sub>3</sub> .	389
B.8 Two plots showing the initial conditions yielding the family of Halo orbits centered about L <sub>3</sub> .	389
B.9 Horseshoe-shaped orbits with varying numbers of upper and lower loops.	390
B.10 Four perspectives of the family of prograde three-dimensional Class 2 orbits.	392
B.11 Two plots showing the initial conditions yielding the family of prograde three-dimensional Class 2 orbits.	392
B.12 Four perspectives of the family of retrograde three-dimensional Class 2 orbits that contain no L <sub>4</sub> / L <sub>5</sub> loops.	393
B.13 Two plots showing the initial conditions yielding the family of retrograde three-dimensional Class 2 orbits shown in Figure B.12.	393

B.14 A few characteristic orbits in the families that make periodic lunar flybys as well as $n$ loops in the vicinity of $L_4 / L_5$ . . . . .	394
B.15 Four perspectives of the first family of retrograde three-dimensional Class 3 orbits. . . . .	396
B.16 Two plots showing the initial conditions yielding the first family of ret- rograde three-dimensional Class 3 orbits shown in Figure B.15. . . . .	396
B.17 Four perspectives of the second family of retrograde three-dimensional Class 3 orbits. . . . .	398
B.18 Two plots showing the initial conditions yielding the second family of retrograde three-dimensional Class 3 orbits shown in Figure B.17. . . . .	398
B.19 Four perspectives of the third family of retrograde three-dimensional Class 3 orbits. . . . .	399
B.20 Two plots showing the initial conditions yielding the third family of ret- rograde three-dimensional Class 3 orbits shown in Figure B.19. . . . .	399
B.21 Four perspectives of the family of Halo orbits centered about $L_1$ . . . . .	400
B.22 Two plots showing the initial conditions yielding the family of Halo or- bits centered about $L_1$ . . . . .	400
B.23 Four perspectives of the family of prograde three-dimensional Class 5 orbits. . . . .	402
B.24 Two plots showing the initial conditions yielding the family of prograde three-dimensional Class 5 orbits shown in Figure B.23. . . . .	402
B.25 Four perspectives of the family of retrograde three-dimensional Class 5 orbits. . . . .	403
B.26 Two plots showing the initial conditions yielding the family of retro- grade three-dimensional Class 5 orbits shown in Figure B.25. . . . .	403
B.27 Four perspectives of the family of Halo orbits centered about $L_2$ . . . . .	405

B.28 Two plots showing the initial conditions yielding the family of Halo orbits centered about $L_2$ .	405
B.29 Four perspectives of a family of prograde M1 orbits, each of which makes two oscillations per orbit.	406
B.30 Four perspectives of a family of prograde M1 orbits, each of which makes three oscillations per orbit.	407
B.31 Four perspectives of a family of prograde M1 orbits, each of which makes four oscillations per orbit.	407
B.32 Four perspectives of a family of prograde M1 orbits, each of which makes four oscillations per orbit.	408
B.33 Four perspectives of a family of prograde M1 orbits, each of which makes six oscillations per orbit.	408
B.34 Four perspectives of an example orbit in a family of retrograde M1 orbits that resemble horseshoe orbits.	409
B.35 Four perspectives of a family of retrograde M2 orbits, each of which makes two oscillations per orbit.	410
E.1 Six sample trajectories that have been produced using each of the four propagation methods.	437
E.2 Example exterior and interior BLT Maps produced in the Patched Three-Body model.	441

# **Chapter 1**

## **Introduction**

The transportation of material to the Moon has become a topic of increasing attention in recent years. There are several well-known methods to transfer a spacecraft from a low Earth orbit (LEO) to an orbit about the Moon, including direct transfers, low-thrust transfers, and low-energy ballistic transfers. The conventional direct method has been used by many missions, including the Apollo program. Its greatest advantage when compared with other lunar transfers is its short transfer time; its greatest weakness is its high fuel cost. A second class of lunar transfers makes use of low-thrust engines to spiral away from the Earth and toward the Moon. The European Space Agency's SMART-1 spacecraft performed such a transfer. The primary advantage of a low-thrust mission is the implementation of engines that use fuel far more efficiently than conventional chemical engines. The disadvantages with such methods include the large transfer times involved and the complexity of a mission design that involves long periods of continuous thrust. The third lunar transfer method, and the method that is the focus of this dissertation, makes use of low-energy ballistic trajectories to reach the Moon. A ballistic lunar transfer generally balances the advantages and disadvantages of the first two lunar transfer methods: it requires less fuel than a direct transfer and it requires less transfer time than a modern low-thrust transfer.

Ballistic lunar transfers (BLTs) have been constructed before: the Japanese Hiten spacecraft implemented one in 1991 to reach the Moon. In recent years, several strate-

gies have been developed to construct BLTs, yet in general these strategies are only useful to construct missions for a set of specific requirements and are not as useful for broad trade studies. This dissertation provides a new method to model, analyze, and construct low-energy ballistic lunar transfers. The application of dynamical systems theory allows one to construct many BLTs in a simple, systematic fashion. In this way, full **families** of BLTs may be constructed and surveyed quickly to determine what types of BLTs exist that meet one's lunar mission design requirements.

This dissertation develops a tool called a BLT State Space Map, or **BLT Map** for short, which may be used to compare BLTs in a design space comparable to the traditional porkchop plot analysis. Where solutions to Lambert's Problem are the fundamental building blocks of porkchop plots, ballistic lunar transfers are the fundamental building blocks of BLT Maps. BLT Maps may then be used to quickly identify the particular ballistic lunar transfers that may be used to satisfy mission requirements.

The dynamical systems methodology that is used in this dissertation to systematically construct and analyze BLTs may be applied to other astrodynamical problems. Example problems include the design of a transfer between two or more Galilean moons, or the design of a mission to explore a binary star system.

Section 1.1 describes a typical BLT in more detail to provide a heuristic understanding of low-energy ballistic lunar transfers. Section 1.2 presents an example of a typical BLT Map. These sections provide preliminary background in order to understand the motivation for introducing the models, methodology, and conventional lunar transfers presented in Chapters 2 – 4. Section 1.3 then proceeds to discuss the organization of the dissertation.

## 1.1 Ballistic Lunar Transfers (BLTs)

A **Ballistic Lunar Transfer** is a transfer from the Earth to an orbit temporarily captured by the Moon that requires no deterministic maneuvers beyond the Trans-Lunar Injection maneuver. The transfer may begin from the surface of the Earth or any type of orbit about the Earth. In order to directly compare the performance of each transfer in this study, this dissertation ensures that all transfers begin in circular 185-km LEO parking orbits. From an initial parking orbit, a spacecraft following a BLT performs a single maneuver to send it 1 – 1.5 million kilometers toward the Earth’s  $L_1$  or  $L_2$  Lagrange points (see Section 2.3.1.5 for information about the Lagrange points). It remains out at that distance for a period of time while being pulled by the Earth, Moon, and the Sun. As the spacecraft falls back to the Moon, it ballistically arrives at the Moon and becomes temporarily captured in one of a variety of different unstable lunar orbits. This research applies dynamical systems theory to the construction of these transfers by requiring that the spacecraft’s destination – be it the final destination or an intermediate staging orbit – be an unstable three-body orbit near the Moon. The orbits that are available to the spacecraft include the well-known libration orbits, e.g., Halo and Lissajous orbits, as well as distant retrograde orbits, resonant orbits, and any of the unstable orbits presented in Appendices A and B.<sup>1</sup> The transfer between the Earth and the lunar three-body orbit requires much less energy than a conventional direct transfer, allowing payloads to be 25% to 40% larger in mass, depending on mission hardware and which particular transfer is taken.

Figures 1.1 – 1.3 show three perspectives of the same example ballistic lunar transfer. Figure 1.1 shows the BLT in the frame of reference that is centered at the Sun-Earth/Moon barycenter, co-rotating with the Sun and the Earth. Figure 1.2 shows the BLT in the inertial, Earth-centered frame of reference. Figure 1.3 shows the BLT in the

---

<sup>1</sup> The Appendices include collections of simple periodic symmetric orbits, a subset of all possible lunar three-body orbits. Only the unstable orbits may be used in ballistic lunar transfers.

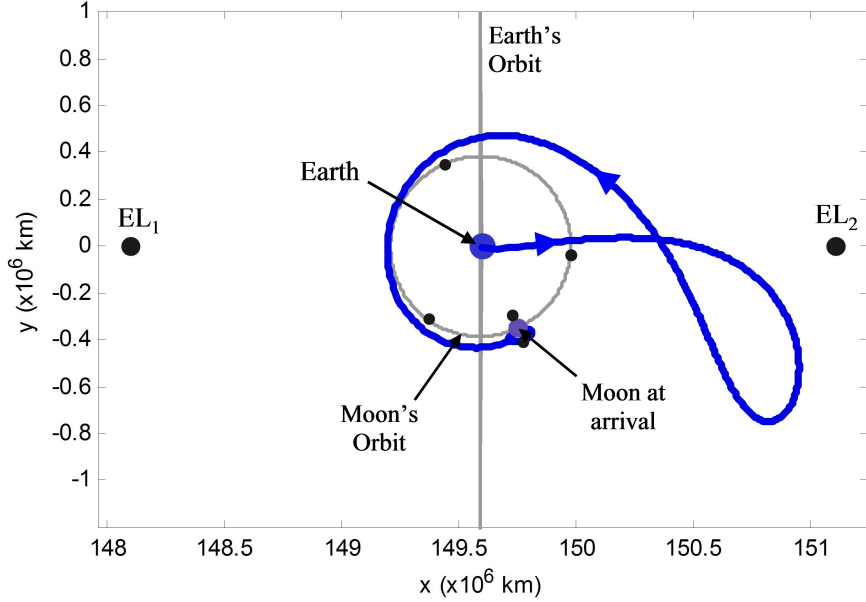


Figure 1.1: An example ballistic lunar transfer, viewed in the Sun-Earth rotating frame.

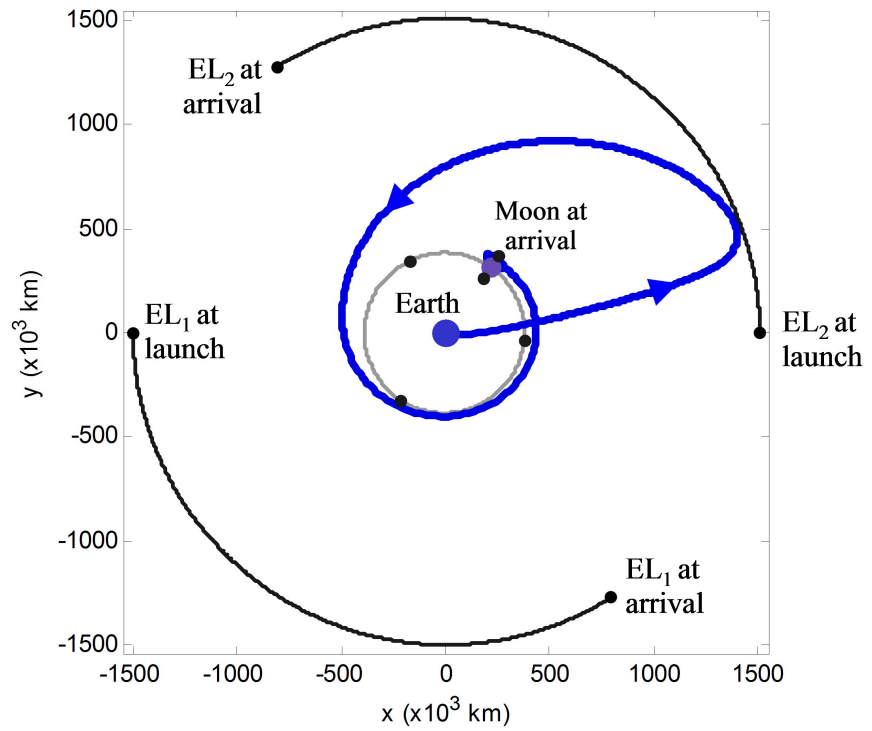


Figure 1.2: The same BLT shown in Figure 1.1 now viewed in the Earth-centered inertial frame.

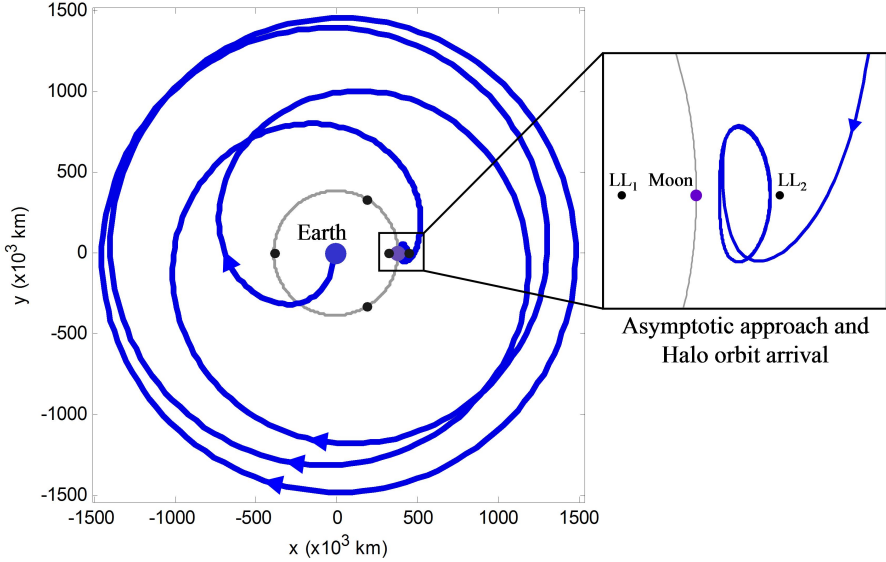


Figure 1.3: The same BLT shown in Figures 1.1 and 1.2 now viewed in the Earth-Moon rotating frame.

frame of reference that is centered at the Earth-Moon barycenter, co-rotating with the Earth and the Moon. Each frame offers different insight into the motion of a spacecraft on a BLT. From Figure 1.1, one can see that the spacecraft departs the Earth and lingers near the Earth’s second Lagrange point,  $L_2$ , before falling back toward the Moon’s orbit and eventually arriving at the Moon. From Figure 1.2, one can see that the spacecraft departs the Earth on a very eccentric orbit, which becomes highly-perturbed by the Sun’s gravity – so much so that the perigee of the orbit is raised enough to intersect the Moon. In this frame, one can see that a BLT may be described as a bi-elliptic or bi-parabolic transfer where the Sun provides the spacecraft’s intermediate  $\Delta V$ . From Figure 1.3, one can see that as the spacecraft approaches the Moon, the spacecraft does indeed enter its lunar orbit, becoming temporarily captured by the Moon without performing any insertion maneuver beyond LEO.

The method presented in this research requires that a spacecraft visit an unstable three-body orbit in the Earth-Moon system. Once the spacecraft has transferred to

this orbit, it has many available options. First, it may certainly remain in that orbit. Alternatively, since the orbit is unstable, the spacecraft may depart the orbit using very little energy. If it does depart the orbit, it may transfer to another three-body orbit, to a low lunar orbit, to the surface of the Moon, or it may even follow a symmetric BLT and return to the Earth. Transfers to other stable orbits do require a second maneuver, albeit smaller than a conventional transfer to such stable orbits. Details of these transfers are given in Chapter 5.

The results of this research show that a BLT may be used to transfer a spacecraft to a low lunar orbit for less energy than a direct transfer. In addition, one launch vehicle may be used to place many spacecraft into low lunar orbits with vastly different planes using a BLT. Although missions to low lunar orbits and missions to the surface of the Moon benefit by the application of a BLT, the missions that gain the greatest benefit from a BLT are missions to lunar three-body orbits, such as Halo orbits. Many considerations of practical mission designs are addressed in Chapter 7.

## 1.2 BLT Maps

A **BLT Map** is an effective tool developed in this dissertation that may be used to design missions to the Moon in much the same way as porkchop plots are used to design two-body trajectories. Where solutions to Lambert's Problem are the fundamental building-blocks of porkchop plots, ballistic lunar transfers are the fundamental building-blocks of BLT Maps.

Figure 1.4 shows a representation of all possible BLTs that may be constructed throughout a month of opportunities, each targeting the same lunar Halo orbit. The plot in the center is a BLT Map, colored according to the altitude of the LEO parking orbit used. The black regions represent BLTs that depart straight from the surface of the Earth, or very near the surface of the Earth, i.e., from 185-km LEO parking orbits; altitudes above the surface are colored in lighter shades. The plots surrounding the

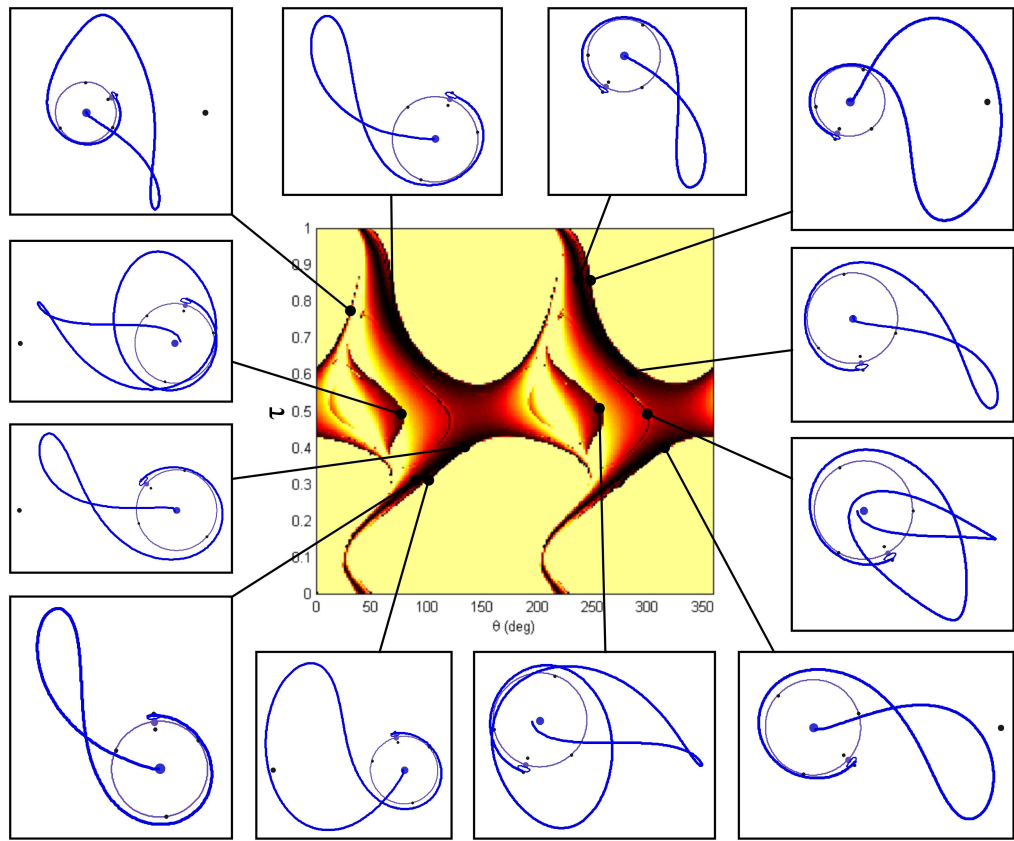


Figure 1.4: A **BLT Map**, shown in the center, where the darkest regions encompass all trajectories that depart from LEO parking orbits and transfer ballistically to a lunar Halo orbit. The plots surrounding the central map indicate where example transfers exist in the BLT Map.

central BLT Map show example BLTs that exist to this single lunar Halo orbit. One may construct families of BLTs by tracing contours in the BLT Map, corresponding to specific LEO altitudes. Once mission designers have access to such families of transfers, they may be able to quickly conduct trade studies and swiftly determine if a BLT exists that meets their mission design requirements.

### 1.3 Dissertation Organization

The remainder of this chapter provides a brief history of dynamical systems methods, the circular restricted three-body problem (CRTBP), orbital transfers, and practical mission designs. It ends by summarizing how this research contributes to the field of lunar mission design and interplanetary mission design in general.

Chapter 2 describes the models that are used in this dissertation, including the CRTBP and the Jet Propulsion Laboratory's Ephemeris model (JPL Ephemeris) of the solar system. The dynamical systems approach to constructing BLTs uses the circular restricted three-body model as an approximation to the solar system much like conic sections are used to initially approximate orbits about planetary and celestial bodies. This dissertation frequently uses the Patched Three-Body model to approximate the Sun-Earth-Moon system.

Chapter 3 presents the dynamical systems methodology that has been used to model, analyze, and construct different types of orbits and orbit transfers throughout this study.

Chapter 4 discusses conventional transfers, i.e., direct transfers from the Earth to low lunar orbits and to lunar three-body orbits. Very little information may be found in the literature regarding direct transfers to lunar three-body orbits. Hence, Chapter 4 develops a method to build a two-maneuver ballistic transfer between the Earth and a lunar three-body orbit. The chapter focuses on transfers between 185-km LEO parking orbits and Halo orbits about both the Moon's L<sub>1</sub> and L<sub>2</sub> points. The same dynamical systems methods are implemented to build the direct transfers as are used to build low-energy BLTs.

Chapter 5 discusses how to use dynamical systems methods to model, analyze, and build low-energy BLTs in the solar system using CRTBP approximations. The chapter also discusses how to build BLTs in the JPL Ephemeris model in order to vali-

date the transfers built in the simplified solar system model.

Chapter 6 discusses how to use dynamical systems methods to systematically build entire families of BLTs. The chapter introduces BLT Maps and studies how BLT Maps change under varying conditions.

Chapter 7 studies the applications of low-energy transfers and BLT Maps to practical spacecraft mission designs. The chapter discusses the impact that a low-energy ballistic lunar transfer might have on a spacecraft system, compared with a conventional, direct lunar transfer. The chapter then discusses several useful ways to implement BLT Maps into one's lunar mission design. The discussions conclude with an example case of a mission that may be designed to take advantage of low-energy lunar orbit transfers to construct a low-cost lunar navigation and communication system.

Finally, Chapter 8 summarizes the contributions that this research makes within the field of low-energy orbit transfers.

## 1.4 History / Literature Review

The purpose of this section is to provide a background of the history and of the work that has been accomplished in the fields of interplanetary mission design and dynamical systems theory in order to understand how this dissertation contributes to these fields.

The history of the three-body problem may be found in most textbooks that describe the system. The following sections summarize many of the important contributions that led to the development of the three-body problem and to practical three-body mission designs. A huge number of authors have contributed to this field; the work cited here has either been directly applied to this research or is fundamental to the research leading to this dissertation.

### 1.4.1 Classical Work in the Three-Body Problem

The complexity of the general three-body problem was first identified by Isaac Newton in the publication of his **Principia** in 1687 (Newton, 1687). Although Newton solved the general two-body problem, no closed-form solutions to the general three-body problem have ever been found. Nevertheless, much progress has been made and many solutions have been found under certain simplifications of the three-body problem.

In the 1760s and the 1770s, Leonhard Euler and Joseph-Louis Lagrange identified the locations of the five libration points, namely, the five fixed-point solutions to the circular restricted simplification of the three-body problem (Euler is given credit for identifying the three collinear points, Lagrange is given credit for identifying the two equilateral points). In 1836, Carl Gustav Jacobi identified an integral of motion that exists in the circular restricted problem, henceforth known as the Jacobi integral of motion. A search for more integrals of motion began, concluding in 1887 when Heinrich Bruns proved that no other integrals of motion could exist expressible as algebraic functions of the positions and velocities of the bodies (Julliard-Tosel, 2000). In the mid-1890s, Henri Poincaré extended the proof to show that no other integrals of motion could exist expressible as algebraic functions of the mass-fraction of the primaries. It is likely that the excess of free variables in the three-body system compared to integrals of motion leads the three-body problem to have no closed-form solution. In 1912, Karl Sundman did, however, derive an infinite series that could be theoretically summed to give a solution to the three-body problem in most cases, but the series converges exceptionally slowly – the series requires on the order of  $10^{8,000,000}$  terms to produce a solution with sufficient precision for practical applications (Sundman, 1912).

Further understanding of the three-body problem was gained in the development of theories of lunar motion; notable contributions include Charles Delaunay

(1860, 1867) and George W. Hill (1878). Other research studied the motion of comets in the three-body problem, including the work of Félix Tisserand (Tisserand, 1889–1896). In the 1890s, Poincaré contributed substantial advancement to the understanding of the three-body problem, most notably by describing the existence of chaos in the dynamical system (Poincaré, 1890, 1892). The existence of chaos helped to explain why a solution to the general three-body problem was so evasive. The classical period of research in the three-body problem ended at the end of the nineteenth century.

#### 1.4.2 Modern Work in Dynamical Systems

By the beginning of the twentieth century, the three-body problem was well-defined, but unwieldy to study all at once. Many modern techniques have been used to simplify the problem, or to analyze the problem using an organized method. This dissertation uses dynamical systems methods; hence a brief history of those methods is given here.

Dynamical systems methods of analysis involve finding simple solutions to a complex system, such as fixed-point solutions or periodic orbit solutions. Then those simple solutions may be used to assist in the analysis of the more complex features of the full system. The five fixed-point solutions of the circular restricted three-body problem were identified in the classical period of research. Many people have since identified and studied periodic orbit solutions to the CRTBP (see Section 1.4.4 for more details). The unstable libration points and unstable orbits have additional dynamical structures associated with them, such as invariant manifolds (described in more detail in Section 3.9). Since the 1960s, the mathematics of invariant manifolds have been applied to unstable periodic orbits in the three-body problem (see, e.g., Lo and Ross, 2001). Overviews of additional tools and algorithms that are useful to analyze dynamical systems may be found in the works of Szebehely (1967), Llibre et al. (1985), Strogatz (1994), Gómez et al. (2003), and Marsden and Ross (2005), among others.

### 1.4.3 Astronomical Observations of Three-Body Dynamics

Many unusual astronomical phenomena have been observed and attributed to chaotic transport mechanisms observed in the three-body problem. Several of the natural satellites of Jupiter, for instance, have orbits that do not fit in with the accepted theories explaining the origin of typical satellites. It is expected that each natural satellite should orbit the planet in a prograde, low-inclined, near-circular orbit. However, satellites have been observed in all combinations of retrograde, highly-inclined, and highly-eccentric orbits. Other unusual astronomical behavior has been observed in the orbits of comets. Several comets, such as comet Oterma, have been observed with orbits that change dramatically over time, deviating substantially from two-body, conic orbits. The motion of comets that appear to be following three-body trajectories has been studied in several papers, including Howell et al. (2001) and Jaffé et al. (2002).

In the early 1900s Moulton argued that some of the atypical satellites of Jupiter are captured asteroids. In 1930, Hopf proved that gravity cannot solely stabilize a temporarily-captured orbit, such as an orbit that might exist in the three-body problem (Hopf, 1930). This left researchers without an easy mechanism to explain the existence of those satellites. Many studies in the 1970s worked to explain how those satellites could become captured using non-conservative mechanisms, including mass-loss of the Sun, mass-accretion of Jupiter, and various forms of drag in the Jovian system (see, e.g., Bailey 1971a,b, Byl and Ovenden 1975, Horedt 1976, Heppenheimer and Porco 1977, and Pollack et al. 1979). Heppenheimer (1975) concluded that the capture mechanisms for atypical prograde and atypical retrograde satellites must be different. In most studies, the captured satellites were originally transported to temporarily-captured orbits about Jupiter via three-body trajectories.

The origin of the Moon has also been attributed to three-body dynamics. Many studies have assumed that the Moon arrived at the Earth in some sort of temporar-

captured three-body orbit prior to becoming captured (e.g., Szebehely and Evans, 1980, Malcuit et al., 1989, and Belbruno and Gott III, 2005). Szebehely and Evans (1980) present a case for how much mass the Sun would have had to have lost to transfer the Moon from a temporarily-captured orbit to a permanently-captured orbit. Malcuit et al. (1989) discuss how one or more dissipative interactions between the Earth and the Moon could have transferred the Moon into a permanently-captured orbit. Belbruno and Gott III (2005) suggest that a Mars-sized object accumulated at the Earth's L<sub>4</sub> or L<sub>5</sub> point before being perturbed onto an impact trajectory with the Earth. The impact could have then resulted in the current Earth-Moon system. Each of these origin theories involves three-body dynamics to bring the Moon into close proximity with the Earth.

These astronomical observations provide natural demonstrations of many types of three-body trajectories. Some of these transport mechanisms may be very useful to use as models when developing practical trajectories for future spacecraft missions.

#### **1.4.4 A Brief History of Periodic Orbits**

Poincaré considered periodic orbits to be the best avenue to understand the dynamics of the complex three-body problem (Howell, 1998). The first periodic orbits in the restricted three-body problem (RTBP) were found at the end of the nineteenth century. Between the 1890s and the 1930s, George Darwin (1897,1911), George Hill (1898), Henry Plummer (1903), Forest Moulton (1920), Elis Strömgren (1935), and their colleagues contributed to the discovery of the first known periodic orbits in the circular restricted three-body problem. Each of these orbits exists in a system where the two primary bodies have equal, or close to equal, mass; many of them also restrict the third, massless body to the orbital plane of the primaries (particularly Plummer, 1903 and Strömgren, 1935). Over the course of 40 years, it is unlikely that more than 150 orbits were ever computed (Broucke, 1968), however, the general aspects of orbits in

the three-body problem became well-understood.

In the 1960s, modern computers became accessible and numerical techniques could be used to swiftly identify and compute periodic orbits. In 1968, Roger Broucke published a large catalog of families of planar periodic orbits that exist in the CRTBP with Earth-Moon masses (Broucke, 1968). Also in the 1960s, researchers computed and cataloged a large number of three-dimensional periodic orbits; significant contributors include Michel Hénon (1965a, 1965b, 1966a, 1966b, 1969), Arenstorf (1963), Goudas (1963), Bray and Goudas (1967a,b), and Kolenkiewicz and Carpenter (1968), among others. In 1969, Broucke published a catalog of periodic orbits in the elliptical RTBP (Broucke, 1969). Researchers continued to identify and catalog periodic orbits in the 1970s, including planar orbits in the CRTBP (e.g., Markeev, 1979) and three-dimensional orbits in the CRTBP (e.g., Guillaume 1974, Zagouras and Kalogeropoulou 1978, and Lidov and Rabinovich 1979). Halo and quasi-halo orbits were discovered and analyzed beginning in the late 1960s (see, e.g., Farquhar 1968, Farquhar and Kamel 1973, Breakwell and Brown 1979, and Howell 1984). In 1980, David Richardson used the Lindstedt-Poincaré method to analytically produce periodic orbits, such as Halo orbits, about the collinear libration points (Richardson, 1980). Additional work was accomplished toward the end of the 20th century studying Lissajous and other quasihalo orbits (see, e.g., Farquhar and Kamel 1973, Howell and Pernicka 1988, and Gómez et al. 1998). In recent years, these periodic orbits have been computed in the real Earth-Moon system (see, e.g., Andreu, 2003).

After decades of work, many families of periodic orbits have been computed and classified in the CRTBP. However, these families generally only include the simplest classes of periodic orbits that exist; numerous families of periodic orbits exist that have never been identified. Most of the complex periodic orbits are not generally useful, since only the simplest are used in dynamical systems methods. To the best of the author's knowledge, no studies have been conducted to show that all of the simplest

classes of periodic orbits have been discovered; there may yet be some undiscovered classes of simple periodic orbits that are potentially useful to orbital analysts.

#### 1.4.5 A Brief History of Orbital Transfers

The subject of orbit transfers is very useful for practical mission designers and is useful for this dissertation; hence a brief review is given here covering the history of research into orbit transfers.

In 1925, Walter Hohmann developed what has become known as the **Hohmann Transfer**, a transfer from one circular orbit to another about a single point-mass using an elliptical transfer (Hohmann, 1925). In many theoretical cases, the Hohmann Transfer is the most cost-effective orbit transfer given a single primary body.

In the three-body problem, trajectories are rarely **on** periodic orbits, as they are in the two-body problem, and they are never on conic orbits. Hence, three-body transfers are not as easy to characterize as two-body transfers. To combat this problem, many studies have chosen to simplify the transfer problem to a problem of constructing a transfer on or off of a given periodic orbit. In 1969, McGehee studied trajectories that would take a particle off of a periodic orbit and then return the particle back onto that same orbit at a later time, i.e., **homoclinic** transfer trajectories (McGehee, 1969). In 1994, studies had been performed to construct transfers from low Earth parking orbits to Halo orbits in the Sun-Earth three-body system (see, e.g., Howell et al., 1994). By 2000, several papers had been published describing transfers between three-dimensional libration orbits, i.e., **heteroclinic** transfer trajectories (see, e.g., Gómez and Masdemont 2000 and Koon et al. 2000a). Several texts in recent years describe an object's invariant manifolds, which may be used to build homoclinic and heteroclinic transfer trajectories (see, e.g., Parker and Chua 1989, Wiggins 1990, and Gómez et al. 2003).

The construction of an efficient, practical transfer for a spacecraft in a three-body system is still an open problem. Most studies in recent years use targeting techniques to

construct a transfer, implementing tools such as the differential corrector (e.g., Howell and Pernicka 1988, Ocampo and Rosborough 1993, Serban et al. 2002, and Gómez et al. 2003).

#### 1.4.6 A Brief History of Orbital Captures

Orbital captures in a two-body sense are similar to orbital transfers in an  $n$ -body system. There have been many studies conducted to understand the mechanisms that cause one celestial body, such as a comet or asteroid, to become captured by another celestial body, such as a planet. In some cases, an asteroid or comet becomes fully captured by a planet (see, e.g., Bailey 1971a,b, Byl and Ovenden 1975, Horedt 1976, Heppenheimer 1975, Szebehely and Evans 1980, Malcuit et al. 1989, and Vieira Neto and Winter 2001); in other cases, the capture is temporary (see, e.g., Howell et al. 2001 and Jaffé et al. 2002). A variety of capture techniques have been studied dating back to 1946 when Fesenkov hypothesized that the possibility of capture existed with the close passage of several attracting bodies (Fesenkov, 1946). In a close passage of several bodies, two bodies may become gravitationally bound to each other if they transfer their relative energy to another body. In 1947, Schmidt also posed the hypothesis that celestial bodies could become captured given the dynamics of only three attracting bodies (Schmidt, 1947). In 1953, Sitnikov provided the first rigorous result showing the possibility of asymptotic capture in the three-body problem. In 1963, Alexeyev demonstrated several capture phenomena in the three-body problem using analytical methods (Alexeyev, 1963). More recently, in the early 1990s, Yamakawa presented a very descriptive discussion of gravitational capture of a body in the three-body problem (Yamakawa 1992 and Yamakawa et al. 1993). Yamakawa observed how the gravitational attraction of one of the primary bodies causes the third body's two-body energy to diminish with respect to the other primary until capture occurs when the two-body energy becomes negative.

#### 1.4.7 A Brief History of Lunar Transfers

Since orbital captures exist in celestial mechanics, mission designers have posed the question of how to construct a transfer that would place a spacecraft into some kind of captured orbit about the Moon using three-body dynamics, i.e., a ballistic lunar transfer.

As early as 1968, Charles Conley began using dynamical systems methods to construct a trajectory that a spacecraft could follow to transfer from an orbit about the Earth to an orbit about the Moon (Conley, 1968) in the planar circular restricted three-body problem. A spacecraft with the proper energy could target the neck region near one of the collinear libration points in the Earth-Moon system. A planar periodic orbit exists in each of those regions that acts as a separatrix, separating the interior of the Moon's region from the rest of the Earth-Moon region. Conley's method implemented dynamical systems techniques to construct the transfer by targeting the gateway periodic orbit.

In the late 1980s and early 1990s, Edward Belbruno began developing a method to construct lunar transfers using his Weak Stability Boundary (WSB) theory (e.g., Belbruno 1987, Belbruno and Carrico 2000, Belbruno 2004, and others). The method involves targeting the region of space that is in gravitational balance between the Sun, Earth, and Moon, without involving any three-body periodic orbits or other dynamical structures, e.g., invariant manifolds of orbits. Ballistic capture occurs when the spacecraft's two-body energy becomes negative, as described by Yamakawa et al. (1993). The lunar transfers presented in this dissertation are very similar to the transfers constructed by Belbruno, but the present work has implemented a completely different methodology to construct them.

In the early 2000s, Ivashkin also developed a method to construct transfers between the Earth and Moon using the Sun's gravitational influence (Ivashkin, 2002,

2003, 2004b,a). His methods involve beginning from a low lunar orbit, or from the surface of the Moon, and numerically targeting trajectories that depart the Moon in the direction of the Earth's L<sub>1</sub> or L<sub>2</sub> points. A spacecraft on such a trajectory departs the Moon with a negative two-body energy with respect to the Moon, but as it climbs away from the Moon, it gains energy from the effect of the Earth's and Sun's gravity. Eventually, it gains enough energy to escape the Moon's vicinity. The trajectory is then targeted such that it lingers near the chosen Lagrange point long enough to allow the Sun to lower the perigee radius of the next perigee passage down to an altitude of approximately 50 km. Ivashkin's methods are very similar to Belbruno's targeting methods.

In the mid 1990s, other methods were developed to construct a lunar transfer that take advantage of the chaos in the Earth-Moon three-body system. Bollt and Meiss (1995b) constructed a trajectory that sent a spacecraft into an orbit without sufficient energy to immediately reach the Moon, but with enough to get close enough to become substantially perturbed by the Moon. Using a series of four very small maneuvers, the spacecraft could then hop between nearby trajectories in the chaotic sea to become captured by the Moon using far less energy than standard direct transfers. In 1997, Schroer and Ott (1997) reduced the time of transfer for the chaotic lunar transfer by targeting specific three-body orbits near the Earth. The total cost remained approximately the same as the transfer constructed by Bollt and Meiss (1995b), but the transfer duration was reduced from approximately 2.05 years to 0.8 years.

In 2000, Koon et al. constructed a planar lunar transfer that was almost entirely ballistic using the techniques involved in Conley's method (Koon et al., 2000b, 2001). Similar to Conley, Koon et al. observed that the planar libration orbits act as a gateway between the interior and exterior regions of space about the Moon. Koon et al. constructed a trajectory that targets the interior of the stable invariant manifold of a planar libration orbit about the Earth-Moon L<sub>2</sub> point. Once inside the interior of the stable

manifold, the spacecraft ballistically arrives at a temporarily-captured orbit about the Moon.

#### **1.4.8 A Brief History of Control, Station-Keeping, and Rendezvous in Three-Body Orbits**

Practical mission designs in the three-body system require knowledge of control, station-keeping, and rendezvous techniques, among many other things. George W. Hill was among the first to provide insight into these practical problems. In 1886, he developed a set of equations that has become to be known as Hill's equations, which are still used today (Hill, 1886). Much later, in 1960, Clohessy and Wiltshire published a set of equations that are very useful for approximating rendezvous maneuvers in close proximity in the presence of a single gravitational body (Clohessy and Wiltshire, 1960). Many papers have since been produced that elaborate or improve upon these equations.

In the early 1990s, many studies began giving attention to the problem of control in **chaotic** dynamical systems, such as the three-body problem. It was found that a particle in a chaotic system could be controlled using a series of small perturbations (see, e.g., Ott et al., 1990; Shinbrot et al., 1993; Ott and Spano, 1995; Ditto et al., 1995). Later in the 1990s, studies demonstrated how to construct a trajectory in a chaotic dynamical system that would **target** a desired state in the given phase space (see, e.g., Shinbrot et al., 1990; Kostelich et al., 1993; Barreto et al., 1995; Boltt, 1995; Boltt and Meiss, 1995a; Schroer and Ott, 1997).

Additional work on control, station-keeping, and rendezvous was performed for applications to real spacecraft missions. These details are provided in Sections 1.4.9 and 1.4.10.

#### 1.4.9 A Brief History of Theoretical Mission Designs

As early as 1950, Arthur C. Clarke suggested using the Earth-Moon L<sub>2</sub> point to broadcast radio and TV signals to colonies at the far-side of the Moon (Clarke, 1950). In 1954, Cross considered using libration orbits to host observatories. In the early 1960s, researchers began to seriously consider placing a satellite at either of the two libration points near the Moon. Columbo (1961) showed that the station-keeping costs of a satellite placed at L<sub>1</sub> could be as low as 10 m/s per year, indicating that such a mission was viable. Additional studies were conducted in the 1960s to demonstrate the practical application of having a communication relay satellite at the Moon's L<sub>2</sub> point in support of the Apollo missions (e.g., Farquhar, 1966, 1967). In 1971, studies considered ways to optimize the station-keeping costs of a spacecraft in a libration orbit (see, e.g., Euler and Yu, 1971).

Since 1969, many studies have considered missions to put space stations or other human-occupied spacecraft in libration orbits (e.g., Farquhar 1969, 1971, 2000, D'Amario 1973, Farquhar and Dunham 1990, Bond et al. 1991, and Condon and Pearson 2001). In the 1970s, studies considered each aspect of real missions that would implement libration orbits, including guidance, navigation, trajectory correction maneuvers, etc. (e.g., Heppenheimer and Kaplan 1977, and Heppenheimer 1978a,b,c).

Since the 1980s, many studies have been conducted to advance the state of technology of mission designs incorporating three-body trajectories and orbits. In 1982, Tanabe et al. demonstrated methods to reach lunar libration orbits using lunar swingbys (Tanabe et al., 1982). In 1990, Pernicka and Howell developed a strategy to place a satellite in a Sun-Earth libration orbit that would avoid the solar-exclusion zone (Pernicka and Howell, 1990). Current research is focusing on the role of invariant manifolds of three-body orbits in low-thrust mission design (e.g., Lo et al. 2004, Anderson and Lo 2004, and Lo et al. 2006). Several references contain a compilation of useful information

for constructing libration-point missions and other missions in the presence of chaotic dynamics, including Gómez et al. (2001a, 2003) and Howell et al. (1997a).

#### 1.4.10 A Brief History of Real Mission Designs

Since the 1970s, several spacecraft have been placed on three-body trajectories to conduct their scientific and technological missions, including ISEE-3, Hiten, SOHO, ACE, WMAP, Genesis, and SMART-1. A brief description of these missions and how they have implemented three-body trajectories is given here. Beckman (2003) provides a good overview of the guidance and navigation involved with the ISEE-3, SOHO, ACE, and WMAP missions.

**ISEE-3.** On August 12, 1978, the International Sun-Earth Explorer 3 (ISEE-3) spacecraft was launched and placed in a Halo orbit about the Sun-Earth L<sub>1</sub> point. On June 10, 1982, the spacecraft began performing a series of 15 very small maneuvers to ride the chaos in the Sun-Earth system and eventually transfer to the Earth-Moon L<sub>1</sub> point. Once there, the spacecraft orbited the Earth-Moon L<sub>1</sub> point five times, performing slight maneuvers at each lunar flyby. On its fifth and final lunar flyby, on December 22, 1983, the spacecraft was renamed the International Cometary Explorer (ICE) as it readied for its encounter with the comet Giacobini-Zinner. On June 5, 1985, ICE entered the comet's tail and collected scientific information about the tail. ICE is expected to return to the vicinity of the Earth in 2014, when it may be captured and brought back to Earth. Figure 1.5 shows a plot of the trajectory of ISEE-3/ICE. For more information, see Farquhar et al. (1977) and Dunham (1979).

**Hiten.** In 1991, the Japanese spacecraft Hiten was the first spacecraft to transfer to the Moon using a low-energy ballistic lunar transfer. The spacecraft was not designed to go to the Moon, but rather to send a probe to the Moon. After the probe's communication system failed, mission designers scrambled to find a new mission for Hiten. Edward Belbruno constructed a new trajectory – a "WSB transfer" – that re-

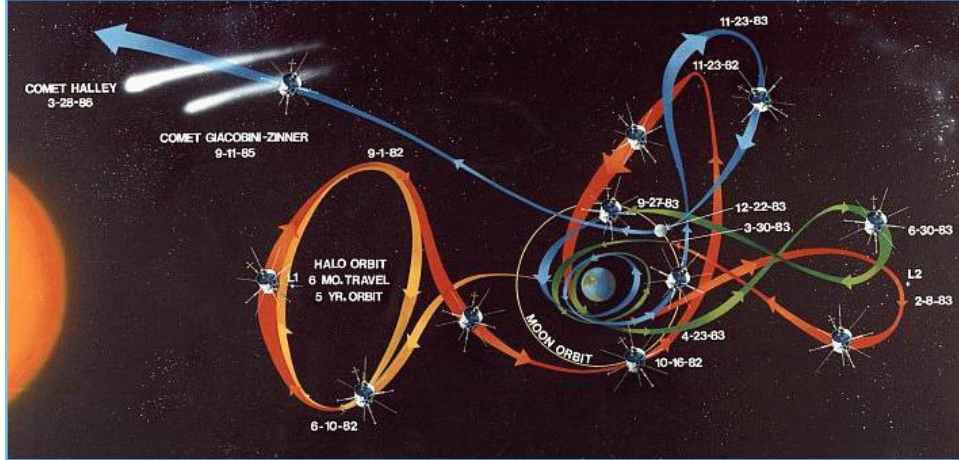


Figure 1.5: The trajectory of ISEE-3 / ICE (GSFC, 2007a).

quired less fuel than traditional lunar transfers. The spacecraft Hiten did not have the fuel required for a conventional lunar transfer, but had the fuel to use this new lunar transfer to reach the Moon. Hiten became Japan's first lunar mission. For more information, see Belbruno and Miller (1990) and Uesugi (1991).

**SOHO.** On December 2, 1995, the Solar and Heliospheric Observatory (SOHO) was launched and placed in a Halo orbit<sup>2</sup> about the Sun-Earth L<sub>1</sub> point. The L<sub>1</sub> Halo orbit is ideal for the observatory because it provides an unobstructed view of the Sun on one side and a near-constant view of the Earth on the other side. Hence, it can collect scientific data about the Sun continuously, while being able to communicate with the Earth at any time. Figure 1.6 shows a plot of the trajectory that SOHO used to transfer to its Halo orbit. For more information, see Simó et al. (1987), Dunham et al. (1992), Bonnet and Felici (1997), and Gómez et al. (2001a).

**ACE.** In 1997, the Advanced Composition Explorer (ACE) was launched and placed in a Lissajous orbit about the Sun-Earth L<sub>1</sub> point. Its mission, much like SOHO's, is dedicated to collecting energetic particles to study the solar corona, interplanetary

<sup>2</sup> The orbit is sometimes referred to as a "quasi-Halo" orbit since in the real solar system the orbit is not perfectly periodic, but quasi-periodic.

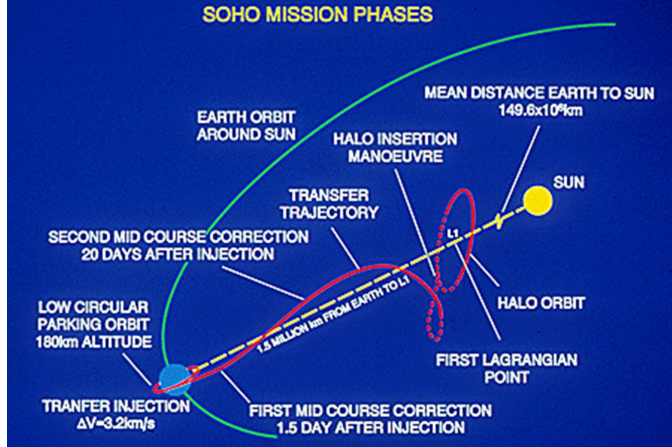


Figure 1.6: The transfer trajectory of SOHO (NASA, 2007a).

medium, solar wind, and cosmic rays. Its transfer appears very similar to SOHO's transfer, shown in Figure 1.6. For more information, see Murdin (2000).

**WMAP.** Launched on June 30, 2001, The Wilkinson Microwave Anisotropy Probe (WMAP) is currently residing in a small-amplitude Lissajous orbit about the Sun-Earth L<sub>2</sub> point. From this orbit, WMAP continues to measure the cosmic background radiation, unobstructed by the radiation originating from the Sun, Earth, or Moon. Figure 1.7 shows a plot of the trajectory that WMAP used to reach its libration orbit about L<sub>2</sub>. For more information, see Bennett (1996).

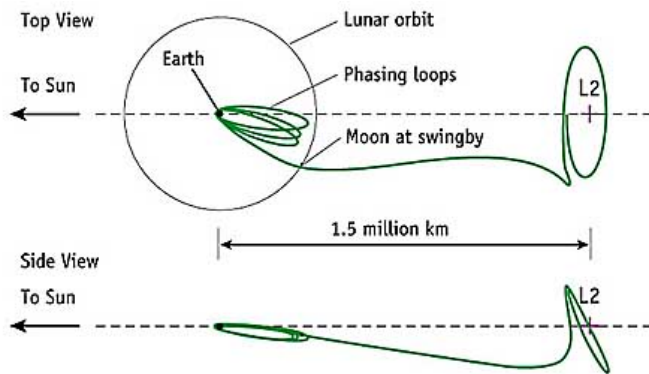


Figure 1.7: The transfer trajectory of WMAP (GSFC, 2007b).

**Genesis.** On August 8, 2001, Genesis launched and was quickly injected into a Halo orbit about the Sun-Earth L<sub>1</sub> point. It traversed the Halo orbit approximately five times, spending over two years in the libration orbit collecting solar wind samples, before turning back toward the Earth. Before returning to the Earth, however, it made a 3-million-mile detour to visit the Sun-Earth L<sub>2</sub> point. The detour allowed it to deposit its science payload on the sunlit-side of the Earth. Figure 1.8 shows a plot of the trajectory that Genesis followed during its primary mission. For more information, see Howell et al. (1997a) and Lo et al. (2001).

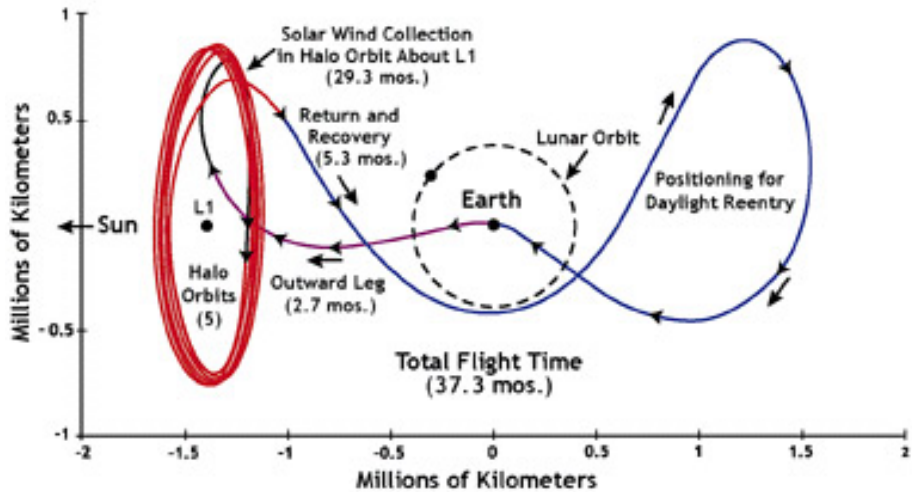


Figure 1.8: The trajectory that the Genesis spacecraft followed (JPL, 2007).

**SMART-1.** On September 27, 2003, the European Space Agency's SMART-1 spacecraft followed a low-thrust two-year trajectory to reach the Moon, becoming the first low-thrust spacecraft to transfer to the Moon. For more information, see Foing and Racca (1999).

**Future Missions.** In the future, there are plans to place the Herschel Space Observatory (Pilbratt et al., 2004), the proposed James Webb Space Telescope (Gardner, 2003), and the proposed Terrestrial Planet Finder (Beichman et al., 2004) missions, among others, at the Sun-Earth L<sub>2</sub> point.

## 1.5 Contributions of this Dissertation

The purpose of this dissertation is to advance the current state of technology in the fields of astrodynamics and dynamical systems theory, and in the more specific field of low-energy ballistic trajectory design. This research contributes to these fields in many ways. First and foremost, the focus of the dissertation is to demonstrate how to use dynamical systems theory to model, analyze, and construct low-energy ballistic transfers between the Earth and the Moon in three dimensions. The dynamical systems methodology provides the means to systematically characterize families of such transfers. This dissertation develops the BLT Map to be used as a tool for mission designers to quickly evaluate many BLTs simultaneously in order to identify a lunar transfer that meets the given mission design requirements. These contributions are the focus of this dissertation.

In the process of developing BLTs, this dissertation also contributes additional tools to the field of interplanetary mission design. This research provides validation for the Patched Three-Body model for its use as a simplified model of the Sun-Earth-Moon-spacecraft four-body system. It demonstrates that a Three-Body Sphere of Influence may be used to switch between three-body systems in order to take advantage of desirable three-body mission design tools, while still designing realistic trajectories. This dissertation also applies dynamical systems methods to the design of two-maneuver, direct transfers between the Earth and lunar three-body orbits. Although direct transfers between the Earth and low lunar orbits have been studied in great depth, this dissertation provides the first robust survey of direct, two-maneuver transfers between the Earth and lunar three-body orbits. The survey is then used as a baseline to evaluate the performance of low-energy single-maneuver transfers, i.e., BLTs, to the same lunar three-body orbits. Finally, this dissertation contributes several mission design concepts for practical spacecraft missions that include low-energy BLTs.

## Chapter 2

### Models

#### 2.1 Introduction

The present study of low-energy pathways in the near-Earth environment uses several models and moves between them frequently. The following list summarizes these models and where they are most frequently used in this work:

- The Two-Body Model. Used for modeling the motion of a particle, i.e., a space-craft, in the presence of one massive body. The model assumes that the particle is not exposed to any other massive bodies nor any other significant perturbations.
- The Circular Restricted Three-Body Model. Used for modeling the motion of a massless object near two massive bodies where the two massive bodies orbit their barycenter in circular orbits.
- The Patched Three-Body Model. Used for modeling the motion of a massless object in the presence of three or more massive bodies. The motion of the massless object is approximated by the gravitational attraction of the two most influential massive bodies at any given time using the dynamics of the circular restricted three-body model.
- The Bicircular Model. Used for modeling the motion of a massless object in the presence of three massive bodies, such as the Sun, Earth, and Moon. This

model assumes that two of the three massive bodies, i.e., the Earth and Moon, orbit their barycenter in circular orbits, and that the barycenter of that system and the third massive body, i.e., the Sun, orbit their collective barycenter in circular orbits.

- The JPL Ephemeris approximation of the Solar System. Used for modeling the motion of a massless object in the presence of the planets and moons in the real solar system, where the motion of the planets and moons are approximated by the most accurate ephemeris constructed by the Jet Propulsion Laboratory to date. It is a computationally-intensive model, but the most accurate model used in this study.

Many other models have been used by other researchers to study low-energy trajectories in the three-body problem, including the elliptic restricted three-body model (Makó and Szenkovits, 2004) and the inclined bicircular problem (Hill et al., 2006a). The models outlined above are used frequently in the present research; these will be summarized in the following sections.

## 2.2 The Two-Body Problem

The two-body problem is presented in great detail in many texts (see, e.g., Bate et al. 1971 or Vallado 1997). The full two-body problem describes the motion of two arbitrarily-shaped bodies in mutual gravitational attraction. The scope of this dissertation is restricted to studying the dynamics about massive bodies that are nearly spherically-symmetric, such as the Sun, Earth, and Moon. The more basic two-body problem describes the motion of two point-masses in mutual gravitational attraction. Newton's Law of Universal Gravitation states that any two bodies attract one another with a force proportional to the product of their masses and inversely proportional to

the square of the distance between them. This is written mathematically as:

$$\vec{F}_g = -\frac{Gm_1m_2}{r^2} \frac{\vec{r}}{r} \quad (2.1)$$

where  $\vec{F}_g$  is the force of gravity on each of the two bodies,  $m_1$  and  $m_2$ , due to their mutual attraction,  $\vec{r}$  is the vector distance between the two bodies, and  $G$  is the universal gravitational constant, equal to approximately  $6.673 \times 10^{-11} \text{ m}^3/\text{kg}\cdot\text{s}^2$  (Bate et al., 1971; Vallado, 1997). When this formula is applied to the case of two masses in the presence of no other forces, then one may arrive at a simple equation relating each body's position over time with respect to the center of mass of the system:

$$\ddot{\vec{r}}_{cm} = -\frac{G(m_1 + m_2)}{r_{cm}^3} \vec{r}_{cm}, \quad (2.2)$$

where  $\vec{r}_{cm}$  is the vector distance between the body of interest and the center of mass of the system. When the relationship given in Equation 2.2 is applied to the motion of a spacecraft,  $m_2$ , in orbit about a planet,  $m_1$ , then the simplification  $m_1 + m_2 \approx m_1 \equiv M$  may be made. Equation 2.2 may then be written as:

$$\ddot{\vec{r}} + \frac{GM}{r^3} \vec{r} = 0, \quad (2.3)$$

where  $r$  is now the vector position of the spacecraft with respect to the planet. Manipulating Equation 2.3 yields the trajectory equation, an equation describing the shape of all two-body orbits (Vallado, 1997):

$$r = \frac{p}{1 + e \cos(\nu)}, \quad (2.4)$$

where  $p$  is the semi-parameter defined by the quantity  $a(1 - e^2)$ ,  $a$  is the semi-major axis of the orbit,  $e$  is the eccentricity of the orbit, and  $\nu$  is the true anomaly. This relationship indicates that all two-body trajectories are conic sections: ellipses, circles, parabolas, and hyperbolas. This relationship does not indicate how a trajectory is oriented; it only gives an analytic expression for the trajectory's shape. Consequently, if the state of the two-body system is known at any time  $t_0$ , including the orientation of

the trajectory, then the state may be determined at any other time  $t$  using this analytic expression.

The well-characterized solution of the two-body problem is demonstrated in another way, which will be useful as background for the three-body and the general  $n$ -body problem. Each body in a three-dimensional system has six degrees of freedom: three position coordinates and three velocity coordinates. These degrees of freedom originate from the fact that each body's motion is characterized by three second-order differential equations. Thus, the two-body problem has a total of 12 degrees of freedom. In order to have the analytic expression given in Equation 2.4, one must have at least as many integrals of motion as there are degrees of freedom in the system. In the case of two bodies, one must have 12 integrals of motion in order to uniquely describe the two-body motion. Conservation of linear momentum provides six integrals of motion, which describe the motion of the barycenter of the system for all time. Using that information, one can translate an arbitrary inertial coordinate frame to the barycenter of the two-body system since it is also an inertial reference frame. Conservation of energy provides one integral of motion. Conservation of angular momentum and Kepler's first two laws provide the remaining five integrals of motion (Vallado, 1997). Kepler's first two laws state that a particle orbits in a conic section and sweeps out equal areas in equal times. Another way to observe this is to define an eccentricity vector,  $\vec{e}$ :

$$\vec{e} = \frac{1}{GM} \left[ \left( v^2 - \frac{GM}{r} \right) \vec{r} - (\vec{r} \cdot \vec{v}) \vec{v} \right]. \quad (2.5)$$

The magnitude of this vector is equal to the scalar eccentricity of the orbit; its direction points toward the orbit's perapse. If one differentiates Equation 2.5 with respect to time, one finds that the eccentricity vector is also conserved. Ultimately, one finds that there are 12 integrals of motion and 12 degrees of freedom, producing a very well-characterized system.

### 2.3 The Three-Body Problem (TBP)

The three-body problem describes the motion of three bodies under mutual gravitational attraction. The problem may be laid out in a similar manner to the two-body problem. Equation 2.1 may be used to describe the force of gravity acting on one body due to the mutual attraction of two bodies; similarly, Equation 2.6 describes the force of gravity acting on one body,  $m_1$ , due to the mutual attraction of all three bodies:

$$\vec{F}_1 = m_1 \ddot{\vec{r}}_1 = -\frac{Gm_1m_2}{r_{12}^3} \vec{r}_{12} - \frac{Gm_1m_3}{r_{13}^3} \vec{r}_{13}, \quad (2.6)$$

where  $\vec{r}_1$  is the position vector of the first body with respect to the origin,  $\vec{r}_{12}$  is the relative position vector of the second body with respect to the first, and  $\vec{r}_{13}$  is the relative position vector of the third body with respect to the first.

In the case of a satellite in orbit about the Earth under the influence of the Moon, the two primary masses move in two-body motion about each other, and the satellite is significantly affected by both masses. In this case, Equation 2.6 may be used to derive the following relationship for the satellite's acceleration:

$$\ddot{\vec{r}}_{\oplus-\mathcal{S}} = -\frac{G(m_{\oplus} + m_{\mathcal{S}})}{r_{\oplus-\mathcal{S}}^3} \vec{r}_{\oplus-\mathcal{S}} + Gm_{\mathbb{C}} \left( \frac{\vec{r}_{\mathcal{S}-\mathbb{C}}}{r_{\mathcal{S}-\mathbb{C}}^3} - \frac{\vec{r}_{\oplus-\mathbb{C}}}{r_{\oplus-\mathbb{C}}^3} \right), \quad (2.7)$$

where the subscripts  $\oplus$ ,  $\mathbb{C}$ , and  $\mathcal{S}$  describe the Earth, the Moon, and the satellite, respectively, and the subscript  $\oplus - \mathcal{S}$  indicates a vector that originates at the Earth and ends at the satellite. The first term in Equation 2.7 is the familiar two-body equation of motion; the second term is the third-body perturbation and it is composed of two parts. The left part is called the **direct effect** because it is the contribution of the Moon's gravity pulling on the spacecraft itself; the right part is called the **indirect effect** because it is the contribution of the Moon's gravity pulling on the Earth, indirectly influencing the spacecraft's trajectory (Vallado, 1997). This third-body effect is very small when the spacecraft is very close to the Earth or when the third body is very far away from the system. Figure 2.1 shows a trajectory that is only slightly perturbed by the Moon's

influence, although perturbed enough to no longer be truly periodic. The third-body effect becomes increasingly influential as the orbit of the spacecraft moves closer to the region of space that is equally influenced by both primary bodies. A dramatic example of such a third-body interaction is shown in Figure 2.2, below. It is in that region that a new model of the three-body system becomes desirable.

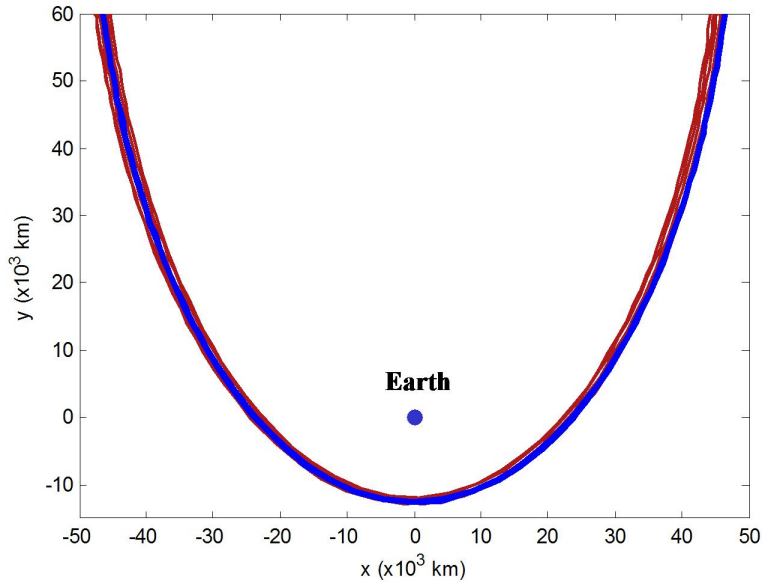


Figure 2.1: A trajectory about the Earth that is perturbed by the Moon. The trajectory shown in blue is not perturbed by the Moon; the trajectory shown in red is perturbed.

The full three body problem includes 18 degrees of freedom. Additionally, since Kepler's laws do not apply to systems of more than two bodies, only ten integrals of motion exist: six due to conservation of linear momentum, one due to conservation of energy, and three due to conservation of angular momentum. Thus, the system with 18 degrees of freedom only has 10 known integrals of motion. The full three-body problem has eight unconstrained degrees of freedom and is therefore impossible to represent analytically. Several simplifications are generally made in order to make progress studying the system.

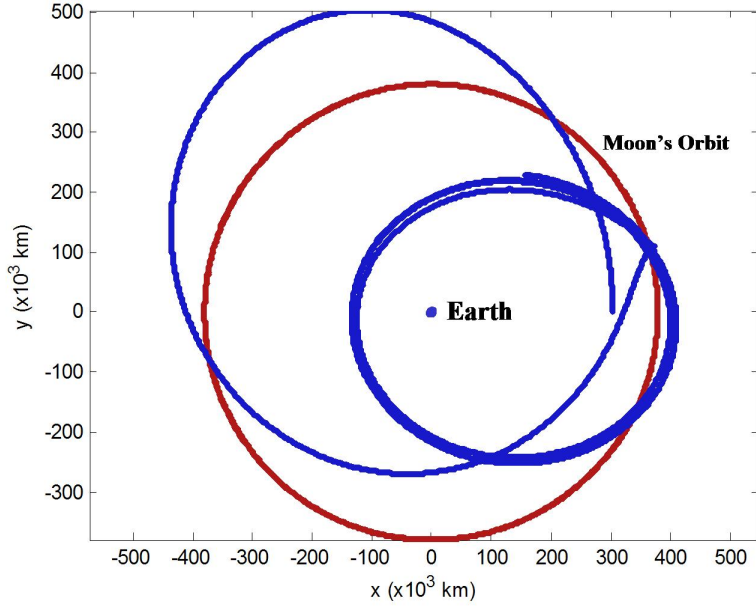


Figure 2.2: A dramatic example of third-body interactions. The trajectory shown in blue is a trajectory of a spacecraft influenced by the Earth and the Moon; the Moon's orbit is shown in red.

The first simplification made to the three-body problem is to restrict the mass of one of the bodies to a negligible value; this simplified problem is known as the restricted three-body problem (RTBP). This simplification is frequently made in astrodynamics when modeling the motion of a small asteroid, comet, or a spacecraft in the presence of two massive bodies. In this RTBP the two massive bodies (called the primaries) move in two-body orbits about their barycenter. This doesn't change the number of degrees of freedom in the system, but it adds two integrals of motion because Kepler's laws once again apply to the motion of the two primaries. The system still has six unconstrained degrees of freedom, however, so more simplifications are generally made to assist in analyzing the possible solutions to the problem.

The next simplification is to restrict the motion of the two primaries to circular orbits about their barycenter. This model is known as the circular restricted three-body problem (CRTBP). The CRTBP still models the motion in the solar system well

because the orbits of the planets are nearly circular. When this simplification is made it is convenient to model the motion of the spacecraft in the synodic frame, i.e., the frame of reference that rotates about the barycenter at the same rate as the rotation rate of the primaries. In this new system an additional integral of motion emerges, called the Jacobi constant, described in more detail in Section 2.3.1.2. The system now only has five unconstrained degrees of freedom.

The final simplification that is typically made is to restrict the motion of all three bodies to a plane. This model is known as the planar circular restricted three-body problem (PCRTBP). This simplification reduces the total number of degrees of freedom to 12 (four for each body), but it also reduces the number of integrals of motion to 9: four due to conservation of linear momentum, one due to conservation of energy, one due to conservation of angular momentum, two due to Kepler's first two laws, and one due to Jacobi's integral. There are now only three unconstrained degrees of freedom. This model is about as simple as one can get before reducing it to the two-body problem.<sup>1</sup> These simplifications are summarized in Table 2.1.

Table 2.1: A summary of the degrees of freedom and integrals of motion in two-body and three-body systems.

System	Two-Body Problem	Three-Body Problem	RTBP: 3 <sup>rd</sup> Body Massless	CRTBP: Circular Orbits	PCRTBP: 2D Motion
Degrees of Freedom	<b>12</b>	<b>18</b>	<b>18</b>	<b>18</b>	<b>12</b>
Integrals of Motion	<b>12</b>	<b>10</b>	<b>12</b>	<b>13</b>	<b>9</b>
Linear Momentum	6	6	6	6	4
Angular Momentum	3	3	3	3	1
Energy	1	1	1	1	1
Kepler's Integrals	2	0	2	2	2
Jacobi's Integral	N/A	N/A	N/A	1	1

---

<sup>1</sup> Szebehely describes an additional reduction where time is removed from the equations to reduce the PCRTBP to a second-order problem (Szebehely, 1967).

### 2.3.1 Circular Restricted Three-Body Problem (CRTBP)

The research presented in this dissertation uses the CRTBP as a foundation. The CRTBP captures most of the dynamics observed in real systems such as the environment near the Earth and Moon. The CRTBP's simplified equations of motion allow mission designers to identify useful trajectories quickly. Those trajectories are then later moved into more realistic systems, such as the JPL ephemeris model of the solar system.

This section describes the details of the planar and full CRTBP, including the equations of motion, a description of the Jacobi integral of motion, and a description of the basic solutions found in the system.

#### 2.3.1.1 Equations of Motion

The coordinate system of the CRTBP and PCRTBP is centered at the barycenter of the primaries and set to rotate with the motion of the primaries about the origin. When viewed from above, the synodic frame rotates in a counter-clockwise fashion compared to the inertial frame, assuming the conventional right-hand rule for the angular momentum in the system. The  $x$ -axis, also known as the syzygy axis (Szebehely, 1967), extends from the origin through the smaller primary, the  $z$ -axis (which is not used in the PCRTBP model except to set up the axes) extends in the direction of the angular momentum of the system, and the  $y$ -axis completes the right-hand coordinate frame. It is convenient to normalize the units in the system such that the following metrics are equal to one: the distance between the two primaries, the sum of the mass of the two primaries, the rotation rate of the system, and the gravitational parameter. The orbital period of the two primaries is then equal to  $2\pi$ . The three-body constant,  $\mu$ , is defined as the ratio of the smaller primary's mass ( $m_2$ ) to the sum of the mass of the two primaries ( $m_1 + m_2$ ), approximately equal to 0.0121506 for the Earth-Moon

Table 2.2: The parameters of the Earth-Moon and Sun-Earth/Moon three-body systems (Vallado, 1997).

System	Earth-Moon		Sun-Earth/Moon	
Parameter	SI units	3-Body normalized units	SI units	3-Body normalized units
$\mu$	0.0121506037932213		$3.04040249992936 \times 10^{-6}$	
Distance between two primaries	384,400 km	$1 d_{3B}$	149,597,870 km	$1 d_{3B}$
Orbital Period	27.28 days	$2\pi t_{3B}$	365.24 days	$2\pi t_{3B}$
$M_1 + M_2$	$6.04768 \times 10^{24}$ kg	$1 m_{3B}$	$1.989106 \times 10^{30}$ kg	$1 m_{3B}$
Primary Mass	$5.9742 \times 10^{24}$ kg	$1 - \mu m_{3B}$	$1.9891 \times 10^{30}$ kg	$1 - \mu m_{3B}$
Secondary Mass	$7.3483 \times 10^{22}$ kg	$\mu m_{3B}$	$6.04768 \times 10^{24}$ kg	$\mu m_{3B}$
Location of $M_1$	$x = -4670.692$ km $y = 0$ km $z = 0$ km	$x = -\mu d_{3B}$ $y = 0 d_{3B}$ $z = 0 d_{3B}$	$x = -454.8377379$ km $y = 0$ km $z = 0$ km	$x = -\mu d_{3B}$ $y = 0 d_{3B}$ $z = 0 d_{3B}$
Location of $M_2$	$x = 379,729.31$ km $y = 0$ km $z = 0$ km	$x = 1 - \mu d_{3B}$ $y = 0 d_{3B}$ $z = 0 d_{3B}$	$x = 149,597,415.16$ km $y = 0$ km $z = 0$ km	$x = 1 - \mu d_{3B}$ $y = 0 d_{3B}$ $z = 0 d_{3B}$

system and  $3.0404 \times 10^{-6}$  for the Sun-Earth system (Vallado, 1997). Since the system has been normalized, the coordinates of the primaries in the rotating axes are therefore equal to  $[-\mu, 0]$  and  $[1 - \mu, 0]$  for the larger and smaller primary, respectively. The mass of the larger and smaller primaries are equal to  $1 - \mu$  and  $\mu$  normalized mass units ( $m_{3B}$  units), respectively. The mass of the third body is neglected in the model. This information is summarized in Table 2.2 for the Earth-Moon and Sun-Earth/Moon three-body systems.

The equations of motion for the third body in the rotating frame are equal to (Szebehely, 1967):

$$\ddot{x} = 2\dot{y} + x - (1 - \mu) \frac{x + \mu}{r_1^3} - \mu \frac{x - 1 + \mu}{r_2^3} \quad (2.8)$$

$$\ddot{y} = -2\dot{x} + y - (1 - \mu) \frac{y}{r_1^3} - \mu \frac{y}{r_2^3} \quad (2.9)$$

$$\ddot{z} = -(1 - \mu) \frac{z}{r_1^3} - \mu \frac{z}{r_2^3} \quad (2.10)$$

where  $r_1$  and  $r_2$  are equal to the distance from the third body to the larger and smaller

primary, respectively:

$$\begin{aligned} r_1^2 &= (x + \mu)^2 + y^2 + z^2 \\ r_2^2 &= (x - 1 + \mu)^2 + y^2 + z^2 \end{aligned}$$

In this form it is clear that the dynamics of the system depend only on the mass fraction  $\mu$ . Furthermore, as  $\mu$  goes to zero, the dynamics approach two-body dynamics, although represented in a rotating frame.

### 2.3.1.2 Jacobi Integral of Motion

The dynamics of the CRTBP permit an integral of motion to exist in the synodic reference frame, namely, the Jacobi constant. The Jacobi constant may be derived by taking the three equations of motion given in Equations 2.8 - 2.10, multiplying them by  $2\dot{x}$ ,  $2\dot{y}$ , and  $2\dot{z}$ , respectively, summing the results together, and integrating. The result of this process produces the well-known Jacobi integral equation:

$$\dot{x}^2 + \dot{y}^2 + \dot{z}^2 - (x^2 + y^2) = \frac{2(1 - \mu)}{r_1} + \frac{2\mu}{r_2} - C \quad (2.11)$$

Equation 2.11 is the Jacobi integral of motion represented in the normalized, synodic reference frame; the constant of integration,  $C$ , is known as Jacobi's constant.

The Jacobi constant may be written simply as:

$$C = 2U - V^2 \quad (2.12)$$

where

$$\begin{aligned} U &= \frac{1}{2} (x^2 + y^2) + \frac{1 - \mu}{r_1} + \frac{\mu}{r_2} \\ V^2 &= \dot{x}^2 + \dot{y}^2 + \dot{z}^2 \end{aligned}$$

In this form, one can see that if a spacecraft performs a maneuver to increase its velocity with respect to the synodic reference frame, the spacecraft's Jacobi constant goes down;

hence, in some respects the Jacobi constant is inversely proportional to the spacecraft's energy. Furthermore, a spacecraft at a particular location in space cannot raise its Jacobi constant above a value of  $2U$  since it cannot acquire an imaginary velocity.

The Jacobi constant of a spacecraft cannot change unless the spacecraft is perturbed in some way other than by the gravitational attraction of the two primary bodies. The spacecraft's Jacobi constant may change in the presence of additional massive bodies, radiation pressure, drag, or if the spacecraft performs a maneuver. If no perturbations exist, the spacecraft's motion is restricted to only those regions of space that permit the spacecraft's Jacobi constant. Regions that a spacecraft cannot reach, such as those that would require imaginary velocity, are known as **forbidden regions** and will be discussed in Section 2.3.1.4.

This dissertation uses Equation 2.12 as the definition of the Jacobi constant; however, some texts (e.g., Vallado, 1997) separate the constant of integration into two parts, such that a different constant  $C^*$  is defined as:

$$C^* = 2U - V^2 - \mu(1 - \mu)$$

and thus  $C^* = C - \mu(1 - \mu)$ . This alternate definition of the Jacobi constant facilitates certain mathematical properties, but has no effect on the equations of motion (see, e.g., Koon et al., 2007).

### 2.3.1.3 Zero-Velocity Curves

If one maps out the potential of the circular restricted three-body system in the inertial frame, one observes that the two primary bodies produce potential wells that follow them as they orbit their barycenter. In the synodic frame, those two potential wells hold still; the potential of the system also falls off as a function of distance due to the centrifugal motion of the reference frame. One can see this by mapping the Jacobi constant throughout the neighborhood of the primaries for particles that are at

rest in the synodic frame. The contours of such a map are thus known as zero-velocity curves. Figure 2.3 shows the zero-velocity curves for the circular restricted three-body system with Earth-Moon masses. The contours near the Earth and near the Moon have been removed to give better depth to the interesting regions. Figure 2.4 shows a three-dimensional view, but with the  $z$ -axis reversed to mimic the potential of the system. The five Lagrange points are labeled in these plots, but will be further discussed in Section 2.3.1.5.

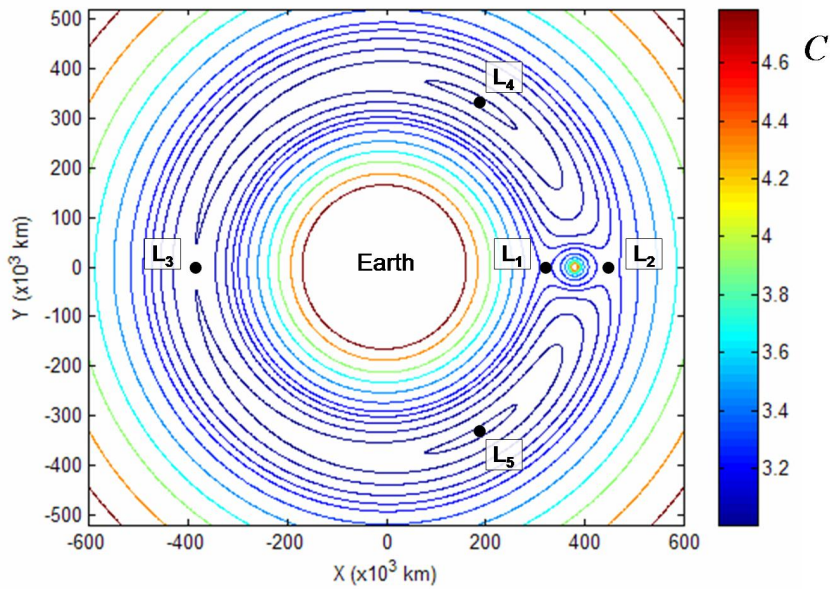


Figure 2.3: The zero-velocity curves for the circular restricted three-body system with Earth-Moon masses, shown in the synodic frame.

#### 2.3.1.4    Forbidden Regions

A spacecraft on a ballistic trajectory in the circular restricted three-body system cannot change its Jacobi constant. As such, the spacecraft's motion is bound to the region of space that permits such a Jacobi constant. The forbidden regions are those regions of space which require the spacecraft to have an imaginary velocity in order to retain its Jacobi constant. In reality, the spacecraft slows down as it approaches the

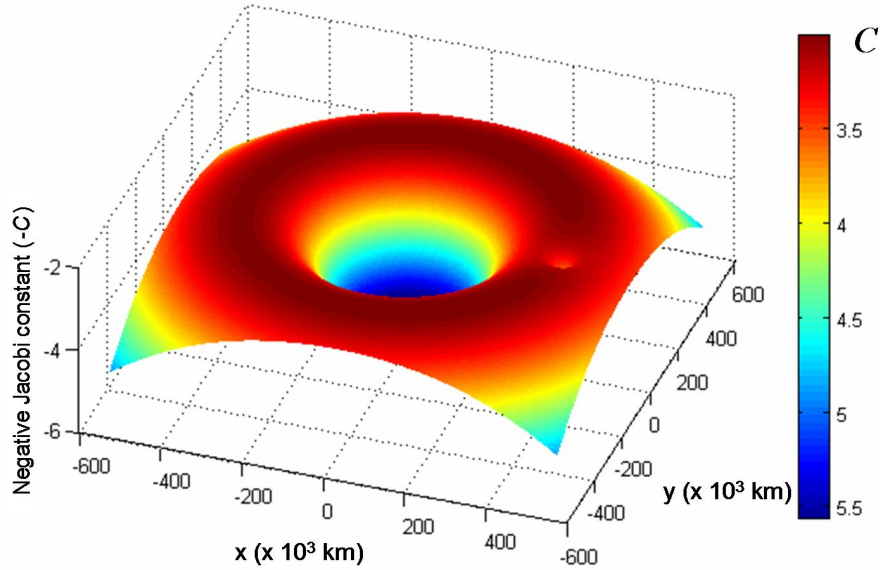


Figure 2.4: A three-dimensional view of the zero-velocity surface, reversed about the  $z$ -axis to mimic the potential of the CRTBP system.

forbidden region. In order to encounter the boundary of the forbidden region, the spacecraft must come to rest in the synodic frame, i.e., it must encounter the zero-velocity curve for its Jacobi constant.

The plots shown in Figure 2.5 demonstrate the notion of the forbidden region in the CRTBP. The trajectories shown have been propagated for particles in the Earth-Moon system with Jacobi constants equal to approximately 3.12 (left) and 3.19 (right); observe that the particles never enter the forbidden region for their Jacobi constant value.

Figure 2.6 shows plots of the forbidden region in the Earth-Moon system for a variety of values of the Jacobi constant. It may be observed that a particle with a Jacobi constant greater than approximately 3.18834 is either trapped in the Earth's or Moon's vicinity and cannot transfer between them. With slightly smaller Jacobi constant values, the particle is permitted to transfer between each body's vicinity through the neck at  $L_1$ , but cannot escape the interior of the Earth-Moon system. A particle with a Ja-

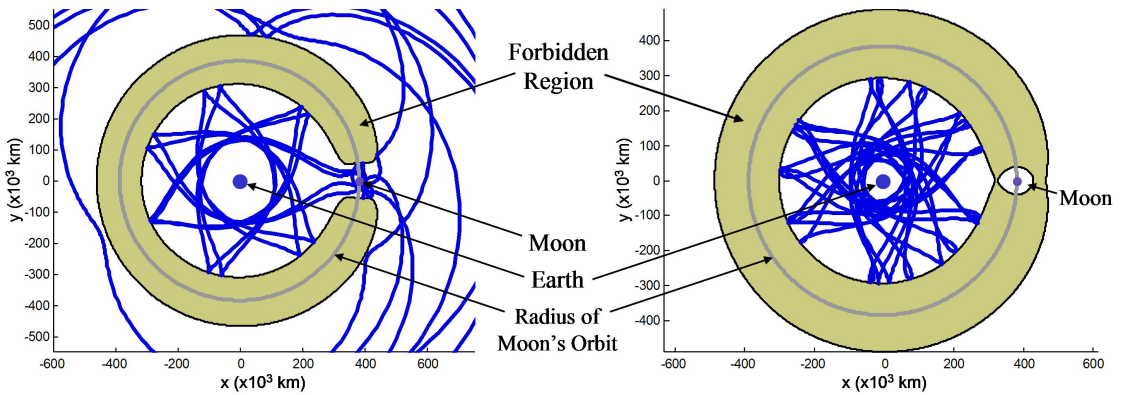


Figure 2.5: Example trajectories of particles with Jacobi constants equal to approximately 3.12 (left) and 3.19 (right) in the Earth-Moon system. The forbidden regions for the respective Jacobi constants are shaded and labeled.

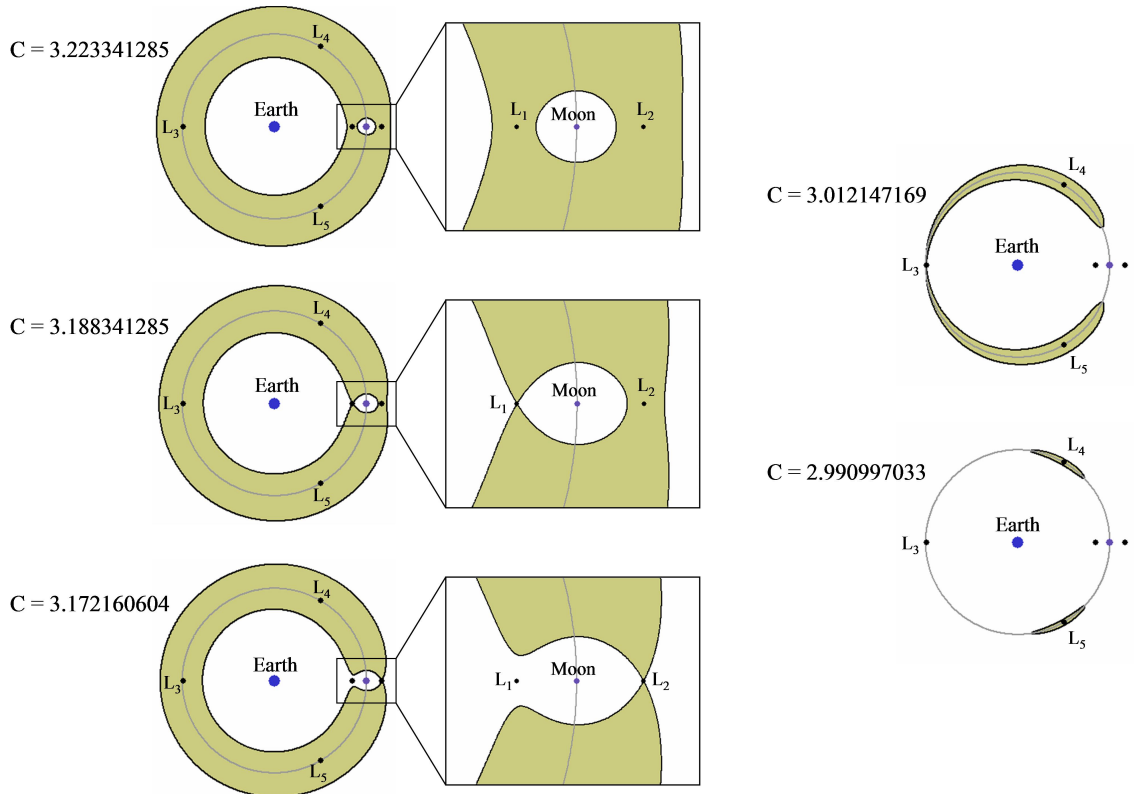


Figure 2.6: The forbidden region in the Earth-Moon system for five values of the Jacobi constant.

cobi constant lower than approximately 3.17216 is permitted to transfer to the exterior region of the Earth-Moon system through the neck at  $L_2$ . Finally, a particle is only permitted to reach any position in the system, including the  $L_4$  and  $L_5$  points, if it has a Jacobi constant lower than approximately 2.98800.

### 2.3.1.5 The Lagrange Points

The zero-velocity plots shown in Figures 2.3 and 2.4 reveal five interesting points in the state space. The contours show three saddle-points that are collinear with the Earth and Moon as well as two peaks that are off-axis: one on each side of the syzygy axis. These five points are the fixed-point equilibrium solutions to the CRTBP, commonly known as the Lagrange points. These points are the five locations in the CRTBP where the centripetal and gravitational accelerations are equal and opposite. If a particle were placed precisely at any of these points with no velocity in the synodic frame, then the particle would stay there indefinitely. However, given a slight perturbation the particle would fall off of the position due to the unstable nature of the dynamics at those locations.

In this study we adopt the nomenclature that  $L_1$  lies between the Earth and the Moon,  $L_2$  beyond the Moon,  $L_3$  beyond the Earth,  $L_4$  above the syzygy-axis, and  $L_5$  below the syzygy-axis. To further clarify any possible ambiguities between Lagrange points of several nearby three-body systems, the Earth-Moon Lagrange points are referred to as  $LL_i$ , the Sun-Earth Lagrange points are referred to as  $EL_i$ , the Sun-Mars Lagrange points  $ML_i$ , etc. Figure 2.7 shows a plot of the locations of the five Lagrange points in the Earth-Moon rotating coordinate system.

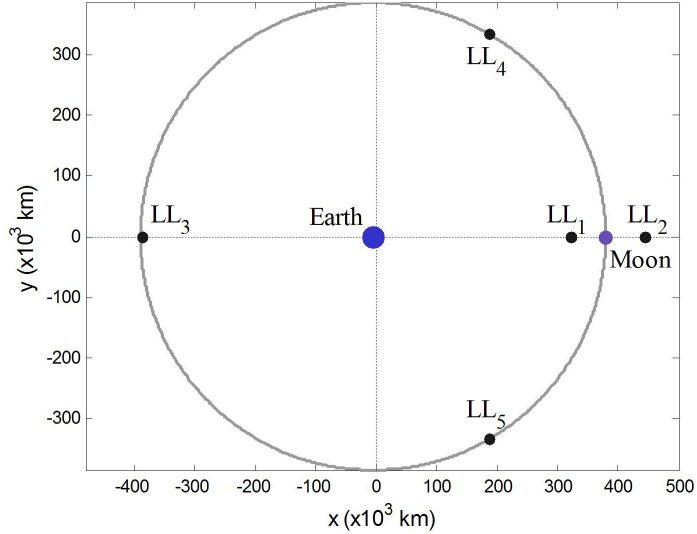


Figure 2.7: The Earth, Moon, and five Lagrange points in the rotating coordinate system of the CRTBP.

The locations of the five Lagrange points vary as functions of the mass parameter  $\mu$ . In the extreme case where  $\mu$  is equal to 0.5, the collinear Lagrange points are equally-spaced; in the case as  $\mu$  approaches zero, the two Lagrange points  $L_1$  and  $L_2$  approach the smaller primary. This dependency on the value of  $\mu$  is shown in Figure 2.8; the  $\mu$ -values of the planets in the solar system, as well as the Earth-Moon three-body system, are plotted on top of the curves for comparison. Figure 2.9 shows the  $\mu$ -values of the Jovian and Saturnian systems as well. It is clear that the Earth-Moon system is very unusual because of its high  $\mu$ -value.

The positions of  $L_4$  and  $L_5$  always make equilateral triangles with the two primaries. Analytical expressions for the collinear Lagrange points can be found in Appendix C; Szebehely (1967) provides a good description for the derivation of the analytical expressions.

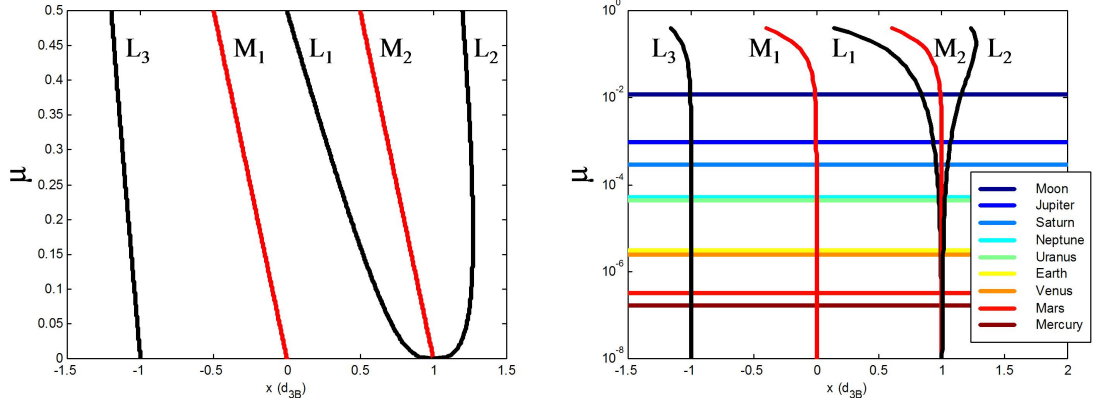


Figure 2.8: The locations of the collinear Lagrange points, the larger primary  $M_1$ , and the smaller primary  $M_2$ , as functions of the mass parameter  $\mu$ . The plots are shown on a linear axis, left, and a logarithmic axis, right. The solar system's planetary three-body mass parameters are shown on the logarithmic plot for comparison.

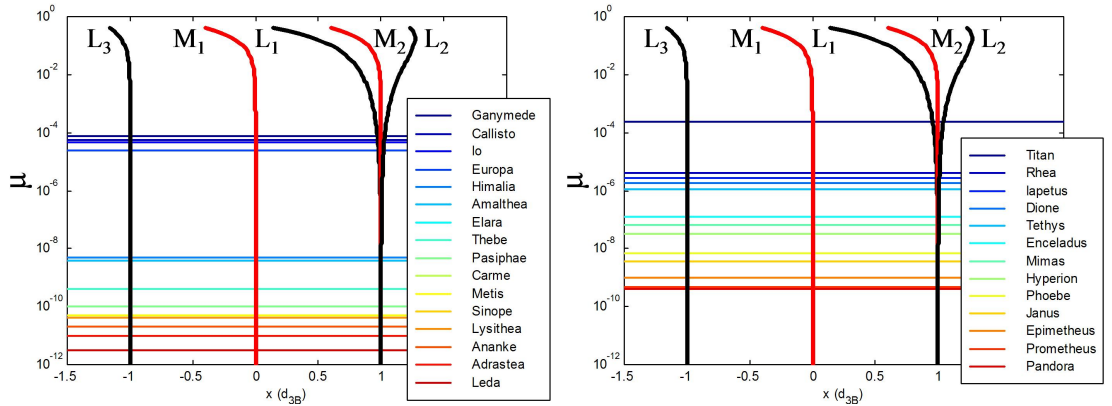


Figure 2.9: The locations of the collinear Lagrange points in the Jovian (left) and Satelian (right) three-body systems.

## 2.4 The Four-Body Problem

The Sun-Earth-Moon system is very interesting because the motion of a spacecraft in the Earth's vicinity may be significantly affected by all three bodies. A spacecraft that has enough energy to reach any of the Earth-Moon Lagrange points most likely has sufficient energy to reach the Sun-Earth Lagrange points as well. Figure 2.10

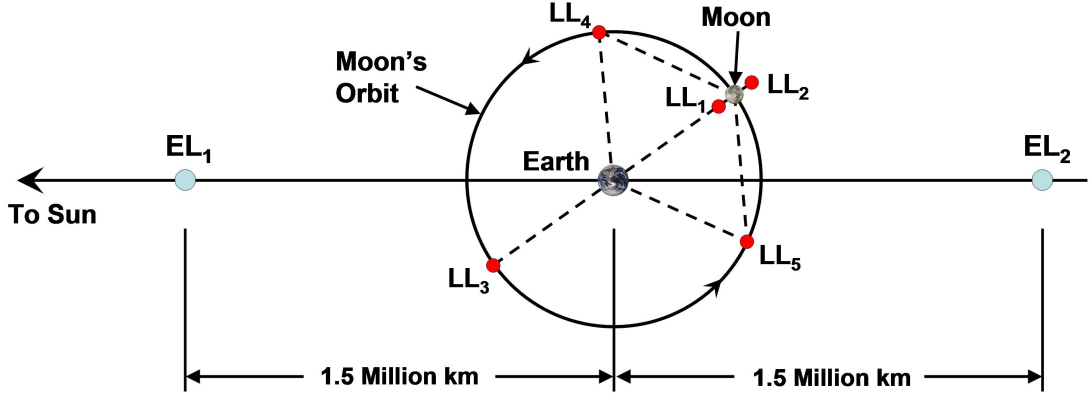


Figure 2.10: A plot depicting the relative proximity of the five Earth-Moon Lagrange points and the two nearby Sun-Earth Lagrange points. The average distance between the Earth and the Moon is equal to approximately 384,400 km (Vallado, 1997). Planetary images courtesy of NASA (2007b).

shows a plot depicting the relative proximity of the seven nearby Lagrange points.

The Sun-Earth-Moon-Spacecraft four-body problem may be approximated by many different models, including the bicircular model, the Patched Three-Body Model, and the JPL Ephemeris model. Each of these models is discussed in the following sections.

#### 2.4.1 Bicircular Model

The bicircular model artificially places the Earth and Moon in circular orbits about their barycenter and places the Sun and Earth/Moon system in circular orbits about the barycenter of the whole system. The Sun's gravity does not perturb the motion of the Earth or the Moon about their barycenter; hence the system does not satisfy Newton's equations. Nevertheless, the model may be used to approximate the true near-Earth environment, and it is a better approximation than either the Earth-Moon CRTBP or the Sun-Earth/Moon CRTBP for trajectories in the near-Earth environment.

It is useful to view trajectories in the bicircular model in three different reference

frames: the Sun-centered inertial frame, the Earth-Moon synodic reference frame (the same reference frame as the Earth-Moon CRTBP), and the Sun-Earth/Moon synodic frame. The equations of motion given in Section 2.4.1.1 are derived assuming the Earth-Moon synodic reference frame. The trajectories may then be easily converted to the other two reference frames using the conversions given in Appendix D.

#### 2.4.1.1 Equations of Motion

Gómez et al. provides a detailed description of the derivation of the equations of motion of the bicircular model (Gómez et al., 2001c). The derivation given here is abbreviated, but should be sufficient to construct the model.

We begin with the Earth-Moon CRTBP described in Section 2.3.1.1, where  $\mu$  is the mass-parameter for the Earth-Moon masses. The parameter  $m_S$  is defined to be the mass of the Sun in the same non-dimensional mass units as the Earth-Moon CRTBP. In this frame, the Earth and Moon hold still and the Sun moves about the barycenter of the Earth-Moon system on a circle with radius  $a_S$ , in non-dimensional distance units. The Sun moves with mean motion  $n_S$  such that  $a_S^3 n_S^2 = 1 + m_S$ , since both the gravitational parameter and the sum of the normalized masses of the Earth and Moon are equal to 1. The  $x$ - and  $y$ -coordinates of the Sun may then be described by  $x_S$  and  $y_S$ , respectively, given by the equations:

$$x_S = a_S \cos \theta$$

$$y_S = -a_S \sin \theta$$

where  $\theta = (1 - n_S)t + \theta_0$  and  $\theta_0$  is the value of  $\theta$  at time  $t = 0$ . The Sun remains in the same plane as the Earth and Moon at all times in this model.

The equations of motion of a massless particle in the bicircular system in the Earth-Moon synodic reference frame are then equal to the equations of motion of the same particle in the Earth-Moon CRTBP with new contributions due to the Sun,

namely:

$$\ddot{x} - 2\dot{y} - x = -(1-\mu) \frac{x+\mu}{r_{PE}^3} - \mu \frac{x-1+\mu}{r_{PM}^3} - m_S \frac{x-x_S}{r_{PS}^3} - \frac{m_S}{a_S^2} \cos \theta \quad (2.13)$$

$$\ddot{y} + 2\dot{x} - y = -(1-\mu) \frac{y}{r_{PE}^3} - \mu \frac{y}{r_{PM}^3} - m_S \frac{y-y_S}{r_{PS}^3} + \frac{m_S}{a_S^2} \sin \theta \quad (2.14)$$

$$\ddot{z} = -(1-\mu) \frac{z}{r_{PE}^3} - \mu \frac{z}{r_{PM}^3} - m_S \frac{z}{r_{PS}^3} \quad (2.15)$$

where  $r_{PE}$ ,  $r_{PM}$ , and  $r_{PS}$  are the distances between the particle and the Earth, Moon, and Sun, respectively, equal to:

$$\begin{aligned} r_{PE}^2 &= (x+\mu)^2 + y^2 + z^2 \\ r_{PM}^2 &= (x-1+\mu)^2 + y^2 + z^2 \\ r_{PS}^2 &= (x-x_S)^2 + (y-y_S)^2 + z^2 \end{aligned}$$

The bicircular model effectively bridges the gap between the Earth-Moon and the Sun-Earth/Moon circular restricted three-body systems and does so in a simple, computationally efficient manner. The main disadvantage of the bicircular model is that it destroys simple solutions that exist in the CRTBP without providing the realism of more-complicated models, such as the JPL ephemeris model.

#### 2.4.2 Patched Three-Body Model

The Patched Three-Body Model uses purely three-body dynamics to model the motion of a spacecraft in the Sun-Earth-Moon-Spacecraft four-body system. When the spacecraft is near the Moon, the spacecraft's motion is modeled by the Earth-Moon three-body system. Otherwise, the spacecraft's motion is modeled by the Sun-Earth/Moon three-body system. For simplicity it is assumed that the Earth-Moon system is coplanar with the Sun-Earth system. The boundary of these two systems is referred to as the three-body sphere of influence (3BSOI), and is computed much like the two-body sphere of influence. Once the spacecraft breaches the 3BSOI, its state is transferred to the other three-body system. In this way, a spacecraft in the near-Earth

environment may be affected by all three massive bodies, but the desirable characteristics of the CRTBP may be exploited during mission planning. Like the patched-conic method of constructing interplanetary missions, the Patched Three-Body Model ignores the small gravitational perturbations that exist in order to use well-known mission analysis tools. Then, once a trajectory has been constructed that meets mission requirements, the trajectory is transferred into a more realistic model of the solar system.

#### 2.4.2.1 Three-Body Sphere of Influence (3BSOI)

A body's sphere of influence (SOI) is qualitatively described as the region of space within which the motion of a particle is governed more by its gravity than by any other gravitational body. If a spacecraft's motion is influenced by two massive bodies, then its motion is characterized by Equation 2.7 (repeated here as Equation 2.16), namely:

$$\ddot{\vec{r}}_{\oplus-\mathcal{S}} = -\frac{G(m_{\oplus} + m_{\mathcal{S}})}{r_{\oplus-\mathcal{S}}^3} \vec{r}_{\oplus-\mathcal{S}} + Gm_{\mathcal{C}} \left( \frac{\vec{r}_{\mathcal{S}-\mathcal{C}}}{r_{\mathcal{S}-\mathcal{C}}^3} - \frac{\vec{r}_{\oplus-\mathcal{C}}}{r_{\oplus-\mathcal{C}}^3} \right). \quad (2.16)$$

The first term in Equation 2.16 is the dominant 2-body equation of motion and the second term is the perturbation due to the second massive body. In this case the dominant primary is the Earth ( $m_{\oplus}$ ), the perturbing body is the Moon ( $m_{\mathcal{C}}$ ), and the mass of the spacecraft,  $m_{\mathcal{S}}$ , may be effectively ignored. The Moon's SOI is thus characterized by the surface in space where the spacecraft's motion is equally affected by the Earth and the Moon, namely, the set of all  $r_{\oplus-\mathcal{S}}$  values that make the following expression true:

$$\frac{G(m_{\oplus} + m_{\mathcal{S}})}{r_{\oplus-\mathcal{S}}^3} \vec{r}_{\oplus-\mathcal{S}} = Gm_{\mathcal{C}} \left( \frac{\vec{r}_{\mathcal{S}-\mathcal{C}}}{r_{\mathcal{S}-\mathcal{C}}^3} - \frac{\vec{r}_{\oplus-\mathcal{C}}}{r_{\oplus-\mathcal{C}}^3} \right) \quad (2.17)$$

After some simplifications, the Moon's SOI is roughly equal to a sphere centered at the

Moon with a radius equal to  $r_{SOI}$ :

$$r_{SOI} \approx a_{\mathbb{C}} \left( \frac{m_{\mathbb{C}}}{m_{\oplus}} \right)^{2/5}$$

where  $a_{\mathbb{C}}$  is equal to the semimajor axis of the Moon's orbit about the Earth. The radius of the Moon's sphere of influence is therefore equal to approximately 66,000 km. Hence, the motion of a spacecraft within about 66,000 km of the Moon is dominated by the Moon's gravity, and the Earth is the perturbing third body.

The general approximation of a body's sphere of influence with respect to the body that it's orbiting is equal to:

$$r_{SOI} \approx a_2 \left( \frac{m_2}{m_1} \right)^{2/5} \quad (2.18)$$

where  $m_2$  is the mass of the minor body, in an elliptical orbit about the major body  $m_1$  with a semimajor axis equal to  $a_2$ .

If one is interested in transferring from one three-body system to another, one is interested in finding some relationship that describes the strength of one primary in the first three-body system relative to another primary in the second three-body system. For example, let's say we are interested in computing the Earth-Moon three-body sphere of influence, i.e., the surface where we would transfer from the Earth-Moon three-body system to the Sun-Earth/Moon three-body system, and vice versa. One way to do this is to compute the surface where the third-body perturbation of the Sun and the third-body perturbation of the Moon are equal, namely, the distance  $r_{S-\mathbb{C}}$  such that the following expression is true:

$$Gm_{\oplus} \left( \frac{\vec{r}_{S-\odot}}{r_{S-\odot}^3} - \frac{\vec{r}_{\oplus-\odot}}{r_{\oplus-\odot}^3} \right) = Gm_{\mathbb{C}} \left( \frac{\vec{r}_{S-\mathbb{C}}}{r_{S-\mathbb{C}}^3} - \frac{\vec{r}_{\oplus-\mathbb{C}}}{r_{\oplus-\mathbb{C}}^3} \right), \quad (2.19)$$

where the symbol  $\odot$  represents the Sun. The surface that includes all values of  $r_{S-\mathbb{C}}$  that make Equation 2.19 true is approximately equal to a sphere centered at the Moon with a radius of 20,240 km. The radius of the Moon is approximately equal to 1,738 km; hence this 3BSOI is not a lot larger than the Moon. In fact, this sphere doesn't

even contain the lunar Lagrange points. However, Equation 2.19 does not include any information about the motion or timescale in the dynamics of the system. The Sun's gravitational perturbation may be stronger, since it is responsible for keeping the Earth, Moon, and spacecraft in their heliocentric orbits, but the timescale corresponding with the Sun's perturbation is so much longer than the Moon's perturbation's timescale that in the short run, the Moon will still oftentimes influence a spacecraft's motion outside of this sphere greater than the Sun. For this reason, we have adopted another form to approximate the Earth-Moon three-body sphere of influence.

The form we have used to approximate the Earth-Moon 3BSOI is that of Equation 2.18, where the dominant body,  $m_1$ , is the Sun and the secondary body,  $m_2$ , is the Moon. In this form the Earth is treated as a perturbing body. Using this relationship, the 3BSOI may be approximated as a sphere centered at the Moon with a radius equal to about 159,198 km. A sphere of that radius centered at the Moon includes the Moon's  $L_1$  and  $L_2$  points, but not the other three Lagrange points. This is satisfactory for the purposes of this study, and is consistent with other studies (e.g., Yamakawa et al., 1993), but should be further studied for missions that require use of the other three Lagrange points. This model is further validated in Section 5.8 when trajectories are compared between the Patched Three-Body model using this formulation of the 3BSOI and the more-realistic JPL Ephemeris model of the solar system.

#### **2.4.2.2 Passing Through the 3BSOI Boundary**

A particle's Earth-Moon Jacobi constant,  $C_{EM}$ , remains constant while the particle's motion remains within the Earth-Moon 3BSOI boundary; however, the value of  $C_{EM}$  will change over time once the particle passes through the 3BSOI. Conversely, the particle's Sun-Earth/Moon Jacobi constant,  $C_{SE}$ , will vary in time while the particle travels within the Earth-Moon three-body system; the value of  $C_{SE}$  becomes fixed once the particle pierces the 3BSOI and enters the Sun-Earth/Moon three-body system. It

is interesting to consider that as the particle is about to pass from the Earth-Moon three-body system into the Sun-Earth/Moon three-body system, the fixed value of  $C_{SE}$  depends on where the particle crosses the 3BSOI. In a similar sense, the particle could theoretically depart the Earth-Moon three-body system with one value of  $C_{EM}$  and re-enter the system at a later time with a new value of  $C_{EM}$ .

This change in Jacobi constant suggests several things about mission designs in the four-body system. First off, if a trajectory is being designed to pass through the 3BSOI boundary, then mission designers have a range of Jacobi constant values that they can target, yielding much different orbits. Secondly, mission designers may use the Earth-Moon three-body system to change the spacecraft's Sun-Earth/Moon Jacobi energy, or vice versa, in a similar way that a gravity swingby about a planet changes a spacecraft's heliocentric energy.

## 2.5 The Full Solar System

The full solar system differs from the previously-described models in several ways. First off, there are many massive bodies that contribute gravitational forces to a particle. In general, the gravitational influence of all additional bodies apart from those already being modeled is small and can normally be safely neglected when performing a preliminary trajectory design. More importantly, the planets and moons in the real solar system are not in circular, coplanar orbits. The non-zero eccentricities and non-zero inclinations of real orbits leads to the most dramatic deviations in a trajectory that is being compared in several models.

### 2.5.1 JPL Ephemeris Model

The JPL Ephemeris model being used in this dissertation is the JPL Planetary and Lunar Ephemerides, "DE405/LE405," which was constructed in 1998 (Standish, 1998). The model uses the International Celestial Reference Frame as its coordinate

system. As of 2006, the model has included ephemerides of the positions and velocities of the Sun, the four terrestrial planets, the four gas-giant planets, the Pluto/Charon system, and the Moon, as well as ephemerides for a pair of nutation angles and the three physical libration angles for the Moon. Standish claims that the entire ephemeris system of DE405 for the inner planets is accurate to approximately 0.001 arcseconds, which was verified by the 0.001-arcsecond error in the ephemeris upon the arrival of the Pathfinder spacecraft at Mars in July 1997 (Standish, 1998).

The ephemerides are stored in files as Tchebyshev coefficients. The interpolation scheme given here is fully explained by Hoffman in the User's Manual of the JPL Ephemeris DE405 system (Hoffman, 1998).

Each component of the position of a body in the ephemeris, as well as each libration or nutation angle, at a given moment in time is given by a Tchebyshev series. For instance, the  $x$ -component of the position vector of a body at a time  $t$  may be interpolated using the summation:

$$R_x(t) = \sum_{k=0}^n a_k T_k(t), \quad (2.20)$$

where the functions  $T_k(t)$  are Tchebyshev polynomials of the first kind and the coefficients  $a_k$  are stored in the ephemeris data files. Each component of the velocity of a body in the ephemeris at a given moment in time is given by a slightly different Tchebyshev series. This new series is constructed from the derivative of the series given in Equation 2.20. For instance, the  $x$ -component of the velocity vector of a body at a time  $t$  may be interpolated using the summation:

$$V_x(t) \equiv \dot{R}_x(t) = \sum_{k=0}^n a_k \dot{T}_k(t), \quad (2.21)$$

where the derivatives of the Tchebyshev polynomials are given by:

$$\dot{T}_k(t) = k U_{k-1}(t). \quad (2.22)$$

The function  $U_k(t)$  is known as a Tchebyshev polynomial of the second kind. The

definition of the Tchebyshev polynomials of the first and second kinds are given as:

$$T_k(t) = \cos(k \cos^{-1} t) \quad (2.23)$$

$$U_k(t) = \frac{\sin((k+1)\cos^{-1} t)}{\sin(\cos^{-1} t)} \quad (2.24)$$

The time,  $t$ , used in the JPL Ephemeris is a normalized time, such that  $-1 \leq t \leq 1$ . If  $JD$  is the Julian date at the interpolation epoch,  $JD_0$  is the Julian date of the start of the coefficient granule (Hoffman, 1998), and  $\Delta T$  is the interval spanned by the coefficient record, then the time  $t$  may be computed using the equation:<sup>2</sup>

$$t = \frac{JD - JD_0}{\Delta T} - 1. \quad (2.25)$$

The International Celestial Reference Frame (ICRF) is consistent with the FK5 J2000.0 optical reference frame, within the limits of the link accuracy (Ma et al., 1998). Hence, the axes are oriented with respect to the Earth's mean equatorial orientation at noon on January 1st, 2000 terrestrial time. The ICRF is a quasi-inertial reference frame that is defined using radio observations of the positions of 212 extragalactic sources in the sky (Ma et al., 1998). The sources are distributed across the entire sky. The observations are made using very long baseline interferometry and are accurate to within one milli-arcsecond in both coordinates. Appendix D describes the process of converting between the ICRF coordinate frame and the standard synodic reference frame.

## 2.6 Discussion

This dissertation studies the three-body problem using dynamical systems theory. Hence, the majority of the work is performed using the circular restricted three-body model. The initial designs of ballistic lunar transfers are also constructed in the CRTBP, even though they involve the gravitational influences of the Earth, Moon, and Sun. To use the dynamical systems tools, such transfers are constructed in the Patched

---

<sup>2</sup> Note: this equation may be missing a factor of two in the numerator. If  $JD$  exists in the range  $JD_0 \leq JD \leq JD_0 + \Delta T$ , then the equation should read  $t = 2(JD - JD_0)/\Delta T - 1$ .

Three-Body model of the Earth's vicinity. Finally, any trajectory in this dissertation that requires validation, e.g., any trajectory that could be proposed for a real practical mission, is then re-constructed in the JPL Ephemeris model of the solar system. This re-construction demonstrates that although the design-work is completed using a simplified model of the solar system, most trajectories indeed exist in the real solar system, albeit somewhat perturbed.

## **Chapter 3**

### **Methodology**

#### **3.1 Introduction**

This chapter discusses the methodology used in this dissertation for modeling, analyzing, and constructing three-body orbits and low-energy orbit transfers. Orbit transfers in the three-body problem are much different than orbit transfers in the two-body problem. The two-body problem's conic solutions yield well-characterized orbit transfers, such as Hohmann Transfers, bi-elliptical transfers, and the various solutions to Lambert's Problem (Vallado, 1997). Orbit transfers built in the three-body problem, however, are not well-characterized since there is a lack of any analytical solution to the three-body problem. Mission designers and researchers have had to choose a method to combat the problem; each method yields certain classes of solutions and misses others.

Dynamical systems methods have been shown to be useful when constructing transfers to/away from periodic orbits in the three-body problem. As introduced in Section 1.4.5, McGehee studied homoclinic transfer trajectories, i.e., trajectories that could be used to take a particle off of a periodic orbit and then return the particle back onto that same orbit at a later time (McGehee, 1969). By 2000, several papers had been published describing heteroclinic transfer trajectories, e.g., transfers between different three-dimensional libration orbits (see, e.g., Gómez and Masdemont 2000 and Koon et al. 2000a). Homoclinic and heteroclinic orbit transfers are generally constructed us-

ing dynamical systems theory.

This chapter introduces the fundamentals of dynamical systems theory in Section 3.2. This discussion leads into an exploration of several types of orbit solutions to the circular restricted three-body problem in Section 3.3. Many tools are required in order to construct periodic orbits and orbit transfers using dynamical systems theory. Sections 3.4 – 3.8 discuss many of these tools and procedures to use them. A discussion about how to construct the set of an orbit’s invariant manifolds is given in Section 3.9. From there, one has the tools needed to produce orbit transfers. Section 3.10 provides a discussion and examples about how to build transfers from the surface of a body to a three-body orbit and transfers between three-body orbits. There is considerable interest in orbit transfers that result in one body becoming captured by another body. Furthermore, many authors use very different definitions of what it means to be captured or temporarily captured by another body. Section 3.11 discusses these definitions and provides some examples of ballistic mechanisms that result in different types of captured trajectories. Finally, Section 3.12 provides an overall discussion about how the methodology presented in this chapter may be used to construct practical interplanetary trajectories.

### 3.2     Dynamical Systems Theory

A dynamical system may be described as a state space with a set of rules, where the rules govern the evolution of objects’ states through time within the system. The rules are deterministic; that is, the evolution of a state through a particular amount of time yields only one future state.

There are different types of dynamical systems depending on the mathematics involved and the allowable values of time. If time is continuous, capable of taking any value in the set of real numbers, then the dynamical system is smooth and is called a **flow**. If time may only take discrete values, then the dynamical system is a **map**.

The CRTBP and other models of the solar system are generally described by flows. A particle's trajectory in such dynamical systems is the set of states that the particle will take as it moves through time given its initial state. When integrating the equations of motion for a particle through time using a machine, time cannot truly take on any value in the set of real numbers. The process of integration is a mapping of the particle's state from one point in the state space to another point. A spacecraft's mapped trajectory is therefore only an approximation of the true trajectory.

There are many techniques that are commonly used to analyze dynamical systems. In this dissertation, we begin our analysis of the CRTBP by identifying fixed points and periodic orbits that exist in the system. We continue by studying the stability of those solutions. These techniques provide an understanding of the motion of trajectories near those solutions. Further analysis gradually provides more information about the motion of trajectories throughout the dynamical system.

### 3.3 Solutions to the CRTBP

The CRTBP is a good example of a system in which dynamical systems methods of analysis work well. The CRTBP contains five fixed-point solutions and an infinite quantity of periodic orbit solutions. The characterization of these solutions helps to understand the flow of particles in the system. Useful trajectories may then be constructed that take advantage of the flow in the system, rather than forcing their way through the system. The following sections describe some of the simplest solutions to the CRTBP.

#### 3.3.1 Fixed-Point Solutions: Five Lagrange Points

The most basic solutions to the CRTBP are fixed-point solutions, that is, the trajectories in the CRTBP that particles may follow such that they stay at rest in the system indefinitely. There are five such fixed-point solutions in the CRTBP, namely, the five La-

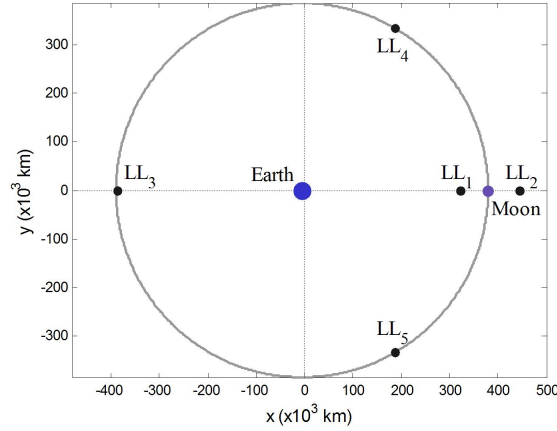


Figure 3.1: The locations of the five Lagrange points in the Earth-Moon CRTBP.

grange points. These points were introduced in Section 2.3.1.5 and are displayed again in Figure 3.1 for the case of the Earth-Moon CRTBP.

The locations of the five Lagrange points in the Sun-Earth and Earth-Moon circular three-body systems are given in Table 3.1, using the planetary masses and distances provided in Section 2.3.1.

Table 3.1: The locations of the five Lagrange points in the Sun-Earth and Earth-Moon circular three-body systems. The positions are given in non-dimensional normalized units and kilometers with respect to the barycenter of the system, assuming the masses and distances given in Section 2.3.1.

Lagrange Point	Position in normalized units			Position in kilometers		
	$x$	$y$	$z$	$x$	$y$	$z$
Sun-Earth	$L_1$	0.9899860052	0	0	148,099,797.7	0
	$L_2$	1.0100751768	0	0	151,105,095.0	0
	$L_3$	-1.000001267	0	0	-149,598,059.5	0
	$L_4$	0.4999969596	0.8660254038	0	74,798,480.2	129,555,555.8
	$L_5$	0.4999969596	-0.8660254038	0	74,798,480.2	-129,555,555.8
Earth-Moon	$L_1$	0.8369150363	0	0	321,710.140	0
	$L_2$	1.1556822354	0	0	444,244.251	0
	$L_3$	-1.0050626534	0	0	-386,346.084	0
	$L_4$	0.4878493962	0.8660254038	0	187,529.308	332,900.165
	$L_5$	0.4878493962	-0.8660254038	0	187,529.308	-332,900.165

### 3.3.2 Sample Periodic and Quasiperiodic Orbit Solutions

The CRTBP permits the existence of numerous families of periodic and quasiperiodic orbits. Appendices A and B provide many examples of families of two-dimensional and three-dimensional periodic orbits that exist. Many other classes of orbits also exist. In this section, we demonstrate how to analytically construct one set of periodic and quasiperiodic orbits that exist about each of the collinear Lagrange points. This demonstration sheds light on why many of the orbits in Appendices A and B exist. Several authors have described this analytical construction in various forms, including Moulton (1920), Richardson (1980), and Howell and Pernicka (1988).

We begin by translating the origin of the synodic frame to one of the collinear libration points  $L_i$ . The parameter  $\gamma$  is defined to be equal to the distance from  $L_i$  to the smaller primary. The value of  $\gamma$  is positive when referring to  $L_2$  and negative when referring to  $L_1$  and  $L_3$ . The new position coordinates  $x'$ ,  $y'$ , and  $z'$  are thus defined by the following:

$$\begin{aligned}x' &= x - (1 - \mu + \gamma) \\y' &= y \\z' &= z\end{aligned}$$

If we now linearize the equations of motion of the CRTBP given in Equations 2.8 – 2.10 under this transformation, we find the following:

$$\begin{aligned}\ddot{x}' - 2\dot{y}' - (1 + 2c)x' &= 0 \\ \ddot{y}' + 2\dot{x}' + (c - 1)y' &= 0 \\ \ddot{z}' + cz' &= 0\end{aligned}\tag{3.1}$$

where  $c$  is a constant coefficient. The analytical solution to the out-of-plane  $z$  motion describes simple harmonic motion. The solution for the in-plane  $x - y$  motion involves a characteristic equation that has two real roots and two imaginary roots. The roots

represent modes of motion: one divergent and one nondivergent. If the nondivergent mode is excited, then the solution is bounded and may be written as:

$$\begin{aligned}x' &= -kA_y \cos(\lambda t + \phi) \\y' &= A_y \sin(\lambda t + \phi) \\z' &= A_z \sin(\nu t + \psi)\end{aligned}\tag{3.2}$$

This motion is described by six variables: the amplitudes of the in-plane and out-of-plane motion  $A_y$  and  $A_z$ , the frequency of oscillation in the in-plane and out-of-plane motion  $\lambda$  and  $\nu$ , and the phase angles for the in-plane and out-of-plane motion  $\phi$  and  $\psi$ . The linearized approximation to the analytical solution for periodic motion about a Lagrange point may thus be characterized by oscillatory motion. If the two frequencies  $\lambda$  and  $\nu$  are equal or otherwise commensurate, the resulting motion will be periodic; if the frequencies are incommensurate, the resulting motion will be quasiperiodic. The periodic orbits whose frequencies are **equal** are known as Halo orbits, the more general quasiperiodic trajectories are known as Lissajous orbits or quasi-Halo orbits. A portion of the family of Halo orbits about the Earth-Moon  $L_2$  is shown in Figure 3.2, and characteristic views of several types of Lissajous orbits are shown in Figure 3.3.

It should also be noted that there is a symmetry that exists in the CRTBP. If the CRTBP permits an orbit to exist, then it also permits a symmetric orbit to exist that is a reflection across the  $x - y$  plane. Hence, there are two families of Halo orbits: a Northern and a Southern family. By convention, if a spacecraft spends more than half of its time above the  $x - y$  plane in an average Halo orbit, then the spacecraft is in orbit about a Northern Halo orbit.

If  $A_z$  is set to zero in Equation 3.2 the resulting orbits are planar and are known as Lyapunov orbits. Figure 3.4 shows a portion of the family of Lyapunov orbits about  $L_2$  in the Earth-Moon system.

These orbits may be constructed analytically since the linearization process near

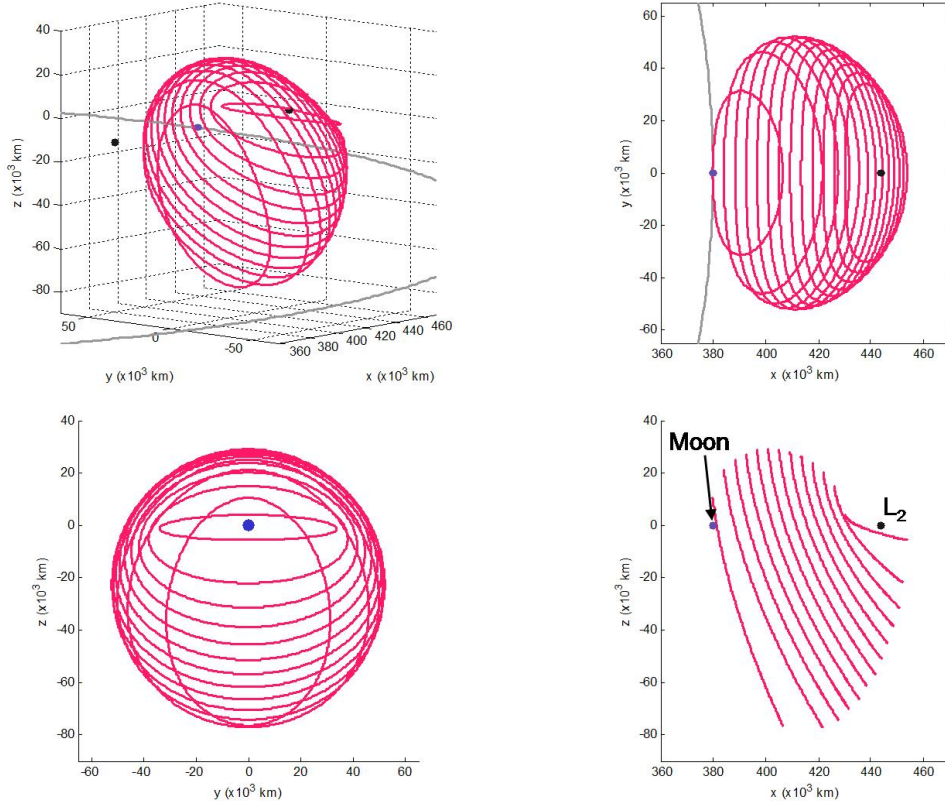


Figure 3.2: A portion of the family of Halo orbits about  $L_2$  in the Earth-Moon system, shown from four perspectives.

one of the Lagrange points produces a good approximation of the true dynamics found in the system. Other orbits presented in Appendices A and B do not have as good of a linear approximation and must be constructed numerically. The process of numerically constructing simple periodic orbits is discussed in Section 3.6.

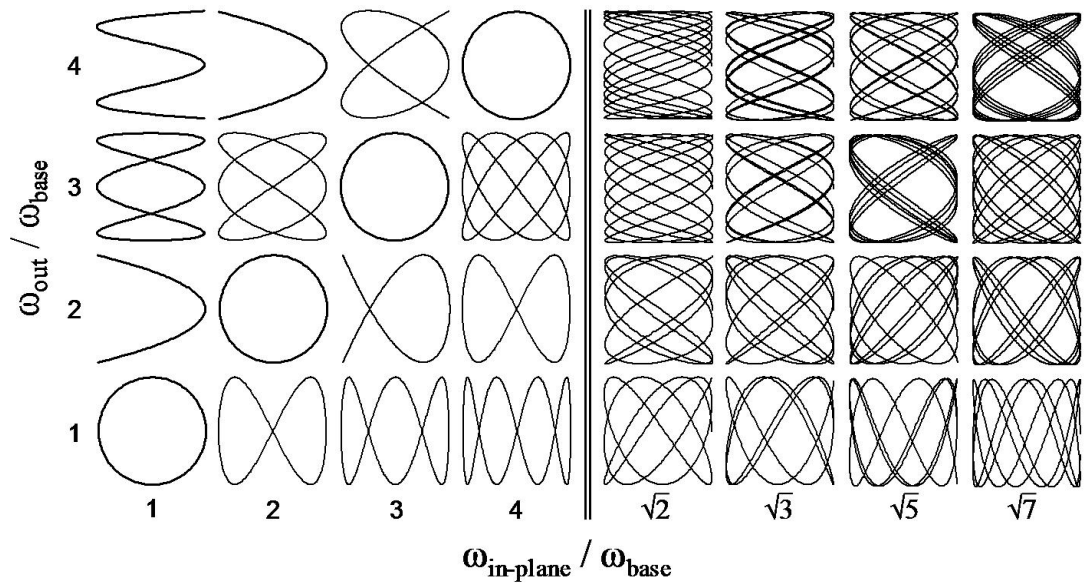


Figure 3.3: A sample of Lissajous curves representing the view of Lissajous orbits in the Earth-Moon system viewed in the  $y - z$  plane;  $\omega_{\text{in-plane}}$  and  $\omega_{\text{out}}$  are multiples of some base frequency  $\omega_{\text{base}}$ . The curves on the left are perfectly periodic; the curves on the right have incommensurate frequencies and have only been propagated for a short amount of time.

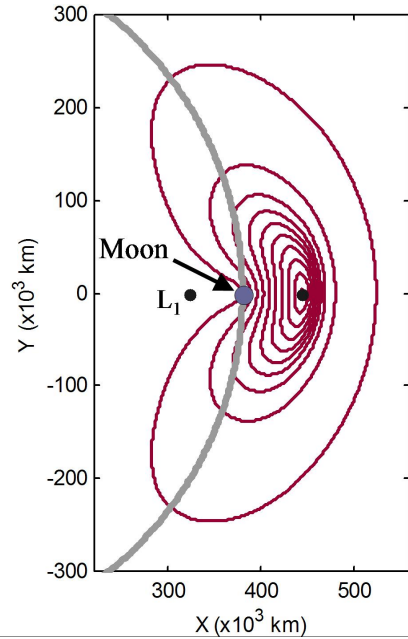


Figure 3.4: A portion of the family of Lyapunov orbits about  $L_2$  in the Earth-Moon system.

### 3.3.3 Orbit Parameters

An orbit and a position in that orbit may be uniquely specified in the two-body problem using six parameters. Typical sets of two-body parameters include the Cartesian and Keplerian sets. Parameterization of orbits in the three-body problem has proven to be much more difficult, since there are no general analytical solutions to the system. Dynamical systems theory is very useful in this regard because the methodology lends itself to many useful parameters. One such parameter,  $\tau$ , is useful when describing periodic orbit solutions to the CRTBP. This parameter is described here; others are introduced in later chapters as their uses become apparent.

The parameter  $\tau$  mimics the two-body mean anomaly. When a spacecraft is following a perfectly periodic orbit in the CRTBP, its position along that orbit may be identified by  $\tau$ . In some studies, e.g., Hill et al. (2006b),  $\tau$  takes on values in the range of  $0 - 360$  degrees or  $0 - 2\pi$  radians, much like the mean anomaly. In this study,  $\tau$  is defined to take on values in the range of  $0 - 1$ , indicating the periodic revolution number. Most libration orbits, e.g., Halo and Lyapunov orbits, have a shape that resembles a conic section; in those cases it makes the most sense to use an angular unit of measurement for  $\tau$ . However, in this study there are many classes of periodic orbits that do not resemble any sort of conic section and it may be confusing to refer to  $\tau$  in angular units. Hence, for this study,  $\tau$  is represented in revolution numbers. Figure 3.5 shows two orbits, demonstrating how  $\tau$  advances along each orbit.

## 3.4 The State Transition and Monodromy Matrices

The state transition matrix  $\Phi(t, t_0)$  monitors the divergent dynamics along a trajectory. Essentially, it approximates how a slight deviation in any of the state variables propagates along the trajectory. Its practical uses are twofold in this study: (1) to provide a means of adjusting the initial conditions of a trajectory to correct for unwanted

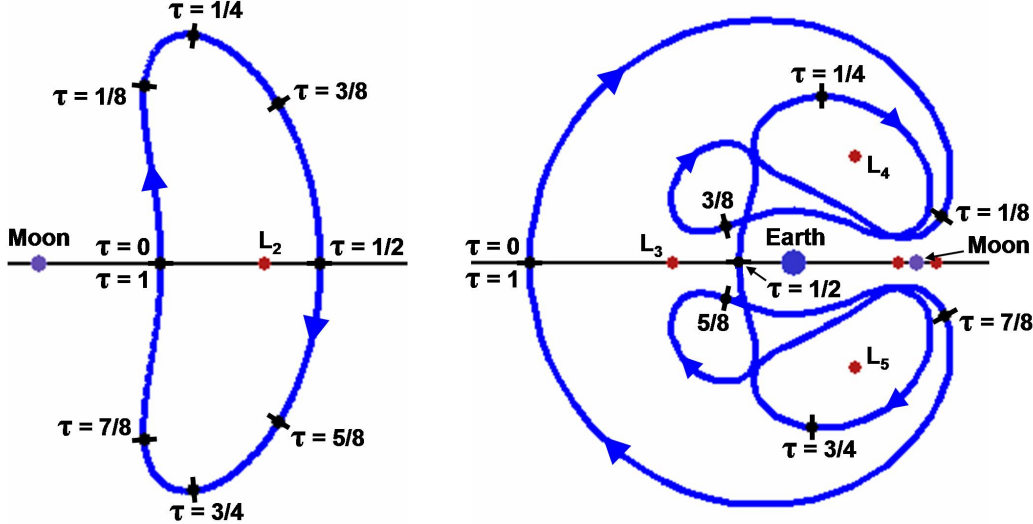


Figure 3.5: The two orbits shown demonstrate how the parameter  $\tau$  moves from 0 to 1 about an orbit.

motion, and (2) to provide information about the stability of an orbit, including the orientation of the eigenvectors along the orbit. The second use involves the **monodromy matrix**, a special case of the state transition matrix. We will explore (1) in Sections 3.5 and 3.6 and (2) in Sections 3.8 and 3.9. This section discusses how to construct the state transition matrix and the monodromy matrix.

Let us define the state vector  $\mathbf{X}$  to be a column vector that contains all of the state variables of interest in the system. In the CRTBP, one is usually only interested in computing the six state variables of the third body in the three-body system. Hence,  $\mathbf{X}$  is defined as:

$$\mathbf{X} = [x \quad y \quad z \quad \dot{x} \quad \dot{y} \quad \dot{z}]^T.$$

Then the state transition matrix is a  $6 \times 6$  matrix composed of the partial derivatives of the state:

$$\Phi(t, t_0) = \frac{\partial \mathbf{X}(t)}{\partial \mathbf{X}(t_0)}, \quad (3.3)$$

with initial conditions  $\Phi(t_0, t_0) = I$ . The state transition matrix is propagated using

the following relationship:

$$\dot{\Phi}(t, t_0) = A(t)\Phi(t, t_0), \quad (3.4)$$

where the matrix  $A(t)$  is equal to:

$$A(t) = \frac{\partial \dot{\mathbf{X}}(t)}{\partial \mathbf{X}(t)}. \quad (3.5)$$

In the CRTBP,  $A(t)$  is equal to:

$$A(t) = \begin{bmatrix} 0 & I \\ U_{XX} & 2\Omega \end{bmatrix}, \quad \text{where} \quad \Omega = \begin{bmatrix} 0 & 1 & 0 \\ -1 & 0 & 0 \\ 0 & 0 & 0 \end{bmatrix}, \quad (3.6)$$

and  $U_{XX}$  is the symmetric matrix composed of second partial derivatives of  $U$  with respect to the third body's position evaluated along the orbit:

$$U_{XX} = \begin{bmatrix} \frac{\partial \ddot{x}}{\partial x} & \frac{\partial \ddot{x}}{\partial y} & \frac{\partial \ddot{x}}{\partial z} \\ \frac{\partial \ddot{y}}{\partial x} & \frac{\partial \ddot{y}}{\partial y} & \frac{\partial \ddot{y}}{\partial z} \\ \frac{\partial \ddot{z}}{\partial x} & \frac{\partial \ddot{z}}{\partial y} & \frac{\partial \ddot{z}}{\partial z} \end{bmatrix}. \quad (3.7)$$

The monodromy matrix,  $M$ , exists for periodic orbits and is computed by propagating the state transition matrix one entire orbit:  $M = \Phi(t_0 + P, t_0)$  (see, e.g., Nayfeh and Balachandran, 1995). After being propagated for a full orbit, the matrix contains information about every region that a particle would pass through along that orbit. This matrix's use is further explored in Sections 3.8 and 3.9.

### 3.5 Differential Correction

Differential correction is a process by which the state transition matrix is used to change a set of initial conditions in order to better satisfy a set of criteria. It is a targeting scheme that converges on its constraints very swiftly within the basin of convergence. Two types of differential correction routines are used in this research: single-shooting and multiple-shooting correction routines.

### 3.5.1 Single-Shooting Differential Correction

In the standard single-shooting differential correction routine used in this research, a spacecraft begins at some state  $\mathbf{X}_0$ , following a nominal trajectory  $T(t)$ , where  $\mathbf{X}_0$  is composed of a position vector  $\mathbf{R}_0$  and a velocity vector  $\mathbf{V}_0$ . It is desired that the spacecraft's trajectory be shifted such that at a later time  $t_f$ , the trajectory encounters a desired state  $\hat{\mathbf{X}}_f$  (including a desired position vector  $\hat{\mathbf{R}}_f$  and a velocity vector  $\hat{\mathbf{V}}_f$ ). There are usually two constraints to the problem: (1) that the spacecraft's initial position may not change, and (2) that the spacecraft's new trajectory leads it to a final specified position vector  $\hat{\mathbf{R}}_f$ . The routine is allowed to vary the initial velocity of the spacecraft (simulating a  $\Delta V$  in the mission design), and is oftentimes allowed to vary the time at which the spacecraft arrives at its final desired position. The velocity of the spacecraft at the final position is usually a free variable and mission designers typically plan to perform an additional  $\Delta V$  at that time. If the routine converges, a new ballistic trajectory is constructed,  $\hat{T}(t)$ , that satisfies the two conditions:

$$\hat{T}(\hat{t}_0) = \hat{\mathbf{X}}_0 \quad \text{with } \hat{t}_0 = t_0, \hat{\mathbf{R}}_0 = \mathbf{R}_0, \text{ and } \hat{\mathbf{V}}_0 \text{ free}$$

$$\hat{T}(\hat{t}_f) = \hat{\mathbf{X}}_f \quad \text{with } \hat{t}_f \text{ constrained or fixed, } \hat{\mathbf{R}}_f \text{ constrained, and } \hat{\mathbf{V}}_f \text{ free}$$

This routine is diagrammed in Figure 3.6.

The single-shooting method uses the state transition matrix  $\Phi(t_f, t_0)$  to estimate what change to make in the initial velocity of the state,  $\Delta \mathbf{V}_0$ , in order to eliminate the deviation in position at the end of the trajectory  $\delta \mathbf{R}_f$ . The state transition matrix maps perturbations in the state over time using the following linearized equations:

$$\begin{aligned} \delta \mathbf{X}_f &= \Phi(t_f, t_0) \Delta \mathbf{X}_0 \quad \text{or} \\ \begin{bmatrix} \delta \mathbf{R}_f \\ \delta \mathbf{V}_f \end{bmatrix} &= \begin{bmatrix} \Phi_{RR}(t_f, t_0) & \Phi_{RV}(t_f, t_0) \\ \Phi_{VR}(t_f, t_0) & \Phi_{VV}(t_f, t_0) \end{bmatrix} \begin{bmatrix} \Delta \mathbf{R}_0 \\ \Delta \mathbf{V}_0 \end{bmatrix} \end{aligned} \quad (3.8)$$

Since  $\Delta \mathbf{R}_0 = 0$  and  $\delta \mathbf{V}_f$  is unconstrained, we may simplify Equation 3.8 and solve for

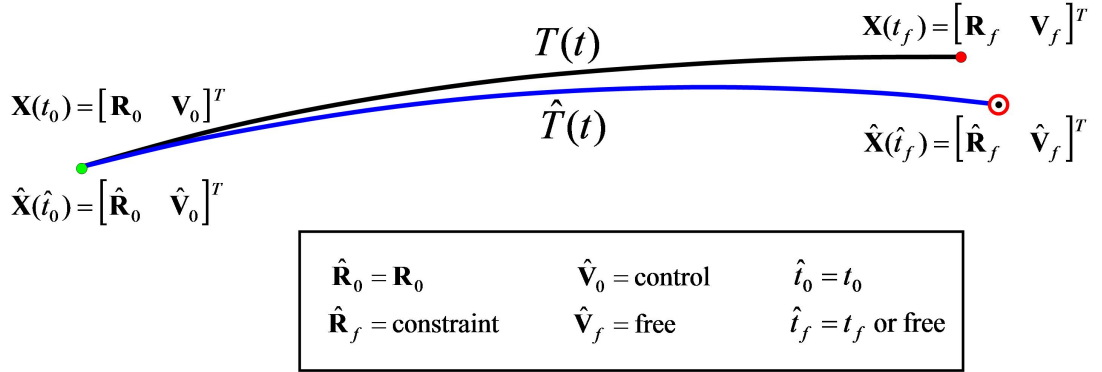


Figure 3.6: The single-shooting differential-correction routine. The black trajectory,  $T(t)$ , is the initial trajectory; the blue trajectory,  $\hat{T}(t)$ , is the corrected trajectory that encounters the target position, indicated by a bull's eye, at the target time.

$\Delta\mathbf{V}_0$  to find:

$$\Delta\mathbf{V}_0 = [\Phi_{RV}(t_f, t_0)]^{-1} \delta\mathbf{R}_f. \quad (3.9)$$

Since the state transition matrix is propagated with linearized equations, the algorithm must be iterated until convergence. When the algorithm is converging, each iteration typically improves the solution by a factor of 10, although factors anywhere between 2 and 100 have been observed in this research.

### 3.5.2 Multiple-Shooting Differential Correction

Multiple-shooting differential correction takes a series of states and adjusts them all simultaneously to construct a complicated trajectory that satisfies a set of constraints. It is very useful when mission designers wish to construct a long trajectory in an unstable environment in the presence of machine precision. For example, the Genesis spacecraft departed the Earth, traversed a quasi-Halo orbit about the Sun-Earth L<sub>1</sub> point several times, transferred to the vicinity of the Sun-Earth L<sub>2</sub> point, and then returned to Earth. This entire trajectory may in theory be constructed without a single maneuver. However, in this unstable environment, deviations even as small as round-off

errors due to machine precision grow exponentially. A computer using finite-precision mathematics does not normally have the precision required to propagate the spacecraft through its entire trajectory before the round-off errors grow large enough to create a large-scale deviation in the spacecraft's trajectory. To get around this numerical problem, mission designers break the trajectory into many segments and patch the segments together with very small maneuvers. The maneuvers counter-act the build-up of propagated round-off errors. They may be as small as desired, depending on the length of each patched segment, and are typically much smaller than any expected station-keeping maneuver. Hence, they are not normally considered to be deterministic maneuvers in the mission.

The multiple-shooting differential correction method is described in detail by Pernicka (1986) and by Wilson (2003), among other authors; we present a summary of the process here and leave the details to the reader.

The first step in the process of differentially correcting a complicated trajectory is to define a series of patchpoints. Several things must be considered when setting up the patchpoints; a discussion of these considerations is given below. From then on, a two-level process is iterated until either the differential corrector fails or each constraint in the system is satisfied. The first level of the process adjusts the patchpoints' velocities; the second level of the process adjusts the patchpoints' positions and epochs. If the patchpoints fall into some basin of convergence for the differential corrector, then the process converges on a continuous trajectory swiftly.

The following paragraphs provide more details about the two-level process:

**Level 1.** The velocities of every patchpoint along the trajectory except the last one are adjusted using the single-shooting differential corrector given in Section 3.5.1. The velocities are set such that the position of each segment ends at the follow-

ing patchpoint. When this step has been completed, the trajectory is continuous, although a spacecraft must perform a  $\Delta V$  at each patchpoint in order to follow the trajectory.

**Level 2.** The positions and epochs of every patchpoint, including the last patchpoint, are adjusted using a least-squares method that is designed to reduce the total  $\Delta V$  cost of the trajectory. The result is a discontinuous trajectory that should require less total  $\Delta V$  after the following iteration of Level 1.

This iteration process is repeated until the discontinuity at each patchpoint in position and velocity is below some tolerance.

The choice of patchpoints has a strong effect on the differential corrector's performance. First of all, since the single-shooting method is invoked between every adjacent patchpoint, the patchpoints must be close enough to permit the single-shooting method to converge within the desirable tolerance given the numerical precision of the machine. That is, if the patchpoints are too far apart, Level 1 will not converge. Secondly, Level 2 of the two-level process is generally designed with the assumption that each patchpoint is evenly spaced in time. If the patchpoints are not evenly spaced, then their epochs should be normalized in some way. This ensures that the least-squares method succeeds at reducing the total  $\Delta V$  in the trajectory between iterations. Finally, it has been observed that the differential corrector converges more readily if there are more patchpoints where the dynamics become more unstable, e.g., near massive bodies.

Section 3.5.1 provides the details of Level 1. In order to shed some light onto the functionality of Level 2, let us assume that we have a trajectory built from three patchpoints. The two segments meet in the middle at the second patchpoint, but are not continuous in velocity, i.e., there is some velocity deviation  $\Delta V_2$ . Let us assume that it is desirable to remove that discontinuity, and to do so we allow the positions

and epochs of all three patchpoints to be adjusted. Wilson provides details about how to numerically compute the variations of the target ( $\Delta\mathbf{V}_2$ ) to the controls ( $\mathbf{R}_1, t_1, \mathbf{R}_2, t_2, \mathbf{R}_3, t_3$ ). In this way, one can construct the following partial derivatives:

$$\begin{aligned} \frac{\partial \Delta\mathbf{V}_2}{\partial \mathbf{R}_1}, & \quad \frac{\partial \Delta\mathbf{V}_2}{\partial t_1}, \\ \frac{\partial \Delta\mathbf{V}_2}{\partial \mathbf{R}_2}, & \quad \frac{\partial \Delta\mathbf{V}_2}{\partial t_2}, \\ \frac{\partial \Delta\mathbf{V}_2}{\partial \mathbf{R}_3}, & \quad \frac{\partial \Delta\mathbf{V}_2}{\partial t_3}. \end{aligned}$$

With these partial derivatives, one can build an approximation of the change in  $\Delta\mathbf{V}_2$  when each of the control parameters are perturbed:

$$[\delta\Delta\mathbf{V}_2] = \underbrace{\begin{bmatrix} \frac{\partial \Delta\mathbf{V}_2}{\partial \mathbf{R}_1} & \frac{\partial \Delta\mathbf{V}_2}{\partial t_1} & \frac{\partial \Delta\mathbf{V}_2}{\partial \mathbf{R}_2} & \frac{\partial \Delta\mathbf{V}_2}{\partial t_2} & \frac{\partial \Delta\mathbf{V}_2}{\partial \mathbf{R}_3} & \frac{\partial \Delta\mathbf{V}_2}{\partial t_3} \end{bmatrix}}_{[M]} \begin{bmatrix} \delta\mathbf{R}_1 \\ \delta t_1 \\ \delta\mathbf{R}_2 \\ \delta t_2 \\ \delta\mathbf{R}_3 \\ \delta t_3 \end{bmatrix}. \quad (3.10)$$

In general, we wish to determine the appropriate changes to make to each of the control variables in order to reduce the value of  $\Delta\mathbf{V}_2$  to zero. The linear system given in Equation 3.10 is underdetermined; Wilson suggests using the smallest Euclidean norm to produce a good solution:

$$\begin{bmatrix} \delta\mathbf{R}_1 \\ \delta t_1 \\ \delta\mathbf{R}_2 \\ \delta t_2 \\ \delta\mathbf{R}_3 \\ \delta t_3 \end{bmatrix} = M^T (MM^T)^{-1} [\delta\Delta\mathbf{V}_2]. \quad (3.11)$$

These deviations in position and epoch are then added to the patchpoints' states to complete the Level 2 iteration. This example included only three patchpoints; additional patchpoints may be added on indefinitely. With many patchpoints in the system, the majority of the matrix  $M$  is filled with zeros, since each velocity discontinuity is only dependent on the positions and epochs of the three nearest patchpoints.

In its simplest form, the Level 2 corrections are only constrained by the velocity discontinuities at each patchpoint. Wilson (2003) describes how to add many other types of constraints to the differential corrector. Some examples of constraints that may be added include:

- Desirable Position Vector. One may target a particular position vector or position magnitude for any patchpoint in the trajectory. This may be with respect to a point in the coordinate axes or with respect to another body.
- Desirable Inclination. One may target many different orbital parameters, such as the inclination of one or more specified patchpoints.
- Maximum Change in Position. One may limit the differential corrector's capability to change one or more patchpoints' positions during each iteration of Level 2. This helps to keep a trajectory near some initial guess.

Many other types of constraints may be placed on the system. The addition of additional constraints is very useful for practical spacecraft missions, where the trajectory must be designed to begin from a particular state or to end at a particular state; however, it does often make it more difficult for the differential corrector to converge.

This research has implemented the multiple-shooting differential corrector in a variety of situations. To demonstrate its use, we will examine its performance as it is used to differentially correct a periodic Halo orbit from the CRTBP into a quasi-Halo orbit in the JPL Ephemeris model of the solar system. Figure 3.7 provides several representative plots of the differential corrector in action. The plots are exaggerated to demonstrate the procedure clearly. The plot shown in (a) depicts the initial periodic Halo orbit in the CRTBP. The trajectory is broken into four segments, separated by five patchpoints as shown in (b), where the fifth patchpoint is coincident with the first. The first iteration of Level 1, shown in (c), forces the new trajectory to be continuous in position and time in the JPL Ephemeris model, but permits velocity discontinuities at

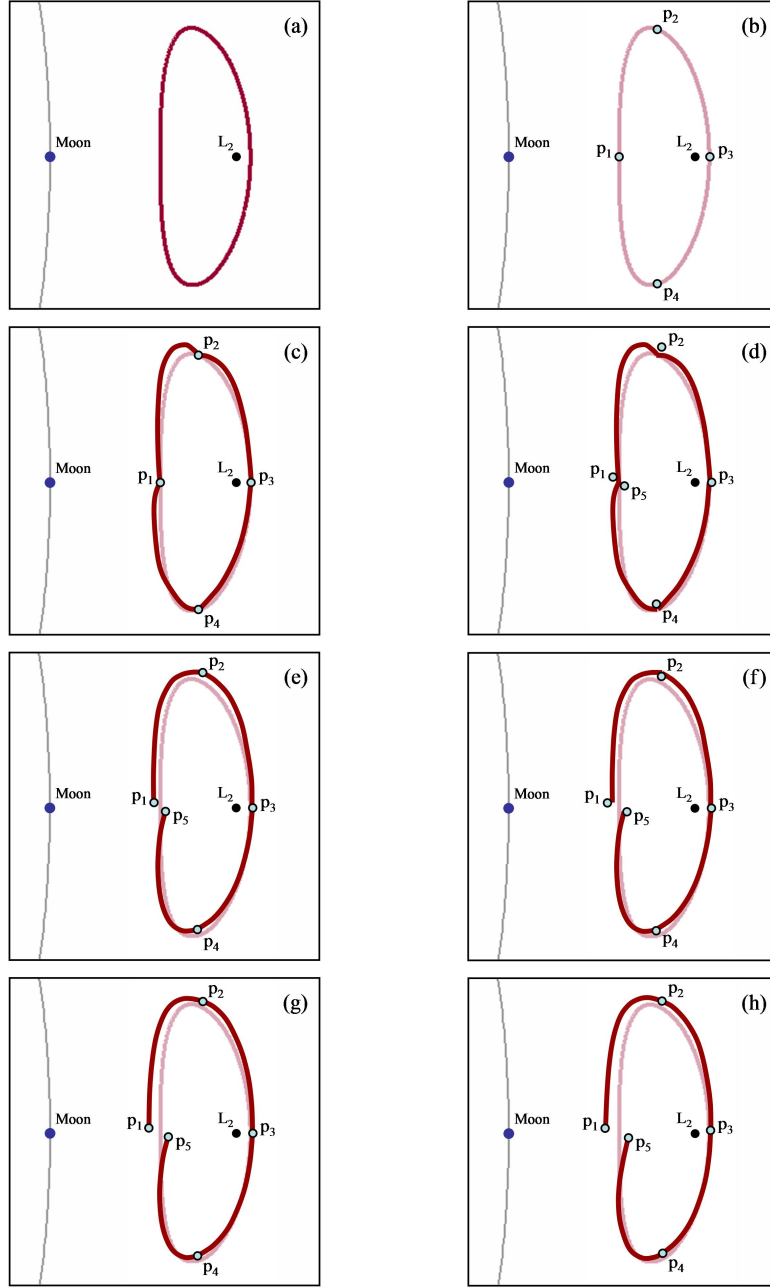


Figure 3.7: An exaggerated demonstration of the implementation of the multiple-shooting differential corrector used to convert a Halo orbit from the CRTBP into the JPL Ephemeris.

- (a) The initial CRTBP Halo orbit.
- (b) The initial placement of patchpoints in the JPL Ephemeris model.
- (c) Level 1: Differential correction to determine the  $\Delta V$ s necessary to make the trajectory continuous in the JPL Ephemeris model.
- (d) Level 2: The adjustments of the patchpoints' positions and epochs to reduce the total  $\Delta V$ .
- (e) Level 1: The second adjustments of the patchpoints' velocities to make the trajectory continuous.
- (f) Level 2: The second adjustments of the patchpoints' positions and epochs to reduce the total  $\Delta V$ .
- (g) Level 1: The third adjustments of the patchpoints' velocities to make the trajectory continuous.
- (h) The final converged trajectory in the JPL Ephemeris model after several additional iterations.

each interior patchpoint. The five patchpoints' positions and epochs are then adjusted in the first iteration of Level 2 as shown in (d). The plots shown in (e) and (f) give an exaggerated representation of the second iteration of Levels 1 and 2. The plot shown in (g) depicts the trajectory after the third iteration of Level 1; one can see that the trajectory is approaching a continuous trajectory. Finally, the plot shown in (h) depicts the final, converged trajectory that is continuous in the JPL Ephemeris model within some tolerance limits.

Studying Figure 3.7, one can see that the differential corrector permits the ends of the trajectory to be altered substantially, since there are no boundary conditions. If more revolutions of the Halo orbit were originally sent into the differential corrector, then the final trajectory would resemble the original Halo orbit more closely. This process is shown in more detail in Section 3.6.3.

### 3.6 Constructing Periodic Orbits

Periodic orbits are important when analyzing and constructing trajectories using dynamical systems methods, since they help to characterize the flow in the system. There are many methods that are frequently used to identify and construct periodic orbits. Three categories of methods are described here:

- (1) Analytical Expansion Techniques. The discussion given in Section 3.3.2 demonstrates how to use basic analytical techniques to identify planar and three-dimensional periodic orbits in the CRTBP. Many authors have constructed analytical expansions that may be used to approximate periodic orbits in the CRTBP or in more complex systems, including Richardson and Cary (1975), Richardson (1980), and Gómez et al. (2001a), among others.

- (2) Shooting Techniques. One may numerically construct a periodic orbit by targeting a single state as both the initial and final states in a trajectory using either a single- or multiple-shooting technique. This technique is difficult without any constraints, but has proven to be very useful when numerically constructing certain types of periodic orbits, such as the orbits presented in Appendices A and B.
- (3) The Poincaré Method. A very notable method that has proven to be very successful at identifying periodic and quasiperiodic orbits, especially stable orbits. Poincaré's technique involves numerically integrating many trajectories for a large amount of time. Trajectories that are close to periodic tend to linger near the same regions of the state space. One can readily identify stable periodic orbits or trajectories near such orbits if one places a plane in the state space, i.e., a **Poincaré Surface of Section**. Then one records the state of each trajectory as the trajectory pierces the plane. A periodic orbit appears as a fixed-point in the plane; a quasiperiodic orbit appears as a closed loop in the plane. Regions that are unstable in the state space appear as a chaotic sea of points, since unstable trajectories are very sensitive to their initial conditions.

Many other types of methods certainly exist, but these three categories provide a good overview of the variety of methods that are used in this research.

### 3.6.1 Periodic Orbits in the CRTBP

If the Lagrange points represent the five simplest solutions to the CRTBP, it may be argued that the next set of solutions to introduce is the set of simple periodic symmetric orbits in the CRTBP. Simple periodic symmetric orbits are orbits that are symmetric about the  $x - z$  plane, pierce the  $x - z$  plane exactly twice per orbit, and pierce the plane orthogonally each time. Libration orbits, such as Halo and Lyapunov or-

bits, are good examples of such orbits. Each orbit presented in Appendix A is a planar simple periodic symmetric orbit unless otherwise stated; each orbit presented in Appendix B is a three-dimensional simple periodic symmetric orbit unless otherwise stated. A simple single-shooting differential correction scheme may be used to construct these orbits by taking advantage of their well-defined structure. Section 3.6.2 provides more information about this differential correction scheme. It should be noted that although this class of orbits does include what might be argued to be the simplest periodic orbits in the CRTBP, this class of orbits also includes families of very complex orbits.

Many other types of periodic orbits exist in the CRTBP, including orbits that pierce the  $x - z$  plane multiple times per orbit and orbits that are not symmetric, such as orbits about the triangular Lagrange points. Lo and Parker (2005) demonstrate a method to chain simple periodic orbits together in order to build more complex periodic orbits.

### **3.6.2 Single-Shooting Method for Constructing Simple Periodic Symmetric Orbits in the CRTBP**

This research has implemented several shooting techniques in order to identify periodic orbits. The simple periodic orbits presented in Appendices A and B have been identified using a single-shooting targeting scheme that is presented in detail by several authors (e.g., Howell, 1984). Since it is a very common and straight-forward procedure, and since it has been used repeatedly in this research to construct Halo orbits and other similar orbits, it is reviewed here.

As mentioned earlier, simple periodic symmetric orbits are orbits that are symmetric about the  $x - z$  plane, pierce the  $x - z$  plane exactly twice per orbit, and pierce the plane orthogonally each time. Let us define  $\mathbf{X}(t_0)$  to be the state of a simple periodic symmetric orbit at the  $x - z$  plane-crossing with a positive  $\dot{y}$  and  $\mathbf{X}(t_{T/2})$  to be the state

of the orbit half of its orbital period later at the  $x - z$  plane-crossing with a negative  $\dot{y}$ . For this orbit to be periodic and symmetric, these states must have the following form:

$$\begin{aligned}\mathbf{X}(t_0) &= [x_0 \ 0 \ z_0 \ 0 \ \dot{y}_0 \ 0]^T, \\ \mathbf{X}(t_{T/2}) &= [x_{T/2} \ 0 \ z_{T/2} \ 0 \ \dot{y}_{T/2} \ 0]^T.\end{aligned}$$

Let us assume that we have an initial guess,  $\hat{\mathbf{X}}(t_0)$ , that is near the initial state of a desirable orbit. When we integrate this state forward in time until the next  $x - z$  plane, we obtain the state  $\hat{\mathbf{X}}(\hat{T}/2)$ :

$$\hat{\mathbf{X}}(\hat{T}/2) = [x_{\hat{T}/2} \ 0 \ z_{\hat{T}/2} \ \dot{x}_{\hat{T}/2} \ \dot{y}_{\hat{T}/2} \ \dot{z}_{\hat{T}/2}]^T.$$

We now wish to adjust the initial state of the trajectory in such a way as to drive the values of  $\dot{x}_{\hat{T}/2}$  and  $\dot{z}_{\hat{T}/2}$  to zero. One notices that by adjusting the initial state, not only do the values of  $\dot{x}$  and  $\dot{z}$  change, but the propagation time,  $\hat{T}/2$ , needed to pierce the  $x - z$  plane also changes. In order to target a proper state  $\mathbf{X}(t_{T/2})$ , one may vary the initial values of  $x$ ,  $z$ , and/or  $\dot{y}$ .

The linearized system of equations relating the final state to the initial state may be written as:

$$\delta\mathbf{X}(t_{T/2}) \approx \Phi(t_{T/2}, t_0) \delta\mathbf{X}(t_0) + \frac{\partial\mathbf{X}}{\partial t} \delta(T/2), \quad (3.12)$$

where  $\delta\mathbf{X}(t_{T/2})$  is the deviation in the final state due to a deviation in the initial state,  $\delta\mathbf{X}(t_0)$ , and a corresponding deviation in the orbit's period,  $\delta(T/2)$ . The time-derivative of the state,  $\partial\mathbf{X}/\partial t$ , may be computed at the second plane-crossing, namely, at time  $t = T/2$ . Equation 3.12 may be used as the driver for a differential corrector by setting  $\delta\mathbf{X}(t_{T/2})$  to be the desired change in the final state's components and solving for  $\delta\mathbf{X}(t_0)$ , the approximate correction to the initial state needed to produce such a change.

We now consider what the desired change in the final state's components should be. For our purposes, the only desired change in the final state is a change in the values of  $\dot{x}$  and  $\dot{z}$ , but it isn't important if the other components of the final state change.

However, we know that the deviation in the final value of  $y$  will always be equal to zero since the trajectory is always propagated to that point. Thus we set  $\delta\mathbf{X}(t_{T/2})$  to:

$$\delta\mathbf{X}(t_{T/2}) = \begin{bmatrix} \delta x_{T/2} & 0 & \delta z_{T/2} & -\dot{x}_{T/2} & \delta \dot{y}_{T/2} & -\dot{z}_{T/2} \end{bmatrix}^T.$$

Furthermore, in order to restrict our search to simple periodic symmetrical orbits we restrict the allowed correction in the initial conditions to:

$$\delta\mathbf{X}(t_0) = \begin{bmatrix} \delta x_0 & 0 & \delta z_0 & 0 & \delta \dot{y}_0 & 0 \end{bmatrix}^T.$$

Now Equation 3.12 simplifies to:

$$\begin{bmatrix} \delta x_{T/2} \\ 0 \\ \delta z_{T/2} \\ -\dot{x}_{T/2} \\ \delta \dot{y}_{T/2} \\ -\dot{z}_{T/2} \end{bmatrix} \approx \begin{bmatrix} \phi_{11} & \phi_{12} & \phi_{13} & \phi_{14} & \phi_{15} & \phi_{16} \\ \phi_{21} & \phi_{22} & \phi_{23} & \phi_{24} & \phi_{25} & \phi_{26} \\ \phi_{31} & \phi_{32} & \phi_{33} & \phi_{34} & \phi_{35} & \phi_{36} \\ \phi_{41} & \phi_{42} & \phi_{43} & \phi_{44} & \phi_{45} & \phi_{46} \\ \phi_{51} & \phi_{52} & \phi_{53} & \phi_{54} & \phi_{55} & \phi_{56} \\ \phi_{61} & \phi_{62} & \phi_{63} & \phi_{64} & \phi_{65} & \phi_{66} \end{bmatrix} (t_{T/2}, t_0) \begin{bmatrix} \delta x_0 \\ 0 \\ \delta z_0 \\ 0 \\ \delta \dot{y}_0 \\ 0 \end{bmatrix} + \begin{bmatrix} \dot{x} \\ \dot{y} \\ \dot{z} \\ \ddot{x} \\ \ddot{y} \\ \ddot{z} \end{bmatrix} \delta(T/2). \quad (3.13)$$

The value of  $\delta(T/2)$  may be determined from the second line of Equation 3.13 to be:

$$\delta(T/2) = \frac{-\phi_{21}\delta x_0 - \phi_{23}\delta z_0 - \phi_{25}\delta \dot{y}_0}{\dot{y}}. \quad (3.14)$$

Substituting this value into the fourth and sixth lines of Equation 3.13 yields:

$$-\dot{x}_{T/2} \approx \left( \phi_{41} - \phi_{21} \frac{\ddot{x}}{\dot{y}} \right) \delta x_0 + \left( \phi_{43} - \phi_{23} \frac{\ddot{x}}{\dot{y}} \right) \delta z_0 + \left( \phi_{45} - \phi_{25} \frac{\ddot{x}}{\dot{y}} \right) \delta \dot{y}_0 \quad (3.15)$$

$$-\dot{z}_{T/2} \approx \left( \phi_{61} - \phi_{21} \frac{\ddot{z}}{\dot{y}} \right) \delta x_0 + \left( \phi_{63} - \phi_{23} \frac{\ddot{z}}{\dot{y}} \right) \delta z_0 + \left( \phi_{65} - \phi_{25} \frac{\ddot{z}}{\dot{y}} \right) \delta \dot{y}_0 \quad (3.16)$$

Equations 3.15 and 3.16 give expressions for the approximate deviation in the final  $x$ - and  $z$ -velocities as functions of the deviation in all three initial conditions  $x_0$ ,  $z_0$ , and  $\dot{y}_0$ . It is sufficient to change only two of the initial conditions, if that is desirable, or a combination of all three. In this research, we have chosen to keep  $x_0$  constant and permit  $z_0$  and  $\dot{y}_0$  to vary, but it is straightforward to derive the appropriate formulae for any combination of these conditions. The following expression summarizes the

approximate changes that must be made to  $z_0$  and  $\dot{y}_0$  to produce a desirable change in the final state (while keeping the other initial conditions constant):

$$\begin{bmatrix} \delta z_0 \\ \delta \dot{y}_0 \end{bmatrix} \approx \begin{bmatrix} \phi_{43} - \phi_{23} \frac{\dot{x}}{\dot{y}} & \phi_{45} - \phi_{25} \frac{\dot{x}}{\dot{y}} \\ \phi_{63} - \phi_{23} \frac{\ddot{z}}{\dot{y}} & \phi_{65} - \phi_{25} \frac{\ddot{z}}{\dot{y}} \end{bmatrix}^{-1} \begin{bmatrix} -\dot{x}_{T/2} \\ -\dot{z}_{T/2} \end{bmatrix}. \quad (3.17)$$

Since the system was linearized in order to produce this procedure, the adjustments will not correct the unwanted motion perfectly; this procedure must be iterated until it converges on an orbit.

### 3.6.3 Differentially-Correcting Orbits into the JPL Ephemeris Model

An orbit that is perfectly periodic in the CRTBP is not perfectly periodic in the real solar system since the planets and moons in the real solar system do not move in circular, coplanar orbits. Various perturbations lead the orbit to diverge from being periodic; the most notable of which is the non-zero eccentricity of the orbits of the primary bodies in the system. The JPL Ephemeris model of the solar system is described in more detail in Section 2.5.1.

To produce a quasiperiodic orbit in the real solar system, one can use a multiple-shooting differential corrector with the periodic CRTBP orbit as the initial guess of the real trajectory. This technique was demonstrated in Section 3.5.2. The differential corrector takes the CRTBP orbit and perturbs it to keep it near its initial guess while eliminating the need to perform large maneuvers.

Figure 3.8 shows the difference between a Halo orbit about the lunar L<sub>2</sub> point produced in the CRTBP compared with the same Halo orbit differentially-corrected into the JPL Ephemeris model of the real solar system. One can see that the real Halo orbit is quasiperiodic, tracing out the same vicinity of space on each orbit, but never truly retracing itself.

The perfectly-periodic CRTBP orbit is typically a very close approximation of the real quasiperiodic orbit, enough so that the early mission design may be developed in

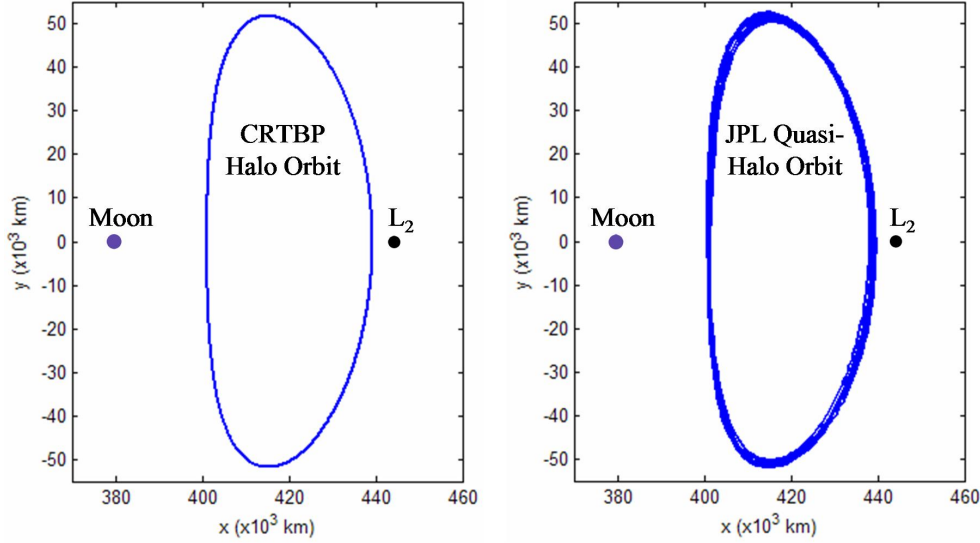


Figure 3.8: A comparison between a Halo orbit produced in the CRTBP and a quasi-Halo orbit produced in the JPL Ephemeris model of the real solar system. The orbits are shown in the Earth-Moon synodic reference frame.

the CRTBP. This is convenient because the motion of a spacecraft in a perfectly periodic orbit is more predictable than the motion of a spacecraft in a quasiperiodic orbit.

On several occasions, it has been observed that some of the structure of a periodic orbit in the CRTBP becomes lost or significantly altered as the orbit is differentially-corrected into the JPL Ephemeris model. This is often seen when a single revolution of a periodic orbit is sent into the differential corrector. Ordinarily, a differential corrector converges on a continuous trajectory more readily if the trajectory's endpoints are not constrained. Without the boundary values constrained, it is often the case that the differential corrector significantly alters the states of the trajectory's endpoints. The resulting trajectory, although continuous, may not resemble the original orbit much at all. This effect may be observed in Figure 3.9.

One way to combat this effect is to differentially-correct several orbits of the periodic orbit together. For the purpose of this discussion, let us say that four periodic

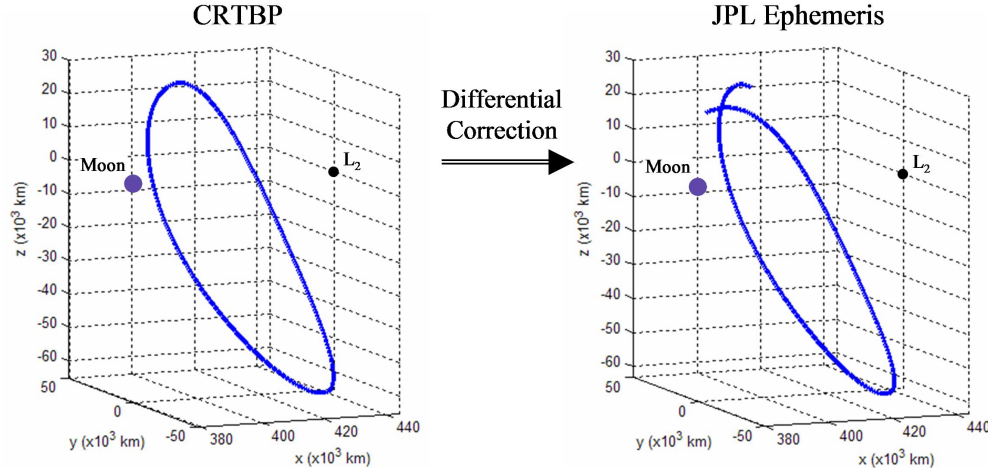


Figure 3.9: A single L<sub>2</sub> Halo orbit in the Earth-Moon CRTBP (left) is differentially-corrected into the JPL Ephemeris model (right).

orbits are differentially-corrected together. Then, two of the orbits are “outer” orbits (the first and last orbits) that are vulnerable to substantial changes in the differential correction process, and two of the orbits are “inner” orbits (the second and third orbits) that are more protected from significant alteration in the process. Normally, the differential corrector converges on a continuous trajectory before the inner orbits are substantially altered. Once the differential corrector has converged on the final trajectory, then the outer orbits may be pruned off in order to observe the structure of the resulting quasiperiodic orbit. Ordinarily, this procedure results in quasiperiodic orbits that exist in the JPL Ephemeris model that retain the same structure as the periodic orbits that exist in the CRTBP. This procedure has been used with much success in this dissertation; Figure 3.10 shows an example of this process.

Since Halo orbits are used frequently in later chapters of this thesis, some discussion is given here regarding the largest observable deviations between the perfectly periodic Halo orbit in the CRTBP and the quasi-Halo orbit in the real solar system. Arguably the most substantial deviation between the CRTBP and the real solar system, at

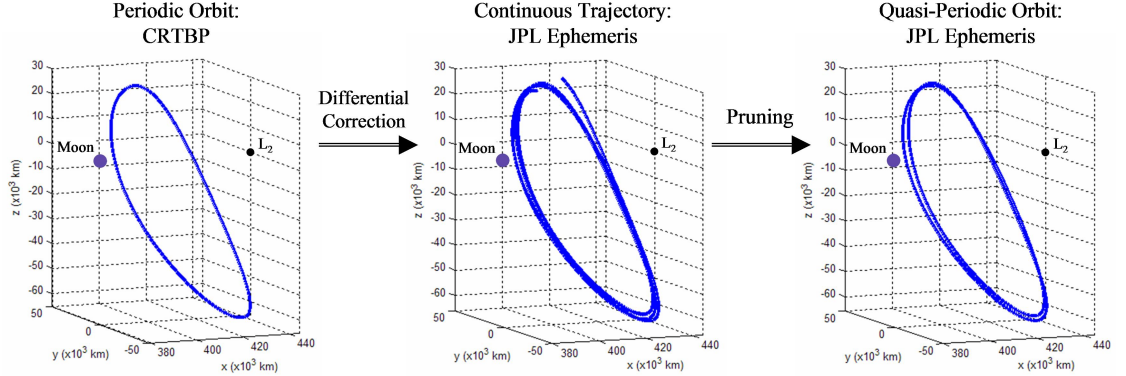


Figure 3.10: An example of the process of differentially-correcting and pruning a Halo orbit from the Earth-Moon CRTBP into the JPL Ephemeris model. Left: the nominal periodic Halo orbit in the Earth-Moon CRTBP; Center: the differentially-corrected trajectory in the JPL Ephemeris model; Right: the pruned quasiperiodic Halo orbits in the JPL Ephemeris model.

least in the case of the Sun-Earth and Earth-Moon three-body systems, is the non-zero eccentricity of the orbits of the primary bodies in the system. The real, eccentric orbit of the primaries imparts a deviation in the quasi-Halo orbits that has a period equal to the orbital period of the primaries. Since most Halo orbits have a period equal to approximately half of the orbital period of the primaries, this dynamic perturbation tends to appear as a resonant pulsation. One quasi-Halo revolution tends to deviate from the perfectly periodic Halo orbit in one direction, and the next revolution tends to deviate in the opposite direction. The result is that a spacecraft on a quasi-Halo orbit tends to retrace its path very closely every other revolution. This effect is less visible when the reference frame is centered on a Lagrange point rather than the barycenter, since the Lagrange point pulses in and out as the primary bodies follow their non-circular orbits.

### 3.7 The Continuation Method

Periodic orbits in the CRTBP may be grouped into families, where a family consists of an infinite number of periodic orbits whose properties vary continuously from one end of the family to the other. All orbits in the same family may be uniquely identified by a single parameter of that family, e.g., their position on a perpendicular  $x - z$  plane crossing, their velocity at that crossing, or some other specified parameter. This property of the CRTBP is due to the existence of the Jacobi constant, the CRTBP's unique integral of motion. Hénon provides more discussion about the existence of families of solutions in the CRTBP (Hénon, 1969).

Once a single periodic orbit is known in the CRTBP then the continuation method may be used to traverse that orbit's family. The method starts by perturbing some parameter of the known periodic orbit and then differentially correcting the new conditions to find that periodic orbit's neighbor in its family. The differential corrector presented in Section 3.6 is well-suited to this method for simple periodic symmetrical orbits because one may vary the initial position and correct for the initial velocity that corresponds to the next periodic orbit in the family (or vice versa, if desired).

To demonstrate this method, the continuation method has been applied to the family of Lyapunov orbits that exist about the Earth-Moon  $L_2$  point. First, a single Lyapunov orbit is identified, e.g., the green orbit in Figures 3.11 and 3.12; the orbit's initial position,  $x_0$ , is then systematically varied while a differential corrector fills out the curve shown in Figure 3.11. The initial conditions in the curve correspond to the family of orbits shown in Figure 3.12.

The continuation method works well when the perturbations are small; in practice it is beneficial to predict the differential corrector's adjustment to the perturbation because this allows larger jumps in the varying parameter. Furthermore, if the perturbations are too large, the differential corrector may converge on a solution of a differ-

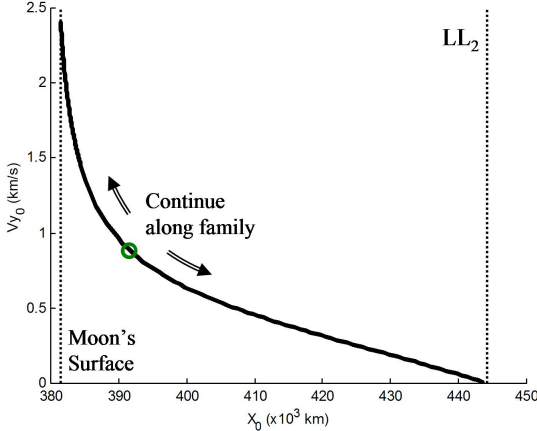


Figure 3.11: A plot of the initial conditions of the family of Lyapunov orbits about the Earth-Moon L<sub>2</sub> point (LL<sub>2</sub>).

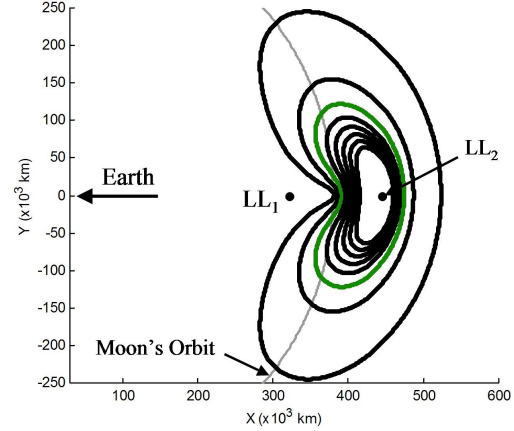


Figure 3.12: Plots of the orbits in the family of LL<sub>2</sub> Lyapunov orbits corresponding to those initial conditions shown in Figure 3.11.

ent family. Thus smaller steps or better prediction methods may be required to make the continuation method more reliable. The work for this study has implemented a quadratic prediction method that uses the three previous data points of the family to predict the next data point. This has been sufficient to allow the differential corrector to converge quickly while allowing the curve of the family to evolve naturally over the state space.

The research completed by Paffenroth et al. discusses additional ways to improve the continuation method, including methods that extrapolate curves using a constant arc-length of two parameters rather than a constant step in some single parameter (Paffenroth et al., 2001).

### 3.8 Stability

The stability of a periodic orbit may be determined by analyzing the eigenvalues of the orbit's monodromy matrix. A random perturbation in the state of a particle on an unstable orbit will cause the particle's state to exponentially diverge from that of the original orbit over time; hence, the monodromy matrix of an unstable orbit in-

cludes at least one eigenvalue whose real component is outside of the unit circle. This section explores the stability characteristics of periodic orbits via the eigenvalues of their monodromy matrices.

### 3.8.1 Eigenvalues of an Orbit's Monodromy Matrix

The monodromy matrices of orbits in the CRTBP have six eigenvalues,  $\lambda_i$  for  $i = 1, 2, \dots, 6$ , corresponding to the eigenvectors  $\mathbf{v}_i$ . The eigenvalues of the monodromy matrix occur in reciprocal pairs (see, e.g., Broucke, 1969), which is a direct consequence of the symplectic nature of the monodromy matrix, and of the state transition matrix in the CRTBP in general (Battin, 1987). Additionally, a pair of eigenvalues of the monodromy matrix will be equal to unity because of the Jacobi integral of motion in the CRTBP (see, e.g., Broucke, 1969; Nayfeh and Balachandran, 1995). The eigenvalues are thus related in the following way:

$$\lambda_2 = \frac{1}{\lambda_1} \quad \lambda_4 = \frac{1}{\lambda_3} \quad \lambda_5 = \lambda_6 = 1. \quad (3.18)$$

The monodromy matrices of periodic orbits in the planar CRTBP only have four eigenvalues:  $(\lambda_1, 1/\lambda_1, 1, 1)$ . Since those orbits may be computed in the spatial CRTBP by setting their  $z$ - and  $\dot{z}$ -components to zero, the remainder of this section only considers orbits in the full three-dimensional system.

The eigenvalues of the monodromy matrix of a periodic orbit in the CRTBP are the roots of a characteristic equation; furthermore, each has a characteristic exponent,  $\alpha$ , where  $\lambda = e^{\alpha T}$  and  $T$  is the period of the orbit. Then, the reciprocal of that eigenvalue is equal to:  $1/\lambda = e^{-\alpha T}$ . The characteristic exponents are sometimes referred to as Lyapunov Characteristic Exponents (see, e.g., Scheeres et al., 2001).

The monodromy matrices of Keplerian orbits, such as low Earth orbits, have three pairs of eigenvalues that are all equal to 1, indicating that after a full orbit any given perturbation neither grows nor decays exponentially. The monodromy matrices

Table 3.2: A summary of the resulting motion of a particle in a periodic orbit, whose state is perturbed along the eigenvector corresponding to a given eigenvalue. The result of a perturbation along the eigenvector corresponding to a complex eigenvalue includes a combination of the imaginary result and one of the real results listed.

Eigenvalue	Result of the perturbation
Real, within the range $(-1, 1)$	The perturbation exponentially decays.
Real, equal to 1 or $-1$	The perturbation neither exponentially decays nor grows.
Real, outside of the range $(-1, 1)$	The perturbation exponentially grows.
Imaginary	After each orbital period, the perturbation oscillates about the particle's original state.

of periodic orbits in the CRTBP may have other eigenvalue pairs, including real values not equal to 1 and pairs of complex numbers. Table 3.2 provides a summary of the resulting motion of a particle in a periodic orbit, whose state is perturbed along the eigenvector corresponding to any type of given eigenvalue.

The stability of a periodic orbit may be identified by observing the resulting motion of a perturbed particle in that orbit or by computing the eigenvalues of the orbit's monodromy matrix and comparing those eigenvalues to the results given in Table 3.2. The following classification scheme for an orbit's stability is used in this dissertation:

- If an eigenvalue exists whose real component is outside of the range  $[-1, 1]$ , then the periodic orbit is asymptotically unstable, referred to here as **unstable**, along the corresponding eigenvector.
- If the real component of each and every eigenvalue of the monodromy matrix is between  $-1$  and  $1$ , then the orbit is **stable**. Given the relationships in Equations 3.18, an orbit may only be stable in the CRTBP if each and every eigenvalue pair is complex with real components in the range  $(-1, 1)$ .
- If the orbit is not unstable and there is at least one eigenvalue pair whose real

component is equal to 1, then the periodic orbit is **neutrally stable**, or a **center** (Strogatz, 1994).

Since every periodic orbit in the CRTBP has at least one pair of eigenvalues whose values are equal to unity, then it is customary to ignore that pair of eigenvalues when classifying the stability of the orbit (Broucke, 1968; Russell, 2005).

To determine the eigenvalues of the monodromy matrix, it is useful to consider the characteristic equation, since many of the roots of this equation are already known:

$$\begin{aligned}\det(M - \lambda I) &= (\lambda - \lambda_1)(\lambda - \lambda_2)(\lambda - \lambda_3)(\lambda - \lambda_4)(\lambda - \lambda_5)(\lambda - \lambda_6) = 0 \\ &= (\lambda - 1)^2(\lambda - \lambda_1)(\lambda - 1/\lambda_1)(\lambda - \lambda_3)(\lambda - 1/\lambda_3) = 0\end{aligned}\quad (3.19)$$

The relationship given in Equation 3.19 may be re-written in terms of the new parameters  $p$  and  $q$ , keeping consistent with the nomenclature found in Bray and Goudas (1967a):

$$(\lambda - 1)^2 (\lambda^2 + p\lambda + 1) (\lambda^2 + q\lambda + 1) = 0. \quad (3.20)$$

Thus,  $p = -(\lambda_1 + 1/\lambda_1)$  and  $q = -(\lambda_3 + 1/\lambda_3)$ . Equation 3.20 may also be factored in the following manner:

$$(\lambda - 1)^2 \left( \lambda^4 + (p+q)\lambda^3 + (pq+2)\lambda^2 + (p+q)\lambda + 1 \right) = 0. \quad (3.21)$$

Equation 3.21 may be re-written using the new parameters  $\alpha$ ,  $\beta$ , and  $\gamma$ , once again to keep consistent with the nomenclature found in Bray and Goudas (1967a) (where  $\alpha$  should not be confused with the characteristic exponent that corresponds to each eigenvalue):

$$(\lambda - 1)^2 \left( \lambda^4 + \alpha\lambda^3 + \beta\lambda^2 + \alpha\lambda + \gamma \right) = 0. \quad (3.22)$$

In this form it is clear that  $\alpha = p + q$ ,  $\beta = pq + 2$ , and  $\gamma = 1$ . The benefits of factoring the characteristic equation into the parameters  $\alpha$ ,  $\beta$ , and  $\gamma$  arises at this point. Bray and Goudas derive a fast and simple method to compute  $\alpha$  and  $\beta$  using the monodromy

matrix (Bray and Goudas, 1967a; Russell, 2005):

$$\alpha = 2 - \text{trace}(M); \quad (3.23)$$

$$\beta = \frac{\alpha^2 - \text{trace}(M^2)}{2} + 1. \quad (3.24)$$

It is then simple to determine the parameters  $p$  and  $q$  using knowledge of  $\alpha$  and  $\beta$ :

$$\left. \begin{array}{c} p \\ q \end{array} \right\} = \frac{\alpha \pm \sqrt{\alpha^2 - 4\beta + 8}}{2}. \quad (3.25)$$

It then follows that with knowledge of  $p$  and  $q$  one may determine the corresponding eigenvalues:

$$\left. \begin{array}{c} \lambda_1 \\ 1/\lambda_1 \end{array} \right\} = \frac{-p \pm \sqrt{p^2 - 4}}{2}; \quad (3.26)$$

$$\left. \begin{array}{c} \lambda_3 \\ 1/\lambda_3 \end{array} \right\} = \frac{-q \pm \sqrt{q^2 - 4}}{2}. \quad (3.27)$$

The final two eigenvalues have already been pre-determined and are given in Equation 3.18 as  $\lambda_5 = \lambda_6 = 1$ . Thus, Equations 3.23 – 3.27 provide a fast and simple method to compute the six eigenvalues of the monodromy matrix. The corresponding eigenvectors may be computed in any standard way using the equation  $M\mathbf{v}_i = \lambda_i \mathbf{v}_i$ . It should be noted that the stable and unstable eigenvalues,  $\lambda^S$  and  $\lambda^U$ , of an orbit's monodromy matrix are equal to the pair of real eigenvalues with the smallest and largest values, respectively, if they exist.

### 3.8.2 The Stability Index

An orbit's **stability index** is defined in various ways in the literature depending on the author. Several authors, e.g., Broucke (1968), define the stability of a periodic orbit on the value of  $k$ , where  $k$  is equal to the sum of the real eigenvalues of the orbit. If  $|k| > n$ , where  $n$  is equal to the number of real eigenvalues in the orbit's monodromy

matrix, then the orbit is unstable; if  $|k| < n$ , the orbit is stable; otherwise  $|k| = n$  and the orbit is neutrally stable. One problem with such a definition is that the value of  $n$  may change depending on the orbit.

The stability index in this dissertation is based on the definition found in Howell's work (Howell, 1984). If one considers the definition  $k_i = \lambda_i + 1/\lambda_i$ , one notices several things. First, the values of  $k_i$  may be easily computed using the parameters  $p$  and  $q$  that were introduced above, namely:  $k_1 = -p$ ,  $k_2 = -q$ , and  $k_3 = 2$ . Next, the value of  $k_i$  is always real and in the range  $-2 \leq k \leq 2$  for stable orbits since the sum of a real pair is real and the sum of a complex conjugate pair is also real. Furthermore, if  $|k_i| > 2$ , then the real component of at least one of the eigenvalues summed is greater than 1 and the orbit is unstable. Since two of the eigenvalues of the orbit's monodromy matrix are equal to unity and it is conventional to ignore them, the stability index,  $k$ , may then be given by:

$$k = \sup\{|\operatorname{Re}(k_1)|, |\operatorname{Re}(k_2)|\}, \quad (3.28)$$

where the operator  $\operatorname{Re}()$  only observes the real component of the operand. We have the final test: if  $k > 2$  the orbit is unstable, if  $k = 2$  the orbit is neutrally stable, and if  $k < 2$  the orbit is stable.

### 3.8.3 The Perturbation Doubling Time

The stability index defined in Equation 3.28 certainly provides information about the stability of the orbit in question. However, it only provides limited information about the relative stability of different orbits. A highly unstable orbit may appear to be more stable than a weakly unstable orbit if the weakly unstable orbit's period is much greater than the highly unstable orbit's period. It is now of interest to find a parameter that may be used to directly compare the stability of two orbits regardless of their relative orbital periods.

The eigenvalues of the monodromy matrix of a periodic orbit are a function of the orbit's period,  $T$ , and a characteristic exponent,  $\alpha$ , as follows:

$$\lambda = e^{\alpha T}. \quad (3.29)$$

To compare the stability of several orbits directly, one may either normalize the eigenvalues of the monodromy matrices, or, equivalently, compare the characteristic exponents in some way.

An intuitive measure for comparison is the orbit's **Perturbation Doubling Time** (for unstable orbits) or the orbit's **Perturbation Halflife** (for stable orbits). In this dissertation, we refer to this time measurement as  $\hat{\tau}$  for two reasons: first, to indicate that it is a normalized measurement and second, to distinguish it from the parameter  $\tau$  that is used to identify points along an orbit (see Section 3.3.3). Given a particle in an unstable orbit, the Perturbation Doubling Time characterizes the length of time that is required for a perturbation in the particle's state to double in magnitude. Similarly, given a particle in a stable orbit, the Perturbation Halflife characterizes the length of time that is required for a perturbation in the particle's state to be reduced by one half. For simplicity, we refer to this time measurement only as the Perturbation Doubling Time, since it is generally more useful when designing real missions to compare this time measurement for unstable orbits.

After one determines the eigenvalues of the orbit's monodromy matrix, one may use Equation 3.29 to determine the corresponding characteristic exponents. If a particle's state is perturbed at time  $t = t_0$  from its nominal state by a perturbation with magnitude  $\delta(t_0)$  along the eigendirection corresponding to the characteristic exponent  $\alpha$ , then the magnitude of that perturbation grows over time by the following expression:

$$\delta(t) = \delta(t_0)e^{\alpha(t-t_0)}. \quad (3.30)$$

Given a random perturbation in the particle's state, the particle's deviation over time is

dominated by the component of that deviation that exists in the most unstable eigendirection, namely, by the direction indicated by the unstable eigenvalue  $\lambda^U$ . The Perturbation Doubling Time may be computed by identifying the time  $t = t_0 + \hat{\tau}$  when the particle's perturbed state is twice as far from its nominal position compared to its perturbed state at time  $t = t_0$ . One can find the Perturbation Doubling Time by solving for  $\hat{\tau}$  in Equation 3.31, derived as follows:

$$\begin{aligned}\delta(t) &= \delta(t_0)e^{\alpha(t-t_0)} \\ 2\delta(t_0) &= \delta(t_0)e^{\alpha\hat{\tau}} \\ 2 &= e^{\alpha\hat{\tau}}\end{aligned}\tag{3.31}$$

where  $\alpha$  is the characteristic exponent that corresponds to the unstable eigenvalue,  $\lambda^U$ , of the orbit's monodromy matrix. The value of  $\alpha$  may be computed using the simple relationship  $\alpha T = \ln \lambda^U$ , derived from Equation 3.29. Hence, the time duration  $\hat{\tau}$  may be computed using the expression:

$$\hat{\tau} = \frac{\ln 2}{\ln \lambda^U} T.\tag{3.32}$$

### 3.9 Invariant Manifolds

The dynamics in the circular restricted three-body system permit the existence of five fixed points (Section 3.3.1) and numerous periodic orbits (Section 3.6.1). The three collinear libration points and many of the periodic orbit solutions in the Earth-Moon three-body system are unstable (§3.8). An unstable orbit has at least one stable and one unstable eigenvalue with corresponding eigenvectors. A particle traveling along an unstable orbit that experiences a perturbation even slightly in the unstable direction will exponentially fall away from its nominal position on that orbit, tracing out a smooth trajectory away from the orbit. In a similar sense, a particle that has the right initial conditions will follow a smooth trajectory that exponentially approaches

an unstable orbit and eventually arrives on that orbit seemingly from the orbit's stable direction. These two trajectories describe what is known as an orbit's stable and unstable invariant manifolds.

An orbit's **unstable invariant manifold** ( $W^U$ ) contains the set of all trajectories that a particle may take if it was perturbed anywhere on that orbit in the direction of the orbit's unstable eigenvector. Similarly, an orbit's **stable invariant manifold** ( $W^S$ ) contains the set of all trajectories that a particle may take to arrive onto that orbit. Put another way, the orbit's stable invariant manifold is the set of all trajectories that a particle may take backward through time after a perturbation in the direction of the orbit's stable eigenvector.

Mathematically, the invariant manifolds are defined as follows. First of all, the CRTBP may be defined as a vector field bound in  $\mathbb{R}^6$ . One and only one vector is bound to every point in the vector field. Thus, the integration of any point  $p$  in the vector field with respect to time generates only one trajectory. Let us define  $T_p$  as the trajectory generated by the point  $p$ . The  $\alpha$ - and  $\omega$ -limits are defined to be the set of points in  $\mathbb{R}^6$  as  $T_p$  tends toward  $-\infty$  and  $+\infty$ , respectively. The  $\alpha$ - and  $\omega$ -limits may include a single point, a periodic orbit, or, if  $T_p$  has no asymptotic behavior, they may include a large portion of the state space. The set of all points defining trajectories that have the same  $\alpha$ -limit set is called the unstable manifold of that limit set. Similarly, the set of all points defining trajectories that have the same  $\omega$ -limit set is called the stable manifold of that limit set.

### 3.9.1 Invariant Manifolds of the Unstable Lagrange Points

The three collinear Lagrange points are unstable in both the Sun-Earth and Earth-Moon three-body systems; hence, they have associated invariant manifolds. Since the Lagrange points are single points in space, their invariant manifolds are one-dimensional structures. To produce them, one first computes the eigenvalues of the Jaco-

bian of their states. If  $\mathbf{X}$  is the state of one of the collinear Lagrange points, equal to  $[x \ y \ z \ \dot{x} \ \dot{y} \ \dot{z}]^T$ , then its Jacobian is equal to:

$$J = \frac{\partial \dot{\mathbf{X}}}{\partial \mathbf{X}} = \begin{bmatrix} \frac{\partial \dot{x}}{\partial x} & \frac{\partial \dot{x}}{\partial y} & \dots & \frac{\partial \dot{x}}{\partial z} \\ \frac{\partial \dot{y}}{\partial x} & \frac{\partial \dot{y}}{\partial y} & \dots & \frac{\partial \dot{y}}{\partial z} \\ \vdots & \vdots & \ddots & \vdots \\ \frac{\partial \dot{z}}{\partial x} & \frac{\partial \dot{z}}{\partial y} & \dots & \frac{\partial \dot{z}}{\partial z} \end{bmatrix} \quad (3.33)$$

After plugging in the equations of motion of the CRTBP given in Equations 2.8 – 2.10 in Section 2.3.1.1, Equation 3.33 simplifies to:

$$J = \begin{bmatrix} 0 & 0 & 0 & 1 & 0 & 0 \\ 0 & 0 & 0 & 0 & 1 & 0 \\ 0 & 0 & 0 & 0 & 0 & 1 \\ \frac{\partial \dot{x}}{\partial x} & \frac{\partial \dot{x}}{\partial y} & \frac{\partial \dot{x}}{\partial z} & 0 & 2 & 0 \\ \frac{\partial \dot{y}}{\partial x} & \frac{\partial \dot{y}}{\partial y} & \frac{\partial \dot{y}}{\partial z} & -2 & 0 & 0 \\ \frac{\partial \dot{z}}{\partial x} & \frac{\partial \dot{z}}{\partial y} & \frac{\partial \dot{z}}{\partial z} & 0 & 0 & 0 \end{bmatrix} \quad (3.34)$$

It is apparent that the Jacobian is the same as the  $A$ -matrix given in Equation 3.6.

The eigenvalues of the Jacobian for each of the three collinear Lagrange points include two pairs of imaginary numbers and one pair of real numbers. The eigenvector corresponding to the larger real eigenvalue indicates the unstable direction:  $\mathbf{v}^U$ ; the eigenvector corresponding to the other real eigenvalue indicates the stable direction:  $\mathbf{v}^S$ . The unstable manifold of the Lagrange point,  $W^U$ , may be mapped by propagating the state  $\mathbf{X}^U$  forward in time, where  $\mathbf{X}^U = \mathbf{X} \pm \epsilon \mathbf{v}^U$  and  $\epsilon$  is some small perturbation. Similarly, the stable manifold,  $W^S$ , may be mapped by propagating the state  $\mathbf{X}^S$  backward in time, where  $\mathbf{X}^S = \mathbf{X} \pm \epsilon \mathbf{v}^S$ .

The perturbation  $\epsilon \mathbf{v}$  may be applied to the state  $\mathbf{X}$  in either a positive or a negative sense, corresponding to two halves of each manifold. One perturbation will result in motion that departs the Lagrange point toward the smaller body, e.g., toward the

Moon in the Earth-Moon system, and one will result in motion that departs the Lagrange point away from the smaller body. It is conventional to refer to the half of the manifold that moves toward the smaller body as the **Interior** manifold, since it remains in the interior of the smaller body's influence, at least for a short while, and to refer to the half that moves away from the smaller body as the **Exterior** manifold (see, e.g., Koon et al., 2000b).

The process of analyzing and constructing the invariant manifolds of the unstable Lagrange points may be visualized by considering that each unstable Lagrange point is a dynamical saddle point, as illustrated by the plot shown in Figure 3.13. One can see that a particle's motion will follow the unstable manifold when propagated forward in time after a perturbation, and it will follow the point's stable manifold when propagated backward in time. Figure 3.13 also demonstrates how there are two halves of each manifold.

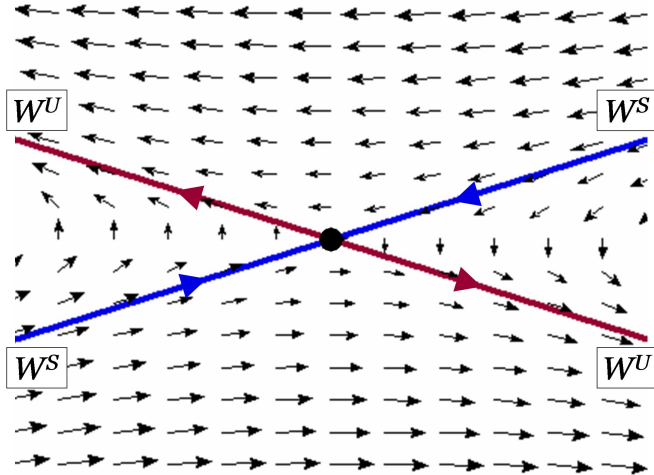


Figure 3.13: A dynamical saddle point, such as that of the unstable Lagrange points in the CRTBP, with a vector field shown that indicates the motion of a particle near the point. The stable and unstable manifolds of the saddle point are shown in blue and red, respectively.

Figures 3.14 – 3.16 show plots of the stable and unstable manifolds of the first three Lagrange points in the Earth-Moon three-body system. The forbidden region is shown shaded in gold in each plot.

The eigenvalues of the Jacobian of the triangular Lagrange points include three imaginary pairs for the Sun-Earth and Earth-Moon three-body systems; hence, they do not have interesting associated invariant manifolds. A particle following a trajectory near one of these Lagrange points will oscillate about the point. If the particle is perturbed, its motion will change but it will not exponentially deviate from its nominal path.

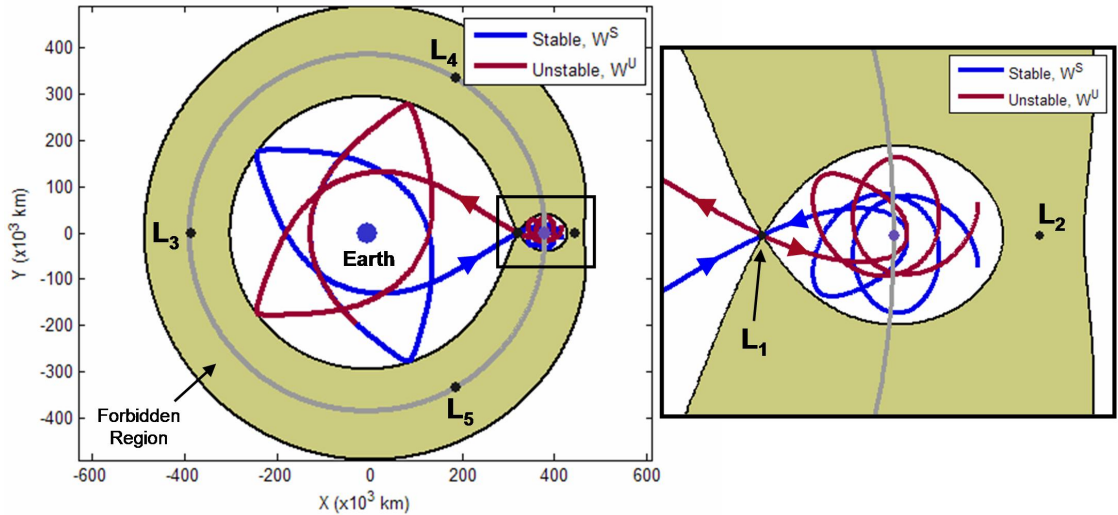


Figure 3.14: The stable and unstable invariant manifolds of the first Lagrange point of the Earth-Moon three-body system.

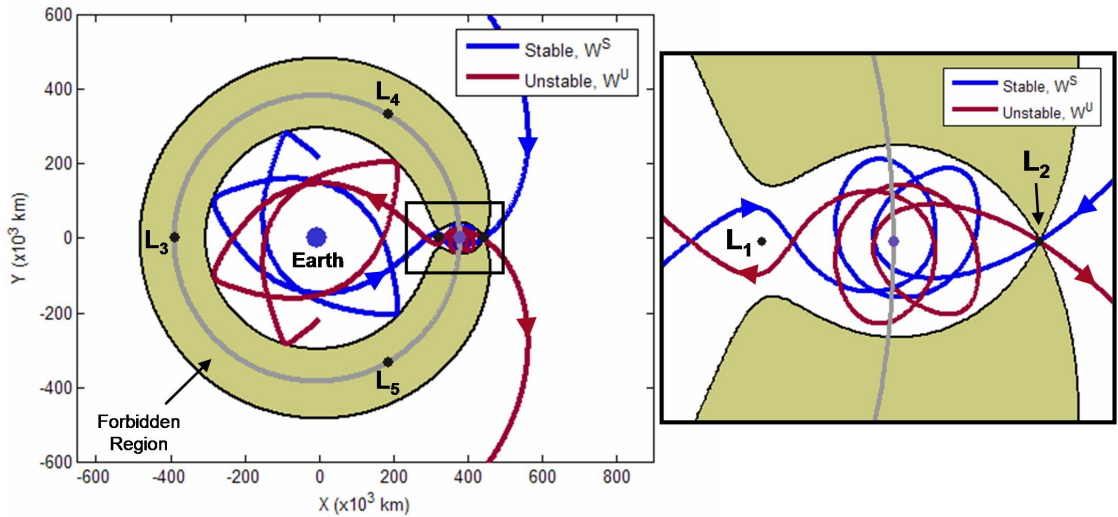


Figure 3.15: The stable and unstable invariant manifolds of the second Lagrange point of the Earth-Moon three-body system.

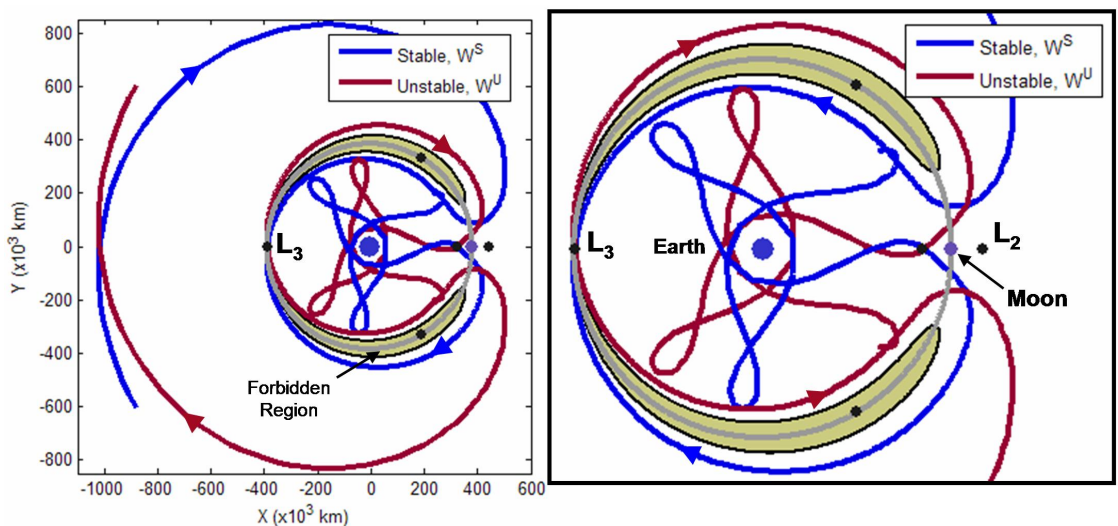


Figure 3.16: The stable and unstable invariant manifolds of the third Lagrange point of the Earth-Moon three-body system.

### 3.9.2 Invariant Manifolds of Unstable Periodic Orbits

Every unstable periodic orbit in the CRTBP has a set of invariant manifolds, much like the Lagrange points. The only substantial difference between the invariant manifolds of periodic orbits and of the Lagrange points is that an additional dimension is added when considering periodic orbits: periodic orbits are one-dimensional structures where the Lagrange points are zero-dimensional structures. Consequently, the invariant manifolds of unstable periodic orbits are two-dimensional structures. They are constructed of a set of trajectories, where each trajectory corresponds to a point along the periodic orbit. The set of trajectories wraps about itself, forming a topological tube. This is further explained below.

To produce the invariant manifolds of an unstable periodic orbit, one requires information about the local stability characteristics of each point along the orbit. In theory, one may evaluate the eigenvalues and eigenvectors of the Jacobian at each and every state along the orbit, and use that information to produce the orbit's invariant manifold. However, evaluating so many eigenvalues requires a great deal of computation. A more efficient manner of producing the invariant manifolds uses the eigenvalues and eigenvectors of the monodromy matrix (see, e.g., Gómez et al., 2004; Ross, 2004).

Since the monodromy matrix is produced by propagating the state transition matrix all the way around the orbit, from time  $t = t_0$  to time  $t = t_0 + T$ , it contains information about the stability of the entire orbit. To determine the stable and unstable directions at each point along the orbit, one only has to propagate the stable and unstable eigenvectors of the monodromy matrix about the orbit using the state transition matrix. That is, the stable and unstable vectors at time  $t_i$  about the orbit,  $\mathbf{v}_i^S$  and  $\mathbf{v}_i^U$ , respectively, may be determined using the stable and unstable eigenvectors of the

monodromy matrix,  $\mathbf{v}^S$  and  $\mathbf{v}^U$ , respectively, using the following equations:

$$\mathbf{v}_i^S = \Phi(t_i, t_0)\mathbf{v}^S \quad (3.35)$$

$$\mathbf{v}_i^U = \Phi(t_i, t_0)\mathbf{v}^U. \quad (3.36)$$

A small perturbation,  $\epsilon$ , is then applied to the state of the orbit at that time,  $\mathbf{X}_i$ , and the result is propagated in time. Since the state transition matrix grows exponentially along an unstable orbit, the magnitudes of the vectors  $\mathbf{v}_i^S$  and  $\mathbf{v}_i^U$  grow along the orbit. It is therefore important to normalize the vectors so that a consistent perturbation is applied to each orbit state. The final equations to produce the initial conditions for the stable and unstable manifolds at time  $t_i$  about the orbit,  $\mathbf{X}_i^S$  and  $\mathbf{X}_i^U$ , respectively, are then equal to:

$$\mathbf{X}_i^S = \mathbf{X}_i \pm \epsilon \frac{\mathbf{v}_i^S}{|\mathbf{v}_i^S|} \quad (3.37)$$

$$\mathbf{X}_i^U = \mathbf{X}_i \pm \epsilon \frac{\mathbf{v}_i^U}{|\mathbf{v}_i^U|}. \quad (3.38)$$

The sign of the perturbation differentiates between Interior and Exterior manifolds, as discussed in Section 3.9.1.

Some discussion should be provided regarding the magnitude of the perturbations applied to the state to produce the manifolds. The theoretical invariant manifolds of the orbit include the set of all trajectories that asymptotically approach the orbit as time goes either forward or backward. In fact, they never truly arrive on the orbit in finite time, but just come arbitrarily close to the orbit. To map them, one approximates the manifolds by perturbing a state slightly off of the orbit and then propagating that state in time. The smaller the perturbation, the closer the approximation comes to mapping the true manifolds; however, small perturbations tend to diverge from the orbit much slower than larger perturbations. When designing practical missions, one is less interested in precisely mapping the invariant manifolds of the orbits, and generally more interested in computationally-swift algorithms. Additionally, the dynamics

of the trajectories depend the greatest on the largest eigenvalues since motion in those directions grows exponentially faster than motion in any other direction. Hence, somewhat large perturbations may be used to map out the motion of the trajectories in the manifolds, e.g., on the order of 100 km in the Earth-Moon system and 1000 km in the Sun-Earth system. In practice, the perturbation magnitudes are given in either units of position or units of velocity, but the perturbation is applied proportionally to all six components. A 100-km perturbation means that the magnitude of the perturbation applied to the position coordinates is equal to 100 km, and the resulting proportionality is used to apply the perturbation to the velocity components, i.e.,

$$\epsilon = \frac{100 \text{ km}}{\sqrt{v_x^2 + v_y^2 + v_z^2}}. \quad (3.39)$$

The structure of the manifolds of an orbit greatly depends on the stability characteristics of each portion of the orbit. Orbits such as libration orbits are fairly uniformly unstable; that is, the local Lyapunov exponent does not vary much along the orbit (for a more detailed exploration about the local Lyapunov exponent of libration orbits, see Anderson 2005). Consequently, their manifolds are fairly smooth as they extend from the orbit. Various other orbits are unstable due to a close flyby of one of the primary bodies. The local stability of these orbits changes drastically, becoming very unstable as the orbit approaches one of the massive bodies. Hence, their manifolds spread out quickly near the body and remain fairly close together elsewhere.

Figure 3.17 shows the stable and unstable manifolds of a two-dimensional Lyapunov orbit about the Earth-Moon L<sub>2</sub> point. One can see that the manifolds are smooth and form a tube-like structure. They remain well-defined until they encounter the Moon, at which time they spread out very rapidly and the tube-like structure becomes less obvious. One can also see that the stable and unstable manifolds are symmetric about the  $x$ -axis, due to the symmetry in the CRTBP. For comparison, Figure 3.18 shows the stable manifold of a resonant flyby orbit, which shows how the structure of the

manifolds depends on the local stability of the orbit. One notices that the trajectories in the manifold diverge quickly near the Moon, but remain near the orbit elsewhere. The unstable manifold is not shown, but is symmetric to the stable manifold.

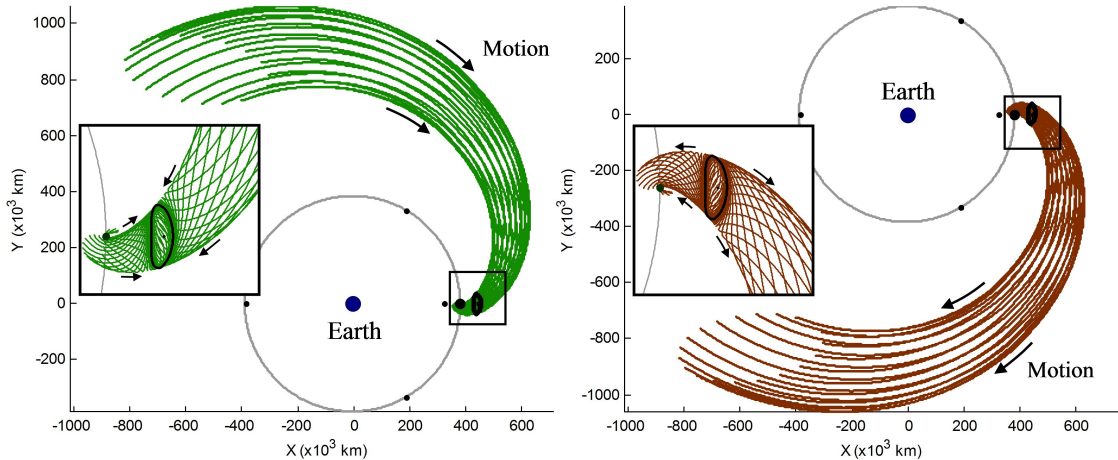


Figure 3.17: The stable (left) and unstable (right) manifolds of a Lyapunov orbit about the Earth-Moon L<sub>2</sub> point.

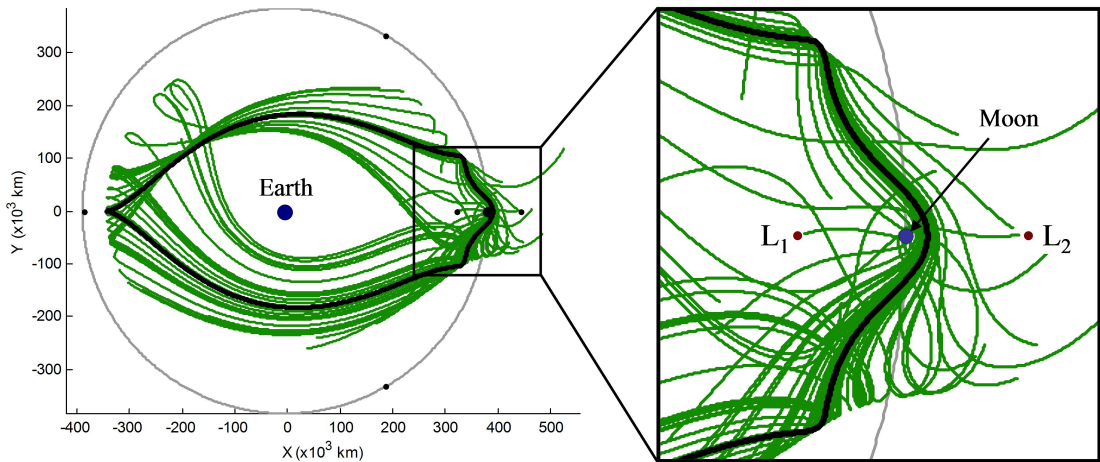


Figure 3.18: The stable manifold of a resonant lunar flyby orbit.

### 3.9.3 Invariant Manifolds of Unstable Quasiperiodic Orbits

Unstable quasiperiodic orbits have associated stable and unstable invariant manifolds, much like unstable periodic orbits, however, the structure and the procedures required to produce them are slightly different. Quasiperiodic Lissajous and quasi-Halo orbits in the CRTBP are two-dimensional structures (Gómez et al., 1998). Hence, their invariant manifolds are three-dimensional structures. The additional dimension adds benefits as well as complexity when using them in practical mission designs.

Since quasiperiodic orbits never retrace their path, one cannot produce them entirely, although one can use a variety of numerical tools to represent them and to produce desirable segments of them (e.g., Kolemen et al., 2007). Since these orbits are not periodic, they do not have associated monodromy matrices. Hence, one cannot use the same simplified procedures to produce their invariant manifolds as those procedures discussed in Section 3.9.2.

To produce a quasiperiodic orbit's invariant manifolds, one may always compute the eigenvectors of the Jacobian of the states at each point along sample segments of the orbit, and follow the same procedures as given in the previous sections. However, that procedure is numerically intensive and slow. Alternatively, to reduce the computational load, one may approximate the manifolds by producing an analog to the monodromy matrix. One may propagate the state transition matrix from one  $x - z$  plane crossing in the synodic frame to the next (or to any later crossing) and use the resulting matrix as a pseudo-monodromy matrix. When one propagates this matrix's stable and unstable eigenvectors about the orbit segment, and then follows the process outlined in Section 3.9.2, one produces approximations of the invariant manifolds of the quasiperiodic orbit. These approximations are often good enough to be used for preliminary spacecraft mission design, such as that used for the Genesis spacecraft mission (Howell et al., 1997b).

## 3.10 Orbit Transfers

Dynamical systems theory provides the tools needed to systematically produce transfers to/from unstable orbits in the CRTBP. This section discusses several example orbit transfers as demonstrations of the application of dynamical systems theory. Section 3.10.1 discusses the construction of a transfer from the Earth to a Halo orbit about the Sun-Earth L<sub>2</sub> point. Section 3.10.2 discusses the construction of a chain of periodic orbits in the CRTBP. That is, trajectories are constructed that transfer a spacecraft back and forth between several periodic orbits in the CRTBP. These examples demonstrate the procedures that may be followed to construct any type of orbit transfer in the CRTBP using dynamical systems theory.

### 3.10.1 Surface to Orbit Transfers

Several missions have been proposed to operate in a libration orbit about the Sun-Earth L<sub>2</sub> (EL<sub>2</sub>) point, including the James Webb Space Telescope and the Terrestrial Planet Finder. In this section, we demonstrate how to construct a ballistic transfer from the Earth to a Halo orbit about EL<sub>2</sub>, a transfer that might prove to be very useful for missions such as these proposed missions. The transfers produced here do not require any orbit insertion maneuvers: after their LEO-departures, each transfer is thereafter entirely free of any deterministic maneuvers. The process used here may be generalized to compute a transfer from the surface of the secondary body in most three-body systems into many unstable three-body periodic orbits, or vice-versa.

We first consider the family of Halo orbits about the EL<sub>2</sub> point. The family begins as a bifurcation of the family of planar libration orbits about EL<sub>2</sub> as shown in Appendices A and B. The orbits in the family gradually move farther out of the plane until they eventually make close approaches with the Earth. Example orbits in the family of Northern EL<sub>2</sub> Halo orbits are shown in Figure 3.19. Southern EL<sub>2</sub> Halo orbits are

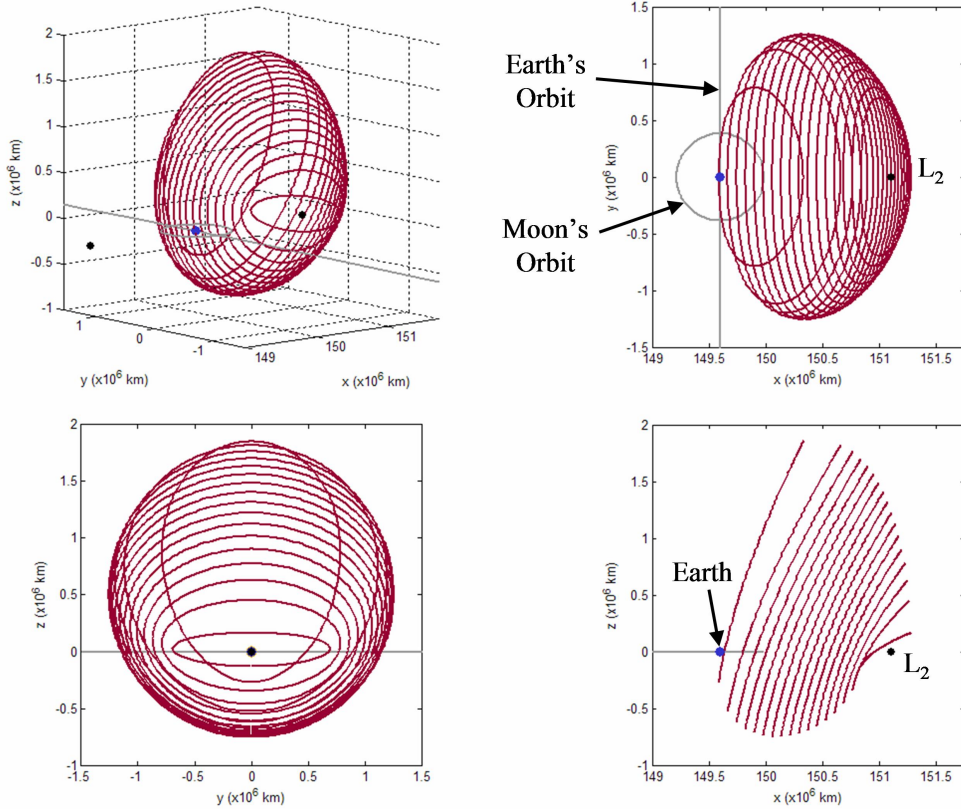


Figure 3.19: Example Halo orbits in the family of Northern Halo orbits about the Sun-Earth L<sub>2</sub> point. The orbits are shown from four perspectives.

identical to Northern orbits except they are symmetric about the  $x - y$  plane.

We next consider a single unstable Halo orbit and produce its stable invariant manifold. This manifold includes all the trajectories that a spacecraft may take to arrive onto the orbit. A plot of the example Halo orbit and its stable manifold is shown in Figure 3.20. The trajectories shown in blue have a perigee altitude below 500 km. The Halo orbit chosen here has a Jacobi constant equal to approximately 3.00077207, given the assumptions about this three-body system (§2.3.1). The CRTBP is a good model of the real solar system for trajectories propagated for a reasonably short amount of time, namely, for one orbital period of the two primary masses about their barycenter. Beyond that, the accumulation of errors due to perturbations in the real solar system

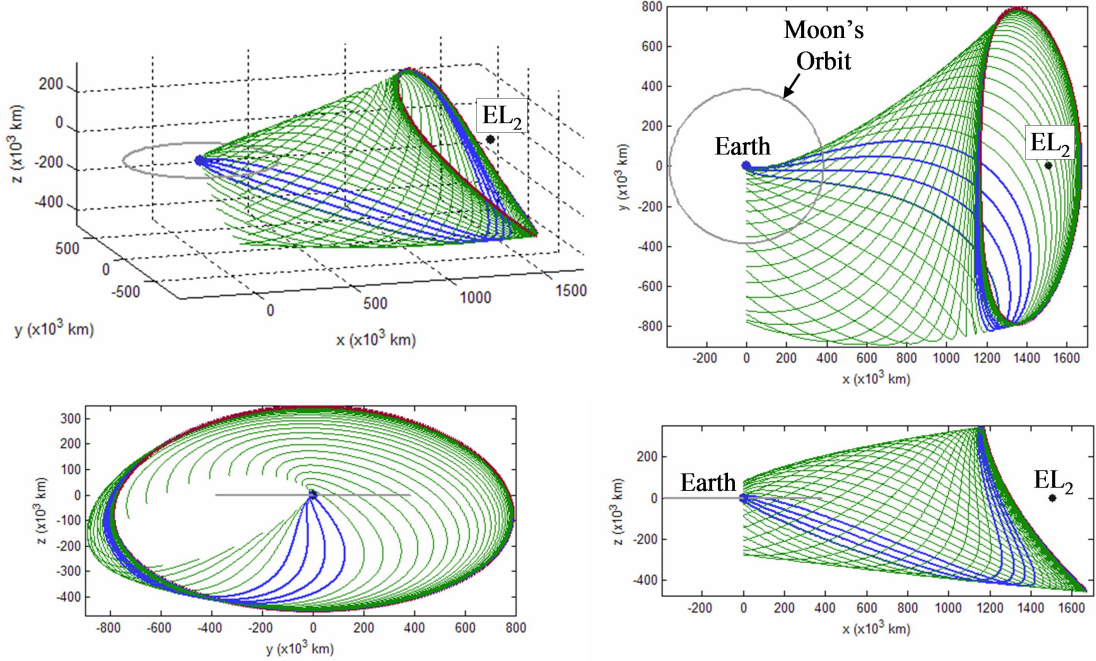


Figure 3.20: An example unstable Halo orbit about the Sun-Earth L<sub>2</sub> point and its stable invariant manifold.

causes the CRTBP approximation to break down. The trajectories shown in Figure 3.20 have been propagated for at most 365 days – they are only plotted in the figure until they cross the plane of the Earth for clarity. A brief study has shown that this propagation time yields good approximations of true trajectories that exist in the real solar system.<sup>1</sup> As the propagation time is increased, the trajectories may make additional close approaches to the Earth. In some cases the second or third perigee passes closer to the Earth than the first. This is explored in more depth momentarily.

Each trajectory shown in Figure 3.20 may be characterized using several parameters. The parameter  $\tau$ , defined in Section 3.3.3, indicates the point where the trajectory arrives at the Halo orbit. The closest approach of each trajectory with the Earth is identified to compute the perigee altitude and ecliptic inclination with respect to the Earth.

<sup>1</sup> Trajectories in the manifold have been differentially-corrected from the CRTBP into the JPL Ephemeris model of the solar system and nearly all have been found to be heuristically unchanged. Exceptions include trajectories that pass very close to the Earth.

These two parameters are useful because they indicate the altitude and inclination of a low Earth orbit that may be used as a staging orbit to transfer a spacecraft to the Halo orbit. Figure 3.21 shows two plots: one of the perigee altitude and one of the corresponding ecliptic inclination as functions of  $\tau$ , where the vertical bars indicate the locations in the manifold that have perigee altitudes between 0 and 500 kilometers. For example, one can see that the trajectory with a  $\tau$ -value of 0.751 encounters a closest approach with the Earth with a perigee altitude of approximately 185 km and an ecliptic inclination of approximately 34.8 degrees. Hence, a spacecraft in a circular low Earth parking orbit with an altitude of 185 km and an ecliptic inclination of  $34.8^\circ$  may perform a tangential  $\Delta V$  to transfer onto the manifold; once on the manifold, the spacecraft ballistically follows it and asymptotically arrives onto the Halo orbit.

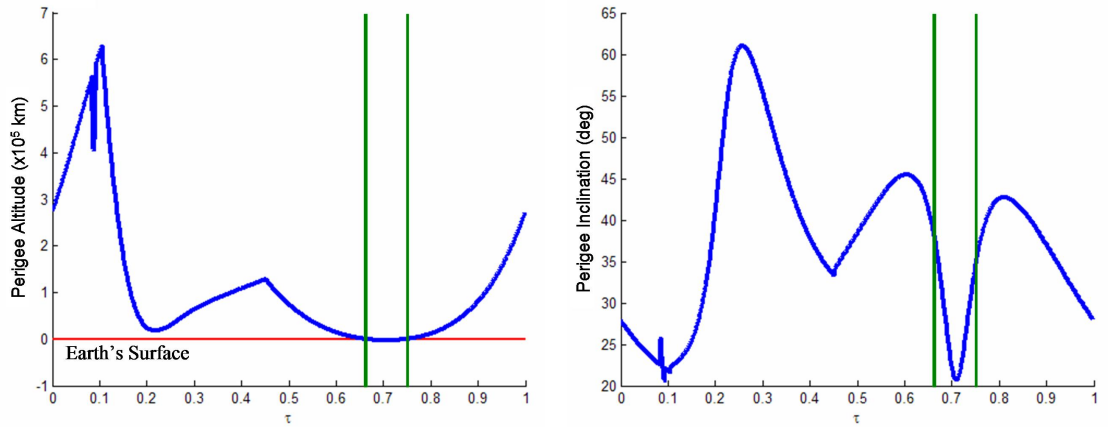


Figure 3.21: The perigee altitude (left) and corresponding ecliptic inclination (right) of the trajectories in the stable manifold shown in Figure 3.20 as functions of  $\tau$ .

There are two statements in these results that need to be addressed. The first is that the inclination values displayed in Figure 3.21 are the inclination values computed in the axes of the CRTBP, namely, with respect to the ecliptic. The equatorial inclination values of these perigee points depend on which date a spacecraft launches. Since the Earth's rotational axis is tilted by approximately  $23.45^\circ$  with respect to the ecliptic (Val-

lado, 1997), many equatorial inclinations may be used to inject onto a desired trajectory depending on the date. The second statement that should be addressed is that the results shown in Figure 3.21 depend greatly on the perturbation magnitude,  $\epsilon$ , described in Section 3.9: implementing a different perturbation magnitude results in a change in the  $\tau$ -values required to obtain a certain trajectory. For example, if  $\epsilon$  were reduced, the trajectories modeling the orbit's manifold would spend more time asymptotically approaching/departing the orbit. Once the trajectories are sufficiently far from the orbit, their characteristics are nearly unchanged. The result is that the  $\tau$ -value for a desired trajectory is strongly related to the value of  $\epsilon$ . This has no significant effect for practical spacecraft mission designs; a spacecraft following a trajectory in the Halo orbit's stable manifold will asymptotically approach the Halo orbit – the value of  $\epsilon$  is only used for modeling the stable manifold.

It is now of interest to identify how the manifolds change and how the plots shown in Figure 3.21 change as the manifold's propagation time is varied. Figure 3.22 shows plots of the stable manifold of the same Halo orbit propagated for successively longer amounts of time. One can see that the trajectories on the manifold spend some amount of time near the Halo orbit (where, once again, the amount of time depends on the value of  $\epsilon$ ), and then depart. It may be seen that many of the trajectories in the manifold make closer approaches with the Earth after their first perigee. Figure 3.23 shows many plots of the closest approach each manifold makes with the Earth for varying amounts of propagation time. It is clear that the longer propagation times yield closer perigee passages.

The procedures given in this section may be repeated for each Halo orbit in the entire family of Halo orbits and maps may be produced showing the range of perigee altitudes and the range of inclination values obtainable for each Halo orbit. These are useful for identifying the approximate location of desirable trajectories in the real solar system.

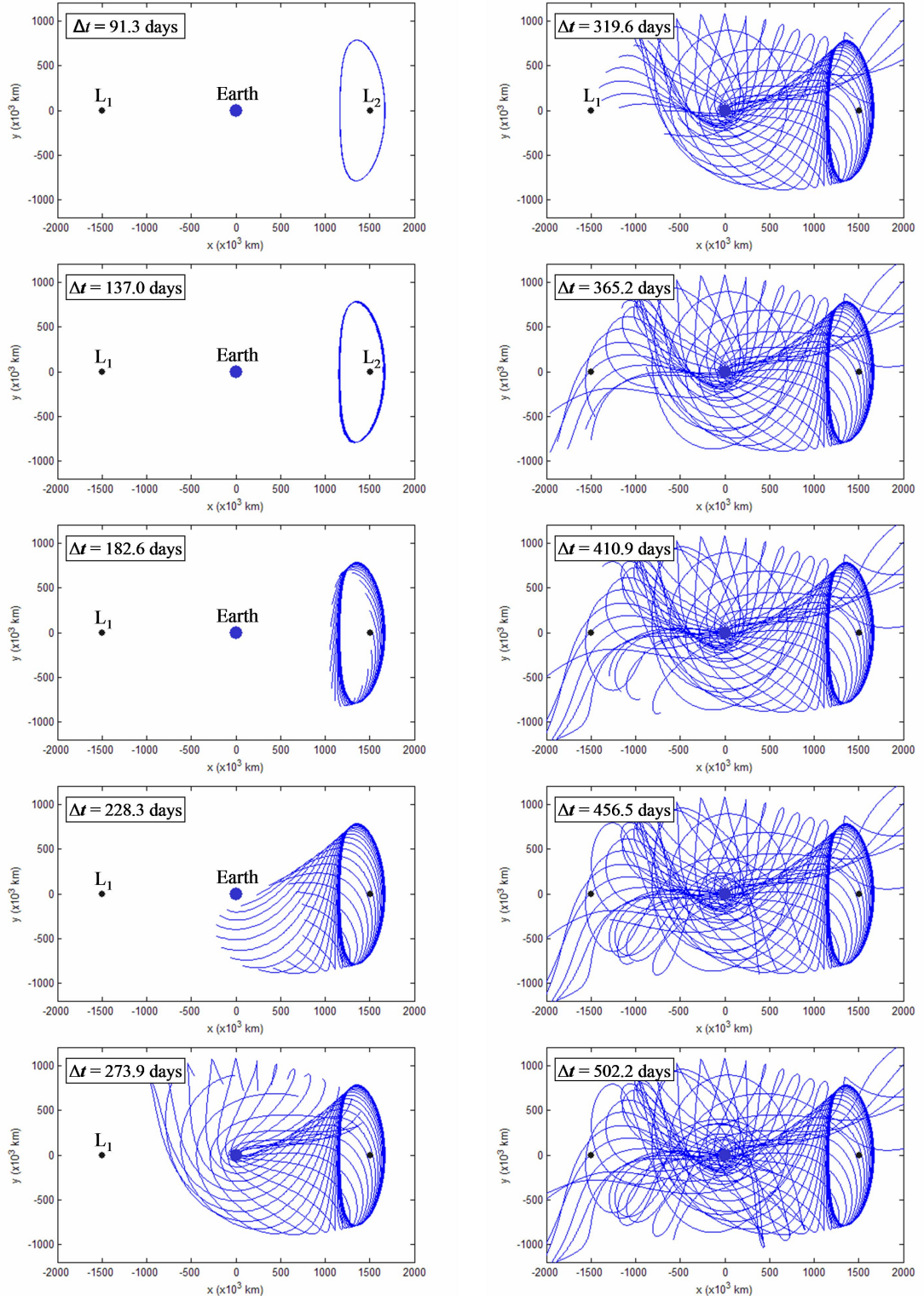


Figure 3.22: The stable manifold of a Sun-Earth L<sub>2</sub> Halo orbit propagated for successively longer amounts of time. The duration of each propagation is indicated in each plot by the value  $\Delta t$ .

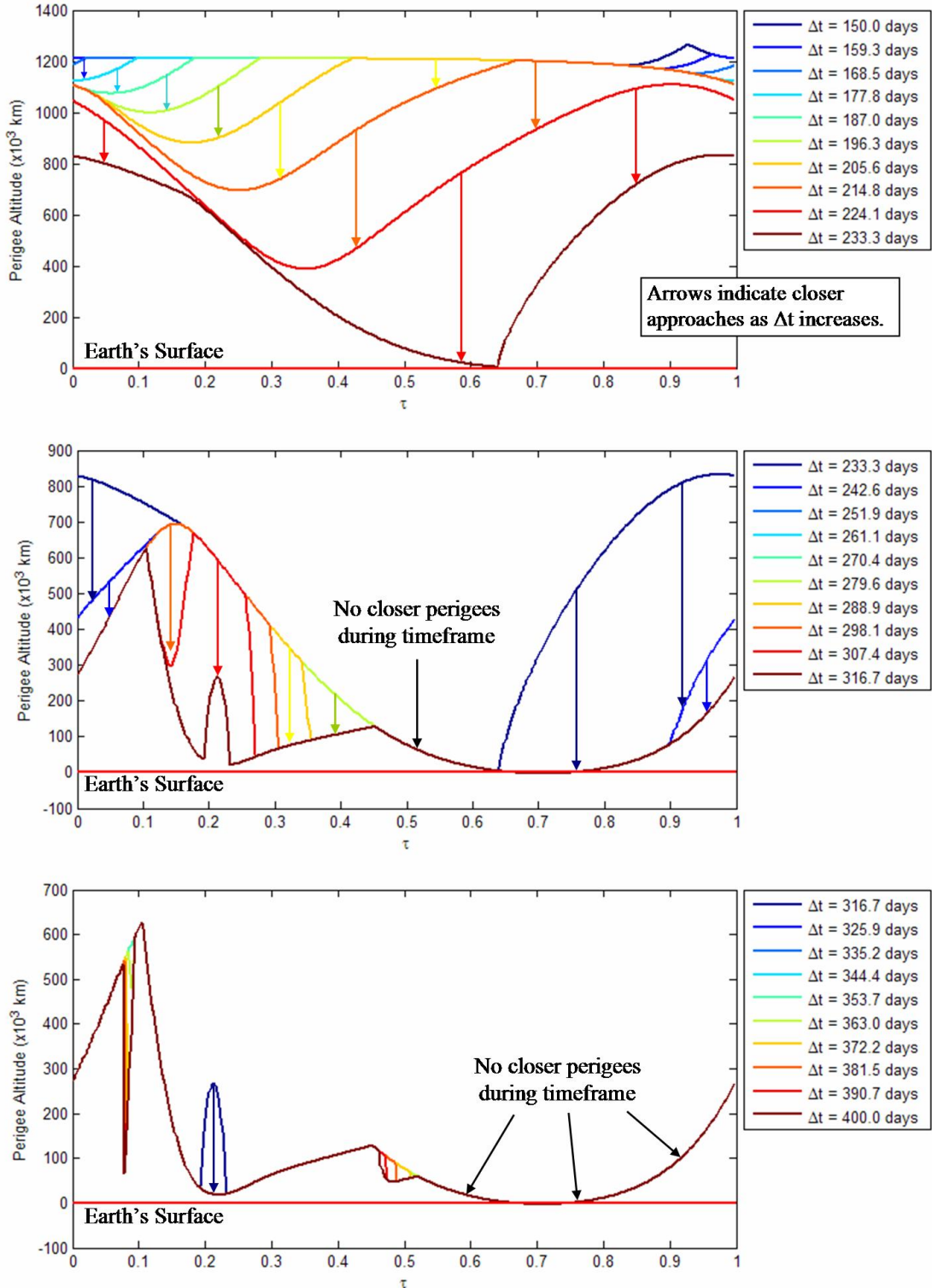


Figure 3.23: The altitude of closest approach of each trajectory in the stable manifolds shown in Figure 3.22 with respect to the Earth. The propagation times of each manifold are shown in the legend. Longer propagation times yield closer perigee passages.

### 3.10.2 Orbit Transfers and Chains

Once a particle or spacecraft is on an unstable periodic orbit in the three-body system, then it may theoretically stay there for an arbitrarily long time or it may fall off of that orbit by following any trajectory on that orbit's unstable manifold. The cost for a spacecraft to transfer off of an orbit is the same as the cost of station-keeping to remain on that orbit: both are arbitrarily small given good navigational support. These considerations are further explored in Chapter 7.

Section 3.9.2 shows several examples of stable and unstable invariant manifolds of unstable periodic orbits. One may notice by studying these manifolds that by controlling exactly when the spacecraft departs from its periodic orbit, it may be able to transfer to numerous other locations in the state space, including, but not limited to, the surface of the Moon, any of the five lunar Lagrange points, another unstable periodic orbit in the system, or an escape trajectory away from the vicinity of the Moon or Earth. If the spacecraft were carefully navigated onto the correct trajectory within the unstable manifold of one orbit, it may encounter the stable manifold of a different unstable three-body orbit.

After considering a spacecraft's options, several categories of orbit transfers may be identified. Table 3.3 summarizes a few characteristic categories of orbit transfers. In the table, a "Stable Orbit" includes conventional two-body orbits about either of the two primaries in the system as well as stable three-body orbits and even transfers to/from the surface of one of the primary bodies. The minimum number of  $\Delta V$ s indicates the fewest number of maneuvers that may typically be used to perform the given transfer. There are many cases when a particular transfer might require more maneuvers, such as a transfer from the surface of a body to a particular orbit in space with a time constraint. There are also certain special cases when a transfer might require fewer maneuvers, such as a transfer between two stable orbits where the two orbits in-

Table 3.3: A summary of several categories of orbit transfers in the CRTBP.

Orbit 1	Orbit 2	Constraints	Minimum # of $\Delta V$ s
Stable Orbit	Stable Orbit	None	2
Stable Orbit	Unstable Orbit	None	1
Unstable Orbit	Stable Orbit	None	1
Unstable Orbit	Unstable Orbit	None	1
Any Orbit	Any Orbit	Transfer Time	2
Unstable Orbit	Unstable Orbit	Transfer Time*	1
Unstable Orbit	Unstable Orbit	Same Jacobi Constant	0

\*Transfers between two unstable orbits with a very short specified transfer time usually require two maneuvers; for longer transfer times, one maneuver is often all that is required.

tersect in space. Nonetheless, Table 3.3 gives a good idea about the minimum number of required maneuvers for orbit transfers in several circumstances.

In this section, low-energy orbit transfers are introduced that may be useful for practical mission design, and which are useful background for the discussions of ballistic lunar transfers in later sections of this dissertation. These orbit transfers are in the category represented by the last row of Table 3.3: transfers that are free of deterministic maneuvers.

Free transfers between unstable periodic orbits may be identified using knowledge of their unstable manifolds and their Jacobi constants. Figure 3.24 shows a plot of several families of three-body orbits in the Earth-Moon CRTBP, where the orbits' Jacobi constant values are plotted as a function of their  $x_0$ -values (the value of their  $x$ -axis crossing that has a positive  $y$ -value as explained in Appendix A). The curves shaded in black correspond to unstable three-body orbits; the curves shaded in gray correspond to neutrally stable three-body orbits. The blue line indicates a particular Jacobi constant value. One can see that several unstable orbits exist at this Jacobi constant within different families of orbits. Free transfers may be constructed between these orbits using their invariant manifolds.

We now consider the case of a spacecraft in orbit about a two-dimensional Lyapunov orbit about the Earth-Moon L<sub>1</sub> point (an orbit in the family classified as a Ret-

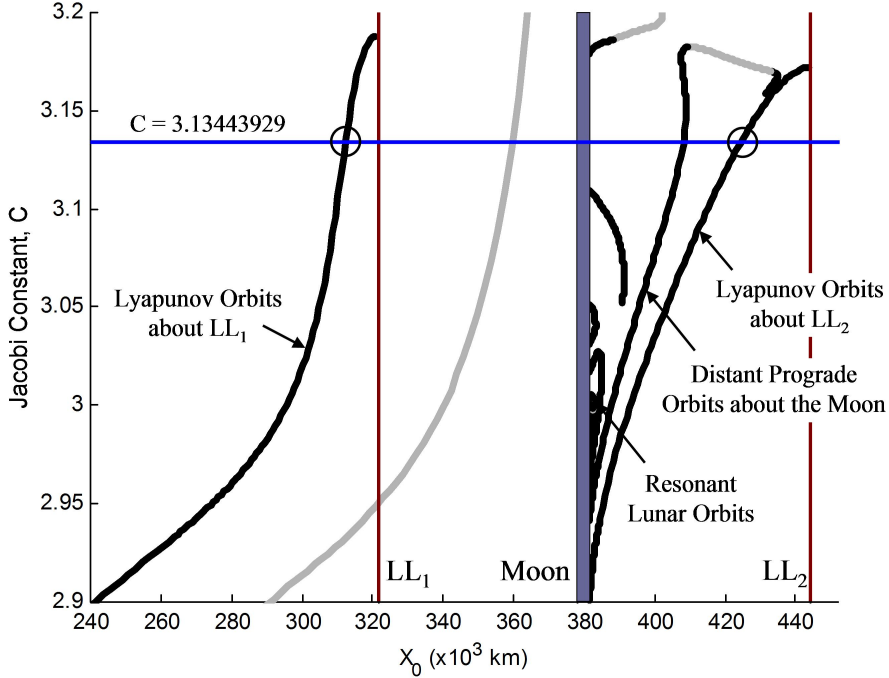


Figure 3.24: A plot of several families of three-body orbits in the Earth-Moon CRTBP, where the orbits' Jacobi constant values are plotted as a function of their  $x_0$ -values (the value of their  $x$ -axis crossing that has a positive  $j$ -value as explained in Appendix A). The curves shaded in black correspond to unstable three-body orbits; the curves shaded in gray correspond to neutrally stable three-body orbits.

rograde Class 4 Orbit in Appendix A), aiming to transfer to a Lyapunov orbit about the  $L_2$  point (a Retrograde Class 6 Orbit in Appendix A). Figure 3.25 shows a plot of both orbits, the unstable manifold of the  $L_1$  Lyapunov orbit, and the stable manifold of the  $L_2$  Lyapunov orbit. The spacecraft may transfer from the  $L_1$  orbit to the  $L_2$  orbit by departing its initial orbit along a trajectory in the orbit's unstable manifold that intersects a trajectory in the final orbit's stable manifold. If the trajectories intersect in space, then the spacecraft can indeed perform a maneuver to make the connection. If the trajectories intersect in both position and velocity, i.e., in phase space, then the spacecraft may make the transfer without any deterministic maneuver. Two free transfers between these orbits are shown in Figure 3.26. Many other free transfers exist that

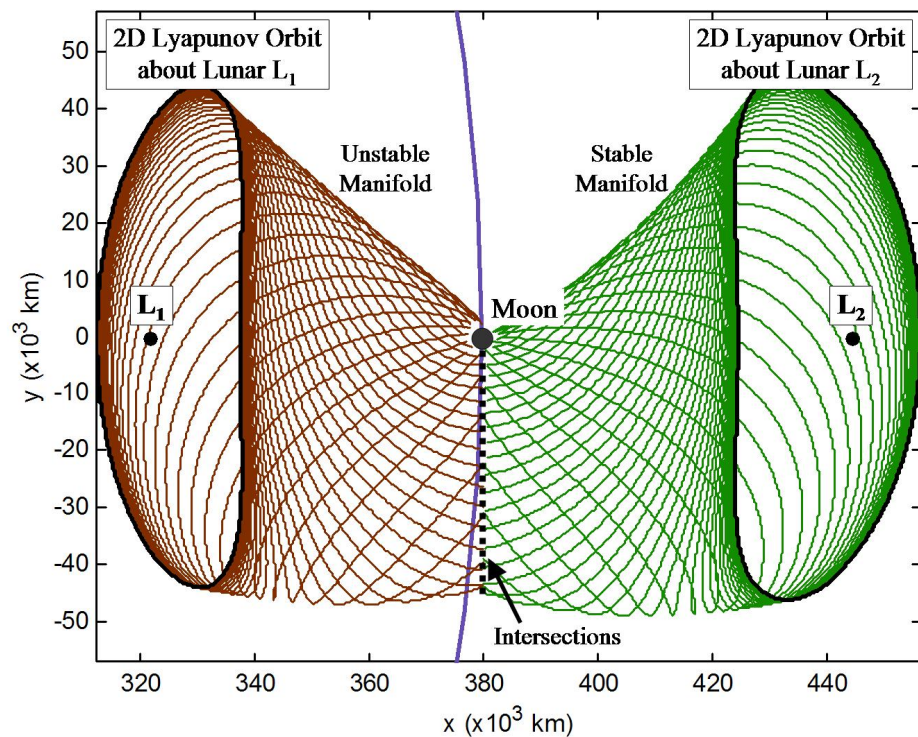


Figure 3.25: The intersection of the unstable manifold (red) of a Lyapunov orbit about the Earth-Moon  $L_1$  point and the stable manifold (green) of a Lyapunov orbit about the Earth-Moon  $L_2$  point.

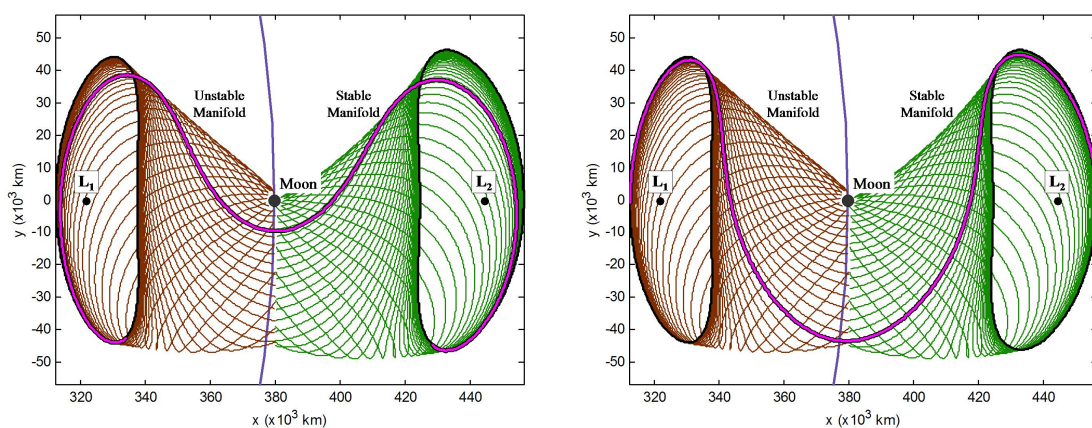


Figure 3.26: Two example free transfers between the orbits shown in Figure 3.25.

require larger transfer durations.

Figure 3.27 shows free transfers between the same two Lyapunov orbits shown in Figures 3.24 – 3.26 and a Distant Prograde Orbit with the same Jacobi constant. A Distant Prograde Orbit is an orbit in the family of three-body orbits classified as a Prograde Class 5 Orbit in Appendix A.

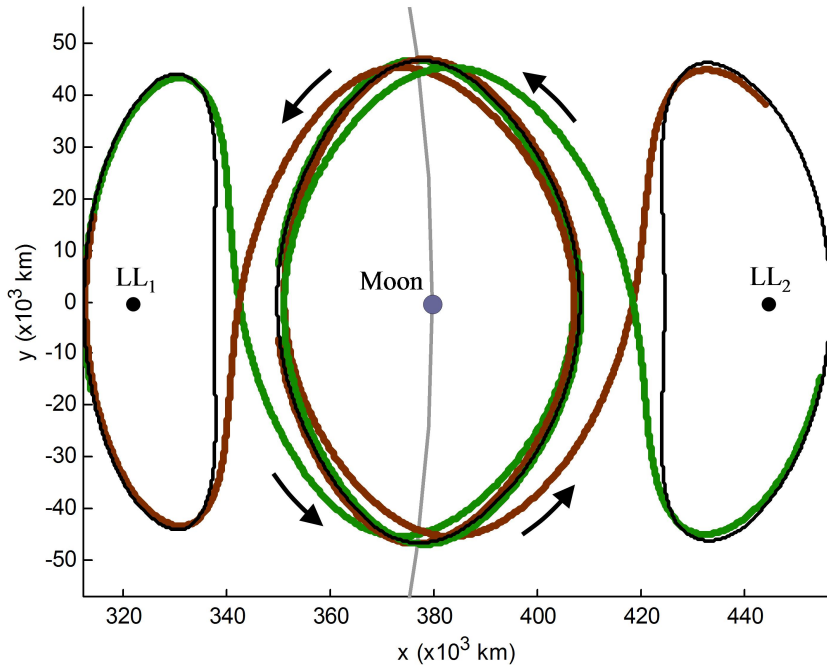


Figure 3.27: Free transfers between a Lyapunov orbit about  $LL_1$ , a Distant Prograde Orbit about the Moon, and a Lyapunov orbit about  $LL_2$ , where each orbit and every trajectory shown have the same Jacobi constant,  $C = 3.13443929$ .

Free transfers between two distinct periodic orbits are heteroclinic connections between those orbits (Koon et al., 2000a). A free transfer from a periodic orbit back onto itself is a homoclinic connection. Because heteroclinic connections exist between these example periodic orbits, one can construct any arbitrary transfer itinerary between these orbits (Lo and Parker, 2005). For instance, one can build a continuous trajectory that a spacecraft may follow to traverse the  $L_1$  orbit  $n_1$  times, followed by the Distant Prograde Orbit  $n_2$  times, followed by the  $L_2$  orbit  $n_3$  times, where  $n_1$ ,  $n_2$ , and  $n_3$  may

be any natural number. The sequence may continue as long as desired without any pattern. If any transfers exist, then the spacecraft is never truly **on** any of the periodic orbits, but is following a trajectory that **shadows** the periodic orbits. If one of the natural numbers  $n_i$  is large, then the spacecraft's trajectory shadows that generating orbit very closely.

A complex periodic orbit may be constructed by repeating a given sequence of  $n_i$ 's ad infinitum. For instance, the sequence  $\{\dots, 2^{L_1}, 1^{DPO}, 2^{L_1}, 1^{DPO}, \dots\}$  represents a periodic orbit that consists of two revolutions about the  $L_1$  Lyapunov orbit, followed by one revolution about the Distant Prograde Orbit, before it repeats itself. Figure 3.28 shows a plot of such a periodic orbit. One can see that a trajectory following a complex itinerary gets very close to one of its generating three-body orbits even with  $n_i$  as low as two; that is, the trajectory shown in Figure 3.28 comes very close to the generating  $L_1$  Lyapunov orbit before transferring away again.

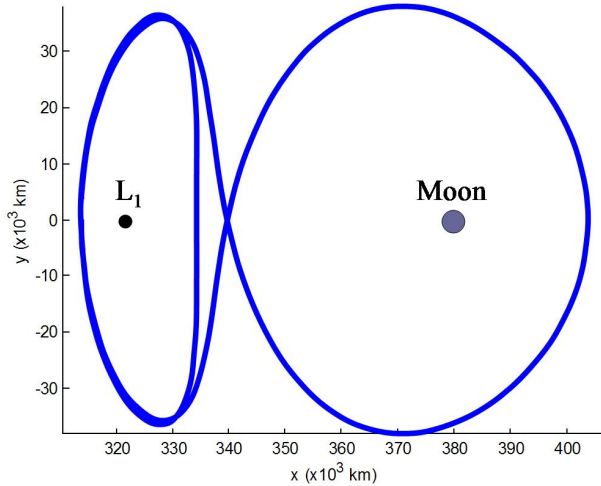


Figure 3.28: A complex periodic orbit that consists of two revolutions about the  $L_1$  Lyapunov orbit, followed by one revolution about the Distant Prograde Orbit, before it repeats itself.

Since each unstable three-body orbit exists in a family, it is apparent that complex periodic orbits also exist in families. Figure 3.29 shows several example complex periodic orbits that exist in the same family as the orbit shown in Figure 3.28.

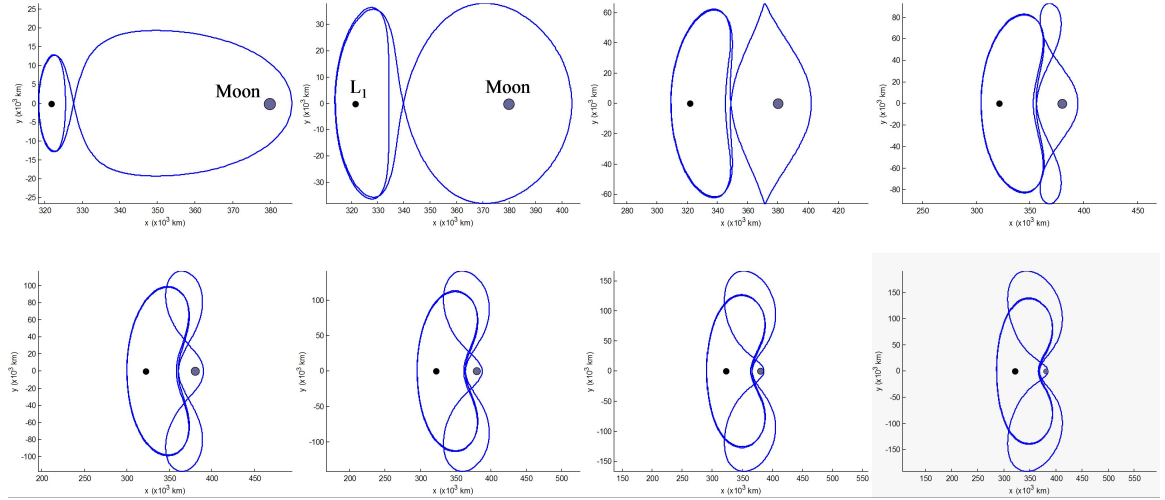


Figure 3.29: Several example complex periodic orbits that exist in the same family as the orbit shown in Figure 3.28.

### 3.11 Becoming Captured or Temporarily Captured

This dissertation studies transfers from one orbit to another, either by implementing an orbit-insertion maneuver or by way of an asymptotic ballistic insertion. Chapter 5 discusses methods that may be used to construct transfers between the Earth and lunar orbits using ballistic means. Since the spacecraft is in a conservative system and does not perform a capture maneuver, the spacecraft cannot transfer into an orbit fully captured by the Moon. Hence, many authors refer to these orbits as being **temporarily captured** by the Moon. There is a good deal of ambiguity in the literature surrounding the definition of a temporarily captured orbit about the Moon. Some discussion is therefore necessary to identify what is meant here by the labels **captured** and **temporarily captured** regarding trajectories and periodic orbits near the Moon.

Orbits in the two-body problem are neutrally stable orbits, using the terminology introduced in Section 3.8. A spacecraft in an elliptical two-body orbit will repeat its track periodically over time. Given a perturbation in its state, the spacecraft will remain near its original orbit over time; that is, the spacecraft's motion will not exponentially diverge from its nominal orbit. Furthermore, a spacecraft in an elliptical two-body orbit has a negative value for its two-body specific energy. The spacecraft is considered to be captured by the primary body. If the spacecraft were to increase its specific energy to a value greater than zero, then the spacecraft could escape the primary body. Hence, in the two-body system, a spacecraft can either be captured by the body or can have sufficient energy to escape; the concept of being temporarily captured is not generally used.

In the three-body problem, a spacecraft's specific energy with respect to either of the primary bodies changes over time. A spacecraft may have an amount of energy sufficient to escape one of the bodies, yet not enough energy to escape the entire system. Furthermore, a spacecraft's energy with respect to one of the bodies may be transferred to the other massive body in the same sense that a gravity flyby transfers energy between a massive body and the spacecraft. Hence, a spacecraft traveling in a three-body environment may have its two-body energy drop temporarily below zero, implying a gravitational capture by one of the bodies – or its energy may rise above zero and it may escape the body.

For now, this discussion considers a spacecraft in the Earth-Moon system, although this discussion may be generalized to any three-body system. One may clearly use the plots of the Forbidden Regions of the CRTBP, such as those given in Section 2.3.1.4, to classify whether or not a spacecraft is fully captured by one of the primary bodies in a three-body system. In the Earth-Moon system, a spacecraft that has a Jacobi constant greater than approximately 3.18834 is either trapped in the Earth's or Moon's vicinity and cannot transfer between them. Such a spacecraft is considered to

be captured by the corresponding body. With slightly smaller Jacobi constant values, the spacecraft is permitted to transfer between each body's vicinity through the neck at LL<sub>1</sub>, but cannot escape the interior of the Earth-Moon system. Such a spacecraft is considered to be captured by the Earth-Moon system, but not captured by either the Earth or the Moon. A spacecraft with a Jacobi constant lower than approximately 3.17216 is permitted to transfer to the exterior region of the Earth-Moon system through the neck at LL<sub>2</sub>. Such a spacecraft may still be considered to be captured by the system if its orbit is within the interior of the system and does not lead it through the LL<sub>2</sub> neck; but since it has sufficient energy to depart the system through the neck, it is more accurate to say that the spacecraft is temporarily captured by the system.

In literature, authors define a spacecraft as being temporarily captured in a system in different ways. Many authors define a spacecraft to be temporarily captured by the Moon if the spacecraft's two-body energy with respect to the Moon falls below zero (see, e.g., Alexeyev, 1963; Belbruno, 1987; Vieira Neto and Prado, 1998; Vieira Neto, 1999; Yamakawa et al., 1993). Other authors require that a spacecraft make at least one revolution about the Moon before escaping in order to be temporarily captured (see, e.g., Koon et al., 2000b). In some cases, the spacecraft must also get within a certain minimum-proximity to the Moon, e.g., within the Moon's sphere of influence (Koon et al., 2001). These requirements are often sufficient, but there are cases when authors may easily argue that a spacecraft has become temporarily captured by the Moon without meeting one or more of these requirements. For instance, a spacecraft in a lunar Halo orbit completes a full revolution about the Moon only after a full month, due to the unique location of the Halo orbits, although the spacecraft's specific energy with respect to the Moon falls below zero during a portion if not all of the orbit. Some might argue, then, that if the spacecraft only visited the Halo orbit for two weeks and then departed that orbit, that the spacecraft was not temporarily captured by the Moon during its time on the Halo orbit. Others may argue that the moment the spacecraft's

two-body specific energy with respect to the Moon dropped below zero that the spacecraft became temporarily captured. Still others will argue that the spacecraft can only be temporarily captured by the Moon in a lunar Halo orbit if that lunar Halo orbit's perilune distance is below some threshold.

To assist in the identification of a temporarily captured orbit, Figure 3.30 shows a survey of six example periodic three-body orbits that exist near the Moon in the Earth-Moon three-body system. In each case, the orbit's Jacobi constant and its two-body specific energy with respect to both primaries have been computed. For brevity, only the minimum and maximum energy-values are displayed in the figure. One can see that each of these six orbits remains within some maximum distance from the Moon. This implies that they are captured by the Moon, although, the Earth's gravitational influence is required to keep a spacecraft in such an orbit. Hence, it is difficult to qualitatively claim that a spacecraft in any of these orbits is truly captured or temporarily captured by the Moon. Certainly over a sufficient length of time, a spacecraft in each of these orbits will completely revolve around the Moon in some sense. One can also see by studying the caption of Figure 3.30 that a spacecraft in any of these orbits can have a variety of two-body specific energy values with respect to the Moon: the energy of a spacecraft in orbits (a) – (c) is always below zero; the energy of a spacecraft in orbits (d) and (e) oscillates about zero; the energy of a spacecraft in orbit (f) is always greater than zero. Some orbits in these families certainly approach within the Moon's sphere of influence, but others do not. It is not immediately clear how to classify these orbits.

It may be argued that a spacecraft is temporarily captured by the Moon when it has negative energy with respect to the Moon and the Moon's gravitational influence dominates the motion of the spacecraft, i.e., it is within the Moon's sphere of influence. A spacecraft in another type of orbit, such as orbits (d) and (f) from Figure 3.30, may have its motion dominated by the gravitational influence of the Earth rather than the Moon. However, a spacecraft in an unstable three-body orbit that persists outside of

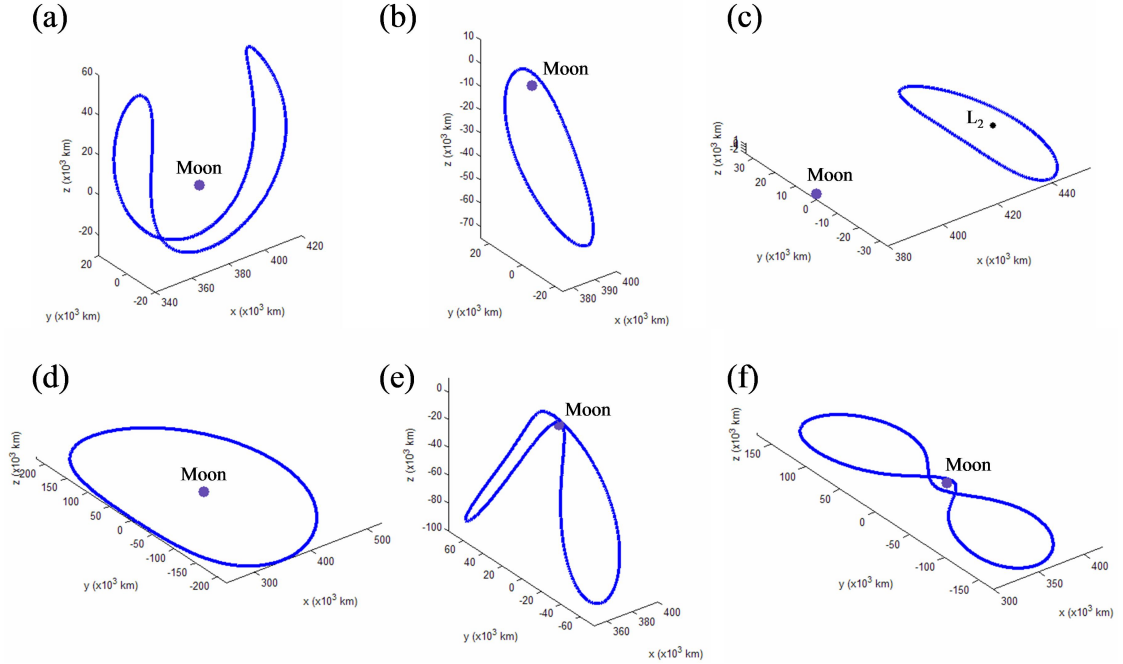


Figure 3.30: A survey of six example three-body orbits near the Moon. The following table summarizes the appropriate information about each orbit. The two-body energy range gives the minimum and maximum specific energy that a spacecraft has when following the orbit with respect to the given primary.

Plot	Orbit Type	Jacobi Constant	Two-Body Energy Range w.r.t. Earth (J/kg)	Two-Body Energy Range w.r.t. Moon (J/kg)
(a)	Retrograde, Class M2 (§B.8)	3.084927	[−0.7531, −0.2479]	[−0.0656, −0.0515]
(b)	Large $z$ -amplitude L <sub>2</sub> Halo, Class 6 (§B.6)	3.032580	[−0.5324, 1.4915]	[−0.0606, −0.0436]
(c)	Small $z$ -amplitude L <sub>2</sub> Halo, Class 6 (§B.6)	3.151994	[−0.3048, −0.0167]	[−0.0653, −0.0462]
(d)	Distant Retrograde Orbit, Class 5 (§A.5.2)	2.842410	[−0.5438, −0.4377]	[−0.0066, 0.0679]
(e)	Distant Prograde Orbit, Class 5 (§B.5.1)	2.970770	[−1.0482, 3.6427]	[−0.0366, 0.0023]
(f)	Distant Prograde Orbit, Class 5 (§A.5.1)	2.986649	[−1.0638, 1.5867]	[0.0013, 0.0150]

the Moon's sphere of influence, such as orbit (c), is freely able to follow a trajectory in the orbit's unstable manifold that may be chosen to meet all of the set requirements of a temporarily captured trajectory. An example of this sort of transfer is shown in Figure 3.31. The unstable three-body orbit may not be classified as a temporarily captured orbit since it extends beyond the Moon's sphere of influence, but it may be used to lead a spacecraft to a trajectory that is generally accepted to be temporarily captured.

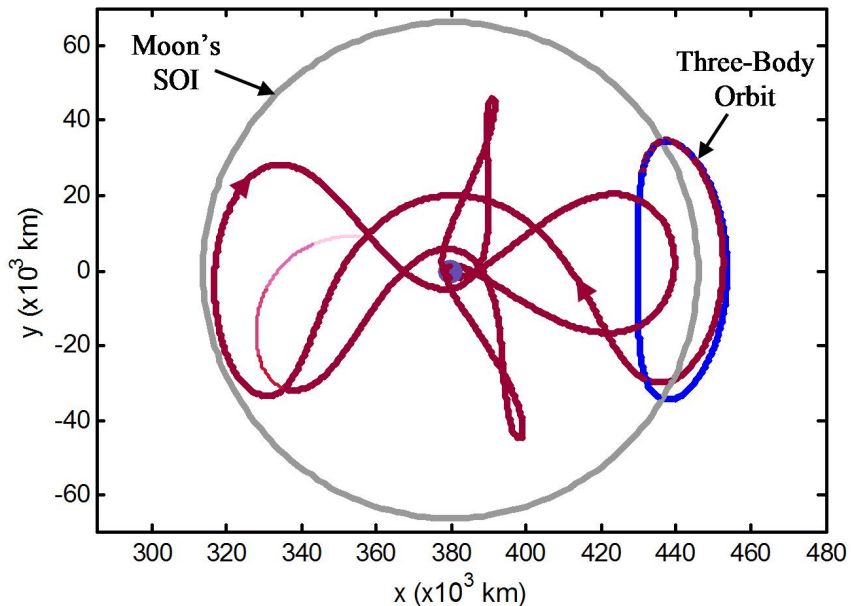


Figure 3.31: An example of a trajectory that a spacecraft may follow to transfer from an unstable orbit that is not always classified as a temporarily captured orbit to a trajectory that is generally accepted to be temporarily captured. The Moon's sphere of influence (SOI) is shown in gray for reference.

Since the definition of a temporarily captured orbit / trajectory is elusive and possibly only even useful for semantic purposes, we offer no final judgment about how to classify orbits / trajectories. For the purposes of this dissertation, we will consider that a spacecraft becomes temporarily captured by the Moon when its motion becomes bounded within some maximum distance from the Moon that does not include the Earth, yet it still has the capability of escaping that bound. This definition

closely matches the requirement that the spacecraft's two-body energy with respect to the Moon fall below zero, but it also allows other three-body orbits to be considered temporarily captured by the Moon. In any case, this dissertation is focused on constructing transfers to unstable periodic three-body orbits near the Moon, whatever their classification; from there a spacecraft has the option of transferring to a captured orbit if the mission calls for it.

### 3.12 Discussion

This chapter introduced the tools that may be used to construct interplanetary transfers in the CRTBP using dynamical systems theory. It introduced the basic solutions of the CRTBP, including the Lagrange points and simple periodic orbits. It discussed several methods that may be used to build periodic orbits in the CRTBP. The stability of a trajectory or an orbit may be evaluated using the eigenvalues of the state transition or monodromy matrices. The state transition matrix is also very useful when implementing targeting tools such as the differential corrector. The unstable nature of many trajectories in the CRTBP leads to divergent behavior and chaos. Invariant manifolds are structures that exist in the chaos surrounding unstable orbits in the CRTBP. Mission designers may use the manifolds of an unstable periodic orbit to target a transfer to/from that orbit. Such transfers require very little energy and may be used to move a spacecraft a great distance around the three-body system without expending much fuel. These transfers are the basis for building ballistic transfers between the Earth and the Moon, which is the topic of the next few chapters.

## **Chapter 4**

### **Direct Ballistic Lunar Transfers**

#### **4.1 Introduction**

The focus of this dissertation is on the study of low-energy ballistic transfers between the Earth and the Moon. In order to relate such low-energy transfers with conventional lunar transfers, this chapter explores the performance of conventional lunar transfers.

This chapter provides a robust survey of two types of short-duration, direct transfers from the Earth to the Moon. The first type, explored in Section 4.2, consists of direct ballistic transfers between the Earth and low lunar orbits about the Moon. The majority of historical missions to the Moon used this type of transfer. The second type, explored in Section 4.3, includes ballistic transfers between the Earth and lunar Halo orbits about both the L<sub>1</sub> and L<sub>2</sub> points. These transfers are very similar to the first type of transfer, but these are the transfers that may be directly compared with low-energy BLTs presented in this dissertation.

Direct ballistic transfers are the shortest class of conventional lunar transfers, requiring fewer than six days of transfer time. The direct ballistic transfers surveyed in Section 4.2 require two large maneuvers: the first is required to inject a spacecraft from the Earth's surface or from a LEO parking orbit onto the transfer; the second is required to remove the spacecraft's excess velocity at the Moon to place it into its desired orbit.

There is very little information about direct ballistic transfers to lunar Halo or-

bits in the literature. The transfers surveyed in Section 4.3 are constructed using the same dynamical systems theories as will be used in later chapters to construct BLTs. In this way, their performance parameters may be directly compared with the performance of low-energy ballistic lunar transfers. The survey of direct ballistic transfers in Section 4.3 includes short-duration ballistic transfers as well as more efficient, longer-duration ballistic transfers. Every transfer surveyed requires two maneuvers, just as the direct transfers to low lunar orbits require two maneuvers.

These two types of lunar transfers are certainly not the only types of lunar transfers that may be constructed. The transfers that we have chosen to survey here provide a good baseline for quick, uncomplicated transfers to the Moon. They only require two maneuvers and use purely ballistic arcs. Other types of lunar transfers are either too unrealistic, too complicated, or unrelated to the study of low-energy ballistic transfers to be studied here. Such transfers include bi-elliptic and bi-parabolic transfers, since they are greatly affected by the Sun's gravity and by optional lunar flyby's – although, such transfers are studied in detail by Sternfeld (1934, 1937, 1956). Low-thrust transfers are also not presented here due to their complexity and the fact that they involve completely different propulsion systems. Additional information about some of these transfer types may be found in literature (see, e.g., Loucks et al., 2005).

In order to directly relate the performance of each transfer presented in this chapter with each other and with other low-energy ballistic lunar transfers presented in this dissertation, it is assumed that each transfer begins from a 185-km LEO parking orbit. The transfers may certainly be constructed to depart from other orbits or from the Earth's surface if needed, but the performance parameters will change.

The discussions in these sections are not intended to provide full trade studies of direct ballistic lunar transfers; the intention is only to provide examples of such transfers to give a good idea of the costs and the benefits associated with each.

## 4.2 Direct Transfers to Low Lunar Orbits

This section studies direct transfers from a 185-km LEO parking orbit to 100-km prograde and retrograde orbits about the Moon. The transfers presented here may be used as baseline estimates for the costs of various direct lunar transfers.

The Earth-Moon system is very interesting because the Moon's mass is so great relative to the Earth's mass, and the distance between the two bodies is relatively small, considering the location of the Earth-Moon system in the solar system. Consequently, it is not accurate to use two-body mission design techniques to construct a direct transfer to the Moon. The simulations produced in this section have been constructed in the Earth-Moon circular restricted three-body system. Hence, the trajectories have been propagated in the presence of both the Earth's and the Moon's masses at all times. The dynamics of the CRTBP yield trajectories that are very similar to trajectories that exist in the real solar system (see Section 3.6.3 for an example comparison). The CRTBP has been used to model these motions since the system is so predictable. Transfers in the real solar system vary depending on the launch date since the Moon's orbit is both eccentric and inclined with respect to the Earth.

For simplicity, the simulations produced here are in the plane of the Moon's orbit; very little additional energy is required to reach polar orbits at the Moon, although that study is not presented here for brevity.

The lunar transfers produced in this section simulate a spacecraft that begins in a prograde, equatorial, 185-km circular LEO parking orbit. The spacecraft performs exactly two deterministic maneuvers: the first from LEO to inject onto the transfer and the second at the lunar periapse to inject into a final 100-km circular lunar orbit. Each maneuver is performed instantaneously in a tangential direction. The spacecraft departs its LEO orbit at a point indicated by the angle  $\theta$ , defined in Figure 4.1.

Depending on the value of  $\theta$ , we have found up to four types of direct transfers that the spacecraft could use to reach the Moon, each requiring a different  $\Delta V$ . Figure 4.2 shows the four transfer types for an angle  $\theta = 125^\circ$ . At that departure point the spacecraft could perform any of the following maneuvers: (1) a  $\Delta V$  of approximately 3.136832 km/s to enter a 3.79-day transfer to a prograde 100-km orbit; (2) a  $\Delta V$  of approximately 3.141458 km/s to enter a 3.70-day transfer to a retrograde 100-km orbit; (3) a  $\Delta V$  of approximately 4.061151 km/s to enter a 0.884-day transfer to a retrograde 100-km orbit; or (4) a  $\Delta V$  of approximately 4.109348 km/s to enter a 0.862-day transfer to a prograde 100-km orbit. Table 4.1 provides some additional data regarding the costs associated with performing a transfer from various values of  $\theta$ .

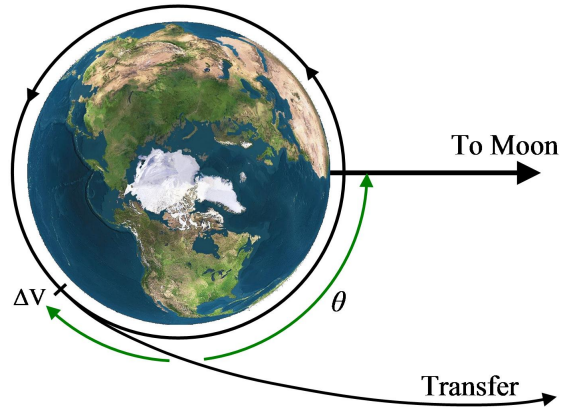


Figure 4.1: The definition of the angle  $\theta$  when describing direct lunar transfers. Planetary image courtesy of NASA (2007b).

Observing Table 4.1, one notices that for a given  $\theta$ -value, it is always less expensive to transfer to a prograde lunar orbit. However, given a specific transfer duration, the cost is very similar to transfer to either a prograde or a retrograde orbit. The transfer identified with the lowest total  $\Delta V$  departs its LEO orbit at an angle  $\theta = 117^\circ$ , arrives at a prograde lunar orbit, and requires a total  $\Delta V$  of approximately 3.9475 km/s. Figure 4.3 shows plots of five different transfers in rotating and inertial frames to compare their performances. Each transfer begins at the same circular 185-km LEO orbit and transfers to the same prograde 100-km lunar orbit.

Many historical missions have implemented direct lunar transfers, such as those described in this section. Table 4.2 provides information about the transfer durations of

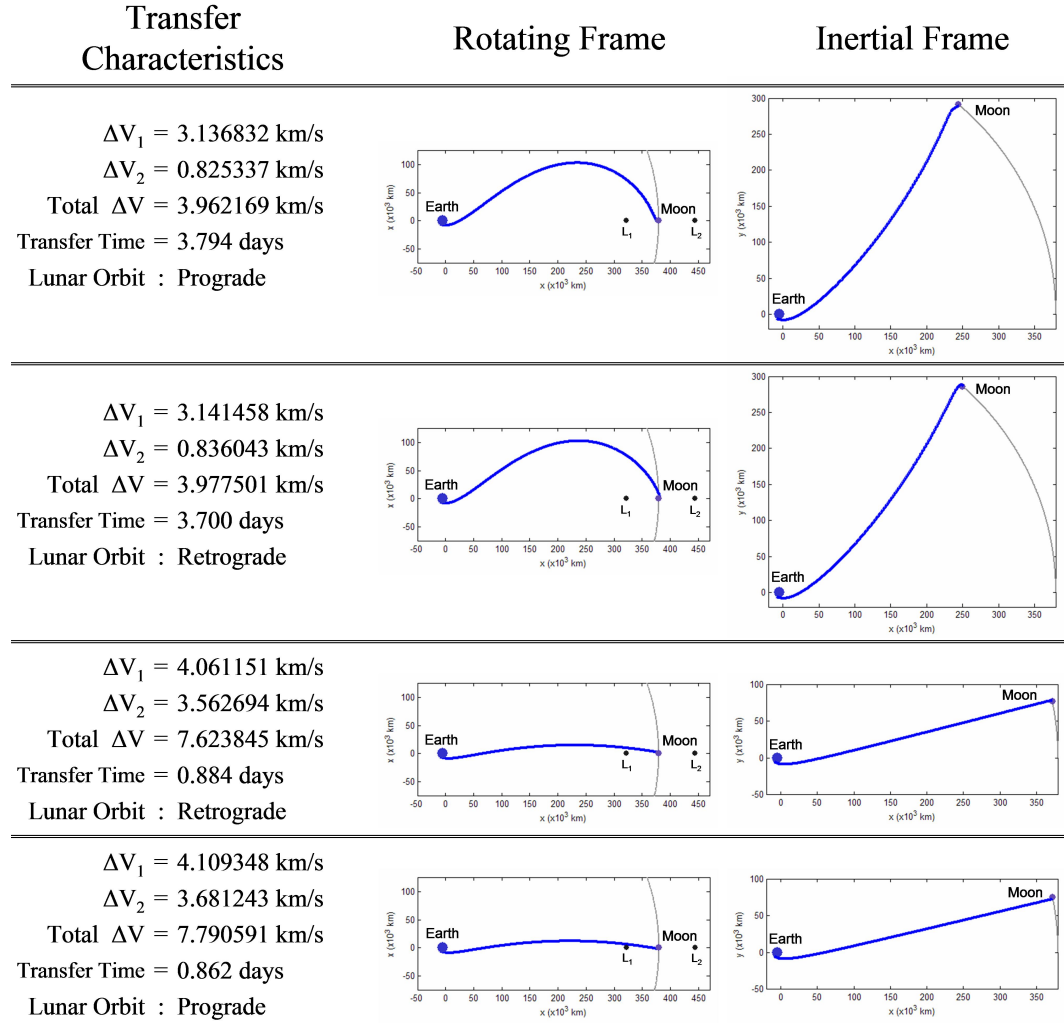


Figure 4.2: A summary of four different lunar transfers that each depart from the same LEO orbit at an angle,  $\theta$ , of  $125^\circ$ .

Table 4.1: A summary of the costs associated with departing the 185-km circular LEO parking orbit at various values of  $\theta$ , transferring directly to a 100-km circular lunar orbit.

$\theta$ -value (deg)	Long Transfer to a Prograde Lunar Orbit				Long Transfer to a Retrograde Lunar Orbit			
	$\Delta V_1$ (km/s)	$\Delta V_2$ (km/s)	Total $\Delta V$ (km/s)	Duration (days)	$\Delta V_1$ (km/s)	$\Delta V_2$ (km/s)	Total $\Delta V$ (km/s)	Duration (days)
100°	3.1378	0.8287	3.9664	6.00	3.1391	0.8265	3.9656	6.00
110°	3.1349	0.8167	3.9516	5.14	3.1371	0.8168	3.9540	5.11
115°	3.1342	0.8135	3.9477	4.70	3.1369	0.8158	3.9527	4.66
117°	3.1341	0.8133	3.9475	4.52	3.1371	0.8167	3.9538	4.47
120°	3.1345	0.8149	3.9493	4.25	3.1379	0.8203	3.9582	4.19
125°	3.1368	0.8253	3.9622	3.79	3.1415	0.8360	3.9775	3.70
130°	3.1439	0.8567	4.0006	3.30	3.1511	0.8781	4.0292	3.17
135°	3.1666	0.9547	4.1214	2.68	3.1838	1.0165	4.2003	2.49
136°	3.1775	1.0004	4.1779	2.52	3.2034	1.0965	4.2999	2.28
136.5°	3.1854	1.0329	4.2182	2.42	3.2230	1.1741	4.3971	2.12
137°	3.1964	1.0781	4.2745	2.31	N/A	N/A	N/A	N/A
137.5°	3.2156	1.1549	4.3705	2.15	N/A	N/A	N/A	N/A
137.75°	3.2430	1.2613	4.5043	1.98	N/A	N/A	N/A	N/A
$\theta$ -value (deg)	Quick Transfer to a Prograde Lunar Orbit				Quick Transfer to a Retrograde Lunar Orbit			
	$\Delta V_1$ (km/s)	$\Delta V_2$ (km/s)	Total $\Delta V$ (km/s)	Duration (days)	$\Delta V_1$ (km/s)	$\Delta V_2$ (km/s)	Total $\Delta V$ (km/s)	Duration (days)
137.75°	3.2573	1.3153	4.5726	1.90	N/A	N/A	N/A	N/A
137.5°	3.2957	1.4560	4.7518	1.75	N/A	N/A	N/A	N/A
137°	3.3367	1.6002	4.9369	1.62	N/A	N/A	N/A	N/A
136.5°	3.3705	1.7145	5.0849	1.53	3.3071	1.4870	4.7942	1.72
136°	3.4012	1.8157	5.2169	1.47	3.3492	1.6332	4.9825	1.59
135°	3.4596	2.0006	5.4603	1.36	3.4153	1.8513	5.2666	1.44
130°	3.7557	2.8337	6.5894	1.05	3.7145	2.7163	6.4308	1.08
125°	4.1093	3.6812	7.7906	0.86	4.0612	3.5627	7.6238	0.88
120°	4.5591	4.6233	9.1823	0.72	4.4993	4.4947	8.9940	0.74
117°	4.8952	5.2628	10.1580	0.65	4.8247	5.1226	9.9473	0.67
115°	5.1551	5.7298	10.8849	0.61	5.0761	5.5802	10.6563	0.62
110°	5.9796	7.0978	13.0774	0.51	5.8697	6.9137	12.7834	0.52
100°	9.2018	11.6069	20.8087	0.34	8.9157	11.2282	20.1440	0.35

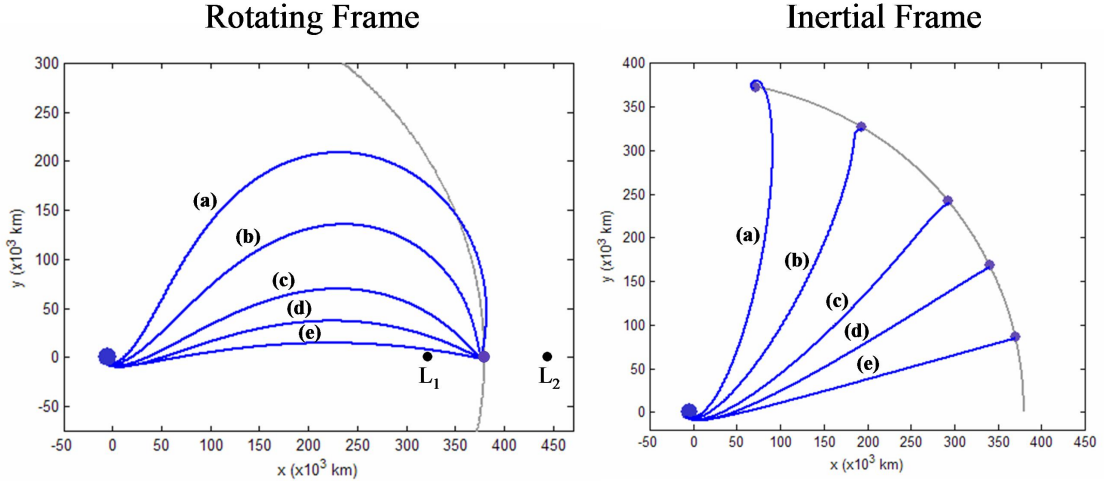


Figure 4.3: Five example direct transfers to 100-km prograde lunar orbits, shown in the rotating frame (left) and inertial frame (right). The following information applies to the labeled trajectories:

Traj. (a): Duration = 6.0 days;	$\Delta V_1 = 3.138 \text{ km/s}$	$\Delta V_2 = 0.829 \text{ km/s}$	Total $\Delta V = 3.966 \text{ km/s}$
Traj. (b): Duration = 4.5 days;	$\Delta V_1 = 3.134 \text{ km/s}$	$\Delta V_2 = 0.813 \text{ km/s}$	Total $\Delta V = 3.948 \text{ km/s}$
Traj. (c): Duration = 3.0 days;	$\Delta V_1 = 3.152 \text{ km/s}$	$\Delta V_2 = 0.893 \text{ km/s}$	Total $\Delta V = 4.045 \text{ km/s}$
Traj. (d): Duration = 2.0 days;	$\Delta V_1 = 3.240 \text{ km/s}$	$\Delta V_2 = 1.248 \text{ km/s}$	Total $\Delta V = 4.488 \text{ km/s}$
Traj. (e): Duration = 1.0 days;	$\Delta V_1 = 3.831 \text{ km/s}$	$\Delta V_2 = 3.024 \text{ km/s}$	Total $\Delta V = 6.854 \text{ km/s}$

many historical lunar missions that implemented direct transfers. The  $\Delta V$  information about each mission is not very useful in the comparison, since each mission departed the Earth from different LEO orbits and/or launch configurations and each mission arrived at the Moon in very different arrival conditions. Nevertheless, by studying the information presented in Table 4.2, one notices that only a handful of lunar missions used a transfer faster than 34 hours, including the early attempts at impacting the Moon. Many missions were sent to the Moon using transfers with durations between 60 and 72 hours. Only in recent years have missions been designed to implement longer, more energy efficient transfers. This is perhaps due to the improved technology levels in the spacecraft and ground station hardware, as well as improved navigation procedures.

Table 4.2: The transfer durations, among other information, of several historical missions that have implemented direct lunar transfers. Sources of the information shown here include: Lozier et al. (1998), Godwin (1999), and NASA (2006).

Launch Date	Spacecraft	Nation	Transfer Duration	Notes
There were 24 Soviet <b>Luna</b> missions; examples include:				
2 Jan. 1959	Luna 1	Soviet Union	34 hrs. (1.42 days)	First Lunar Flyby (5995 km)
12 Sept. 1959	Luna 2	Soviet Union	33.5 hrs. (1.40 days)	First Lunar Impact (29.10 N, 0.00 E)
4 Oct. 1959	Luna 3	Soviet Union	60 hrs. (2.50 days)	Flyby (6200 km)
2 Apr. 1963	Luna 4	Soviet Union	77.3 hrs. (3.22 days)	Flyby (8336.2 km)
31 Jan. 1966	Luna 9	Soviet Union	79 hrs. (3.29 days)	First Soft-Landing (7.08 N, 295.63 E)
There were eight Soviet <b>Zond</b> missions; little accurate information is available.				
18 July 1965	Zond 3	Soviet Union	33 hrs. (1.38 days)	Flyby (9200 km)
There were nine American <b>Ranger</b> missions; examples include:				
26 Jan. 1962	Ranger 3	USA	2-3 days	Flyby (~36,800 km)
23 Apr. 1962	Ranger 4	USA	64 hrs. (2.67 days)	Impact (15.5 S, 229.3 E)
18 Oct. 1962	Ranger 5	USA	2-3 days	Flyby (725 km)
30 Jan. 1964	Ranger 6	USA	65.5 hrs. (2.73 days)	Impact
28 July 1964	Ranger 7	USA	68.6 hrs. (2.86 days)	Impact (10.70 S, 339.33 E)
17 Feb. 1965	Ranger 8	USA	64.9 hrs. (2.70 days)	Impact (2.71 N, 24.81 E)
21 Mar. 1965	Ranger 9	USA	64.5 hrs. (2.69 days)	Impact (12.91 S, 357.62 E)
There were seven American <b>Surveyor</b> missions, including:				
30 May 1966	Surveyor 1	USA	63 hrs. (2.63 days)	Landed (2.45 S, 316.79 E)
20 Sept. 1966	Surveyor 2	USA	2-3 days	Impact
17 Apr. 1967	Surveyor 3	USA	64.5 hrs. (2.69 days)	Landed (3.01 S, 336.66 E)
14 July 1967	Surveyor 4	USA	2-3 days	Impact
8 Sept. 1967	Surveyor 5	USA	64.8 hrs. (2.70 days)	Landed (1.41 N, 23.18 E)
7 Nov. 1967	Surveyor 6	USA	65.0 hrs. (2.71 days)	Landed (0.49 N, 358.6 E); First powered take-off
7 Jan. 1968	Surveyor 7	USA	66.0 hrs. (2.75 days)	Landed (40.86 S, 348.53 E)
There were five American <b>Lunar Orbiter</b> missions; examples include:				
10 Aug. 1966	Lunar Orbiter 1	USA	91.6 hrs. (3.82 days)	Orbiter
6 Nov. 1966	Lunar Orbiter 2	USA	92.5 hrs. (3.85 days)	Orbiter
5 Feb. 1967	Lunar Orbiter 3	USA	92.6 hrs. (3.86 days)	Orbiter
There were 17 American <b>Apollo</b> missions; examples include:				
21 Dec. 1968	Apollo 8	USA	66.3 hrs. (2.76 days)	First manned lunar orbiter
18 May 1969	Apollo 10	USA	73.3 hrs. (3.05 days)	Orbit & Return
16 July 1969	Apollo 11	USA	73.1 hrs. (3.04 days)	First manned landing
Additional missions that have or will implement direct transfers include:				
7 Jan. 1998	Lunar Prospector	USA	105 hrs. (4.38 days)	Orbiter
14 Sept. 2007	KAGUYA	Japan	127 hrs. (5.29 days)	Orbiter
24 Oct. 2007	Chang'e 1	China	~120 hrs. (~5 days)	Orbiter
~ Apr. 2008	Chandrayaan-1	India	132 hrs. (5.50 days)	Orbiter
~ Oct. 2008	LRO/LCROSS	USA	~96 hrs. (~4 days)	Orbiter/Impactor

### 4.3 Direct Transfers to Lunar Halo Orbits

This section provides a robust survey of short-duration ballistic transfers from 185-km LEO parking orbits to lunar Halo orbits about both the  $L_1$  and  $L_2$  points. The author knows of no missions that have implemented direct transfers to lunar Halo orbits prior to 2007, but such transfers are of interest in this dissertation because they may be directly compared with low-energy transfers to the same Halo orbits. Furthermore, very little information is available about such orbit transfers in the literature as of 2007, although Edelbaum has studied the case of a direct transfer from the Earth to the  $L_1$  point itself (Edelbaum, 1970). Therefore, this dissertation has developed the techniques used to construct such transfers and will survey those transfers that have been constructed.

#### 4.3.1 Constructing Direct Lunar Halo Transfers

Direct lunar Halo orbit transfers are constructed in this section using the dynamical systems methodology presented in Chapters 2 and 3. The transfers are constructed by targeting states within the stable manifold of a desirable Halo orbit. Section 3.10.1 demonstrated how one may use this technique to construct a transfer from the Earth to a Sun-Earth Halo orbit. In that scenario the Earth is the smaller of the two primary bodies and the stable manifolds of many Halo orbits intersect it within a short amount of time. In the Earth-Moon system, where lunar Halo orbits exist, the Earth is the larger of the two primary bodies. When the stable manifolds of lunar Halo orbits are propagated backwards in time, one notices that the trajectories do not intersect the Earth or any reasonable low Earth orbits within a short amount of time. Consequently, at least two maneuvers must be performed to directly transfer onto the lunar Halo orbit's stable manifold from an initial LEO parking orbit.

Figure 4.4 shows two perspectives of an example scenario that may be used to

transfer a spacecraft from a 185-km LEO parking orbit to a lunar  $L_1$  Halo orbit. The scenario requires a large maneuver at the LEO injection point ( $\Delta V_{LEO}$ ; also known as the Trans-Lunar Injection maneuver) and a second large maneuver at the manifold injection point ( $\Delta V_{MI}$ ). The two mission segments are referred to as the **Bridge** segment and the **Manifold** segment. The spacecraft launches from an inclined LEO parking orbit onto the Bridge segment. Once the spacecraft arrives onto the Manifold segment, after performing the  $\Delta V_{MI}$  maneuver, it asymptotically transfers onto the lunar Halo orbit.

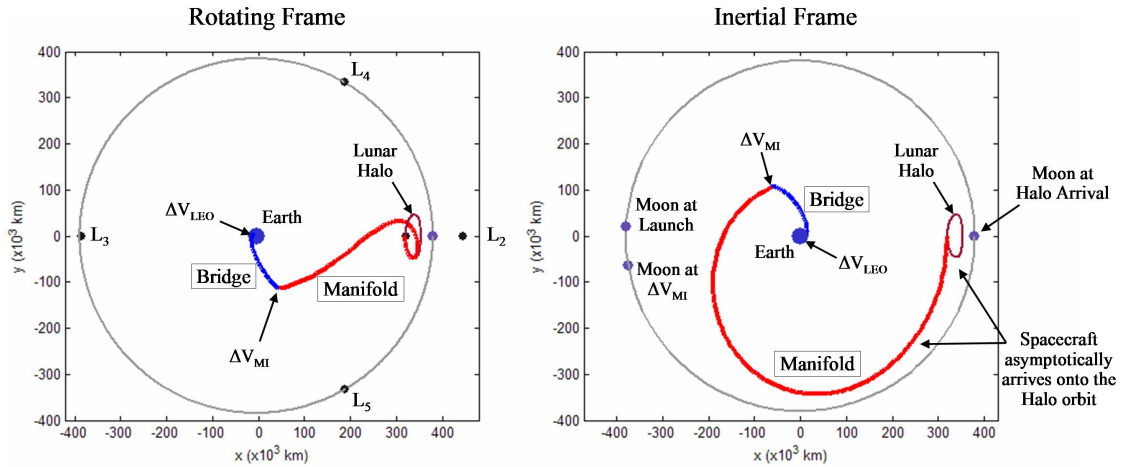


Figure 4.4: Two perspectives of an example scenario that may be used to transfer a spacecraft from a 185-km LEO parking orbit to a lunar  $L_1$  Halo orbit. The transfer is shown in the Earth-Moon rotating frame (left) and the corresponding inertial frame of reference. The Halo orbit is shown in the inertial frame only for reference.

The goal of this study is to construct optimal direct lunar Halo transfers. This is a very difficult task if there are no additional constraints, since the two deterministic maneuvers may be performed at any time in nearly any direction. To simplify the search for optimal transfers, only tangential maneuvers have been explored in this study. The following strategy has been followed to construct direct transfers to lunar Halo orbits:

**Step 1.** Construct the desired Halo orbit.

**Step 2.** Construct the **Manifold** segment:

- (1) Choose a  $\tau$ -value, i.e., a point along the Halo orbit as defined in Section 3.3.3; choose a manifold propagation duration,  $\Delta t_m$ ; and choose a direction, i.e., either “Interior” or “Exterior” as discussed in Section 3.9.
- (2) The Manifold segment is constructed by propagating the specific trajectory in the Halo orbit’s stable manifold that corresponds to the given  $\tau$ -value. The trajectory is propagated backwards in time for the given duration and departs the Halo orbit either in the interior or exterior direction, as indicated.

**Step 3.** Define  $X_{MI}$  to be the final state of the Manifold segment. This is the state that a spacecraft would need to obtain in order to inject onto the Manifold segment.

**Step 4.** Construct  $\Delta V_{MI}$  and the **Bridge** segment:

- (1) Define  $\Delta V_{MI}$  to be the tangential  $\Delta V$  that may be applied to  $X_{MI}$  in order to construct the Bridge segment.
- (2) When propagated further backwards in time, the Bridge segment should encounter the prograde 185-km LEO orbit at the Bridge’s perigee point.
- (3) It has been found that two-body dynamics may be used effectively to approximate the value of  $\Delta V_{MI}$ ; the value of  $\Delta V_{MI}$  may then be fine-tuned in the Earth-Moon CRTBP to include the gravitational influence of the Moon.

**Step 5.** Construct  $\Delta V_{LEO}$ , the tangential  $\Delta V$  that may be applied to transfer the spacecraft from its LEO orbit onto the Bridge segment.

This process works very well to construct arbitrary lunar transfers given a specified Halo orbit, a  $\tau$ -value, the length of time to propagate the Manifold segment, and the direction of motion of the Manifold segment. There are rare occasions when the process fails to converge on a successful Bridge segment, most likely because the two-body approximation fails to account for a very close lunar flyby.

Several scenarios have been explored to identify optimal transfers. The first suspicion is that the optimal transfer may be constructed by building a Bridge segment that connects the LEO departure with the Manifold segment's perigee point. Since energy-change maneuvers are more efficient when spacecraft are traveling faster (Val-lado, 1997), then the perigee of the Manifold segment seems like a good location to perform the  $\Delta V_{MI}$  maneuver. Then, the best transfer for a specific Halo orbit would be the one that requires the least total  $\Delta V$  over all  $\tau$ -values. This **perigee-point** scenario is presented first.

#### 4.3.1.1 The Perigee-Point Scenario

Figure 4.5 shows two perspectives of several example trajectories that may be used to transfer onto a single lunar  $L_1$  Halo orbit using the perigee-point scheme. Each transfer implements a different  $\tau$ -value about the same Halo orbit. For reference, the Halo orbit is a Northern  $L_1$  Halo orbit with an  $x_0$ -value of approximately 319,052 km

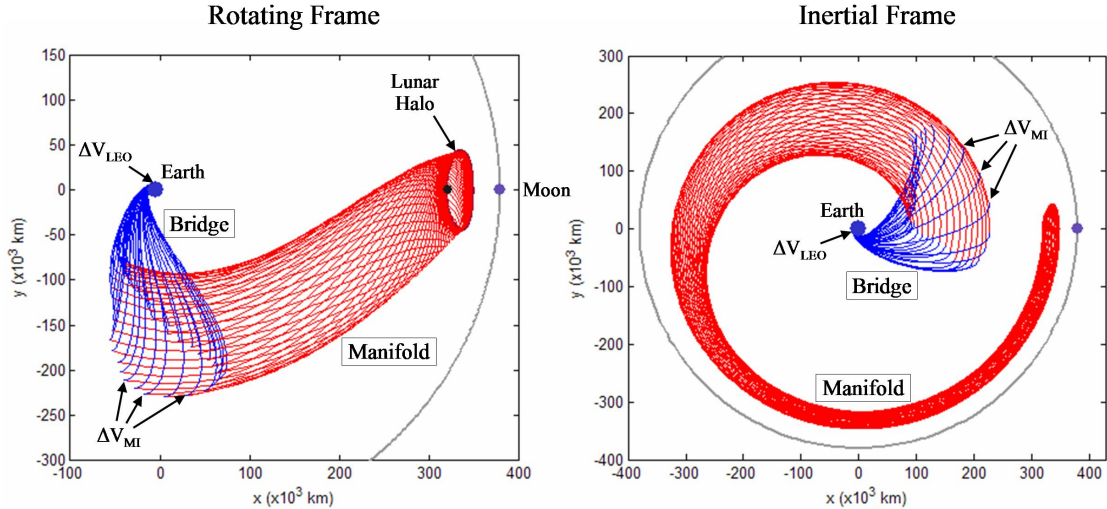


Figure 4.5: Example trajectories that implement the **perigee-point** scheme to directly transfer from LEO to a lunar  $L_1$  Halo orbit. The transfers are shown in the Earth-Moon rotating frame (left) and the corresponding inertial frame of reference (right).

(see Appendix B.6). The Manifold segment in each case has been propagated to its perigee point, and the corresponding Bridge segment has been constructed to transfer from a 185-km prograde LEO orbit to that perigee point. The trajectories are shown in both the Earth-Moon rotating frame and the corresponding inertial frame of reference.

Figure 4.6 shows plots of the magnitudes of the two required maneuvers,  $\Delta V_{\text{LEO}}$  and  $\Delta V_{\text{MI}}$ , as well as the total maneuver cost as functions of the parameter  $\tau$ . One can see that the minimum cost to transfer from the 185-km LEO orbit to this Halo orbit using the perigee-point scheme is approximately 4.14 km/s. One can also see that this minimum occurs at the point where  $\Delta V_{\text{LEO}}$  is at its maximum.

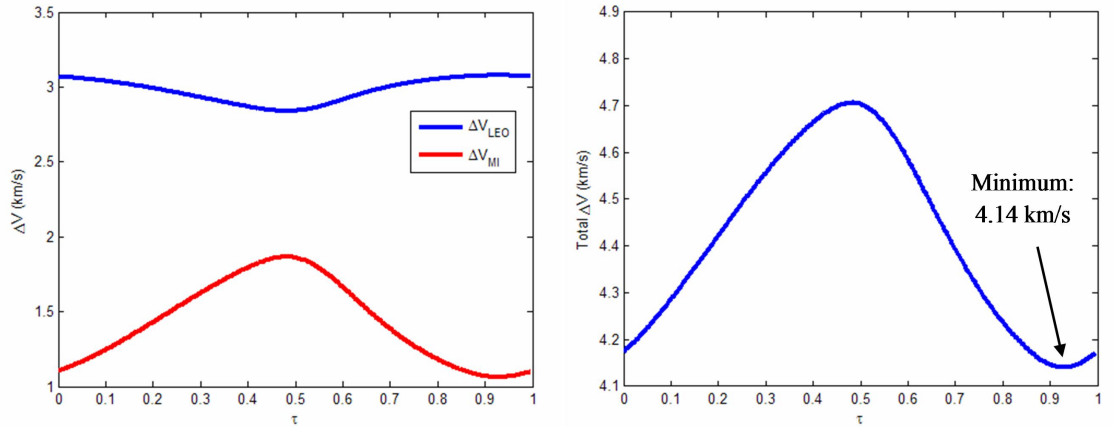


Figure 4.6: Plots of the maneuver requirements to transfer onto a lunar  $L_1$  Halo orbit using the perigee-point scheme. Left: The magnitudes of the two maneuvers  $\Delta V_{\text{LEO}}$  and  $\Delta V_{\text{MI}}$  as functions of  $\tau$ ; Right: The total  $\Delta V$  cost as a function of  $\tau$ .

#### 4.3.1.2 The Open-Point Scenario

It turns out that although it may be intuitive to perform  $\Delta V_{\text{MI}}$  at the Manifold segment's perigee point because of the energy considerations, it is actually better to perform a larger  $\Delta V_{\text{LEO}}$  and a smaller, although less-efficient,  $\Delta V_{\text{MI}}$ . This is because the maneuver at LEO can take advantage of its close proximity to the Earth to make the

total energy-change required in the transfer as efficient as possible. That is, it is most efficient to change as much of the spacecraft's energy at LEO as possible, since that is almost always the location where the spacecraft travels the fastest during the lunar transfer.

A second, more complicated scheme has been developed where the second maneuver,  $\Delta V_{MI}$ , may be placed anywhere along the stable manifold of the Halo orbit. The Manifold segment may be propagated well beyond its perigee point, although it has an imposed maximum propagation time of one or two months: one month for Exterior manifolds since they depart the Moon's vicinity quickly and two months for Interior manifolds since they linger near the Moon for longer amounts of time and may be more accurately modeled by the Earth-Moon system. The transfers have an additional degree of freedom compared with the perigee-point scheme but are otherwise constructed in exactly the same manner as listed above. This new scheme is referred to as the **open-point** scheme, since the manifold insertion point has had its position constraint opened.

To demonstrate the **open-point** transfer strategy, Figure 4.7 shows several transfers that may be constructed from LEO to an arbitrary trajectory within the stable manifold of a particular Halo orbit: in this case, the same Halo orbit used in Figures 4.5 and 4.6. For reference, the manifold shown in Figure 4.7 has a  $\tau$ -value of 0.3 and the Halo orbit is the same Northern L<sub>1</sub> Halo orbit presented in Section 4.3.1.1. The transfers are shown in both the Earth-Moon rotating frame and the inertial frame of reference. Figure 4.8 shows the maneuver cost associated with transferring to various points along the manifold. The location of  $\Delta V_{MI}$  is specified by the parameter  $\Delta t_m$ , which has been defined to be the duration of time that is required to traverse the Manifold segment before arriving within 100 kilometers of the Halo orbit. One can see that there are two local minima that correspond to low-energy lunar transfers: one at a  $\Delta t_m$  of approximately 10.0 days and the next at a  $\Delta t_m$  of approximately 22.7 days, neither of

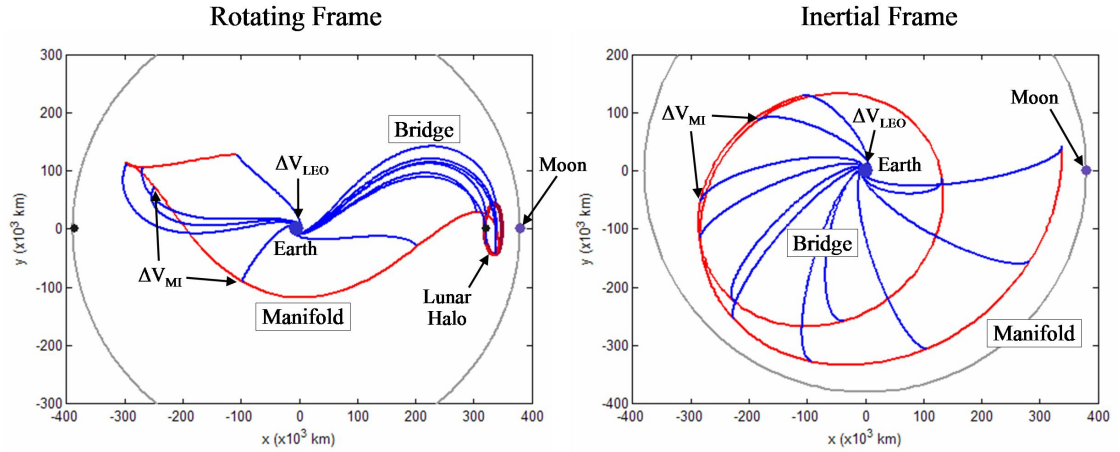


Figure 4.7: Example trajectories that implement the **open-point** scheme to directly transfer from LEO to a specific manifold of a specific lunar L<sub>1</sub> Halo orbit. The transfers are shown in the Earth-Moon rotating frame (left) and the corresponding inertial frame of reference (right).

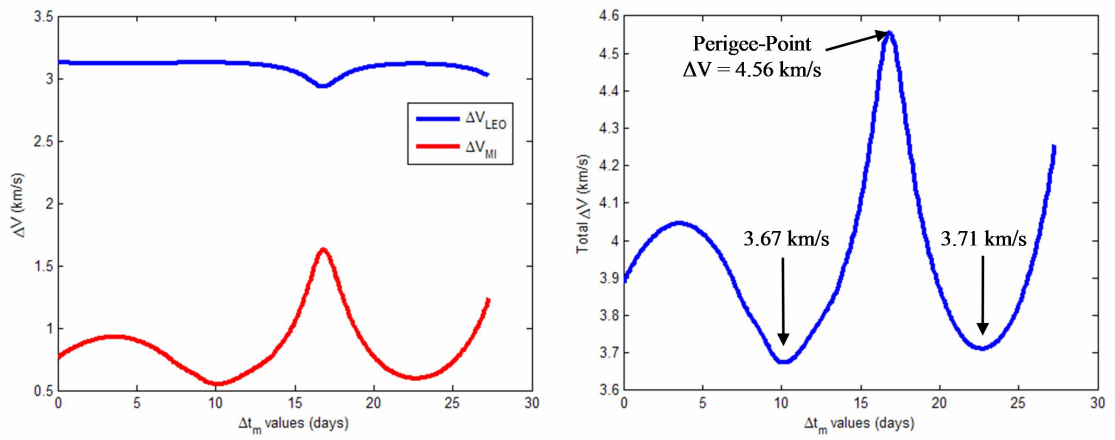


Figure 4.8: Plots of the maneuver requirements to transfer onto a specific manifold of a specific lunar L<sub>1</sub> Halo orbit using the open-point scheme. Left: The magnitudes of the two maneuvers  $\Delta V_{LEO}$  and  $\Delta V_{MI}$  as functions of  $\Delta t_m$ ; Right: The total  $\Delta V$  cost as a function of  $\Delta t_m$ .

which correspond to a mission that transfers to the Manifold segment's perigee point (which has a  $\Delta t_m$  of approximately 16.86 days). In fact, these transfers correspond to missions where the Bridge segment connects the spacecraft very near the **apogee** of the Manifold segment. Figure 4.9 shows plots of the distance between the spacecraft and the two massive bodies for each  $\Delta t_m$ -point along the Manifold segment. One can see that the two local minima observed in Figure 4.8 coincide very near to the Manifold segment's apogee locations.

Figures 4.7 – 4.9 have demonstrated the open-point scheme applied to a single trajectory (where  $\tau = 0.3$ ) on the stable manifold of a single Halo orbit (the Northern lunlar  $L_1$  Halo orbit with an  $x_0$ -value of approximately 319,052 km). The open-point scheme is easily extended to cover many trajectories along the Halo orbit's stable manifold. Figure 4.10 summarizes the required maneuvers and the total maneuver cost associated with the least expensive lunar transfer for each trajectory on the stable manifold of the same Halo orbit. The following observations may be made:

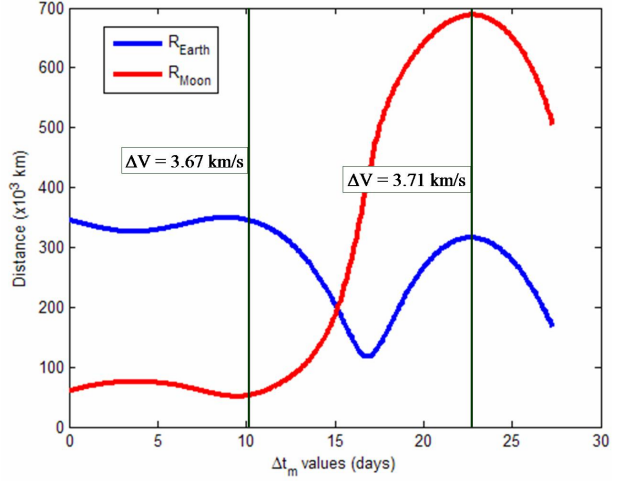


Figure 4.9: Plots of the distance between the spacecraft and the two massive bodies for each  $\Delta t_m$ -point along the Manifold segment. The minimum-energy transfers observed in Figure 4.8 are indicated by vertical bars.

- One can see that the lowest-energy open-point transfer constructed to this particular Halo orbit requires a total  $\Delta V$  of approximately 3.62 km/s. This transfer implements the trajectory in the orbit's stable manifold with a  $\tau$ -value of approximately 0.48. For verification, Figure 4.10 shows that the trajectory with a  $\tau$ -value of 0.3 requires a minimum  $\Delta V$  of approximately 3.67 km/s: the same

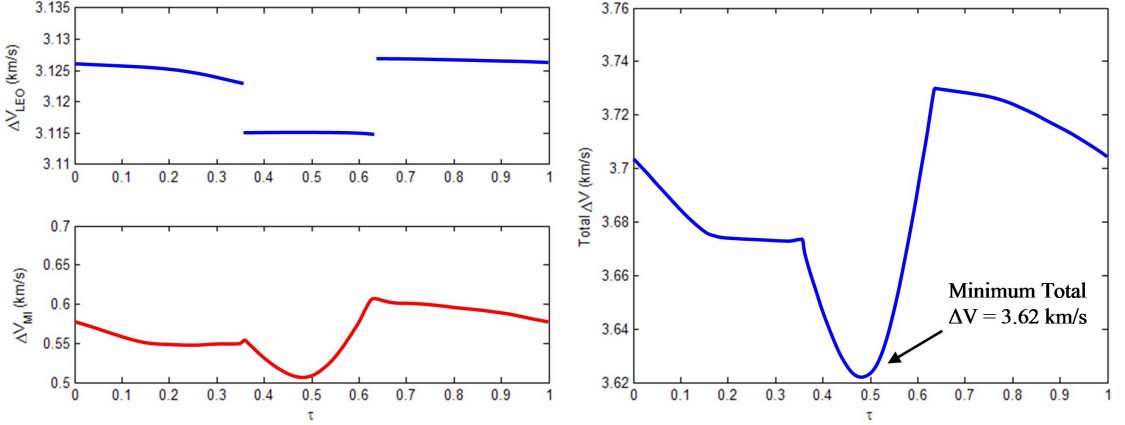


Figure 4.10: Plots summarizing the required maneuvers and the total maneuver cost associated with the least expensive open-point lunar transfer for each trajectory on the stable manifold of a single lunar L<sub>1</sub> Halo orbit. The plots show the magnitudes of the two required maneuvers  $\Delta V_{LEO}$  and  $\Delta V_{MI}$  (left) and the total  $\Delta V$  cost (right) associated with the least-expensive transfer for each manifold indicated by its  $\tau$ -value.

result as that shown in Figure 4.8.

- When the result shown in Figure 4.10 is directly compared with the result of the perigee-point scheme shown in Figure 4.6, one can see that the open-point scheme out-performs the perigee-point scheme for each and every  $\tau$ -value.
- It is interesting to observe in Figure 4.10 that the least-expensive transfers to this Halo orbit use the first maneuver,  $\Delta V_{LEO}$ , to perform the vast majority of the spacecraft's energy-change. This is consistent with the notion that the most efficient transfer performs as much  $\Delta V$  as possible deep within the Earth's gravity well where the spacecraft is traveling fast.
- One may also observe when comparing Figures 4.10 and 4.6 that the open-point scheme allows more of its total  $\Delta V$  to be performed at LEO than any transfer produced from the perigee-point scheme.

### 4.3.2 Surveying Direct Lunar Halo Orbit Transfers

Section 4.3.1.2 illustrated the open-point scheme applied to a single Halo orbit about the Earth-Moon L<sub>1</sub> point using the Halo orbit's exterior stable manifold. The process results in a low-energy, two-maneuver, direct lunar transfer to that Halo orbit, following the exterior stable manifold. This section surveys low-energy direct lunar transfers to orbits within the entire families of Halo orbits about both the Earth-Moon L<sub>1</sub> and L<sub>2</sub> points, taking advantage of both the exterior and interior stable manifolds.

A Halo orbit's interior stable manifold passes very near the Moon en route to the Halo orbit. The corresponding lunar flyby may reduce the total ΔV cost of the lunar transfer. This paper considers each half of the target orbit's stable manifold separately when searching for low-energy direct lunar transfers.

The following sections summarize the results of each of the four surveys performed here:

Section	Halo Family	Interior/Exterior Stable Manifold
Section 4.3.2.1	L <sub>1</sub>	Exterior
Section 4.3.2.2	L <sub>1</sub>	Interior
Section 4.3.2.3	L <sub>2</sub>	Exterior
Section 4.3.2.4	L <sub>2</sub>	Interior

In each of these four cases, it would be ideal to perform an exhaustive search for the very best transfer to each Halo orbit implementing the given stable manifold. However, it is very time-consuming to construct a transfer to each point along each trajectory in each Halo orbit's stable manifold. The corresponding phase space is three-dimensional and every combination of parameters takes a significant amount of computation time. To reduce the computation load, while still performing a survey of a large portion of the phase space, several numerical optimization routines have been implemented.

It has been found that a combination of hill-climbing and genetic algorithms performs very well at identifying the least-expensive transfers to a given Halo orbit very swiftly. The numerical algorithms use the state  $X = [x_0, \tau, \Delta t_m]^T$  to define a direct two-maneuver lunar transfer, given the procedure outlined in Section 4.3.1. The numerical optimization process begins by implementing a genetic algorithm to identify a local  $\Delta V$ -minimum in the phase space. The implementation of the genetic algorithm will not be discussed here for brevity, but may be found in many sources in literature, e.g., Winter et al. (1995). After several iterations of the genetic algorithm, the state that corresponds to the least-expensive lunar transfer is refined using a dynamic hill-climbing algorithm, also known as the steepest descent algorithm (e.g., Avriel, 2003). In this way, the local minima of the three-dimensional phase space are quickly explored. In order to survey specific orbits within a family of Halo orbits, the parameter  $x_0$  is held constant and the remaining two parameters are varied.

The numerical optimization routine is not guaranteed to converge on the most efficient transfer, but it easily converges on relatively efficient transfers. The results given in the following sections include the most efficient transfers identified, as well as somewhat less efficient transfers. The results then trace out a Pareto front of optimal solutions, where a Pareto front describes a curve of optimal combinations of two or more parameters (for more information on Pareto optimality, see, e.g., Coello et al., 2002). Other non-optimal points have been added to the results to give an impression of the range of costs of transfers that exist. Each result is discussed in more detail in the following sections.

#### 4.3.2.1    Exterior Transfers to L<sub>1</sub> Halo Orbits

This section presents the results of **open-point** transfers constructed between 185-km LEO parking orbits and the exterior stable manifold of Halo orbits in the family of lunar L<sub>1</sub> Halo orbits. Figure 4.11 shows the cost of many such example transfers to

each Halo orbit in the family, including a Pareto front of optimal transfers. One can see that there are several types of efficient transfers one can construct. To help identify the differences between each type of transfer, Figure 4.12 shows plots of several example transfers.

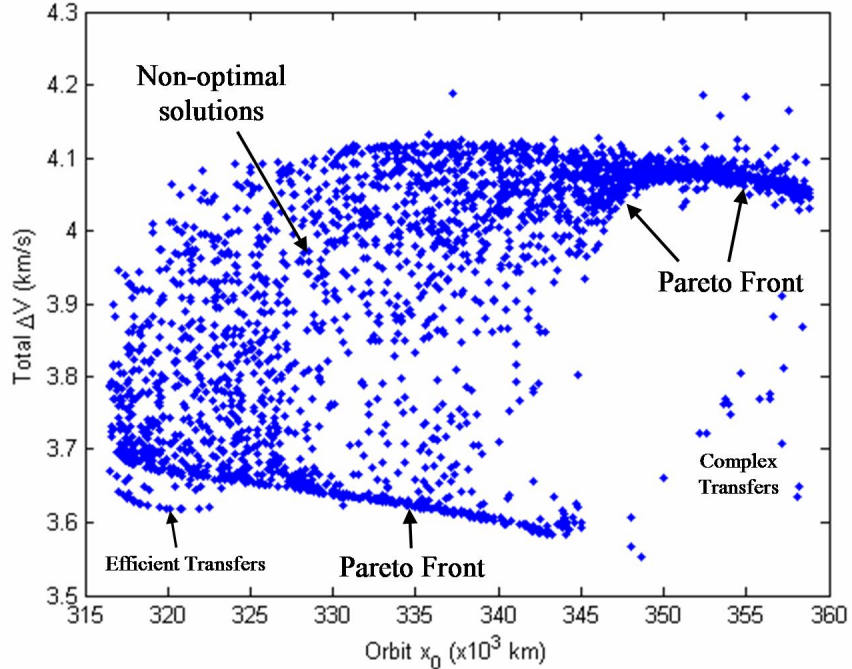


Figure 4.11: The total  $\Delta V$  cost of many transfers to the exterior stable manifold of each orbit in the family of lunar  $L_1$  Halo orbits, including a Pareto front of optimal solutions.

Figures 4.11 and 4.12 show many interesting patterns. After studying the transfers presented in these figures, the following observations have been made:

- The majority of the least-expensive transfers of this type are very fast transfers, requiring only about five days to reach the Halo orbit. Their Bridge segments take the spacecraft nearly directly to the Halo orbit. These transfers compose the majority of the Pareto front observed in the figures.
- The Bridge segments that do connect the spacecraft nearly directly with the

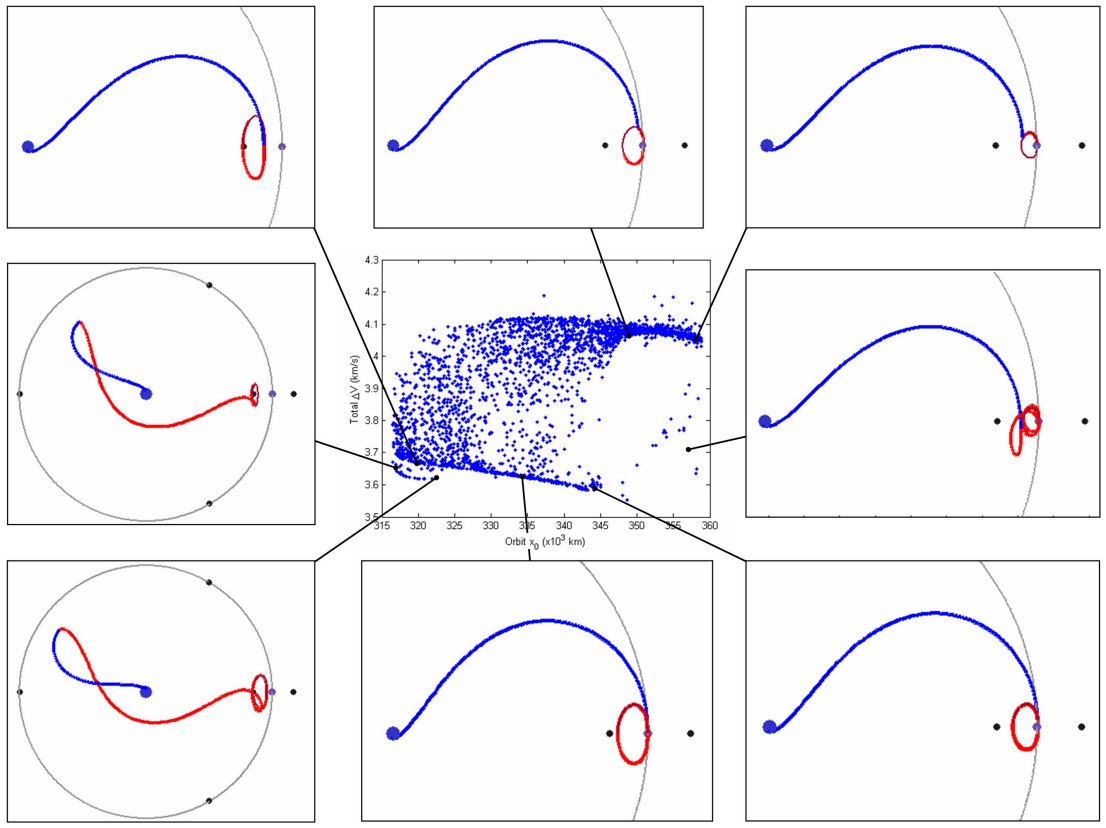


Figure 4.12: Several example transfers between 185-km LEO parking orbits and the exterior stable manifold of lunar  $L_1$  Halo orbits.

Halo orbit appear to do so in an organized manner. For Halo orbits with  $x_0$ -values below a value of approximately 345,000 km, the Bridge segments connect the spacecraft with the far-side of the Halo orbit. Beyond  $x_0$ -values of 345,000 km, i.e., for very large  $z$ -amplitude Halo orbits, the optimal direct transfers tend to connect closer to the near-side of the Halo orbit. This pattern may be observed in the plots shown around the perimeter of Figure 4.12.

- A family of very efficient direct transfers of this kind appears for transfers to Halo orbits with  $x_0$ -values between approximately 316,000 km and approximately 323,000 km. The Bridge segments of these transfers connect the spacecraft with the first apogee of the Manifold segments after the Manifold seg-

ments traverse to the opposite side of the Earth-Moon system. This family of transfers may be seen on the left side of the figures and corresponds to Halo orbits that have small  $z$ -amplitudes.

- A few transfers have been found that require less total  $\Delta V$  than the vast majority of locally-optimal transfers. These transfers appear toward the lower-right portion of the plot shown in Figure 4.11 and are labeled as complex transfers. These transfers tend to involve several close flybys of the Moon. This dissertation has not explored these transfers in detail, since they are much more complicated by nature.
- The transfers shown in Figures 4.11 and 4.12 implement LEO parking orbits with ecliptic inclinations anywhere between  $0^\circ$  and  $50^\circ$ . The equatorial inclination, by comparison, depends on the specific launch date and varies from the ecliptic inclination by as much as  $\pm 23.45$  degrees (Berger, 1976; Wittmann, 1979).
- The duration of time required to transfer within 100 km of the Halo orbit may be anywhere between 5 – 30 days. Transfers may certainly be constructed that require more time, however, these transfers are not considered in this study since they may be more influenced by the Sun's gravity.
- The least-expensive transfers to lunar  $L_1$  Halo orbits following their exterior stable manifolds generally require a total  $\Delta V$  no smaller than approximately 3.60 km/s, depending on the Halo orbit of choice. Halo orbits with  $x_0$ -values greater than approximately 345,000 km tend to require more total  $\Delta V$ : in the range of  $4.05 \text{ km/s} \leq \Delta V \leq 4.08 \text{ km/s}$ . The least-expensive transfer identified in this study requires a total  $\Delta V$  of approximately 3.552 km/s.

In many practical missions, the launch vehicle provides a set amount of  $\Delta V$ , given a payload mass, and mission designers must optimize their transfer trajectories around that performance. Hence, many times it is useful to consider the two transfer maneuvers separately as well as the total cost of the transfer. Figure 4.13 shows the magnitudes of the two maneuvers separately, which combine to produce the total  $\Delta V$  cost of the transfers shown in Figures 4.11 and 4.12. One can see that nearly all of the transfers require the magnitude of the Trans-Lunar Injection maneuver ( $\Delta V_{\text{LEO}}$ ) to be between 3.120 and 3.136 km/s. This suggests that the same launch vehicle can perform the Trans-Lunar Injection maneuver for nearly all of these transfers given the same payload mass. Although it is difficult to see in these plots, the least-expensive transfers require the most-expensive  $\Delta V_{\text{LEO}}$ -magnitudes. The second maneuver,  $\Delta V_{\text{MI}}$ , contributes most of the variations seen in the total cost of the lunar transfer.

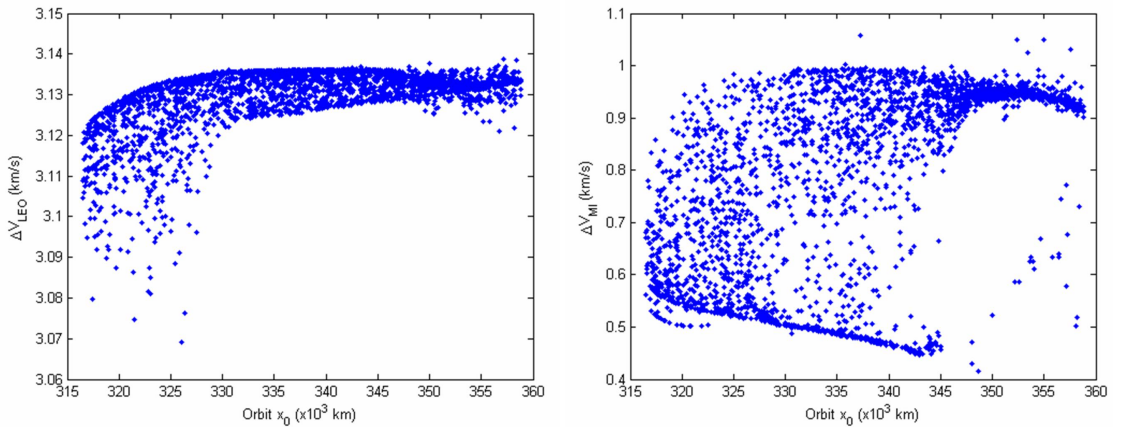


Figure 4.13: The two transfer maneuver magnitudes that combine to produce the total  $\Delta V$  cost of the transfers shown in Figures 4.11 and 4.12. Left: The magnitudes of the Trans-Lunar Injection maneuvers ( $\Delta V_{\text{LEO}}$ ) in each transfer; Right: The magnitudes of the Manifold-Insertion maneuvers ( $\Delta V_{\text{MI}}$ ) in each transfer.

### 4.3.2.2 Interior Transfers to L<sub>1</sub> Halo Orbits

This section presents the results of transfers constructed between 185-km LEO parking orbits and the interior stable manifold of Halo orbits in the family of lunar L<sub>1</sub> Halo orbits. Figure 4.14 shows the cost of many such example transfers, where several families of locally-optimal transfers have been plotted in a more prominent shade. Other non-optimal transfers have been scattered about the plot to demonstrate that an entire field of options are available. To help identify the differences between each type of transfer, Figure 4.15 shows plots of several example transfers.

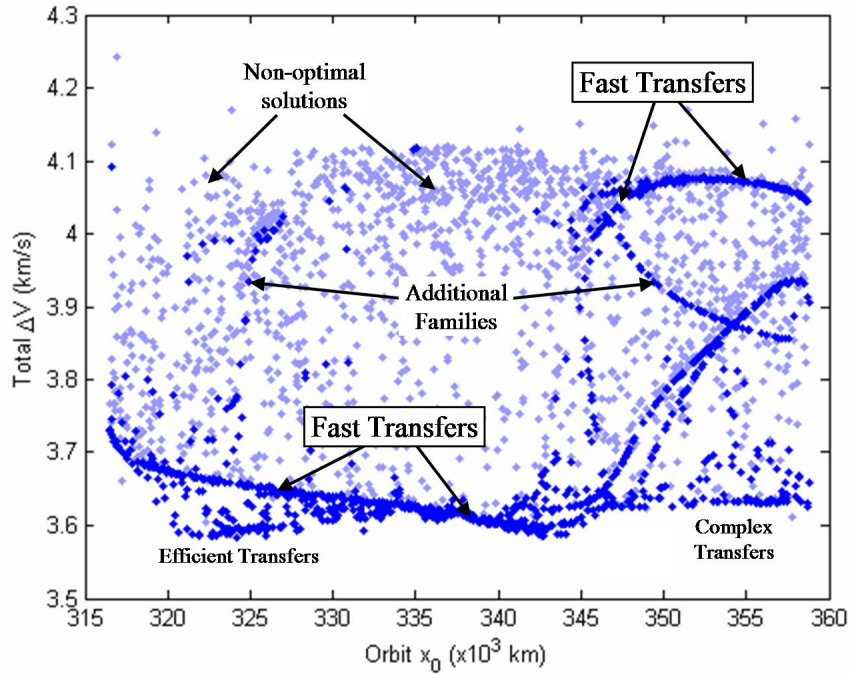


Figure 4.14: The total  $\Delta V$  cost of many transfers to the interior stable manifold of each orbit in the family of lunar L<sub>1</sub> Halo orbits.

The following observations may be made after studying the plots shown in Figures 4.14 and 4.15:

- The same types of **fast** transfers exist to L<sub>1</sub> Halo orbits via their interior sta-

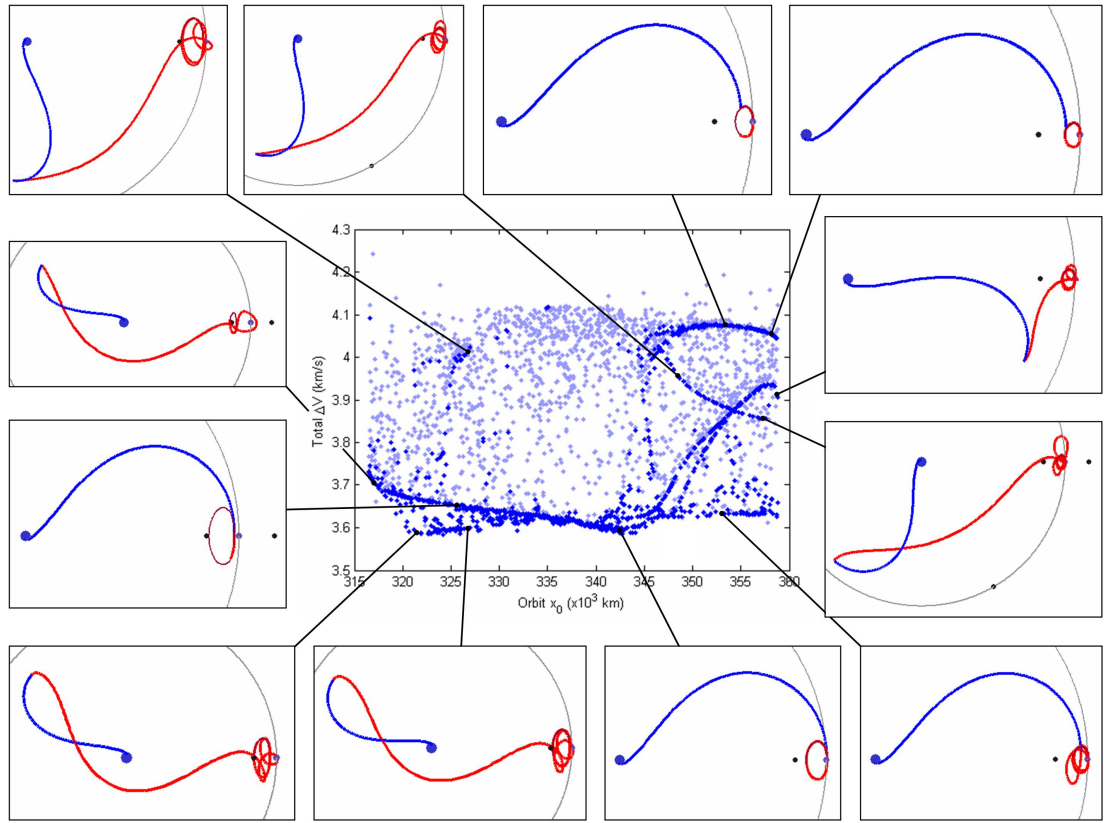


Figure 4.15: Several example transfers between 185-km LEO parking orbits and the interior stable manifold of lunar  $L_1$  Halo orbits.

ble manifolds as via their exterior stable manifolds, because the Manifold segments of those transfers do not extend far beyond the Halo orbits. Hence, the cost of such fast transfers closely resemble the cost of the fast transfers explored in Section 4.3.2.1.

- Many families of longer-duration transfers exist as may be seen in the lower-left and lower-right regions of Figures 4.14 and 4.15. Many of these transfers require less total  $\Delta V$  than the faster transfers. In general, each of these transfers is constructed by intersecting the transfer's Bridge segment with a point very near apogee of the transfer's Manifold segment.

- The least-expensive transfers, e.g., those transfers seen in the lowest regions on the left and right sides of the two figures, require several lunar flybys to reach the corresponding Halo orbits. These transfers are more logically difficult since a spacecraft will need to be carefully navigated through the lunar flybys.
- The transfers shown in Figures 4.14 and 4.15 implement LEO parking orbits with ecliptic inclinations anywhere between  $0^\circ$  and  $60^\circ$ . Again, the equatorial inclinations of the LEO parking orbits depend on the launch date.
- The duration of time required to transfer within 100 km of the Halo orbit may be anywhere between 5 – 60 days. Transfers may certainly be constructed that require more time, however, these transfers are not considered in this study since they may be more influenced by the Sun’s gravity.
- The least-expensive transfers to lunar  $L_1$  Halo orbits following their interior stable manifolds generally require a total  $\Delta V$  no smaller than approximately 3.60 km/s, depending on the Halo orbit of choice. The trend is very similar to that presented in Section 4.3.2.1 for short-duration lunar Halo transfers. The least-expensive transfer identified in this study requires a total  $\Delta V$  of approximately 3.583 km/s.

To continue this analysis, Figure 4.16 shows the magnitudes of the two deterministic maneuvers separately. One can see that the total  $\Delta V$  cost of each transfer is divided between the two maneuvers in a very similar way as the exterior transfers shown in Section 4.3.2.1. Many of the transfers require a Trans-Lunar Injection maneuver magnitude ( $\Delta V_{LEO}$ ) between 3.120 and 3.136 km/s. Some of the families of more-efficient transfers require smaller  $\Delta V_{LEO}$ -magnitudes. Even with these slight reductions, the second maneuver,  $\Delta V_{MI}$ , still contributes most of the variations seen in the total cost of the lunar transfer.

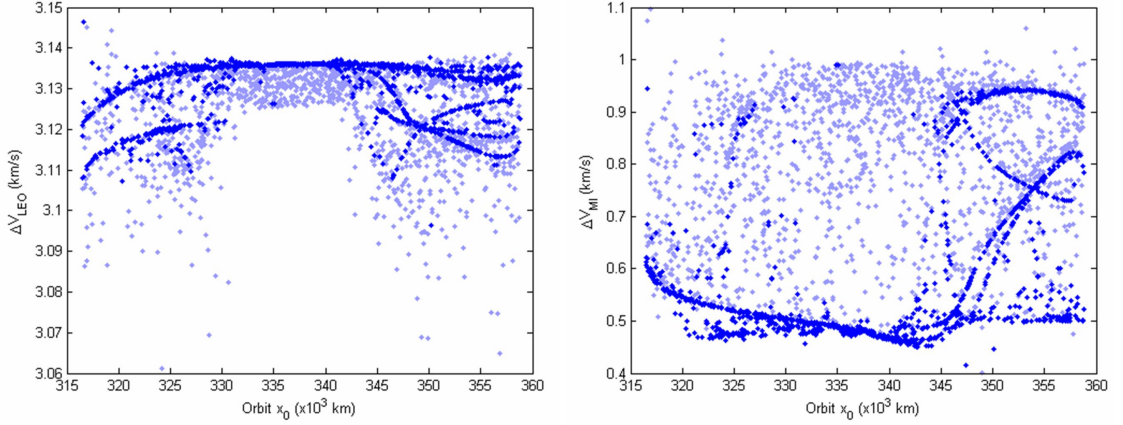


Figure 4.16: The two transfer maneuver magnitudes that combine to produce the total  $\Delta V$  cost of the transfers shown in Figures 4.14 and 4.15. Left: The magnitudes of the Trans-Lunar Injection maneuvers ( $\Delta V_{LEO}$ ) in each transfer; Right: The magnitudes of the Manifold-Insertion maneuvers ( $\Delta V_{MI}$ ) in each transfer.

#### 4.3.2.3 Exterior Transfers to L<sub>2</sub> Halo Orbits

This section presents the results of transfers constructed between 185-km LEO parking orbits and the exterior stable manifold of Halo orbits in the family of lunar L<sub>2</sub> Halo orbits. Figure 4.17 shows the cost of many such example transfers to each Halo orbit in the family, including a Pareto front of optimal transfers. One can see that there are several types of efficient transfers one can make. To help identify the differences between each type of transfer, Figure 4.18 shows plots of several example transfers.

Figures 4.17 and 4.18 show many interesting patterns. After studying the transfers presented in these figures, the following observations have been made:

- Two dominant types of efficient transfers exist that transfer to the Halo orbits' exterior stable manifold. The first one, indicated by the upper prominent curve in Figure 4.17, includes transfers whose Bridge segments connect the spacecraft directly with the far side of the L<sub>2</sub> Halo orbit. These are short-duration transfers, similar to the short-duration transfers explored in Sections 4.3.2.1 and 4.3.2.2. The second dominant type of transfer, indicated by the lower

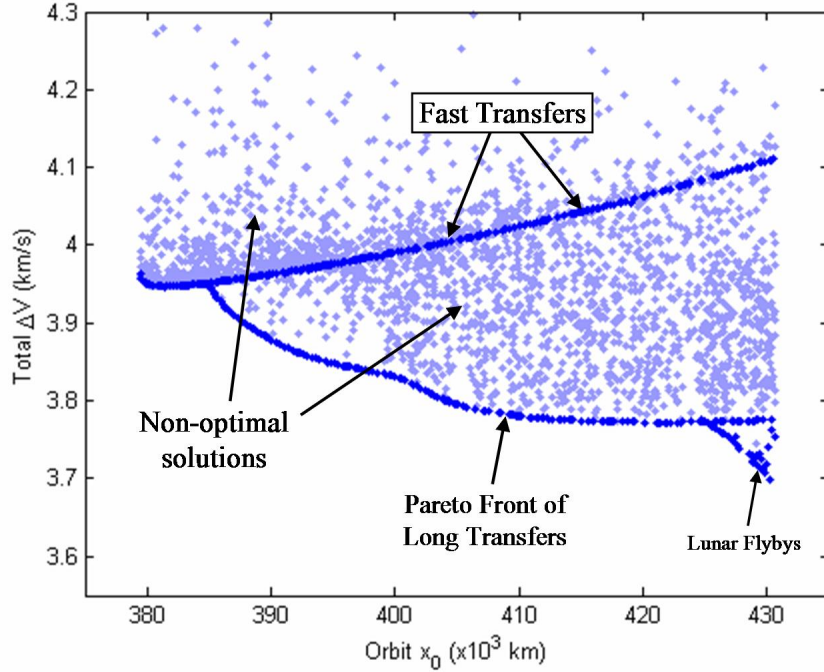


Figure 4.17: The total  $\Delta V$  cost of many transfers to the exterior stable manifold of each orbit in the family of lunar  $L_2$  Halo orbits, including a Pareto front of optimal solutions.

prominent curve in Figure 4.17, includes trajectories whose Bridge segments send the spacecraft well beyond the Moon, where they intersect the corresponding Manifold segments near the segments' apogee points. The first type of transfer requires only 5 – 6 days to accomplish, whereas the second type requires as many as 35 – 45 days before the spacecraft is within 100 km of the lunar Halo orbit.

- Additional benefit may be obtained for transfers to  $L_2$  Halos with  $x_0$ -values greater than approximately 425,000 km by flying near the Moon en route to the  $\Delta V_{MI}$  maneuver. The lunar flyby reduces the total required  $\Delta V$ , albeit at the expense of more sensitive navigation requirements near that lunar flyby. These transfers may be seen in the lower-right portion of Figure 4.17; two example plots are shown in the lower-right portion of Figure 4.18, where one transfer

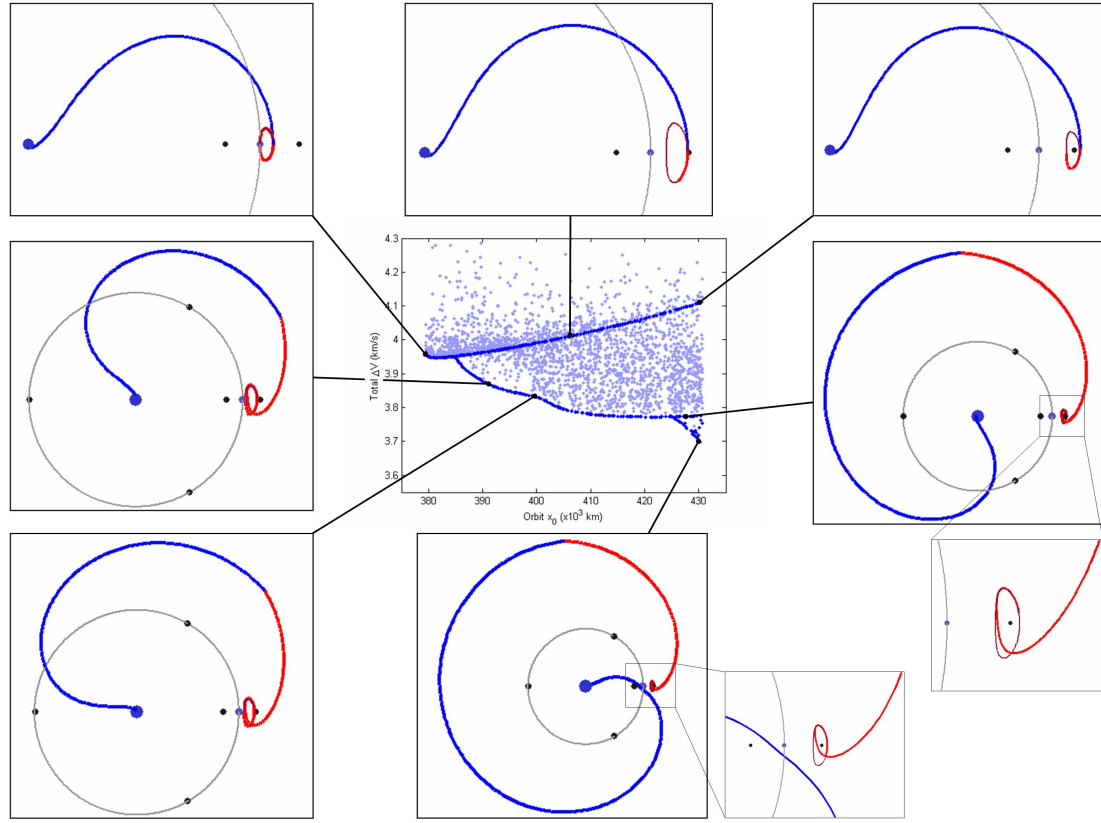


Figure 4.18: Several example transfers between 185-km LEO parking orbits and the exterior stable manifold of lunar L<sub>2</sub> Halo orbits.

includes the lunar flyby and the other does not.

- The transfers shown in Figures 4.17 and 4.18 implement LEO parking orbits with different ranges of ecliptic inclinations. The transfers indicated by the upper prominent curve in Figure 4.17 may be launched from LEO parking orbits with ecliptic inclination values anywhere in the range of 0° – 25°. Those transfers indicated by the lower prominent curve may implement LEO inclination values anywhere in the range of 0° – 19°. Finally, those transfers shown in the lower-right portion of the figures, e.g., those transfers with lunar flybys en route to the  $\Delta V_{MI}$  maneuver, may implement LEO parking orbits with a much more broad range of ecliptic inclinations: anywhere in the range of 20° – 120°

and possibly beyond.

- The total  $\Delta V$  cost of the least-expensive transfers to lunar L<sub>2</sub> Halo orbits following their exterior stable manifolds greatly depend on which Halo orbit is being targeted. Halo orbits with  $x_0$ -values less than 385,000 km, i.e., very large  $z$ -amplitude Halo orbits, require no less than approximately 3.95 km/s to reach in this way. The cost steadily goes down for Halo orbits with  $x_0$ -values between 385,000 – 415,000 km. Halo orbits with  $x_0$ -values greater than approximately 415,000 km, i.e., very low  $z$ -amplitude Halo orbits, require no less than approximately 3.77 km/s to reach in this way. Finally, those Halo orbits that may be reached using an additional lunar flyby en route have a total  $\Delta V$  requirement that may be reduced to as low as approximately 3.69 km/s.

Once again, to continue this analysis, Figure 4.19 shows the magnitudes of the two transfer maneuvers separately. One can see that the total  $\Delta V$  cost of each transfer is divided between the two maneuvers in a similar way as the transfers shown in

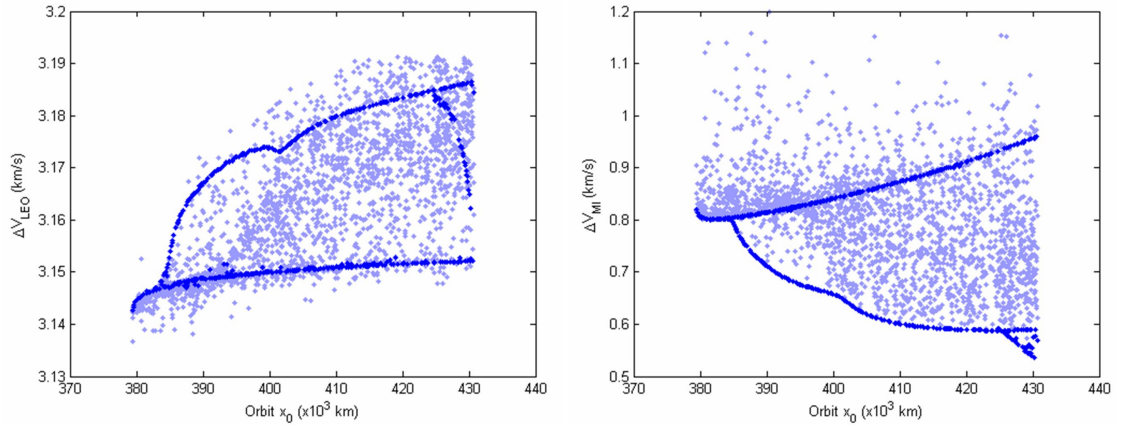


Figure 4.19: The two transfer maneuver magnitudes that combine to produce the total  $\Delta V$  cost of the transfers shown in Figures 4.17 and 4.18. Left: The magnitudes of the Trans-Lunar Injection maneuvers ( $\Delta V_{\text{LEO}}$ ) in each transfer; Right: The magnitudes of the Manifold-Insertion maneuvers ( $\Delta V_{\text{MI}}$ ) in each transfer.

Sections 4.3.2.1 and 4.3.2.2. However, in these exterior transfers to the L<sub>2</sub> Halo orbits, the first maneuver,  $\Delta V_{LEO}$ , must perform somewhat larger  $\Delta V$ s than it did for transfers to L<sub>1</sub> Halo orbits: between 3.145 and 3.185 km/s. The second maneuver,  $\Delta V_{MI}$ , still contributes most of the variations seen in the total cost of the lunar transfer.

#### 4.3.2.4 Interior Transfers to L<sub>2</sub> Halo Orbits

This section presents the results of transfers constructed between 185-km LEO parking orbits and the interior stable manifold of Halo orbits in the family of lunar L<sub>2</sub> Halo orbits. Figure 4.20 shows the cost of many such example transfers to each Halo orbit in the family. Several families of locally-optimal transfers have been highlighted in a more prominent shade to be distinguished from the scattered non-optimal transfers. To help identify the differences between each type of transfer, Figure 4.21 shows plots of several example transfers.

The following observations may be made after studying the plots shown in Figures 4.20 and 4.21:

- The most prominent upper curve in Figure 4.20 is nearly identical to the most prominent curve in Figure 4.17 from Section 4.3.2.3. This is because the Manifold segments of the transfers along both of those curves do not depart far from the corresponding Halo orbits. Both of these curves correspond to the shortest-duration transfers to lunar L<sub>2</sub> Halo orbits, although they are certainly not the least-expensive in most cases.
- Many transfers exist that may be modeled as a transfer from LEO to an orbit about the Moon's L<sub>1</sub> point, followed by a transfer from L<sub>1</sub> to L<sub>2</sub>. It makes sense, then, that many transfers to L<sub>2</sub> require no more  $\Delta V$  than transfers to L<sub>1</sub>. These transfers require more transfer-time than the shortest-duration transfers previously described.

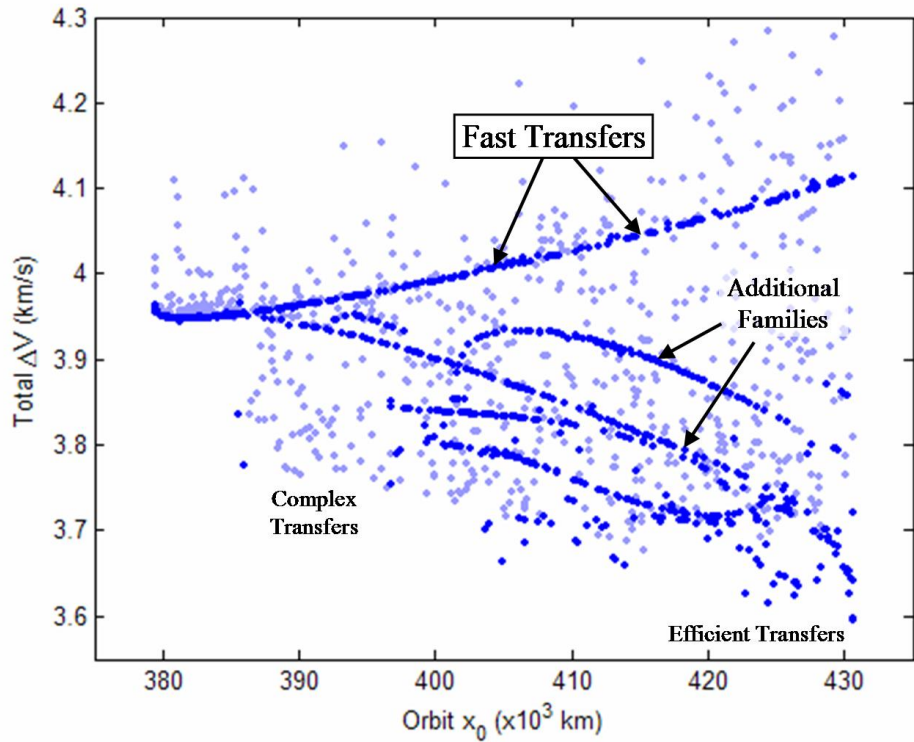


Figure 4.20: The total  $\Delta V$  cost of many transfers to the interior stable manifold of each orbit in the family of lunar L<sub>2</sub> Halo orbits.

- The transfers shown in the lower-left plots in Figure 4.21 include Manifold segments that extend well-beyond the lunar vicinity. The Bridge segments in those transfers connect with a point near one of the apogee points of the corresponding Manifold segments. Several such families exist; in fact, a different family may be produced for transfers that connect with any given apogee of the corresponding Manifold segments. Figure 4.21 shows two plots of transfers that connect with the Manifold segment's first apogee point opposite of the Moon as well as one plot of a transfer that connects with the Manifold segment's second apogee point. In this case, the second family requires slightly less total  $\Delta V$  than the first family. Families of transfers that intersect the third or later apogee passages have not been produced here.

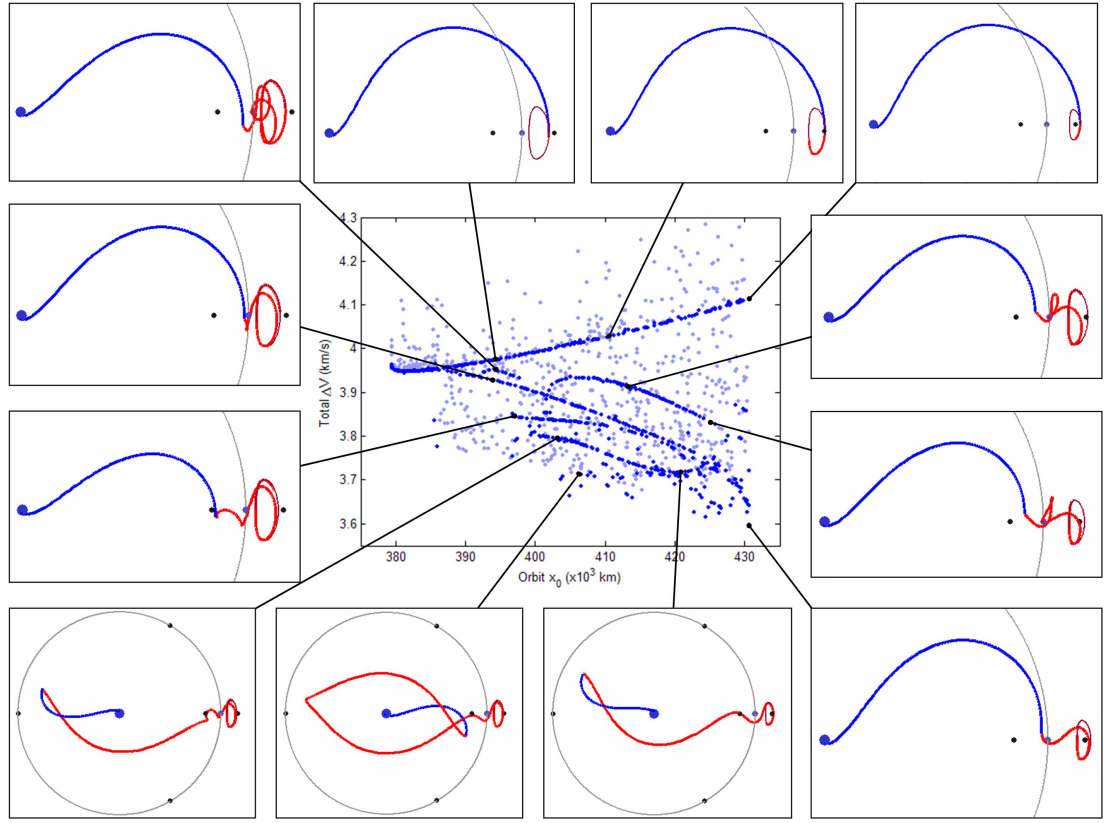


Figure 4.21: Several example transfers between 185-km LEO parking orbits and the interior stable manifold of lunar L<sub>2</sub> Halo orbits.

- There exist many types of transfers that make at least one close lunar passage en route to the L<sub>2</sub> Halo orbit. It is apparent when studying the figures that the total required  $\Delta V$  of a transfer is very dependent on the distance between the Moon and the Manifold-Insertion maneuver. That is, as the proximity of  $\Delta V_{MI}$  with the Moon is reduced the total required  $\Delta V$  in the transfer is reduced. This makes sense because more of the energy-change in the transfer is performed deeper in a gravity well, where the spacecraft is traveling faster. The transfer shown in the lower-right plot of Figure 4.21 is a good example of this effect: its  $\Delta V_{MI}$  is performed very close to the Moon; hence its total  $\Delta V$  cost is lower.
- Several of the non-optimal transfers (plotted in a lighter shade in Figure 4.20)

appear to require less total  $\Delta V$  than other locally-optimal transfers. It is likely that those non-optimal transfers are in a different class of transfer, e.g., they require a different combination of lunar flybys en route to the L<sub>2</sub> Halo orbit, such that the optimized transfers of that class require a longer transfer time. Only transfers requiring fewer than 60 days are plotted in the figures; the locally-optimal transfers that require more than 60 days, and perhaps less total  $\Delta V$ , are hence not displayed.

- The transfers shown in Figures 4.20 and 4.21 implement LEO parking orbits with ecliptic inclinations generally in the range of  $0^\circ - 55^\circ$ .
- The duration of time required to transfer within 100 km of the Halo orbit may be anywhere between 5 – 60 days. Transfers may certainly be constructed that require more time, however, these transfers are not considered in this study since they may be more influenced by the Sun's gravity.
- The least-expensive transfers to lunar L<sub>2</sub> Halo orbits following their exterior stable manifolds generally require a total  $\Delta V$  no smaller than approximately 3.60 or 3.65 km/s, depending on the Halo orbit of choice. The least-expensive transfer identified in this study requires a total  $\Delta V$  of approximately 3.585 km/s.

The final analysis in this section is to study the performance of the two maneuvers separately for each interior lunar L<sub>2</sub> Halo transfer. Figure 4.22 shows the magnitudes of the two transfer maneuvers. One can see that the majority of each transfer's  $\Delta V$  cost is performed in the first maneuver,  $\Delta V_{LEO}$ , but the variations in the magnitude of  $\Delta V_{LEO}$  between transfers is very small, ranging between approximately 3.11 and 3.15 km/s. The second maneuver,  $\Delta V_{MI}$ , although much smaller, has a great deal more variability and therefore determines the total cost of the transfer.

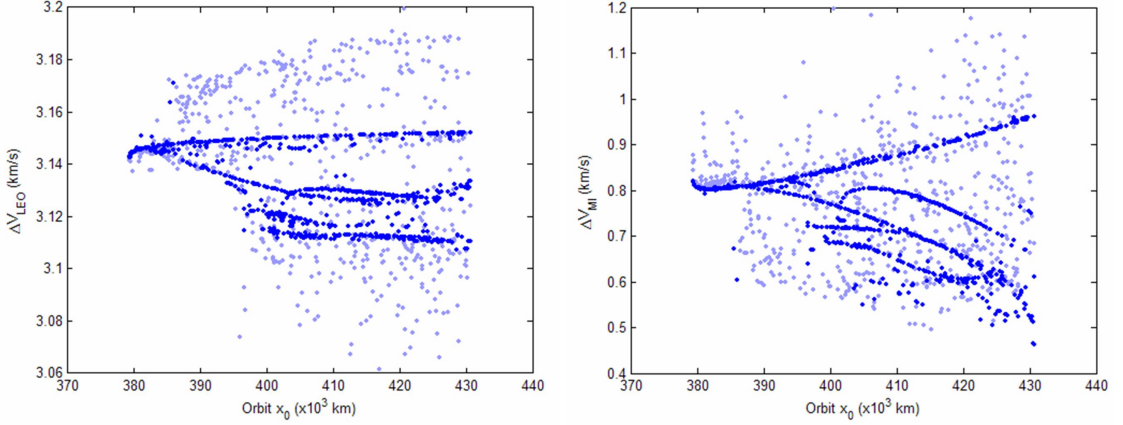


Figure 4.22: The two transfer maneuver magnitudes that combine to produce the total  $\Delta V$  cost of the transfers shown in Figures 4.20 and 4.21. Left: The magnitudes of the Trans-Lunar Injection maneuvers ( $\Delta V_{LEO}$ ) in each transfer; Right: The magnitudes of the Manifold-Insertion maneuvers ( $\Delta V_{MI}$ ) in each transfer.

### 4.3.3 Discussion of Results

Sections 4.3.2.1 and 4.3.2.2 surveyed direct transfers to lunar L<sub>1</sub> Halo orbits; Sections 4.3.2.3 and 4.3.2.4 surveyed direct transfers to lunar L<sub>2</sub> Halo orbits; this section summarizes all of the results together.

Each of the results presented in Sections 4.3.2.1 – 4.3.2.4 implemented direct lunar transfers found by searching through only one half of the stable manifold of the targeted Halo orbits. In reality, it most likely doesn't matter whether a particular trajectory implements an interior or an exterior transfer – just that the spacecraft arrives at the Halo orbit in some way. Figure 4.23 shows a summary of the  $\Delta V$  requirements for both interior and exterior transfers plotted in the same axes. Hence, Figure 4.23 may be used to identify the least-expensive transfers to any lunar L<sub>1</sub> Halo orbit, no matter which type of manifold is taken. Granted, one should still consider the transfer duration and whether any lunar flybys are required. Figure 4.24 shows the same  $\Delta V$  summary for transfers to lunar L<sub>2</sub> Halo orbits.

Theoretically, it is possible to transfer to any given lunar L<sub>2</sub> Halo orbit from a

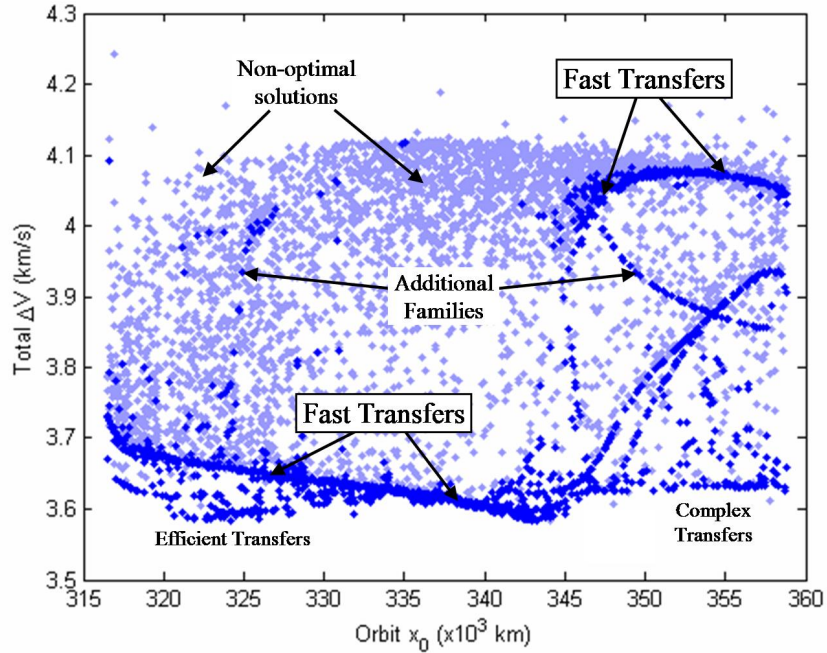


Figure 4.23: The total  $\Delta V$  cost of many transfers to lunar  $L_1$  Halo orbits using either interior or exterior transfers.

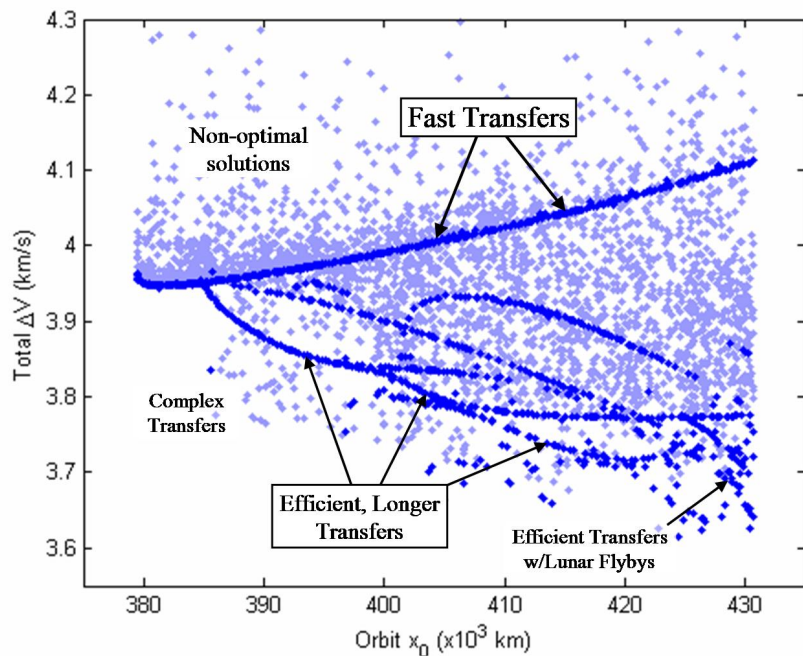


Figure 4.24: The total  $\Delta V$  cost of many transfers to lunar  $L_2$  Halo orbits using either interior or exterior transfers.

lunar L<sub>1</sub> Halo orbit with the same Jacobi constant, and vice versa. See Section 3.10.2 for more details about constructing such transfers. To explore this concept further, Figure 4.25 shows a plot of the Jacobi constant,  $C$ , of each lunar Halo orbit as a function of the Halo orbits'  $x_0$ -values. One can see that there is a lunar L<sub>1</sub> Halo orbit with the same Jacobi constant as each and every lunar L<sub>2</sub> Halo orbit in this study. The family of lunar L<sub>2</sub> Halo orbits includes orbits with Jacobi constants in the approximate range  $3.015 < C < 3.152$ ; the family of lunar L<sub>1</sub> Halo orbits spans that entire range and then extends a bit further in each direction. In theory, it is thus possible to transfer to any lunar L<sub>2</sub> Halo orbit from the corresponding lunar L<sub>1</sub> Halo orbit for very little energy.

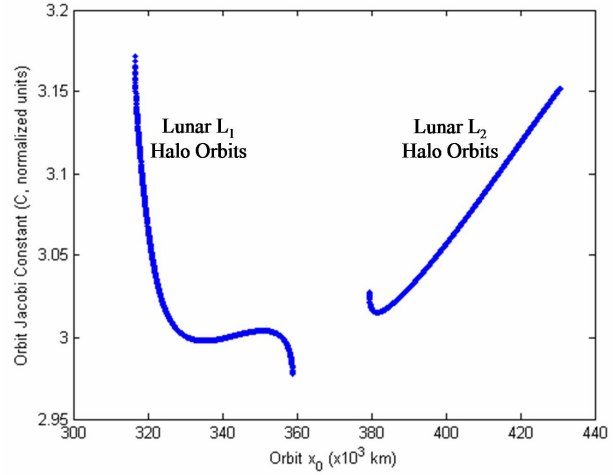


Figure 4.25: The Jacobi constant of each lunar Halo orbit as a function of the Halo orbits'  $x_0$ -values.

Figure 4.26 shows the same results shown in Figures 4.23 and 4.24, but now plotted as a function of the Halo orbits'  $C$ -values rather than their  $x_0$ -values. In this way, one can observe the minimum total  $\Delta V$  required to reach any Halo orbit of a particular Jacobi constant. Then, once in that orbit, one can theoretically transfer to a different desired orbit, provided the desired orbit has the same Jacobi constant. The left part of Figure 4.26 shows transfers that may be used to reach only lunar L<sub>1</sub> Halo orbits, since there are no lunar L<sub>2</sub> Halo orbits with Jacobi constant values below 3.015. Figure 4.26 also shows that if a low-energy transfer can be found between Halo orbits about L<sub>1</sub> and L<sub>2</sub> of a given Jacobi constant, it is almost always more efficient to transfer directly to the lunar L<sub>1</sub> Halo orbit first, and then take the low-energy transfer over to the lunar L<sub>2</sub> Halo orbit.

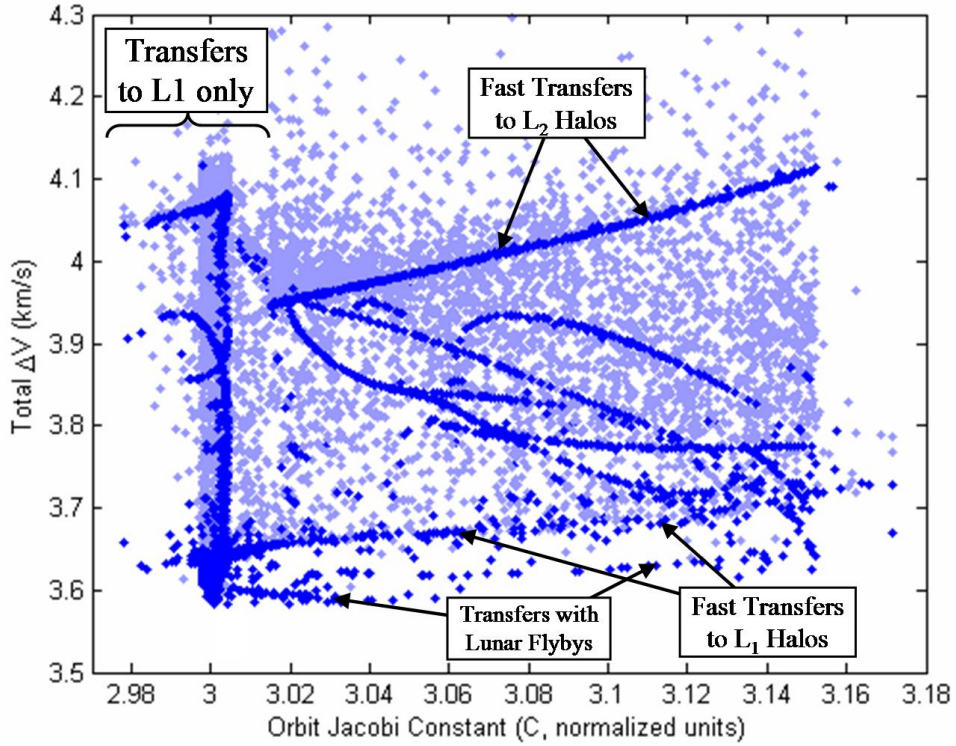


Figure 4.26: The total  $\Delta V$  cost of direct lunar Halo orbit transfers as a function of the Halo orbits' Jacobi constant values.

Halo orbits exist in two families: a Northern and a Southern family as described in Section 3.3.2. Every lunar L<sub>1</sub> Halo orbit explored in this chapter has been a member of the Northern family; every lunar L<sub>2</sub> Halo orbit has been a member of the Southern family. To access the symmetric family of Halo orbits, in either case, the transfer must be reflected about the  $x - y$  plane. The only difference that would be noticeable in such a symmetric transfer would be that the LEO parking orbit's ecliptic inclination would have the opposite sign.

Each transfer surveyed in this section has been constructed in the circular restricted three-body model. This model approximates the real solar system well in general, but there are several significant differences between real lunar transfers and the modeled transfers (see Section 3.6.3 for more details). The most significant differ-

ences between the real solar system and the modeled system for lunar transfers are the Moon’s non-circular orbit about the Earth and the gravitational forces of the Sun and of the other planets in the solar system. One may convert a trajectory from the CRTBP into a more realistic model of the solar system, e.g., the JPL Ephemeris model (§2.5.1), using a multiple-shooting differential corrector (§3.5.2 and §3.6.3). Periodic orbits such as Halo orbits that exist in the CRTBP become quasiperiodic in the real solar system. A particular lunar transfer modeled in the CRTBP varies in the real solar system based on the reference date of the real transfer. The majority of the variability observed in the parameters of real lunar transfers, including the transfer’s total  $\Delta V$  cost, varies on a monthly cycle. Other parameters, such as the inclination of the LEO parking orbit, depend on the Earth’s position in its orbit about the Sun.

#### 4.4 Conclusions

This chapter has explored direct transfers to lunar orbits. Section 4.2 surveyed the performance of historical lunar missions as well as conventional direct transfers between 185-km LEO parking orbits and 100-km low lunar orbits. Section 4.3 constructed and surveyed many types of short-duration direct transfers between 185-km LEO parking orbits and lunar Halo orbits about the  $L_1$  and  $L_2$  libration points.

Section 4.2 explored a variety of different direct transfers to 100-km circular low lunar orbits. It was found that the transfer that required the least  $\Delta V$  was a 4.5-day transfer that required a total  $\Delta V$  of approximately 3.947 km/s, including an initial 3.134 km/s maneuver to depart LEO and a final 0.813 km/s maneuver to insert into the lunar orbit. This estimation was produced in the Earth-Moon circular restricted three-body model; the performance of real missions will vary depending on the launch date, the arrival conditions, and various sources of error throughout the mission. Missions with shorter durations may require more  $\Delta V$ , although the  $\Delta V$  penalty is not large until the transfer duration is shortened to fewer than three days. Nevertheless, this dissertation

assumes that transfers to 100-km low lunar orbits require no less than 3.947 km/s using conventional methods.

Section 4.3 explored many types of direct transfers between 185-km LEO parking orbits and lunar Halo orbits. It has been found that short-duration transfers exist to both lunar L<sub>1</sub> and L<sub>2</sub> Halo orbits, requiring approximately five days of transfer time. Such short-duration transfers require between 3.6 and 4.1 km/s, depending on the Halo orbit. It has also been found that transfers exist between LEO and every Halo orbit that require as little as 3.59 to 3.65 km/s, although many of these transfers require three or more weeks of transfer time. Figure 4.27 summarizes the results, showing the least amount of total  $\Delta V$  required to reach any Halo orbit using the fastest optimized transfers, i.e., transfers with a duration of approximately five days, as well as an envelope of longer low- $\Delta V$  transfers that require at most two months of transfer time. The curve representing the longer transfers is very approximate – it was produced by tracing out points that were produced successfully and interpolating between those points. Some of these transfers may be difficult to construct; other lower-cost transfers may also exist that are not shown. Figure 4.28 summarizes the same results as a function of the Halo orbits' C-values rather than their  $x_0$ -values. This representation is useful when mission designers are more interested in which Jacobi constant they obtain rather than which Halo orbit in particular they are targeting.

The fast transfers may be useful for missions with human occupants; the more efficient, longer transfers may be useful for robotic missions to the lunar Halo orbits. If the transfer length increases much beyond one month, it would most likely be preferable to use a more efficient Ballistic Lunar Transfer discussed in the remainder of this dissertation.

In general, it is hereafter assumed that a fast direct transfer may be constructed from a 185-km LEO parking orbit to any given Halo orbit for approximately 3.65 km/s. For specific examples, the cost of fast direct transfers is obtained by studying the results

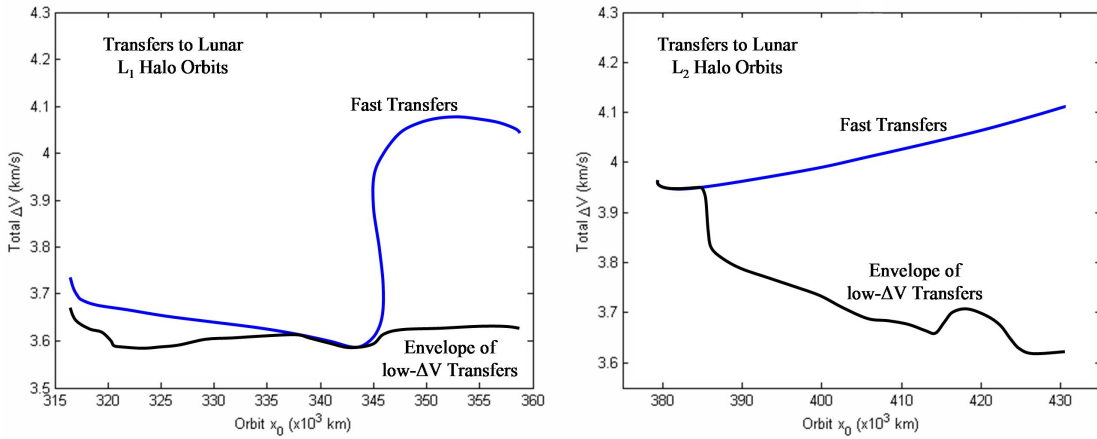


Figure 4.27: A summary of the minimum amount of total  $\Delta V$  required to reach any Halo orbit using the fastest optimized transfers (approximately 5 days) as well as an envelope of longer low- $\Delta V$  transfers (1 – 2 months).

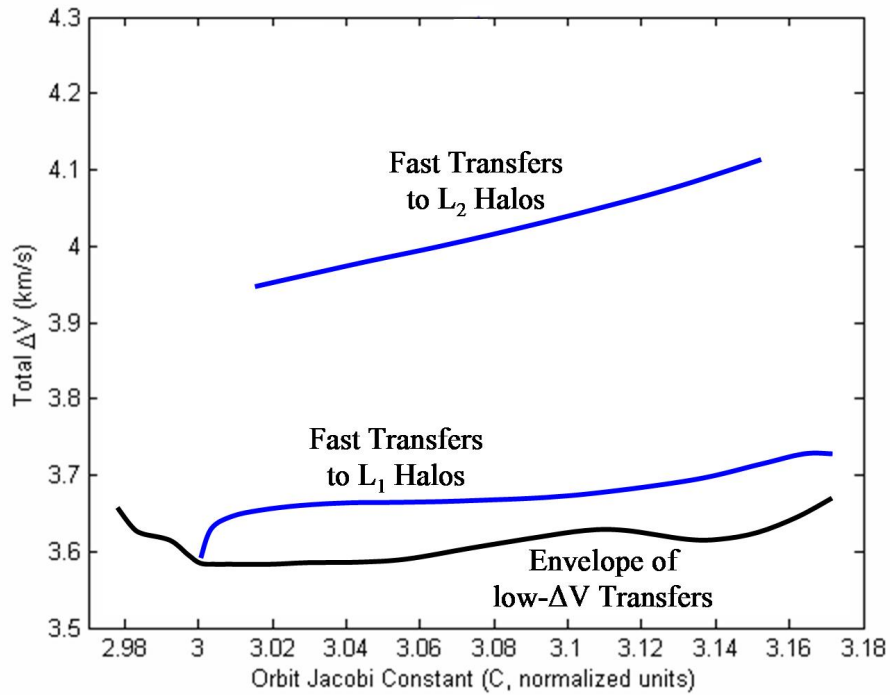


Figure 4.28: A summary of the minimum amount of total  $\Delta V$  required to reach Halo orbits with a given Jacobi constant.

given in this chapter. When appropriate, the cost of more complicated trajectories, i.e., trajectories that implement one or more lunar gravity assists en route to the Halo orbit, will also be used for comparison.

## Chapter 5

### Low-Energy Ballistic Lunar Transfers

#### 5.1 Introduction

The purpose of this chapter is to demonstrate how to use dynamical systems theory to model, analyze, and construct low-energy ballistic transfers between the Earth and the Moon. Chapter 4 presented information about direct transfers to the Moon and to lunar Halo orbits. This chapter studies trajectories that accomplish the same goal, namely, to transfer a spacecraft from a 185-km LEO parking orbit to an orbit about the Moon, but this chapter studies how to harness the Sun’s gravity to reduce the transfer’s  $\Delta V$  cost.

In Chapter 4, it was observed that conventional direct transfers to lunar orbits require at least two large maneuvers, where the second maneuver is required to inject the spacecraft into the final desired orbit. By extending the transfer’s duration and utilizing the Sun’s gravity, one can substantially reduce or even eliminate the need for a second large maneuver. More specifically, a spacecraft implementing a low-energy BLT to a **low lunar** orbit requires a much smaller orbit-insertion maneuver than a spacecraft implementing a conventional transfer; a spacecraft implementing a low-energy BLT to a **lunar Halo** orbit – or to another unstable three-body orbit – requires no orbit-insertion maneuver at all. The spacecraft arrives and is injected into the lunar Halo orbit entirely ballistically. For this reason, these transfers are called low-energy ballistic lunar transfers (BLTs).

Ballistic lunar transfers, as defined in Chapter 1, are trajectories that a spacecraft may use to go from a low Earth orbit to an unstable three-body orbit about the Moon using only one large injection maneuver at LEO. In this chapter, the transfers are constructed to an example Halo orbit about the Earth-Moon L<sub>2</sub> point, but the same sorts of transfers may be produced from the Earth to a variety of different unstable three-body orbits. Such transfers will be explored in Section 6.5.

Several authors have constructed ballistic transfers to the Moon in the past using a variety of strategies. A brief background that outlines some of these strategies will be presented in Section 5.2. To the author's knowledge, none of these strategies uses dynamical systems theory to construct transfers to three-dimensional unstable three-body orbits. Most of the work done previously has been accomplished with the intention of constructing a transfer to any temporarily captured orbit about the Moon (see Section 3.11 for more information about temporarily captured orbits). In some respects, many unstable three-body orbits **are** temporarily captured orbits about the Moon and hence, the BLTs studied in this dissertation may be classified as a particular type of transfers to temporarily captured lunar orbits. Nonetheless, the dynamical systems methods used in this dissertation are substantially different than those strategies used previously: they offer many insights when modeling BLTs, and they offer many advantages when constructing BLTs. These topics will be discussed in detail in this chapter.

This chapter is organized in the following manner. Section 5.2 discusses the background of low-energy ballistic lunar transfers and outlines the strategies used by other authors to construct low-energy lunar transfers. Section 5.3 discusses the different segments of a BLT, qualitatively describing a BLT from different perspectives. The discussion introduces some of the most compelling reasons why it might be beneficial to transfer to a lunar three-body orbit rather than an arbitrary temporarily captured lunar orbit. Section 5.4 discusses how to model a BLT using dynamical systems the-

ory. This discussion introduces another significant benefit of using dynamical systems theory when constructing BLTs: one may compartmentalize the transfers in the same way that patched-conic methods compartmentalize each segment of an interplanetary transfer. That is, one may analyze each segment of a BLT independently. Section 5.5 provides an analysis of an example BLT from an energy perspective. This analysis gives insight into how a spacecraft ballistically changes its energy with respect to the Earth and Moon. Sections 5.6 and 5.7 discuss how to construct BLTs in the Patched Three-Body model (§5.6) and in the JPL Ephemeris model (§5.7). Section 5.8 compares the performance of an example BLT constructed in different models of the solar system. Section 5.9 compares the example BLT with conventional methods to transfer to the Moon. Finally, Section 5.10 summarizes the conclusions that may be drawn from this chapter.

## 5.2 Background

Low-energy lunar transfers have been constructed in the past using a variety of strategies. As early as 1968, Charles Conley began using dynamical systems methods to construct such transfers, although the transfers he constructed were limited to the planar problem. He developed a method that may be used to transfer a spacecraft from an orbit about the Earth to an orbit about the Moon by way of transferring through the neck region about one of the collinear libration points in the Earth-Moon system (Conley, 1968). If a spacecraft has a proper Jacobi energy, then a “neck region” opens up in the forbidden region of the Earth-Moon three-body system, as one can see in Figure 2.6 on page 39 and in Figures 3.14 – 3.16 on pages 92 – 93. Two-dimensional Lyapunov orbits exist in this neck-region that effectively separate the region of space near the Moon from the region of space exterior to the Moon. Conley’s method implements dynamical systems techniques to construct the transfer by targeting the gateway periodic orbit, which then permits the spacecraft to transfer from the exterior region to the

region of space near the Moon.

In the late 1980's and early 1990's, Edward Belbruno began developing a method to construct lunar transfers using his Weak Stability Boundary (WSB) theory (e.g., Belbruno 1987, Belbruno and Carrico 2000, Belbruno 2004, and others). The method involves targeting the region of space that is in gravitational balance between the Sun, Earth, and Moon, without involving any three-body periodic orbits or other dynamical structures, e.g., invariant manifolds of orbits. Ballistic capture occurs when the spacecraft's two-body energy becomes negative, as described by Yamakawa et al. (1993). The lunar transfers presented in this dissertation are very similar to the transfers constructed by Belbruno, but this dissertation implements a completely different method to construct them.

In the early 2000's, Viacheslav Ivashkin also developed a method to construct transfers between the Earth and Moon using the Sun's gravitational influence (Ivashkin, 2002, 2003, 2004b,a). His methods involve beginning from a low lunar orbit, or from the surface of the Moon, and numerically targeting trajectories that depart the Moon in the direction of the Earth's L<sub>1</sub> or L<sub>2</sub> points. A spacecraft on such a trajectory will depart the Moon with a negative two-body energy with respect to the Moon, but as it climbs away from the Moon it gains energy from the effect of the Earth's and Sun's gravity. Eventually, it gains enough energy to escape the Moon's vicinity. The trajectory is then targeted such that it lingers near the chosen Lagrange point long enough to allow the Sun to lower the perigee radius of the next perigee passage down to an altitude of approximately 50 km. Ivashkin's methods are very similar to Belbruno's targeting methods.

In the mid 1990's, other methods were developed to construct a lunar transfer that take advantage of the chaos in the Earth-Moon three-body system. Boltt and Meiss (1995b) constructed a trajectory that sent a spacecraft into an orbit without sufficient energy to immediately reach the Moon, but with enough to get close enough to become

substantially perturbed by the Moon. Using a series of four very small maneuvers, the spacecraft could then hop between nearby trajectories in the chaotic sea to become captured by the Moon using far less energy than standard direct transfers. In 1997, Schroer and Ott (1997) reduced the time of transfer for the chaotic lunar transfer by targeting specific three-body orbits near the Earth. The total cost remained approximately the same as the transfer constructed by Boltt and Meiss (1995b), but the transfer duration was reduced from approximately 2.05 years to 0.8 years.

In 2000, Koon et al. constructed a planar lunar transfer that was almost entirely ballistic using the techniques involved in Conley's method (Koon et al., 2000b, 2001). Similar to Conley, Koon et al. observed that the planar libration orbits act as gateways between the interior and exterior regions of space about the Moon. Koon et al. constructed a transfer by targeting a trajectory within the interior of the stable invariant manifold of a planar libration orbit about the Earth-Moon L<sub>2</sub> point. Once inside the interior of the stable manifold, the spacecraft ballistically arrives at a temporarily-captured orbit about the Moon.

Dynamical systems theory proved to be very useful in the planar problem because the system is very well defined. The four-dimensional phase space of the planar CRTBP is reduced to three dimensions by specifying a particular Jacobi energy to use in the problem. Koon et al. took advantage of that topological reduction and showed that the two-dimensional invariant manifolds of a Lyapunov orbit act as a separatrix, dividing the three-dimensional energy surface into interior and exterior regions. A spacecraft in the exterior region of the Earth-Moon system could then target a trajectory within the interior region of the energy surface in order to transfer through the neck of the forbidden region into the interior of the system. Unfortunately, the algorithms presented in the study cannot be trivially moved into the three-dimensional CRTBP system. The spatial CRTBP has a phase space with six dimensions; by specifying a particular Jacobi energy the system is reduced to a five-dimensional energy

surface. The invariant manifolds of periodic orbits in the CRTBP, such as Halo orbits, are two-dimensional; the invariant manifolds of quasiperiodic orbits, such as Lissajous orbits, are three-dimensional. Even the three-dimensional manifolds of Lissajous orbits cannot clearly divide a five-dimensional energy surface into well-defined interior and exterior regions. Hence, the methods developed by Conley and Koon et al. fail to produce the same kind of success in three dimensions as they demonstrated in the planar problem.

The present dissertation uses the same dynamical systems methodology used by Conley (1968) and Koon et al. (2000b), but instead of attempting to identify each and every type of trajectory that may be used to transfer a spacecraft into a temporarily-captured orbit about the Moon, this dissertation studies the more localized problem of transferring a spacecraft from the Earth to a particular unstable three-body orbit in the Earth-Moon system. Once the spacecraft reaches the Earth-Moon three-body orbit, the spacecraft can then transfer for free into the interior of the lunar region and even to the surface of the Moon itself. This then completes the problem of constructing a three-dimensional ballistic transfer to a temporarily-captured lunar orbit.

The discussions given here use Halo orbits as the targeted Earth-Moon three-body orbits since they are so easy to visualize, although many other types of orbits may be used as well. Halo orbits are also a logical step to take in the analyses presented here because they are the three-dimensional bifurcation of the family of Lyapunov orbits. Furthermore, Halo orbits have been shown to be useful for many types of practical mission designs in the Earth-Moon system, such as lunar communication or navigation system designs, which will be discussed further in Chapter 7.

### 5.3 The Mission Segments of a BLT

This section qualitatively describes the motion of a spacecraft on a low-energy ballistic lunar transfer. Figure 5.1 shows two example BLTs, viewed in the Sun-Earth rotating frame from above the ecliptic. The main aspects of a BLT may be summarized by discussing the LEO parking orbit (§5.3.1), the outbound trajectory (§5.3.2), the encounter with the Moon (§5.3.3), and then the options that a spacecraft has once it arrives at its lunar orbit (§5.3.4). Finally, an example of a transfer from the Earth-Moon orbit to a low lunar orbit is given in Section 5.3.5 to demonstrate one option that a spacecraft has once it arrives at its lunar three-body orbit.

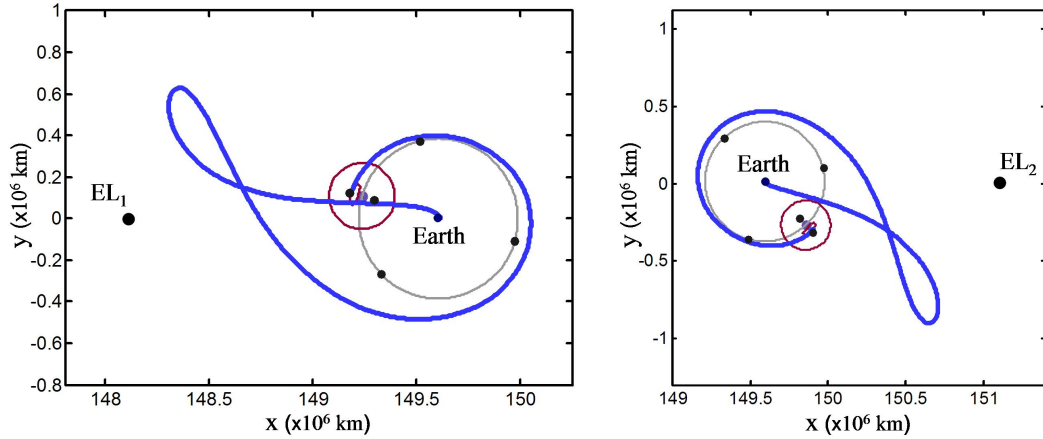


Figure 5.1: Two example low-energy ballistic lunar transfers, viewed in the Sun-Earth rotating frame from above the ecliptic. The 3BSOI is shown in red encircling the Moon.

#### 5.3.1 The LEO Parking Orbit

Ballistic lunar transfers may begin in any LEO parking orbit, including orbits with an inclination compatible with a launch from Cape Canaveral or any other launch facility, provided that the spacecraft injects onto the outbound trajectory at the right time. In this study, it has been found that ballistic lunar transfers may be constructed that depart LEO during most days of each month and during any month of the year.

Some departure dates correspond to BLTs with shorter transfer durations or to BLTs that require less energy than others.

A particular BLT has a small injection window of opportunity, but mission designers have many options available to them if this window is missed. In the event of a delayed launch, a similar BLT may be found that will open a new launch window; this new BLT may have very different characteristics than the original one, but it may still be used to reach the desired lunar orbit. Or if the launch is delayed by more than a few days, the original BLT's launch window will re-open one month later, albeit with slight differences due to the orbit of the Earth and other perturbations. As an additional alternative for a short launch delay, the mission may implement the same BLT with a small maneuver performed en route to correct the trajectory to reach the proper lunar orbit.

### 5.3.2 The Outbound Trajectory

After the spacecraft performs the injection maneuver from its LEO parking orbit, or from the surface of the Earth, the spacecraft travels well beyond the orbit of the Moon and into the region of space that is substantially influenced by the Sun's gravity as well as the Earth's. It is beneficial to describe the spacecraft's motion from both two-body and three-body perspectives, since both perspectives help to paint the full picture.

From a two-body perspective, the spacecraft begins by transferring from its LEO orbit onto a highly-eccentric orbit about the Earth: an orbit with an apogee far beyond the Moon's orbital radius. As the spacecraft approaches and traverses the apogee of this orbit, the spacecraft lingers long enough to give the Sun a large amount of time to perturb its orbit. During this time, the Sun's gravity effectively raises the perigee of the spacecraft's orbit. By the time the spacecraft has returned to its orbital perigee, the spacecraft's orbit will have changed so much that its perigee is now near the radius

of the Moon's orbit about the Earth. As the spacecraft approaches this new perigee, it encounters the Moon.

From a three-body perspective, the spacecraft begins by transferring from its LEO orbit onto a trajectory that shadows the stable manifold of a Sun-Earth/Moon three-body orbit (typically a quasiperiodic libration orbit). The spacecraft approaches this orbit as it approaches the Earth's L<sub>1</sub> or L<sub>2</sub> point, but the spacecraft does not enter the orbit. The spacecraft then ballistically transfers to a trajectory that shadows the three-body orbit's unstable manifold. This trajectory takes the spacecraft to the lunar encounter. The observed transfers occur for free due to the unstable nature of this three-body orbit.

The outbound trajectory travels well beyond the orbital radius of the Moon. With some clever planning, the outbound trajectory may therefore be designed to pass by the Moon on its way out. By performing a lunar flyby during the outbound trajectory, the launch costs can be even further reduced.

During this transfer, the spacecraft requires station-keeping to remain on its proper trajectory. The station-keeping cost is minimal and may be accounted for by typical trajectory correction maneuvers; the Genesis spacecraft followed a similar low-energy transfer and required only approximately 8.87 m/s of  $\Delta V$  per year (Howell et al., 1997a; Lo et al., 2001; Williams et al., 2005).

### 5.3.3 Lunar Encounter

As the spacecraft approaches the Moon, it arrives on the stable manifold of an Earth-Moon three-body orbit, such as a lunar Halo orbit. As the spacecraft follows this stable manifold, it asymptotically approaches the three-body orbit; hence, the transfer requires no final orbit-insertion maneuver to inject into the lunar three-body orbit.

The target Earth-Moon three-body orbit may be planar or three-dimensional; it may orbit the Moon's L<sub>1</sub> point, its L<sub>2</sub> point, or the Moon itself. One of the only require-

ments is that the orbit must be unstable; otherwise, it will not have useful invariant manifolds and an orbit-insertion maneuver will be required. The orbit is typically chosen to either meet mission requirements (such as the requirements of a communication satellite at  $L_1$  or  $L_2$ ) or to be used as a staging orbit before transferring to a final lunar orbit.

#### **5.3.4 Available Options from the Lunar Three-Body Orbit**

Once a spacecraft has arrived at the lunar three-body orbit, the spacecraft has several options. First of all, it may remain there for as long as desired, or at least until its station-keeping fuel budget is exhausted (which may be years). Lunar Halo orbits may be a desirable location for communication and/or navigation satellites; they may also be a desirable location for space stations or servicing satellites.

The spacecraft may transfer from the three-body orbit to a different three-body orbit in the Earth-Moon system for very little energy, provided that both orbits are unstable and have the same Jacobi constant (see Section 3.10 for more information). For instance, the spacecraft might arrive at a lunar  $L_2$  Halo orbit and then later transfer to a lunar  $L_1$  Halo orbit.

The spacecraft may also transfer from the nominal three-body orbit onto its unstable manifold and follow that trajectory to a desirable stable orbit. For instance, the unstable manifolds of  $L_2$  Halo orbits intersect nearly any low lunar orbit, including polar orbits as well as equatorial orbits. The spacecraft may follow the manifold until it intersects the desirable orbit and then perform an injection maneuver to complete the orbit transfer. Such an injection maneuver is typically much smaller than the same injection maneuver performed from a direct lunar transfer rather than performed from a low-energy BLT.

Similarly, the spacecraft may follow the unstable manifold of the three-body orbit down to the surface of the Moon. It has been found that any point on the surface of

the Moon may be reached, although some points require one or two orbits about the Moon prior to touch-down. Again, the required  $\Delta V$  to land from the lunar three-body orbit is smaller than the required  $\Delta V$  to land following a conventional direct transfer from the Earth.

Finally, the spacecraft has the option to return to the Earth following an Earth-return trajectory. Every BLT has a symmetric Earth-return counterpart; the Earth-return trajectory does not need to be the same type that was used to arrive at the lunar orbit.

If the spacecraft's final destination is not the lunar three-body orbit then the spacecraft does not need to inject into that orbit. Instead, the orbit's stable manifold may be used to guide the spacecraft to its final destination rather than to inject the spacecraft onto the three-body orbit. The stable manifold may be used as an initial guess into a trajectory-optimization routine, such as the multiple-shooting differential corrector introduced in Section 3.5.2.

### 5.3.5 Example Transfer from the Lunar Three-Body Orbit

This section provides a demonstration of an example transfer from a lunar  $L_2$  Halo staging orbit to a low lunar orbit. Figure 5.2 shows the example lunar Halo staging orbit and its unstable manifold. A spacecraft on this Halo orbit may depart along any one of these trajectories. These trajectories fly by the Moon at different radii and inclinations, indicating that many different final lunar orbits are accessible from this staging orbit. Figure 5.3 shows one such trajectory that a spacecraft may take to depart the lunar Halo staging orbit. If a maneuver is performed at perilune (or most other places along the trajectory) the spacecraft may become captured into a stable orbit about the Moon.

Additionally, since each Halo orbit in the family of all  $L_2$  Halo orbits has a different unstable manifold, the transfer can access nearly any lunar orbit. Figure 5.4 shows

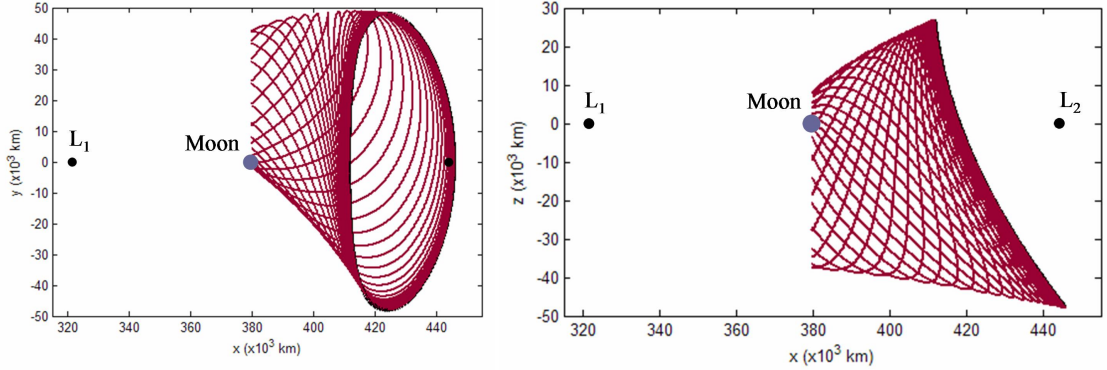


Figure 5.2: An example lunar Halo staging orbit and its unstable manifold, viewed in the Earth-Moon rotating frame from above (left) and from the side (right). A spacecraft on this Halo orbit may depart along any one of the trajectories shown.

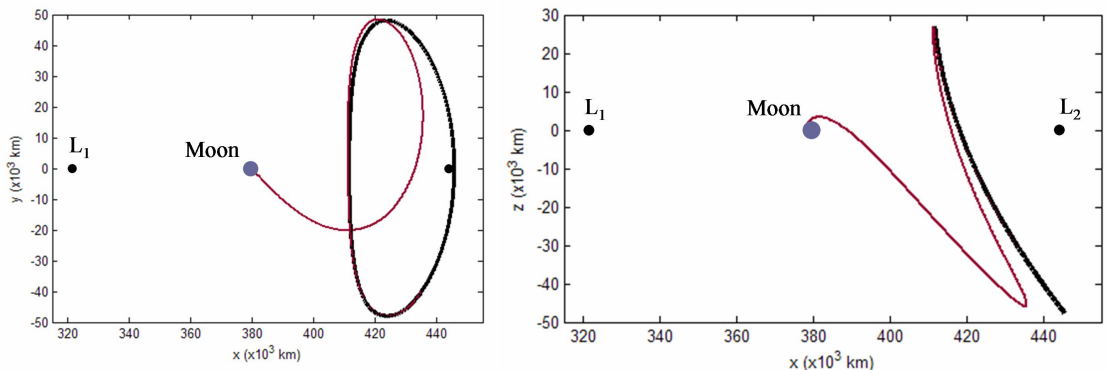


Figure 5.3: One particular trajectory that a spacecraft may take to depart the lunar Halo staging orbit, viewed in the Earth-Moon rotating frame from above (left) and from the side (right). This trajectory intersects a polar low lunar orbit.

some available options for the radius and inclination of lunar orbits that may be accessed by Northern lunar L<sub>2</sub> Halo orbits. The highlighted points are those that are accessible from the example Halo staging orbit shown in Figures 5.2 and 5.3. Southern Halo orbits can access the same set of lunar orbits except with a negative inclination. In each case, it is assumed that the orbit-insertion maneuver is performed at the perilune of the unstable manifold.

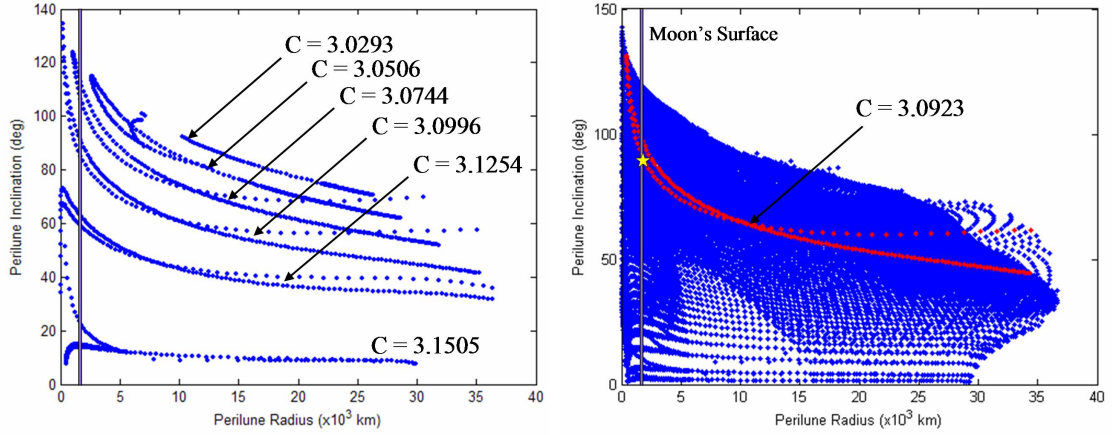


Figure 5.4: Left: The radii and inclination combinations that may be obtained at perilune of the unstable manifolds of six different lunar L<sub>2</sub> Halo orbits, where each orbit's available options are labeled with that orbit's Jacobi constant. Right: The radii and inclination combinations that may be obtained at perilune of the unstable manifolds of many orbits in the family of Northern Halo orbits. The highlighted options in the figure at right correspond to the available options for the Halo orbit shown in Figure 5.2; the star corresponds to the specific trajectory shown in Figure 5.3.

## 5.4 Modeling and Analyzing a Ballistic Lunar Transfer

Section 5.3 qualitatively described each portion of a low-energy ballistic lunar transfer; this section describes how to use dynamical systems theory to model a BLT.

A BLT may be modeled as a series of transfers from one three-body orbit to another. After the spacecraft launches from its LEO parking orbit, the spacecraft transfers to the vicinity of a three-body orbit in the Sun-Earth system, referred to in this section as the **Earth staging orbit**. The spacecraft's LEO departure trajectory follows the flow of the Earth staging orbit's stable manifold. Once in the vicinity of the Earth staging orbit, the spacecraft falls away from the staging orbit, following the flow of that orbit's unstable manifold. The trajectory is chosen so that it encounters the stable manifold of a three-body orbit in the Earth-Moon system, referred to in this section as the **Lunar staging orbit**. The spacecraft may use the Lunar staging orbit as a final destination or

as a transitory orbit, as summarized in Section 5.3.4. To generalize the modeling process even further, a BLT may be modeled as a transfer from Earth to one or more Earth staging orbits to one or more Lunar staging orbits and then to some final destination.

This section considers the use of libration orbits in the modeling, analysis, and construction of BLTs, although many types of three-body orbits may be used. The selection of the type of libration orbits for the staging orbits must be given careful consideration due to the topology of the problem. An Earth staging orbit must be selected with the requirements that its stable manifold intersects the Earth and its unstable manifold intersects the Moon's orbit. The Lunar staging orbit must be selected with the requirement that its stable manifold intersects the unstable manifold of the Earth's staging orbit in full phase space. Only then can the transfer be free of deterministic maneuvers. In a five-dimensional energy surface, it is much easier to intersect three-dimensional invariant manifolds than two-dimensional manifolds. This suggests that quasiperiodic orbits such as Lissajous orbits have a better chance of successfully intersecting their manifolds than periodic orbits such as Halo orbits.

Sections 5.4.1 and 5.4.2 discuss viable Earth and Lunar staging orbits, respectively; Section 5.4.3 shows an example of a simple BLT modeled using a single Earth staging orbit and a single Lunar staging orbit. An end-to-end solution has been constructed using a Lissajous orbit about the Sun-Earth  $L_2$  point and a Halo orbit about the Earth-Moon  $L_2$  point. Finally, Section 5.4.4 provides some more details about the modeling of BLTs using dynamical systems theory.

### 5.4.1 Earth Staging Orbits

Many types of three-body orbits may be used as Earth staging orbits in the process of modeling or constructing a BLT. A proper staging orbit must meet the following requirements:

- (1) The orbit must be unstable;
- (2) If the orbit is the first Earth staging orbit, then the orbit's stable manifold must intersect LEO or the launch asymptote; otherwise, the orbit's stable manifold must intersect the preceding staging orbit's unstable manifold;
- (3) The orbit's unstable manifold must intersect the following staging orbit's stable manifold, be it another Earth staging orbit or a Lunar staging orbit.

A quasiperiodic Lissajous orbit has been selected for the example in Section 5.4.3 because it meets each of these requirements. Unfortunately, quasiperiodic orbits and their invariant manifolds are difficult to visualize since they never retrace their paths. This section illustrates the validity of a Lissajous orbit by showing that Halo orbits are viable candidates to be used as Earth staging orbits.

Figure 5.5 shows four perspectives of the family of Northern Halo orbits centered about the Sun-Earth L<sub>2</sub> point. Lissajous orbits span a very similar region of space, but typically do not extend as far in the *z*-axis. Many of these libration orbits may be used in a lunar transfer depending on the requirements of the mission. The specific orbit may only be chosen once one has identified the origin and destination of the spacecraft in its mission.

Most libration orbits in the Sun-Earth system are unstable and hence meet Requirement 1 given above. This discussion will assume that a Halo orbit from the family shown in Figure 5.5 will be used as the only Earth staging orbit en route to a Lunar staging orbit. This is the itinerary of the transfer developed in Section 5.4.3. Figure 5.6

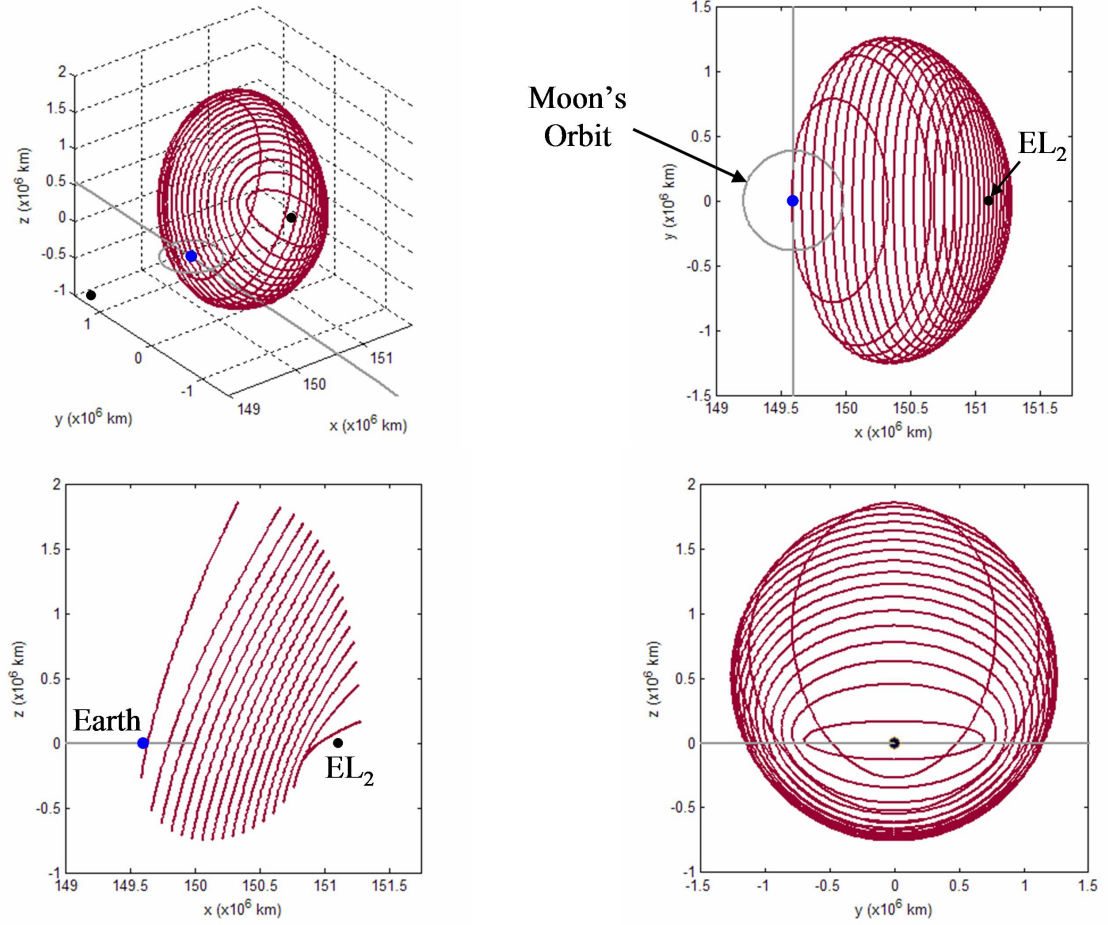


Figure 5.5: Four perspectives of the family of Northern Halo orbits about the Sun-Earth L<sub>2</sub> point.

shows two plots of an example Halo orbit about the Sun-Earth L<sub>2</sub> point and the interior half of its stable manifold. One can see that this stable manifold intersects the Earth. Thus, a spacecraft may make a single maneuver to transfer from a LEO parking orbit to a trajectory on this Halo orbit's stable manifold; this satisfies Requirement 2 for this itinerary. Similarly, Figure 5.7 shows two plots of the same Halo orbit's unstable manifold, showing that trajectories exist that intersect the Moon's orbit about the Earth. Thus, a spacecraft on, or sufficiently near, the Halo orbit may use the orbit's unstable manifold to guide it to intersect the Moon (satisfying Requirement 3). The invariant

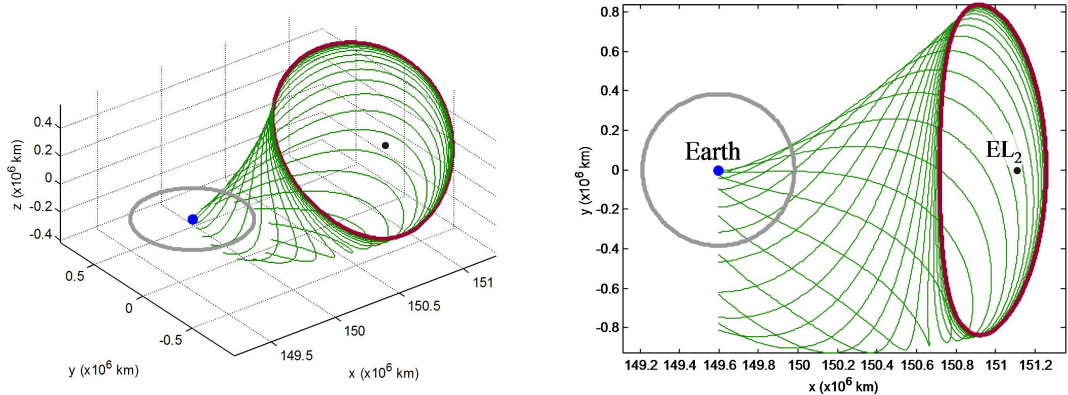


Figure 5.6: Two perspectives of an example Northern Halo orbit about the Sun-Earth L<sub>2</sub> point, shown with the interior half of its stable manifold. One can see that the stable manifold intersects the Earth.

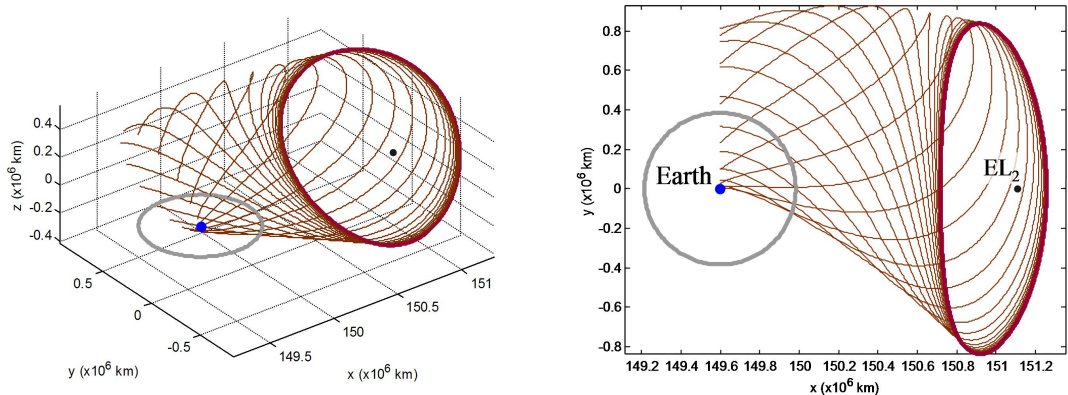


Figure 5.7: Two perspectives of the same Northern EL<sub>2</sub> Halo orbit shown in Figure 5.6, this time shown with the interior half of its unstable manifold. One can see that the unstable manifold intersects the Moon's orbit.

manifolds of Lissajous orbits with similar Jacobi constants also demonstrate the same properties, making them viable candidates for BLT staging orbits.

This section has demonstrated that a three-dimensional libration orbit about the Sun-Earth L<sub>2</sub> point can be used as a staging orbit to transfer a spacecraft from a LEO parking orbit to a trajectory that encounters the Moon. The next section explores Lunar staging orbit options.

### 5.4.2 Lunar Staging Orbits

Many different Earth-Moon three-body orbits may be used as Lunar staging orbits; the example BLT modeled in Section 5.4.3 uses a Halo orbit about the Earth-Moon L<sub>2</sub> point as its Lunar staging orbit because it meets all of the requirements.

The requirements for a Lunar staging orbit typically come from the requirements of the mission itself as summarized in Section 5.3.4. The following list summarizes the additional requirements imposed on the Lunar staging orbit:

- (1) The orbit must be unstable;
- (2) The orbit's stable manifold must intersect the unstable manifold of the preceding staging orbit, be it an earlier Lunar staging orbit or the previous Earth staging orbit;
- (3) If the orbit is the final Lunar staging orbit, then it must meet any requirements derived from the mission; otherwise, the orbit's unstable manifold must intersect the following Lunar staging orbit's stable manifold.

There are many families of Earth-Moon three-body orbits that satisfy Requirement 1, including the family of lunar L<sub>2</sub> Halo orbits. This section demonstrates that these Halo orbits are viable candidates to be used as Lunar staging orbits.

The family of Halo orbits about the Earth-Moon L<sub>2</sub> point closely resembles the family of Halo orbits about the Sun-Earth L<sub>2</sub> point shown in Figure 5.5 and will not be shown here for brevity. Plots of this family appear in Appendix B.6.

Figure 5.8 shows two perspectives of an example LL<sub>2</sub> Halo orbit along with its exterior stable manifold, propagated in the Patched Three-Body model. If a spacecraft targeted a trajectory on this manifold it would asymptotically approach and eventually arrive onto the staging orbit. Thus, if a spacecraft were able to transfer from the Earth staging orbit's unstable manifold onto this LL<sub>2</sub> Halo orbit's stable manifold, then

the spacecraft would have achieved a ballistic transfer to this lunar orbit from LEO. By phasing the Moon properly, one may align and intersect the two manifolds to accomplish this task.

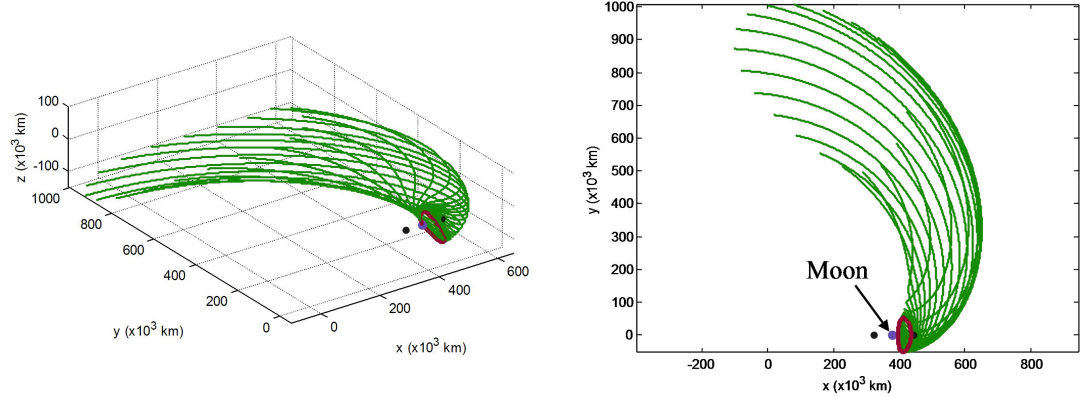


Figure 5.8: Two perspectives of an example Northern Halo orbit about the Earth-Moon L<sub>2</sub> point, shown with the exterior half of its stable manifold. One can see that the stable manifold quickly departs the Moon's vicinity and may then intersect the unstable manifold of the Earth staging orbit.

If one propagates the stable manifold backward in time, i.e., in the process of intersecting it with the Earth staging orbit's manifold, one notices that it quickly departs the Moon's vicinity. As the spacecraft departs the Moon's vicinity, the gravitational perturbations of the Sun grow until such time that the Sun's gravity plays a stronger role in the motion of the spacecraft than the Moon's gravity. When producing trajectories in models that include all planetary bodies, such as the JPL Ephemeris model, this change happens naturally. However, this change must be modeled carefully when producing trajectories in a simpler model, such as the CRTBP. This dissertation therefore propagates a spacecraft's trajectory in the Patched Three-Body model, which is designed to switch from the Earth-Moon three-body system to the Sun-Earth three-body system once the trajectory passes through the three-body sphere of influence (3BSOI). The trajectory is then propagated in such a way that it continues to switch coordinate

systems anytime it crosses the 3BSOI boundary. See Section 2.4.2 for more information about the Patched Three-Body model of the Earth's neighborhood.

#### 5.4.3 An Example Modeled BLT

An example BLT has been modeled using dynamical systems theory and will be presented here. This BLT will continue to be used throughout this chapter. It is a fairly simple example of a BLT: it consists of a single Earth staging orbit and a single Lunar staging orbit. A Lissajous orbit about the Sun-Earth  $L_2$  point has been selected to be the Earth staging orbit, although it will be visualized here by a Halo orbit with the same Jacobi constant. A lunar  $L_2$  Halo orbit has been selected to be the only Lunar staging orbit. This Halo orbit may be used as a staging orbit to transfer the spacecraft to any type of orbit mentioned in Section 5.3.5.

Figure 5.9 shows the first portion of the three-dimensional BLT in two perspectives. The spacecraft is launched from a 185-km low Earth orbit, travels outward toward the Sun-Earth  $L_2$  point along a trajectory that shadows the stable manifold of an

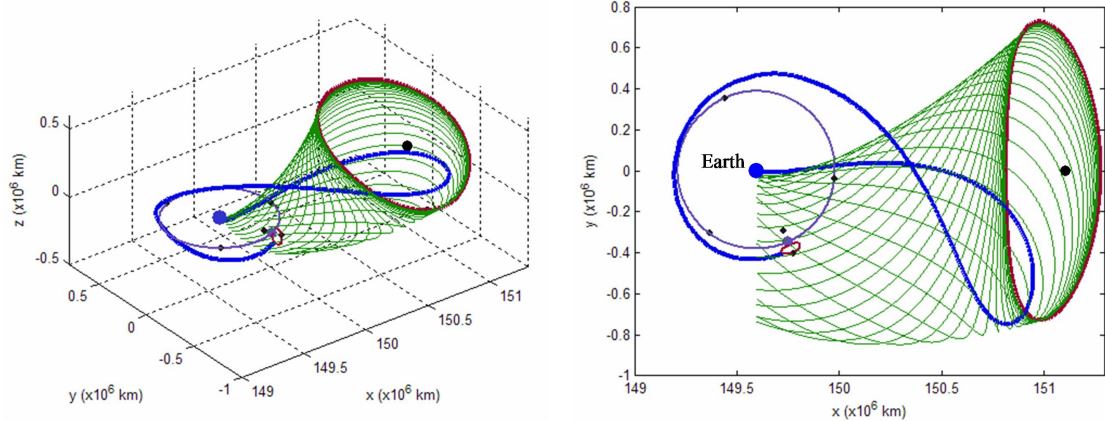


Figure 5.9: Two perspectives of the first portion of the example BLT, modeled using the stable manifold of a Halo orbit about the Sun-Earth  $L_2$  point. One can see that the spacecraft's outbound motion shadows the Halo orbit's stable manifold.

$\text{EL}_2$  libration orbit, skims the periodic orbit and then travels toward the Moon. Figure 5.9 shows the representative Halo orbit and its stable manifold,  $W_{\text{EL}_2}^S$ ; the stable manifold of the actual Lissajous staging orbit does an even better job of mapping out the flow of the spacecraft's motion in space.

Figure 5.10 shows two perspectives of the same transfer trajectory, but this time plotted with the  $\text{EL}_2$  Halo orbit's unstable manifold,  $W_{\text{EL}_2}^U$ . One can see that as the spacecraft departs the vicinity of the Earth staging orbit and approaches the Moon, its trajectory shadows the unstable manifold of the Earth staging orbit. Once again, the manifold of the representative Halo orbit demonstrates the flow in the system, but not as well as the actual Lissajous staging orbit.

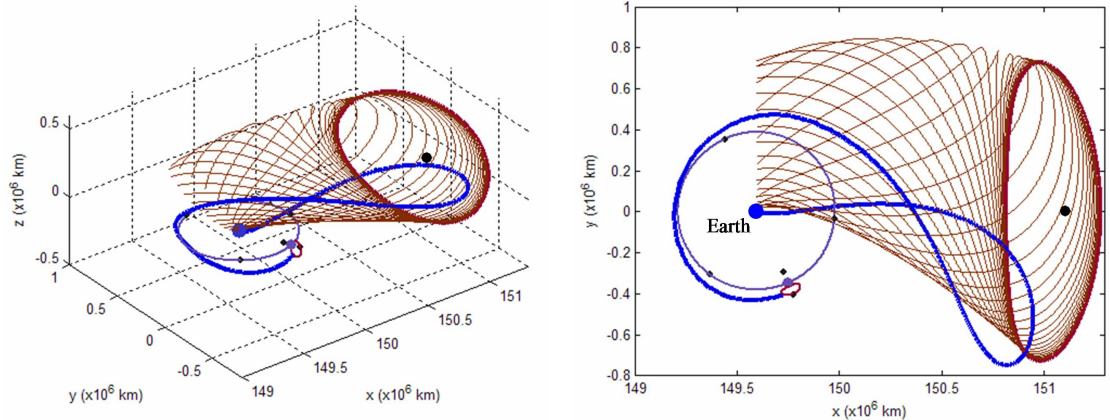


Figure 5.10: Two perspectives of the second portion of the example BLT, modeled using the unstable manifold of a Halo orbit about the Sun-Earth  $L_2$  point. One can see that as the spacecraft departs the vicinity of the Earth staging orbit and approaches the moon, its trajectory shadows the unstable manifold of the Earth staging orbit.

Figure 5.11 shows the same two perspectives of the three-dimensional BLT plotted alongside the Lunar staging orbit's stable manifold,  $W_{LL_2}^S$ . One can see that the BLT intersects the manifold in full phase space, indicating that the spacecraft has injected into the  $LL_2$  Halo orbit. Once in the final Earth-Moon Halo orbit, the spacecraft has all of the options presented in Section 5.3.4 available to it. By following a trajectory

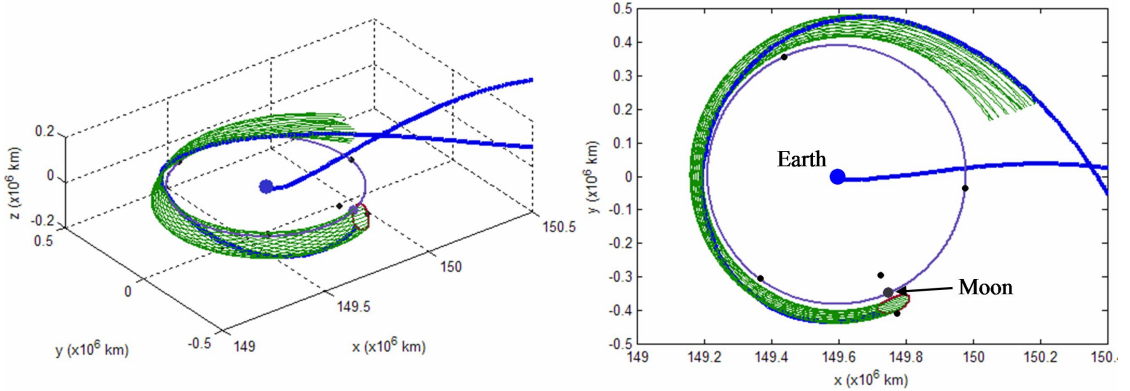


Figure 5.11: Two perspectives of the third portion of the example BLT, modeled using the stable manifold of a Halo orbit about the Earth-Moon L<sub>2</sub> point. One can see that the BLT intersects the manifold in full phase space, indicating that the spacecraft has injected into the LL<sub>2</sub> Halo orbit.

similar to that shown in Figure 5.3, the spacecraft can complete its goal of becoming temporarily captured by the Moon. Finally, Figure 5.12 shows a top-down perspective of the entire three-dimensional BLT with all three manifolds displayed.

#### 5.4.4 Discussion

The dynamical systems method of modeling, analyzing, and constructing BLTs takes advantage of three-body structures. The three-body orbits and their corresponding invariant manifolds exist in families, as may be seen in Appendices A and B. A BLT constructed using these three-body orbits is also, therefore, a member of a family of similar BLTs. This concept has driven the research presented in Chapter 6.

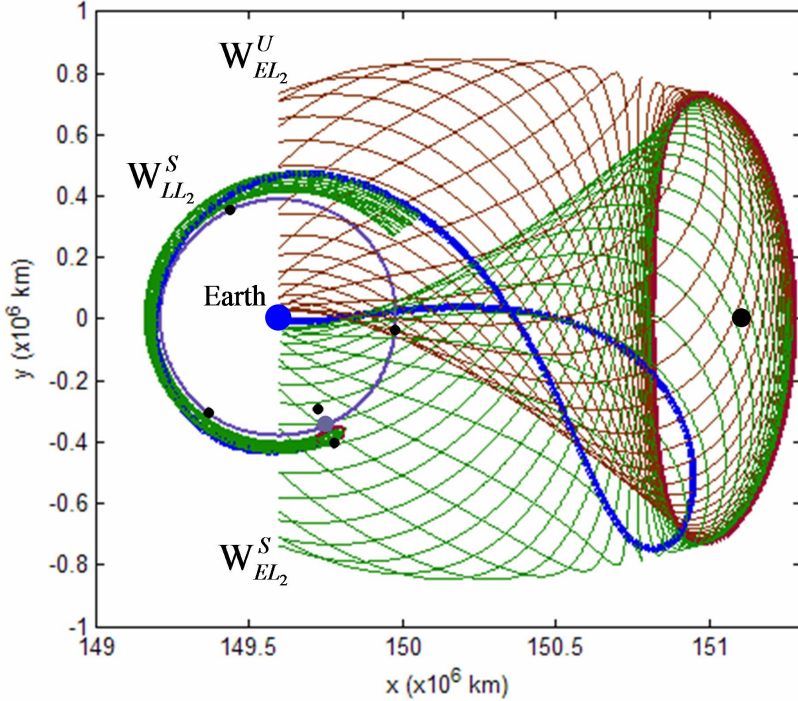


Figure 5.12: A top-down perspective of the example BLT, shown with all three manifolds that are used to model it.

## 5.5 Energy Analysis of a BLT

Ballistic lunar transfers harness the Sun's gravity to reduce the  $\Delta V$  requirements of a lunar transfer. It is useful to observe how the two-body energy of the spacecraft with respect to each of the massive bodies changes throughout the transfer. It is also useful to observe how the Moon affects the spacecraft's Sun-Earth Jacobi constant and especially how the Sun affects the spacecraft's Earth-Moon Jacobi constant. These energy changes are explored in this section.

The BLT used as an example in Section 5.4 will be analyzed again here for consistency; other BLTs have been found to behave in a very similar fashion.

To begin this analysis, Figure 5.13 shows plots of the distance between the spacecraft and both the Earth and Moon as the spacecraft traverses the BLT. This is a useful illustration since both the spacecraft's two-body energy and its Jacobi constant vary

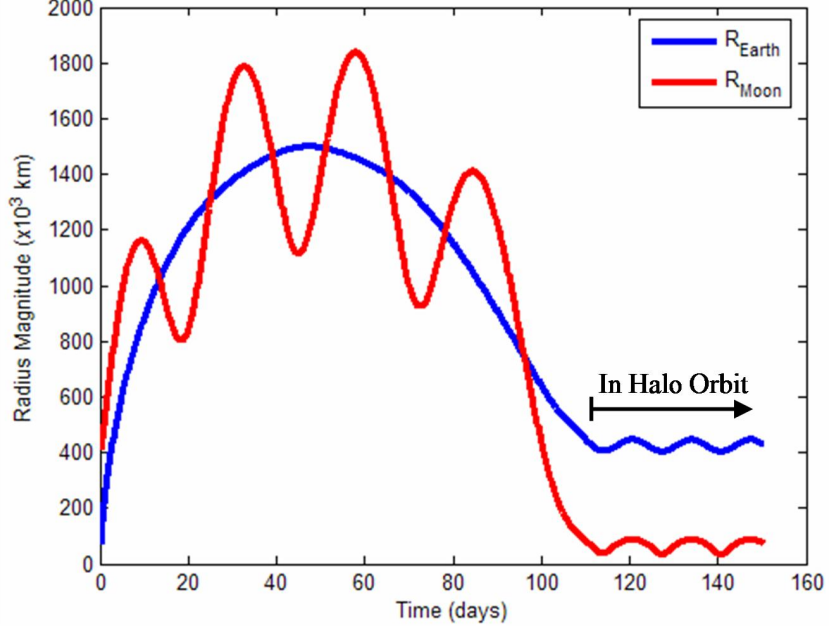


Figure 5.13: The magnitude of the radius vector of the spacecraft with respect to both the Earth and the Moon as the spacecraft traverses the example BLT.

as functions of distance to these bodies. After studying Figure 5.13, one notices that the large variation in the distance between the spacecraft and the Moon is due to the Moon's motion in its orbit about the Earth. As the spacecraft approaches the Moon, approximately 110 days into the transfer, the distance between the spacecraft and the Moon ceases to oscillate about the spacecraft's distance from the Earth. Figure 5.13 may thus be used to approximate the time at which the spacecraft arrives at its lunar Halo orbit destination.

It is expected that the two-body energy of a spacecraft with respect to the Earth increases over time due to the Sun's gravity, since the spacecraft's perigee radius gradually rises throughout the transfer. Figure 5.14 shows the two-body specific energy of the spacecraft with respect to the Earth throughout the BLT. One can see that the spacecraft's energy does indeed rise while it is in the vicinity of the Earth staging orbit. The energy then begins to vary wildly once it enters the lunar Halo orbit, which

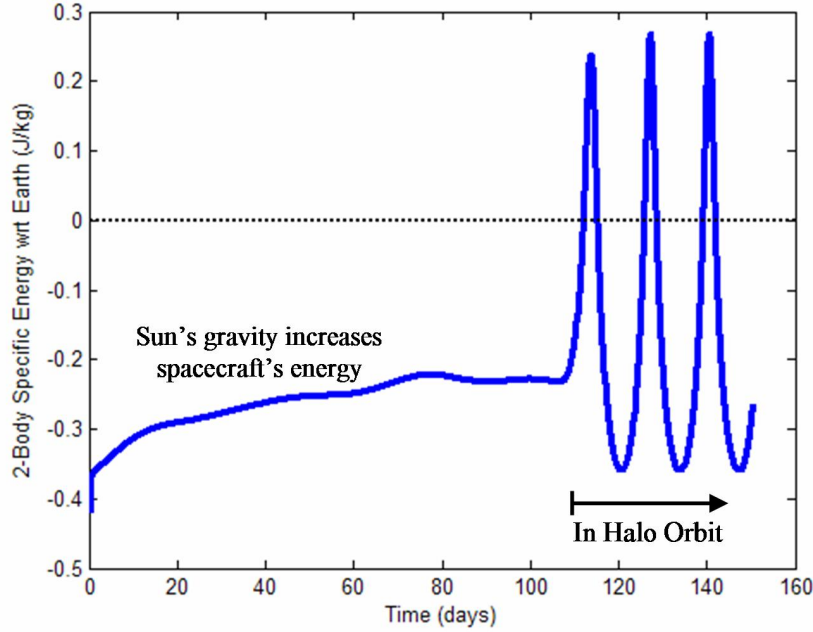


Figure 5.14: The two-body specific energy of a spacecraft with respect to the Earth over time as it traverses an example BLT.

makes sense because the Halo orbit only exists in the presence of both the Earth and the Moon, balancing the gravity of both bodies. Figure 5.15 shows four other two-body orbital elements of the spacecraft with respect to the Earth as the spacecraft traverses the BLT, including the spacecraft's semi-major axis, perigee radius, eccentricity, and ecliptic inclination. One can see that the Sun's gravity increases the spacecraft's semi-major axis and perigee radius as the spacecraft traverses the Earth staging orbit. The Sun's gravity reduces the spacecraft's eccentricity and inclination with respect to the Earth. The spacecraft enters the lunar Halo orbit at approximately 110 days after launch, beyond which the Moon's gravity is the dominant source causing each of the spacecraft's orbital elements to vary over time.

It is also expected that the spacecraft's two-body energy with respect to the Moon decreases as the spacecraft approaches the lunar Halo orbit. This makes sense because the spacecraft transitions from well beyond the Moon's sphere of influence into a lu-

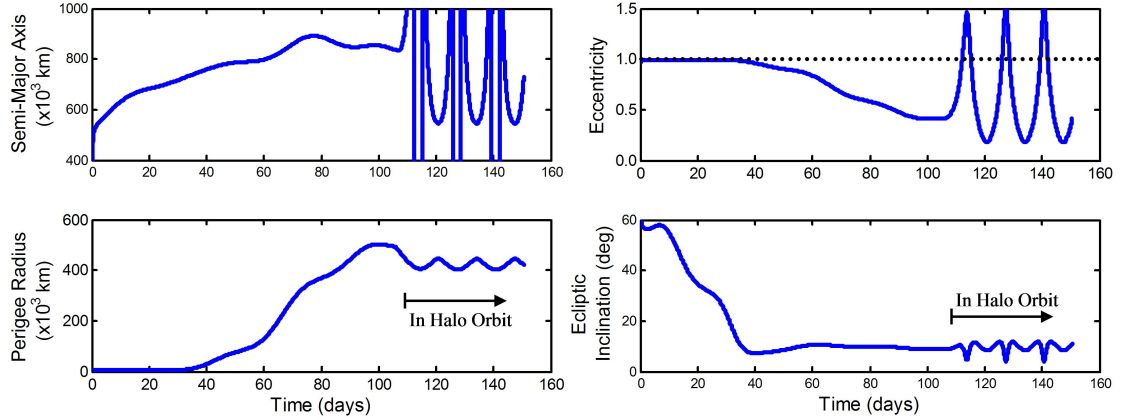


Figure 5.15: Four two-body orbital elements of the spacecraft with respect to the Earth as the spacecraft traverses the example BLT, including the spacecraft’s semi-major axis (top-left), perigee radius (bottom-left), eccentricity (top-right), and ecliptic inclination (bottom-right).

nar Halo orbit, which can then be used as a staging orbit en route to a temporarily captured orbit about the Moon. Figure 5.16 shows the two-body specific energy of the spacecraft with respect to the Moon throughout the BLT. The energy of the spacecraft varies greatly during the first 90 days of the transfer because the spacecraft is not in any sort of lunar orbit. However, as the spacecraft approaches the lunar Halo orbit one can certainly see that the spacecraft’s energy diminishes. Furthermore, its energy drops below zero, satisfying some authors’ requirements to be temporarily captured by the Moon.

Figure 5.17 shows the evolution of the spacecraft’s Jacobi constant with respect to the Sun-Earth three-body system as the spacecraft traverses the example BLT.<sup>1</sup> One can see this value is constant during the first 105 days of the transfer. This makes sense because the first portion of the BLT has been constructed in the Sun-Earth CRTBP and the corresponding Jacobi constant must indeed be constant. However, once the spacecraft crosses the Earth-Moon 3BSOI its motion is then modeled by the Earth-Moon

<sup>1</sup> As usual, the smaller primary of this system is actually the Earth-Moon barycenter, but for brevity we refer to this system as the Sun-Earth three-body system.

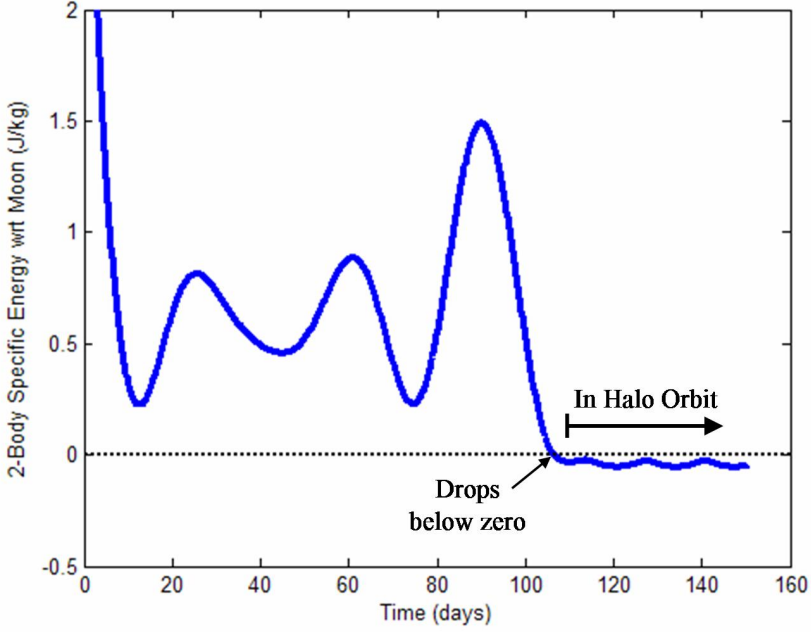


Figure 5.16: The two-body specific energy of a spacecraft with respect to the Moon over time as it traverses an example BLT.

CRTBP; after that point, the Jacobi constant with respect to the Sun-Earth three-body system no longer remains constant. Conversely, the Jacobi constant with respect to the Earth-Moon three-body system **should** be constant. This may be seen in Figure 5.18, which shows the evolution of the spacecraft's Jacobi constant with respect to the Earth-Moon three-body system as the spacecraft traverses the BLT. By comparing Figures 5.17 and 5.18, one can see that the spacecraft's Jacobi constant remains constant in one system and varies in the other, depending on the spacecraft's location with respect to the Earth-Moon three-body sphere of influence.

It is interesting to consider that the Earth-Moon three-body system may be used as a tool to change the Jacobi constant of a spacecraft in the Sun-Earth three-body system, and vice versa. If the spacecraft traversing the example BLT presented in this chapter were to arrive at the Earth-Moon 3BSOI slightly earlier or slightly later, it would enter the Earth-Moon system with a different Jacobi constant. In this way, the

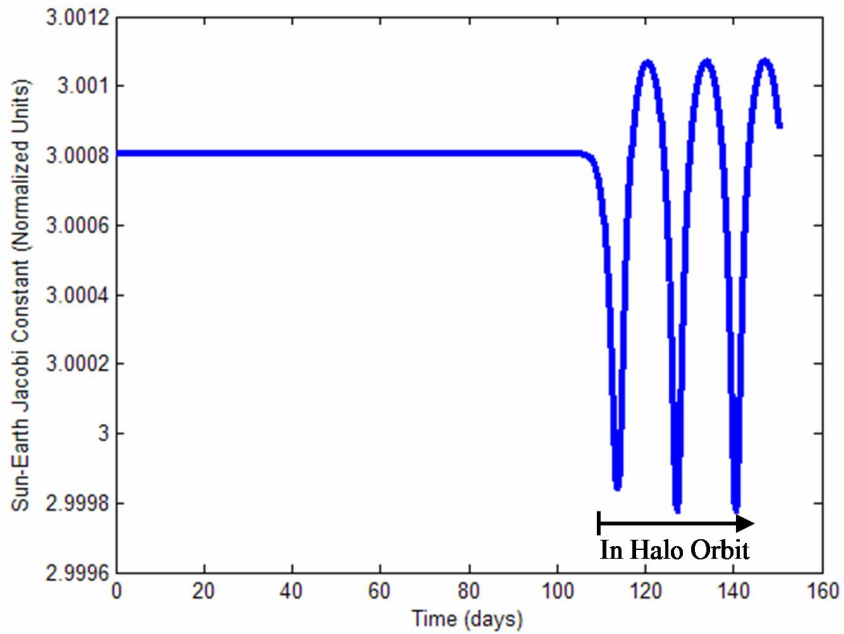


Figure 5.17: The evolution of the spacecraft's Jacobi constant with respect to the Sun-Earth three-body system as the spacecraft traverses the example BLT.

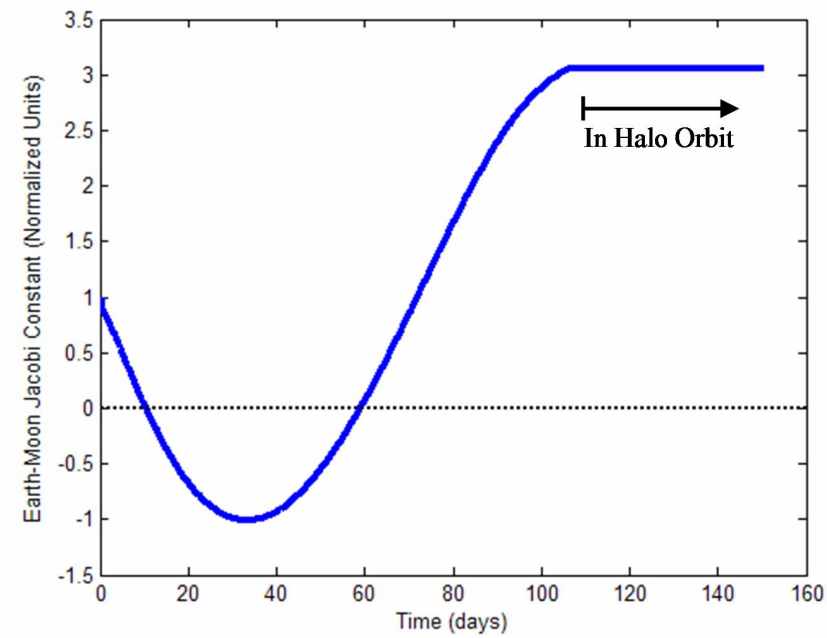


Figure 5.18: The evolution of the spacecraft's Jacobi constant with respect to the Earth-Moon three-body system as the spacecraft traverses the example BLT.

spacecraft may target a lunar Halo orbit with a different Jacobi constant. Perhaps a spacecraft in a lunar Halo orbit can transfer to a different Halo orbit by departing the Earth-Moon system and traversing through the Sun-Earth three-body system for a period of time. Later on, the spacecraft may re-enter the Earth-Moon three-body system with a different Jacobi constant. It may be possible to perform such a transfer without spending months traversing the Sun-Earth system, but that study has not been completed here.

## 5.6 Constructing a BLT in the Patched Three-Body Model

Modeling a BLT involves the use of several staging orbits in the Earth-Moon and Sun-Earth systems and their corresponding invariant manifolds. If a mission designer wishes to construct a BLT that intentionally visits certain staging orbits, then the BLT may be constructed in the same manner that it is modeled. More often, a mission designer only wishes for the spacecraft to reach the final lunar orbit, no matter its route through the Sun-Earth system. In that case, the methods used to construct a BLT may be simplified.

Ballistic lunar transfers have been constructed in this dissertation by propagating the stable manifold of the final lunar Halo orbit (or other three-body orbit) backward in time for a set amount of time. This is a simple process for trajectories propagated in the JPL Ephemeris model of the solar system or any other model that includes at least the gravity of the Sun, Earth, and Moon. In the Patched Three-Body model, care must be taken to ensure that the trajectories in the stable manifold are propagated in the appropriate three-body system during the transfer.

After each trajectory has been propagated from the Earth-Moon system through the Sun-Earth system and hopefully toward the Earth, the perigee point of the trajectory is identified. A proper BLT may be identified as one whose perigee point corresponds to some desired value, e.g., an altitude of 185 km. In this manner, a practical

BLT may be constructed between the Earth and the lunar three-body orbit without identifying any required staging orbit.

### 5.6.1 Parameters

The dynamical systems method of constructing ballistic lunar transfers provides a natural set of parameters that may be used to define each BLT. In the Patched Three-Body model, this set may be described by the parameters:  $[F, C, \theta, \tau, p, \Delta t_m]$ . Each of these parameters will be described in this section.

#### 5.6.1.1 Orbit Family Parameter: $F$

Depending on the mission requirements, one may wish to target any type of Earth-Moon three-body orbit. The first parameters of the set must therefore describe which orbit is being targeted; there are many ways to do that. In this dissertation, the parameter  $F$  is defined to be a discrete variable describing the family of unstable three-body orbits that contains our desired orbit. In the example used in this chapter,  $F$  is set to describe the family of Southern Halo orbits about the Earth-Moon L<sub>2</sub> point. There are certainly symbolic ways to represent each family of three-body orbits, but using text to do so provides a clear description of which family is being used.

#### 5.6.1.2 Orbit Parameter: $C$

As described by Section 3.7, a particular orbit within a family may be specified by a single parameter. In this dissertation, the Jacobi constant,  $C$ , of the targeted orbit is used to specify which orbit is being targeted within the family. Appendices A and B provide plots showing how the Jacobi constant changes throughout each family presented. There are several families that contain more than one orbit with the same Jacobi constant; in these cases, one must specify which orbit is being targeted. A different parameter may always be defined that uniquely specifies each orbit in any family, but

the Jacobi constant is generally more useful since it also provides information about the corresponding forbidden regions and the allowable motion of spacecraft with that Jacobi constant (see Section 2.3.1.4 for more information).

#### 5.6.1.3 Sun-Earth-Moon Angle: $\theta$

The parameter  $\theta$  is defined to be the angle between the Sun-Earth line and the Earth-Moon line. It is a required parameter needed to convert between the two three-body systems in the Patched Three-Body model. Figure 5.19 shows an example of the geometry and the definition of  $\theta$ . A  $\theta$ -value of  $0^\circ$  corresponds to a full Moon and a  $\theta$ -value of  $180^\circ$  indicates a new Moon.

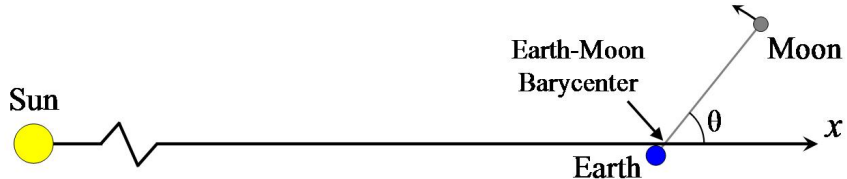


Figure 5.19: The definition of  $\theta$ , the Sun-Earth-Moon angle.

#### 5.6.1.4 Arrival Location: $\tau$

Each point on a periodic orbit may be uniquely described by the parameter  $\tau$ , where in this dissertation  $\tau$  ranges from 0 to 1. More information about  $\tau$  is provided in Section 3.3.3. Figure 5.20 shows a plot of the definition of  $\tau$  when applied to two types of symmetric orbits.

#### 5.6.1.5 Perturbation Direction: $p$

To construct a trajectory in an invariant manifold of a given unstable orbit, one takes the state of the orbit at a given  $\tau$ -value and perturbs that state in either the stable or unstable direction. More information about this process is given in Section 3.9.

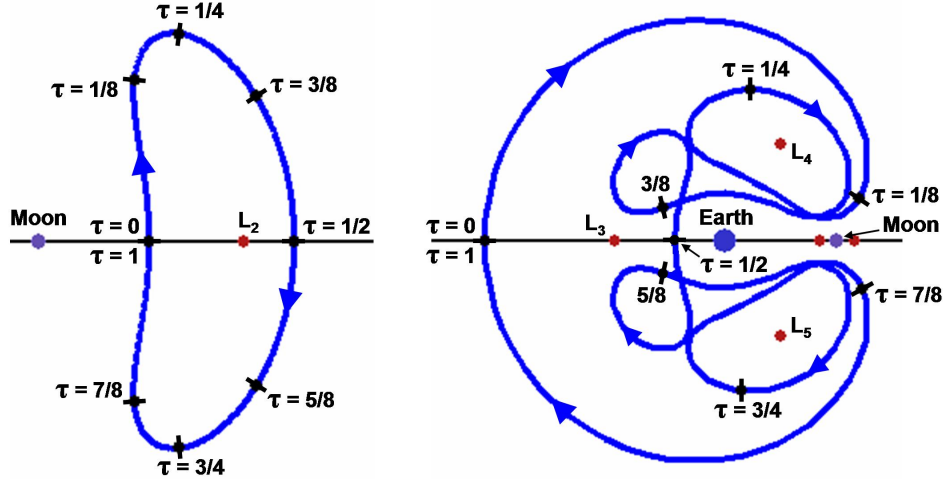


Figure 5.20: The two orbits shown demonstrate how the parameter  $\tau$  moves from 0 to 1 about an orbit.

When the state of the orbit is perturbed, the perturbation can occur in two directions: an interior or an exterior direction. A trajectory on the **interior** manifold travels immediately from the orbit toward the vicinity of the Moon; a trajectory on the **exterior** manifold travels immediately away from the vicinity of the Moon. The parameter  $p$  is a discrete variable that contains information about the direction of the perturbation:  $p$  may be set to “**Interior**” or “**Exterior**”, corresponding to an interior perturbation or an exterior perturbation, respectively. Figure 5.21 shows a plot of the two halves of an example stable invariant manifold.

#### 5.6.1.6 Manifold Propagation Time: $\Delta t_m$

The trajectory in the given three-body orbit’s stable manifold is propagated backward in time for an amount of time equal to  $\Delta t_m$ . Typically when propagated backward in time, the trajectories that lead to desirable BLTs depart the vicinity of the Moon, traverse their apogee, fall toward the Earth, and then intersect a desirable altitude above the surface of the Earth. However, BLTs may also be constructed that pass near the Earth once or several times before intersecting the desirable altitude above the surface

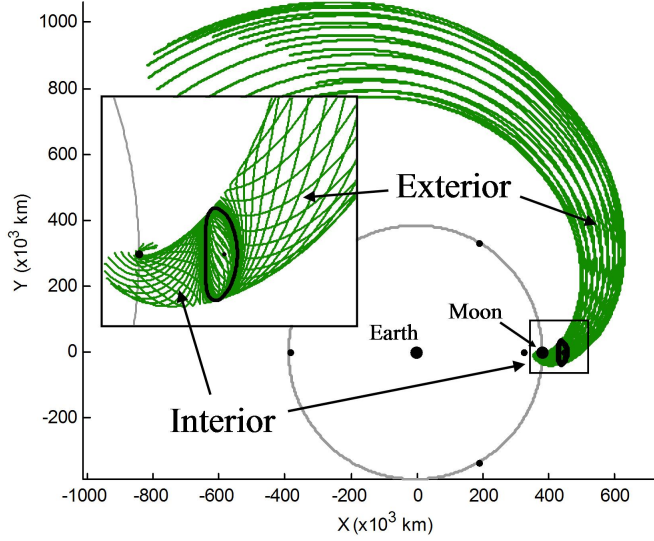


Figure 5.21: An example stable invariant manifold with the Interior and Exterior halves identified.

of the Earth. Such trajectories must be propagated long enough to allow the desirable perigee passage to occur. Thus, the parameter  $\Delta t_m$  is important in order to ensure that the proper perigee passage is being implemented in the BLT.

#### 5.6.1.7 Discussion Regarding Parameters

The set of parameters used in this dissertation does not contain all continuous variables as other sets of orbital elements do, such as the Keplerian orbital element set of a two-body orbit. Other than the Cartesian element set, no continuous sets of variables have been found that uniquely describe families of three-body orbits without some *a priori* knowledge about the shape or structure of the orbits in each family. The present parameter set also requires knowledge about how to use it, but given that knowledge, this set may be used to uniquely describe any low-energy ballistic transfer between the Earth and an unstable three-body orbit. Table 5.1 summarizes the parameter set.

One additional note will be given here. The perturbation magnitude, given as

Table 5.1: A summary of the six parameters used to produce BLTs in the Patched Three-Body model.

Parameter	Domain	Description
$F$	Discrete	Target three-body orbit family
$C$	Continuous	Jacobi constant of target orbit
$\theta$	Continuous $[0^\circ, 360^\circ]$	Sun-Earth-Moon angle
$\tau$	Continuous $[0, 1]$	Arrival location on the target orbit
$p$	Discrete	Perturbation direction
$\Delta t_m$	Continuous	Propagation duration

$\epsilon$  in Section 3.9, must also be set properly to reproduce a particular BLT. The reason becomes clear with an example. The value of  $\epsilon$  corresponds to the perturbation magnitude that is applied to the state of the orbit at the given value of  $\tau$ . Since trajectories depart the unstable three-body orbit at an exponential rate, then a trajectory that is given a perturbation with a magnitude of 100 km will depart quicker than a trajectory that is given a perturbation with a magnitude of 50 km. However, both perturbations can lead to very similar trajectories if the parameters  $\theta$ ,  $\tau$ , and  $\Delta t_m$  are also set correctly. As long as  $\epsilon$  is set to be the same each time – and set to be a reasonable value as described in Section 3.9 – then a given BLT may be reproduced.

### 5.6.2 Producing the BLT

The process of producing a BLT given the parameter set  $[F, C, \theta, \tau, p, \Delta t_m]$  is very simple and will be described henceforth.

**Step 1.** First of all, one must build the target Earth-Moon orbit. The desired orbit must be unstable and can be identified using the parameters  $F$  and  $C$ , as defined above. The example BLT presented in this paper has been produced using an orbit in the family,  $F$ , of Southern Halo orbits about the Earth-Moon  $L_2$  point. The specific orbit has been identified in its family by the value of  $C$ , equal to 3.05.

**Step 2.** The parameter  $\theta$  specifies the location of the Moon, and hence the target orbit,

with respect to the Earth and Sun in the Patched Three-Body model. As time moves forward, the value of  $\theta$  advances with the motion of the Moon about the Earth-Moon barycenter. The example BLT has used an initial  $\theta$ -value of approximately 293.75 degrees. This may be verified by inspecting the final location of the Moon in Figures 5.9 – 5.12. Since the BLT is produced backward in time, the value of  $\theta$  specifies the **final** position of the Moon.

**Step 3.** The parameter  $\tau$  specifies a particular state in the unstable three-body orbit. The example BLT has implemented a  $\tau$ -value of approximately 0.74, corresponding to a point roughly three quarters around the Halo orbit from the orbit's reference point (the point where the orbit crosses the  $x$ -axis orthogonally with positive  $y$ ).

**Step 4.** The particular state in the target orbit is then perturbed in order to construct a single trajectory in the stable manifold of the orbit. The magnitude of this perturbation is given by  $\epsilon$ ; the direction is given by the orbit's monodromy matrix and the parameter  $p$ . The orbit's monodromy matrix is used to compute the orbit's stable and unstable eigenvectors (see Section 3.4 for more information); the stable eigenvector is then mapped to the given  $\tau$ -value using the orbit's state transition matrix. The perturbation is applied along the stable eigenvector either in the interior or exterior direction, as characterized by the parameter  $p$ . The example BLT has implemented a trajectory in the Halo orbit's exterior manifold with the value of  $\epsilon$  set to 100 km.

**Step 5.** The resulting state is then used as the initial condition to construct a trajectory in the stable manifold of the three-body orbit. This trajectory is propagated backward in time for a duration of time equal to  $\Delta t_m$ . The trajectory that has produced the example BLT has been propagated for approximately 28.53 non-dimensional Earth-Moon time units (approximately 123.9 days) before encountering the desired perigee point, i.e., the desired LEO injection point.

**Step 6.** The final step in the construction of a BLT is to connect this trajectory with a LEO parking orbit or with the surface of the Earth. Normally, the trajectory is constructed such that its perigee point comes within a desirable radius from the Earth, e.g., 185 km from the Earth, suggesting that the LEO connection be made at that point. A random set of parameters will produce a BLT that normally does not approach within 185 km of the Earth. In that case, either a bridge segment must be constructed between the desirable LEO orbit and the trajectory (as used in the construction of conventional transfers in Chapter 4), or it is assumed that a very high Earth orbit (HEO) is used as the parking orbit. Using a HEO parking orbit is often unrealistic since it is more efficient to transfer onto a BLT directly from the Earth or from a LEO parking orbit. Nevertheless, there may be times when a spacecraft's mission might take it directly from a HEO orbit or a geosynchronous transfer orbit onto a BLT. This dissertation consistently evaluates the performance of a given BLT by assuming the BLT begins from a circular Earth orbit and refers to that orbit as the LEO parking orbit, even though the altitude may be quite high.

Discussions about the computation time needed to build a BLT are provided in Appendix E. This dissertation evaluates the performance of a BLT using several metrics, including the altitude and inclination of the circular LEO parking orbit, the Trans-Lunar Injection  $\Delta V$  required to insert a spacecraft onto the BLT from the circular LEO parking orbit, and the transfer duration of the BLT. Other parameters are also considered, including the duration of the launch window, the stability of the BLT, and the Sun-Spacecraft-Earth angle during the transfer.

## 5.7 Constructing a BLT in the JPL Ephemeris Model

The BLT that has been analyzed in this chapter has been constructed in the Patched Three-Body model in order to take advantage of all dynamical systems tools that exist in the three-body system. The Patched Three-Body model is certainly useful for modeling and analyzing theoretical BLTs, but BLTs need to be constructed in more realistic models of the solar system in order to be useful for real missions. Therefore, this section describes two processes that one may use to build a BLT in the JPL Ephemeris model of the solar system. Section 5.7.1 describes how to build a BLT in the JPL Ephemeris from the ground up using the same methods that have been used to build a BLT in the Patched Three-Body model. Section 5.7.2 describes how to take a BLT constructed in the Patched Three-Body model and convert it into the JPL Ephemeris model. Both of these methods have specific advantages and disadvantages; Section 5.7.3 provides a discussion about when each of these methods is particularly useful.

### 5.7.1 Building a BLT in the JPL Ephemeris Model

A BLT may be produced in the JPL Ephemeris model using the same techniques that were summarized in Section 5.6 to build a BLT in the Patched Three-Body model. The basic steps are precisely the same, namely:

- (1) Build the desired Earth-Moon three-body orbit in the JPL ephemeris system.
- (2) Construct the orbit's stable invariant manifold.
- (3) Search for locations in the orbit's stable manifold that intersect the desired LEO parking orbit.

Although the basic steps are the same, the implementation of these steps is not as simple in the JPL Ephemeris model as it is in the Patched Three-Body model of the

solar system. The differences will be described henceforth.

The first step in the construction of a practical BLT is to construct the desired Earth-Moon three-body orbit in the JPL Ephemeris model. Periodic Earth-Moon three-body orbits, such as Halo orbits, are only periodic in the CRTBP; they are quasiperiodic in the JPL Ephemeris model, as described in Sections 2.5 and 3.6. Most periodic three-body orbits may be produced as quasiperiodic orbits in the JPL Ephemeris model by differentially-correcting states from their CRTBP representation into the JPL Ephemeris model. In order to retain as much of the same structure as possible, it is generally beneficial to differentially-correct many revolutions of the orbit and then prune off unwanted motion at the ends of the final, converged trajectory. This process is described in detail in Section 3.6.3.

Since three-body orbits are not periodic in the JPL Ephemeris model of the solar system, their characteristics vary slightly from revolution to revolution about the orbit. In this discussion, let us define the parameter  $\tilde{\tau}$  to be equal to 0 at each  $x$ -axis crossing of the orbit whose  $\dot{y}$  component is positive, advancing linearly in time until the next such crossing at which point the value returns from a value of 1 to a value of 0. Then, the rate of change of  $\tilde{\tau}$  varies slightly from revolution to revolution, but  $\tilde{\tau}$  describes a revolution number as  $\tau$  has in this dissertation. Then, let's say that a trajectory may be identified in the orbit's manifold that intersects a desirable LEO parking orbit. That trajectory's  $\tilde{\tau}$ -value will vary from revolution to revolution about the quasiperiodic orbit. In fact, it may be the case that certain revolutions permit such a manifold to exist and other revolutions do not. Furthermore, those trajectories that do encounter a desirable LEO parking orbit may encounter that orbit at different inclination values, different velocities, etc. The Patched Three-Body model generally provides a good estimate of the parameters of a BLT, but the real parameters vary as a function of the reference Julian Date in the JPL Ephemeris model of the solar system.

In the Patched Three-Body model of the solar system, the Lunar staging orbit may be constructed independently of the parameter  $\theta$  (the Sun-Earth-Moon angle). In the JPL Ephemeris model, the orbit and the positions of each of the planets are all dependent on the reference Julian Date. As a consequence, the parameter sets used to uniquely describe a BLT in the Patched Three-Body and in the JPL Ephemeris models are slightly different. In this dissertation, the JPL Ephemeris parameter set is given as:  $[F, C, \text{JD}_0, \tilde{\tau}, p, \Delta t_m]$ , where the parameter  $\text{JD}_0$  has replaced the Patched Three-Body model's parameter  $\theta$  and the parameter  $\tilde{\tau}$  has replaced  $\tau$ . Each of the other four parameters is the same as the corresponding parameter defined in Section 5.6.1, although, several changes must be made in the procedures used to build the represented BLT.

First of all, the particular three-body orbit that is used as a final Lunar staging orbit is selected in the same way as in Section 5.6 – using parameters  $F$  and  $C$  – but once it has been selected it must be converted to the JPL Ephemeris model. The value of  $\text{JD}_0$  provides a reference Julian Date for this conversion. The value of  $\text{JD}_0$  also defines the relative positions of each of the planets and of the Sun. In this way, the Lunar staging orbit is no longer just a theoretical orbit in space that is independent of time, but it is a trajectory that is propagated through time. Thus, the parameter  $\tilde{\tau}$  now specifies a certain Julian Date as well as a point about the orbit. The result is that the trajectories in the manifolds that are propagated from each  $\tilde{\tau}$ -value will each begin at a different Julian Date. The BLTs produced in this way will be studied in Section 6.6 and a practical example will be presented in Chapter 7.

Although this method successfully produces BLTs in the JPL Ephemeris model, it is difficult to compare the results of this method directly with any Patched Three-Body BLT since both are built independently from the ground up. However, the next section provides a method that may be used to **directly** compare BLTs produced in each model.

### 5.7.2 Converting a BLT from the Patched Three-Body Model Directly into the JPL Ephemeris Model

A BLT may be constructed in the JPL Ephemeris model by first constructing it in the Patched Three-Body model and then converting it into the JPL Ephemeris model. It has been found that a multiple-shooting differential corrector may be used to perform this conversion, such as the corrector discussed in Section 3.5.2.

The first step in this process is to convert the Patched Three-Body BLT into the JPL Ephemeris model to be used as an initial guess into the differential corrector. It has been found that it is best to convert the Earth-Moon segments of the BLT into the JPL reference frame separately from the Sun-Earth/Moon segments, since the segments have different reference bodies. The conversions for both synodic reference frames may be found in Appendix D.6. Then the only difficult task is to find a reference Julian Date that minimizes the gaps between each of these segments. To visualize this task, Figure 5.22 shows plots of the states of the Patched Three-Body BLT given in this chapter converted into the JPL reference frame for four different reference Julian Dates. One can see that a gap exists where the BLT pierces the Earth-Moon 3BSOI, and the gap's size changes based on the location of the Moon in its orbit. Given the proper reference Julian Date, the Moon will be properly phased to minimize that gap. However, since the Moon's orbit about the Earth is inclined with respect to the ecliptic, it is unlikely that the gap will disappear entirely. Figure 5.23 shows a plot of the minimum gap-distance that exists during each month for 86 consecutive months. One can see that a smaller gap appears approximately every six months, most likely corresponding to points where the Moon's position in its inclined orbit matches the incoming trajectory closely. It has been found that any of these opportunities, even the worst ones, may be used as reference Julian Dates into the differential corrector to produce continuous trajectories in the JPL Ephemeris model, although, each reference Julian Date yields

a slightly different trajectory. In this section, we arbitrarily chose to use a reference Julian Date of 2454186.57 (March 27, 2007 at 1:42:51.636), corresponding to the Julian Date that minimized the gap at month “0” in Figure 5.23.

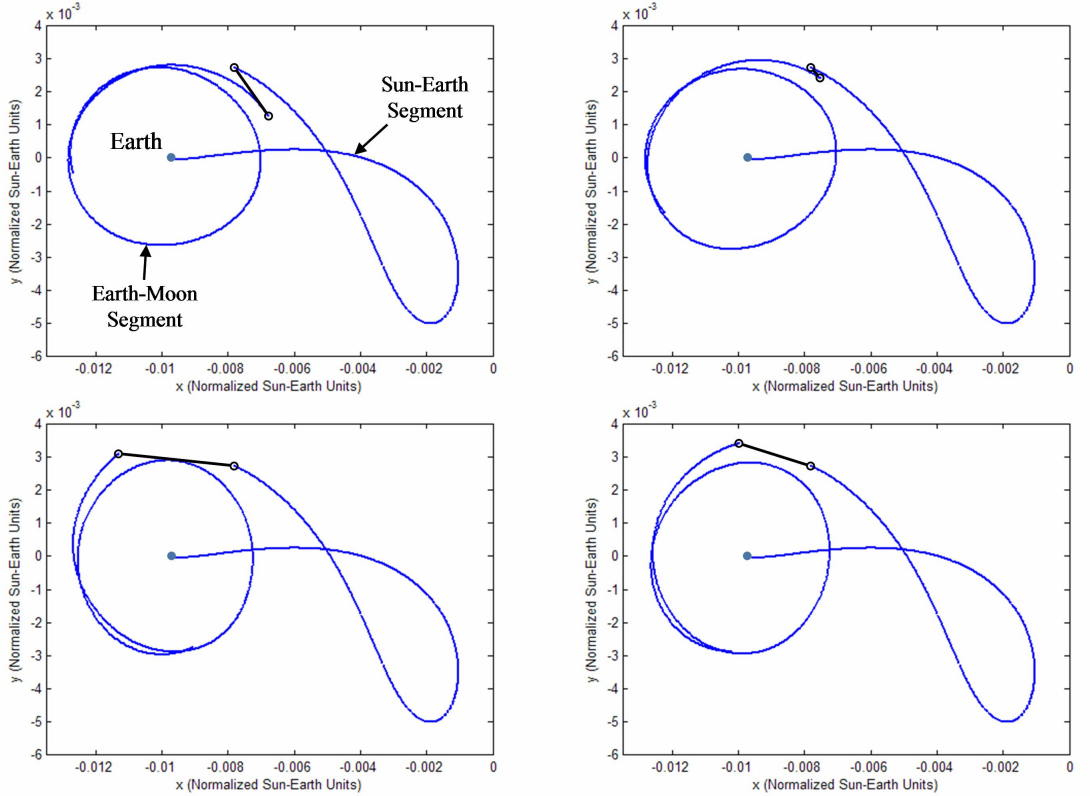


Figure 5.22: The Patched Three-Body BLT converted into the JPL reference frame using four different reference Julian Dates. The gaps shown in black correspond to the points where the trajectories cross the Earth-Moon 3BSOI. Beginning in the top-left plot, the reference Julian Date increases for each plot in a clockwise fashion.

Once a reference Julian Date has been chosen that minimizes the gap across each Earth-Moon 3BSOI crossing, then the states on that trajectory may be inserted into the differential corrector. The multiple-shooting differential corrector presented in Section 3.5.2 has been used in this dissertation to converge on a continuous trajectory. The differential corrector is very sensitive; several techniques have been used in this dissertation to assist the differential corrector to converge on a desirable trajectory. These

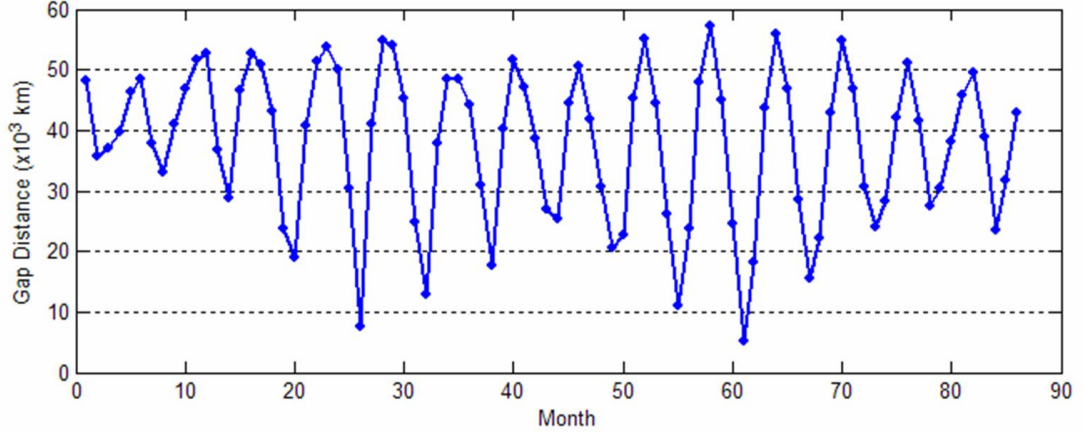


Figure 5.23: The minimum gap distance that exists in each month for 86 consecutive months when patching the Earth-Moon BLT segments with the Sun-Earth BLT segments.

techniques will be summarized in the following paragraphs.

Assuming that the final lunar three-body orbit is a Halo orbit, then there should be at least three patchpoints per lunar Halo orbit and preferably more. Additionally, the differential corrector converges more successfully when the time duration of each segment is approximately the same. One can either ensure that the physical time duration of each segment is initially the same or one can normalize the time duration of each segment at each step during the correction process. In this dissertation, we have opted to use the same physical time duration for each segment, including the long transit period in the Sun-Earth system. An initial duration of 1.75 days has been used for each segment, which has successfully converged on a BLT in the JPL Ephemeris model in many simulations. This time duration results in approximately eight patchpoints per lunar Halo orbit.

Without boundary constraints, the differential corrector typically alters the end-points of a trajectory to a substantial extent in order to converge quickly. However, a BLT must begin in a proper LEO parking orbit and should end in the desired lunar

three-body orbit. Hence, constraints should be placed on each end of the BLT. It has been found that placing a constraint on the distance between the first patchpoint and the Earth keeps the LEO radius constant, which keeps the injection  $\Delta V$  fairly constant. Additional constraints can also be used, such as a constraint on the LEO orbit's inclination, but each additional constraint makes the conversion process more difficult. It has also been found that the final lunar orbit can be constrained by stringing several lunar orbits together. Then the differential corrector can alter the end of the trajectory in order to assist its convergence, while allowing at least a few lunar orbits to retain their initial shape. Then after the differential corrector has converged, the end of the trajectory may be pruned off to keep the spacecraft on the desired lunar orbit. This procedure is described in more detail in Section 3.6.3 – it is also described in more detail during an example given below.

In addition, it has been found that the differential corrector converges more readily when the corrections are scaled down during the first few iterations. In this way, the large gap that exists at each Earth-Moon 3BSOI crossing is spread to several nearby patchpoints, and the conversion is more successful.

Finally, it has been found that the differential corrector converges more successfully if a constraint is placed on the maximum allowable change that the corrector may apply to the positions and times of each patchpoint during each iteration. This is very important for the patchpoints nearest to the Earth. The differential corrector tends to adjust those patchpoints out of the basin of convergence very quickly. By restraining the movement of those patchpoints, the trajectory remains near the basin of convergence longer and has a better chance of landing within that basin.

An example of the differential correction process is shown in Figures 5.24 and 5.25. Figure 5.24 shows several of the iterations that the differential corrector went through converting the Patched Three-Body BLT into the JPL Ephemeris model, viewed in the Sun-Earth synodic reference frame. Figure 5.25 shows the same iterations viewed

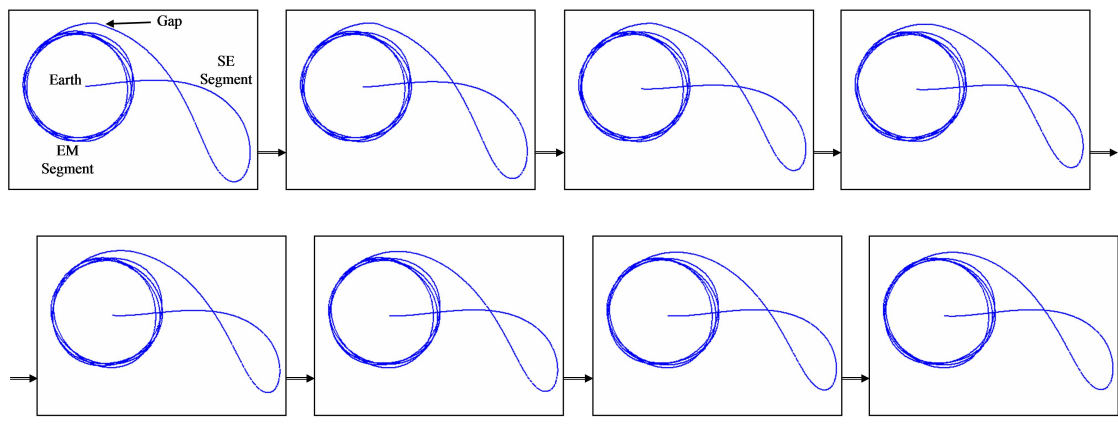


Figure 5.24: Several iterations in the process of differentially correcting the Patched Three-Body BLT into the JPL Ephemeris model. The initial trajectory is shown in the top-left; the final, continuous trajectory is shown in the bottom-right; each trajectory is shown in the Sun-Earth synodic reference frame.

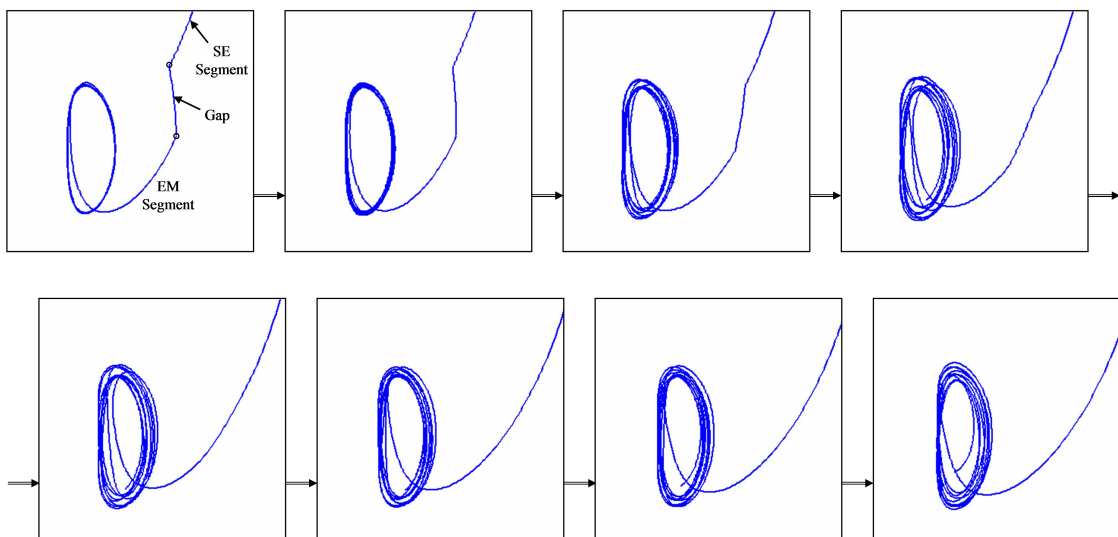


Figure 5.25: Several iterations in the process of differentially correcting the Patched Three-Body BLT into the JPL Ephemeris model. The initial trajectory is shown in the top-left; the final, continuous trajectory is shown in the bottom-right; each trajectory is shown in the Earth-Moon synodic reference frame.

in the Earth-Moon synodic reference frame in order to view the convergence of the trajectory near the lunar Halo orbit.

By observing the plots shown in Figure 5.24, one can see that the differential corrector retains the majority of the shape of the initial trajectory. The region of the trajectory near apogee, i.e., the region of the trajectory in the lower-right portion of each plot, gradually moves upward and outward in the plots. This indicates that the geometry of the transfer in the JPL Ephemeris is slightly different than the geometry of the transfer in the Patched Three-Body model, although the change appears to be very minor.

The gap that exists at the 3BSOI from the process of converting the Patched Three-Body BLT into the JPL Ephemeris model (discussed in Figures 5.22 and 5.23) is very apparent in the upper-left plot of Figure 5.25. The patchpoints in the JPL Ephemeris model bridge the gap to build a continuous trajectory, but require two substantial maneuvers to do so. As the differential corrector converges on a ballistic trajectory, one can see that the gap gradually smoothes out until the trajectory is fully continuous, as can be seen in the lower-right plot of the figure. To compensate for the gap, the differential corrector adjusts the trajectory on both sides of the gap. One can see this by noticing that the incoming trajectory moves rightward in the plots shown in Figure 5.25 – which is one significant reason why the apogee of the transfer shifts slightly as previously observed in Figure 5.24. One also notices that the differential corrector compensates for the 3BSOI gap by gradually adjusting the patchpoints in the final lunar three-body orbit. The initially periodic Halo orbit gradually shifts into a quasiperiodic “quasi-Halo” orbit.

Once the differential corrector has converged on a continuous trajectory, then the end of the trajectory is pruned off so that the trajectory ends on the lunar quasi-Halo orbit. After convergence, additional lunar Halo orbits may be added to the trajectory and differentially corrected to construct a trajectory that the spacecraft can follow to

remain on the lunar quasi-Halo orbit for an extended amount of time. Theoretically, it is possible to gradually add more quasi-Halo orbits, differentially correcting the trajectory at each addition, and keep the spacecraft in a quasi-Halo orbit indefinitely. In the example shown in Figures 5.24 and 5.25, eight Halo orbits were initially chained together; two were pruned off after the differential correction process converged. Then 30 more orbits were successfully added to the end of the trajectory to verify that a continuous trajectory may be constructed that will stay near the Halo orbit for an extended amount of time.

### 5.7.3 Discussion

The methods presented in Sections 5.7.1 and 5.7.2 both produce BLTs that exist in the JPL Ephemeris model. The method presented in Section 5.7.1 fully constructs a BLT in the JPL Ephemeris model using concepts derived from the Patched Three-Body model; hence, we will refer to that method as the “Construction” method. The method presented in Section 5.7.2 constructs a BLT in the JPL Ephemeris model by converting a BLT from the Patched Three-Body model into the ephemeris; hence, we will refer to that method as the “Conversion” method.

The Patched Three-Body model is a convenient model for constructing BLTs due to its symmetries and particular time-invariances. It may be desirable to do a great deal of mission analysis in the Patched Three-Body model before moving into the JPL Ephemeris model. If a mission designer has gone so far as to design a BLT in the Patched Three-Body model that meets all mission requirements, then the mission designer may wish to use the Conversion method to transfer that BLT into the JPL Ephemeris model. However, the Conversion method is typically more difficult and time-consuming than the Construction method. Thus, if a mission designer has not already chosen a particular BLT to use, it is generally faster to use the methodology derived from the Patched Three-Body model to build a BLT from the ground up in the

JPL Ephemeris.

## 5.8 Comparison Between Different Models

This section compares the performance of the example BLT that has been produced in the Patched Three-Body model in Section 5.4.3 with the BLT that has been differentially corrected into the JPL Ephemeris model of the solar system in Section 5.7.2. For simplicity, these trajectories will be referred to as the Patched Three-Body BLT and the JPL Ephemeris BLT. The Patched Three-Body BLT will then be compared with other JPL Ephemeris BLTs produced in the same manner, but using different reference Julian Dates. Finally, this section will summarize the comparisons and provide some conclusions about the validity of the Patched Three-Body model.

### 5.8.1 Comparing the Patched Three-Body BLT with the Nominal JPL Ephemeris BLT

The process of differentially correcting a trajectory into the JPL Ephemeris model changes some of the characteristics of the trajectory. Each of the two BLTs compared here, namely the Patched Three-Body BLT and the nominal JPL Ephemeris BLT, is a member of a full family of BLTs, where the characteristics of the trajectories vary in a continuous manner from one end of the family to the other. As such, it is very likely that the differential correction process conducted in Section 5.7.2 has converged on a BLT in the JPL Ephemeris model that more closely resembles a neighbor BLT in the family of similar Patched Three-Body BLTs. Nevertheless, these two BLTs are still very similar, and the comparison of these BLTs reveals some very interesting observations.

Figure 5.26 shows the Patched Three-Body BLT and the JPL Ephemeris BLT plotted on the same axes. The trajectories are shown from above in the Sun-Earth synodic reference frame. One can see that the general characteristics of the trajectories are the same. One slight difference that becomes noticeable in later analyses is that the two

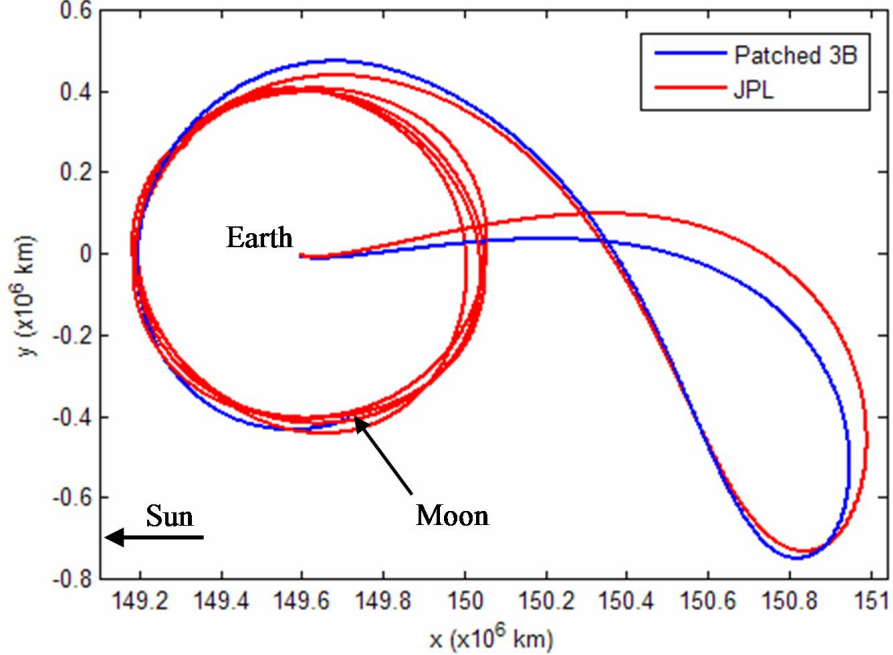


Figure 5.26: A plot comparing the general characteristics of the Patched Three-Body BLT (shown in blue) and the JPL Ephemeris BLT (shown in red). The trajectories are viewed from above in the Sun-Earth synodic reference frame.

trajectories depart the Earth at different angles. Hence, each trajectory passes by the Moon differently. In addition, the Moon's orbit is not circular in the JPL Ephemeris reference frame, which helps to explain the variations in the JPL Ephemeris trajectory as it orbits the final Earth-Moon three-body orbit.

Figure 5.27 shows a three-dimensional view of the LEO-departures of both BLTs in order to compare the different departure characteristics. One can see that the trajectories depart from different longitudes above the Earth and depart on trajectories that have different right ascension and declination values of the departure asymptotes. Table 5.2 compares these parameters as well as other interesting parameters that describe the LEO parking orbits of each trajectory.

By studying Table 5.2, one can see that both BLTs depart the Earth from 185-km circular LEO parking orbits, but most other parameters are slightly different. The eclip-

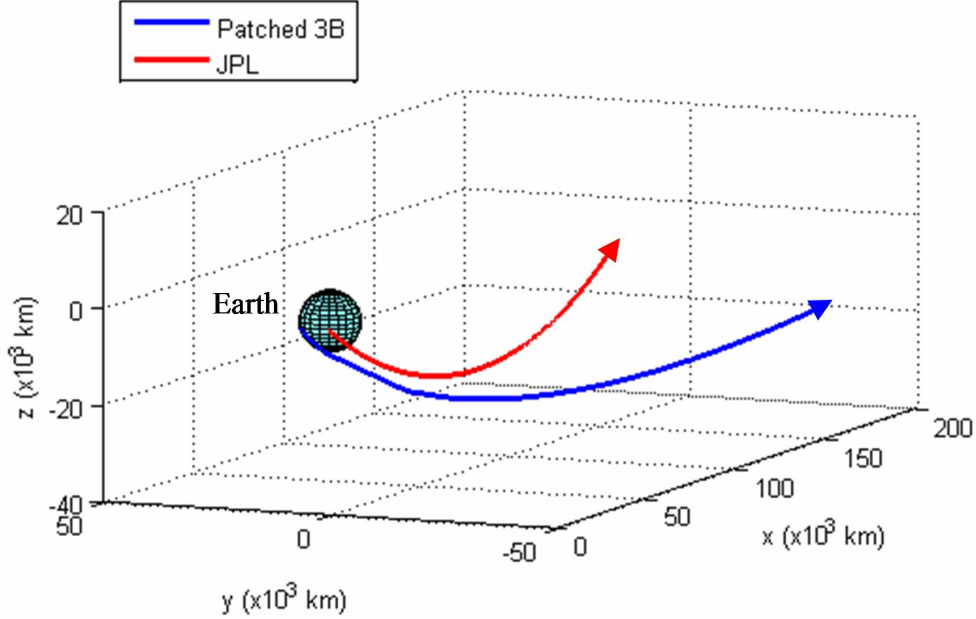


Figure 5.27: A comparison of the departure trajectories of the Patched Three-Body BLT and JPL Ephemeris BLT.

tic inclination of each parking orbit only differs by about  $3.1^\circ$ , but the right-ascension of the ascending node,  $\Omega$ , differs by approximately  $44.3^\circ$ . The difference in  $\Omega$  may be eliminated by adding it as a constraint to the differential correction process, although, that may reduce the chances of the differential corrector converging on a successful BLT in the JPL Ephemeris model. The right-ascension and declination values of the departure asymptote with respect to the ecliptic are also slightly different in each model. To be consistent between models, these values are computed at the point where the trajectories reach a distance of 200,000 km from the Earth. These parameters have also not been included as constraints in the differential correction process. Because the departure trajectory is somewhat different in each model, the trajectories each pass by the Moon differently. Consequently, the two BLTs require slightly different  $\Delta V$  magnitudes at the injection point from their corresponding LEO parking orbits. The JPL Ephemeris BLT requires an injection maneuver approximately 67.5 m/s smaller than the injection

Table 5.2: A comparison of certain parameters of the LEO parking orbit and departure conditions for the BLTs produced in the Patched Three-Body and JPL Ephemeris models. <sup>1</sup>The departure asymptote is defined here to be the state of the spacecraft approximately 200,000 km from the Earth.

<b>The LEO Parking Orbit</b>		
Parameter	Patched Three-Body BLT	JPL Ephemeris BLT
Altitude	185 km	185 km
Ecliptic Inclination	51.249°	54.387°
R.A. of the Ascending Node	7.536°	51.817°
Velocity	7.793 km/s	7.793 km/s
<b>Parameters of the Departure Asymptote with respect to the Ecliptic<sup>1</sup></b>		
Parameter	Patched Three-Body BLT	JPL Ephemeris BLT
Right-Ascension	8.019°	13.119°
Declination	1.654°	4.154°
<b>Additional Orbital Elements of the BLT Departure with respect to the Earth</b>		
Parameter	Patched Three-Body BLT	JPL Ephemeris BLT
Specific Energy	-0.366053 J/kg	-0.349478 J/kg
Eccentricity	0.987947	0.988494
Semi-Major Axis	544,503.0 km	570,328.1 km
<b>Injection ΔV</b>		
Parameter	Patched Three-Body BLT	JPL Ephemeris BLT
Injection ΔV	3.263928 km/s	3.196411 km/s

maneuver required by the Patched Three-Body BLT. It is hypothesized that the reduced injection  $\Delta V$  may be attributed to the Moon's non-zero eccentricity, as well as to a closer lunar passage as the spacecraft departs the Earth. The closer passage is confirmed by studying Figure 5.28, which shows a plot of the distance between the spacecraft and the Earth and Moon during each trajectory. One can see that the spacecraft does indeed make a closer pass by the Moon in the JPL Ephemeris trajectory than it does in the Patched Three-Body trajectory as it departs the Earth. Figure 5.28 also confirms that both trajectories require approximately the same amount of time to transfer from the Earth to the final Earth-Moon three-body orbit. As mentioned in Section 5.7.2, the final three-body orbit in the JPL Ephemeris trajectory is a quasi-Halo orbit that has very

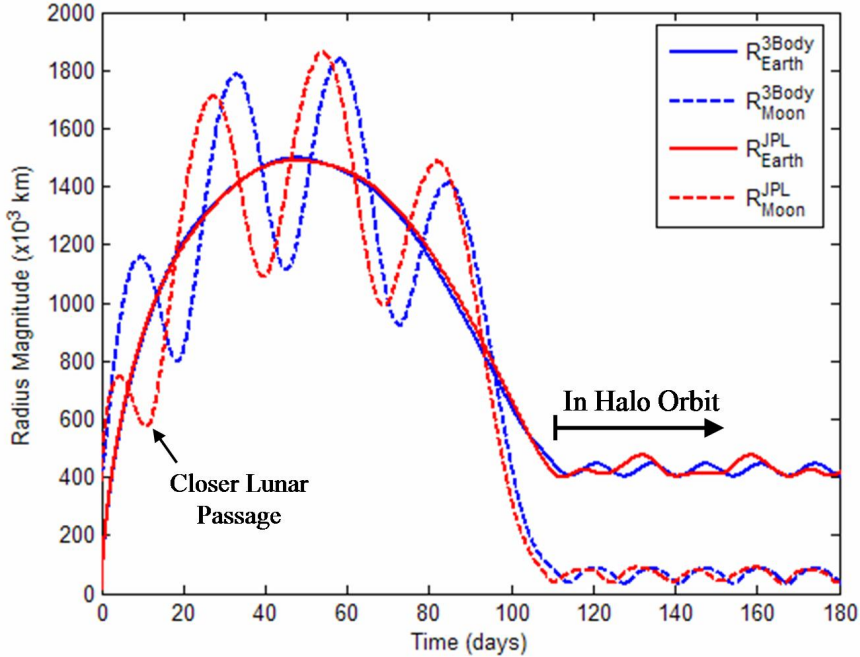


Figure 5.28: A comparison of the distances between the spacecraft and the Earth and Moon during each of the two compared trajectories. One can see that the spacecraft passes nearer to the Moon in the JPL Ephemeris BLT than it does in the Patched Three-Body BLT as the spacecraft departs the Earth.

similar characteristics as the Halo orbit at the end of the Patched Three-Body trajectory.

Table 5.2 shows that the initial two-body specific energy of a spacecraft with respect to the Earth on the BLT in the JPL Ephemeris model is higher than the corresponding specific energy of a spacecraft in the Patched Three-Body model. Figure 5.29 shows a comparison of the specific energy of a spacecraft with respect to the Earth as a spacecraft traverses each BLT. One notices that the specific energy of a spacecraft in the JPL Ephemeris model varies slightly from the specific energy of a spacecraft in the Patched Three-Body model throughout each BLT, but the Patched Three-Body BLT is a good model of the more realistic JPL Ephemeris BLT. The larger variations toward the end of each trajectory are most likely due to the non-circular orbits of the Earth and Moon in the JPL Ephemeris model.

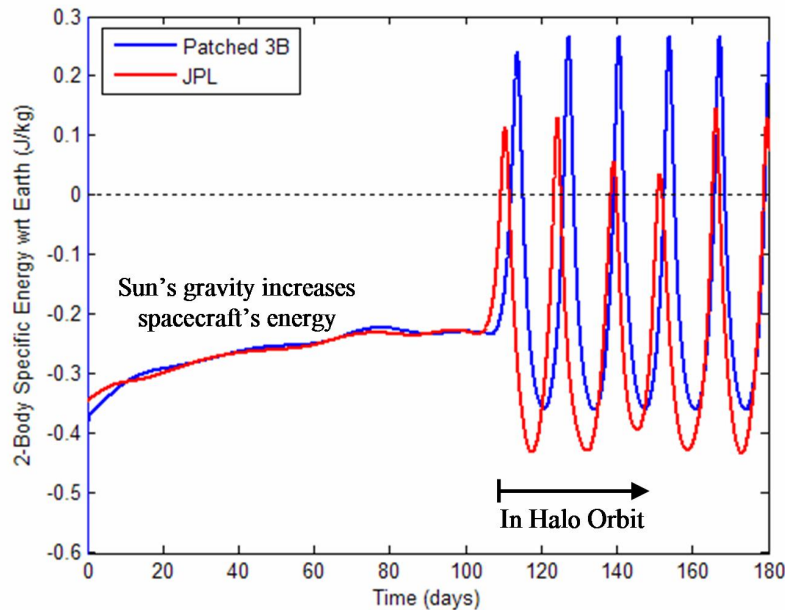


Figure 5.29: A comparison of the two-body specific energy of a spacecraft with respect to the Earth as a spacecraft traverses both the Patched Three-Body BLT and the JPL Ephemeris BLT.

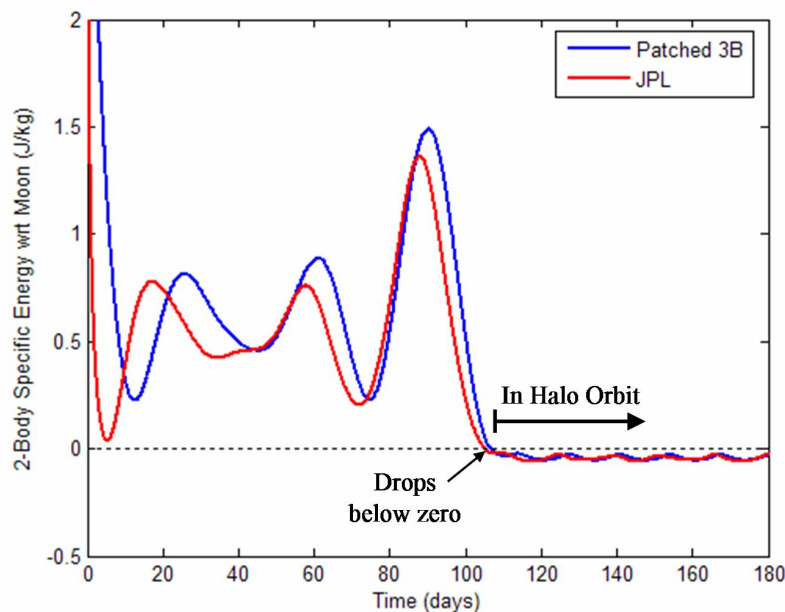


Figure 5.30: A comparison of the two-body specific energy of a spacecraft with respect to the Moon as a spacecraft traverses both the Patched Three-Body BLT and the JPL Ephemeris BLT.

Figure 5.30 shows a similar comparison of the specific energy of a spacecraft with respect to the Moon as a spacecraft traverses each BLT. In this figure, one notices the difference between the differentially-corrected BLT in the JPL Ephemeris model compared with the Patched Three-Body BLT. One can see the effect of the closer lunar passage of the BLT in the JPL Ephemeris model during the early part of the trajectory. It is very interesting to observe that the specific energy of the BLT with respect to the Moon in both models falls below zero as the trajectories arrive at the Earth-Moon three-body orbit. This is additional evidence that the Patched Three-Body model is a good approximation of the JPL Ephemeris model, even though the BLTs have slightly different characteristics in this comparison.

Figures 5.31 and 5.32 show comparisons of the differences between the Jacobi constants of the two BLTs in the Sun-Earth and Earth-Moon synodic frames, respectively. In the Patched Three-Body model, the Jacobi constant only varies in one of these synodic frames, depending on which three-body system the trajectory is propagated in. The Jacobi constant should **not** be constant in any synodic frame when the trajectory is produced in the JPL Ephemeris model, since more than two massive bodies are included in the model and each body moves in a non-circular orbit. It is very interesting to notice the level of variability of the Jacobi constant in each synodic frame for the JPL Ephemeris BLT. The inset shown in Figure 5.31 displays the early portion of each trajectory dramatically zoomed in; one notices that the Sun-Earth Jacobi constant in the JPL Ephemeris model varies very little. Furthermore, one notices that the Patched Three-Body BLT captures the sudden change in the Sun-Earth Jacobi constant as the spacecraft crosses into the Earth-Moon three-body vicinity. In Figure 5.32, one notices that the Earth-Moon Jacobi constant is very similar in both models. The Patched Three-Body model also captures the point where the Earth-Moon Jacobi constant becomes fairly constant in the JPL Ephemeris model. These two figures provide very strong evidence that the Patched Three-Body model is a good approximation of the

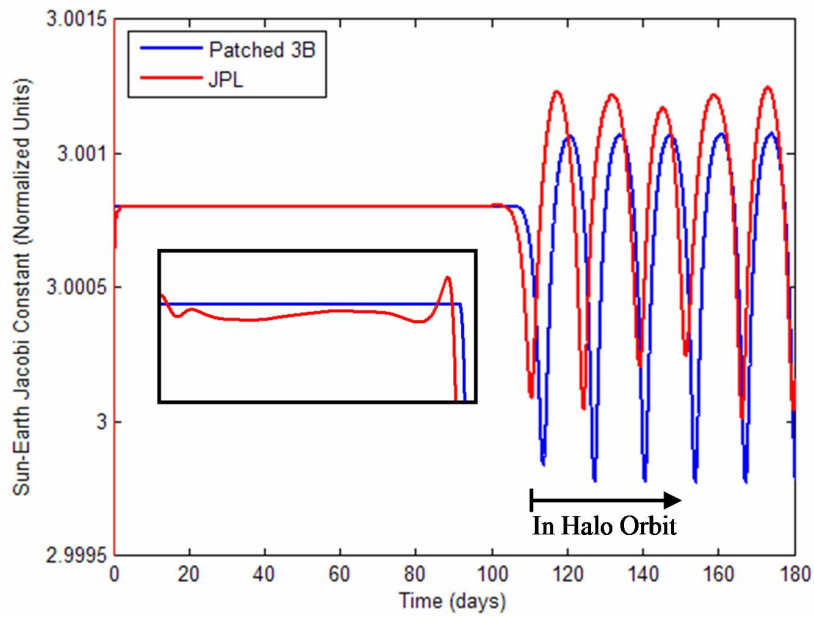


Figure 5.31: A comparison of a spacecraft's Jacobi constant with respect to the Sun-Earth three-body system as a spacecraft traverses both the Patched Three-Body BLT and the JPL Ephemeris BLT. The inset shows a zoomed-in view of the first 112 days of both transfers. The  $y$ -axis of the inset spans a Jacobi constant range of only  $1.2 \times 10^{-5}$ , demonstrating how flat the curve is even in the JPL Ephemeris model.

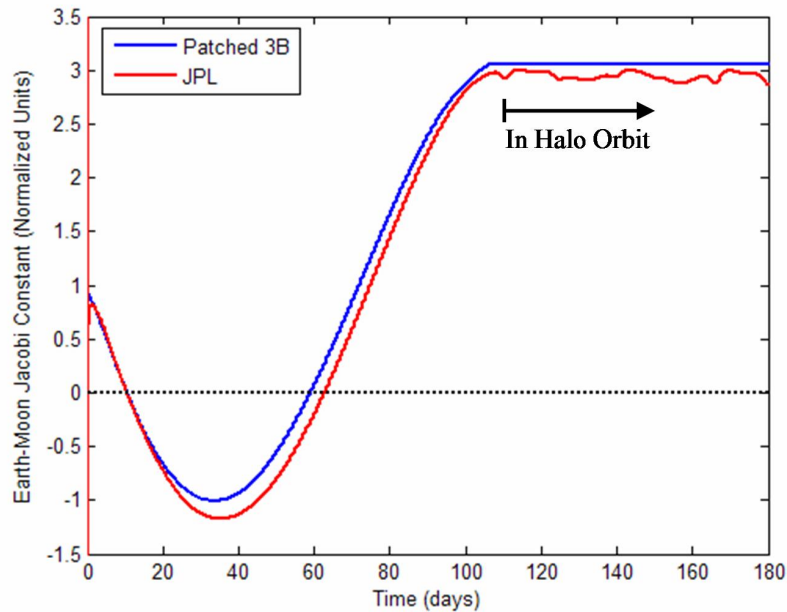


Figure 5.32: A comparison of a spacecraft's Jacobi constant with respect to the Earth-Moon three-body system as a spacecraft traverses both the Patched Three-Body BLT and the JPL Ephemeris BLT.

JPL Ephemeris model. These two figures also provide strong evidence that the Earth-Moon Three-Body Sphere of Influence defined in Section 2.4.2 has been constructed very appropriately to model ballistic lunar transfers in the Patched Three-Body model.

### 5.8.2 Comparing the Patched Three-Body BLT with Several JPL Ephemeris BLTs

The nominal JPL Ephemeris BLT presented in Section 5.8.1 has been constructed by converting the Patched Three-Body BLT into the JPL Ephemeris model on a particular nominal reference Julian Date. However, this conversion process is dependent on the reference Julian Date used. In order to validate the comparison of the two BLTs presented here, further comparisons have been performed between the Patched Three-Body BLT and numerous JPL Ephemeris BLTs where each JPL Ephemeris BLT has been produced using a different reference Julian Date.

Figure 5.23 on page 202 shows a plot of the minimum gap distance that is obtainable when converting the Patched Three-Body BLT into the JPL Ephemeris model using the best reference Julian Dates for each of 86 consecutive months. The process given in Section 5.7.2 has been repeated for many of these months; the results for months 8 – 13 are presented here. This timeframe spans approximately a full oscillation of the minimum gap distance shown in Figure 5.23. In addition, the nominal trajectory (month 0) should match closely with the resulting BLT of month 12, since the Earth will have returned to approximately the same point in its orbit about the Sun. However, since the Moon’s orbit is not in resonance with the Earth’s orbit, the best opportunity to construct this same BLT in the JPL Ephemeris model will not occur on the same day of the year for each year.

Figure 5.33 shows plots of the converged BLTs produced in the JPL Ephemeris model using the best reference Julian Date from each of the example months. The trajectories are very similar, but one can see slight differences that arise from the varying

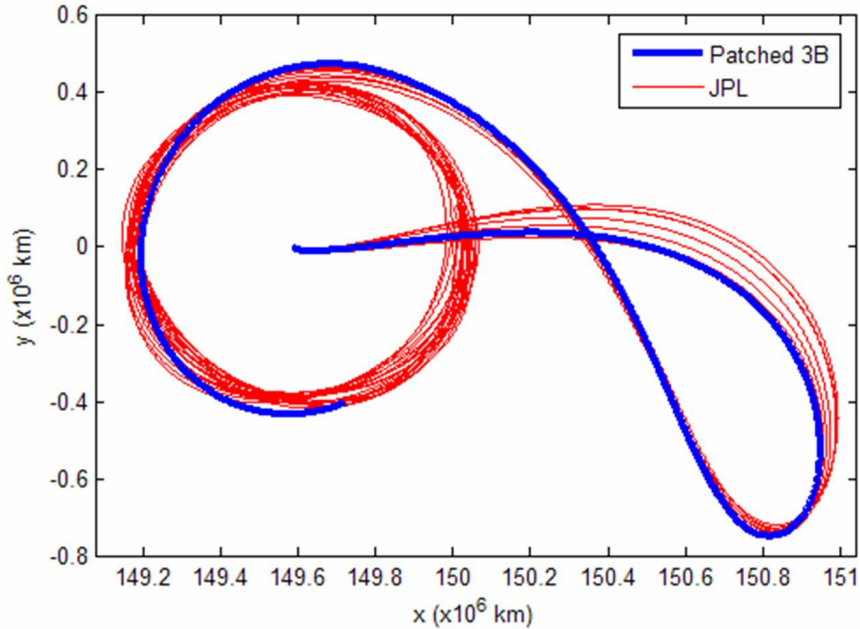


Figure 5.33: The trajectories of several BLTs produced in the JPL Ephemeris model using the Conversion method for several different reference Julian Dates.

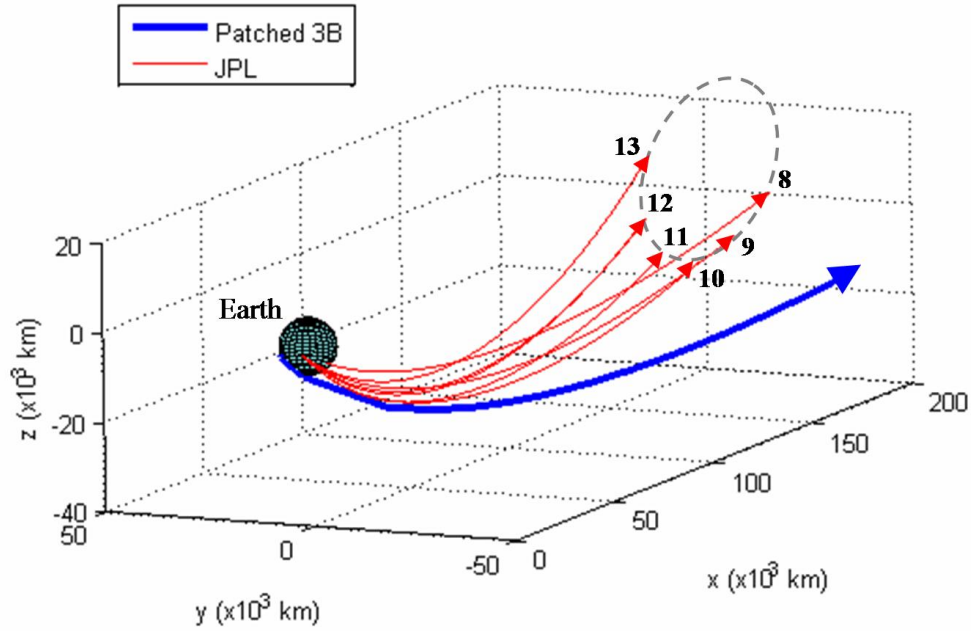


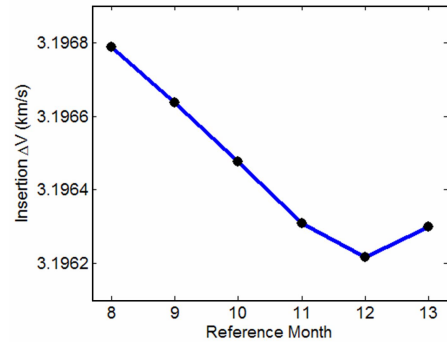
Figure 5.34: The LEO departure segments of the BLTs shown in Figure 5.33. The numbers shown next to each trajectory indicate the reference month used for the conversion process, relative to the nominal date of March 27, 2007.

position of Earth in its orbit about the Sun. Figure 5.34 shows plots of each of these trajectories as they depart the Earth. One can see that the departure asymptote varies in a periodic fashion as the reference Julian Date advances each month. It has been found that the departure asymptote sweeps out a cycle once every 12 months, presumably due to the motion of the Earth in its orbit about the Sun. The trajectory corresponding to month 12 is nearly identical to the nominal JPL Ephemeris BLT shown in Figure 5.27 on page 209.

The plots of the specific energy of each BLT shown in Figure 5.33 with respect to both the Earth and the Moon are nearly identical, as are the plots of the Jacobi constants of each BLT with respect to the Sun-Earth and Earth-Moon synodic reference frames. In addition, the injection  $\Delta V$  magnitudes are also nearly identical. For comparison, the injection  $\Delta V$  magnitudes are shown in Table 5.3. It has been concluded that the differential correction process that has been used to convert the Patched Three-Body BLT into the JPL Ephemeris model results in very similar BLTs no matter which reference Julian Date is used. However, the equatorial inclination of the LEO parking orbit varies per month, depending on the relative orientation of the Earth's pole vector and the departure asymptote of the BLT.

Table 5.3: The injection  $\Delta V$  magnitudes of the JPL Ephemeris BLTs converted from the nominal Patched Three-Body BLT for the optimal reference Julian Date in several consecutive months.

Reference Month	Injection $\Delta V$
0	3.196411 km/s
8	3.196788 km/s
9	3.196638 km/s
10	3.196477 km/s
11	3.196310 km/s
12	3.196217 km/s
13	3.196299 km/s



### 5.8.3 Summary of Comparison

This section has compared the performance of a single Patched Three-Body BLT with several corresponding BLTs differentially corrected into the JPL Ephemeris model. The results indicate that the Patched Three-Body model is a very accurate tool to model realistic BLTs in a simplified model.

The comparison has shown that the trajectories modeled in the Patched Three-Body model closely approximate more realistic trajectories constructed in the JPL Ephemeris model of the solar system. The conversion process used in this section has been shown to change some of the features of the trajectories slightly, such as the BLT's de-parcel asymptote, but the overall characteristics of the BLT remain nearly unchanged. The required Trans-Lunar Injection  $\Delta V$  of the BLTs produced in the JPL Ephemeris model is slightly lower than the required injection  $\Delta V$  of the BLT produced in the Patched Three-Body model: approximately 3.196 km/s compared to approximately 3.264 km/s, respectively.

The comparisons made here have demonstrated that the Patched Three-Body model is well-suited to approximate realistic BLTs in the solar system. The best evidence of the validity of the Patched Three-Body model is seen by observing how well the Patched Three-Body model approximates the Jacobi constant in both the Earth-Moon and the Sun-Earth/Moon synodic reference frames.

## 5.9 Comparison with Conventional Transfers

The example BLT produced in this chapter requires a total  $\Delta V$  of approximately 3.264 km/s to transfer a spacecraft from a 185-km LEO parking orbit to a Halo orbit about the Moon's  $L_2$  point in the Patched Three-Body model. In the JPL Ephemeris model, the cost drops to only 3.196 km/s for the same transfer. The low-energy BLT's cost, in either case, is much lower than any conventional transfer presented in Chap-

ter 4. Conventional transfers between a 185-km LEO parking orbit and this same lunar Halo orbit require a total  $\Delta V$  between approximately 3.6 km/s (for a potentially very complicated transfer) and approximately 3.98 km/s (for a direct 5-day transfer). Furthermore, the entire  $\Delta V$  budget of the ballistic lunar transfer presented here – except for trajectory correction maneuvers and other operational maneuvers – is executed in a single Trans-Lunar Injection maneuver, which enables a simplified spacecraft system compared to a conventional transfer. Additional spacecraft mission design considerations will be explored in Chapter 7.

### 5.10 Conclusions

This chapter has studied how to analyze, model, and construct low-energy ballistic lunar transfers using dynamical systems techniques. We will review each of the conclusions that may be drawn from the material presented in this chapter.

Section 5.2 discussed different strategies that have been used to produce low-energy transfers to the Moon. To the author’s knowledge, no work has been presented in the literature discussing how to build a low-energy ballistic lunar transfer to an Earth-Moon three-body orbit. The dynamical systems method presented in this chapter is a new technique to build low-energy ballistic transfers between the Earth and the Moon.

Section 5.3 discussed the elements of a BLT, qualitatively describing a BLT from different perspectives. The discussions in that section presented information about how dynamical systems techniques may be used to compartmentalize the BLT. That is, mission designers may construct the spacecraft’s route onto the lunar three-body orbit independently from the spacecraft’s departure from that orbit. Once on the lunar three-body orbit, the spacecraft may remain there or it may transfer to another three-body orbit, to a low lunar orbit, to the surface of the Moon, or even back to the Earth. All of these options are available independently of how the spacecraft arrives onto the

lunar three-body orbit. Section 5.4 discussed how to model a BLT using dynamical systems theory. Once again, this discussion demonstrated the compartmentalization of a BLT design. It was shown that many types of three-body orbits may be used as staging orbits throughout a BLT.

Section 5.5 provided an analysis of an example BLT from an energy perspective. It was shown that the Sun's gravity effectively raises a spacecraft's two-body specific energy with respect to the Earth during the early portion of the BLT. Similarly, it was shown that a spacecraft's two-body specific energy with respect to the Moon drops below zero as the spacecraft approaches the lunar Halo orbit. It was also shown that the Moon effectively changes a spacecraft's Sun-Earth Jacobi constant and that the Sun effectively changes a spacecraft's Earth-Moon Jacobi constant. A spacecraft may change its Jacobi constant in one system by transferring to the other system and back again. The boundary of these two systems has been described here as the Earth-Moon three-body sphere of influence. The corresponding Patched Three-Body model approximates the more-realistic energy values computed in the JPL Ephemeris model very well. This section gives validation to the assumptions that went into designing the Patched Three-Body model and the Earth-Moon 3BSOI.

Sections 5.6 and 5.7 discussed how to construct BLTs in the Patched Three-Body model and in the JPL Ephemeris model, respectively. It was shown that the Patched Three-Body model allows mission designers to use three-body modeling techniques in the Sun-Earth-Moon-Spacecraft four-body system. Furthermore, dynamical systems techniques provide a means for mission designers to parameterize BLTs. The parameter set varies slightly between the JPL Ephemeris model and the Patched Three-Body model of the solar system. Two techniques have been demonstrated here to construct a BLT in the JPL Ephemeris model. The first technique is to build the entire trajectory from the ground up in the JPL Ephemeris model, mimicking the process of building a BLT in the Patched Three-Body model. The second technique is to first build a BLT in

the Patched Three-Body model and then convert the trajectory into the JPL Ephemeris model. Section 5.8 compared the performance of an example BLT constructed in different models of the solar system. It was found that the same Patched Three-Body BLT may be constructed in the JPL Ephemeris model using different reference Julian Dates. Each JPL Ephemeris BLT is very similar, only differing by slight deviations in the departure asymptote and the equatorial inclination of the LEO parking orbit used.

Finally, Section 5.9 compared the example BLT with conventional methods to transfer to the Moon. A low-energy BLT may be used to transfer material to the Moon using much less  $\Delta V$  than if that material were transferred to the Moon using conventional methods. The main trade-off is transfer time. The example BLT produced in this chapter required a transfer duration of about 100 days and a total  $\Delta V$  of approximately 3.196 km/s compared with a conventional 5-day transfer that requires approximately 3.98 km/s to the same three-body orbit. The BLT requires about 19.7% less  $\Delta V$  than the conventional transfer. The result is that the same launch vehicle can send much more payload to a lunar three-body orbit using a BLT rather than a conventional transfer. Further analysis of the benefits of BLTs in practical lunar missions is provided in Chapter 7.

## Chapter 6

### Families of Ballistic Lunar Transfers

#### 6.1 Introduction

In Chapter 5, the dynamical systems method of analysis was applied to the construction of low-energy ballistic lunar transfers (BLTs). An example BLT was used for the modeling, analysis, and validation demonstrations presented in the chapter. The example BLT was first constructed in the Patched Three-Body model and was later converted into the JPL Ephemeris model (§5.7.2); however, no real discussion was given in Chapter 5 about how to identify the initial parameters in the Patched Three-Body model that may be used to build that BLT in the first place. This chapter demonstrates how to identify those parameters.

The purpose of this chapter is to examine a method that may be used to identify families of BLTs using dynamical systems theory. This method yields parametric maps that one may use to identify combinations of parameters that yield desirable BLTs. This chapter explores those maps, surveying many thousands of BLTs for their applications to practical lunar missions.

The BLT State Space Maps (or **BLT Maps** for short) presented in this chapter are analogous to porkchop plots that are used in conventional interplanetary mission design. Where conic sections are the fundamental building block of porkchop plots, BLTs are the fundamental building block of these State Space Maps. After constructing a BLT Map, one may use it to identify useful transfers from desirable LEO parking

orbits to desirable Earth-Moon three-body orbits.

The analysis begins in Section 6.2 by discussing what a BLT State Space Map is, how to build one, and how to extract families of BLTs from such a map. Then Section 6.3 provides an initial examination of two example BLT Maps, comparing families of **Exterior** BLTs with families of **Interior** BLTs. These BLTs are produced in the Patched Three-Body model, targeting a particular Halo orbit about the Earth-Moon L<sub>2</sub> point. Section 6.4 explores the variations in a BLT Map as changes are made to both the maximum propagation duration and the Jacobi constant of the underlying BLTs. Section 6.5 explores different BLT Maps for different Earth-Moon three-body orbit destinations, i.e., Halo orbits about the Earth-Moon L<sub>1</sub> point and distant prograde orbits about the Moon.

Every BLT presented between Sections 6.2 and 6.5 is produced in the Patched Three-Body model. Section 6.6 validates these BLT Maps by comparing them with BLT Maps produced in the JPL Ephemeris model using the same dynamical systems techniques. It is found that the dynamical systems techniques work well to identify families of BLTs that exist in the JPL Ephemeris model. Finally, Section 6.7 summarizes the results and provide some final conclusions that may be drawn from this work.

## 6.2 BLT State Space Maps

This section describes what a BLT Map is, how to build one, and how to extract families of BLTs from one. This section begins with a review about how BLTs may be parameterized (§6.2.1); an experiment is then conducted, which demonstrates that BLTs do indeed exist in families (§6.2.2). Next, the results of the experiment are extended to demonstrate how to build a BLT Map using knowledge of the parameterization of BLTs (§6.2.3). Finally, this section explores a wide variety of BLT families that are discovered (§6.2.4).

### 6.2.1 Parameterization

The dynamical systems method provides a natural set of parameters that may be used to build a BLT in the Patched Three-Body model:  $[F, C, \theta, \tau, p, \Delta t_m]$  (see Section 5.6.1 for more information). A similar set exists for the JPL Ephemeris model:  $[F, C, \text{JD}_0, \tilde{\tau}, p, \Delta t_m]$  (see Section 5.7.1). The discussions here remain focused on the Patched Three-Body model until Section 6.6, at which point the discussions switch to the JPL Ephemeris model for validation purposes.

The example Patched Three-Body BLT presented in Chapter 5 has the following set of parameters:  $F$  describes the family of Southern Halo orbits about the Earth-Moon L<sub>2</sub> point;  $C = 3.05$ ;  $\theta = 293.75^\circ$ ;  $\tau = 0.74$ ;  $p$  = “Exterior”; and  $\Delta t_m = 123.9$  days. These parameters yield a trajectory that begins in a circular LEO parking orbit with an altitude of 185 km and an ecliptic inclination of  $51.249^\circ$ . If one were to change one of the BLT’s parameters slightly, say, the value of  $\tau$ , the resulting BLT would require a different LEO parking orbit. However, by simultaneously varying two or more of the BLT’s parameters, e.g., both  $\tau$  and  $\theta$ , one can construct a different BLT that also uses a 185-km LEO parking orbit.

A BLT Map is produced by setting the parameters  $F, C, p$ , and  $\Delta t_m$  constant and allowing  $\theta$  and  $\tau$  to vary throughout their corresponding ranges. By keeping  $F$  and  $C$  constant, the only BLTs being constructed are those that arrive at the same Earth-Moon three-body orbit destination. Since  $p$  is held constant, a BLT Map only shows information about either exterior or interior transfers. Hence, two BLT Maps are typically necessary to study any type of ballistic transfer to a given three-body orbit. Finally, with the value of  $\Delta t_m$  held constant, all of the BLTs constructed require no more than a specified transfer duration. That is, the specified  $\Delta t_m$  value is a limit to the transfer duration: a particular BLT may indeed encounter the optimal perigee prior to the  $\Delta t_m$  value and thus have a shorter transfer duration. The transfer duration is the amount

of time needed to depart the LEO parking orbit and approach within 100 km of the targeted Halo orbit along its stable invariant manifold.

Using this method, a BLT Map is useful for identifying transfers between LEO and a particular Earth-Moon three-body orbit. As previously mentioned, it is useful to produce two BLT Maps for each case: both an exterior BLT Map ( $p$  set to “Exterior”) and an interior BLT Map ( $p$  set to “Interior”). It is also useful to set  $\Delta t_m$  to be the maximum mission duration that one would permit for a practical spacecraft mission. Studies of how BLT Maps vary as one changes the values of  $C$  and  $\Delta t_m$  are presented in Section 6.4. A study of how BLT Maps vary as one considers different Earth-Moon orbits is presented in Section 6.5.

### 6.2.2 Slight Perturbations

Let us consider the example BLT studied in Chapter 5 and consider what happens if its parameters are slightly changed. For this discussion, the parameters  $F$ ,  $C$ , and  $p$  are kept unchanged from those used to build the example BLT so that only topologically-similar BLTs are considered. We construct a grid of  $\theta$  and  $\tau$  values and build trajectories at each point in the grid. For this experiment, the parameter  $\theta$  has been set to vary by up to  $1^\circ$  about its nominal value:  $\theta \in 293.75^\circ \pm 1^\circ$ . Similarly, the parameter  $\tau$  has been set to vary by up to 0.01 about its nominal value:  $\tau \in 0.74 \pm 0.01$ . Finally, in order to consider BLTs that may require slightly longer transfer durations, each trajectory in the grid is integrated for  $\Delta t_m = 140$  days to ensure that a similar perigee point is reached. These parameters are summarized in Table 6.1. The closest perigee point is then identified for each integrated trajectory using the procedures outlined in Section 5.6.2. Several performance parameters are evaluated at the perigee point, including the altitude of closest approach with the Earth (representing the altitude of the LEO parking that may be used to inject onto the corresponding BLT), the ecliptic inclination of the perigee point, and the transfer duration.

Table 6.1: The parameters used to produce the results shown in Figures 6.1 and 6.2.

Parameter	Value
$F$	The family of Earth-Moon L <sub>2</sub> Halo Orbits
$C$	3.05
$\theta$	$292.75^\circ \leq \theta \leq 294.75^\circ$
$\tau$	$0.73 \leq \tau \leq 0.75$
$p$	“Exterior”
$\Delta t_m$	140 days

Figure 6.1 shows two plots of the main result of this experiment. The plot on the left is a contour map of the perigee altitude that each trajectory encounters as a function of  $\theta$  and  $\tau$ , including a contour of 185 km to match the nominal BLT given above. The plot on the right shows the same perigee altitude function, but plotted as a surface for a different perspective. This demonstrates that one can perturb  $\theta$  and  $\tau$  in a systematic way to arrive at a new BLT that encounters the Earth at the same altitude. The new BLT most likely encounters its perigee point at a different ecliptic inclination and require a different transfer duration. These parameters are explored below.

Another interpretation of the plots shown in Figure 6.1 is that if the LEO park-

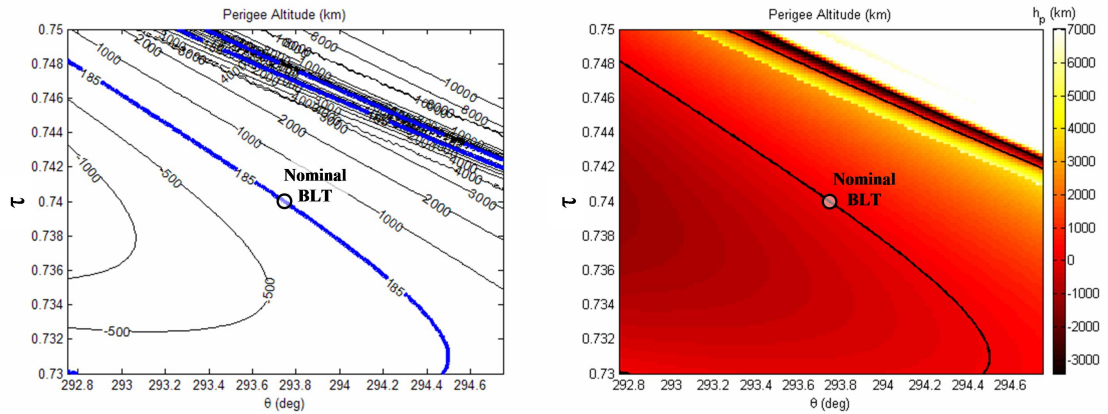


Figure 6.1: Two plots showing the BLT State Space near the nominal BLT. Left: A contour map of the perigee altitude that each trajectory encounters as a function of  $\theta$  and  $\tau$ ; Right: A surface map colored as a function of perigee altitude. The 185-km contour is highlighted in each plot.

ing orbit needs to be lowered slightly, then the trajectory should implement a slightly smaller  $\tau$ -value or a slightly smaller  $\theta$ -value to ballistically transfer to the same Earth-Moon three-body orbit.

One also notices in the plots shown in Figure 6.1 that other combinations of  $\theta$  and  $\tau$  reveal other families of BLTs that encounter a 185-km perigee altitude. In the lower-left region of each plot, a small curve may be observed that also encounters 185-km LEO orbits – this curve is an extension of the same family of BLTs that contains the nominal BLT; the curves will meet if the limits of the plots are extended. However, toward the upper-right of each plot, one can see two other curves of BLTs. These curves are members of one or two families that are very different from the nominal family of BLTs.

Figure 6.2 shows four additional plots of results from this experiment. The four curves are identified as Family 1 – Family 4, where once again, Family 1 and Family 2 are most likely curves within the same family. The plot in the upper-left is the same  $\theta$  vs.  $\tau$  plot as shown in Figure 6.1, used as a reference for defining each family. The other three plots show performance parameters of the BLTs in each family, including the Trans-Lunar Injection  $\Delta V$  (top-right), the ecliptic inclination of the corresponding LEO parking orbit (bottom-left), and the transfer duration (bottom-right). The nominal BLT is indicated in each plot for reference. One notices that by increasing  $\theta$  slightly and reducing  $\tau$  by a corresponding amount, one can reduce the injection  $\Delta V$  magnitude of the nominal BLT; by doing so, one also reduces the ecliptic inclination and the transfer duration of the BLT. It is interesting to notice that BLTs in Family 4 require very similar ecliptic inclination values as BLTs in the nominal family, and smaller injection  $\Delta V$  magnitudes, implying that they would likely be better BLTs to use in practical lunar missions. However, the BLTs in Family 4 also require longer transfer durations, which may make them less desirable after all.

More trade-studies are conducted later in this chapter. The purpose of this ex-

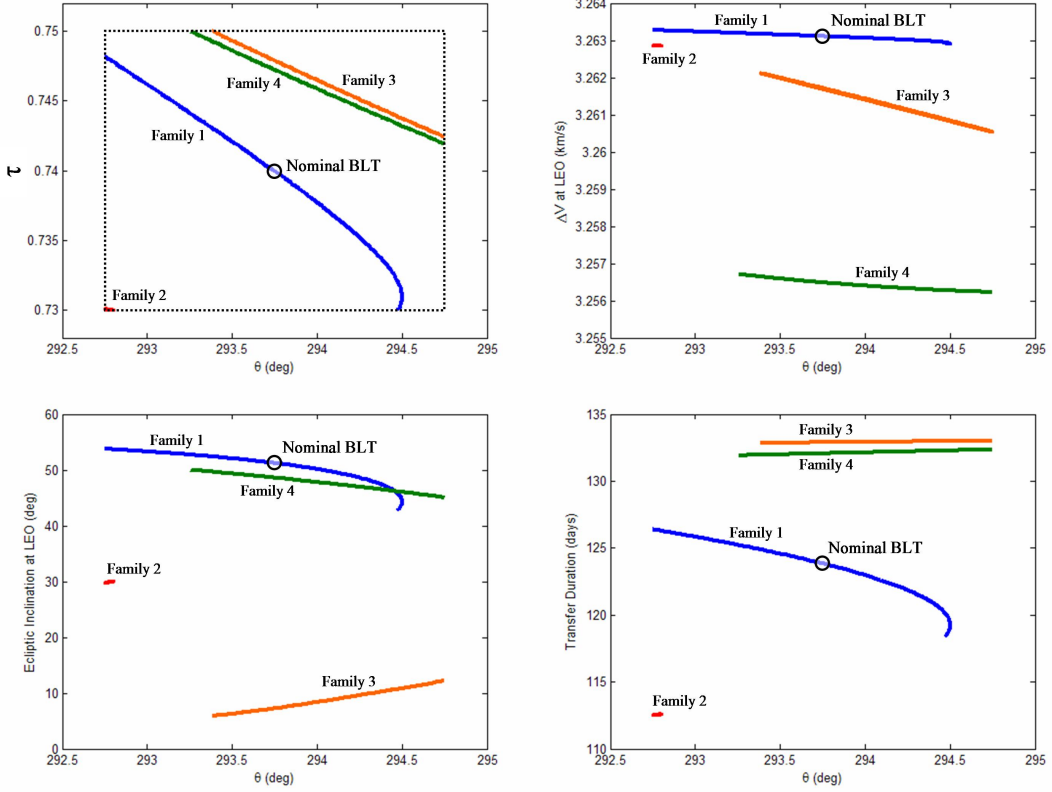


Figure 6.2: Four plots displaying the performance parameters of families that may be extracted from the plots shown in Figure 6.1. The plot in the upper-left is the same  $\theta$  vs.  $\tau$  plot as shown in Figure 6.1. The other three plots show performance parameters of the BLTs in each family, including the Trans-Lunar Injection  $\Delta V$  (top-right), the ecliptic inclination of the corresponding LEO parking orbit (bottom-left), and the transfer duration (bottom-right). The nominal BLT is indicated in each plot for reference.

periment is to verify that BLTs do indeed exist in families and BLT Maps are useful for extracting those families.

### 6.2.3 Example Full BLT Maps

The experiment given in Section 6.2.2 may be extended to allow  $\theta$  and  $\tau$  to vary throughout each parameter's range, namely,  $0^\circ \leq \theta \leq 360^\circ$  and  $0 \leq \tau \leq 1$ . In this way, trajectories are sampled from every point of the lunar three-body orbit's stable manifold and for each position of the Moon about the Earth. To further extend the ex-

periment, the trajectory at each  $(\theta, \tau)$  grid point is integrated for approximately 195.4 days (exactly 45 Earth-Moon nondimensional time units). Finally, two sets of results are produced: one for  $p$  set to “Exterior” and one for  $p$  set to “Interior”. Figures 6.3 and 6.4 show the resulting BLT Map for the exterior BLTs; Figures 6.5 and 6.6 show the resulting BLT Map for the interior BLTs. The parameters used in this experiment are summarized in Table 6.2. The closest perigee point of the trajectory at each  $(\theta, \tau)$  grid point in the integration timespan is identified and its perigee altitude is recorded. Figure 6.3 shows a plot that is shaded according to the altitude of the closest perigee point of each trajectory in the grid. The darkest regions represent trajectories that approach very near the Earth. Each contour in the plot represents a set of families of BLTs that depart the Earth from a particular altitude, e.g., from 185-km LEO parking orbits. Figure 6.4 shows the same BLT Map as Figure 6.3 with additional plots of sample BLTs displayed around the perimeter. This demonstrates how to interpret the BLT Map. One can see that there are a wide variety of BLTs that depart the Earth from 185 km orbits and ballistically transfer to the Moon in fewer than 195 days. Finally, Figures 6.5 and 6.6 show the same results but for interior BLTs rather than exterior BLTs. That is, the trajectories summarized by the BLT Map of Figures 6.5 and 6.6 arrive at the final lunar Halo orbit from the interior of the Moon’s vicinity rather than from the exterior.

The BLT Maps are explored in much more detail in later discussions. Neverthe-

Table 6.2: The parameters used to produce the results shown in Section 6.2.3.

Parameter	Value
$F$	The family of Earth-Moon $L_2$ Halo Orbits
$C$	3.05
$\theta$	$0^\circ \leq \theta \leq 360^\circ$
$\tau$	$0 \leq \tau \leq 1$
$p$	$\begin{cases} \text{“Exterior”} : \text{ Figures 6.3 and 6.4} \\ \text{“Interior”} : \text{ Figures 6.5 and 6.6} \end{cases}$
$\Delta t_m$	195.4 days (45 Earth-Moon time units)

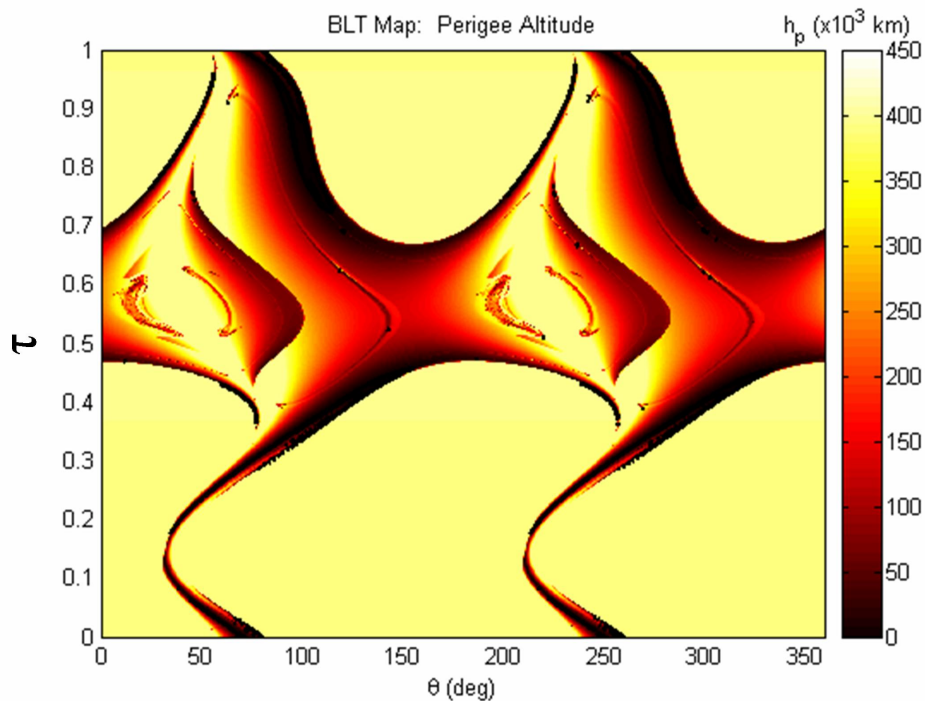


Figure 6.3: An example BLT Map using the parameters shown in Table 6.2 for the “Exterior” case. The shading indicates the lowest perigee altitude that each trajectory encounters, such that points shaded darkest approach the closest to the Earth.

less, there are many interesting features that may be immediately observed in these maps and some discussion is given here.

This discussion begins by considering the exterior BLT Map shown in Figures 6.3 and 6.4. The most prominent features in the map are the darkest black curves. As previously mentioned, the darkest regions in the map represent trajectories that make very close approaches with the Earth, including the BLTs that mission designers find desirable. The lightest regions in the plot, conversely, represent trajectories that do not approach the Earth within the integration timespan. Most of those light-colored trajectories escape from the lunar Halo orbit into various heliocentric orbits (when propagated backward in time); thus, in the integration timespan, their closest perigee passages are

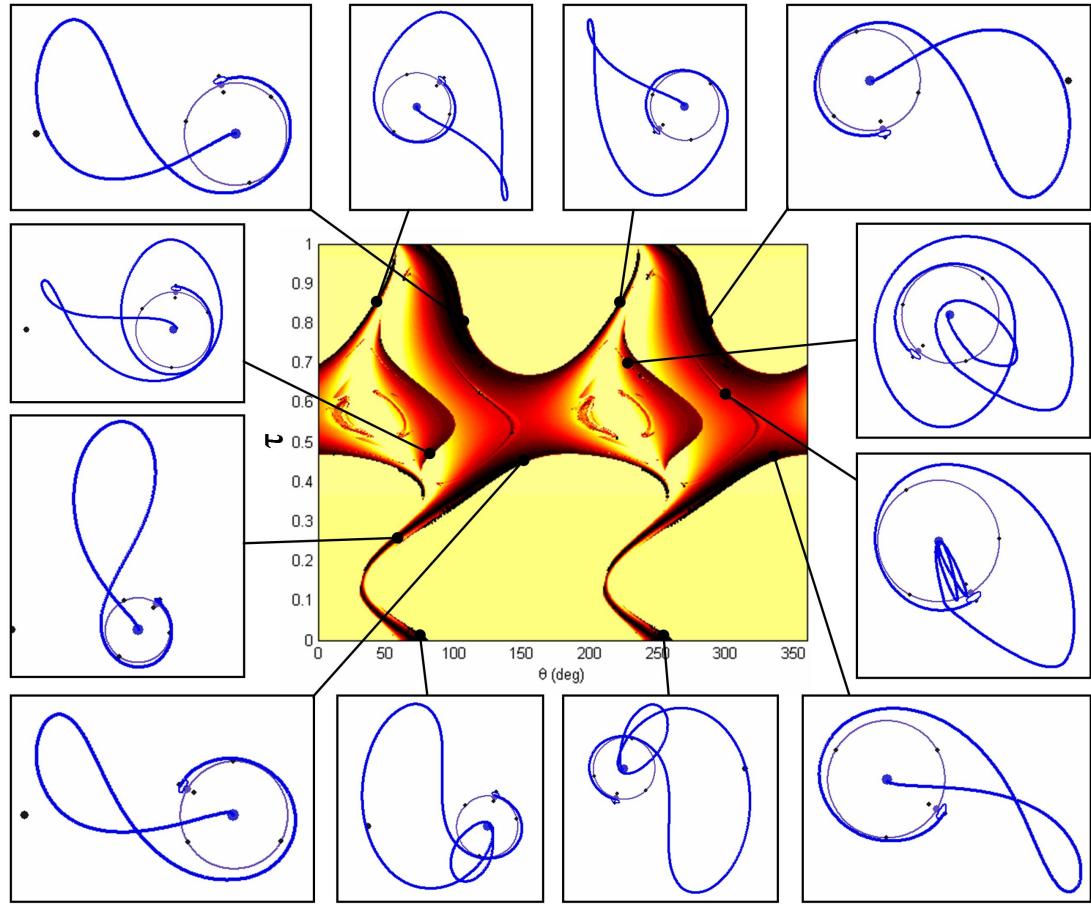


Figure 6.4: The same plot shown in Figure 6.3 with example trajectories shown, indicating the variety of BLT families that exist.

at the distance of the lunar Halo orbit itself.

The largest, most pronounced black curves observed in the BLT Map shown in Figures 6.3 and 6.4 correspond to the shortest-duration class of exterior BLTs. The outer-most plots shown in the four corners of Figure 6.4 are four examples of such short-duration BLTs. One can see that they depart the Earth, traverse their apogee, and then approach the Moon, immediately arriving at the lunar Halo orbit. They perform neither phasing loops nor any lunar flybys en route to the Moon. On the other hand, there are many families of BLTs shown in the example trajectories of Figure 6.4 that demonstrate alternative routes to the lunar Halo orbit. The two middle plots shown

on the lower edge of Figure 6.4 are two examples of trajectories that depart the Earth into a phasing orbit. These trajectories traverse a single phasing orbit and then pass by the Earth again before completing the remainder of the BLT. Other trajectories may be computed that traverse several orbits of a phasing orbit prior to completing the BLT – although, many of those trajectories require more than 195 days to complete and therefore have not been computed in this BLT Map. Another alternate BLT type includes one or more lunar flybys. The two middle plots on the right side of Figure 6.4 are two examples of trajectories that pass near the Moon during the ballistic lunar transfer. The lower of these two plots shows a trajectory that departs the Earth, traverses a phasing orbit for two orbits, then passes by the Moon and completes the remainder of the exterior BLT from there. The upper of these two plots shows a trajectory that passes near the Moon twice during the BLT before being ballistically inserted into the lunar Halo orbit. Many other examples of BLTs exist that are not shown in the example plots.

One additional observation that may be made about the BLT Maps shown in Figures 6.3 and 6.4 is that every feature appears to be repeated as  $\theta$  changes by  $180^\circ$ . The features are not exactly identical, but they are very similar. This is due to the fact that the dynamics in the Sun-Earth three-body system are nearly symmetric on either side of the Earth – toward the Earth's  $L_1$  point and toward the Earth's  $L_2$  point. Mission designers may take advantage of this and notice that a nearly-symmetric trajectory exists that departs the Earth toward the Earth's  $L_2$  point compared with one that departs the Earth two weeks earlier/later toward the Earth's  $L_1$  point.

The BLT Map shown in Figures 6.5 and 6.6 is more complicated than the exterior BLT Map shown in Figures 6.3 and 6.4. As one can see by carefully studying the example trajectories shown in Figure 6.6, the BLT Map explores trajectories that exist within the lunar Halo orbit's **interior** stable manifold. They are heuristically identical to the exterior transfers shown in the example plots of Figure 6.4 from their LEO-departure until they arrive at the Moon. Instead of directly inserting into the lunar Halo orbit,

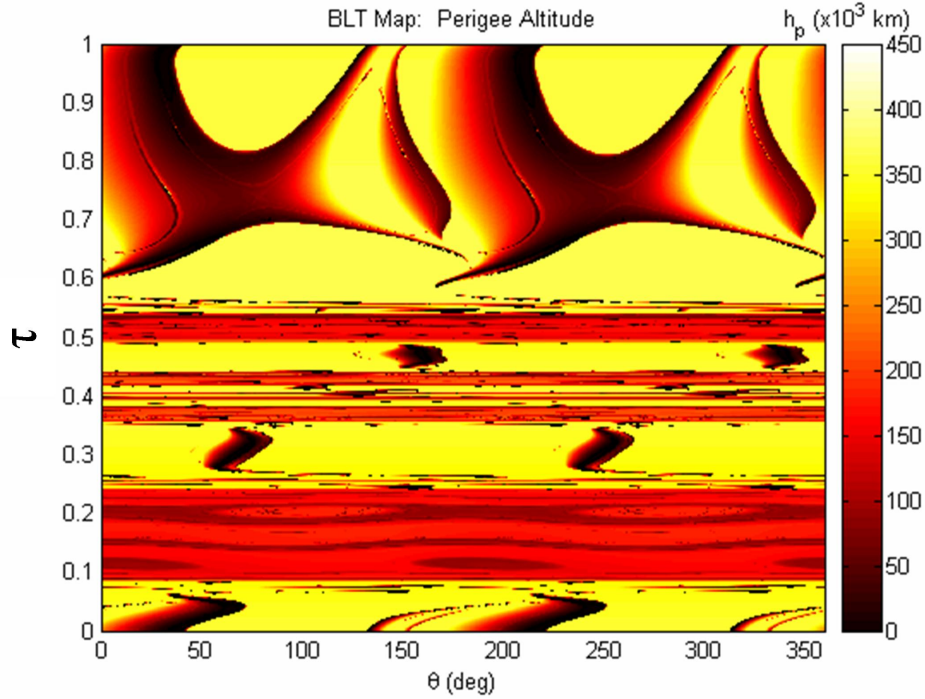


Figure 6.5: An example BLT Map using the parameters shown in Table 6.2 for the “Interior” case. The shading indicates the lowest perigee altitude that each trajectory encounters, such that points shaded darkest approach the closest to the Earth.

these interior transfers first pass near the Moon. They all fly by the Moon at least once prior to the lunar Halo orbit insertion; some fly by the Moon many times. These lunar encounters are the reason that this BLT Map is so complex compared with the exterior BLT Map. Trajectories that pass near the Moon have sensitive dependence on their initial conditions – meaning that slight changes in  $\theta$  and/or  $\tau$  result in very different trajectories.

By studying the BLT Map shown in Figures 6.5 and 6.6, one notices many of the same features that have been observed in Figures 6.3 and 6.4. One notices several black curves that are more pronounced than others, as well as darker regions that are smaller and/or less pronounced. Similar to the exterior BLTs, the most-pronounced black curves in this interior BLT Map correspond to the shorter-duration interior BLTs.

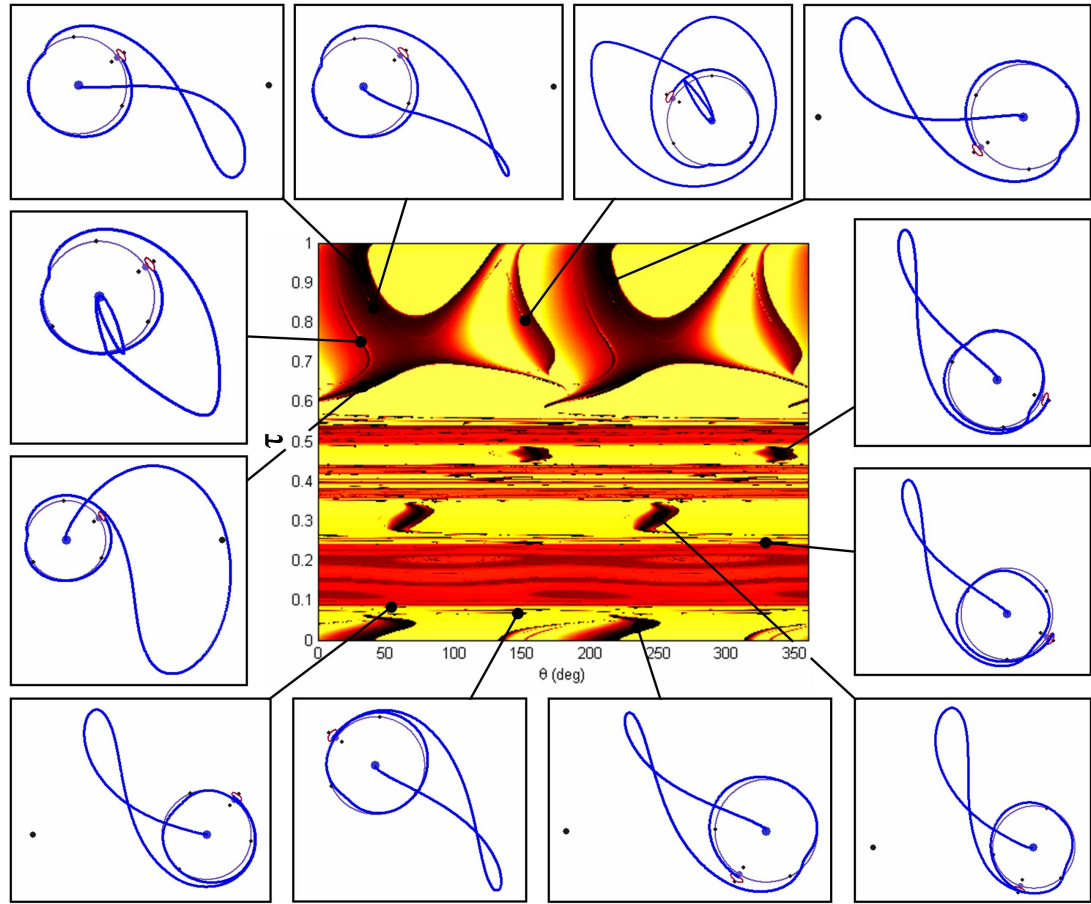


Figure 6.6: The same plot shown in Figure 6.5 with example trajectories shown, indicating the variety of BLT families that exist.

The less-pronounced curves in this BLT Map correspond to more complex – hence, more sensitive – interior BLTs. It is also quite apparent that features appear to be repeated throughout this BLT Map in a seemingly fractal pattern. This characteristic of the BLT Map is caused by the fact that trajectories may arrive at the Moon after following very complicated itineraries through space, including any number of lunar flybys and phasing orbits. The fractal pattern is further explored in Section 6.3.4.

Interior BLTs are generally more complex than exterior BLTs. Interior BLTs allow mission designers the flexibility to design trajectories that include any of the following options:

- Phasing orbits about the Earth;
- Lunar flybys en route to the Moon;
- Lunar flybys during the ballistic capture portion of the BLT;
- Phasing orbits in the Earth-Moon system.

The latter two options are not generally observed in exterior BLTs. The example trajectories shown around the perimeter of Figure 6.6 demonstrate just a few possible schemes. The trajectories with  $\tau$ -values between about 0.6 and 1.0, wrapping to include trajectories with  $\tau$ -values between 0.0 and about 0.08, are very similar to the exterior transfers previously studied. None of these trajectories implements phasing orbits at the Moon – they all fly by the Moon just once upon arrival at the Moon before ballistically inserting into the lunar Halo orbit. This feature may be observed by carefully studying the example trajectories shown in these regions of the BLT Map: the trajectories visibly only make one lunar flyby during the final capture. These trajectories may, however, include any combination of phasing orbits at the Earth and/or lunar flybys en route to the Moon.

The other regions of the interior BLT Map are much more sensitive and may be composed of much more complicated BLT itineraries. At first glance, the four example BLTs shown in the lower-right perimeter plots of Figure 6.6 appear to be nearly identical. The LEO-departure segments and the apogee segments are indeed very similar. However, each trajectory encounters the Moon differently, performing a series of lunar flybys and/or lunar phasing orbits prior to the lunar Halo orbit insertion.

To demonstrate the highly sensitive nature of other regions within the interior BLT Map, we have chosen to present a particularly complex ballistic lunar transfer that exists at the point ( $\theta = 120^\circ, \tau = 0.417505$ ). Figure 6.7 shows the example trajectory in the Sun-Earth synodic reference frame. One notices that this trajectory departs

the Earth, traverses its apogee, flies past the Moon, traverses a very large phasing orbit within the Earth-Moon system, transfers to a phasing orbit about the Moon, and then finally inserts into the lunar Halo orbit. Figure 6.8 shows the trajectory in the Earth-Moon synodic reference frame. The middle plot clearly shows the large phasing orbit in the Earth-Moon system; the right-most plot shows the phasing orbit about the Moon. Finally, Figure 6.9 shows the trajectory in three dimensions in the Earth-Moon synodic reference frame. It is not surprising that this trajectory is very sensitive to initial conditions due to its highly complex nature.

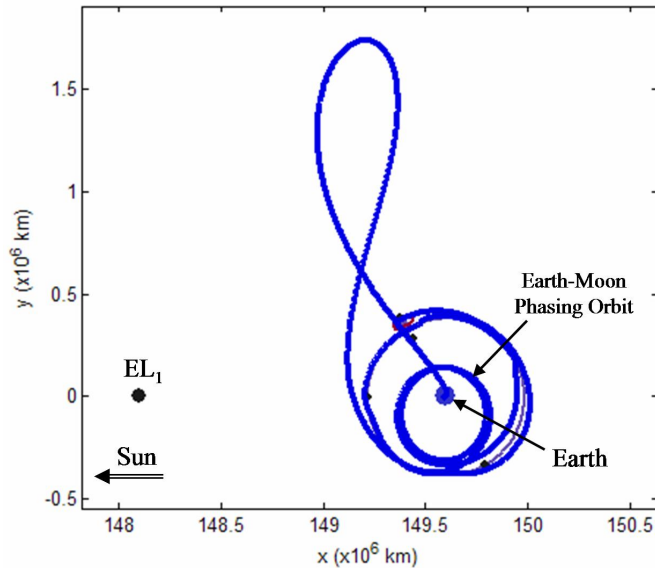


Figure 6.7: An example interior ballistic lunar transfer that is particularly complicated, demonstrating the sensitivity of such BLTs to their initial conditions. The trajectory is shown in the Sun-Earth synodic reference frame.

The BLT Maps presented here provide a means to systematically identify numerous types of BLTs. The next section demonstrates the process of extracting families of BLTs. The families are then surveyed in order to identify which families include BLTs with desirable parameters for practical spacecraft missions.

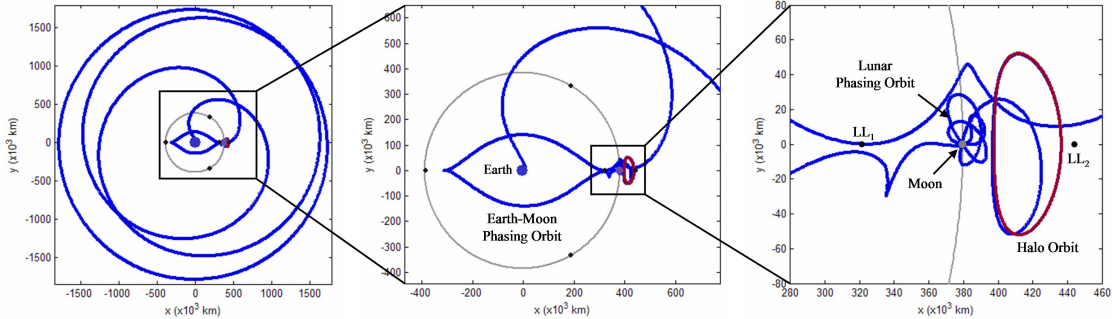


Figure 6.8: The same interior BLT shown in Figure 6.7 plotted in the Earth-Moon synodic reference frame at three different scales.

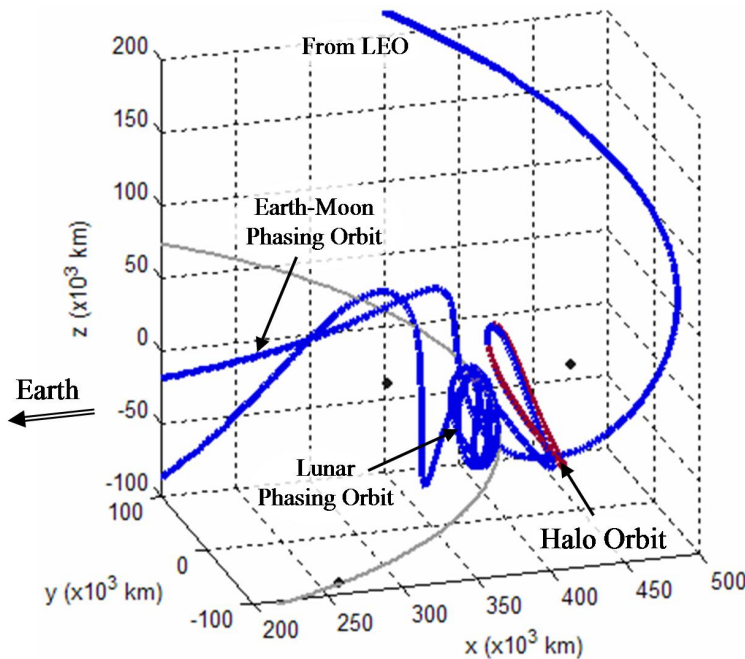


Figure 6.9: The same interior BLT shown in Figures 6.7 and 6.8 plotted in three dimensions in the Earth-Moon synodic reference frame.

#### 6.2.4 Extracting Families

The BLT Maps presented in Figures 6.3 – 6.6 are colored according to the closest approach that each trajectory makes with the Earth. In order to identify each BLT that departs the Earth from an altitude of 185 km, one only needs to identify the 185-km contour in the map. Figure 6.10 shows the same BLT Map presented in Figure 6.3 with

the 185-km contour superimposed. This contour indicates all of the available ballistic lunar transfers that depart the Earth from 185-km LEO parking orbits, arrive at the same lunar Halo orbit along its exterior stable manifold, and require no more than 195.4 days to complete the transfer.

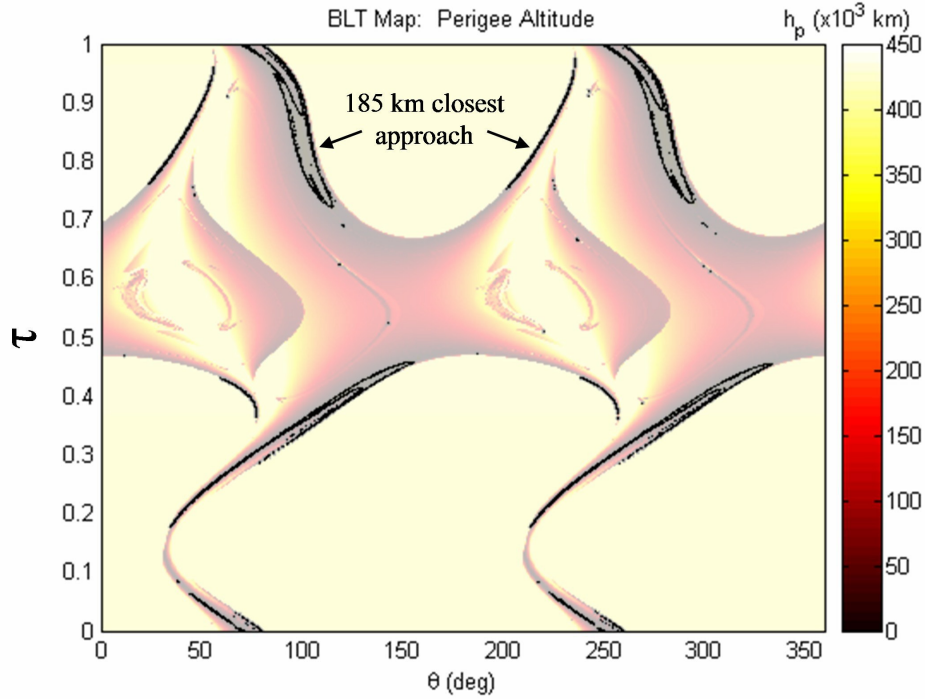


Figure 6.10: The BLT Map shown in Figure 6.3 with a contour superimposed, indicating all available ballistic lunar transfers that depart the Earth from 185-km LEO parking orbits.

One can see that the 185-km contour shown in Figure 6.10 contains many individual curves. Each continuous curve along one contour segment represents a **family** of BLTs, where the parameters of each BLT in the family vary in a continuous fashion across the curve. Every BLT in a family is topologically identical; two neighboring BLTs in the same family have nearly identical parameters, including their transfer durations, their Trans-Lunar Injection  $\Delta V$  cost, the inclination of their injection points, etc. Two unconnected families of BLTs are similar in that they both contain BLTs that

depart the Earth at an altitude of 185 kilometers and arrive at the same Halo orbit. However, an example BLT within one family may be topologically different from an example BLT within another family; their performance parameters are also likely to be very different. One might consider that the two unconnected families contain BLTs that are cousins since they share the same perigee altitude and the same destination. The collection of all of the families of BLTs, namely, the entire 185-km contour shown in Figure 6.10, comprises the **set** of all BLTs with the same perigee altitudes and transfer destinations.

The 185-km contour shown in Figure 6.10 has been produced by interpolating between grid points that span a LEO altitude of 185 km. Hence, the contour only provides approximate values of  $\theta$  and  $\tau$  that may be used to produce an actual BLT within the family. More precise parameters may be obtained in many ways, including a variety of numerical methods (Winter et al., 1995; Avriel, 2003). In this dissertation we have explored several methods to numerically determine very precise parameters for a BLT, including the following methods:

**One-dimensional Secant/bisection method.** This method begins by identifying two  $(\theta, \tau)$ -combinations that span a perigee altitude of 185 kilometers. The Secant method is then used to numerically converge on the 185-km crossing. If the method appears to be converging slowly, a bisection of the interval is introduced in an attempt to speed up the convergence process.

**Two-dimensional hill-climbing/simulated-annealing optimization method.** This method begins by identifying one  $(\theta, \tau)$ -combination that is used as an initial estimate of the BLT. Then each parameter is perturbed in a positive and negative direction and four new BLTs are produced. The nominal  $(\theta, \tau)$  state is updated if one of the new BLTs has a perigee altitude closer to the desired 185-km value. The hill-climbing process is repeated until the best BLT is identified given the current perturbation values. The

perturbation values are then reduced and the hill-climbing process is repeated.

**Two-dimensional genetic algorithm optimization method.** This method begins by producing a population of  $(\theta, \tau)$ -combinations near an estimated solution. The population is then “mated” to produce new  $(\theta, \tau)$ -combinations. The mating procedure that we have followed takes two “parent” states in the population,  $(\theta_1, \tau_1)$  and  $(\theta_2, \tau_2)$ , and operates on them in the following manner to produce a new “child” state,  $(\hat{\theta}, \hat{\tau})$ :

$$\begin{aligned}\hat{\theta} &= p\theta_1 + (1 - p)\theta_2; \\ \hat{\tau} &= q\tau_1 + (1 - q)\tau_2,\end{aligned}$$

where  $p$  and  $q$  are two random numbers between 0 and 1. A small mutation in the state is also introduced anytime the new state is equal to a state already in the population. After several matings have occurred, a new population, i.e., a new “generation”, is constructed that consists of the best-known states, including either the new children or the older parents.

In this dissertation, the values of  $\theta$  and  $\tau$  have been adjusted by one of these numerical methods until a BLT has been identified that encounters the Earth within 0.1 meters of the target 185 kilometers. The Secant method has been implemented in any case where the parameters need to be optimized in only one dimension. It has been found that the other two numerical methods may be used interchangeably; there are cases when either of the two-dimensional methods works better than the other.

Each of these methods has several numerical problems. First of all, every trajectory presented in this dissertation has been propagated using a numerical integrator, as discussed in Appendix E. Even the most precise integrators introduce small errors while propagating a trajectory. We have implemented a variable time-step eighth-order Runge-Kutta integration method that has a very small relative error (Wilson and Turcotte, 1997). Nevertheless, since the CRTBP is inherently chaotic, these small numerical

errors grow – sometimes very rapidly. The result is that the  $\tau$ - and  $\theta$ -values that one of the numerical schemes converges on will have some small errors associated with them. Therefore, the trajectories produced here only approximate true trajectories that exist in the system being modeled. The numerical errors are small enough that they may be generally absorbed by a spacecraft's trajectory-correction maneuvers (Howell et al., 1997a).

A second numerical problem that is very relevant to this dissertation is the problem that occurs in some situations where it becomes numerically impossible to target a ballistic trajectory that has a perigee altitude within 0.1 meters of 185 km using accessible computers. That is, it is observed that a change in  $\theta$  or  $\tau$  as small as  $1 \times 10^{-15}$  units results in a perigee altitude change greater than 0.1 meters. In those situations, we have chosen to record the best estimates of  $\theta$  and  $\tau$  for mapping purposes, but not to include them in the surveys presented later in this dissertation since their performance parameters are not as accurate as desired. If such a BLT is indeed so desirable that a mission designer wishes to construct it, then the BLT may be constructed without this numerical problem by implementing a multiple-shooting method, such as that presented in Section 3.5.2.

Even in the presence of numerical problems, the majority of the families observed in Figure 6.10 have been constructed and categorized. In many cases, more work may be done to enhance the features of each family. Furthermore, it is likely that some families have yet to be identified. Nevertheless, a survey of the families that have been categorized, including families of both exterior and interior BLTs, is presented in Section 6.3.

### 6.3 A Survey of Families of BLTs

Figure 6.11 shows the two BLT Maps previously studied, each with the 185-km contour superimposed. One can see that there are a very large number of families of BLTs that exist within these BLT Maps. It is difficult to compare each and every curve with each other directly. We have surveyed many of the families in each BLT Map and will present them in the following manner. Section 6.3.1 presents families of exterior BLTs that are visible in the left-half of the exterior BLT Map. Section 6.3.2 characterizes the differences between families on either half of a BLT Map. Section 6.3.3 presents families of interior BLTs. Section 6.3.4 continues to study the interior BLT Map by exploring the chaotic regions found within it. Finally, Section 6.3.5 discusses the results of this survey and provides some concluding remarks.

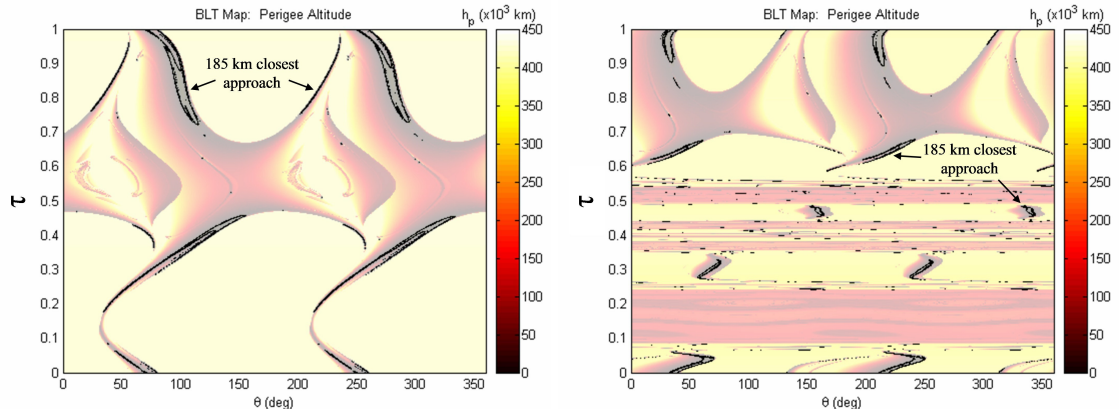


Figure 6.11: The families of BLTs that depart the Earth from 185-km LEO parking orbits, encountering the lunar Halo orbit from the exterior (left) and interior (right).

#### 6.3.1 Families of Exterior BLTs

This section explores the set of families of BLTs that depart the Earth from 185-km LEO parking orbits and arrive at the lunar  $L_2$  Halo orbit via its exterior stable manifold. Figure 6.12 shows the numerically-converged  $(\theta, \tau)$ -combinations, which correspond

to BLTs that exist along the 185-km contour of the exterior BLT Map. As discussed in Section 6.2.4, the parameters of each of the BLTs shown in Figure 6.12, and all BLTs presented in this section, have been numerically adjusted until each BLT's perigee altitude is within 0.1 meters of the desired 185 kilometers. Substantially more effort has been spent converging on actual BLTs on the left half of Figure 6.12 compared with the right half; hence, the density of points is greater on that side. Most of the features of the right side of the figure are symmetric to the left; a discussion about any subtle differences is presented in Section 6.3.2. In some places, curves that appear in the interpolated contour plot shown in Figures 6.10 and 6.11 could not be computed to within the desired 0.1-meter accuracy and are thus not shown. Nevertheless, approximately 200 families of BLTs have been identified and are surveyed here. One final note when studying Figure 6.12: the revolution number  $\tau$  has been adjusted such that any  $\tau$ -values below 0.1 have been increased by 1. This adjustment has been made so that the curves of

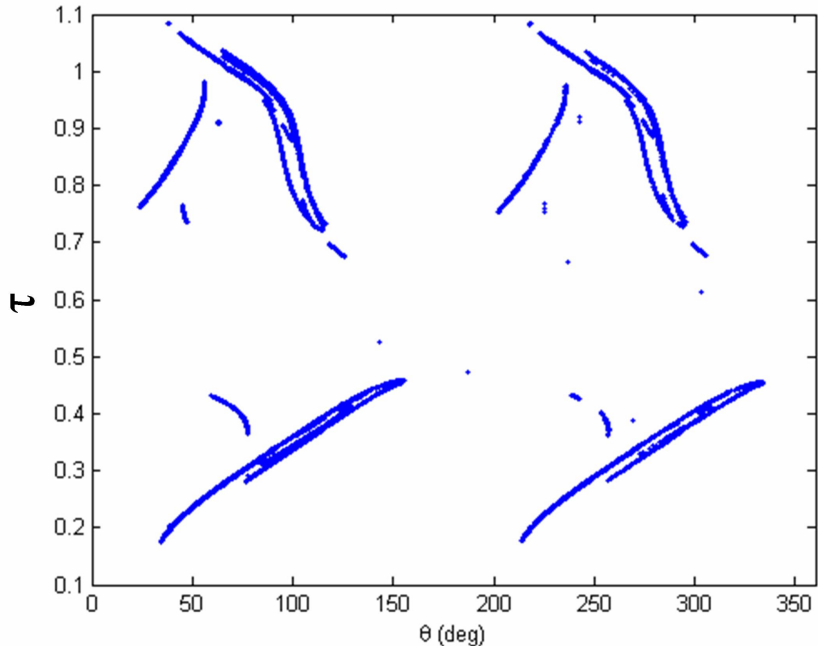


Figure 6.12: The numerically-converged  $(\theta, \tau)$ -combinations, which yield BLTs that depart from LEO altitudes within 0.1 meters of the desired 185 kilometers.

the families that cross the top/bottom boundary of the plots are now continuous. The adjustment is purely aesthetic and is made possible because Halo orbits are perfectly periodic in the CRTBP.<sup>1</sup>

Since there are so many different families, each with widely varying parameters, it is difficult to directly compare them all graphically. We present the families by first exploring a few representative families to demonstrate how the BLT parameters can vary across a family; then we compare a larger number of families together.

Figures 6.13 – 6.17 show several example trajectories in five representative families of BLTs, each shown in the Sun-Earth synodic reference frame viewed from above the ecliptic. Each figure also contains four plots that show how four particular parameters vary as functions of  $\theta$  within each family. The top-left parametric plot in each figure is a plot of  $\theta$  vs.  $\tau$ , which is useful to identify the family in the BLT Map. The other three parameters shown, in clockwise order, are the Trans-Lunar Injection  $\Delta V$  magnitude that would be executed to transfer the spacecraft from its LEO parking orbit onto the BLT, the ecliptic inclination of the Trans-Lunar Injection point, and the transfer duration. A brief description of each of these families follows.

**Example Family A.** Figure 6.13 shows an example family of exterior BLTs that require a relatively short transfer duration of about 100 days. The required  $\Delta V$  magnitudes range between approximately 3.263 and 3.2685 km/s. The parameter that varies the most within these four considered parameters is the ecliptic inclination of the Trans-Lunar Injection point, which ranges between approximately 10 and 120 degrees.

**Example Family B.** Figure 6.14 shows an example family of BLTs that require considerably greater durations of time than those presented in Figure 6.13. Each of these BLTs

---

<sup>1</sup> There is, however, a slight discontinuity that appears between BLTs with  $\tau$ -values on either side of the  $\tau$ -boundary. This is caused by small numerical errors that are introduced when propagating the state transition matrix about the periodic orbit. When the stable eigenvectors of the monodromy matrix are mapped all the way around the orbit, they should theoretically return to their nominal values. Numerically, they do not return precisely to those values due to the numerical propagation errors. Hence, a small discontinuity is observed.

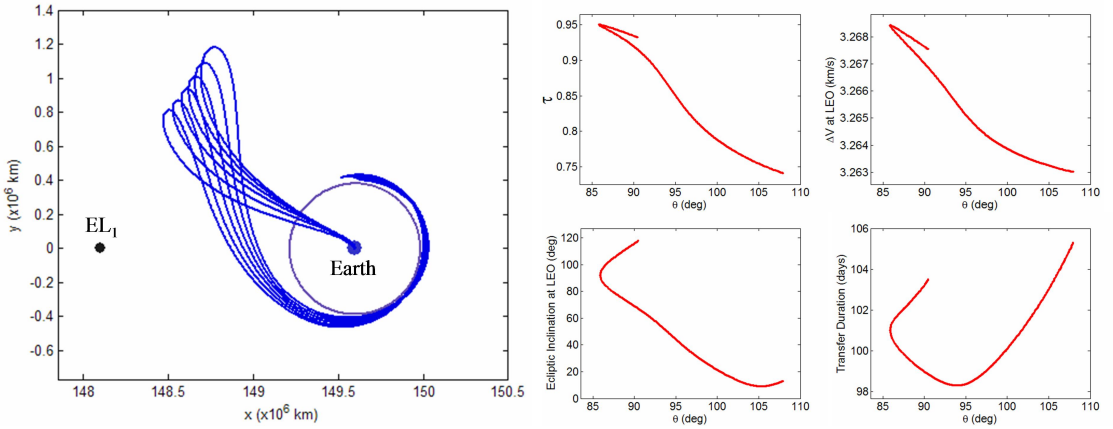


Figure 6.13: Several example trajectories in Family A of exterior BLTs. The four plots shown on the right indicate how four parameters vary as functions of  $\theta$  for this family. Starting with the top-left plot and continuing clockwise, the four presented parameters are the BLT's  $\tau$ -value, the  $\Delta V$  magnitude of the Trans-Lunar Injection maneuver, the ecliptic inclination of the Trans-Lunar Injection point, and the transfer duration.

traverses two apogee passages prior to encountering the Moon. Although the transfer durations are long, ranging between approximately 178 and 190 days, the Trans-Lunar Injection  $\Delta V$  magnitudes are somewhat smaller than the first family, ranging between approximately 3.235 and 3.275 km/s. The ecliptic inclination of the injection point varies anywhere between 0 and 180 degrees.

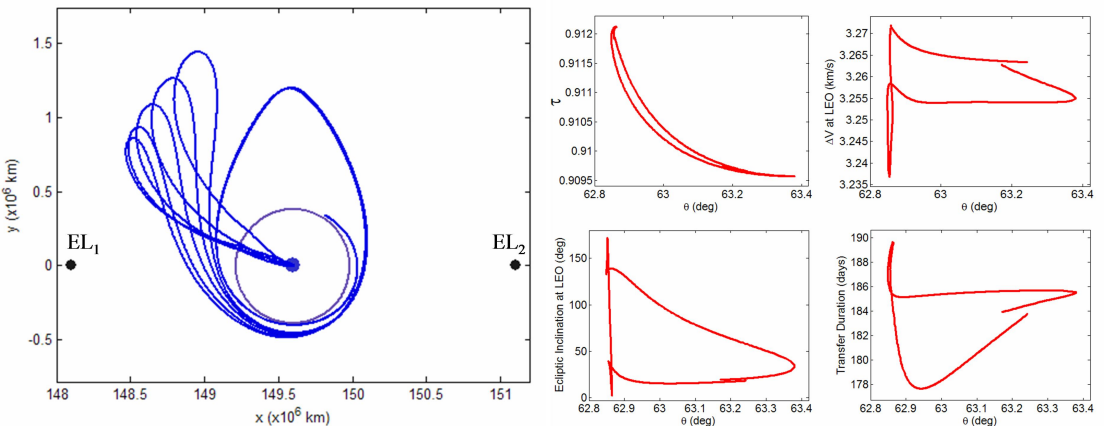


Figure 6.14: Several example trajectories in Family B of exterior BLTs, with the same four parametric plots presented for this family as shown in Figure 6.13.

**Example Family C.** Figure 6.15 shows an example family of BLTs that approach the Sun-Earth L<sub>2</sub> point rather than the L<sub>1</sub> point. In general, if a family of BLTs exists that approaches EL<sub>1</sub>, a very similar family of BLTs also exists that approaches EL<sub>2</sub>. This family includes transfers that hit the maximum propagation time used in this study of 195.4 days.

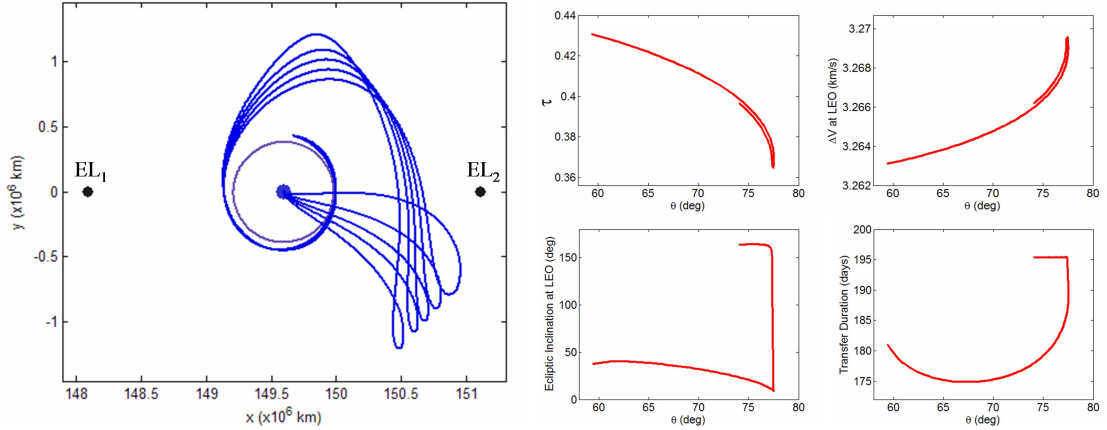


Figure 6.15: Several example trajectories in Family C of exterior BLTs, with the same four parametric plots presented for this family as shown in Figure 6.13.

**Example Family D.** Figure 6.16 shows an example family of BLTs that pass near the Moon en route to their first apogee passage. This lunar flyby reduces the magnitude of the Trans-Lunar Injection maneuver required by each transfer: the reduced  $\Delta V$  magnitude ranges between approximately 3.200 and 3.235 km/s. Similar to the third family presented here, this family includes transfers that hit the maximum transfer duration, which helps to explain the odd features observed in the parametric plots on the right.

**Example Family E.** Finally, Figure 6.17 shows an example family of BLTs that includes transfers which vary widely in their required transfer durations. In addition, this family demonstrates some interesting features in its parametric plots: each plot varies in a predictable, systematic fashion except at several  $\theta$ -regions, where each plot deviates

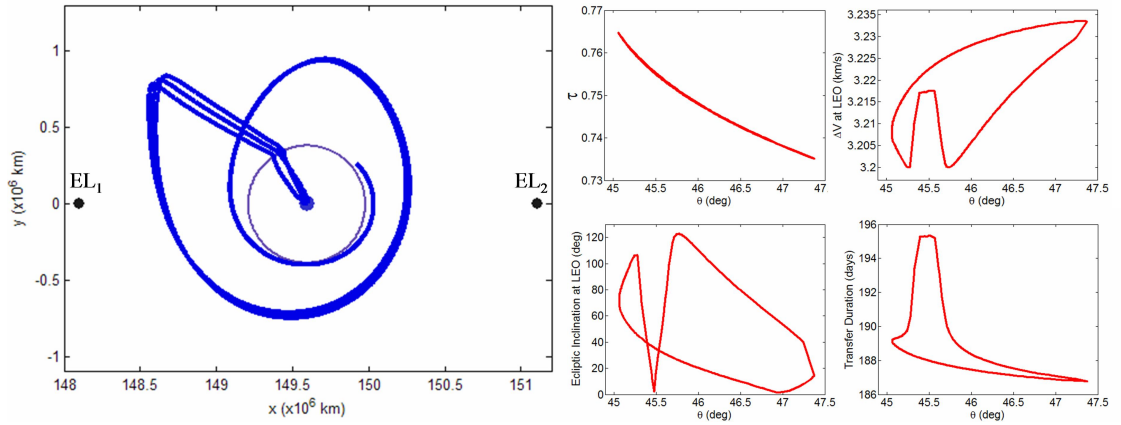


Figure 6.16: Several example trajectories in Family D of exterior BLTs, with the same four parametric plots presented for this family as shown in Figure 6.13.

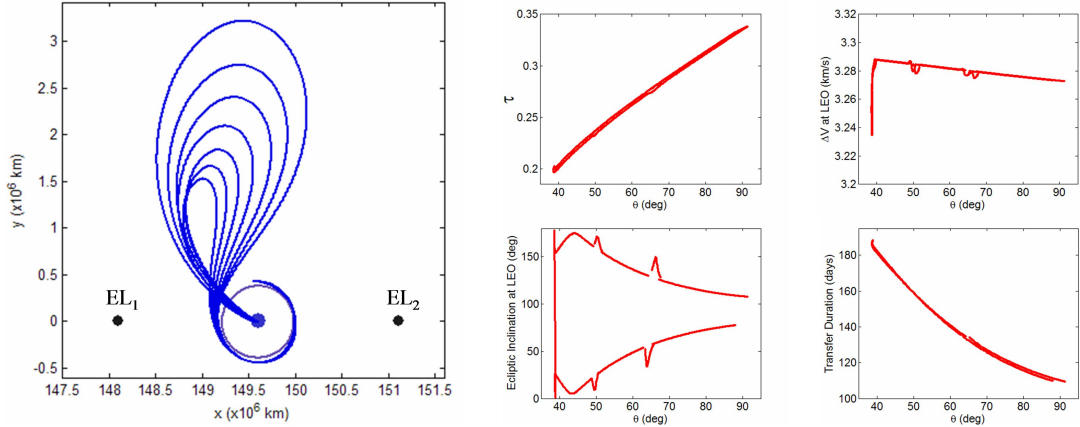


Figure 6.17: Several example trajectories in Family E of exterior BLTs, with the same four parametric plots presented for this family as shown in Figure 6.13.

considerably. It is hypothesized that these deviations are caused by the gravitational influence of the Moon as the transfer departs the Earth. The  $\theta$ -regions that demonstrate the deviations may be those regions where the Moon is considerably closer to the BLTs during their outbound segments.

Figures 6.13 – 6.17 have demonstrated how BLTs can vary throughout a particular family. We now present the parameters of many families of BLTs together in order to give an impression of the combinations of parameters that a mission designer may use to ballistically transfer to this particular lunar Halo orbit. Figures 6.18 and 6.19 show several parametric plots of approximately 50 families of exterior BLTs each. Each family of BLTs is colored the same in each plot to assist in identifying its various characteristics. The five example families presented earlier are also indicated on the two figures, where the example families A, B, and D appear on Figure 6.18 and the example families C and E appear on Figure 6.19. The top-left plot in each figure shows the main exterior BLT Map for this lunar Halo orbit and the location that is studied in the other plots. Continuing about the figure in a clockwise fashion, the plots show the parameters  $\tau$ , Trans-Lunar Injection  $\Delta V$  magnitude, transfer duration, and ecliptic inclination of the injection point all as functions of  $\theta$ . Each of these plots uses the parameter  $\theta$  as the independent variable in order to readily compare the families' characteristics from plot to plot. Finally, the sixth plot (the middle plot on the left of each figure) shows a parametric plot of each transfer's  $\Delta V$  cost as a function of its transfer duration – two very important parameters when comparing the families.

The main results of this survey are represented in the sixth plot of each figure. One can see that the majority of the quicker exterior BLTs, i.e., those that require fewer than 120 days to approach within 100 km of the Halo orbit, require approximately 3.265 km/s to reach the lunar Halo orbit. If the transfer duration may be extended to as much as 190 days, then transfers may be constructed that require a Trans-Lunar Injection maneuver with a magnitude as small as 3.200 km/s.

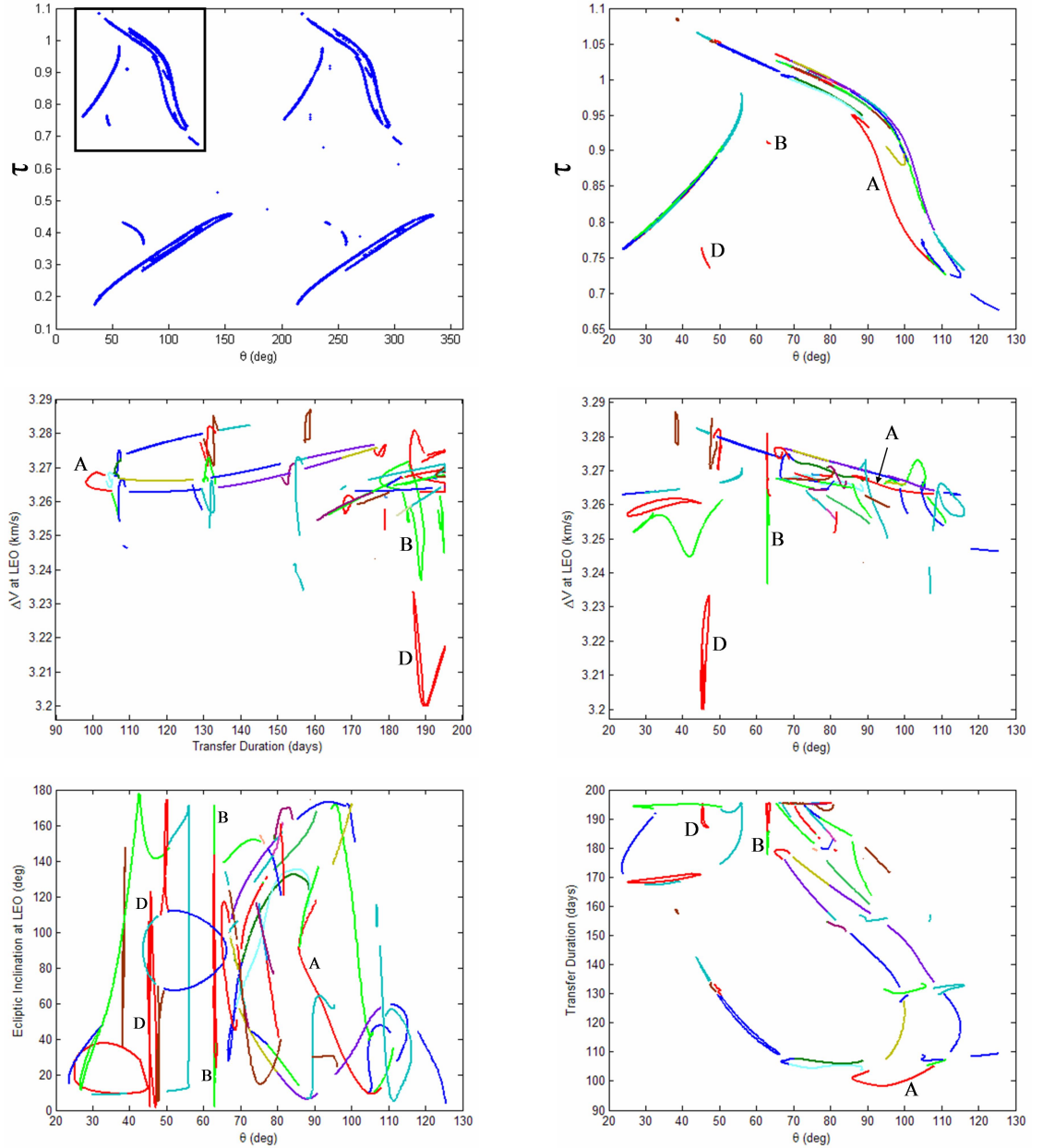


Figure 6.18: Six plots comparing approximately 50 families of exterior BLTs. The exterior BLT Map is shown in the top-left; the map shown in the top-right is a blown-up region of the BLT Map containing the studied families. Continuing clockwise, the plots show the  $\Delta V$  cost vs.  $\theta$ , the transfer duration vs.  $\theta$ , the ecliptic inclination of the injection point vs.  $\theta$ , and the  $\Delta V$  cost vs. the transfer duration. Each family is colored the same in each of the plots. The letters correspond to the example families presented in Figures 6.13 – 6.17.

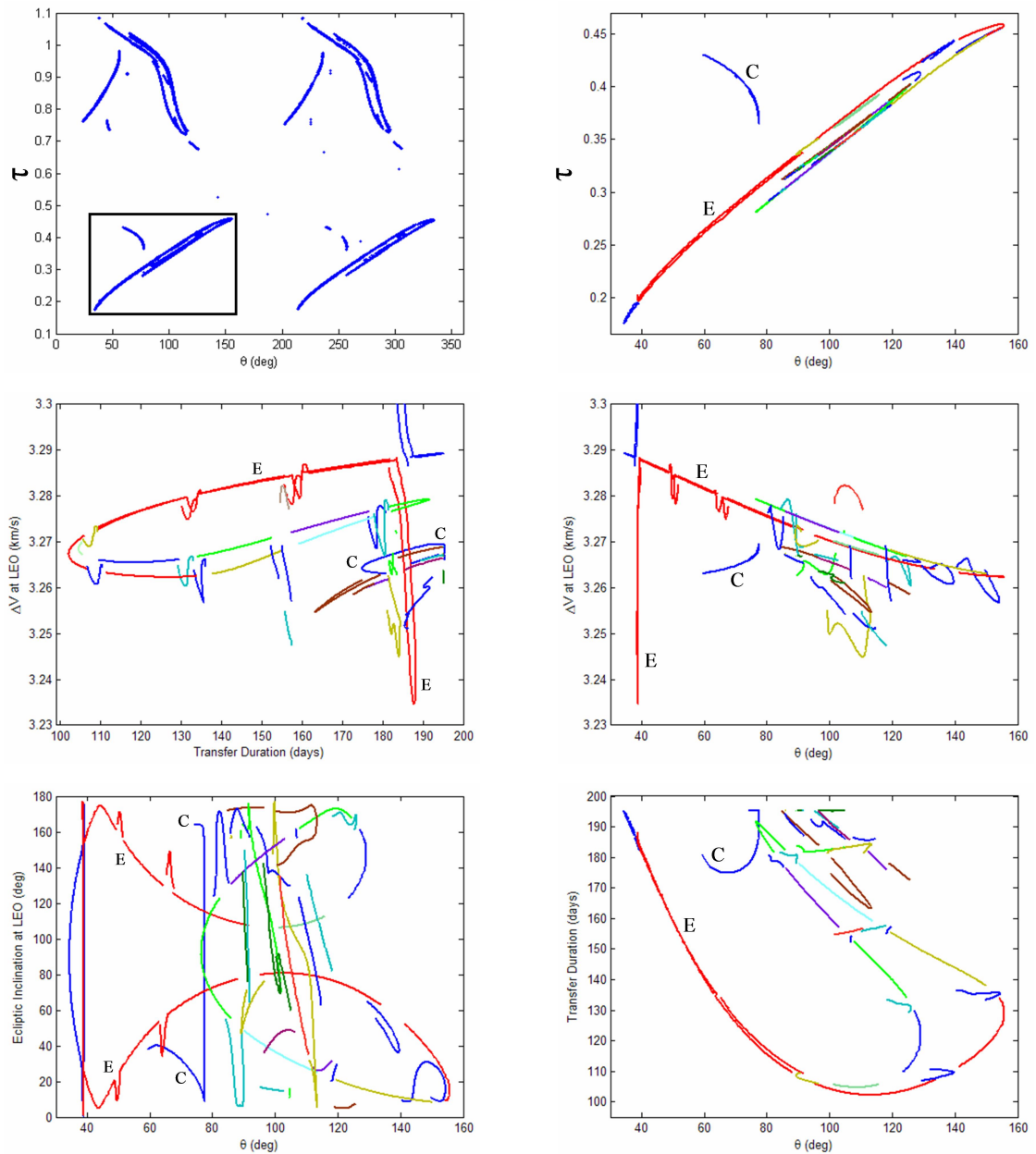


Figure 6.19: The same six plots presented in Figure 6.18 but for approximately 50 new families, as indicated by the BLT Map shown in the top-left.

### 6.3.2 Comparing Symmetric Families on Either Side of the BLT Map

The analysis of exterior BLTs given in Section 6.3.1 only considered families of BLTs within the left half of the exterior BLT Map, i.e., families of BLTs that have  $\theta$ -values between 0 and 180 degrees. The families on the right half have very similar parameters, except of course that the parameter  $\theta$  has an approximate 180° phase difference. The ballistic lunar transfers arrive at the Moon when the Moon is on the other side of the Earth, implying that each BLT takes a symmetric route through the Sun-Earth system. That is, if a BLT on the left side of the BLT Map approaches the Earth's L<sub>1</sub> point during its transfer, then the corresponding BLT on the right side of the BLT Map approaches the Earth's L<sub>2</sub> point during its transfer.

This discussion will now directly compare one family of BLTs that exists on the left half of the exterior BLT Map with the family of BLTs that appears to have very similar parameters on the right side of the Map (except that  $\theta_{\text{right}} \approx \theta_{\text{left}} + 180^\circ$ ). Figure 6.20 shows a plot of one example BLT from both families. The BLTs are labeled "Left" and "Right" according to which half of the BLT Map they exist in. One can quickly see that the two trajectories are nearly symmetric. Figure 6.21 shows four plots of different parameters of each family, all as functions of  $\theta$ . The  $\theta$ -values of each BLT in the "Right" family have all been reduced by 180° to directly compare their parameters with those in the "Left" family. One can see that the  $\theta$ -values are not quite phased by 180°, but they are close. It makes sense that they are not perfectly phased by 180° since the force field on either side of the Earth is not perfectly symmetric. After inspecting other families of BLTs, we have noticed that the difference in  $\theta$ -values may be above or below 180°. Finally, Figure 6.22 shows a parametric plot comparing the transfer duration with the total  $\Delta V$  cost of each of these two families of BLTs. One can see that these parameters are very comparable.

It is convenient that the majority of the transfers on either side of a BLT Map

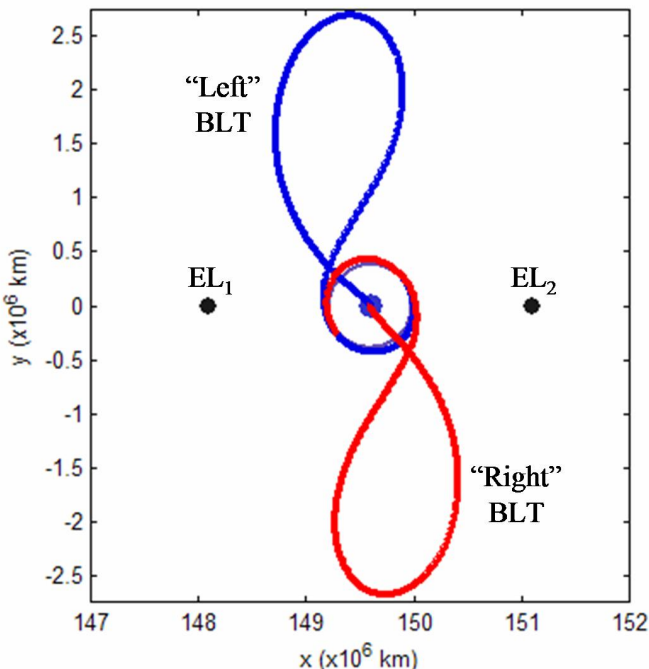


Figure 6.20: A plot of two BLTs that are nearly symmetric, where the two BLTs are labeled according to which half of the exterior BLT Map they exist in.

are nearly symmetric. When one constructs a single BLT, one may evaluate the performance of **four** very similar BLTs. To demonstrate, let's assume that we have constructed a BLT that visits the Sun-Earth L<sub>1</sub> point en route to a Northern lunar Halo orbit, then we may evaluate the following two BLTs immediately:

- The nominal BLT that visits EL<sub>1</sub> en route to a Northern Halo orbit, and
- The symmetric BLT that visits EL<sub>1</sub> en route to a Southern Halo orbit.

In addition, it requires very little additional work to evaluate the following two similar BLTs:

- The BLT that visits EL<sub>2</sub> en route to a Northern Halo orbit, and
- The BLT that visits EL<sub>2</sub> en route to a Southern Halo orbit.

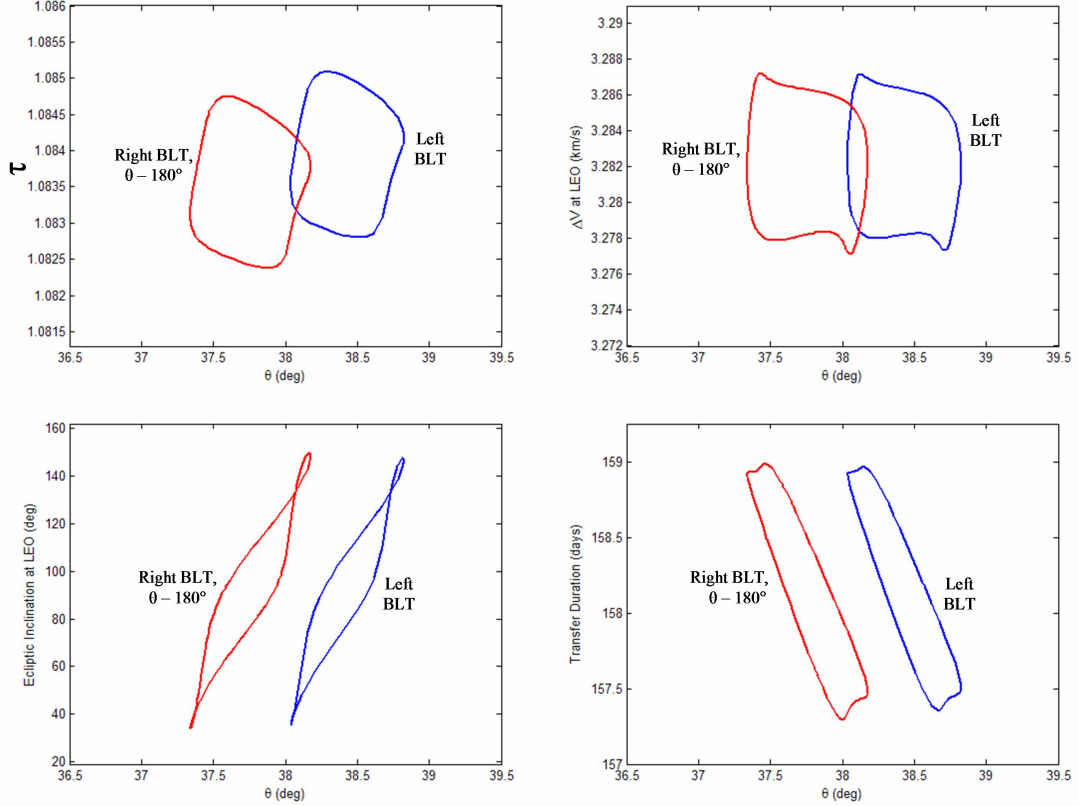


Figure 6.21: Four parametric plots comparing parameters of the families of the two BLTs shown in Figure 6.20. The plot in the top-left shows  $\tau$  vs.  $\theta$  to compare these families on the BLT Map; continuing clockwise, the plots show the  $\Delta V$  cost vs.  $\theta$ , the transfer duration vs.  $\theta$ , and the ecliptic inclination of the BLT-injection point vs.  $\theta$ . In each case, the  $\theta$ -values of the “Right” family of BLTs have been reduced by  $180^\circ$ .

Although the transfer durations and Trans-Lunar Injection maneuver costs are very similar between symmetric transfers, the LEO parking orbit is very different. The altitude of the LEO parking orbit is the same, but the inclination and right-ascension of the ascending node may be very different. Furthermore, the distance and angle to the Sun is different between symmetric transfers, which has some impact on the power, communication, and attitude control systems of the spacecraft.

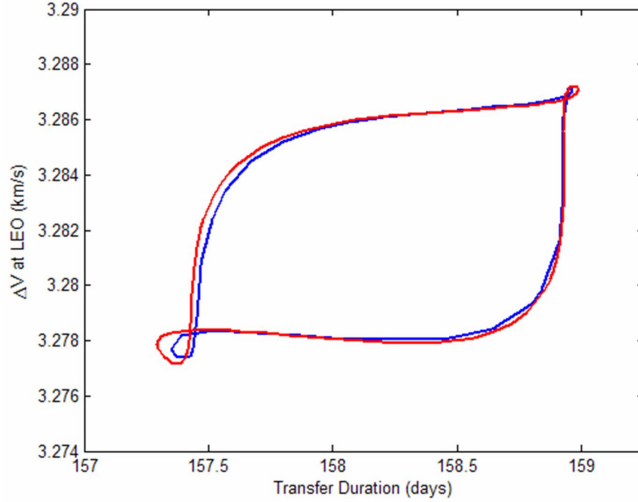


Figure 6.22: A parametric plot comparing the transfer duration with the  $\Delta V$  cost of the families of the two BLTs shown in Figure 6.20. The blue curve corresponds to the “Left” family and the red curve corresponds to the “Right” family.

### 6.3.3 Families of Interior BLTs

This section explores the set of families of BLTs that depart the Earth from 185-km LEO parking orbits and arrive at the Halo orbit along its interior stable manifold. The interior BLT Map is shown in Figures 6.5 and 6.6; the 185-km contour that defines the set of families of interior BLTs is shown in Figure 6.11 on page 242. Looking at the 185-km contour in the interior BLT Map shown in Figure 6.11, one notices that the interior BLT Map is so complex that it would be an enormous task to categorize each and every interior BLT into families. Nevertheless, we have surveyed the BLT Map to produce representative BLTs from many of the observed families. We have applied a  $1000 \times 1000$  grid to the map and used the Secant Method given in Section 6.2.4 between each node where a 185-km BLT existed. This process identified approximately 6000 BLTs, each converged to within 0.1 meters of the targeted 185-km perigee altitude. We then applied all three numerical methods mentioned in Section 6.2.4 to the interesting regions within the BLT Map to increase the density of the identified BLTs. Many of

the identified BLTs may be easily placed into families, but others appear to be isolated examples of other families. In any case, our goal has only been to survey the BLT options that exist; the following discussion presents the results of this survey.

Figure 6.23 shows the locations of each of the numerically-refined interior BLTs within the interior BLT Map. Once again, one can visibly trace numerous curves throughout this map, yet many BLTs appear in isolated locations. Upon closer inspection, it has been found that each BLT that appears to be a single point in the BLT Map is indeed a member of a continuous family of BLTs, where the family exists in a very small region within the parameter space. Figure 6.24 shows a survey of the Trans-Lunar Injection  $\Delta V$  magnitudes for each of the converged BLTs. The vast majority of the BLTs require  $\Delta V$ s with a magnitude between 3.255 and 3.285 km/s, although a few have been found that require  $\Delta V$ s as low as 3.205 km/s. Figure 6.25 shows a survey of the transfer durations of each of the converged interior BLTs. The shortest-duration interior BLTs

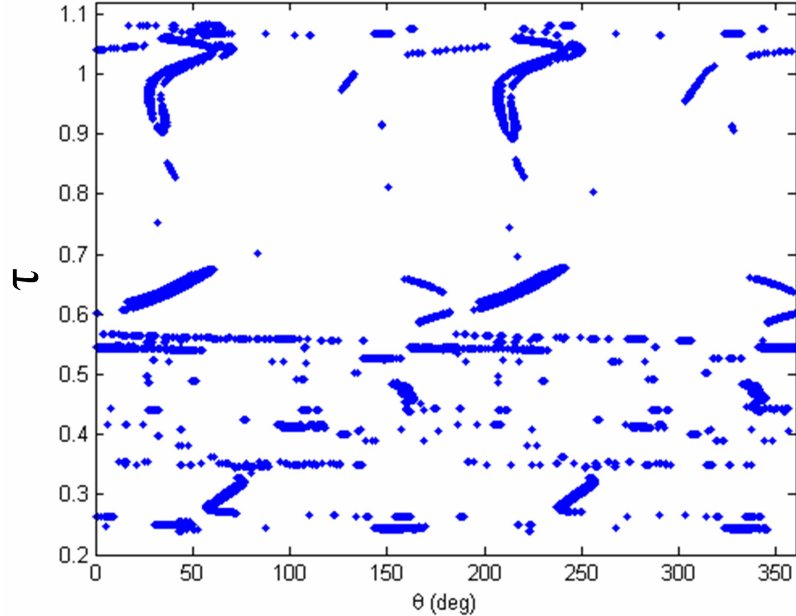


Figure 6.23: The numerically-converged  $(\theta, \tau)$ -combinations, which yield interior BLTs that depart from LEO altitudes within 0.1 meters of the desired 185 kilometers. A huge number of families of interior BLTs appear to exist.

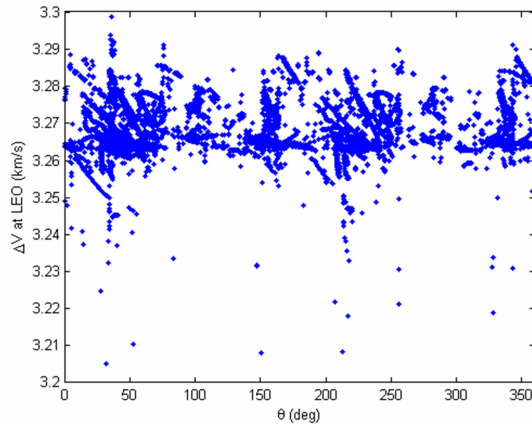


Figure 6.24: A survey of the  $\Delta V$  cost as a function of  $\theta$  for the interior BLTs displayed in Figure 6.23.

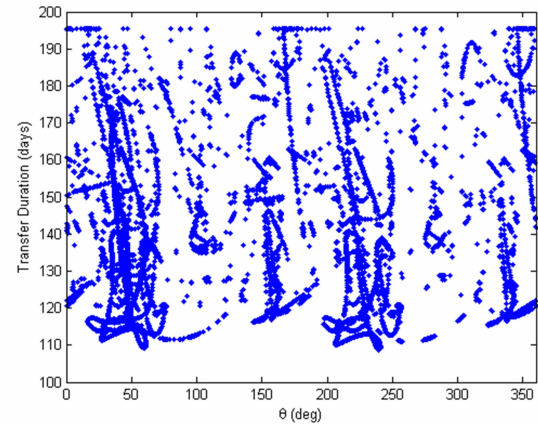


Figure 6.25: A survey of the transfer duration as a function of  $\theta$  for the interior BLTs displayed in Figure 6.23.

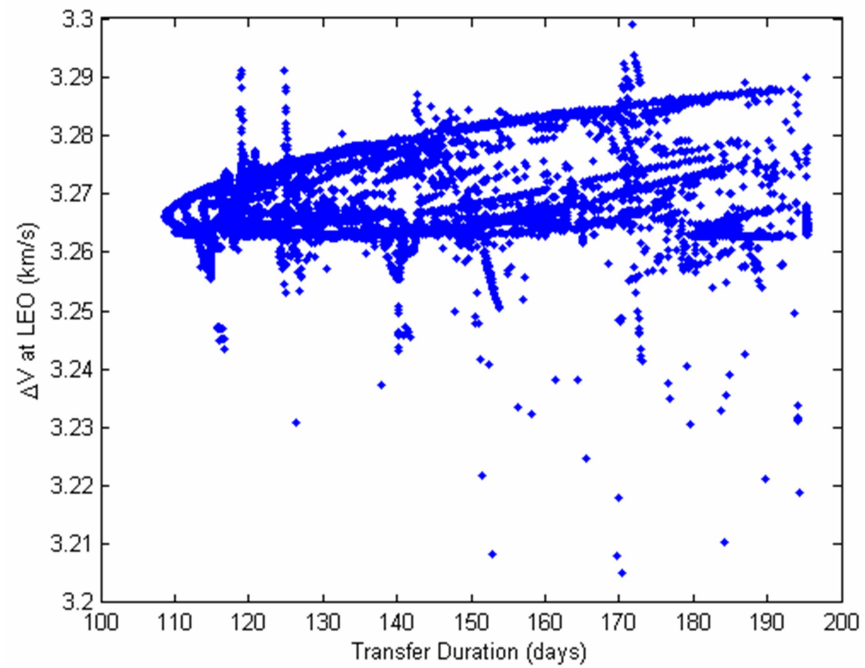


Figure 6.26: A parametric plot comparing the transfer duration with the  $\Delta V$  cost of all of the interior BLTs surveyed in Figures 6.23 – 6.25.

require approximately 109 days to approach within 100 km of the targeted Halo orbit; many BLTs require substantially more time to do so. Finally, Figure 6.26 shows a survey of the  $\Delta V$  cost of each converged BLT as a function of its transfer duration. One can see that the most efficient fast transfers, i.e., those transfers that require only 110 days of transfer time, require approximately 3.265 km/s. By allowing an increased transfer duration, one may construct BLTs with Trans-Lunar Injection maneuvers as small as 3.205 km/s.

Additional care has been taken to identify a particular curve in the interior BLT Map as a demonstration that the points shown in Figures 6.23 – 6.26 do describe families of interior BLTs. We have chosen to explore a curve that exists within a feature of the interior BLT Map, which closely resembles the feature within the exterior BLT Map that contains the example “Family A” of exterior BLTs (seen in Figure 6.13). Figure 6.27 shows the locations of the example families of exterior and interior BLTs in their respective BLT Maps. One can see that they both exist toward the edge of a very similar and prominent feature of both BLT Maps. Figures 6.28 and 6.29 show several plots of the

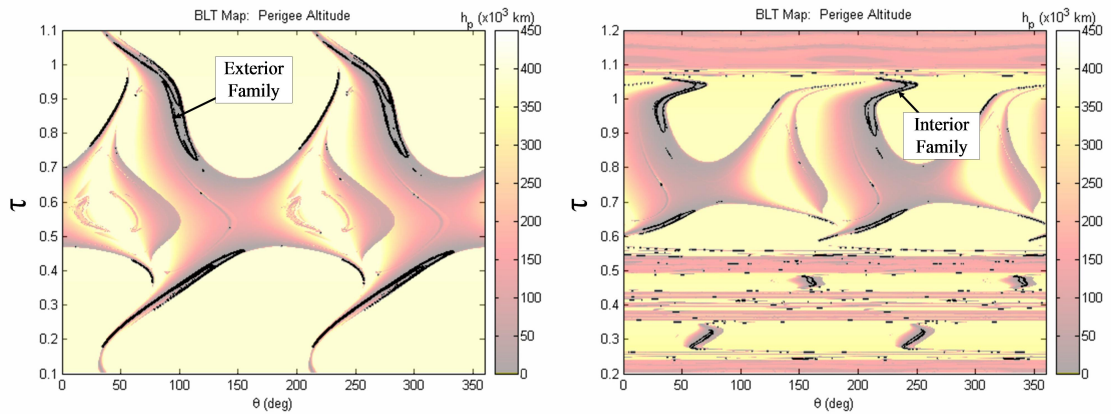


Figure 6.27: The locations of the two example families of BLTs in their respective BLT Maps. The exterior BLT Map is shown on the left and the interior BLT Map is shown on the right. The features of each BLT Map are very comparable at the two indicated locations.

shape and performance parameters of the two example families of BLTs: Figure 6.28 shows the same information as Figure 6.13 and Figure 6.29 shows the example family of interior BLTs. One can see that the BLTs are very similar, with the obvious exception that the interior BLTs make a close passage of the Moon as they arrive at the Halo orbit, whereas the exterior BLTs insert into the Halo orbit directly. Because of this difference, the interior BLTs require larger transfer durations and somewhat larger values of  $\theta$ . It is interesting to notice that the  $\Delta V$  cost of both families of BLTs are very comparable.

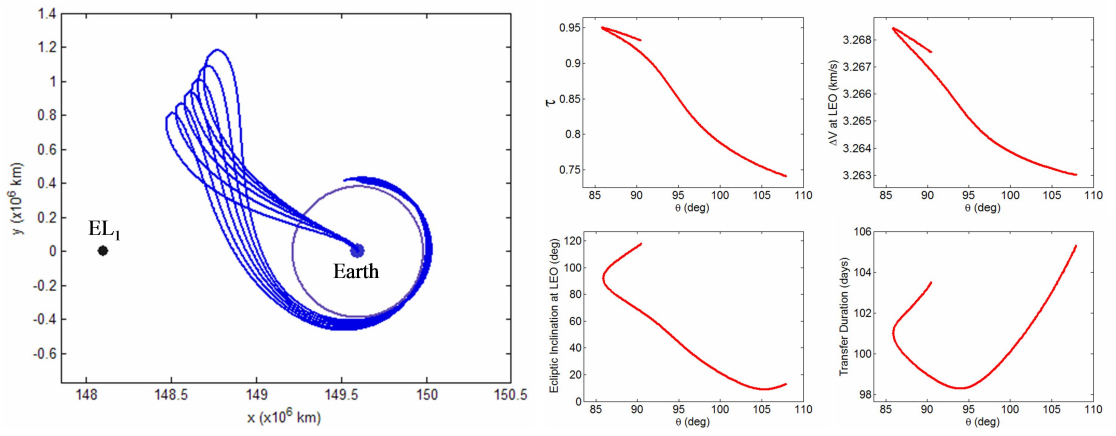


Figure 6.28: The example “Family A” of exterior BLTs along with four parametric plots showing the family’s performance parameters.

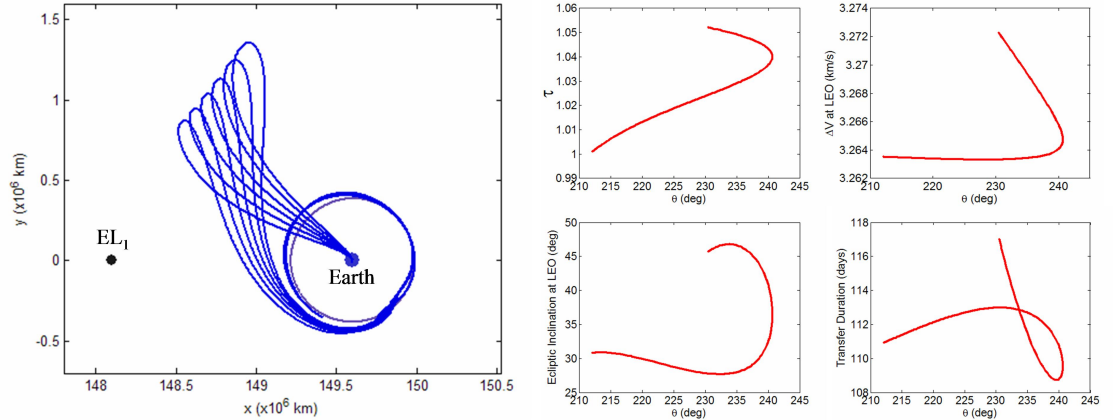


Figure 6.29: An example family of interior BLTs whose transfer characteristics compare very closely with the family of exterior BLTs shown in Figure 6.28.

### 6.3.4 Fractal Patterns Observed in the Interior BLT Map

The interior BLT Map shown in Figures 6.5 and 6.6 includes regions of the state space that appear to be chaotic: regions that are very sensitive to initial conditions. This was introduced in Section 6.2.3 when we explored the complicated interior BLT shown in Figures 6.7 – 6.9. This section explores the fractal characteristics of the interior BLT Map in more detail.

Figure 6.30 shows an example chaotic region within the interior BLT Map that has been explored in very fine detail. One can see that there is repeated structure observed at every level as the interior BLT Map is blown up. This structure would certainly continue to finer levels of detail if the propagation time of the transfer trajectories were increased.

The fractal structure observed in Figure 6.30 may be explained by the existence of

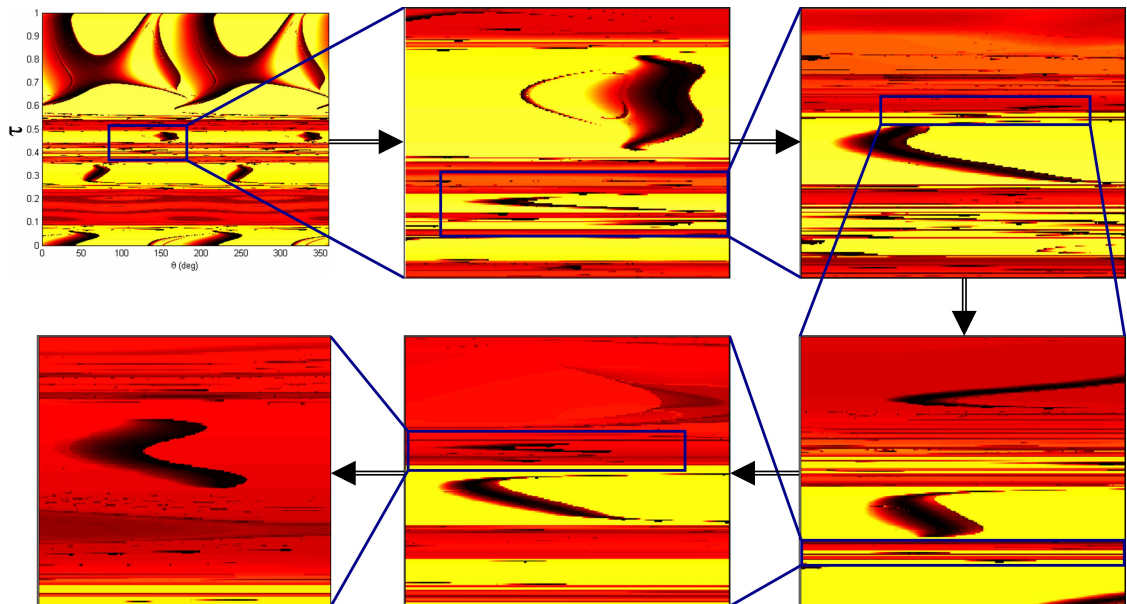


Figure 6.30: An example chaotic region within the interior BLT Map explored to very fine detail. The interior BLT Map is shown in the top-left plot; each plot continuing in a clockwise fashion zooms in to a finer level. One may observe repeating structure at each level of detail.

interior BLTs with very complicated itineraries. Section 3.10 explored how to take advantage of the unstable nature of the three-body system to construct ballistic transfers between one orbit and another. Similarly, one can build ballistic transfers to lunar Halo orbits that include very complicated itineraries, including any number of flybys, lunar staging orbits, and Earth staging orbits. The chaotic regions of the interior BLT Map are filled with these complex trajectories. Despite their chaotic nature, these complex trajectories exist in families, as can be observed in Figure 6.30. Hence, their performance parameters may be compared with other families of BLTs to evaluate their use in practical spacecraft mission designs. Although their initial conditions are very sensitive due to their complex transfer itineraries, they may be just as easy to implement in a real mission as a very simple transfer. It is likely, however, that one of these complex transfers will prove to be much more difficult to convert into the JPL Ephemeris model of the solar system than a simpler BLT.

### 6.3.5 Discussion

This section has explored the families of BLTs that exist in two example BLT Maps: the exterior and interior BLT Maps containing all possible ballistic trajectories between 185-km LEO parking orbits and a single lunar L<sub>2</sub> Halo orbit. Furthermore, these ballistic trajectories have been limited to a duration of approximately 195.4 days.

The results have shown that a very large number of families of BLTs exist that accomplish this transfer. The quickest transfers require fewer than 100 days between the Trans-Lunar Injection maneuver and the point at which the spacecraft is within 100 km of the lunar L<sub>2</sub> Halo orbit; the majority of such transfers follow trajectories in the Halo orbit's exterior stable manifold. The quickest transfers require Trans-Lunar Injection maneuvers with magnitudes of approximately 3.265 km/s. Other BLTs have been constructed that require as little as 3.200 km/s, but have transfer durations closer to 200 days and involve some combination of phasing orbits and/or lunar flybys. Finally,

it has been found that BLTs may be constructed that depart their 185-km LEO parking orbit at any ecliptic inclination with nearly any combination of  $\Delta V$  cost and transfer duration.

The following sections explore the changes in the BLT Maps when the transfer duration and the target orbit are varied.

#### 6.4 Evolving BLT Maps

The BLT Maps that have been studied in this chapter have been produced using the parameter set presented in Table 6.2 and repeated in Table 6.3. This section explores the changes that occur in the exterior and interior BLT Maps as the parameters  $\Delta t_m$  and  $C$  are varied. In every case presented in this section, we continue to permit  $\theta$  and  $\tau$  to vary throughout their full ranges and we construct both the exterior and interior BLT Maps.

Table 6.3: The parameters used to produce the BLT Maps presented in this chapter.

Parameter	Value
$F$	The family of Earth-Moon L <sub>2</sub> Halo Orbit
$C$	3.05
$\theta$	$0^\circ \leq \theta \leq 360^\circ$
$\tau$	$0 \leq \tau \leq 1$
$p$	“Exterior” and “Interior”
$\Delta t_m$	195.4 days (45 Earth-Moon time units)

By varying  $\Delta t_m$ , one studies which BLTs exist that may be used to reach a given Halo orbit in varying amounts of time. When  $\Delta t_m$  is set to a small value, one may only identify those BLTs that reach the target orbit quickly. As  $\Delta t_m$  is increased, the analysis is permitted to consider BLTs that take longer, but which may require less  $\Delta V$ . This exploration is presented in Section 6.4.1.

A change in  $C$  corresponds to a change in the target orbit. If  $C$  is perturbed slightly, the target orbit is only changed slightly and the corresponding BLTs change

very little. One can see, though, that the orbits in each family of orbits presented in Appendices A and B vary quite a bit throughout the family. Hence, the BLTs that may be used to transfer spacecraft between the Earth and each orbit in the family will vary based on the shape and stability of each orbit that is considered. This exploration is presented in Section 6.4.2.

#### 6.4.1 Varying the Transfer Duration

BLT Maps are very dependent on the length of time that each trajectory is propagated. If the value of  $\Delta t_m$  is very short, e.g., 30 days, none of the trajectories will have the time needed to depart the Halo orbit and approach the Earth. When  $\Delta t_m$  is increased to a value near 100 days, then only the quickest BLTs may be identified. The quickest BLTs are those that encounter a desirable LEO altitude at their first perigee passage, when propagated backward in time. If the propagation duration is further increased, BLTs may be identified that encounter the Earth at their second perigee passage or subsequent passages. The longer-duration BLTs may require smaller Trans-Lunar Injection  $\Delta V$ s or may implement LEO parking orbits with more desirable parameters. It is therefore interesting to observe how BLT Maps change as the value of  $\Delta t_m$  is increased.

The plots shown in Figure 6.31 demonstrate how the exterior BLT Map explored in this chapter evolves when one allows the trajectories to be propagated for varying amounts of time. Figure 6.31 includes plots that have a propagation time,  $\Delta t_m$ , between 93.6 days (21.55 nondimensional three-body time units) and 759.9 days (175.0 nondimensional three-body time units). The Jacobi constant of the target orbit has been set to a value of 3.05 in each BLT Map to be consistent with the example BLT Maps already presented in this chapter. Figure 6.32 shows the succession of plots for the same series of propagation durations for the interior BLT Map. One can see that as the time duration increases, new families of BLTs appear.

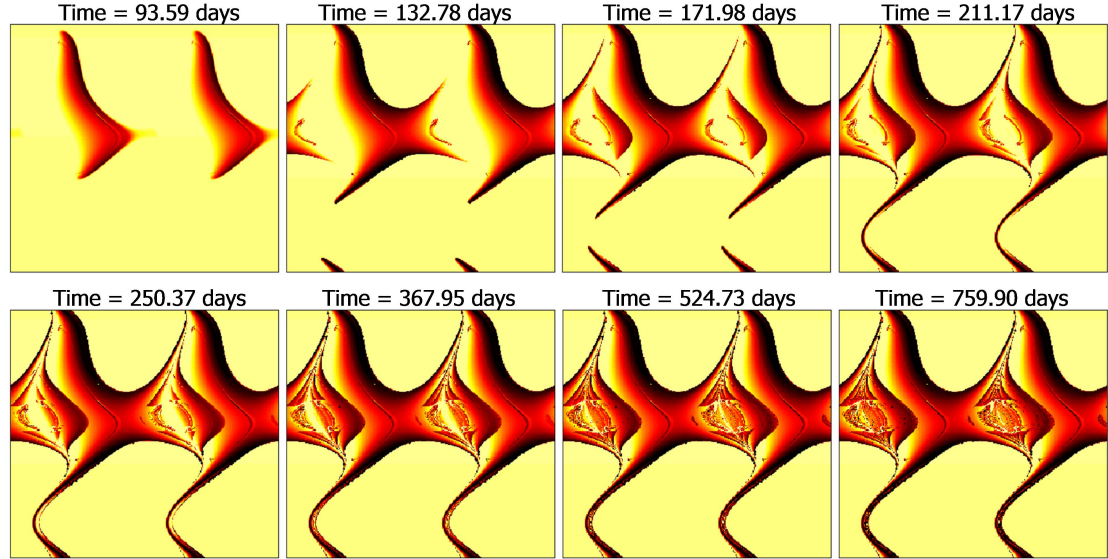


Figure 6.31: A succession of exterior BLT Maps with propagation times between 93.6 days (top-left) and 759.9 days (bottom-right). The propagation time increases from left to right and from top to bottom. For reference, the example exterior BLT Map presented in this chapter has a propagation time equal to 195.4 days.

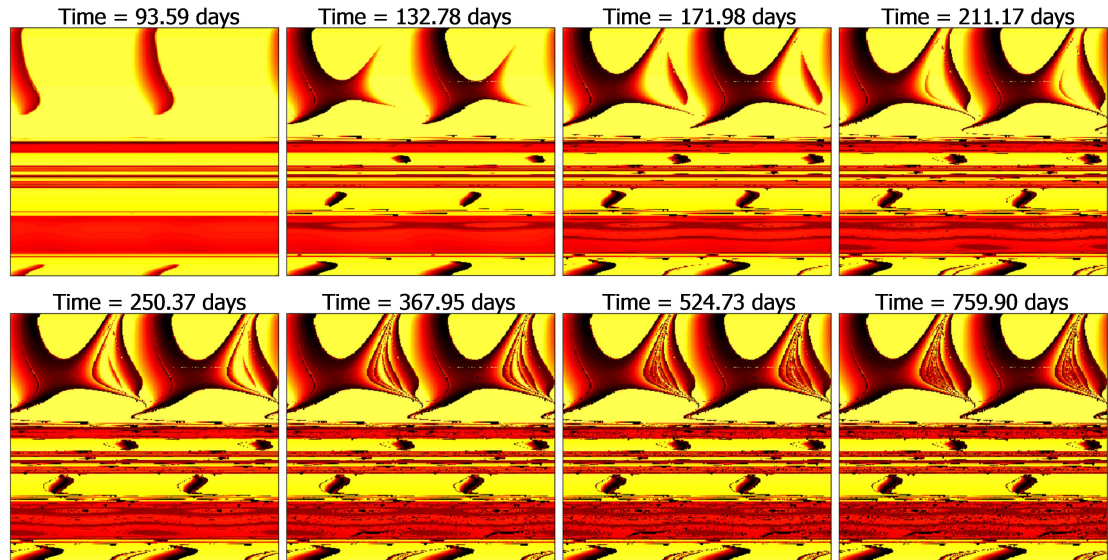


Figure 6.32: A succession of interior BLT Maps with propagation times between 93.6 days (top-left) and 759.9 days (bottom-right). The propagation time increases from left to right and from top to bottom. For reference, the example interior BLT Map presented in this chapter has a propagation time equal to 195.4 days.

The transfer duration is certainly something that mission designers must consider when designing a practical lunar mission. The value of  $\Delta t_m$  should be set to the maximum allowable transfer duration for the mission in order to ensure that all potentially useful BLTs are examined during the mission design process, and to quickly eliminate BLTs that exceed the maximum allowable transfer duration. The quickest BLTs are still considered, since their appropriate perigee passages occur after shorter amounts of time, but longer and potentially more useful BLTs are also constructed in the BLT Map.

#### 6.4.2 Varying the Lunar L<sub>2</sub> Orbit's Jacobi Constant

Each and every BLT Map produced in this chapter up to this point has had the parameter C set at a value of 3.05. That is, every BLT Map produced so far has studied transfers to a single destination: the Northern L<sub>2</sub> Halo orbit with a Jacobi constant, C, of 3.05. Figure 6.33 shows how the exterior BLT Map changes when BLTs are constructed between the Earth and L<sub>2</sub> Halo orbits with other Jacobi constant values. Figure 6.33 shows a succession of exterior BLT Maps, where a BLT Map has been constructed for orbits with Jacobi constant values between 3.022 and 3.152. Each trajectory in each BLT Map has been propagated for a duration  $\Delta t_m$  of 195.4 days to be consistent with the example BLT Maps constructed earlier in the chapter. Figure 6.34 shows a similar succession of interior BLT Maps using the same target orbits and transfer duration.

The Halo orbits with large Jacobi constant values have very low z-altitudes, whereas those with lower Jacobi constant values extend well out of the plane. Examples of different lunar L<sub>2</sub> Halo orbits are given in Appendix B. One can see in Figure 6.33 that exterior BLTs with large Jacobi constant values are more sensitive to their  $\theta$ -values and less sensitive to their  $\tau$ -values. A very interesting result of this study is that practical low-energy BLTs exist to each and every Halo orbit explored in this study.

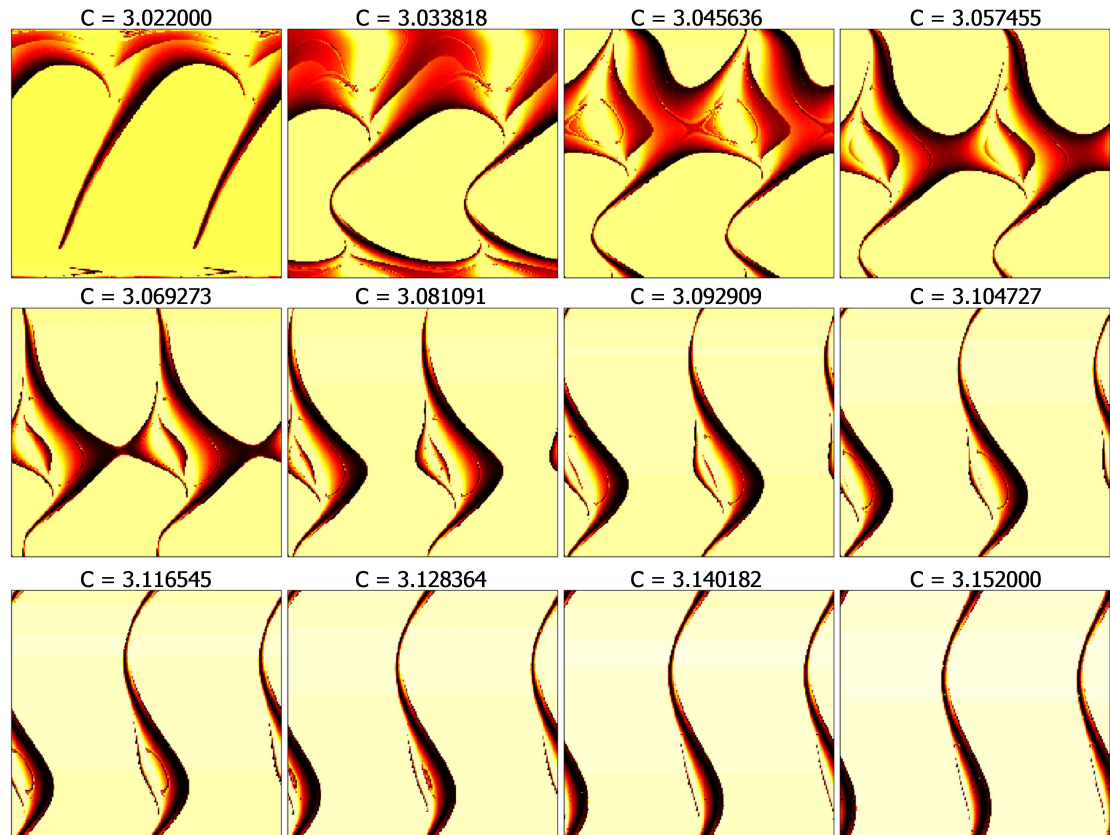


Figure 6.33: A succession of exterior BLT maps, produced by varying the Jacobi constant of the target L<sub>2</sub> Halo orbit. Each target orbit has been constructed from the family of lunar L<sub>2</sub> Halo orbits with Jacobi constant values ranging between 3.022 and 3.152. Each trajectory in each BLT Map has been propagated for 195.4 days. The Jacobi constant value increases from left to right and from top to bottom.

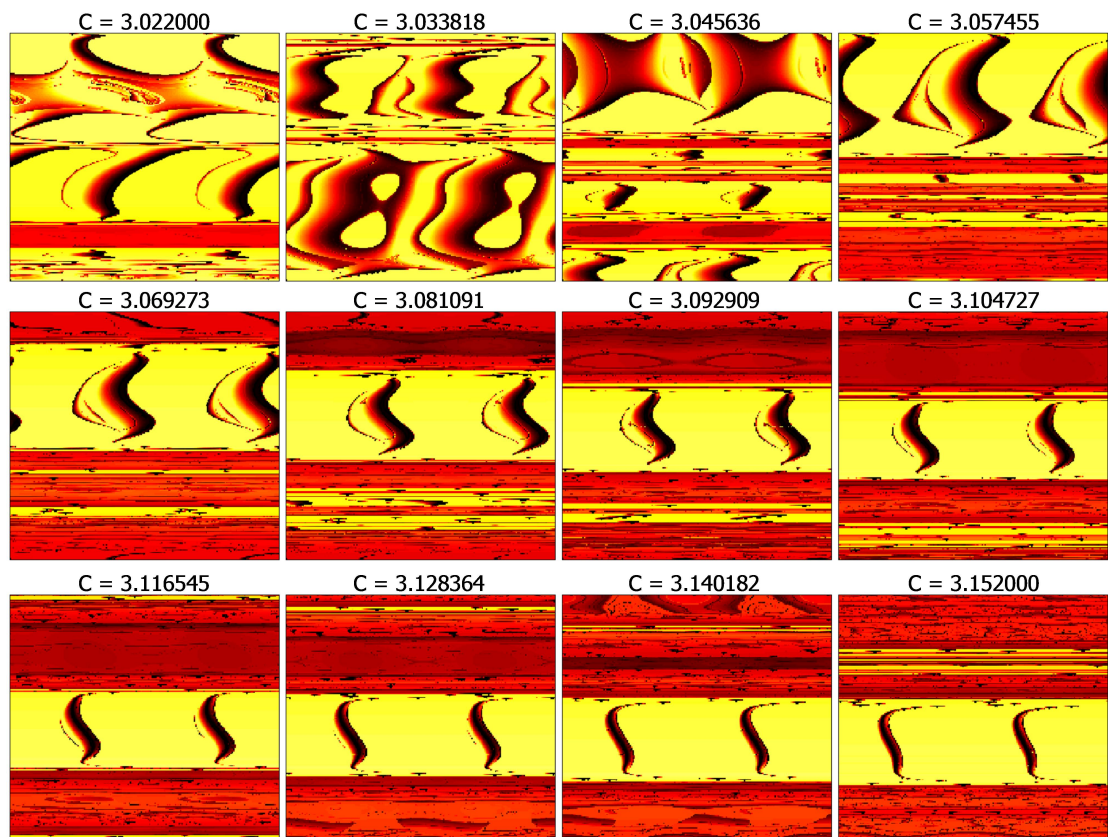


Figure 6.34: A succession of interior BLT Maps using the same parameters as Figure 6.33, but for interior BLTs. The Jacobi constant value increases from left to right and from top to bottom.

## 6.5 BLT Maps for Different Lunar Orbit Families

The example BLT produced and studied in Chapter 5 targeted a particular lunar L<sub>2</sub> Halo orbit – the same lunar L<sub>2</sub> Halo orbit that has been used to produce the two example BLT Maps studied in Sections 6.2 – 6.3 of this chapter. The purpose of this section is to demonstrate that BLTs may be produced between the Earth and nearly any unstable Earth-Moon three-body orbit, including orbits in other families, using the same methodology presented in this dissertation.

The discussion given here provides several examples of low-energy ballistic lunar transfers, as well as full BLT Maps, that have been produced using target orbits within different orbit families. Each trajectory and map produced here may be analyzed with the same techniques presented in this dissertation.

Section 6.5.1 explores BLTs that target an example lunar L<sub>1</sub> Halo orbit. Since this orbit is on the interior side of the Moon, the trajectories that target it must transfer from the lunar L<sub>2</sub> region past the Moon before encountering the target orbit.

Section 6.5.2 explores BLTs that target an example distant prograde orbit about the Moon. Orbits in this family traverse both the near and far sides of the Moon. Hence, BLTs that target these orbits may demonstrate characteristics similar to BLTs that target either L<sub>1</sub> or L<sub>2</sub> Halo orbits.

### 6.5.1 Low-Energy Transfers to a Lunar L<sub>1</sub> Halo Orbit

This section explores low-energy ballistic transfers to an example lunar L<sub>1</sub> Halo orbit. The family of lunar L<sub>1</sub> Halo orbits is classified in Appendix B as a family of Class 4 three-dimensional simple periodic symmetric orbits; they are explored in detail in Appendix B.4. In order to reach a Halo orbit about the L<sub>1</sub> point via a typical BLT, a spacecraft must depart the Earth and arrive in the lunar L<sub>2</sub> vicinity in much the same way as a spacecraft following a BLT to a lunar L<sub>2</sub> Halo orbit. Then from the vicinity of

$L_2$ , the spacecraft must transfer past the Moon before arriving at its target  $L_1$  Halo orbit. As usual, there are two types of transfers: transfers that implement either the exterior or the interior stable manifold of the  $L_1$  Halo orbit. Interior transfers may arrive on the  $L_1$  Halo orbit immediately after passing by the Moon since the interior stable manifold

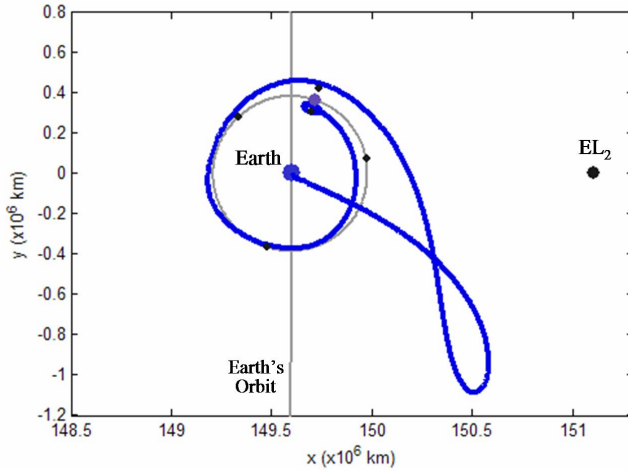


Figure 6.35: An example interior BLT to a lunar  $L_1$  Halo orbit, shown in the Sun-Earth synodic reference frame from above the ecliptic.

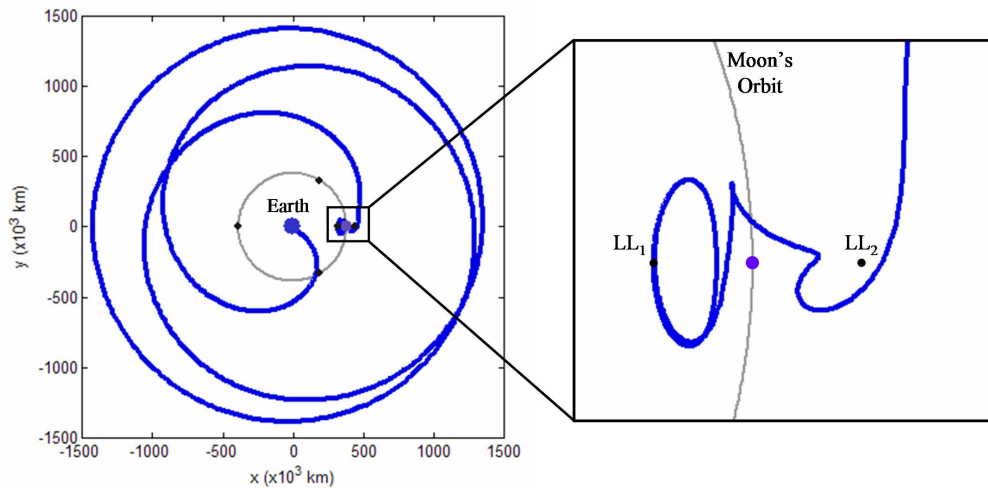


Figure 6.36: The same BLT presented in Figure 6.35, but now shown in the Earth-Moon synodic reference frame from above the ecliptic.

is propagated in that direction. Exterior transfers to most L<sub>1</sub> Halo orbits must first traverse some sort of Earth staging orbit prior to arriving on the L<sub>1</sub> Halo orbit.

Figure 6.35 shows an example interior BLT to a lunar L<sub>1</sub> Halo orbit in the Sun-Earth synodic reference frame. Figure 6.36 shows the same transfer in the Earth-Moon synodic reference frame. The characteristics of this example BLT are very similar to many of the BLTs previously studied in this dissertation that have transferred to L<sub>2</sub> Halo orbits. The only major difference is that this example BLT passes through the L<sub>2</sub> region en route to the L<sub>1</sub> region, where it encounters its target L<sub>1</sub> Halo orbit. For reference, the Halo orbit has a Jacobi constant equal to 3.05 – the same Jacobi constant as the example BLT Maps produced for the transfers to the lunar L<sub>2</sub> Halo orbit.

Figures 6.37 and 6.38 show an example exterior BLT to a lunar L<sub>1</sub> Halo orbit in the Sun-Earth and Earth-Moon synodic reference frames, respectively. One can see that the transfer involves an Earth staging orbit, which permits it to encounter the L<sub>1</sub> Halo orbit along the orbit's exterior stable manifold. Each and every exterior BLT that has been constructed in this dissertation between the Earth and this L<sub>1</sub> Halo orbit requires the use of at least one Earth staging orbit. This is because the forbidden region in the Earth-Moon system for a Jacobi constant of 3.05 only allows transfers between the interior and exterior of the system through the neck region near the Moon (see Figure 2.6 in Section 2.3.1.4). When propagated backward in time, the exterior BLTs depart the L<sub>1</sub> Halo orbit away from the Moon; hence, they must return to the Moon via an Earth staging orbit in order to transfer out of the Earth-Moon system and into the Sun-Earth system.

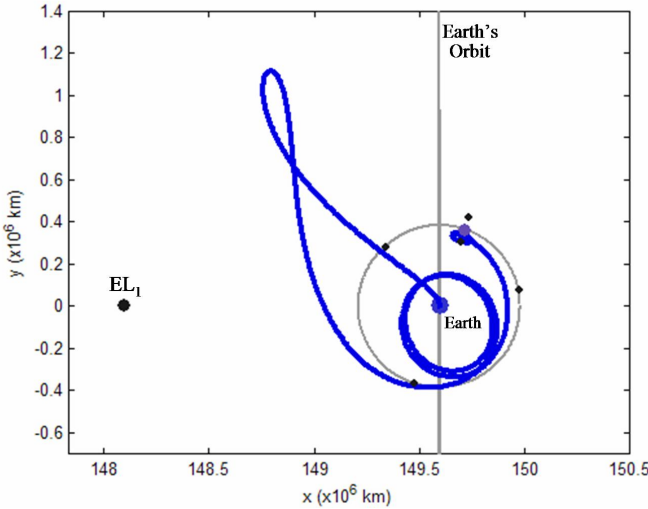


Figure 6.37: An example exterior BLT to a lunar  $L_1$  Halo orbit, shown in the Sun-Earth synodic reference frame from above the ecliptic.

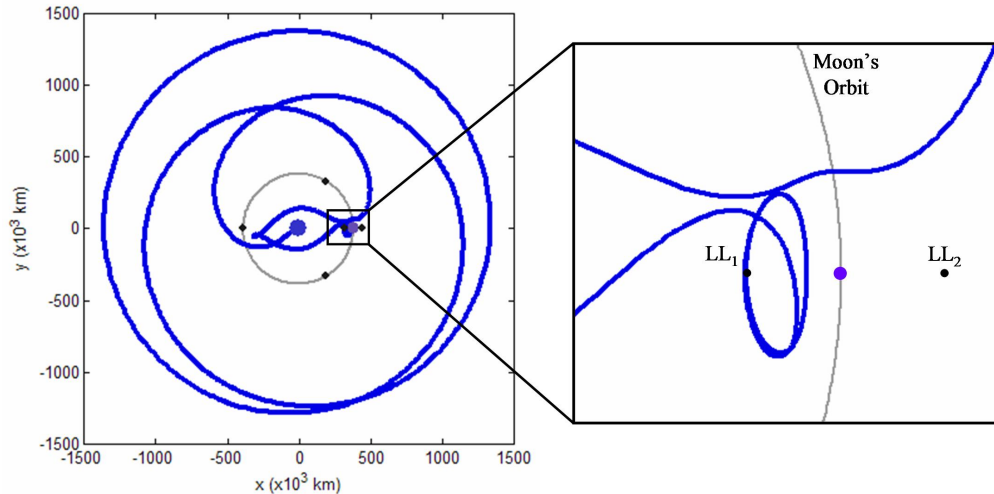


Figure 6.38: The same BLT presented in Figure 6.37, but now shown in the Earth-Moon synodic reference frame from above the ecliptic.

To characterize many BLTs to this example lunar  $L_1$  Halo orbit simultaneously, Figures 6.39 and 6.40 show the interior and exterior BLT Maps, respectively, for low-energy transfers to this Halo orbit. Each figure also shows eight example BLTs to display some of the available transfer options that exist to this Halo orbit. The color scale

in each BLT Map is exactly the same as the scale in each BLT Map presented in this dissertation: points shown in black represent BLTs that encounter the Earth at very low altitudes (including the desirable 185-km perigee altitude); points shown in white have a closest approach with the Earth of 450,000 km. Points shown in orange and yellow encounter the Earth between 150,000 and 350,000 km and are thus still not useful for most practical spacecraft missions between the Earth and this target orbit. The L<sub>1</sub> Halo orbit itself has a closest approach with the Earth of approximately 330,320 km; hence, there are no white regions of either BLT Map and the lightest shade of any BLT in the

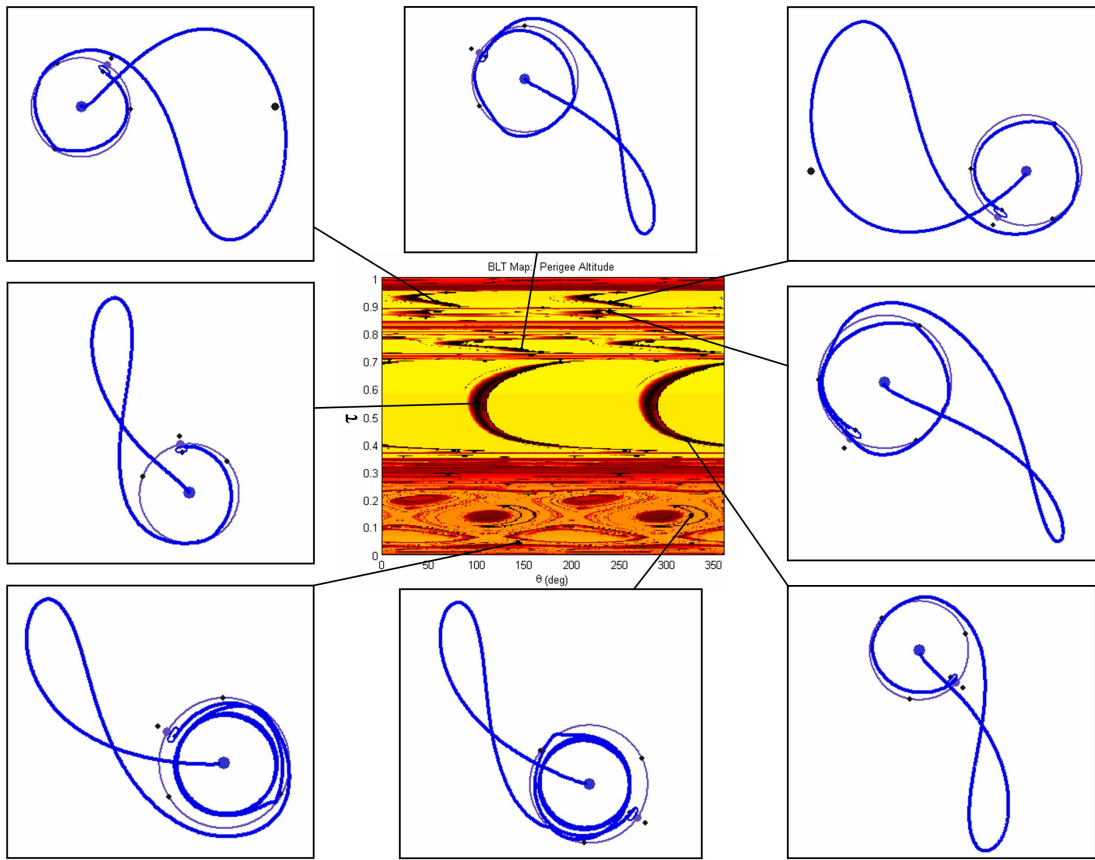


Figure 6.39: The interior BLT Map for low-energy transfers to the example lunar L<sub>1</sub> Halo orbit. The orbit has a Jacobi constant equal to 3.05; the propagation duration for each transfer shown is no greater than 195.4 days. Eight example BLTs are shown around the BLT to demonstrate some of the types of BLTs that may be constructed between 185-km LEO orbits and this Halo orbit.

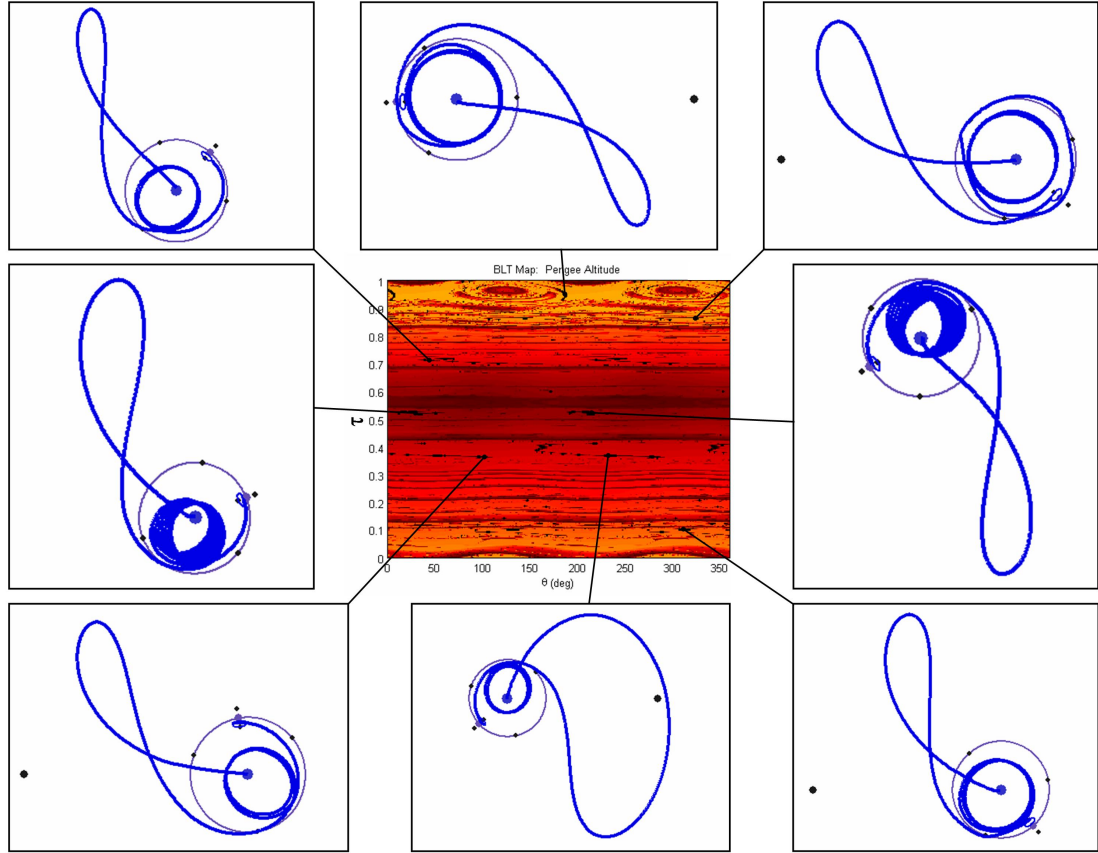


Figure 6.40: The exterior BLT Map for low-energy transfers to the example lunar L<sub>1</sub> Halo orbit. The orbit has a Jacobi constant equal to 3.05; the propagation duration for each transfer shown is no greater than 195.4 days. Eight example BLTs are shown around the BLT to demonstrate some of the types of BLTs that may be constructed between 185-km LEO orbits and this Halo orbit.

color scheme is a bright yellow. As usual, we are only interested in the darkest regions of the BLT Maps because those regions correspond with trajectories that depart from practical low Earth orbits.

One can see that the two BLT Maps shown in Figures 6.39 and 6.40 are very complex. This makes sense because the only ways to construct ballistic transfers between the Earth and this lunar L<sub>1</sub> Halo orbit require some combination of lunar passages and Earth staging orbits.

When studying Figure 6.39, one notices many things. First of all, the BLT Map

is rather simple in the range of  $\tau$ -values between 0.4 and 0.7. This region of  $\tau$ -values includes BLTs that make only a single lunar passage en route to the L<sub>1</sub> Halo orbit. These transfers resemble the simplest BLTs to lunar L<sub>2</sub> Halo orbits and have very similar performance parameters. Somewhat more complex BLTs are shown in the BLT Map for  $\tau$ -values between 0.7 and 0.96: most of these involve several close lunar passages en route to the L<sub>1</sub> Halo orbit. Every BLT constructed with a  $\tau$ -value between 0 and 0.35 involves at least one Earth staging orbit, as may be seen in the two example BLTs shown on the lower-left edge of the figure.

The exterior BLT Map shown in Figure 6.40 is more complex than the interior BLT Map. This is because each BLT must implement at least one Earth staging orbit in addition to whatever lunar passages are required to complete the low-energy transfer. One may verify this by observing that every example trajectory shown around the edge of Figure 6.40 includes at least one Earth staging orbit. Otherwise, these transfers are very similar to other BLTs previously studied.

### 6.5.2 Low-Energy Transfers to a Distant Prograde Orbit

This section explores low-energy ballistic transfers to an example distant prograde orbit about the Moon. The family of distant prograde orbits is classified in Appendix B as a family of Class 5 three-dimensional simple periodic symmetric orbits; they are explored in detail in Appendix B.5.1. Distant prograde orbits are interesting because they traverse both the near and far sides of the Moon. One might suspect that the qualitative nature of a BLT to such an orbit might take on characteristics of BLTs to either L<sub>1</sub> or L<sub>2</sub> Halo orbits, depending on how the specific BLT arrives at the orbit.

We have produced an example distant prograde orbit with a Jacobi constant equal to 3.00; such an orbit has fairly large lobes and is easy to view in the example BLTs presented here. Figure 6.41 shows an example BLT to this distant prograde orbit in the Sun-Earth synodic reference frame. Figure 6.42 shows the same example BLT

in the Earth-Moon synodic reference frame. One can see that this BLT does not enter any staging orbits, nor make any lunar flybys, but rather injects immediately into the distant prograde orbit. Other BLTs may be produced that do use staging orbits or other complex lunar flybys en route to the orbit.

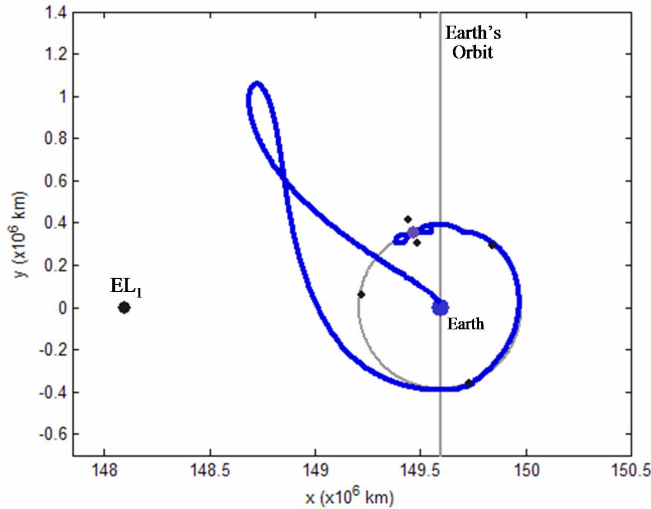


Figure 6.41: An example BLT to a distant prograde orbit, shown in the Sun-Earth synodic reference frame from above the ecliptic.

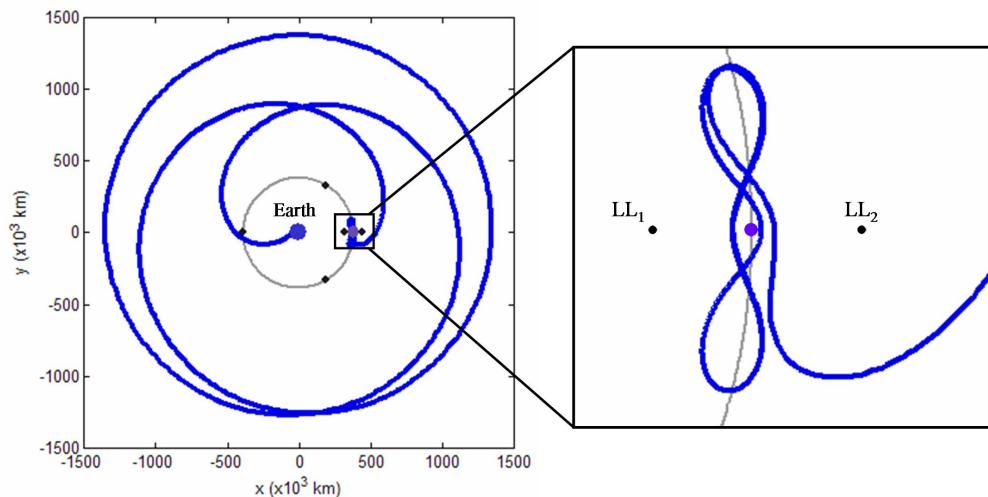


Figure 6.42: The same BLT presented in Figure 6.41, but now shown in the Earth-Moon synodic reference frame from above the ecliptic.

Because of the symmetry in the distant prograde orbit's shape, the two halves of the orbit's stable manifold are not clearly identifiable based on their immediate motion. That is, both halves of the stable manifold include both interior and exterior trajectories. However, the majority of one half of the distant prograde orbit's stable manifold propagates toward the Earth, and the majority of the other half propagates away from the Earth. This discussion refers to the half that propagates toward the Earth as the interior stable manifold and the other half as the exterior manifold. Using this nomenclature, Figures 6.43 and 6.44 show the exterior and interior BLT Maps, respectively, for low-energy transfers to this distant prograde orbit.

Along with the exterior BLT Map, Figure 6.43 also shows eight example exterior transfers that exist to this distant prograde orbit. One can see that these transfers are very simple – they don't require any lunar flybys or staging orbits to reach the target orbit. Because such simple transfers are prevalent in this exterior BLT Map, the map is consequently not nearly as chaotic as some of the previous BLT Maps studied in this chapter. The interior BLT Map shown in Figure 6.44, however, presents some more complex BLTs to this distant prograde orbit, including several examples of BLTs that require Earth staging orbits.

The characteristics of the exterior BLTs shown in Figure 6.43 resemble the characteristics of the exterior BLTs to the lunar L<sub>2</sub> Halo orbit. The only real complexity that may be introduced into the majority of such transfers is the addition of a lunar flyby en route to the transfers' apogee passages. Conversely, the characteristics of many of the interior BLTs shown in Figure 6.44 resemble the characteristics of the exterior BLTs to the lunar L<sub>1</sub> Halo orbit shown in Figure 6.40. This makes sense because the majority of both types of transfers involve Earth staging orbits, among other features.

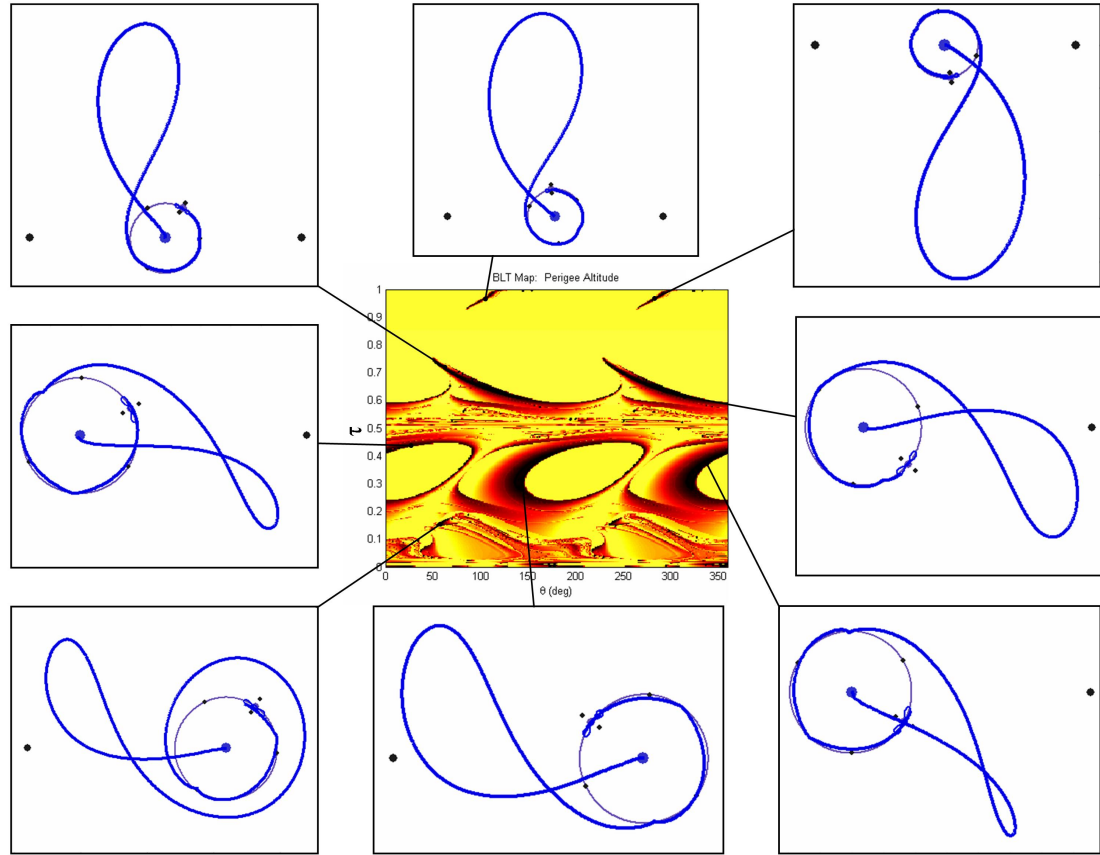


Figure 6.43: The exterior BLT Map for low-energy transfers to the example distant prograde orbit about the Moon. The orbit has a Jacobi constant equal to 3.00; the propagation duration for each transfer shown is no greater than 195.4 days. Eight example BLTs are shown around the BLT to demonstrate some of the types of BLTs that may be constructed between 185-km LEO orbits and this lunar orbit.

### 6.5.3 Discussion

This section has demonstrated that the methodology presented in this dissertation may be applied to many different families of unstable three-body orbits. The low-energy transfers and BLT Maps constructed using different target orbits may appear very different. Nonetheless, families of BLTs may still be identified and systematically evaluated in order to identify good candidates for practical lunar missions.

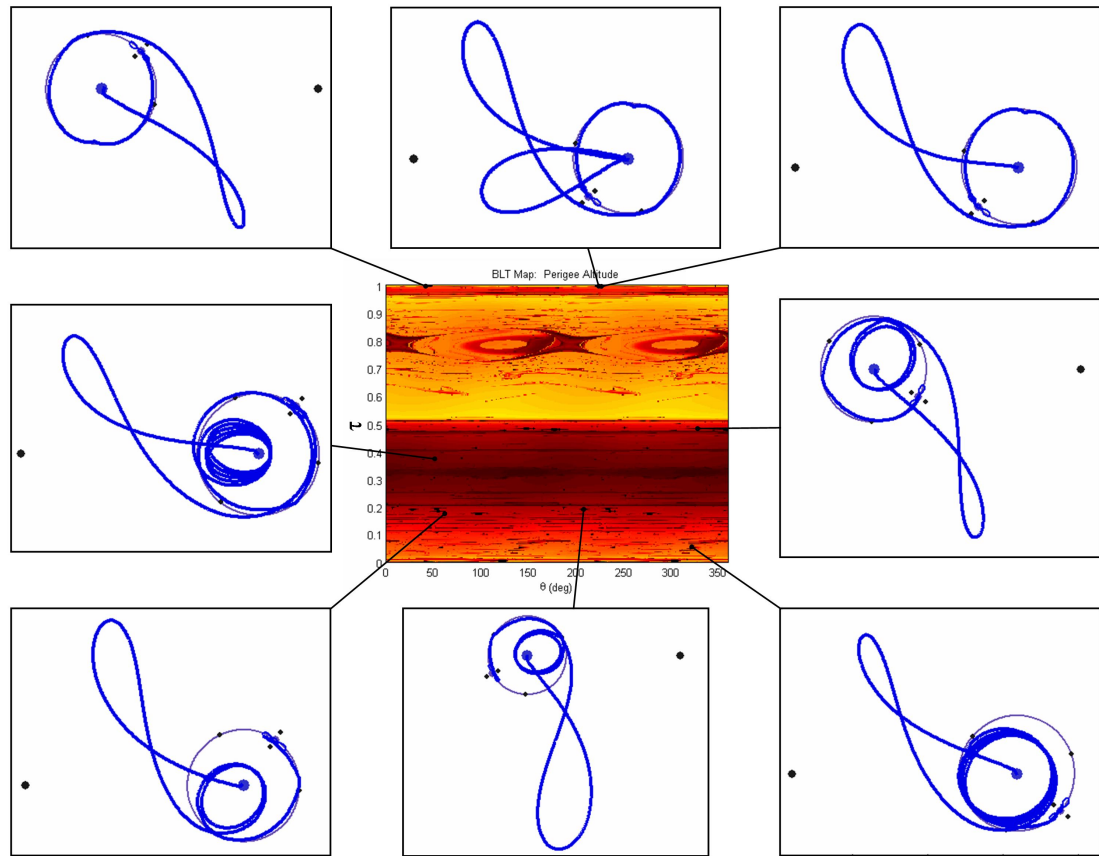


Figure 6.44: The interior BLT Map for low-energy transfers to the example distant prograde orbit about the Moon. The orbit has a Jacobi constant equal to 3.00; the propagation duration for each transfer shown is no greater than 195.4 days. Eight example BLTs are shown around the BLT to demonstrate some of the types of BLTs that may be constructed between 185-km LEO orbits and this lunar orbit.

## 6.6 Validating BLT Maps in the JPL Ephemeris Model

The low-energy transfers and BLT Maps produced in this chapter have been constructed in the Patched Three-Body model (see Section 2.4.2 and Section 5.6 for more information). The Patched Three-Body model is a model that is useful for preliminary mission designs, but it approximates many aspects of the dynamics found in the real solar system. Section 5.8 has demonstrated the validity of a particular BLT produced in the Patched Three-Body model by directly comparing it with a more realistic BLT produced in the JPL Ephemeris model of the solar system. The purpose of this section is to validate the BLT Maps produced in the Patched Three-Body model by comparing them directly with similar BLT Maps produced in the JPL Ephemeris model.

The process of constructing a BLT in the JPL Ephemeris model is described in detail in Section 5.7.1. Dynamical systems theory yields a useful set of six parameters that may be used to describe each JPL Ephemeris BLT:  $[F, C, \text{JD}_0, \tilde{\tau}, p, \Delta t_m]$ . These parameters may be used to build a BLT Map in the JPL Ephemeris model in a very similar manner as presented in Section 6.2.3 for the Patched Three-Body model. First, the parameters  $F$  and  $C$  are set to define the target three-body orbit. This orbit is differentially-corrected into the JPL Ephemeris model using the nominal Julian Date  $\text{JD}_0$  as the reference epoch. The parameter  $p$  is set to either “Exterior” or “Interior” as described in Section 6.2.3. The parameter  $\Delta t_m$ , namely, the manifold propagation duration, is set to the maximum allowable transfer duration. Finally, the two parameters  $\text{JD}_0$  and  $\tilde{\tau}$  are varied throughout some specified range to map out a BLT Map. The parameter  $\text{JD}_0$  mimics the Patched Three-Body parameter  $\theta$ , and the parameter  $\tilde{\tau}$  is the JPL Ephemeris equivalent of the Patched Three-Body parameter  $\tau$ . To build a JPL Ephemeris BLT Map that is comparable to one of the Patched Three-Body BLT Maps presented in this chapter, the parameter  $\text{JD}_0$  is varied through one synodic month of Julian Dates, and the parameter  $\tilde{\tau}$  is varied in the range  $0 \leq \tilde{\tau} \leq 1$ .

Figure 6.45 shows the exterior JPL Ephemeris BLT Map produced using the parameters shown in Table 6.4. This exterior BLT Map has been produced using conditions that closely approximate the exterior Patched Three-Body BLT Map produced in Figures 6.3 and 6.4 in order to validate the Patched Three-Body model as well as possible. The target three-body orbit is approximately the same in both the JPL Ephemeris BLT Map and the Patched Three-Body BLT Map: the quasiperiodic three-body orbit about the Earth-Moon L<sub>2</sub> point has been produced by differentially-correcting the CRTBP L<sub>2</sub> Halo orbit into the JPL Ephemeris model. The parameters  $p$  and  $\Delta t_m$  have been set the same as the corresponding parameters in the Patched Three-Body exterior BLT Map. The main difference between these two models is that the orbits of the Moon about the Earth and the Earth about the Sun are neither circular nor coplanar. Hence, BLTs produced each synodic month are not identical to each other and the JPL Ephemeris BLT Map is not perfectly periodic.

To compare the two BLT Maps directly, Figure 6.46 shows the exterior Patched Three-Body BLT Map next to the exterior JPL Ephemeris BLT Map. One can see that the main features in each map are very similar, but there are several distinct differences between the maps. These differences originate from many sources, including the non-zero inclination of the Moon's orbit about the Earth with respect to the ecliptic and the non-zero eccentricity of the Moon's orbit about the Earth.

The non-zero inclination of the Moon's orbit about the Earth with respect to the ecliptic causes several observed differences between the two BLT Maps being compared. First, the JPL Ephemeris BLT Map varies each month, which is explored further below. Second, the parameters of many of the more complicated trajectories are moved in the state space. This includes the longer-duration transfers toward the middle of each BLT Map.

The non-zero eccentricity of the Moon's orbit results in a quasiperiodic three-body orbit that pulses toward and away from the Moon; more information about this

Table 6.4: The parameters used to produce the exterior JPL Ephemeris BLT Map shown in Figure 6.45. These parameters have been designed to be as close as possible to the parameters given in Table 6.2 that produced the example exterior Patched Three-Body BLT Map presented in Figures 6.3 and 6.4.

Parameter	Value
$F$	The family of $L_2$ Halo orbits differentially-corrected into the JPL Ephemeris model using $JD_0$ as the reference epoch.
$C$	3.05
$JD_0$	$2453694.8643 \leq JD_0 \leq 2453722.8643$
$\tilde{\tau}$	$0 \leq \tilde{\tau} \leq 1$
$p$	“Exterior”
$\Delta t_m$	195.4 days

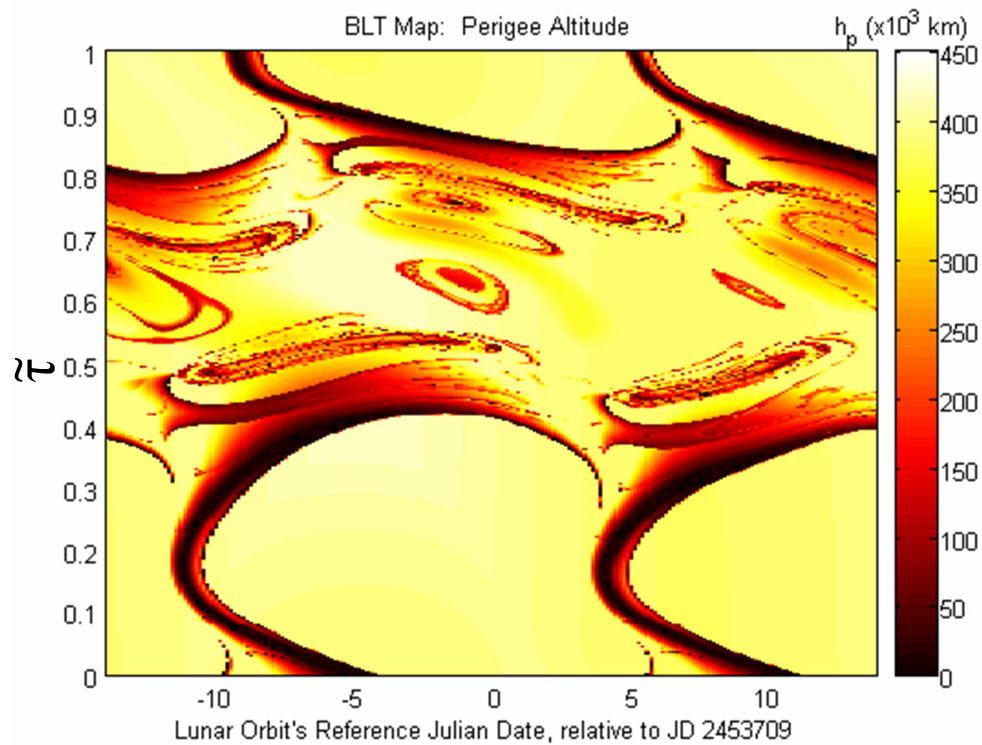


Figure 6.45: The exterior BLT Map produced in the JPL Ephemeris model of the solar system using the parameters shown in Table 6.4.

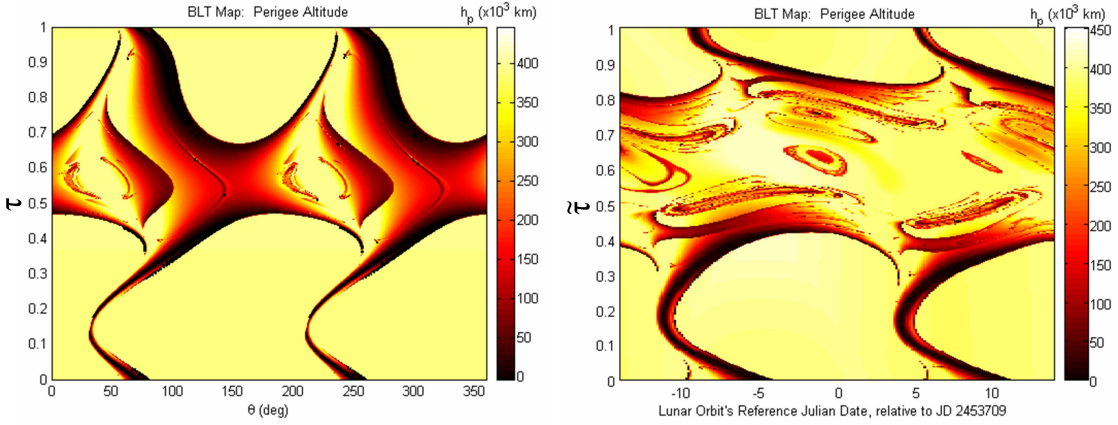


Figure 6.46: A direct comparison between the Patched Three-Body and JPL Ephemeris exterior BLT Maps targeting the L<sub>2</sub> three-body orbit with a nominal Jacobi constant of 3.05.

effect is provided in Section 3.6.3. The pulsation of the quasiperiodic three-body orbit is a major contributor to the fact that the JPL Ephemeris BLT Map is not perfectly cyclic in  $\tilde{\tau}$ . It is clear when observing the JPL Ephemeris BLT Map in Figure 6.45 that the parameters of BLTs near  $\tilde{\tau} = 1$  are somewhat different than the parameters of BLTs near  $\tilde{\tau} = 0$ . However, since the pulsation effect has a period that is approximately twice the period of the quasi-Halo orbit, the parameters of BLTs near  $\tilde{\tau} = 2$  are very similar to the parameters of BLTs near  $\tilde{\tau} = 0$ . The non-zero eccentricity of the Moon's orbit also affects the parameters of many of the more complicated trajectories in the state space.

Figure 6.47 shows the exterior JPL Ephemeris BLT Map continued over three months of reference Julian Date values. Table 6.5 summarizes the parameters that result in this extended BLT Map. One can see that the subtle differences in the BLT Map vary from month to month, although the main features exist in each month.

It is interesting to see how the JPL Ephemeris BLT Maps evolve as the Jacobi constant of the initial CRTBP Halo orbit is varied. Figures 6.48 and 6.49 show two extended three-month JPL Ephemeris BLT Maps that have been produced using initial

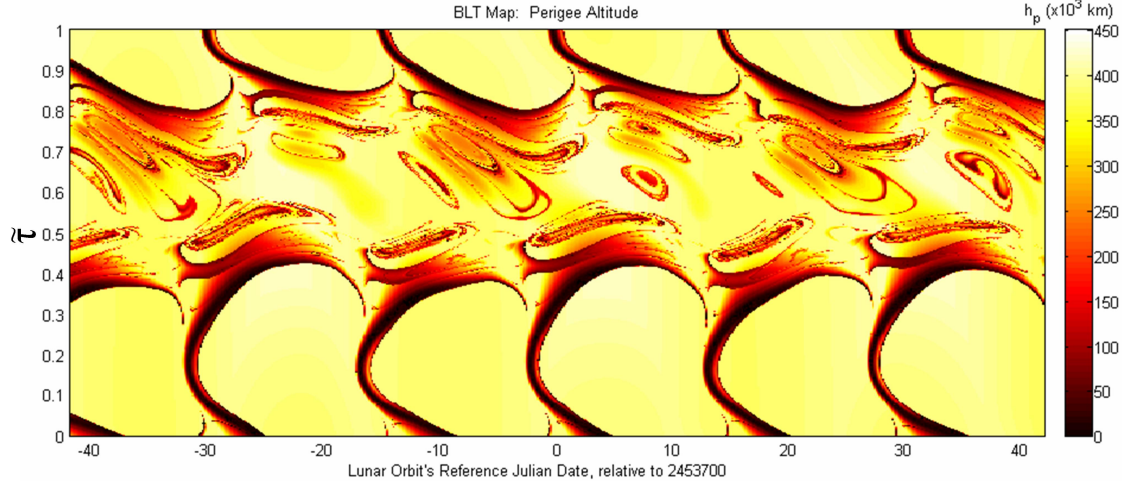


Figure 6.47: The exterior JPL Ephemeris BLT Map shown in Figure 6.45 continued over three months' worth of  $JD_0$ -values.

Table 6.5: The parameters used to produce the three extended exterior JPL Ephemeris BLT Maps shown in Figures 6.47 – 6.49.

Parameter	Value
$F$	The family of $L_2$ Halo orbits differentially-corrected into the JPL Ephemeris model using $JD_0$ as the reference epoch.
$C$	$\begin{cases} 3.05 & \text{Figure 6.47} \\ 3.10 & \text{Figure 6.48} \\ 3.15 & \text{Figure 6.49} \end{cases}$
$JD_0$	$2453658 \leq JD_0 \leq 2453742$
$\tilde{\tau}$	$0 \leq \tilde{\tau} \leq 1$
$p$	"Exterior"
$\Delta t_m$	195.4 days

CRTBP Halo orbits with Jacobi constant values of 3.10 and 3.15, respectively. Table 6.5 summarizes the parameters that result in these two extended BLT Maps, as well as the parameters that result in the original extended BLT Map shown in Figure 6.47. One can see that the same sorts of variations exist from month to month in these two JPL Ephemeris BLT Maps as has been observed in the extended JPL Ephemeris BLT Map shown in Figure 6.47. In addition, one notices that the JPL Ephemeris BLT Maps evolve with their reference Jacobi constant values in much the same way as the Patched

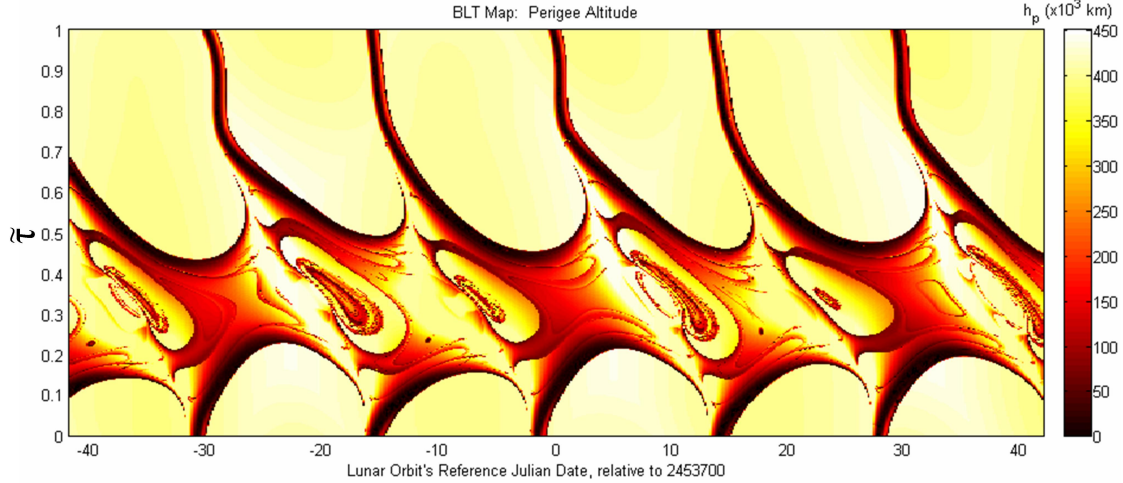


Figure 6.48: The exterior JPL Ephemeris BLT Map with an initial Jacobi constant of 3.10 continued over three months' worth of  $JD_0$ -values.

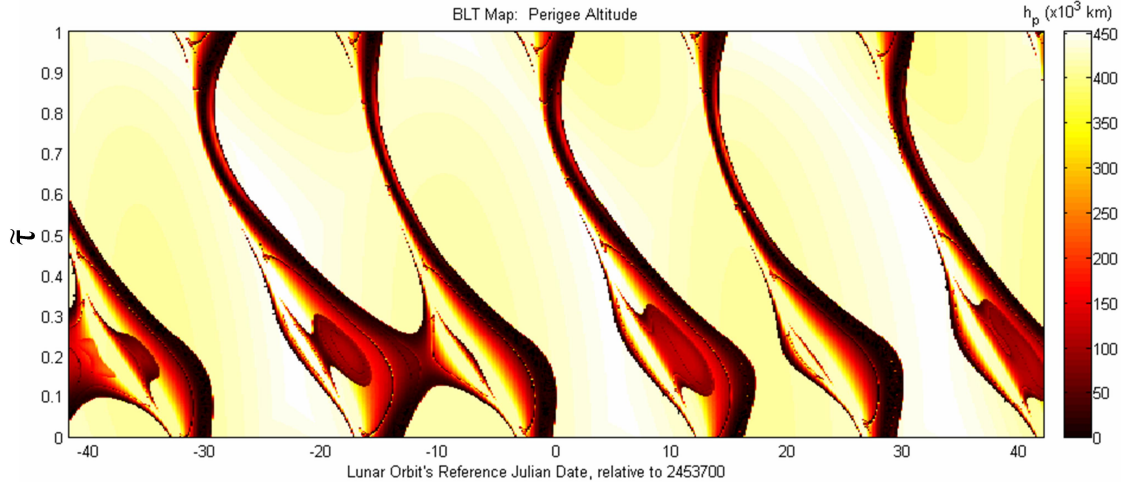


Figure 6.49: The exterior JPL Ephemeris BLT Map with an initial Jacobi constant of 3.15 continued over three months' worth of  $JD_0$ -values.

Three-Body BLT Maps have been observed to do in Section 6.4.2. It is interesting to note, though, that the JPL Ephemeris BLT Map at one Jacobi constant appears more comparable to a Patched Three-Body BLT Map at a lower Jacobi constant value. One hypothesis that would explain this observation is that the discrepancy is caused by the fact that the quasi-Halo orbits in the JPL Ephemeris model are further out of the ecliptic

plane than Halo orbits in the CRTBP due to the non-zero inclination of the Moon's orbit with respect to the ecliptic. The CRTBP Halo orbits at lower Jacobi constant values extend further out of the ecliptic. Hence, the trajectories associated with a particular quasi-Halo orbit in the JPL Ephemeris model may be more comparable to the corresponding trajectories associated with a CRTBP Halo orbit with a lower Jacobi constant value.

Although there are differences between the shapes of the features in the Patched Three-Body BLT Maps and the JPL Ephemeris BLT Maps, each state space map reveals the same qualitative sets of families of BLTs. Figure 6.50 shows the same exterior JPL Ephemeris BLT Map shown in Figure 6.45, but now presented with 12 example exterior BLTs around its perimeter. One can see that the same families of simple exterior BLTs exist in the JPL Ephemeris model as in the Patched Three-Body model. One can also see that families of more complex exterior BLTs also exist in the JPL Ephemeris model as they do in the Patched Three-Body model.

This section has demonstrated that the Patched Three-Body approximation of the BLT Maps results in the same families of BLTs that exist in the JPL Ephemeris BLT Maps. One may either use the Patched Three-Body model to produce a desirable BLT and then convert that BLT into the JPL Ephemeris model using the Conversion method given in Section 5.7.2; or one may begin in the JPL Ephemeris model and build the JPL Ephemeris BLT Map directly. Either process uses knowledge gained from the simplified CRTBP system, but works to produce real trajectories that may be applied to practical spacecraft mission designs.

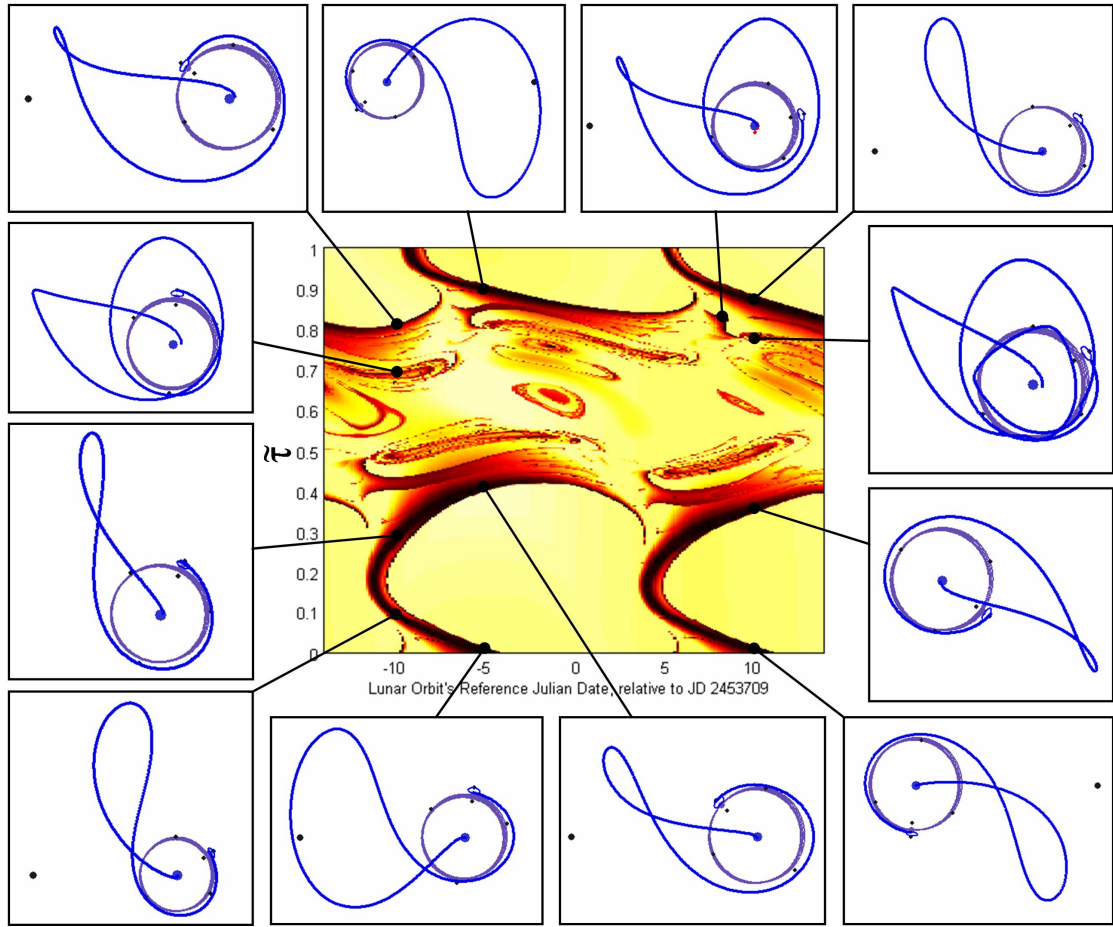


Figure 6.50: The same exterior JPL Ephemeris BLT Map shown in Figure 6.45, but now with 12 example exterior BLTs around its perimeter. One can see that the same families of simple exterior BLTs exist in the JPL Ephemeris model as in the Patched Three-Body model.

## 6.7 Summary and Conclusions

The purpose of this chapter has been to demonstrate that dynamical systems methods may be used to identify families of low-energy ballistic lunar transfers. This is made possible because dynamical systems methods allows one to parameterize a BLT in a simple way. In Section 6.2.2, it was observed that by changing two parameters in a systematic fashion, e.g., the parameters  $\theta$  and  $\tau$ , one can trace out a family of BLTs. In Section 6.2.3, the parameters  $\theta$  and  $\tau$  were varied throughout their entire ranges to

produce two example BLT Maps. One BLT Map included example exterior BLTs and one BLT Map included interior BLTs. Families of BLTs may be identified on a BLT Map by tracing out a contour that corresponds to a desired transfer parameter, i.e., the desired LEO altitude. This chapter has studied the set of families of BLTs that each depart from a point 185 kilometers above the surface of the Earth. In theory, any type of parking orbit may be used, but to compare the performance of each BLT directly, it was assumed that the parking orbit was a 185-km circular low Earth orbit.

Sections 6.3 – 6.5 studied BLT Maps in depth. Section 6.3 surveyed several families of exterior and interior BLTs that were identified from their respective BLT Maps. It also explored the fractal pattern observed in the interior BLT Map (§6.3.4). Section 6.4 studied the evolution of both exterior and interior BLT Maps when their parameters were varied, including the parameters  $\Delta t_m$  (§6.4.1) and  $C$  (§6.4.2). Each BLT Map constructed up to that point was produced using target Earth-Moon orbits in the family of  $L_2$  Halo orbits. Section 6.5 studied BLT Maps for different families of target orbits, including  $L_1$  Halo orbits (§6.5.1) and Distant Prograde Orbits (§6.5.2). It was found that families of BLTs exist to each of these classes of target three-body orbits.

Finally, Section 6.6 discussed how to build a BLT Map in the JPL Ephemeris model. The JPL Ephemeris BLT Maps produced in Section 6.6 were found to be very similar to the corresponding Patched Three-Body BLT Maps. They contain the same large-scale features and evolve in a similar fashion as their parameters are varied. The most significant result of Section 6.6 is that the JPL Ephemeris BLT Maps can be used in the same way as the Patched Three-Body BLT Maps in order to identify families of BLTs. Most of the families identified were qualitatively similar to families of Patched Three-Body BLTs. In conclusion, Section 6.6 showed that the dynamical systems methodology may be used to design real missions in the JPL Ephemeris model of the solar system.

This chapter has demonstrated that a wide variety of BLTs exist. The surveys

of exterior BLTs and interior BLTs in Sections 6.3.1 and 6.3.3, respectively, showed that BLTs can be constructed that may be used to transfer a spacecraft between the Earth and the target L<sub>2</sub> Halo orbit with a wide range of performance parameters. A large number of BLTs exist that may be used to transfer the spacecraft to within 100 km of the Halo orbit in fewer than 120 days. BLTs constructed in the Patched Three-Body model require Trans-Lunar Injection ΔVs with magnitudes as low as 3.2 km/s. The BLTs produced in the JPL Ephemeris model have performance parameters that vary per month based on the location of the Moon. Some BLTs produced in the JPL Ephemeris model have been constructed that require Trans-Lunar Injection ΔVs with magnitudes smaller than 3.2 km/s. Furthermore, BLTs may be produced that depart from LEO parking orbits at any inclination and nearly any day of each month.

Chapter 7 continues this study by addressing specific applications of BLTs to practical spacecraft mission design. The chapter considers which BLTs may be used to depart from a specific LEO parking orbit and how often a departure opportunity presents itself. In addition, the chapter addresses how a low-energy transfer impacts the spacecraft system design when compared with conventional direct transfers.

## **Chapter 7**

### **Applications to Practical Mission Design**

The purpose of this chapter is to study the applications of low-energy orbit transfers and dynamical systems analysis tools to practical spacecraft mission designs. This chapter focuses on spacecraft missions between the Earth and the Moon and in the Earth-Moon environment, however, many of the discussions may be generalized to any type of low-energy transfer in a multi-body system.

This chapter begins in Section 7.1 with a discussion about the impact that low-energy trajectories have on spacecraft systems, when compared to conventional, direct orbit transfers. Section 7.1 considers how a low-energy transfer may increase a spacecraft's payload mass and reduce its propulsion system requirements. The section also considers how a low-energy orbit transfer impacts a spacecraft's mission operations as well as the spacecraft's communication, power, thermal, and attitude determination and control systems.

Section 7.2 studies how to apply knowledge of a BLT Map to the development of practical spacecraft mission designs that implement BLTs. The discussions include how to identify the potential departure opportunities of a spacecraft in a LEO parking orbit (§7.2.1 – §7.2.2) and how to use a BLT Map to build a trajectory to rendezvous with an existing object in a lunar Halo orbit (§7.2.3). Section 7.2 concludes with a discussion about how to transfer a spacecraft from a random initial Earth orbit onto a low-energy BLT using as little energy as possible (§7.2.4).

Finally, Section 7.3 provides a general survey about how to apply the dynamical systems methods and low-energy trajectories presented in this dissertation to a variety of different mission design scenarios.

## 7.1 Spacecraft Systems Considerations

There are many subtle costs and benefits associated with implementing an unstable three-body orbit or a low-energy orbit transfer in a mission rather than using a more conventional orbit or a direct orbit transfer. This section addresses several of the spacecraft system considerations one may encounter when implementing a low-energy trajectory.

The discussions in this section may be applied to many different mission design scenarios. We have chosen three basic mission design concepts to focus these discussions on, when appropriate, since these scenario concepts are very relevant to this dissertation:

**Scenario A.** A spacecraft is to perform a transfer between a circular 185-km LEO parking orbit and the lunar L<sub>2</sub> Halo orbit with a Jacobi constant of 3.05. The main options to be considered are a direct transfer, i.e., one of the transfers studied in Section 4.3, and a low-energy BLT, i.e., one of the transfers studied in Section 6.3.

**Scenario B.** A spacecraft is to perform a transfer between a circular 185-km LEO parking and a circular 100-km lunar orbit. The main options to be considered are a direct transfer, i.e., one of the transfers studied in Section 4.2, and a low-energy transfer. In this scenario, the low-energy transfer consists of a transfer to a lunar Halo orbit followed by a transfer down to the low lunar orbit, similar to the transfer presented in Section 5.3.5.

**Scenario C.** A spacecraft is to perform a transfer between a circular 185-km LEO parking and a frozen lunar orbit (for more information on frozen lunar orbits, see, e.g., Folta and Quinn, 2006, and Russell and Lara, 2006, and the references therein). The transfer options are identical to Scenario B. To keep Scenario C comparable to Scenario B, a  $100 \times 8000$  km frozen orbit has been chosen as the target orbit. This orbit has a semi-major axis of approximately 5789 km, an eccentricity of approximately 0.68 and an inclination of approximately  $55^\circ$ .

The low-energy options of the latter two Scenarios are extensions of Scenario A, since the low-energy options may use any of the same transfers considered in Scenario A to reach the lunar Halo orbit. The simplest BLTs considered in this dissertation transfer from LEO to lunar  $L_2$  Halo orbits, although BLTs may be constructed to any unstable three-body orbit near the Moon. Hence, for simplicity in Scenarios B and C we only consider low-energy transfers that visit the lunar  $L_2$  Halo orbit en route to the target low lunar orbit.

The goals set for Scenario A may be met by numerous trajectory options. Table 7.1 provides several good examples of trajectories that trade transfer time with  $\Delta V$  cost. One can see that the more time is spent in the orbit transfer, the less total  $\Delta V$  is required for the transfer.

Table 7.1: A summary of ballistic transfer options for a transfer between a circular 185-km LEO parking orbit and a lunar  $L_2$  Halo orbit with Jacobi constant of 3.05.

Mission Itinerary	Transfer Duration	$\Delta V_1$ (km/s)	$\Delta V_2$ (km/s)	Total $\Delta V$ (km/s)	Reference Section
LEO – $L_2$	$\sim 5$ days	3.1497	0.8326	3.9823	4.3.2.3
LEO – $L_2$	$\sim 39$ days	3.1733	0.6682	3.8415	4.3.2.3
LEO – $L_2$	$\sim 54$ days	3.1764	0.5817	3.7581	4.3.2.4
LEO – $L_1$ – $L_2$	$\sim 50$ days	3.1176	0.5012	3.6188	4.3.3
LEO – $L_1$ – $L_2$	$\sim 60$ days	3.1178	0.4696	3.5874	4.3.3
LEO – BLT – $L_2$	$\sim 95$ days	3.2650	0.0000	3.2650	6.3.1
LEO – BLT – $L_2$	$\sim 190$ days	3.2006	0.0000	3.2006	6.3.1

The goals set for Scenarios B and C may be met by transferring a spacecraft directly between the low Earth and the low lunar orbits or by visiting the L<sub>2</sub> Halo orbit en route. Table 7.1 already considered the trajectory options that may be used to reach the lunar L<sub>2</sub> Halo orbit; Table 7.2 summarizes the remaining trajectory segments that may be used to complete the goal of the transfer in Scenarios B and C.

Table 7.2: A summary of trajectory segments that may be used to transfer a spacecraft from a circular 185-km LEO parking orbit to a 100-km circular lunar orbit (LLO) or to the 100 × 8000 km frozen orbit, in addition to those segments presented in Table 7.1.

Mission Scenario	Mission Itinerary	Transfer Duration	$\Delta V_1$ (km/s)	$\Delta V_2$ (km/s)	Total $\Delta V$ (km/s)	Reference Section
B:	LEO – LLO	~ 4.5 days	3.1341	0.8133	3.9474	4.2
B:	L <sub>2</sub> – LLO	~ 20 days	0.0000	0.6440	0.6440	5.3.5
C:	LEO – Frozen	~ 4.5 days	3.1341	0.3281	3.4622	4.2
C:	L <sub>2</sub> – Frozen	~ 20 days	0.0000	0.1588	0.1588	5.3.5

The trajectory segments presented in Tables 7.1 and 7.2 are used in the following sections to evaluate the costs and benefits associated with low-energy transfers compared to direct transfers.

### 7.1.1 Increased Payload Mass

If all other factors are the same, a spacecraft's mass may be reduced by reducing the  $\Delta V$  requirements of the mission. Hence, a smaller rocket may be used to send the spacecraft to its destination. Alternatively, if a mission's  $\Delta V$  requirements are reduced, then the same launch vehicle may be used to send a larger spacecraft to the same destination. This discussion first determines the maximum amount of mass that may be placed into a lunar orbit using a direct, conventional lunar transfer. It then evaluates how much additional mass may be placed into the same orbit using a low-energy lunar transfer.

The capabilities of modern launch vehicles vary widely, from being able to place

a small payload into a circular 185-km orbit to being able to send a sizeable spacecraft payload to the Moon. In order to simplify this study, it is assumed that the launch vehicle's only purpose is to place a two-stage spacecraft system into a circular 185-km LEO parking orbit. Then that spacecraft system performs the necessary maneuvers to reach its lunar orbit destination. In reality, the launch vehicle would most likely perform the Trans-Lunar Injection maneuver, but since each launch vehicle performs differently, that trade study would become unwieldy very quickly.

Table 7.3 summarizes the capability of several example launch vehicles to place a spacecraft into a LEO parking orbit. Unless otherwise noted, the table presents the maximum mass that the launch vehicle can place into a circular 185-km LEO parking orbit. This information has been gathered from Encyclopedia Astronautica (2007).

Table 7.3: The maximum mass that several launch vehicles can place into a LEO parking orbit. Those entries marked with a \* indicate an ISS-rendezvous orbit, otherwise the entries represent the maximum mass capability for a circular 185-km LEO parking orbit (Encyclopedia Astronautica, 2007).

Launch Vehicle	LEO Payload (kg)	Launch Vehicle	LEO Payload (kg)
Delta IV Medium	13,600	Delta IV Heavy	25,800
Atlas V 401	12,500	Atlas V 551	20,050
Ariane 42L	8,000	Ariane 5 EC-A	16,000*
PSLV	3,700	Falcon 9	8,000*
H-2A	12,000	Proton 8K82K / Briz-M	21,000*

For this discussion, it will be assumed that the spacecraft system that will transfer to the Moon includes the two propulsion stages shown in Table 7.4. The first stage has been modeled to be similar to the upper stages of many of the modern launch vehicles shown in Table 7.3. It uses a  $\text{LO}_\text{X}/\text{LH}_\text{2}$  bipropellant system and minimizes the inert mass of the stage. The upper stage uses a NTO/Hydrazine bipropellant system that is modeled after several interplanetary spacecraft propulsion systems, such as Mars Odyssey (NASA, 2007c). For simplicity, we will use the approximation that each stage's inert mass, namely, the mass of all parts of the propulsion system except for

Table 7.4: A summary of the two stages of a fictitious spacecraft propulsion system that will be used to transfer the spacecraft from the Earth to the Moon.

<b>Stage 1</b>	
Parameter	Value
Propellant	LOX/LH <sub>2</sub>
$I_{sp}$	450 seconds
Inert Mass Fraction, $f_{inert}$	8%
<b>Stage 2</b>	
Parameter	Value
Propellant	N <sub>2</sub> O <sub>4</sub> /N <sub>2</sub> H <sub>4</sub>
$I_{sp}$	320 seconds
Inert Mass Fraction, $f_{inert}$	14%

the fuel, is equal to some percentage of the mass of the entire propulsion system. We have assumed that the upper stage's inert mass fraction is higher than the first stage's, largely because of the difference in  $\Delta V$  magnitude that each stage must perform.

We would like to derive a relationship for the amount of payload we can send to the Moon as a function of the initial mass of the spacecraft in the LEO parking orbit and the required  $\Delta V$  values for the transfer. The maximum obtainable  $\Delta V$  that each stage of the spacecraft system may impart to its payload, assuming that the stage acts as an ideal rocket, may be found using the ideal rocket relationship (see, e.g., Sutton and Biblarz, 2001):

$$\Delta V = I_{sp}g_0 \ln M_R, \quad (7.1)$$

where  $I_{sp}$  is the specific impulse of the rocket,  $g_0$  is the standard sea level acceleration of gravity equal to approximately 9.80665 m/s<sup>2</sup> (Sutton and Biblarz, 2001), and  $M_R$  is the mass ratio. We will assume that each maneuver depletes that stage's propellant. After the first maneuver, the first stage is discarded. After the second maneuver, any remaining fuel is considered payload to be used for mission operations. Then the mass

ratio for both maneuvers is equal to  $m_i/m_f$ , where

$$m_i = m_{\text{payload}} + m_{\text{propellant}} + m_{\text{inert}} \quad \text{and} \quad (7.2)$$

$$m_f = m_{\text{payload}} + m_{\text{inert}} \quad (7.3)$$

In this discussion, the propellant and inert mass fractions,  $f_{\text{propellant}}$  and  $f_{\text{inert}}$ , respectively, are equal to:

$$f_{\text{propellant}} = \frac{m_{\text{propellant}}}{m_{\text{propellant}} + m_{\text{inert}}} \quad (7.4)$$

$$f_{\text{inert}} = \frac{m_{\text{inert}}}{m_{\text{propellant}} + m_{\text{inert}}} \quad (7.5)$$

such that  $f_{\text{propellant}} + f_{\text{inert}} = 1$ .

After some algebra, one finds the following expression for the payload mass of one stage as a function of the initial mass of that stage:

$$m_{\text{payload}} = m_{\text{initial}} \left( \frac{1 - f_{\text{inert}} e^{\left(\frac{\Delta V}{I_{\text{sp}} g_0}\right)}}{(1 - f_{\text{inert}}) e^{\left(\frac{\Delta V}{I_{\text{sp}} g_0}\right)}} \right). \quad (7.6)$$

The initial mass of the upper stage is equal to the payload mass of the first stage. Equation 7.6 may be used twice to determine the final payload mass of the system as a function of the system's initial LEO mass and the  $\Delta V$  values of the transfer.

To demonstrate, we will determine the final payload mass as a function of the initial LEO mass of a mission that implements the direct five-day transfer to the example L<sub>2</sub> Halo orbit given in Table 7.1. In that transfer,  $\Delta V_1 = 3.1497$  km/s and  $\Delta V_2 = 0.8326$  km/s. The mass ratio for the first stage's maneuver,  $M_{R_1}$ , is equal to:

$$M_{R_1} = e^{\left(\frac{\Delta V_1}{I_{\text{sp}_1} g_0}\right)}$$

$$M_{R_1} \approx 2.0416.$$

This means that the initial mass of the first stage is approximately 2.0416 times greater

than the final mass. After applying Equation 7.6, we find the following:

$$\begin{aligned} m_{\text{payload}_1} &= m_{\text{initial}_1} \left( \frac{1 - f_{\text{inert}_1} e^{\left( \frac{\Delta V_1}{I_{sp_1} g_0} \right)}}{(1 - f_{\text{inert}_1}) e^{\left( \frac{\Delta V_1}{I_{sp_1} g_0} \right)}} \right) \\ m_{\text{payload}_1} &= m_{\text{initial}_1} \left( \frac{1 - f_{\text{inert}_1} M_{R_1}}{(1 - f_{\text{inert}_1}) M_{R_1}} \right) \\ m_{\text{payload}_1} &\approx m_{\text{initial}_1} (0.44545). \end{aligned}$$

Hence, about 44.5% of the initial LEO mass is payload of the first stage. Or, the initial mass of the upper stage is approximately 44.5% of the initial LEO mass of the system. More than half of the initial LEO mass of the spacecraft system is required just to inject the spacecraft onto the lunar transfer.

The mass ratio of the upper stage is somewhat smaller, equal to:

$$M_{R_2} = e^{\left( \frac{\Delta V_2}{I_{sp_2} g_0} \right)}$$

$$M_{R_2} \approx 1.3038.$$

After applying Equation 7.6 a second time, we find the following:

$$\begin{aligned} m_{\text{payload}_2} &= m_{\text{initial}_2} \left( \frac{1 - f_{\text{inert}_2} e^{\left( \frac{\Delta V_2}{I_{sp_2} g_0} \right)}}{(1 - f_{\text{inert}_2}) e^{\left( \frac{\Delta V_2}{I_{sp_2} g_0} \right)}} \right) \\ m_{\text{payload}_2} &= m_{\text{initial}_2} \left( \frac{1 - f_{\text{inert}_2} M_{R_2}}{(1 - f_{\text{inert}_2}) M_{R_2}} \right) \\ m_{\text{payload}_2} &\approx m_{\text{initial}_2} (0.72903). \end{aligned}$$

Since  $m_{\text{initial}_2} = m_{\text{payload}_1}$  and  $m_{\text{payload}_1} \approx (0.44545)m_{\text{initial}_1}$ , we can conclude the following:

$$m_{\text{payload}_2} \approx (0.72903)(0.44545)m_{\text{initial}_1}$$

$$m_{\text{payload}_2} \approx (0.32474)m_{\text{initial}_1}$$

Approximately 32.474% of the initial LEO mass of the system is equal to satellite payload mass in the lunar L<sub>2</sub> Halo orbit. This does not account for any trajectory correction

maneuvers or other operational maneuvers. For the purpose of this discussion, we will define the payload mass fraction,  $f_{\text{payload}}$  to be this resulting fraction.

Table 7.5 summarizes the payload mass for various trajectory options to transfer a spacecraft from LEO to the lunar L<sub>2</sub> Halo orbit (i.e., Scenario A). The table repeats the transfer duration and ΔV information from Table 7.1 and uses the procedure just described to determine the payload mass fraction,  $f_{\text{payload}}$ , for each itinerary. Finally, the table computes the percentage of additional payload mass that each low-energy itinerary may implement compared with the five-day direct transfer. This value is computed using the relationship:

$$\text{Payload Mass \% Increase} = \frac{\text{Mass}_{\text{itinerary}} - \text{Mass}_{\text{direct}}}{\text{Mass}_{\text{direct}}} \times 100\%. \quad (7.7)$$

The results shown in Table 7.5 depend very much on the assumptions of the spacecraft's propulsion system, shown in Table 7.4. However, these results provide a general guideline for the trade-off one might expect between transfer duration and payload mass for various transfer itineraries.

In some cases, mission designers have no control over the launch vehicle. It

Table 7.5: A summary of the final payload mass for a two-stage spacecraft system using various ballistic transfer options for a transfer between a circular 185-km LEO parking orbit and a lunar L<sub>2</sub> Halo orbit with Jacobi constant of 3.05.

Mission Itinerary	Transfer Duration	ΔV <sub>1</sub> (km/s)	ΔV <sub>2</sub> (km/s)	Payload Mass Fraction, $f_{\text{payload}}$	Payload Mass % Increase
LEO – L <sub>2</sub>	~ 5 days	3.1497	0.8326	0.32474	0%
LEO – L <sub>2</sub>	~ 39 days	3.1733	0.6682	0.34390	5.90003%
LEO – L <sub>2</sub>	~ 54 days	3.1764	0.5817	0.35523	9.38779%
LEO – L <sub>1</sub> – L <sub>2</sub>	~ 50 days	3.1176	0.5012	0.37221	14.61681%
LEO – L <sub>1</sub> – L <sub>2</sub>	~ 60 days	3.1178	0.4696	0.37670	15.99849%
LEO – BLT – L <sub>2</sub>	~ 95 days	3.2650	0.0000	0.43172	32.94128%
LEO – BLT – L <sub>2</sub>	~ 190 days	3.2006	0.0000	0.43934	35.28918%

may be the case that the launch vehicle can provide sufficient  $\Delta V$  to inject a spacecraft onto any of these available options. In that case, the mission designers might only care about the trade-off between the mission's transfer duration and the total mass of the spacecraft and its upper stage. Table 7.6 summarizes this trade-off. One notices that the low-energy BLTs provide even more payload mass in this situation.

Table 7.6: A summary of a similar scenario as in Table 7.5, but in this case the Trans-Lunar Injection  $\Delta V$  is performed by the launch vehicle and thus not considered in the spacecraft system trade study.

Mission Itinerary	Transfer Duration	$\Delta V_2$ (km/s)	Payload Mass Fraction, $f_{\text{payload}}$	Payload Mass % Increase
LEO – L <sub>2</sub>	~ 5 days	0.8326	0.72903	0%
LEO – L <sub>2</sub>	~ 39 days	0.6682	0.77699	6.57945%
LEO – L <sub>2</sub>	~ 54 days	0.5817	0.80326	10.18215%
LEO – L <sub>1</sub> – L <sub>2</sub>	~ 50 days	0.5012	0.82836	13.62536%
LEO – L <sub>1</sub> – L <sub>2</sub>	~ 60 days	0.4696	0.83839	15.00130%
LEO – BLT – L <sub>2</sub>	~ 95 days	0.0000	1.00000	37.16930%
LEO – BLT – L <sub>2</sub>	~ 190 days	0.0000	1.00000	37.16930%

When one considers Scenarios B and C, namely, the scenarios where a spacecraft is to transfer between a low Earth orbit and a low lunar orbit, one has been given two main choices. One may transfer directly from the low Earth orbit to the lunar orbit via a 4.5-day direct transfer. Or one may use a low-energy transfer and visit the L<sub>2</sub> Halo orbit en route. One may use any of the transfer options listed in Table 7.5 to perform the transfer to the L<sub>2</sub> Halo orbit. However, a quick calculation shows that all but the last two transfer options to the L<sub>2</sub> Halo orbit become more expensive than the direct option once the additional transfer from L<sub>2</sub> to the lunar orbit is made. Therefore, we will only consider the last two options in Table 7.5 as options for the LEO – L<sub>2</sub> segment. Conveniently, these two options still only require two maneuvers: a Trans-Lunar Injection maneuver and a low lunar orbit insertion maneuver. Table 7.7 summarizes the

Table 7.7: A summary of the mission itineraries for Scenarios B and C.

Mission Scenario	Mission Itinerary	Transfer Duration	$\Delta V_1$ (km/s)	$\Delta V_2$ (km/s)	Total $\Delta V$ (km/s)
B	LEO – LLO	~ 4.5 days	3.1341	0.8133	3.9474
B	LEO – BLT – L <sub>2</sub> – LLO	~ 115 days	3.2650	0.6440	3.9090
B	LEO – BLT – L <sub>2</sub> – LLO	~ 210 days	3.2006	0.6440	3.8446
C	LEO – Frozen	~ 4.5 days	3.1341	0.3281	3.4622
C	LEO – BLT – L <sub>2</sub> – Frozen	~ 115 days	3.2650	0.1588	3.4238
C	LEO – BLT – L <sub>2</sub> – Frozen	~ 210 days	3.2006	0.1588	3.3594

resulting options, combining the information from Table 7.1 with Table 7.2.

We may apply the same techniques to analyze the options presented in Table 7.7 as we did for Scenario A, above. Tables 7.8 and 7.9 show a summary of the results for Scenarios B and C, respectively.

Finally, we again consider the case where the mission designer has no control over the launch vehicle. In this case, the launch vehicle has the capability to provide

Table 7.8: A summary of the final payload mass for a two-stage spacecraft system using various ballistic transfer options for a transfer between a circular 185-km LEO parking orbit and a circular 100-km lunar orbit.

Mission Itinerary	Transfer Duration	$\Delta V_1$ (km/s)	$\Delta V_2$ (km/s)	Payload Mass Fraction, $f_{\text{payload}}$	Payload Mass % Increase
LEO – LLO	~ 4.5 days	3.1341	0.8133	0.32858	0%
LEO – L <sub>2</sub> – LLO	~ 115 days	3.2650	0.6440	0.33858	3.04442%
LEO – L <sub>2</sub> – LLO	~ 210 days	3.2006	0.6440	0.34456	4.86430%

Table 7.9: A summary of the final payload mass for a two-stage spacecraft system using various ballistic transfer options for a transfer between a circular 185-km LEO parking orbit and a 100 × 8000 km frozen lunar orbit.

Mission Itinerary	Transfer Duration	$\Delta V_1$ (km/s)	$\Delta V_2$ (km/s)	Payload Mass Fraction, $f_{\text{payload}}$	Payload Mass % Increase
LEO – Frozen	~ 4.5 days	3.1341	0.3281	0.39570	0%
LEO – L <sub>2</sub> – Frozen	~ 115 days	3.2650	0.1588	0.40695	2.84331%
LEO – L <sub>2</sub> – Frozen	~ 210 days	3.2006	0.1588	0.41413	4.65965%

sufficient  $\Delta V$  to the spacecraft, no matter the spacecraft's course to the Moon. Then the mission designer only has to consider the propulsion system needed to inject the spacecraft into its final lunar orbit. Tables 7.10 and 7.11 provide a summary of this trade-off for Scenarios B and C, respectively. One can see that the low-energy BLTs provide more mass to the final lunar orbit; one can also see that it is no longer necessary to take a longer route through the system in order to reduce the size of the Trans-Lunar Injection maneuver.

Table 7.10: A summary of the simplified Scenario B, where the launch vehicle performs the Trans-Lunar Injection maneuver and the spacecraft's only trade is its orbit-insertion maneuver.

Mission Itinerary	Transfer Duration	$\Delta V_2$ (km/s)	Payload Mass Fraction, $f_{\text{payload}}$	Payload Mass % Increase
LEO – LLO	~ 4.5 days	0.8133	0.73453	0%
LEO – L <sub>2</sub> – LLO	~ 115 days	0.6440	0.78427	6.77162%
LEO – L <sub>2</sub> – LLO	~ 210 days	0.6440	0.78427	6.77162%

Table 7.11: A summary of the simplified Scenario C, where the launch vehicle performs the Trans-Lunar Injection maneuver and the spacecraft's only trade is its orbit-insertion maneuver.

Mission Itinerary	Transfer Duration	$\Delta V_2$ (km/s)	Payload Mass Fraction, $f_{\text{payload}}$	Payload Mass % Increase
LEO – Frozen	~ 4.5 days	0.3281	0.88457	0%
LEO – L <sub>2</sub> – Frozen	~ 115 days	0.1588	0.94262	6.56324%
LEO – L <sub>2</sub> – Frozen	~ 210 days	0.1588	0.94262	6.56324%

The results presented in this section are very sensitive to the assumptions that have been made. Many circumstances may result in an improved relative performance of a low-energy BLT compared with a direct lunar transfer. The following considerations outline several examples of these circumstances:

- First, it has been assumed that a spacecraft can implement any lunar transfer,

including the least-expensive direct transfer available. If the performance of the direct transfer were reduced, that is, if it were found that the direct transfer required more  $\Delta V$  for a particular mission's requirements, then the relative performance of any low-energy transfer would be improved.

- Secondly, if the upper stage's performance were reduced, e.g., by implementing a solid rocket motor with a reduced  $I_{sp}$  value of 250 seconds, then the direct transfer would permit less payload mass. In that situation, the spacecraft's payload mass may be increased by several more percent with the application of a low-energy BLT.
- If more care were put into the trajectory design, one may theoretically construct a BLT that required a Trans-Lunar Injection  $\Delta V$  with a magnitude as little as that used by the direct transfer. Such a BLT would require at least one lunar flyby en route to the L<sub>2</sub> Halo orbit, but this would result in an allowable payload mass several more percent higher than a direct transfer.
- Finally, the results presented in this section have all been produced in the Patched Three-Body model. In the JPL Ephemeris model, the Moon's orbit is neither circular nor coplanar with respect to the ecliptic. In that system, one may construct a BLT that is even more efficient than those presented here, if one chooses an opportunity that has a desirable geometry. Such a BLT has been integrated into the low-cost communication and navigation system presented by Hill et al. (2006b).

Even outside of the presence of any of these circumstances, this section has demonstrated that low-energy transfers may be used to send more mass to the Moon than conventional, direct transfers.

### 7.1.2 Navigation Considerations

When one is considering the use of an unstable three-body orbit or a low-energy orbit transfer in one's mission design, one must consider the consequences that such trajectories have to navigation. When a spacecraft is traversing an unstable region in space, it is important to have good knowledge about the spacecraft's state. The more unstable a region is, the quicker the magnitude of an error in the spacecraft's state grows. Of course, this is the underlying reason that low-energy transfers exist in the first place – a spacecraft requires very little energy to change its trajectory in an unstable environment. The crux of the problem is to ensure that the spacecraft's new trajectory is the desired trajectory and not some nearby exponentially-deviating trajectory.

A trajectory's local stability may be mapped using its local Lyapunov exponent (Anderson, 2005). If a spacecraft's state is perturbed in a random way, the local Lyapunov exponent provides information about how fast that perturbation might grow over a short period of time. There are several numerical methods of computing the local Lyapunov exponent of a given trajectory (see, e.g., Anderson, 2005). More information may be found in Lyapunov (1892), Oseledec (1968), Lichtenberg and Lieberman (1983), Abarbanel et al. (1991), Scheeres et al. (2001), and others.

The local Lyapunov exponent provides information for mission designers about when it will be important to perform station-keeping and/or trajectory correction maneuvers. If the spacecraft is approaching a segment of its trajectory that has a larger local Lyapunov exponent, i.e., a particularly unstable segment, then it becomes cost-effective to ensure that the spacecraft is following a trajectory that is very close to the spacecraft's nominal trajectory. Similarly, if mission designers wish to alter the spacecraft's nominal trajectory, it is cost-effective to perform such changes prior to entering an unstable region because the unstable dynamics may be utilized to reduce the  $\Delta V$  cost of the maneuver. These principles reflect the advantages and difficulties of

conventional gravity flybys: a spacecraft that flies near a massive body can have its trajectory substantially altered, but it must be navigated through the encounter very carefully to ensure that its trajectory is altered in a desirable way.

In this section, the local Lyapunov exponents of a trajectory are approximated by evaluating the eigenvalues of the local state transition matrix,  $\Phi(t_0 + \frac{\delta t}{2}, t_0 - \frac{\delta t}{2})$ , i.e., the state transition matrix that is mapped through a small interval of time,  $\delta t$ , about the nominal state in the trajectory; see Section 3.4 for more information about the state transition matrix. Scheeres et al. points out that although the monodromy matrix contains two eigenvalues equal to unity, the local state transition matrix does not necessarily include any unity eigenvalues (Scheeres et al., 2001). The eigenvalues still come in reciprocal pairs, but otherwise do not follow the same patterns as the eigenvalues of the monodromy matrix.

The absolute value of the real component of each eigenvalue of the local state transition matrix  $\Phi(t_0 + \frac{\delta t}{2}, t_0 - \frac{\delta t}{2})$  is considered; the largest of which, corresponding to  $\lambda_{max}$ , indicates the stability of that segment of the trajectory. This is discussed in more detail in Section 3.8. Because the eigenvalues depend on the length of time that the state transition matrix is propagated, we have chosen to also consider the Perturbation Doubling Time,  $\hat{\tau}$ , as a measure of stability (§3.8.3). The value of  $\hat{\tau}$  is normalized with respect to time and represents a physical characteristic of the system. It is clear that a small value of  $\hat{\tau}$  indicates a trajectory that is more unstable, since it takes less time to double the magnitude of a given perturbation.

Figure 7.1 shows two views of a lunar L<sub>2</sub> Halo orbit, colored according to the value of  $\lambda_{max}$ : the red regions are more unstable than the blue regions, but all regions of the Halo orbit are unstable. The local state transition matrix has been propagated for a day in either direction about each nominal point in the Halo orbit to produce the value of  $\lambda_{max}$  about the orbit. Figure 7.2 shows a comparison of three parameters of the Halo orbit: the distance between a spacecraft and the Moon as the spacecraft

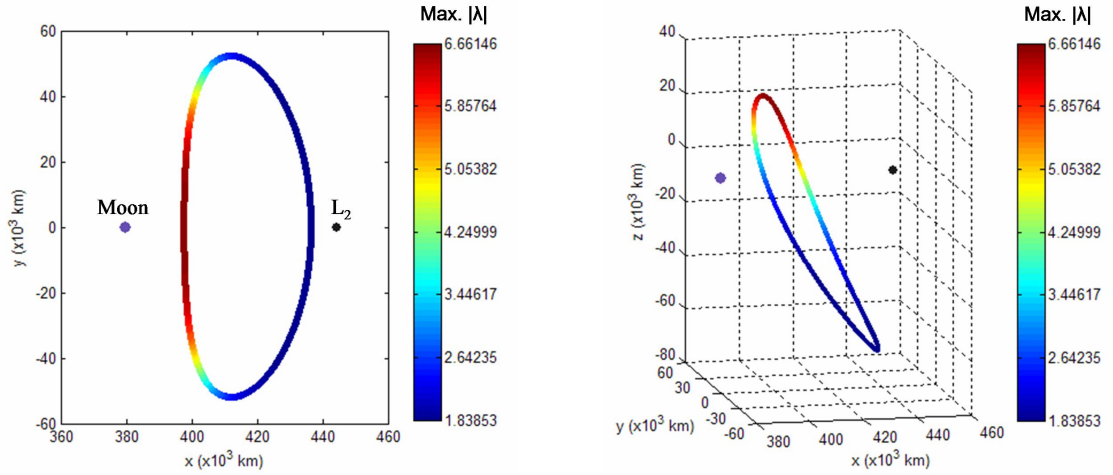


Figure 7.1: Two views of a lunar L<sub>2</sub> Halo orbit, colored according to the value of  $\lambda_{max}$ : the red regions are more unstable than the blue regions, but all regions of the Halo orbit are unstable.

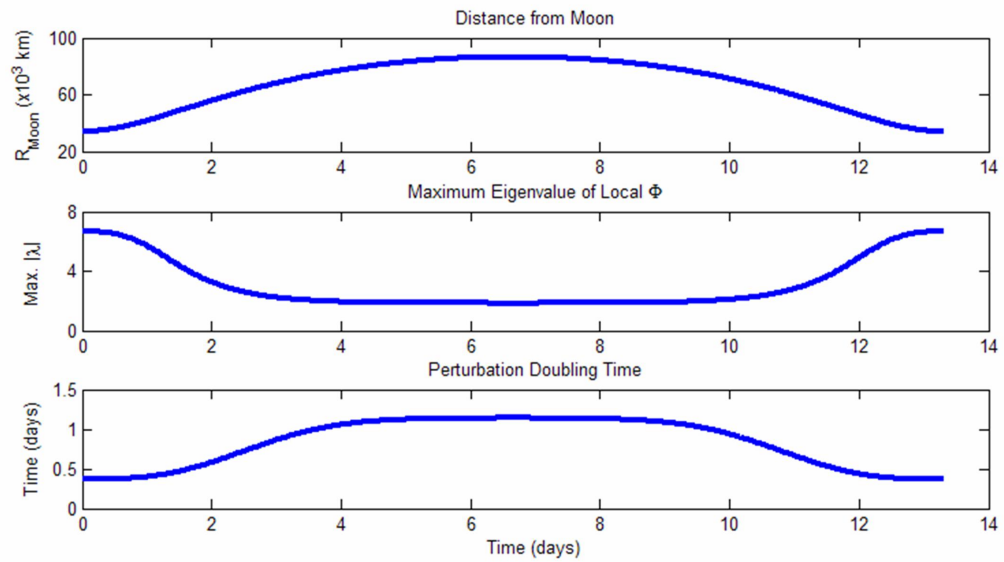


Figure 7.2: A comparison of three parameters of the Halo orbit shown in Figure 7.1. Top: the distance between a spacecraft traversing the Halo orbit and the Moon. Middle: the value of  $\lambda_{max}$ . Bottom: the value of the Perturbation Doubling Time parameter  $\hat{\tau}$ .

traverses the Halo orbit, the value of  $\lambda_{max}$ , and the value of the Perturbation Doubling Time parameter  $\hat{\tau}$ . One can see that the value of  $\hat{\tau}$  is positively correlated with the distance between the spacecraft and the Moon, giving more credibility to the claim that a trajectory is more unstable near a massive body.

Figure 7.3 shows two views of an example interior BLT to a lunar L<sub>2</sub> Halo orbit, colored according to the value of  $\lambda_{max}$ . The local state transition matrix has been propagated for 0.1 days in either direction about each nominal point in the BLT to produce the value of  $\lambda_{max}$ . The view on the left is in the Sun-Earth synodic reference frame; the view on the right is in the Earth-Moon synodic reference frame; the trajectory has been produced in the JPL Ephemeris model of the solar system. This particular BLT includes two lunar flybys en route to the Halo orbit, demonstrating that the trajectory's most unstable segments after departure are those segments that are nearest to the Moon. The BLT is also very unstable as it departs the Earth, which makes sense because a deviation there may result in a very different trajectory. In contrast, it is apparent that the BLT is relatively stable during its traversal of the Sun-Earth system, prior to its first lunar encounter. When the spacecraft finally arrives at its lunar Halo orbit destination, the spacecraft experiences the same stability characteristics in its trajectory as that shown in Figures 7.1 and 7.2.

Figure 7.4 shows a comparison of three parameters of the BLT: the distance between a spacecraft traversing the BLT and the two massive bodies, the value of  $\lambda_{max}$ , and the value of the Perturbation Doubling Time parameter  $\hat{\tau}$ . As was noticed in the stability analysis of the Halo orbit, the value of  $\hat{\tau}$  is positively correlated with the closest proximity between the spacecraft and either of the massive bodies.

The primary purpose of this study is to demonstrate that the navigation requirements are not the same at all points throughout a low-energy trajectory. Anderson has shown that a spacecraft's station-keeping requirements are proportional to the instability of its trajectory (Anderson, 2005). A spacecraft traversing a BLT requires better nav-

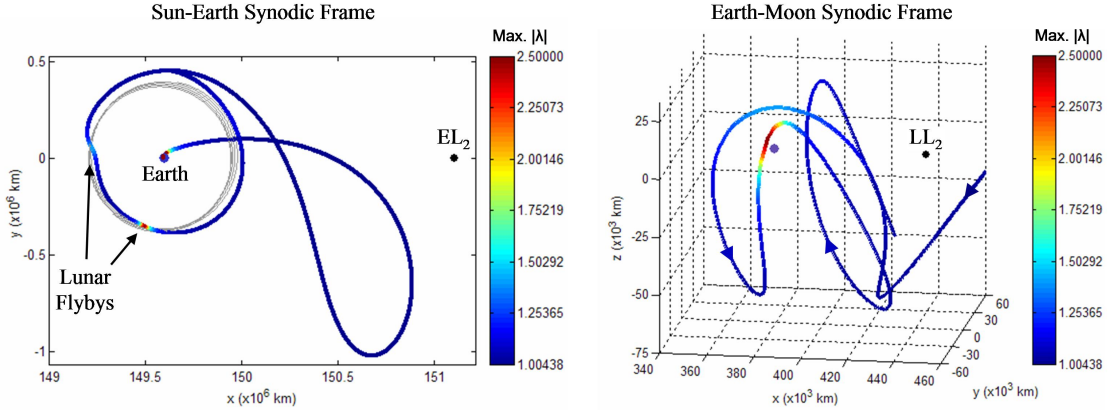


Figure 7.3: Two views of an example interior BLT to a lunar L<sub>2</sub> Halo orbit, colored according to the value of  $\lambda_{max}$ . Left: The BLT viewed in the Sun-Earth synodic reference frame; Right: The BLT viewed in the Earth-Moon synodic reference frame.

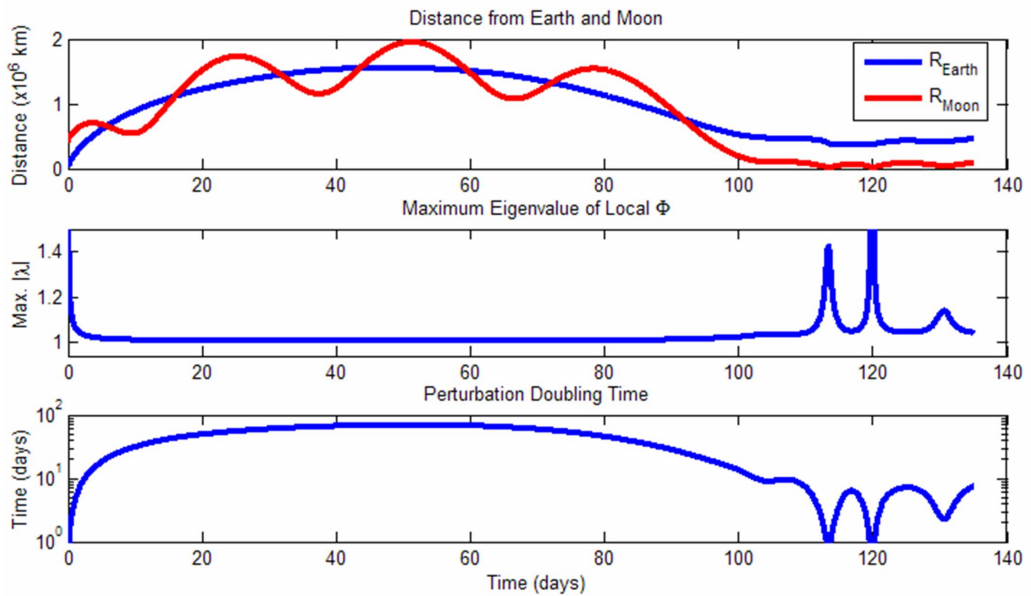


Figure 7.4: A comparison of three parameters of the BLT shown in Figure 7.3. Top: the distance between a spacecraft traversing the BLT and the two massive bodies. Middle: the value of  $\lambda_{max}$ . Bottom: the value of the Perturbation Doubling Time parameter  $\hat{\tau}$ .

igation immediately after launch and during any close approaches with the Moon. The frequency of trajectory correction maneuvers may be reduced during the spacecraft's long traversal through the Sun-Earth system. During that segment of the transfer, the value of  $\hat{\tau}$  is well-above 20 days; which means that a slight deviation in the spacecraft's trajectory takes more than 20 days to double in magnitude.

It is also interesting to consider the navigation trade-off between having a longer transfer duration versus having to perform an orbit-insertion maneuver upon arrival at a lunar Halo orbit. The longer transfer duration implies more trajectory correction maneuvers and larger operations costs for sending the spacecraft to the Moon. But since BLTs do not require an orbit-insertion maneuver at the Halo orbit, there is no critical maneuver to be performed upon arrival. The navigation requirements as the spacecraft approaches the Halo orbit do not increase as dramatically as they would if there were an orbit-insertion maneuver. Additionally, if a mission is to use the Halo orbit as a staging orbit en route to a lower lunar orbit, the mission has much more time prior to its orbit-insertion maneuver to collect tracking data and ensure that it is on its proper trajectory. More discussion about this are given in Section 7.1.8.

### 7.1.3 Station-Keeping Costs

A spacecraft traversing an unstable trajectory in the presence of uncertainty must perform station-keeping maneuvers. Very few spacecraft have traversed three-body trajectories in the Earth-Moon system, and no spacecraft have orbited in an Earth-Moon Halo orbit to date. Hence, there is little historical data on the station-keeping requirements of such spacecraft. There is more historical data on missions within the Sun-Earth three-body system.

The ISEE-3 spacecraft performed 15 station-keeping maneuvers while in a Halo orbit about the Sun-Earth L<sub>1</sub> point (Muhonen, 1983). Those 15 maneuvers had planned  $\Delta V$  magnitudes of approximately  $1.989 \pm 0.791$  m/s and were performed at intervals

in time of approximately  $82.3 \pm 17.1$  days. The Wilkinson Microwave Anisotropy Probe required several station-keeping maneuvers to maintain its Halo orbit about the Sun-Earth L<sub>2</sub> point. Its station-keeping maneuvers had magnitudes of approximately  $0.412 \pm 0.058$  m/s and were performed at intervals of approximately  $97.5 \pm 20.5$  days (Limon, M., et al., 2003). The Genesis spacecraft's station-keeping maneuvers had planned  $\Delta V$  magnitudes of approximately  $1.364 \pm 0.235$  m/s and were performed at intervals of approximately  $50 \pm 17.3$  days (Smith et al., 2003). Additional information about other spacecraft's station-keeping performances may be found in the literature (see, e.g., Dunham and Roberts, 1998). Although these spacecraft implemented unstable trajectories in their respective missions, their station-keeping costs were very reasonable.

Spacecraft in libration orbits have implemented several control strategies to maintain their trajectories. The ISEE-3 spacecraft controllers used a very tight control algorithm that proved that a spacecraft may indeed travel on unstable trajectories. More recent spacecraft missions, including the SOHO spacecraft mission, have implemented looser control algorithms and have demonstrated very low station-keeping requirements (Dunham and Roberts, 1998). SOHO's mission only requires that the spacecraft remain in some sort of libration orbit about the Sun-Earth L<sub>1</sub> point that avoids the solar exclusion zone, i.e., the region of space where the spacecraft would be within approximately  $5^\circ$  of the Sun as viewed from the Earth. Several authors have considered control algorithms that avoid this solar exclusion zone (e.g., Howell and Perenicka, 1990). The station-keeping requirements of spacecraft on these trajectories are certainly looser than spacecraft that must follow a pre-determined path to a particular destination, such as ISEE-3 and the recent Genesis spacecraft mission. The Genesis mission design team constructed each of its station-keeping maneuvers such that the new trajectory would intersect the nominal trajectory at the planned epoch of the next station-keeping maneuver, assuming no additional errors (Lo et al., 2000). The Genesis

mission further required that each of its maneuvers be biased slightly to account for its particular spacecraft bus requirements and the physical location of its thrusters.

It is apparent that most station-keeping control strategies on libration point orbits require 2 – 3 station-keeping maneuvers per orbit. It may be surmised that a spacecraft in a Halo orbit about one of the Earth-Moon libration points would require the same number of station-keeping maneuvers per orbit. The frequency of such maneuvers would be on the order of once every four to seven days. This frequency makes mission operations very difficult if all of the tracking is performed from conventional ground stations. Studies have shown more recently that autonomous navigation may be performed that would allow such missions to operate without considerable ground support (Hill and Born, 2007). It has been shown that missions in a Halo orbit about an Earth-Moon libration point that implement autonomous navigation may require a total station-keeping maneuver cost below 10 m/s per year (Hill et al., 2006b). This result assumes that station-keeping maneuvers may be performed that have magnitudes as small as several millimeters per second. In any case, the station-keeping maneuver demands of spacecraft in Earth-Moon three-body orbits are not unreasonable given this autonomous navigation system.

#### **7.1.4 Communication System**

A spacecraft that uses a typical BLT to transfer between the Earth and Moon travels to distances much greater than the average distance between the Earth and the Moon. Consequently, the spacecraft's communication system must be capable of communicating at those distances. Fortunately, most spacecraft do not need to communicate a great deal of information during their orbit transfers; their largest communication demands are likely to be after they have reached their destination.

We have computed a set of statistics for the maximum apogee distance of the 24,571 exterior BLTs and the 8,851 interior BLTs that have been identified in this disser-

tation between 185-km LEO parking orbits and the lunar L<sub>2</sub> Halo orbit with a Jacobi constant of 3.05. The statistics are presented in Table 7.12. The set of BLTs studied here is scattered fairly evenly throughout the two BLT Maps produced in Chapter 6; the set does not favor any particular type of BLT, and certainly contains BLTs that are probably undesirable for most practical missions. Although not explicitly stated in Table 7.12, a great number of exterior and interior BLTs have a maximum apogee distance between 1.35 and 1.5 million kilometers.

Table 7.12: Statistics for the maximum apogee distance of the BLTs that have been identified in this dissertation between a 185-km LEO parking orbit and the lunar L<sub>2</sub> Halo orbit with a Jacobi constant of 3.05. All distances are given in millions of kilometers.

	# of BLTs	Average	Std. Dev.	Minimum	Maximum
Exterior BLTs	24,571	1.749	0.345	1.106	3.553
Interior BLTs	8,851	1.657	0.350	1.126	3.304

For reference, a direct transfer to the Moon has a maximum apogee distance approximately equal to the distance between the Earth and Moon, namely, approximately 384,400 km. The maximum distance between the Earth and a spacecraft in the example lunar L<sub>2</sub> Halo orbit is equal to approximately 446,000 km. Additionally, the maximum distance between the Earth and a spacecraft traversing the lunar L<sub>1</sub> Halo orbit with the same Jacobi constant is equal to approximately 364,700 km.

The free space loss in a link budget is proportional to the square of the distance in the link. Table 7.13 summarizes the relative free space loss penalty of several types of lunar transfers compared with a direct transfer between the Earth and a low lunar orbit about the Moon. One can see that a direct transfer to a lunar L<sub>1</sub> Halo orbit has a free space loss benefit compared with the baseline lunar mission. Conversely, as expected, a direct transfer to a lunar L<sub>2</sub> Halo orbit has a free space loss approximately 1.346 times worse than the baseline lunar mission. Even the lowest BLTs have a free space loss 10 or more times worse than the baseline lunar mission.

Table 7.13: A summary of the relative free space loss penalty of several types of lunar transfers compared with a direct transfer between the Earth and a low lunar orbit about the Moon.

Mission	Maximum Apogee Distance	Relative Free Space Loss
Direct to LLO	384,400 km	1.000
Direct to $L_1$	364,700 km	0.900
Direct to $L_2$	446,000 km	1.346
Low BLT	1,350,000 km	12.334
Med BLT	1,700,000 km	19.558
High BLT	2,050,000 km	28.441

There are several additional communication trade-offs between a spacecraft in a lunar Halo orbit, or other three-body orbit, compared with a spacecraft in a conventional low lunar or frozen orbit. First of all, a spacecraft in a lunar Halo orbit is always visible from the Earth, whereas a spacecraft in a lower lunar orbit is blocked by the Moon periodically. A spacecraft in a lunar Halo orbit, or other three-body orbit, typically remains in view of a target on the lunar surface for very long periods of time, which is good from a tracking and communication relay perspective. However, the spacecraft is also typically much farther away from the lunar surface than a spacecraft in a lower lunar orbit. Hence, the communication link suffers from a greater free space loss and some measure must be taken to restore the link budget. Either the communication data rates must be reduced or the gain values of the antennas must be improved in order to match the link budget of a spacecraft in a lower lunar orbit.

### 7.1.5 Power System

A spacecraft mission that implements a lunar Halo orbit rather than a conventional low lunar or frozen orbit has an advantage when it comes to the spacecraft's power system, assuming that the spacecraft uses solar power. A lunar Halo orbit may be designed such that a spacecraft in that orbit is always in view of the Sun. Hence, that spacecraft's power system does not require the consistent use of large batteries or

the need to regularly condition those batteries. The spacecraft would probably include a battery back-up power system anyway, particularly in case the spacecraft's solar arrays were inadvertently pointed away from the Sun. Nevertheless, it is beneficial not to have to cycle through the battery's power frequently.

Many satellite missions have been limited in their mission timelines by the operational life of their batteries. For instance, the Topex/Poseidon satellite required several changes in its operating procedures to extend its mission lifetime on account of its battery performance (see, e.g., Deligiannis et al., 1994). It would certainly be advantageous not to have to worry about conditioning the satellite's batteries, or to have to carry large batteries onboard in the first place.

There are many types of BLTs that include lunar flybys. A spacecraft following such a BLT may pass through the Moon's shadow and experience a brief period of time where it must rely on battery power. Although the battery system may be required, the power system may not need to be very robust, since a spacecraft following one of these BLTs may only experience a few eclipses at most.

#### **7.1.6 Thermal System**

A spacecraft's thermal system is often very dependent on the level and variability of energy that it receives from external sources, such as the Earth, Moon, and especially the Sun. In general, a spacecraft's thermal system may be simplified for the same reasons that the spacecraft's power system was simplified in Section 7.1.5. A spacecraft that does not pass through eclipses does not experience the thermal shock that is ordinary for many vehicles in low Earth and low lunar orbits. A spacecraft following a Halo orbit or a BLT still must maintain a healthy thermal environment, but the requirements are often simpler than conventional missions.

### 7.1.7 Attitude Determination and Control System

There are not many claims that can be readily made about a satellite's attitude determination and control system due to its trajectory, since its requirements may vary widely depending on its mission. However, one can argue that a satellite in a Halo orbit may have simpler attitude control requirements when communicating with ground systems on the Earth or Moon. Since the satellite is not moving very quickly relative to either body, its communication link probably has a very slow slew-rate requirement. However, due to the large link distance between the satellite and ground systems on the Moon, the attitude determination requirements of the satellite are probably tighter.

### 7.1.8 Mission Operations

A spacecraft mission that implements a low-energy ballistic lunar transfer to reach its destination has several trade-offs when compared to a mission that implements a direct lunar transfer when considering the cost and complexity of mission operations.

First of all, BLTs have much longer transfer durations than direct lunar transfers. The cost of operating a mission generally has a component that is directly proportional to the mission's duration. It may be possible to add maneuvers to the BLT to reduce its transfer time without increasing its total  $\Delta V$  cost very much, although that study has not been performed here.

A spacecraft following a BLT requires the same sort of trajectory correction maneuvers as a spacecraft following a direct lunar transfer. More discussion of this trade-off is given in Section 7.1.2.

There is one big advantage for a mission implementing a low-energy transfer to a lunar Halo orbit, or other three-body orbit, compared with a mission implementing a direct transfer to the same three-body orbit: the low-energy transfer typically does not

require an orbit-insertion maneuver. An orbit-insertion maneuver is a critical event that requires careful planning, navigation, and execution. A spacecraft following a BLT arrives at its target three-body orbit asymptotically, typically without any need of a large, mission-critical, orbit-insertion maneuver.

A spacecraft following a low-energy transfer from a three-body orbit down to a low lunar orbit does require an orbit-insertion maneuver. But the typical low-energy transfers explored in this dissertation require more transfer time than typical direct transfers. With longer transfer durations, mission operators have more time to accumulate navigation data, which may reduce the risk of trajectory errors as the spacecraft performs the orbit-insertion maneuver.

## 7.2 Applying BLT Maps to Practical Mission Design

Section 7.1 discussed the impact that a low-energy trajectory might have on the design of a spacecraft system. This section discusses how to apply knowledge of BLT Maps to the development of practical spacecraft mission designs. Section 7.2.1 considers how to use a BLT Map to evaluate the various departure opportunities for a mission between a LEO parking orbit with a particular altitude and a particular  $L_2$  Halo orbit destination. Section 7.2.2 constrains the results of Section 7.2.1 to depart from a LEO parking orbit with a particular ecliptic inclination. Section 7.2.3 discusses how to use a BLT Map to construct a BLT to rendezvous with an object already in the lunar three-body orbit destination. Finally, Section 7.2.4 considers how to use a BLT Map to construct a desirable BLT between an arbitrary LEO parking orbit and a particular  $L_2$  Halo orbit destination.

### 7.2.1 Departure Opportunities

A BLT Map may be used to help identify all possible departure dates for the BLTs that may be used to transfer a spacecraft to a desired Earth-Moon orbit. Then if a mission misses its target departure date, it may implement a BLT that departs later to reach its target orbit. In this discussion, the departure date is the date at which the Trans-Lunar Injection  $\Delta V$  is performed, be it a launch from the surface of the Earth or a departure from a LEO parking orbit. This section demonstrates how to perform a departure opportunity analysis using the example BLT Map shown in Figure 6.3 in Section 6.2.3 (repeated as Figure 7.5). This BLT Map summarizes all possible exterior BLTs that require fewer than 195.4 days to reach the lunar  $L_2$  Halo orbit that has a Jacobi constant of 3.05. To be complete, one should also include the interior BLT Map in the analysis, but using just the exterior BLT Map will suffice for this demonstration. The discussion here only considers the available departure opportunities; it doesn't

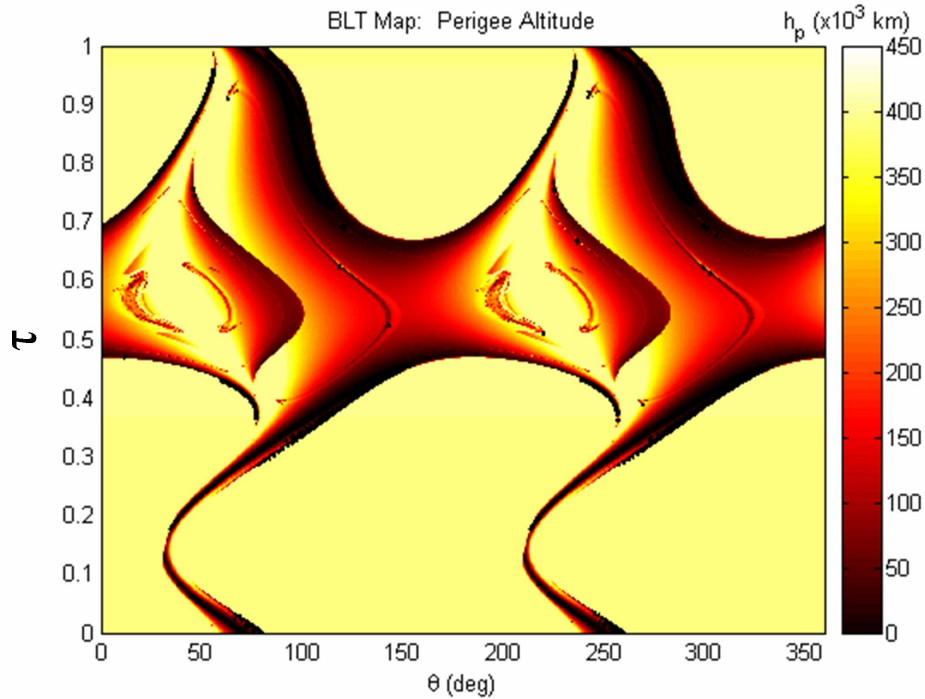


Figure 7.5: The example BLT Map used to demonstrate a departure opportunity analysis. The ballistic lunar transfers shown in this BLT Map target the lunar L<sub>2</sub> Halo orbit via its exterior stable manifold. The Jacobi constant has been set to 3.05 and the maximum transfer duration has been set to 195.4 days.

consider the length of time of the departure **window** for each available departure opportunity. Other researchers have considered the  $\Delta V$  penalty for departing at a non-optimal epoch within a particular departure window (see, e.g., Belbruno and Carrico, 2000).

As usual, we will assume that a mission designer wishes to depart the Earth from a 185-km LEO parking orbit. The families of BLTs that depart from such an orbit and arrive at the targeted lunar L<sub>2</sub> Halo orbit are presented and analyzed in Section 6.3. The Trans-Lunar Injection date of each BLT may be determined by subtracting the BLT's transfer duration from its Halo orbit arrival date. The arrival date has been characterized in this dissertation by the parameter  $\theta$  in order to make the design process more general, where  $\theta$  is the angle of the Moon with respect to the Earth and Sun (see Sec-

tion 5.6.1). A  $\theta$ -value of  $0^\circ$  indicates a full Moon and a  $\theta$ -value of  $180^\circ$  indicates a new Moon. Then the  $\theta$ -value that corresponds to the Trans-Lunar Injection date,  $\theta_{TLI}$ , may be evaluated in the Patched Three-Body model by the expression:

$$\theta_{TLI} = \theta_{\text{Arrival}} - \dot{\theta}\Delta t, \quad (7.8)$$

where  $\Delta t$  is the BLT's transfer duration and  $\dot{\theta}$  is the rate of change of the Moon's angle with respect to the Sun-Earth syzygy axis. The synodic period of the Moon is equal to approximately 29.486 days, assuming circular orbits and the orbital parameters given by Vallado (1997). Hence,  $\dot{\theta}$  is equal to approximately 12.209 degrees/day or approximately  $2.4663 \times 10^{-6}$  radians/second. The parameter  $\theta_{TLI}$  is used throughout the remainder of this discussion in order to keep the analysis generic for each month.

It would be desirable to produce a timeline that shows all of the departure opportunities for the BLTs shown in the example exterior BLT Map. However, there are far too many BLTs in the example BLT Map to show their departure opportunities on a single one-dimensional timeline. Since each departure corresponds with a BLT that has its own particular set of performance parameters, the departure opportunities may be plotted on a two-dimensional timeline. Figures 7.6 – 7.8 show three different two-dimensional timelines, each highlighting a different performance parameter of the exterior BLTs as a function of the BLTs'  $\theta_{TLI}$ -values: Figure 7.6 shows each departure's Trans-Lunar Injection  $\Delta V$  magnitude, Figure 7.7 shows each departure's ecliptic inclination at the Trans-Lunar Injection point, and Figure 7.8 shows each departure's corresponding transfer duration. Since we have permitted the value of  $\theta_{TLI}$  to take on values outside of the range  $[0^\circ, 360^\circ]$ , one can clearly see the different families of BLTs that exist. These families were studied in more detail in Section 6.3. In general, smaller values of  $\theta_{TLI}$  correspond to BLTs with longer transfer durations, as one can infer from Equation 7.8. The  $180^\circ$  symmetry in  $\theta$  that is clearly evident in the BLT Map in Figure 7.5 is also observable in each of the three plots shown in Figures 7.6 – 7.8.

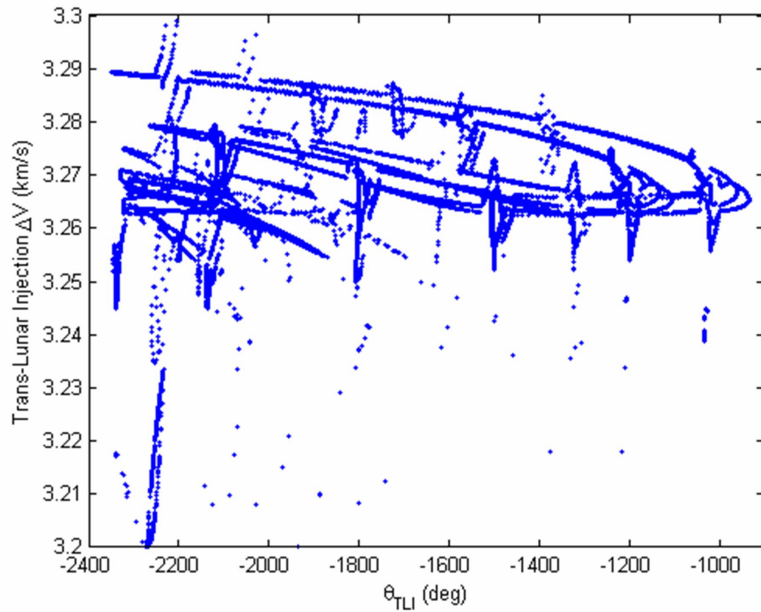


Figure 7.6: The Trans-Lunar Injection  $\Delta V$  value of each exterior BLT in Figure 7.5 as a function of the BLT's corresponding Trans-Lunar Injection  $\theta$ -value,  $\theta_{TLI}$ .

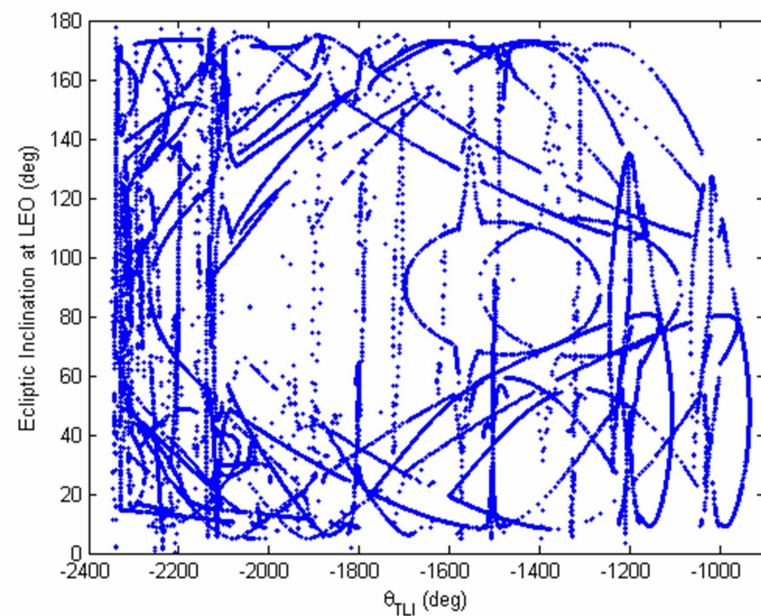


Figure 7.7: The Trans-Lunar Injection ecliptic inclination value of each exterior BLT in Figure 7.5 as a function of the BLT's corresponding Trans-Lunar Injection  $\theta$ -value,  $\theta_{TLI}$ .

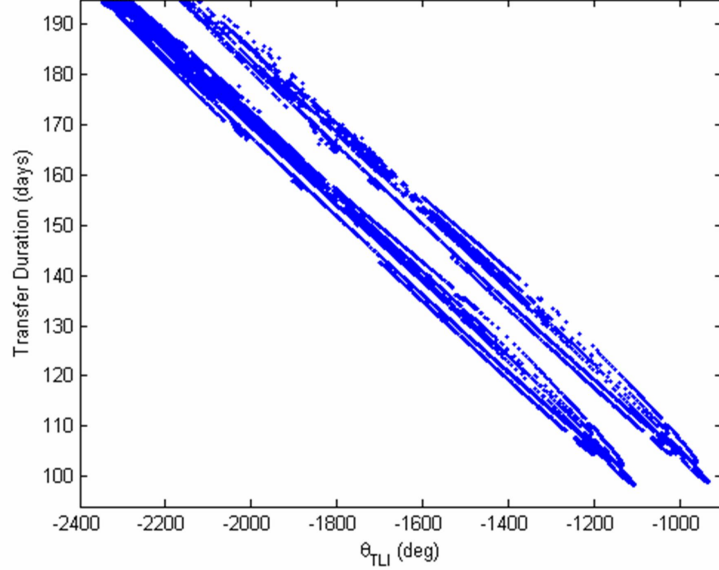


Figure 7.8: The transfer duration of each exterior BLT in Figure 7.5 as a function of the BLT's corresponding Trans-Lunar Injection  $\theta$ -value,  $\theta_{TLI}$ .

Although, as was mentioned in Section 6.3, more care went into producing BLTs on the left half of the BLT Map than in the right half, and the density of the visible points is consequently different in the corresponding families of BLTs.

A spacecraft may implement a given BLT once every month; if it misses a launch one month, and if it must follow that particular BLT, then it may wait until the next month and attempt the launch again. Of course, in the real solar system the dynamics change each month, but a similar BLT is available once each month. In the Patched Three-Body model, a BLT may depart precisely the same each month. Because of this repetition, we may wrap the  $\theta_{TLI}$  angles, i.e., the BLT departure opportunities, into the range  $[0^\circ, 360^\circ]$ . Upon doing so, one observes that there are many BLT departure opportunities each month, even when one only considers departures from a specific ecliptic inclination value. Figures 7.9 – 7.11 show the same two-dimensional departure opportunity timelines as Figures 7.6 – 7.8, but with the values of  $\theta_{TLI}$  wrapped into the range  $[0^\circ, 360^\circ]$ . Each departure opportunity corresponds with a particular **exterior**

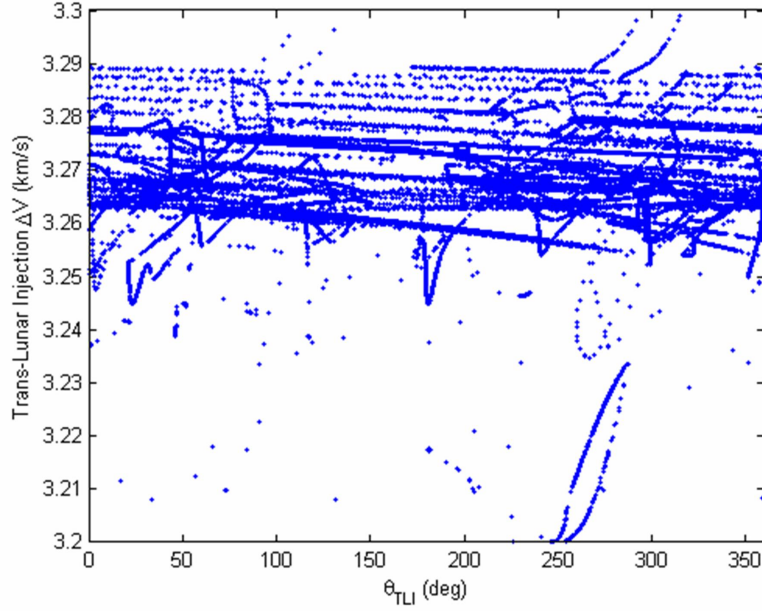


Figure 7.9: The Trans-Lunar Injection  $\Delta V$  value of each exterior BLT in Figure 7.5 as a function of the BLT's corresponding Trans-Lunar Injection  $\theta$ -value,  $\theta_{TLI}$ . The value of  $\theta_{TLI}$  has been wrapped into the range  $[0^\circ, 360^\circ]$ .

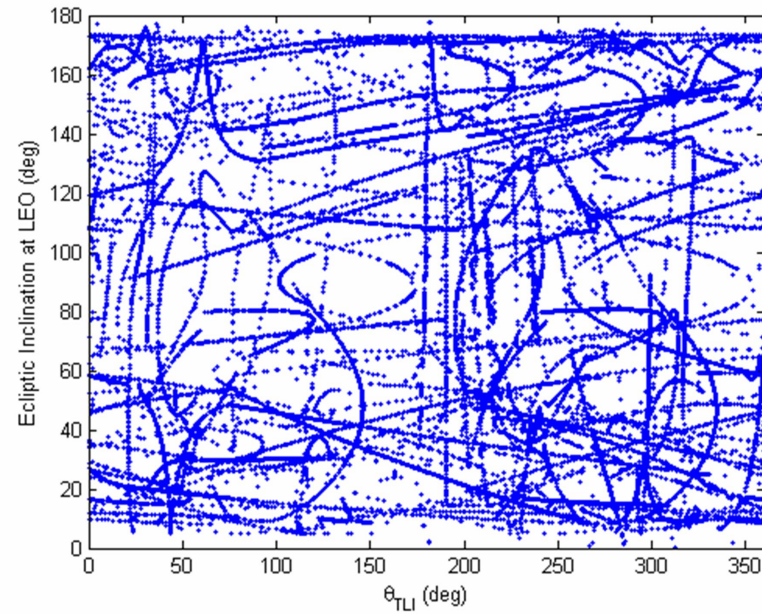


Figure 7.10: The Trans-Lunar Injection ecliptic inclination value of each exterior BLT in Figure 7.5 as a function of the BLT's corresponding Trans-Lunar Injection  $\theta$ -value,  $\theta_{TLI}$ . The value of  $\theta_{TLI}$  has been wrapped into the range  $[0^\circ, 360^\circ]$ .

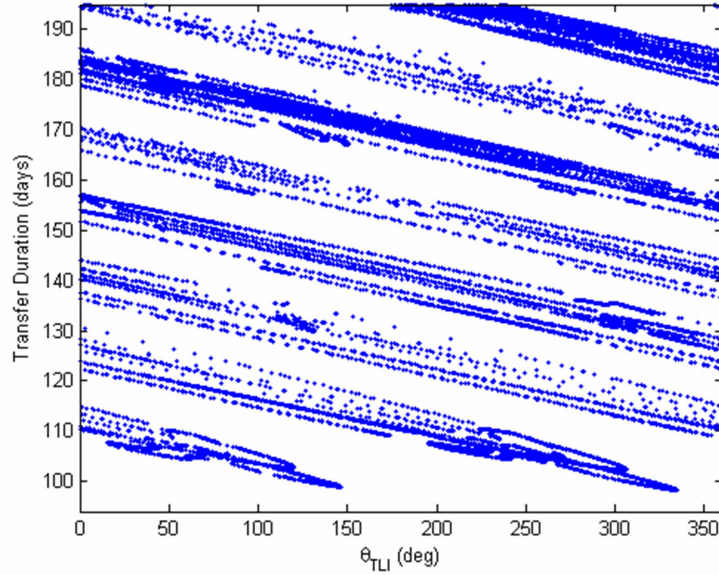


Figure 7.11: The transfer duration of each exterior BLT in Figure 7.5 as a function of the BLT's corresponding Trans-Lunar Injection  $\theta$ -value,  $\theta_{TLI}$ . The value of  $\theta_{TLI}$  has been wrapped into the range  $[0^\circ, 360^\circ]$ .

BLT – these plots don't even consider the options that interior BLTs would permit. It is clear that BLT Maps provide the means to identify a large number of departure opportunities simultaneously.

### 7.2.2 Departure Opportunities from a Particular Inclination

To continue the analysis of Section 7.2.1, we now consider all of the departure opportunities for a spacecraft that is in a LEO parking orbit with a particular ecliptic inclination. Since the Earth's equator is tilted with respect to the ecliptic, this analysis will need to be completed for each specific mission design considered; nevertheless, this example provides a demonstration of the possible options that a spacecraft might have at an arbitrary ecliptic inclination.

Figure 7.12 shows the transfer duration and Trans-Lunar Injection  $\Delta V$  departure options for each BLT that departs from a 185-km LEO parking orbit with an ecliptic

inclination of  $20^\circ \pm 1^\circ$ . One can see that there are many departure options every month for a spacecraft at this inclination. The majority of the transfers require Trans-Lunar Injection  $\Delta V$  magnitudes very close to 3.26 km/s. The transfer duration of each BLT option varies between approximately 100 and 195 days. Figures 7.13 and 7.14 show similar plots of the options that a spacecraft has departing from a 185-km LEO parking orbit with an ecliptic inclination of  $25^\circ \pm 1^\circ$  and  $30^\circ \pm 1^\circ$ , respectively. One can see that the results are very similar for all three LEO parking orbits. As mentioned earlier, these are only the options for exterior BLTs; analyzing the interior BLT Map will provide even more options. Furthermore, these are only the options that have been identified in this research; certainly others exist as well that have not been classified here.

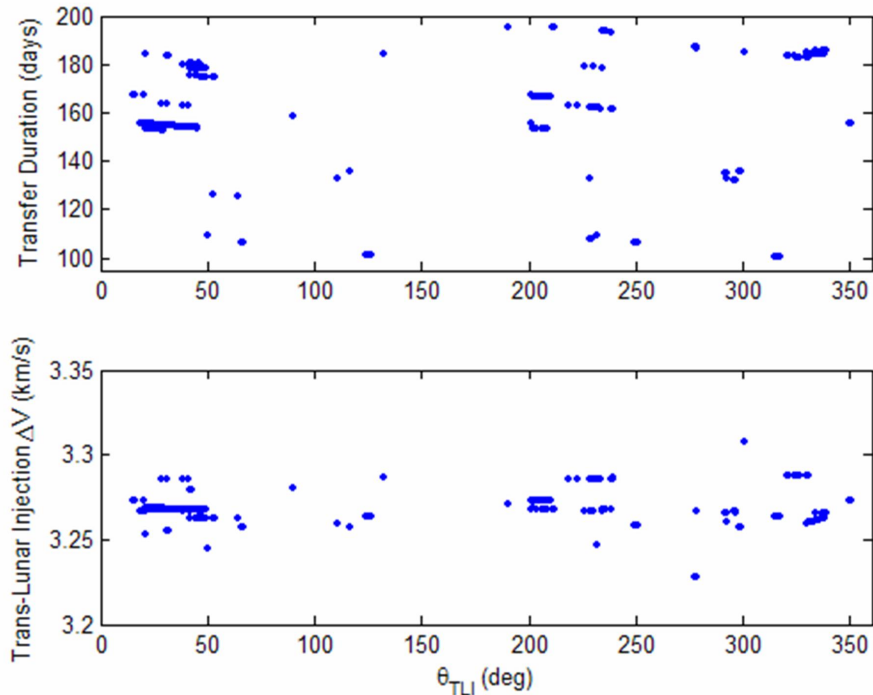


Figure 7.12: The transfer duration and Trans-Lunar Injection  $\Delta V$  departure options for each BLT that departs from a 185-km LEO parking orbit with an ecliptic inclination of  $20^\circ \pm 1^\circ$ .

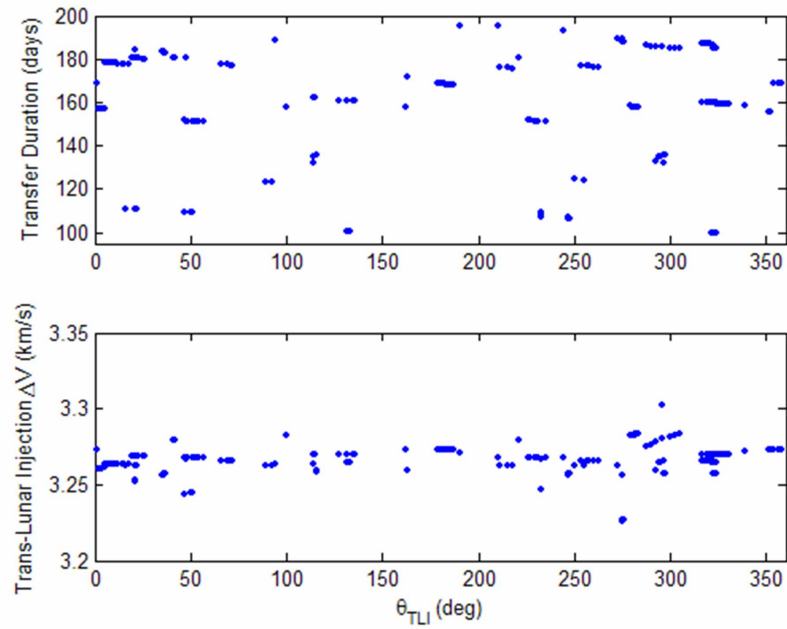


Figure 7.13: The transfer duration and Trans-Lunar Injection  $\Delta V$  departure options for each BLT that departs from a 185-km LEO parking orbit with an ecliptic inclination of  $25^\circ \pm 1^\circ$ .

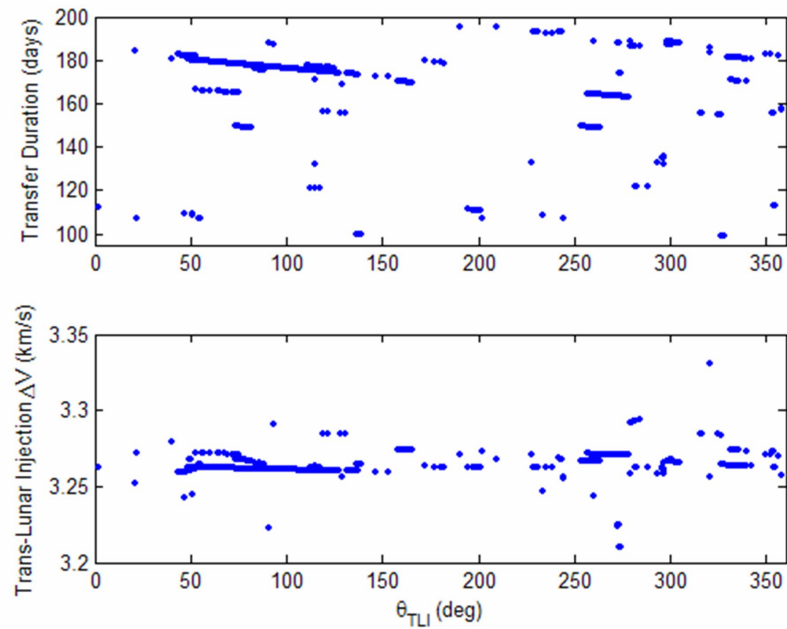


Figure 7.14: The transfer duration and Trans-Lunar Injection  $\Delta V$  departure options for each BLT that departs from a 185-km LEO parking orbit with an ecliptic inclination of  $30^\circ \pm 1^\circ$ .

The next step for a practical spacecraft mission design is to evaluate the available departure opportunities for the given ecliptic inclination to determine which BLTs depart at desirable right-ascension of the ascending node and argument of perigee values. The argument of perigee is not a concern if one uses a circular parking orbit or launches directly from the Earth's surface onto the BLT. Matching the proper right-ascension of the ascending node is not a problem if one launches into a parking orbit at the proper time during the day.

### 7.2.3 Identifying Rendezvous Trajectories

BLT Maps are quite useful when applied to the problem of constructing a mission to rendezvous with an object already in some target three-body orbit. For this discussion, it is assumed that there is some object in orbit about the same example lunar L<sub>2</sub> Halo orbit that produced the exterior BLT Map shown in Figure 7.5. Furthermore, it is assumed that the target object is located at the arbitrary point  $\tau = 0.8$  at an epoch when the Moon is at an angle  $\theta = 300^\circ$ . We wish to construct a BLT that will rendezvous with this object at an epoch prior to that target epoch.

To construct such a BLT, one may take advantage of the motion of the object in its Halo orbit. The angle  $\theta$  changes through time at the rate  $\dot{\theta}$ , identified in Section 7.2.1 to be equal to approximately 12.209 degrees/day or approximately  $2.466 \times 10^{-6}$  radians/second. The period of the object's lunar L<sub>2</sub> Halo orbit is equal to approximately 13.3167 days. Hence, it takes  $\tau$  approximately 13.3167 days to traverse between the values 0 and 1; that is,  $\tau$  changes at a rate of approximately 0.075094 per day or approximately  $8.6914 \times 10^{-7}$  per second. One can use the information about  $\dot{\theta}$  and  $\dot{\tau}$  to determine where the object will be located on the BLT Map prior to the rendezvous epoch. The object's resulting trajectory is superimposed on the exterior BLT Map shown in Figure 7.15.

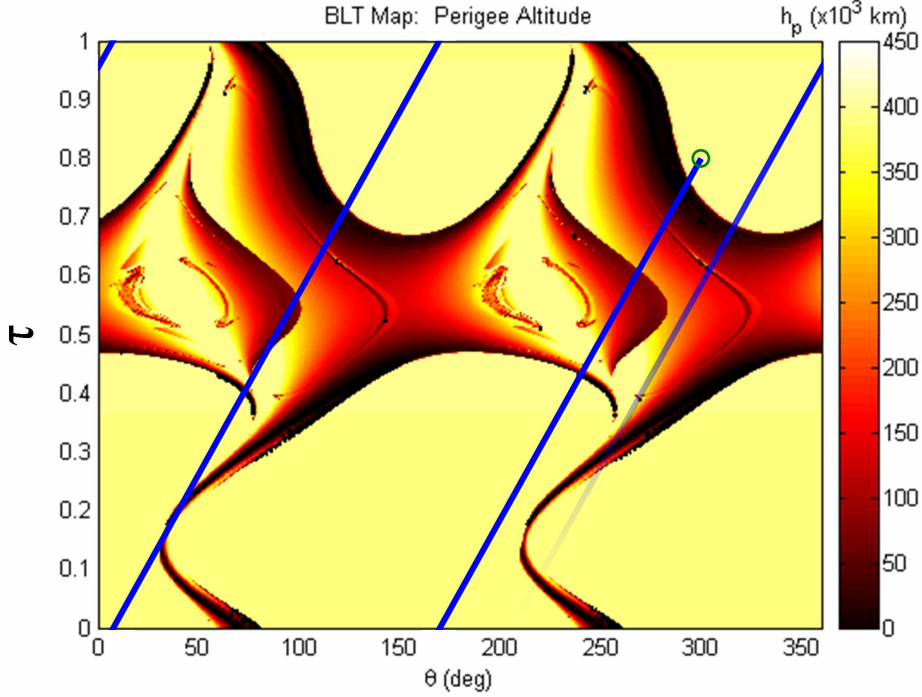


Figure 7.15: The exterior BLT Map shown in Figure 7.5 with a rendezvous trajectory superimposed. Any BLT that intersects this trajectory may be used to rendezvous with the target object prior to the rendezvous epoch (indicated by the green circle).

Figure 7.16 shows several example exterior BLTs that may be used to rendezvous with the object in its Halo orbit. These BLTs have been identified because their parameters intersect the object's trajectory through the BLT Map. Many additional exterior BLTs exist that could make the rendezvous by arriving at the Halo orbit earlier in time. Furthermore, many interior BLTs also exist that could be used to make the rendezvous, although those are not examined here. One can see that a variety of desirable exterior BLTs exist, including trajectories with very different transfer durations. A rendezvous mission may therefore target a launch window for one of the longer transfers, knowing that several backup BLTs exist that the mission may also use in case it missed the nominal launch window.

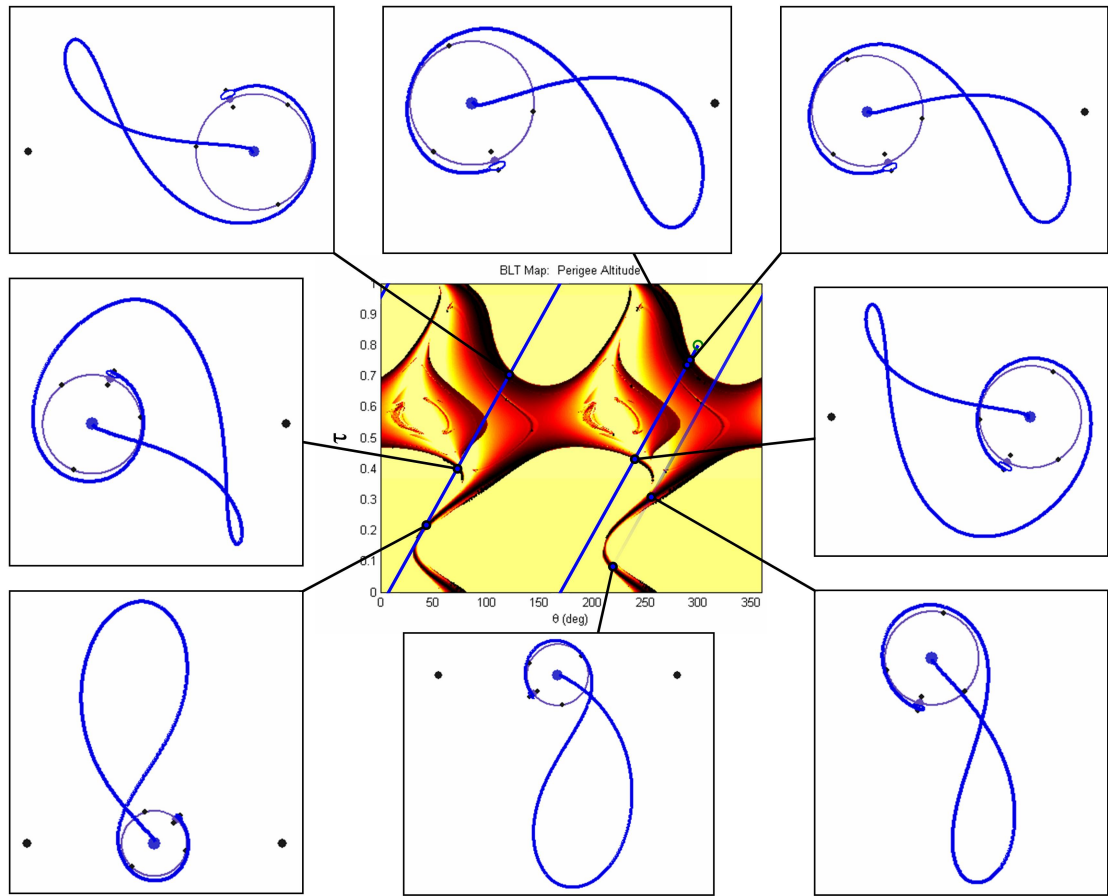


Figure 7.16: The exterior BLT Map and the superimposed rendezvous trajectory from Figure 7.15 with several example BLTs that a spacecraft may follow to successfully rendezvous with the target object prior to the target epoch.

#### 7.2.4 Identifying Desirable BLTs

The BLT Maps presented in Chapter 6 have demonstrated that BLTs may be produced between virtually any LEO parking orbit and a specified lunar three-body orbit. This section considers how to build a BLT between a random initial Earth parking orbit and a particular lunar three-body orbit. This analysis is useful in case a spacecraft may be placed as a secondary payload onto a launch vehicle whose purpose is to deliver its primary payload into a completely unrelated orbit. Then it would be desirable to find a way to target a low-energy BLT for the spacecraft given its arbitrary initial orbit. It

may be safe to assume that the perigee of the initial orbit is near 185 kilometers, but all other orbital parameters are unpredictable.

First of all, the Patched Three-Body model may be used to quickly build a BLT Map for the particular lunar three-body orbit destination, which would be useful for understanding where useful transfers exist in the state space. But for a real spacecraft mission design it would probably be better to build the BLT Map in the JPL Ephemeris model as was done in Section 6.6. In the JPL Ephemeris model, one must have knowledge about the epoch that a transfer needs to occur. With knowledge of the epoch, one can consider the real parameter of the spacecraft's orbit, such as its equatorial inclination rather than its ecliptic inclination.

A spacecraft in a random initial orbit may certainly perform several large, inefficient maneuvers to inject itself onto a BLT. It is more difficult to construct a series of maneuvers that would position the spacecraft to perform a single, efficient Trans-Lunar Injection maneuver. This discussion will address how to take a spacecraft with a set of six random Keplerian orbital elements,  $[a, e, i, \Omega, \omega, \nu]$ , and work to position the spacecraft in such a way that it can perform an efficient Trans-Lunar Injection  $\Delta V$  onto a BLT.

We will first address the spacecraft's semi-major axis,  $a$ , its eccentricity,  $e$ , and its inclination,  $i$ . The spacecraft's semi-major axis and eccentricity define the spacecraft's perigee radius via the relationship  $r_p = a(1 - e)$ . The spacecraft's Trans-Lunar Injection  $\Delta V$  is the most efficient if performed at perigee. Thus, one can use the BLT Map for the target three-body orbit and identify the contour that corresponds with the spacecraft's perigee altitude. One can then use knowledge of the spacecraft's inclination to perform a departure opportunity analysis, such as that given in Section 7.2.2. This analysis should reveal many departure opportunities each month. One might be lucky enough to identify a departure opportunity that matches the spacecraft's other three parameters, but we will assume that such an opportunity is not available.

When a particular departure opportunity has been chosen, one then needs to alter the spacecraft's right-ascension of its ascending node,  $\Omega$ , its argument of perigee,  $\omega$ , and its true anomaly,  $\nu$ , in order to position it such that it may perform its Trans-Lunar Injection  $\Delta V$  in a tangential fashion at its perigee point.

The spacecraft's true anomaly may be adjusted using conventional targeting methods in order to position the spacecraft to be at perigee at the proper injection time. Let us say that in its nominal orbit, the spacecraft will traverse  $n$  orbits before arriving at the perigee point that it should use to perform the Trans-Lunar Injection maneuver. Furthermore, let us say that in its current orbit, the spacecraft will arrive at its perigee point **early** by an amount of time equal to  $\Delta t$  seconds. To place the spacecraft at perigee at the proper time, the spacecraft may perform a small  $\Delta V$  at its perigee point to raise its apogee radius. By raising its orbit, the spacecraft increases its orbital period, say, by an amount of time equal to  $\Delta P$  seconds. If  $\Delta P$  is chosen properly, such that  $\Delta P = \Delta t/n$ , the spacecraft will arrive precisely at perigee of this orbit at the proper injection time after traversing  $n$  orbits. Given enough time, namely, given a large enough value of  $n$ , this repositioning maneuver can be as small as desired. Furthermore, it is desirable to raise the apogee of the orbit, rather than lowering it, since this will reduce the Trans-Lunar Injection  $\Delta V$  by a proportional amount.

The next problem is how to align the spacecraft's right-ascension of its ascending node and its argument of perigee to ensure that the Trans-Lunar Injection maneuver is performed in a tangential fashion. If these are not aligned properly, then the Trans-Lunar Injection maneuver will increase in magnitude or a correction maneuver will be required later during the transfer, which may be a sizeable maneuver.

The spacecraft's right-ascension of its ascending node and argument of perigee change over time due to several natural processes. A very notable natural process is the Earth's non-spherical gravity field. The oblateness of the Earth induces a strong secular perturbation in both parameters; the rate of change of both parameters may be

expressed by the following relationships:

$$\dot{\Omega} = -\frac{3}{2}J_2 \left(\frac{R_e}{p}\right)^2 n \cos(i), \quad (7.9)$$

$$\dot{\omega} = \frac{3}{4}J_2 \left(\frac{R_e}{p}\right)^2 n (4 - 5 \sin^2 i), \quad (7.10)$$

where  $J_2$  is the zonal harmonic coefficient that corresponds to the Earth's oblateness, equal to approximately  $1.08263 \times 10^{-3}$  (Boain, 2004),  $R_e$  is the equatorial radius of the Earth, equal to approximately 6378.1363 km (Vallado, 1997),  $p = a(1 - e^2)$  is the orbit parameter,  $n = \sqrt{\mu_e/a^3}$  is the orbit's mean motion,  $\mu_e$  is the gravitational parameter of the Earth, equal to approximately 398,600.4415 km<sup>3</sup>/s<sup>2</sup> (Vallado, 1997), and  $i$  is the inclination of the orbit. Figures 7.17 and 7.18 show plots of the values of  $\dot{\Omega}$  and  $\dot{\omega}$ , respectively, for orbits that have inclination values between  $0^\circ$  and  $90^\circ$  and apogee altitudes between 100 km and 8000 km. The perigee altitude of each orbit has been set to 185 km, since many realistic parking orbits have a perigee altitude near 185 km. One can see that there may be benefit to raising or lowering the apogee altitude of the orbit in order to hit some desirable value of  $\dot{\Omega}$  or  $\dot{\omega}$ .

As the Earth orbits about the solar system barycenter, the spacecraft's orbit rotates about the Earth as viewed in the Sun-Earth synodic frame of reference. The orbit still retains the same right-ascension of the ascending node value, since  $\Omega$  is defined in an inertial frame of reference. What this does mean is that the Trans-Lunar Injection point of a given BLT moves about the Earth at each of its monthly departure opportunities. In the Patched Three-Body model, a BLT that has an injection point with a right-ascension of the ascending node equal to  $\Omega_0$  degrees in one month will have a right-ascension of the ascending node equal to  $(\Omega_0 + P_M \cdot 360^\circ / P_{EM})$  degrees the next, where  $P_M$  is equal to the synodic period of the Moon's orbit about the Earth, approximately 29.486 days, and  $P_{EM}$  is equal to the period of the Earth-Moon barycenter's orbit about the solar system barycenter, approximately 365.24 days. Hence, each consecutive opportunity of the same BLT implements a right-ascension of the ascending node

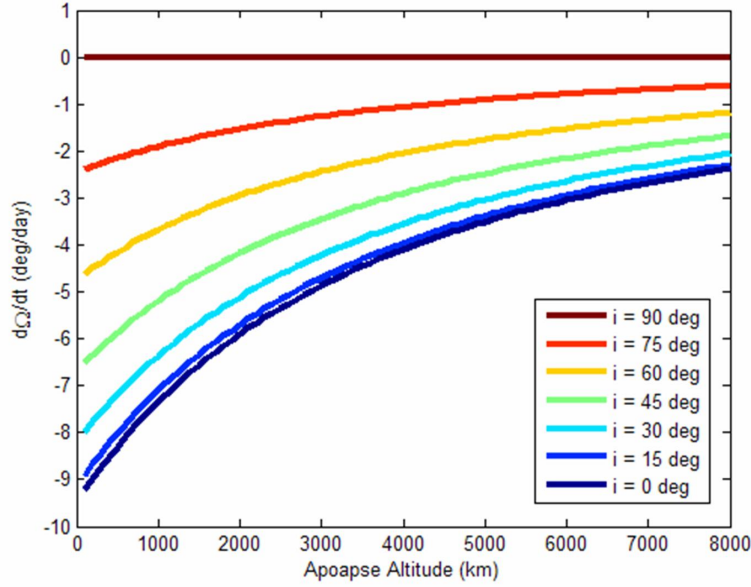


Figure 7.17: Plots of the secular perturbation of the right-ascension of the ascending node,  $\dot{\Omega}$ , for orbits that have inclination values between  $0^\circ$  and  $90^\circ$  and apogee altitudes between 100 km and 8000 km. The perigee altitude of each orbit has been set to 185 km.

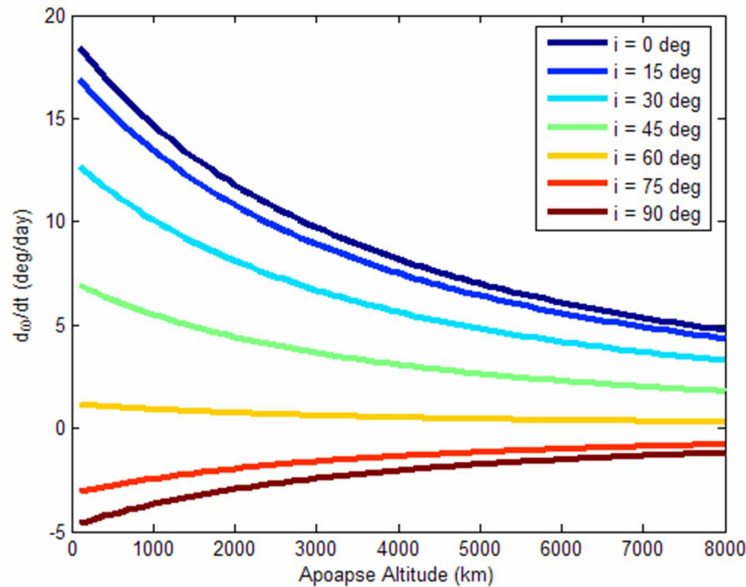


Figure 7.18: Plots of the secular perturbation of the argument of perigee,  $\dot{\omega}$ , for orbits that have inclination values between  $0^\circ$  and  $90^\circ$  and apogee altitudes between 100 km and 8000 km. The perigee altitude of each orbit has been set to 185 km.

value that is approximately  $29.06^\circ$  greater than its last value. It is certainly low-cost to wait for a BLT's departure conditions to meet the spacecraft's orbital parameters, but it may require several months before the conditions line up naturally. Hence, mission designers would probably perform a maneuver at the spacecraft's perigee point, if possible, to target an orbit that had a natural precession rate that would speed up the alignment process.

It may not be possible to align a spacecraft's right-ascension of its ascending node, its argument of perigee, and its true anomaly all with a single maneuver at its perigee point, even with so many departure opportunities every month. But it should be possible to minimize the relative error in each of these parameters, particularly if one is allowed to use several small targeting maneuvers. The result would be a transfer that required greater total  $\Delta V$  than an optimal low-energy transfer, however, it is likely that this process will still result in a mission that requires less total  $\Delta V$  than a direct, conventional lunar transfer.

### 7.3 Applications to Mission Designs

There are many types of mission design concepts that may benefit from the use of low-energy BLTs. This section provides a very top-level description of several example concepts.

**Lunar Libration Point Missions.** Many lunar libration point mission design concepts have been considered in the past, including missions to place a space station at the lunar  $L_1$  point and missions to place communication satellites at either libration point (Clarke, 1950; Columbo, 1961; Farquhar, 1966; Hill et al., 2006b). This research has demonstrated that a mission may benefit substantially by using a BLT rather than a direct transfer in order to transfer a satellite payload into a libration orbit. Section 7.1.1

showed that the same launch vehicle may be used to place up to 35% or possibly 40% more mass into the same libration orbit as a direct transfer. In addition, Section 7.2.3 demonstrated how to use a BLT Map to identify BLTs that may be used to rendezvous with an object already in a libration orbit, such as a space station. Recent studies, e.g., Hill et al. (2006b), have demonstrated how to take advantage of both mission design tools in the JPL Ephemeris model of the solar system.

**Missions to Lunar Science Orbits.** This research has demonstrated that a low-energy trajectory may be used to reduce the orbit-insertion maneuver when a spacecraft intends to insert into a low lunar orbit (§7.1). In this way, BLTs may be used to send larger payloads into low lunar orbits compared with conventional, direct transfers. The low-energy transfers produced in this dissertation use a lunar Halo orbit, or another unstable three-body orbit, as a staging orbit en route to the final lunar orbit. When a spacecraft reaches the lunar staging orbit, the spacecraft may split into several separate satellites. Then, each satellite may follow a different trajectory away from the lunar staging orbit and each may inject into separate low lunar orbits. In this way, a mission designer may be able to construct an entire constellation of lunar satellites using a single launch – further, each of these lunar satellites may be placed into completely different planes without additional cost.

**Missions to the Lunar Surface.** As just mentioned, this research has demonstrated that a low-energy trajectory may be used to reduce the orbit-insertion maneuver when a spacecraft intends to insert into a low lunar orbit (§7.1). Similarly, a low-energy trajectory may be used to reduce the  $\Delta V$  needed to land a vehicle on the surface of the Moon, compared with a conventional, direct transfer. If the proper lunar three-body staging orbit is used in the BLT, then any location on the surface of the Moon may be reached following trajectories in that staging orbit's unstable manifold.

**Repair / Replacement Missions.** A satellite in a lunar three-body orbit may be repaired or replaced using the rendezvous strategies provided in Section 7.2.3. It may also be possible to repair a spacecraft that is in orbit about a Sun-Earth three-body orbit by first transferring the spacecraft to an Earth-Moon three-body using a transfer similar to a BLT; Howell and Kakoi have recently studied such orbit transfers (Howell and Kakoi, 2006). Once the damaged spacecraft is in the Earth-Moon three-body orbit, a repair spacecraft may use a BLT to rendezvous with it to make the repairs. Alternatively, if it requires human contact to repair the satellite, the humans may take a direct transfer to the Earth-Moon three-body orbit while the damaged spacecraft returns from the Sun-Earth libration orbit. The entire servicing mission would require fewer than two weeks for the humans and would require very little energy for the damaged spacecraft.

**Earth-Moon Cyclers.** Every ballistic lunar transfer constructed in the Patched Three-Body model has a symmetric ballistic Earth-return transfer associated with it. Hence, a spacecraft that has used a BLT to reach a lunar Halo orbit may be able to transfer back to the Earth following a symmetric Earth-return transfer. The Earth-return transfer does not need to be in the same family as the spacecraft's initial lunar transfer. In this way, one can build a mission that cycles back and forth between the Earth and the lunar three-body orbit using very little energy.

Many low-energy mission design concepts begin with a transfer from the Earth to an orbit about one of the Sun-Earth libration points. Section 3.10.1 described how to use dynamical systems tools to construct a trajectory that may be used to inject a spacecraft into a Sun-Earth libration orbit using only a single injection maneuver. Once in that orbit, the spacecraft may transfer anywhere along the local Interplanetary Superhighway (Lo and Ross, 2001), including the Moon or other planets. One example of an interesting mission concept is to send many satellites within a Mothership into a

Sun-Earth libration orbit; from there the satellites may be sent back to the Earth along different trajectories in the libration orbit's unstable manifold. In this way, one can construct a complicated constellation of small Earth-observing satellites using a single launch.

Other types of mission designs involve using Earth-Moon orbits as staging orbits, check-out orbits, or quarantine orbits to/from interplanetary space. For example, a spacecraft may be returning from an interplanetary voyage such that it would be desirable to place it into a quarantine orbit before returning it to the Earth. The spacecraft's trajectory may be designed to approach the Earth-Moon system and intersect a trajectory in the stable manifold of a lunar three-body orbit about  $L_2$ . From there, the spacecraft may transfer for free onto a resonant Earth-Moon three-body orbit, for instance. Such an orbit is very stable for weeks at a time. During that time the spacecraft would not require many station-keeping maneuvers. The spacecraft may later transfer back to the  $L_2$  orbit or may divert to its final Earth encounter.

Finally, the dynamical systems methods that have been applied in this research to produce BLTs may be applied in other multi-body systems to design other types of low-energy transfers. For instance, this methodology may be used when designing a transfer between Jovian or Saturnian moons; it may be used to design a tour of a binary asteroid system; or it may even be used to design a transfer to a binary star system outside of the solar system.

#### **7.4 Discussion**

This chapter has discussed how low-energy ballistic lunar transfers and BLT Maps may be applied to practical spacecraft systems design. Section 7.1 addressed how a low-energy transfer might impact the design of a spacecraft system, when compared with conventional transfers. A spacecraft system may benefit with the implementation of a low-energy BLT by experiencing an increase in its payload mass, a reduction

in its propulsion system requirements, a reduction in the complexity of its power and thermal subsystems, longer communication passes, and a potential reduction in the complexity of its mission operations. However, a spacecraft system may experience more difficulty implementing a low-energy transfer due to the large link distances involved with communication, the station-keeping requirements, and the longer transfer durations.

Section 7.2 continued the discussion by introducing several ways to use BLT Maps in the development of practical spacecraft missions. It was found that BLT Maps may be used to help identify the available departure opportunities for a given LEO parking orbit. It was also found that BLT Maps are very helpful with the problem of constructing low-energy rendezvous trajectories between a spacecraft at the Earth and a spacecraft in a lunar three-body orbit.

Finally, Section 7.3 discussed several other top-level mission design scenarios that may benefit with the use of a BLT or other low-energy trajectory.

The purpose of these discussions is to provide some understanding about the costs and benefits associated with implementing a BLT in a practical spacecraft mission. There are certainly many other trade studies that may be performed that would reveal costs and benefits associated with BLTs that have not been outlined here.

## **Chapter 8**

### **Summary and Conclusions**

This research has explored the application of dynamical systems theory to the design of low-energy ballistic lunar transfers. This chapter summarizes the work presented and provides several concluding remarks.

#### **8.1 Contributions to the Field**

This dissertation has contributed to the field of low-energy ballistic trajectory design in many ways. Its most significant contribution is the development of a systematic method that uses dynamical systems tools to model, analyze, and construct low-energy ballistic transfers between the Earth and the Moon in three dimensions. More specifically, the method developed here is the first systematic method that is useful for constructing low-energy ballistic transfers between the Earth and three-dimensional periodic lunar three-body orbits. The dynamical systems methodology has provided the means to parameterize ballistic lunar transfers (BLTs) using a set of six simple parameters. This research has developed the BLT State Space Map (BLT Map) to be used as a tool to identify the parameters that yield desirable BLTs. This dissertation has demonstrated how to use BLT Maps to identify and produce full families of BLTs; the families that have been surveyed in this research have varied widely in their characteristics and performance parameters. Given knowledge of these families of BLTs, a mission designer may be able to quickly identify a low-energy lunar transfer that

meets a given set of mission design requirements.

This research has provided several additional contributions to the field of interplanetary mission design. The BLTs studied here have been used to validate the Patched Three-Body model for trajectories that encounter the Moon and/or the lunar L<sub>1</sub> or L<sub>2</sub> points within the Sun-Earth-Moon-spacecraft four-body system. These studies have also validated the form of the Three-Body Sphere of Influence when applied to ballistic trajectory design within the Sun-Earth-Moon system. An additional contribution of this dissertation has been in the development of two-maneuver ballistic transfers between the Earth and lunar three-body orbits. This dissertation has provided a robust survey of such transfers that have been built using the same dynamical systems methodology that has been used to build low-energy BLTs. As a final contribution to the field, this dissertation has demonstrated how to apply BLTs and BLT Maps to practical spacecraft mission designs.

## **8.2 A Summary of Dynamical Systems Techniques Applied to the Construction of Orbit Transfers**

This section provides a summary of the results of this dissertation, highlighting the results that are new contributions to the field of interplanetary mission design.

### **8.2.1 Parameterization**

Dynamical systems theory has provided the means to parameterize three-body orbit transfers. It is advantageous to be able to parameterize an orbit transfer for several reasons. First, one can easily construct a particular transfer given knowledge of its parameters and knowledge of how to interpret those parameters. Second, one can communicate a particular orbit transfer among mission designers by merely specify-

ing the parameters of that transfer. Finally, one may use the transfer parameters to identify and explore entire families of such transfers. This research has demonstrated that if one has knowledge of full families of orbit transfers, one may be able to quickly identify an orbit transfer that meets one's mission design constraints.

### 8.2.2 Direct Lunar Halo Orbit Transfers

Direct transfers between the Earth and low lunar orbits have been studied and used in the past for many successful lunar missions. However, direct transfers between the Earth and **lunar Halo orbits** have not been thoroughly studied to date. Chapter 4 applies the dynamical systems methodology to the problem of constructing such direct orbit transfers. The chapter presents a robust survey of two-maneuver transfers between 185-km LEO parking orbits and lunar Halo orbits about the lunar L<sub>1</sub> and L<sub>2</sub> points. The technique may certainly be applied to other three-body orbits, although the chapter focused on Halo orbits.

The survey of trajectories presented in Chapter 4 has revealed many types of potentially useful orbit transfers, including quick five-day transfers and longer, more efficient orbit transfers. The results have shown that nearly any lunar libration orbit may be reached for a total transfer  $\Delta V$  of approximately 3.65 km/s, although such transfers may require three or more weeks of time. The quick five-day transfers in the survey require two maneuvers with a total  $\Delta V$  between 3.6 and 4.1 km/s, depending on the target Halo orbit.

The survey provides a baseline cost of the required  $\Delta V$  needed to transfer directly from low Earth orbit to any lunar Halo orbit. Mission designers may use the results of the survey to find a direct transfer that balances their transfer duration constraints with the total  $\Delta V$  cost. This dissertation has used the results of the survey as a performance baseline when compared to the performance of low-energy BLTs.

### 8.2.3 Low-Energy Ballistic Lunar Transfers

Low-energy ballistic transfers between the Earth and various lunar orbits have been studied in the past by many people using a variety of methods. Many researchers have developed targeting schemes to build such transfers; others have used dynamical systems methodology to do so. The dynamical systems strategies that have been implemented in the past to construct ballistic lunar transfers have been limited to the planar problem. This dissertation has presented a new strategy that uses dynamical systems theory to model, analyze, and construct low-energy BLTs in three dimensions. This new strategy is presented in detail in Chapter 5.

The BLTs produced in this dissertation implement three-dimensional staging orbits in the Earth-Moon system, e.g., lunar Halo orbits. This technique provides several key benefits. First, the transfers may be parameterized and constructed in a repeatable, systematic fashion. Second, the mission design process may be compartmentalized such that the transfer between the Earth and the lunar Halo orbit may be constructed separately from the transfer between the lunar Halo orbit and a final destination at the Moon.

This dissertation has also demonstrated the practical application of the Patched Three-Body model, a model that may be used to quickly build trajectories in the Sun-Earth-Moon system. The model takes advantage of the solutions to the circular restricted three-body problem, but is coherent enough to produce realistic trajectories in a four-body system. Chapter 5 validates an example BLT produced in the Patched Three-Body model by converting it into the JPL Ephemeris model and comparing the results directly.

#### 8.2.4 BLT Maps

Since BLTs may be parameterized, they may be organized into families. This dissertation has explored the parameter-space of BLTs and developed a tool called a BLT Map, which is very useful for quickly identifying the parameters that may be used to build useful BLTs. The development and exploration of BLT Maps is presented in Chapter 6.

The example BLT Maps presented in Section 6.3 have been surveyed to determine the characteristics of each of the families of BLTs that exist within those maps. It has been observed that BLTs exist with a wide variety of performance parameters. BLTs may be constructed that depart from orbits at nearly any combination of altitude and inclination. The BLTs that depart from circular 185-km LEO parking orbits require Trans-Lunar Injection maneuvers with magnitudes as little as 3.2 km/s when produced in the Patched Three-Body model. The injection maneuvers may be even lower in the real solar system, depending on the relative locations of the Sun, Earth, and Moon. A wide variety of low-energy ballistic transfers may be constructed that require fewer than 120 days to approach within 100 km of the target three-body orbit. Many require fewer than 100 days to transfer from the Earth to a point where they are considered to be in a temporarily-captured orbit about the Moon. These surveys of BLTs are made possible using the dynamical systems methodology presented in this dissertation.

#### 8.2.5 Applications of BLT Maps to Practical Lunar Missions

It is not necessarily obvious how BLTs and BLT Maps may be applied to practical spacecraft mission designs. The purpose of Chapter 7 is to address several example scenarios that exist where a BLT may be a particularly useful trajectory option and where a BLT Map becomes a pragmatic mission design tool. The discussions in Section 7.1 address the impact that three-body orbits and low-energy transfers have

on spacecraft system designs compared with conventional mission designs. The discussions in Section 7.2 study several applications of BLT Maps to practical spacecraft mission designs. These discussions provide several example conceptual ideas about how to take advantage of the theoretical research presented here and apply it to real mission design problems.

### 8.3 Conclusions

The application of dynamical systems theory to the problem of constructing low-energy ballistic lunar transfers has been shown to be very successful. The dynamical systems methodology results in a systematic way to model, analyze, and build BLTs. It has been found that any given low-energy ballistic transfer to a lunar three-body orbit may be represented using six parameters. These parameters may be systematically varied to identify families of BLTs. Given knowledge of families of BLTs, mission designers should be able to build the BLTs needed to transport material to desirable lunar destinations quickly and easily.

### 8.4 Future Work

The research presented here has targeted a specific goal, namely, to develop a systematic method that uses dynamical systems theory to characterize families of low-energy ballistic lunar transfers. On its path to meeting that goal, many avenues of research have opened up that have not been thoroughly explored. It would be both interesting and potentially very useful to explore many of these avenues.

This research has implemented the Patched Three-Body model to build BLTs using three-body methodology. The Patched Three-Body model approximations have been shown to be valid for the purposes of designing BLTs, but additional work must

be performed for the Patched Three-Body model to be useful when applied to other types of trajectories. The Three-Body Sphere of Influence has been modeled as a sphere centered at the Moon. This model has been exceedingly useful for trajectories that encounter the Moon and/or visit the Earth-Moon L<sub>1</sub> and L<sub>2</sub> points, but it does not permit the design of trajectories near the Earth-Moon L<sub>3</sub>, L<sub>4</sub>, or L<sub>5</sub> points. It would be interesting to study how to extend the Patched Three-Body model to incorporate trajectories that linger near these libration points. In addition, the three-body sphere of influence may be improved if its design considered a spacecraft's velocity as well as its position relative to the Moon.

The two-maneuver direct lunar Halo orbit transfers constructed in Chapter 4 were developed to be used as a performance baseline for low-energy BLTs. However, the application of dynamical systems methodology to the development of such direct lunar transfers is quite new in itself. It would be very interesting to explore the families of such direct transfers further. It may be the case that an alternative technique yields direct lunar transfers that are more efficient than those constructed here. Furthermore, it would be useful to characterize the impact that the gravitational effect of the Sun has on these direct lunar transfers.

A wide variety of low-energy BLTs have been studied in this dissertation. It would be useful to develop a method that could be used to build a BLT with specific requirements without having to search through a BLT Map. For instance, a hypothetical mission may require that the BLT departs a 185-km circular LEO parking orbit at a particular inclination, performs a lunar flyby during its departure phase, and requires no more than 100 days to insert into a desirable lunar orbit. Such a BLT may certainly exist and may even be identifiable from a BLT Map, but it would be interesting to develop a method that could build an initial guess of what such a trajectory might look like. Then that initial guess may be differentially corrected to produce a continuous trajectory.

Further work may also be performed to explore alternative methods to identify and describe the families of BLTs within a BLT Map. This research has introduced the concept that BLTs may be organized into families. It has identified families of BLTs by tracing out contours of a BLT Map. However, other methods, e.g., analytical expansions or iterative schemes, may prove to be more efficient at identifying and characterizing families of BLTs.

The present research may be extended in another way by introducing small maneuvers into the lunar transfer design. Every BLT constructed in this research has been designed to be entirely ballistic. The performance of these BLTs may be significantly improved with the introduction of small maneuvers in the transfer. The introduction of a small maneuver into an otherwise ballistic transfer may reduce the transfer's duration significantly or may alter its Trans-Lunar Injection  $\Delta V$  design. It would be very interesting and potentially very useful to characterize the effects that an introduction of one or more maneuvers would have on the overall performance of a lunar transfer design.

## Bibliography

- Abarbanel, H. D. I., Brown, R., and Kennel, M. B., "Variation of Lyapunov Exponents on a Strange Attractor," *Journal of Nonlinear Science*, Vol. 1, pp. 175–199, 1991.
- Alexeyev, V. M., "New Examples of Capture in the Three-Body Problem," *Soviet Astronomy*, Vol. 6, No. 4, pp. 565–572, 1963.
- Anderson, R. L., *Low Thrust Trajectory Design for Resonant Flybys and Captures Using Invariant Manifolds*, Ph.D. thesis, University of Colorado, Boulder, Colorado, 2005.
- Anderson, R. L. and Lo, M. W., "The Role of Invariant Manifolds in Low Thrust Trajectory Design (Part II)," in *AIAA/AAS Astrodynamics Specialist Conference*, AIAA 2004-5305, AIAA/AAS, Providence, Rhode Island, August 16–19, 2004.
- Andreu, M. A., "New Results on Computation of Translunar Halo Orbits of the Real Earth-Moon System," in *Libration Point Orbits and Applications: Proceedings of the Conference*, edited by G. Gómez, M. W. Lo, and J. J. Masdemont, World Scientific Publishing Company, Aiguablava, Spain, June 2003.
- Arenstorf, R. F., "Existence of Periodic Solutions Passing Near Both Masses of the Restricted Three-Body Problem," *AIAA Journal*, Vol. 1, p. 238, 1963.
- ATK, "ATK Space Systems STAR 27," October 2007.  
URL [http://www.mission.com/starmotors/starmotors\\_star27.asp](http://www.mission.com/starmotors/starmotors_star27.asp)
- Avriel, M., *Nonlinear Programming Analysis and Methods*, Dover Publications, Inc., Mineola, New York, 2003.
- Bailey, J. M., "Jupiter: its Captured Satellites," *Science*, Vol. 173, No. 3999, pp. 812–813, 1971a.
- Bailey, J. M., "Origin of the Outer Satellites of Jupiter," *Journal of Geophysical Research*, Vol. 76, No. 32, pp. 7827–7832, 1971b.
- Barreto, E., Kostelich, E. J., Grebogi, C., Ott, E., and Yorke, J. A., "Efficient Switching Between Controlled Unstable Periodic Orbits in Higher Dimensional Chaotic Systems," in *Phys. Rev. E*, Vol. 51, pp. 4169–4172, 1995.
- Bate, R. R., Mueller, D. D., and White, J. E., *Fundamentals of Astrodynamics*, Dover Publications, Inc., New York, 1971.

- Battin, R. H., *An Introduction to the Mathematics and Methods of Astrodynamics*, American Institute of Aeronautics and Astronautics, Inc., New York, 1987.
- Beckman, M., "Orbit Determination Issues for Libration Point Orbits," in *Libration Point Orbits and Applications: Proceedings of the Conference*, edited by G. Gómez, M. W. Lo, and J. J. Masdemont, World Scientific Publishing Company, Aiguablava, Spain, June 2003.
- Beichman, C., Gómez, G., Lo, M. W., Masdemont, J., and Romans, L., "Searching for Life with the Terrestrial Planet Finder: Lagrange Point Options for a Formation Flying Interferometer," *Advances in Space Research*, Vol. 34, No. 3, pp. 637–644, 2004.
- Belbruno, E. A., "Lunar Capture Orbits, a Method of Constructing Earth Moon Trajectories and the Lunar Gas Mission," in *The 19th AIAA/DGLR/JSASS International Electric Propulsion Conference*, AIAA 87-1054, Colorado Springs, Colorado, May 1987.
- Belbruno, E. A., *Capture Dynamics and Chaotic Motions in Celestial Mechanics*, Princeton University Press, Princeton, NJ, 2004.
- Belbruno, E. A. and Carrico, J. P., "Calculation of Weak Stability Boundary Ballistic Lunar Transfer Trajectories," in *AIAA/AAS Astrodynamics Specialist Conference*, AIAA 2000-4142, AIAA/AAS, Denver, CO, 14-17 August 2000.
- Belbruno, E. A. and Gott III, J. R., "Where did the Moon come from?" *The Astronomical Journal*, Vol. 129, No. 3, pp. 1724–1745, March 2005.
- Belbruno, E. A. and Miller, J., "A Ballistic Lunar Capture Trajectory for the Japanese Spacecraft Hitens," Tech. Rep. IOM 312/90.4-1731-EAB, Jet Propulsion Laboratory, Cal. Tech., 1990.
- Bennett, C. L., "The Microwave Anisotropy Probe (MAP) Mission," in *Bulletin of the American Astronomical Society*, Vol. 28, p. 1391, American Astronomical Society, 189th AAS Meeting, 1996.
- Berger, A. L., "Obliquity & Precession for the Last 5 Million Years," *Astronomy & Astrophysics*, Vol. 51, p. 127, 1976.
- Boain, R. J., "A-B-Cs of Sun-Synchronous Orbit Mission Design," in *AAS/AIAA Space Flight Mechanics Conference*, AAS 04-108, AAS/AIAA, Maui, Hawaii, February 8–12, 2004.
- Bollt, E. M., *Controlling Chaos, Targeting, and Transport*, Ph.D. thesis, University of Colorado, Boulder, CO, 1995, University Microfilms.
- Bollt, E. M. and Meiss, J. D., "Controlling Chaotic Transport Through Recurrence," in *Physica D*, Vol. 81, pp. 280–294, 1995a.
- Bollt, E. M. and Meiss, J. D., "Targeting Chaotic Orbits to the Moon Through Recurrence," in *Physics Letters A*, Vol. 204, pp. 373–378, 1995b.
- Bond, V. R., Sponaugle, S. J., Fraietta, M. F., and Everett, S. F., "Cislunar Libration Point as a Transportation Node for Lunar Exploration," in *AAS/AIAA Spaceflight Mechanics Meeting*, AAS 91-103, AAS/AIAA, February 1991.

- Bonnet, R. M. and Felici, F., "Overview of the SOHO Mission," *Adv. Space Res.*, Vol. 20, pp. 2207–2218, 1997.
- Bray, T. A. and Goudas, C. L., "Doubly-Symmetric Orbits about the Collinear Lagrange Points," *The Astronomical Journal*, Vol. 72, No. 2, March 1967a.
- Bray, T. A. and Goudas, C. L., "Three Dimensional Periodic Oscillations about L1, L2, L3," *Advances in Astronomy and Astrophysics*, Vol. 5, pp. 71–130, 1967b.
- Breakwell, J. V. and Brown, J. V., "The Halo Family of 3-Dimensional Periodic Orbits in the Earth-Moon Restricted 3-Body Problem," *Celestial Mechanics*, Vol. 20, pp. 389–404, 1979.
- Broucke, R. A., "Periodic Orbits in the Restricted Three-Body Problem with Earth-Moon Masses," Tech. Rep. 32-1168, Jet Propulsion Laboratory, Cal. Tech., 1968.
- Broucke, R. A., "Stability of Periodic Orbits in the Elliptic, Restricted Three-Body Problem," *AIAA Journal*, Vol. 7, No. 6, pp. 1003–1009, June 1969.
- Broucke, R. A., Davoust, E., Anderson, J. D., Lass, H., and Blitzer, L., "Periodic solutions about the collinear Lagrangian solution in the general problem of three bodies," *Celestial Mechanics*, Vol. 24, pp. 63–82, May 1981.
- Byl, J. and Ovenden, M. W., "On the Satellite Capture Problem," *Royal Astronomical Society, Monthly Notices*, Vol. 173, No. 3, pp. 579–584, December 1975.
- Clarke, A. C., *Interplanetary Flight*, Temple Press Books Ltd., London, 1950.
- Clohessy, W. H. and Wiltshire, R. S., "Terminal Guidance System for Satellite Rendezvous," *Journal of the Aerospace Sciences*, Vol. 27, No. 9, pp. 653–674, 1960.
- Cobos, J. and Masdemont, J., "Astrodynamical Applications of Invariant Manifolds Associated with Collinear Lissajous Libration Orbits," in *Libration Point Orbits and Applications: Proceedings of the Conference*, edited by G. Gómez, M. W. Lo, and J. J. Masdemont, World Scientific Publishing Company, Aiguablava, Spain, June 2003.
- Coello, C. A. C., Veldhuizen", D. A. V., and Lamont, G. B., *Evolutionary Algorithms for Solving Multi-Objective Problems*, Kluwer Academic / Plenum Publishers, New York, 2002.
- Columbo, G., "The Stabilization of an Artificial Satellite at the Inferior Conjunction Point of the Earth-Moon System," in *Smithsonian Astrophysical Observatory, Special Report No. 80*, November 1961.
- Condon, G. L. and Pearson, D. P., "The Role of Humans in Libration Point Missions with Specific Application to an Earth-Moon Libration Point Gateway Station," in *AIAA/AAS Astrodynamics Specialist Meeting*, AIAA 01-307, AIAA/AAS, Quebec City, Canada, August 2001.
- Conley, C., "Low Energy Transit Orbits in the Restricted Three Body Problem," *SIAM Journal Appl. Math.*, Vol. 16, No. 4, pp. 732–746, 1968.

- Cross, C. A., "Orbits for an Extra-Terrestrial Observatory," *Journal of the British Interplanetary Society*, Vol. 13, No. 4, pp. 204–207, 1954.
- D'Amario, L. A., "Minimum Impulse Three-Body Trajectories," Tech. Rep. T-593, Massachusetts Institute of Technology, June 1973.
- Darwin, G. H., "Periodic Orbits," *Acta Mathematica*, Vol. 21, pp. 99–242, 1897.
- Darwin, G. H., "Periodic Orbits," *Scientific Papers*, Vol. 4, 1911, Cambridge University Press, Cambridge, Mass.
- Delaunay, C. E., *La Théorie du mouvement de la lune, 2 Volumes*, 1860, 1867.
- Deligiannis, F., Sherwood, R., Perrone, D., and Di Stefano, S., "TOPEX/Poseidon NiCd Battery Performance – Comparison of Flight and Ground Test Results," in *AIAA Intersociety Energy Conversion Engineering Conference*, pp. 105–111, AIAA 1994-4038, AIAA, Monterey, CA, August 7–11, 1994.
- Ditto, W., Spano, M., and Lindner, J., "Techniques for the Control of Chaos," *Physica D.*, Vol. 86, pp. 198–211, September 1995.
- Dunham, D. and Roberts, C., "Stationkeeping Techniques for Libration-Point Satellites," in *AIAA/AAS Astrodynamics Specialist Conference*, AIAA 98-4466, AIAA, August 10–12, 1998.
- Dunham, D. W., "Contingency Plans for the ISEE-3 Libration Point Mission," in *AIAA/AAS Astrodynamics Specialist Conference*, AIAA 79-129, AIAA/AAS, 1979.
- Dunham, D. W., Jen, S. J., Roberts, C. E., Seacord, A. W., Sharer, P. J., Folta, D. C., and Muonen, D. P., "Transfer Trajectory Design for the SOHO Libration-Point Mission," in *43rd Congress of the International Astronautical Federation*, IAF Paper 92-0066, 1992.
- Edelbaum, T. N., "Libration Point Rendezvous," Tech. Rep. N70-26184, Report No. 70-12, Analytical Mechanics Associates, Inc., Cambridge, Massachusetts, February 1970.
- Encyclopedia Astronautica, "Encyclopedia Astronautica Orbital Launch Vehicle Index," February 2007.  
URL <http://www.astronautix.com/lvs/orbindex.htm>
- Euler, E. A. and Yu, E. Y., "Optimal Station Keeping at Collinear Points," *Journal of Spacecraft and Rockets*, Vol. 8, pp. 513–517, 1971.
- Farquhar, R. W., "Station-Keeping in the Vicinity of Collinear Libration Points with an Application to a Lunar Communications Problem," in *Space Flight Mechanics, Science and Technology Series*, Vol. 11, pp. 519–535, American Astronautical Society, New York, 1966.
- Farquhar, R. W., "Lunar Communications with Libration-Point Satellites," *Journal of Spacecraft and Rockets*, Vol. 4, No. 10, pp. 1383–1384, 1967.
- Farquhar, R. W., *The Control and Use of Libartion-Point Satellites*, Ph.D. thesis, Department of Aeronautics and Astronautics, Stanford University, Stanford, CA, 1968.

- Farquhar, R. W., "Future Missions for Libration-point Satellites," *Astronautics & Aeronautics*, pp. 52–56, May 1969.
- Farquhar, R. W., "The Utilization of Halo Orbits in Advanced Lunar Operations," Tech. rep., NASA TN D-6365, July 1971.
- Farquhar, R. W., "The Role of the Sun-Earth Collinear Libration Points in Future Space Exploration," in *SPACE TIMES*, pp. 10–12, November–December 2000.
- Farquhar, R. W. and Dunham, D. W., "Use of Libration-Point Orbits for Space Observatories," in *Observatories in Earth Orbit and Beyond*, pp. 391–395, Kluwer Academic Publishers, 1990.
- Farquhar, R. W. and Kamel, A. A., "Quasi-Periodic Orbits about the Translunar Libration Point," *Celestial Mechanics*, Vol. 7, No. 4, pp. 458–473, June 1973.
- Farquhar, R. W., Muhonen, D., and Richardson, D., "Mission Design for a Halo Orbiter of the Earth," *Journal of Spacecraft and Rockets*, Vol. 14, No. 3, pp. 170–177, March 1977.
- Fesenkov, V. G., "On the Possibility of Capture at Close Passages of Attracting Bodies," *Astronomicheskiy Zhurnal*, Vol. 23, No. 1, pp. 45–48, 1946, Astronomical Journal of the Soviet Union.
- Foing, B. H. and Racca, G. R., "The ESA SMART-1 Mission to the Moon with Solar Electric Propulsion," *Advances in Space Research*, Vol. 23, No. 11, pp. 1865–1870, 1999.
- Folta, D. and Quinn, D., "Lunar Frozen Orbits," in *AIAA/AAS Astrodynamics Specialist Conference and Exhibit*, AIAA 2006-6749, AIAA/AAS, Keystone, Colorado, August 21–24, 2006.
- Folta, D. and Vaughn, F., "A Survey of Earth-Moon Libration Orbits: Stationkeeping Strategies and Intra-Orbit Transfers," in *AIAA/AAS Astrodynamics Specialist Conference and Exhibit*, AIAA 2004-4741, AIAA/AAS, Providence, Rhode Island, August 16–19, 2004.
- Gardner, J. P., "The James Webb Space Telescope," in *Large Telescopes and Virtual Observatory: Visions for the Future*, 25th meeting of the IAU, Sydney, Australia, July 2003.
- Godwin, R. (Editor), *Apollo 11 – The NASA Mission Reports, The Apogee Books Space Series*, Vol. 1, Collector's Guide Publishing Inc., 1999.
- Gómez, G., Jorba, A., Llibre, J., Martínez, R., Masdemont, J., and Simó, C., *Dynamics and Mission Design near Libration Points*, Vol. I–IV, World Scientific Publishing Co., Singapore, 2001a.
- Gómez, G., Koon, W. S., Lo, M. W., Marsden, J. E., Masdemont, J., and Ross, S. D., "Invariant Manifolds, the Spatial Three-Body Problem and Space Mission Design," in *AIAA/AAS Astrodynamics Specialist Meeting*, AIAA 01-301, AIAA/AAS, Quebec City, Canada, August 2001b.
- Gómez, G., Koon, W. S., Marsden, J. E., Masdemont, J., and Ross, S. D., "Connecting Orbits and Invariant Manifolds in the Spatial Restricted Three-Body Problem," *Nonlinearity*, Vol. 17, pp. 1571–1606, 2004.

- Gómez, G. and Masdemont, J., "Some Zero Cost Transfers Between Libration Point Orbits," in *AAS/AIAA Spaceflight Mechanics Meeting*, AAS 00-177, AAS/AIAA, Clearwater, Florida, January 2000.
- Gómez, G., Masdemont, J., and Mondelo, J. M., "Libration Point Orbits: A Survey from the Dynamical Point of View," in *Libration Point Orbits and Applications: Proceedings of the Conference*, edited by G. Gómez, M. W. Lo, and J. J. Masdemont, World Scientific Publishing Company, Aiguablava, Spain, June 2003.
- Gómez, G., Masdemont, J., and Simó, C., "Quasihalo Orbits Associated with Libration Points," *The Journal of the Astronautical Sciences*, Vol. 46, No. 2, pp. 135–176, 1998.
- Gómez, G., Simó, C., Llibre, J., and Martínez, R., "Dynamics and Mission Design near Libration Points, Volume II: Fundamentals: The Case of Triangular Libration Points," *World Scientific Monograph Series in Mathematics*, Vol. 3, 2001c.
- Goudas, C. L., "Three Dimensional Periodic Orbits and their Stability," *Icarus*, Vol. 2, pp. 1–18, 1963.
- GSFC, "NASA's High Energy Astrophysics Science Archive Research Center," March 2007a.  
 URL <http://heasarc.gsfc.nasa.gov/>
- GSFC, "Wilkinson Microwave Anisotropy Probe," March 2007b.  
 URL <http://map.gsfc.nasa.gov/>
- Guillaume, P., "New Periodic Solutions of the Three Dimensional Restricted Problem," *Celestial Mechanics*, Vol. 10, No. 4, pp. 475–495, 1974.
- Hénon, M., "Exploration Numérique du Problème des Trois Corps, (I), Masses Égales, Orbites Périodiques," *Ann. Astrophys.*, Vol. 28, No. 3, pp. 499–511, 1965a.
- Hénon, M., "Exploration Numérique du Problème des Trois Corps, (II), Masses Égales, Orbites Périodiques," *Ann. Astrophys.*, Vol. 28, No. 6, pp. 992–1007, 1965b.
- Hénon, M., "Exploration Numérique du Problème des Trois Corps, (III), Masses Égales, Orbites Non Périodiques," *Bull. Astron.*, Vol. 1, No. 1, pp. 57–80, 1966a.
- Hénon, M., "Exploration Numérique du Problème des Trois Corps, (IV), Masses Égales, Orbites Non Périodiques," *Bull. Astron.*, Vol. 1, No. 2, pp. 49–66, 1966b.
- Hénon, M., "Numerical Exploration of the Restricted Problem. V., Hill's Case: Periodic Orbits and Their Stability," *Astron. & Astrophys.*, Vol. 1, pp. 223–238, 1969.
- Hénon, M., "New Families of Periodic Orbits in Hill's Problem of Three Bodies," *Celestial Mech. & Dynamical Astr.*, Vol. 85, pp. 223–246, 2003.
- Heppenheimer, T. A., "On the Presumed Capture Origin of Jupiter's Outer Satellites," *Icarus*, Vol. 24, pp. 172–180, February 1975.
- Heppenheimer, T. A., "Achromatic Trajectories and Lunar Material Transport for Space Colonization," *Journal of Spacecraft and Rockets*, Vol. 15, No. 3, pp. 176–183, 1978a.

- Heppenheimer, T. A., "A Mass-Catcher for Large-Scale Lunar Material Transport," *Journal of Spacecraft and Rockets*, Vol. 15, No. 4, pp. 242–249, 1978b.
- Heppenheimer, T. A., "Steps Toward Space Colonization - Colony Location and Transfer Trajectories," *Journal of Spacecraft and Rockets*, Vol. 15, No. 5, pp. 305–312, 1978c.
- Heppenheimer, T. A. and Kaplan, D., "Guidance and Trajectory Considerations in Lunar Mass Transportation," *AIAA Journal*, Vol. 15, pp. 172–180, February 1977.
- Heppenheimer, T. A. and Porco, C., "New Contributions to the Problem of Capture," *Icarus*, Vol. 30, No. 2, pp. 385–401, February 1977.
- Hill, G. W., "Researches in Lunar Theory," *American Journal of Mathematics*, Vol. 1, pp. 5–26, 1878.
- Hill, G. W., "On the Part of the Motion of the Lunar Perigee which is a Function of the Mean Motions of the Sun and the Moon," *Acta Math.*, Vol. 8, pp. 1–36, 1886.
- Hill, G. W., "Review of Darwin's Periodic Orbits," *Astronomical Journal*, Vol. 18, No. 423, p. 120, 1898.
- Hill, K. and Born, G. H., "Autonomous Interplanetary Orbit Determination Using Satellite-to-Satellite Tracking," *AIAA Journal of Guidance, Control, and Dynamics*, Vol. 30, No. 3, May–June 2007.
- Hill, K., Lo, M. W., and Born, G. H., "Liaison Navigation in the Sun-Earth-Moon Four-Body Problem," in *AAS/AIAA Spaceflight Dynamics Conference*, AAS 06-221, AAS/AIAA, Tampa, FL, January 22–26, 2006a.
- Hill, K., Parker, J. S., Born, G. H., and Demandante, N., "A Lunar L2 Navigation, Communication, and Gravity Mission," in *AIAA/AAS Astrodynamics Specialist Conference*, AIAA 2006-6662, AIAA/AAS, Keystone, Colorado, August 2006b.
- Hoffman, D., *A Set of C Utility Programs for Processing JPL Ephemeris Data*, Johnson Space Center, 1998.
- Hohmann, W., *Die Erreichbarkeit Der Himmelskörper: Untersuchungen über Das Raumfahrtproblem*, Munique, 1925.
- Hopf, E., "Zwei Sätze über den wahrscheinlichen Verlauf der Bewegungen Dynamischer Systeme," *Mathematische Annalen*, Vol. 103, pp. 710–719, 1930.
- Horedt, G. P., "Capture of Planetary Satellites," *Astronomical Journal*, Vol. 81, No. 8, pp. 675–680, August 1976.
- Howell, K. C., "Three-Dimensional, Periodic, 'Halo' Orbits," *Celest. Mech.*, Vol. 32, No. 53, 1984.
- Howell, K. C., "Families of Orbits in the Vicinity of the Collinear Libration Points," in *AIAA/AAS Astrodynamics Specialist Conference and Exhibit*, AIAA 1998-4465, AIAA/AAS, Boston, MA, August 10–12, 1998.

- Howell, K. C., Barden, B. T., and Lo, M. W., "Application of Dynamical Systems Theory to Trajectory Design for a Libration Point Mission," *Journal of Astronautical Sciences*, Vol. 45, No. 2, pp. 161–178, April–June 1997a.
- Howell, K. C., Barden, B. T., Wilson, R. S., and Lo, M. W., "Trajectory Design Using a Dynamical Systems Approach with Application to Genesis," in *AAS/AIAA Astrodynamics Specialist Conference*, AAS 97-709, AAS/AIAA, Sun Valley, Idaho, August 4–7, 1997b.
- Howell, K. C. and Kakoi, M., "Transfers Between the Earth-Moon and Sun-Earth Systems using Manifolds and Transit Orbits," *Acta Astronautica*, Vol. 59, No. 1–5, pp. 367–380, 2006, IAC-05-C1.6.01.
- Howell, K. C., Mains, D. L., and Barden, B. T., "Transfer Trajectories from Earth Parking Orbits to Sun-Earth Halo Orbits," in *AAS/AIAA Spaceflight Mechanics Meeting*, AAS 94-160, AAS/AIAA, Cocoa Beach, Florida, 1994.
- Howell, K. C., Marchand, B. G., and Lo, M. W., "Temporary Satellite Capture of Short-Period Jupiter Family Comets from the Perspective of Dynamical Systems," *Journal of Astronautical Sciences*, Vol. 49, No. 4, 2001.
- Howell, K. C. and Pernicka, H. J., "Numerical Determination of Lissajous Trajectories in the Restricted Three-Body Problem," *Celest. Mech.*, Vol. 41, pp. 107–124, 1988.
- Howell, K. C. and Pernicka, H. J., "Sun-Earth Libration Point Trajectories that Avoid the Solar Exclusion Zone," *Journal of the Astronautical Sciences*, Vol. 38, pp. 269–288, July–September 1990.
- Ivashkin, V. V., "On Trajectories of the Earth-Moon Flight of a Particle with its Temporary Capture by the Moon," *Doklady Physics, Mechanics*, Vol. 47, No. 11, pp. 825–827, 2002.
- Ivashkin, V. V., "On the Earth-to-Moon Trajectories with Temporary Capture of a Particle by the Moon," in *54th International Astronautical Congress*, pp. 1–9, Paper IAC-03-A.P.01, Bremen, Germany, Sept. 29–Oct. 3, 2003.
- Ivashkin, V. V., "On Particle's Trajectories of Moon-to-Earth Space Flights with the Gravitational Escape from the Lunar Attraction," *Doklady Physics, Mechanics*, Vol. 49, No. 9, pp. 539–542, 2004a.
- Ivashkin, V. V., "On Trajectories for the Earth-to-Moon Flight with Capture by the Moon," in *International Lunar Conference 2003, Science and Technology Series*, Vol. 108, edited by Steve M. Durst, et al., pp. 157–166, American Astronautical Society AAS, 2004b.
- Jaffé, C., Ross, S. D., Lo, M. W., Marsden, J., Farrelly, D., and Uzer, T., "Statistical Theory of Asteroid Escape Rates," *Phys. Rev. Lett.*, Vol. 89, July 2002.
- JPL, "Genesis: Search for Origins," March 2007.  
 URL <http://genesismission.jpl.nasa.gov/>

- Julliard-Tosel, E., "Bruns' Theorem: The Proof and Some Generalizations," in *Celestial Mechanics and Dynamical Astronomy*, Vol. 76, pp. 241–281, Springer Netherlands, April 2000.
- Kolemen, E., Kasdin, N. J., and Gurfil, P., "Quasi-Periodic Orbits of the Restricted Three-Body Problem Made Easy," in *New Trends in Astrodynamics and Applications III, American Institute of Physics Conference Series*, Vol. 886, pp. 68–77, February 2007.
- Kolenkiewicz, R. and Carpenter, L., "Stable Periodic Orbits about the Sun Perturbed Earth-Moon Triangular Points," *AIAA Journal*, Vol. 6, No. 7, pp. 1301–1304, 1968.
- Koon, W. S., Lo, M. W., Marsden, J. E., and Ross, S. D., "Heteroclinic Connections Between Periodic Orbits and Resonance Transitions in Celestial Mechanics," *Chaos*, Vol. 10, No. 2, pp. 427–469, 2000a.
- Koon, W. S., Lo, M. W., Marsden, J. E., and Ross, S. D., "Shoot the Moon," in *AAS/AIAA Spaceflight Mechanics 2000*, Vol. 105, part 2, pp. 1017–1030, AAS/AIAA, 2000b.
- Koon, W. S., Lo, M. W., Marsden, J. E., and Ross, S. D., "Low Energy Transfers to the Moon," *Celestial Mechanics and Dynamical Astronomy*, Vol. 81, pp. 63–73, 2001.
- Koon, W. S., Lo, M. W., Marsden, J. E., and Ross, S. D., "Dynamical Systems, the Three-Body Problem and Space Mission Design," 2007, in progress.
- Kostelich, E. J., Grebogi, C., Ott, E., and Yorke, J. A., "Higher-dimensional Targeting," in *Phys. Rev. E*, Vol. 47, pp. 305–310, 1993.
- Lichtenberg, A. J. and Lieberman, M. A., *Regular and Stochastic Motion*, Springer-Verlag, New York, 1983.
- Lidov, M. L. and Rabinovich, V. Y., "Investigation of Families of Three-Dimensional Periodic Orbits of the Three-Body Problem," *Cosmic Research*, Vol. 17, No. 3, 1979.
- Limon, M., et al., "Wilkinson Microwave Anisotropy Probe (WMAP): Explanatory Supplement," Tech. Rep. 1.0, Goddard Space Flight Center, Greenbelt, MD: NASA/GSFC, February 11, 2003.
- Llibre, J., Martínez, R., and Simó, C., "Transversality of the Invariant Manifolds Associated to the Lyapunov Family of Periodic Orbits Near L2 in the Restricted Three-Body Problem," *J. Differ. Eq.*, Vol. 58, pp. 104–156, 1985.
- Lo, M., Serban, R., Petzold, L., Koon, W., Ross, S., Marsden, J., and Wilson, R., "Halo Orbit Mission Correction Maneuvers Using Optimal Control," Tech. rep., Jet Propulsion Laboratory, January 1, 2000.
- Lo, M. W., Anderson, R. L., Lam, T., and Whiffen, G., "The Role of Invariant Manifolds in Low Thrust Trajectory Design (Part III)," in *AAS/AIAA Spaceflight Dynamics Conference*, AAS 06-190, AAS/AIAA, Tampa, Florida, January 22–26, 2006.
- Lo, M. W., Anderson, R. L., Whiffen, G., and Romans, L., "The Role of Invariant Manifolds in Low Thrust Trajectory Design," in *AAS/AIAA Spaceflight Dynamics Conference*, AAS 04-288, AAS/AIAA, Maui, Hawaii, February 8–12, 2004.

- Lo, M. W. and Parker, J. S., "Unstable Resonant Orbits Near Earth and Their Applications in Planetary Missions," in *AIAA/AAS Astrodynamics Specialist Conference*, Vol. 14, AIAA / AAS, Providence, RI, August 16–19, 2004.
- Lo, M. W. and Parker, J. S., "Chaining Simple Periodic Three-Body Orbits," in *AAS/AIAA Astrodynamics Specialist Conference*, AAS 2005-380, AIAA/AAS, Lake Tahoe, California, August 7–11, 2005.
- Lo, M. W. and Ross, S. D., "The Lunar L<sub>1</sub> Gateway: Portal to the Stars and Beyond," in *AIAA Space 2001 Conference*, Albuquerque, NM, 2001.
- Lo, M. W., Williams, B. G., Bollman, W. E., Han, D. S., Hahn, Y. S., Bell, J. L., Hirst, E. A., Corwin, R. A., Hong, P. E., Howell, K. C., Barden, B., and Wilson, R., "Genesis Mission Design," *The Journal of the Astronautical Sciences*, Vol. 49, pp. 169–184, 2001.
- Loucks, M., Carrico, J., Carrico, T., and Deiterich, C., "A Comparison of Lunar Landing Trajectory Strategies Using Numerical Simulations," in *International Lunar Conference*, September 2005.
- Lozier, L., Galal, K., Folta, D., and Beckman, M., "Lunar Prospector Mission Design and Trajectory Support," in *AAS/AIAA Spaceflight Dynamics Conference*, AAS 98-323, AAS/AIAA, 1998.
- Lyapunov, A. M., "The General Problem of the Stability of Motion," *Comm. Soc. Math. Kharkow*, 1892, in Russian, reprinted in English, Taylor & Francis, London, 1992.
- Ma, C., Arias, E. F., Eubanks, T. M., Fey, A. L., Gontier, A. M., Jacobs, C. S., Sovers, O. J., Archinal, B. A., and Charlot, P., "The International Celestial Reference Frame as Realized by Very Long Baseline Interferometry," *The Astronomical Journal*, Vol. 116, pp. 516–546, July 1998.
- Makó, Z. and Szenkovits, F., "Capture in the Circular and Elliptic Restricted Three-Body Problem," *Celestial Mechanics and Dynamical Astronomy*, Vol. 90, No. 1, pp. 51–58, July 2004.
- Malcuit, R. J., Mehringer, D. M., and Winters, R. R., "Numerical Simulation of Gravitational Capture of a Lunar-Like Body by Earth," in *Lunar and Planetary Science Conference*, edited by G. Ryder and V. L. Sharpton, pp. 581–591, Cambridge University Press / Lunar and Planetary Institute, Houston, TX, March 14–15, 1989.
- Markeev, A. P., "Two-Dimensional Periodic Motion of a Satellite Relative to the Center of Mass Near a Collinear Libration Point," *Cosmic Research*, Vol. 17, No. 3, 1979.
- Marsden, J. E. and Ross, S. D., "New Methods in Celestial Mechanics and Mission Design," in *Bulletin of the American Mathematical Society*, Vol. 43, pp. 43–73, 2005.
- Matukuma, T., "On the Periodic Orbits in Hill's Case," *Proceedings of the Imperial Academy of Japan*, Vol. 9, No. 364, 1933.
- Matukuma, T., "Sendai astr. Rap., No. 51, 1957.

- McGehee, R. P., *Some Homoclinic Orbits for the Restricted Three Body Problem*, Ph.D. thesis, University of Wisconsin, Madison, Wisconsin, 1969.
- Meeus, J., *Astronomical Algorithms*, First English ed., William-Bell, Inc., Richmond, VA, 1991.
- Miller, J. K. and Belbruno, E. A., "A Method for the Construction of a Lunar Transfer Trajectory Using Ballistic Capture," in *AAS/AIAA Space Flight Mechanics Meeting*, Vol. 1, pp. 97–109, AAS/AIAA, Houston, TX, Feb 11–13, 1991.
- Moulton, F. R., "Periodic Orbits," *Carnegie Institute of Washington Publications*, No. 161, 1920.
- Muhonen, D. P., "Accelerometer-Enhanced Orbit Control Near the Sun-Earth L<sub>1</sub> Libration Point," in *AIAA 21st Aerospace Sciences Meeting*, AIAA-83-0018, AIAA, Reno, Nevada, January 10–13, 1983.
- Murdin, P., "ACE (Advanced Composition Explorer)," in *Encyclopedia of Astronomy and Astrophysics*, 4518, Bristol: Institute of Physics Publishing, 2000.
- Murison, M. A., "The Fractal Dynamics of Satellite Capture in the Circular Restricted Three-Body Problem," *The Astronomical Journal*, Vol. 98, No. 6, pp. 2346–2386, 1989.
- NASA, "NASA National Space Science Data Center (NSSDC) Lunar and Planetary Home Page," August 2006.  
 URL <http://nssdc.gsfc.nasa.gov/planetary/planets/moonpage.html>
- NASA, "Glenn Research Center Home," March 2007a.  
 URL <http://www.nasa.gov/centers/glenn/>
- NASA, "NASA's Image Access Home Page," February 2007b.  
 URL <http://photojournal.jpl.nasa.gov>
- NASA, J. P. L., "Mars Odyssey: Home," 2007c.  
 URL <http://mars.jpl.nasa.gov/odyssey/>
- Nayfeh, A. H. and Balachandran, B., *Applied Nonlinear Dynamics*, John Wiley and Sons, Inc., New York, 1995.
- Newton, I., *Philosophiae Naturalis Principia Mathematica*, Londoni, 1687.
- Ocampo, C. A., "COPERNICUS: A Trajectory Design and Optimization System," in *First International Conference on Libration Points and Libration Point Missions*, Institut d'Estudis Espacials de Catalunya, Parador d'Aiguablava, Girona, Spain, 10 – 14 June 2002.
- Ocampo, C. A. and Rosborough, G. W., "Transfer Trajectories for Distant Retrograde Orbiters of the Earth," in *AAS/AIAA Spaceflight Dynamics Conference*, AAS 93-344, AAS/AIAA, 1993.
- Orbital, *Pegasus User's Guide*, Orbital Sciences Corporation, release 6.0 ed., June 2007.

- Oseledec, V. I., "A Multiplicative Ergodic Theorem. Lyapunov Characteristic Numbers for Dynamical Systems," in *Transactions of the Moscow Mathematical Society*, Vol. 19, Trudy Moskov. Mat. Obshch., 1968.
- Ott, E., Grebogi, C., and Yorke, J. A., "Controlling Chaos," in *Physical Review Letters*, Vol. 64, pp. 1196–1199, 1990.
- Ott, E. and Spano, M., "Controlling Chaos," *Physics Today*, Vol. 48, pp. 34–40, 1995.
- Paffenroth, R. C., Doedel, E. J., and Dichmann, D. J., "Continuation of Periodic Orbits Around Lagrange Points and AUTO2000," in *AIAA/AAS Astrodynamics Specialist Conference*, AIAA 01-303, AIAA/AAS, Quebec City, July 2001.
- Parker, J. S., "Families of Low-Energy Lunar Halo Transfers," in *AAS/AIAA Spaceflight Dynamics Conference*, AAS 06-132, AAS/AIAA, Tampa, FL, January 22–26, 2006.
- Parker, J. S., *Low-Energy Ballistic Lunar Transfers*, Ph.D. thesis, University of Colorado, Boulder, Colorado, 2007.
- Parker, J. S. and Born, G. H., "Direct Lunar Halo Orbit Transfers," in *AAS/AIAA Spaceflight Mechanics Conference*, AAS 07-229, AAS/AIAA, Sedona, Arizona, January 28 – February 1, 2007.
- Parker, J. S. and Lo, M. W., "Shoot the Moon 3D," in *AAS/AIAA Astrodynamics Specialist Conference*, AAS 05-383, AAS/AIAA, Lake Tahoe, CA, August 7–11, 2005.
- Parker, T. S. and Chua, L. O., *Practical Numerical Algorithms for Chaotic Systems*, Springer-Verlag, New York, 1989.
- Pernicka, H. J., *The Numerical Determination of Lissajous Orbits in the Circular Restricted Three-Body Problem*, Master's thesis, Purdue University, December 1986.
- Pernicka, H. J. and Howell, K. C., "Sun-Earth Libration Point Trajectories that Avoid the Solar Exclusion Zone," *Journal of the Astronautical Sciences*, Vol. 38, No. 3, pp. 269–288, 1990.
- Pilbratt, G. L., Prusti, T., Heras, A. M., Leeks, S., Marston, A. P., and Vavrek, R., "Herschel Space Observatory," in *American Astronomical Society Meeting 204*, Paper 01-81, 2004.
- Plummer, H. C., "On Oscillating Satellites – 1," *Monthly Notices of the Royal Astronomical Society*, Vol. 63, No. 8, pp. 436–443, 1903.
- Poincaré, H., "Sur le problème des trois corps et les équations de la dynamique," *Acta Math*, Vol. 13, pp. 1–27, 1890.
- Poincaré, H., *Les Méthodes Nouvelles de la Mécanique Celeste, 3 Volumes*, 1892.
- Pollack, J. B., Burns, J. A., and Tauber, M. E., "Gas Drag in Primordial Circumplanetary Nebulae: A Mechanism for Satellite Capture," *Icarus*, Vol. 37, pp. 587–611, 1979.
- Richardson, D. L., "Analytical Construction of Periodic Orbits about the Collinear Points," *Celestial Mechanics*, Vol. 22, pp. 241–253, 1980.

- Richardson, D. L. and Cary, N. D., "A Uniformly Valid Solution for Motion of the Interior Libration Point for the Perturbed Elliptic-Restricted Problem," in *AIAA/AAS Astrodynamics Specialist Conference*, AIAA 75-021, AIAA/AAS, July 1975.
- Ross, S. D., *Cylindrical Manifolds and Tube Dynamics in the Restricted Three-Body Problem*, Ph.D. thesis, California Institute of Technology, April 2004.
- Russell, R., "Global Search for Planar and Three-Dimensional Periodic Orbits near Europa," in *AAS/AIAA Astrodynamics Specialist Conference*, AAS 05-290, AAS/AIAA, Lake Tahoe, CA, August 7–11, 2005.
- Russell, R. P. and Lara, M., "Repeat Ground Track Lunar Orbits in the Full-Potential Plus Third-Body Problem," in *AIAA/AAS Astrodynamics Specialist Conference and Exhibit*, AIAA 2006-6750, AIAA/AAS, Keystone, Colorado, August 21–24, 2006.
- Scheeres, D. J., Han, D., and Hou, Y., "Orbit Determination Uncertainty Distributions and Mappings in an Unstable Halo Orbit," Tech. Rep. IPN PR 42-146, The Interplanetary Network Progress Report, April–June 2001.
- Schmidt, Y., "The Possibility of Capture in Celestial Mechanics," *Doklady Akademii Nauk SSSR*, Vol. 58, No. 2, pp. 213–216, 1947.
- Schroer, C. G. and Ott, E., "Targeting in Hamiltonian Systems that have Mixed Regular/Chaotic Phase Spaces," *Chaos*, Vol. 7, No. 4, pp. 512–519, December 1997.
- Serban, R., Koon, W. S., Lo, M. W., Marsden, J. E., Petzold, L. R., Ross, S. D., and Wilson, R. S., "Halo Orbit Mission Correction Maneuvers Using Optimal Control," *Automatica*, Vol. 38, pp. 571–583, 2002.
- Shinbrot, T., Grebogi, C., Ott, E., and Yorke, J. A., "Using Small Perturbations to Control Chaos," *Nature*, Vol. 363, pp. 411–417, 1993.
- Shinbrot, T., Ott, E., Grebogi, C., and Yorke, J. A., "Using Chaos to Direct Trajectories to Targets," in *Physical Review Letters*, Vol. 65, pp. 3215–3218, 1990.
- Simó, C., Gómez, G., Llibre, J., and Martínez, R., "Station Keeping of a Quasiperiodic Halo Orbit Using Invariant Manifolds," Tech. rep., 1987.
- Simó, C., Jorba, A., Masdemont, J., and Gómez, G., *From Newton to Chaos*, p. 343, Plenum Press, New York, 1995.
- Smith, N. G., Williams, K. E., Wiens, R. C., and Rasbach, C. E., "Genesis – The Middle Years," in *IEEE Aerospace Conference*, Vol. 1, IEEE, Big Sky, Montana, 2003.
- Standish, E. M., "JPL Planetary and Lunar Ephemerides, DE405/LE405," Tech. Rep. IOM 312.F-98-048, Jet Propulsion Laboratory, August 1998.
- Sternfeld, A., "Sur les Trajectoires Permettant d'un Corps Attractif Central à Partir d'une Orbite Keplérienne Donnée," *Comptes Rendus de l'Acad. des Sciences*, Vol. 198, pp. 711–713, 1934.
- Sternfeld, A., *Introduction to Cosmonautics*, ONTI NKTP Publishers, Moscow, USSR, 1937.

- Sternfeld, A., *Artificial Satellites of the Earth*, GITTL Publishers, Moscow, USSR, 1956.
- Strogatz, S. H., *Nonlinear Dynamics and Chaos*, Perseus Books Publishing, L.L.C., 1994.
- Strömgren, E., "Connaissance actuelle des orbites dans le problème des trois corps," *Copenhagen Observatory Publications*, , No. 100, 1935, also *Bull. Astr. Vol. 9*, No. 87, 1935.
- Sundman, K., "Recherches sur le Problème des Trois Corps," *Acta Societatis Scientiarum Fennicae*, Vol. 34, 1908.
- Sundman, K., "Nouvelle Recherches sur le Problème des Trois Corps," *Acta Societatis Scientiarum Fennicae*, Vol. 35, 1909.
- Sundman, K., "Mémoire sur le Problème des Trois Corps," *Acta Mathematica*, Vol. 36, pp. 105–179, 1912.
- Sutton, G. P. and Biblarz, O., *Rocket Propulsion Elements*, 7th ed., John Wiley and Sons, Inc., 2001.
- Sweetser, T. H., "Estimate of the Global Minimum DV Needed for Earth-Moon Transfer," in *AAS/AIAA Spaceflight Mechanics Meeting*, AAS 91-101, AAS/AIAA, Houston, TX, February 1991.
- Szebehely, V., *Theory of Orbits: The Restricted Problem of Three Bodies*, Academic Press, New York, 1967.
- Szebehely, V. and Evans, R. T., "On the Capture of the Moon," *Celestial Mechanics*, Vol. 21, pp. 259–264, April 1980.
- Tanabe, T., Itoh, Y., Ishii, N., and Yokota, H., "Visiting Libration Points in the Earth-Moon System Using a Lunar Swingby," in *International Symposium on Space Technology and Science*, Tokyo, Japan, 1982.
- Tisserand, F., *Traité de mécanique céleste, 4 Volumes*, 1889–1896.
- Toppotto, F., Vasile, M., and Bernelli-Zazzera, F., "Interplanetary and Lunar Transfers using Libration Points," in *18th International Symposium on Space Flight Dynamics*, Munich, Germany, October 2004.
- Uesugi, K., "Japanese first double Lunar swingby mission 'HITEN,'" *Acta Astronautica*, Vol. 25, No. 7, pp. 347–355, 1991.
- Vallado, D. A., *Fundamentals of Astrodynamics and Applications*, McGraw-Hill Companies, Inc., 1997.
- Vieira Neto, E., *Estudo Numérico da Captura Gravitacional Temporária Utilizando o Problema Restrito de Três Corpos*, Ph.D. thesis, Instituto Nacional de Pesquisas Espaciais, Brazil, 1999.
- Vieira Neto, E. and Prado, A., "Time-of-Flight Analyses for the Gravitational Capture Maneuver," *Journal of Guidance, Control and Dynamics*, Vol. 21, No. 1, pp. 122–126, 1998.

- Vieira Neto, E. and Winter, O. C., "Time Analysis for Temporary Gravitational Capture: Satellites of Uranus," *The Astronomical Journal*, Vol. 122, pp. 440–448, 2001.
- Wade, M., "Encyclopedia Astronautica," October 2007.  
URL <http://www.astronautix.com>
- Walt, M., *Introduction to Geomagnetically Trapped Radiation*, Cambridge University Press, Cambridge, UK, 2005.
- Wiggins, S., *Introduction to Applied Nonlinear Dynamical Systems and Chaos*, Text in Applied Mathematics, 2, Springer-Verlag, New York, 1990.
- Williams, K. E., Lewis, G. D., Wilson, R. S., Helfrich, C. E., and Potts, C. L., "Genesis Earth Return: Refined Strategies and Flight Experience," in *AAS/AIAA Space Flight Mechanics Conference*, AAS 05-116, AAS/AIAA, Copper Mountain, CO, January 23–27, 2005.
- Wilson, H. and Turcotte, L., *Advanced Mathematics and Mechanics Applications Using MATLAB*, 2nd ed., CRC Press, 1997.
- Wilson, R., *Trajectory Design in the Sun-Earth-Moon Four Body Problem*, Ph.D. thesis, Purdue University, December 1998.
- Wilson, R., "Derivation of Differential Correctors Used in GENESIS Mission Design," Tech. Rep. JPL IOM 312.I-03-002, Jet Propulsion Laboratory, 2003.
- Winter, G., Périaux, J., Galán, M., and Cuesta, P. (Editors), *Genetic Algorithms in Engineering and Computer Science*, John Wiley and Son Ltd., 1995.
- Wittmann, A., "The Obliquity of the Ecliptic," *Astronomy & Astrophysics*, Vol. 73, pp. 129–131, 1979.
- Yamakawa, H., *On Earth-Moon Transfer Trajectory with Gravitational Capture*, Ph.D. thesis, University of Tokyo, 1992.
- Yamakawa, H., Kawaguchi, J., Ishii, N., and Matsuo, H., "On Earth-Moon Transfer Trajectory with Gravitational Capture," in *AIAA/AAS Astrodynamics Specialist Conference*, AIAA 93-633, AIAA/AAS, August 1993.
- Zagouras, C. G. and Kalogeropoulou, M., "Numerical Determination of Families of Three-Dimensional Orbits Bifurcating from Plane Periodic Orbits around Both Primaries," *Astron. Astrophys. Suppl.*, Vol. 32, pp. 307–321, 1978.

## Appendix A

### Planar Simple Periodic Symmetric Orbits

The circular restricted three-body system permits a huge number of different families of periodic orbits to exist. To demonstrate the variety and potential uses of these orbits, while also providing some idea of how many families of general periodic orbits exist, this chapter will give an overview description of many of the families in the CRTB system that contain planar simple periodic symmetric orbits.

As defined by Strömgren (1935), **simple periodic symmetric orbits** are orbits that pierce the  $x$ -axis of the CRTBP's rotating coordinate frame exactly two times each period, and each  $x$ -axis crossing is orthogonal. In general, this type of orbit is one of the most fundamental types of three-body orbits, providing a basis to build more complicated orbits and trajectories. Many of these orbits are unstable and can be chained together – a topic discussed further in Section 3.10. Astronomers have noted in literature that the motion of certain comets and other celestial bodies may be explained using the pathways that approach and depart from simple periodic symmetric orbits (see, e.g., Tisserand, 1889–1896; Howell et al., 2001; Jaffé et al., 2002). Nevertheless, the orbits presented in this section represent a very small sample of orbit solutions to the CRTBP. An infinite number of other families of orbits exist, including three-dimensional orbits (samples provided in Appendix B), asymmetric orbits, orbits that make more revolutions about their centers, etc.

The families presented here have been classified in different ways in previous

studies. Matukuma (1933 and 1957) and Strömgren (1935) classified five families of simple-periodic orbits based on the location of the origin of the family. For instance, one of their families originated from small orbits about one of the primary bodies, another originated from  $L_1$ , etc. The trouble with the classical scheme for classifying symmetric periodic orbit families is that as one moves from one orbit to its neighbor in the family, the orbits gradually move around the system until it may not be clear which object was its origin. Furthermore, if the entire family is not known, it may not be clear at all where the family originated from. Broucke (1968) introduced a classification scheme that avoids these confusions entirely. He conjectured that since this type of orbit pierces the  $x$ -axis two times orthogonally, one could introduce six classes that would contain all such periodic orbits based on the locations of those piercings. The “center” of the orbit would then be clearly defined. Furthermore, one family of orbits is always contained within a single class since it would have to cross a singularity to change classes. The classes and a pictorial description are listed in Table A.1. The family of orbits shown in Figure A.1 may be used as an example for this classification scheme. Since both  $x$ -axis crossings of every Lyapunov orbit about  $LL_2$  occur to the right of  $M_2$ , that family would be classified as a Class 6 family. Table A.2, below, summarizes all of the families of orbits presented in this paper and categorizes them into their appropriate classes. Prograde orbits revolve about their center in a counter-clockwise fashion, keeping step with the conventional right-hand rule for angular momentum.

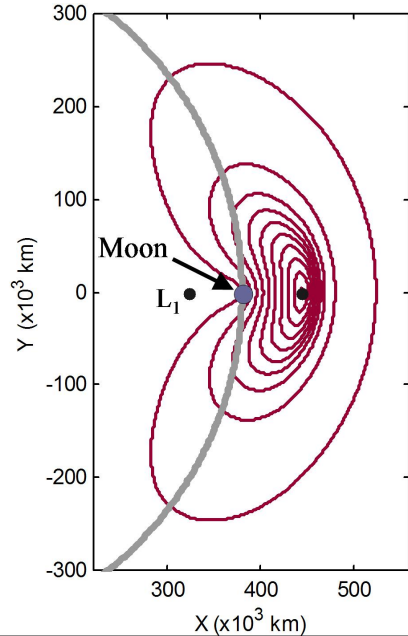


Figure A.1: A portion of the family of Lyapunov orbits about  $L_2$  in the Earth-Moon system.

Table A.1: Classification of symmetric periodic orbits in the PCRTBP based on their orthogonal  $x$ -axis crossings.

Class	Structure	Center
Class 1		$L_3$
Class 2		$M_1$
Class 3		$M_1+M_2$
Class 4		$L_1$
Class 5		$M_2$
Class 6		$L_2$

Table A.2: A summary of the families of simple periodic symmetric orbits presented in this study. The labels in parentheses are used to locate the family-types in Figures A.2 – A.8.

Orbit Class	Center	Family Types	
Class 1	$L_3$	Prograde	Horseshoe Families (1A)
		Retrograde	Lyapunov $L_3$ (1B)
Class 2	$M_1$	Prograde	Near-Earth (2A), Two-Lobed Distant Flybys (2B)
		Retrograde	Retrograde Lunar Flybys, with optional $L_4/L_5$ Loops (2C)
Class 3	$M_1+M_2$	Prograde	Resonant Lunar Flybys (3A)
		Retrograde	Distant Orbits (3B), Short-Period Orbits (3C), Retrograde Lunar Flybys, with optional $L_4/L_5$ loops (3D)
Class 4	$L_1$	Prograde	N/A
		Retrograde	Lyapunov $L_1$ (4A)
Class 5	$M_2$	Prograde	Low-Lunar (5A), Two-Lobed Distant Lunar (5B)
		Retrograde	Distant Retrograde Orbits (5C)
Class 6	$L_2$	Prograde	N/A
		Retrograde	Lyapunov $L_2$ (6A)

As introduced in Section 3.7, each family of orbits in the PCRTBP consists of an infinite number of periodic orbits whose properties vary continuously from one end of the family to the other. All orbits in the same family may be uniquely identified by a single parameter of that family. This study generally uses an orbit's  $x_0$ -position (its  $x$ -position at the orbit's orthogonal  $x$ -axis crossing with positive  $y$ ) or its Jacobi constant to identify it in its family.

The initial conditions of the simple-periodic symmetric orbits found in the Earth-Moon system that did not hit the Earth's surface or the Moon's surface are shown in Figures A.2 – A.6, below. Figure A.3 shows those orbits whose initial conditions lay on the far side of  $L_3$ , Figure A.4 shows the orbits between  $L_3$  and the Earth, Figure A.5 shows the orbits between the Earth and the Moon, and Figure A.6 shows the orbits between the Moon and  $L_2$ . In all of the plots, the gray orbits are neutrally stable and the black orbits are unstable; the labels indicate which type of family the orbits belong to, as defined in Table A.2 above. Some labels apply to more than one actual family of orbits, especially since some families bifurcate endlessly, preventing clear labels.

Figure A.7 shows a plot that compares the Jacobi constant,  $C$ , for all of these periodic orbits. The orbits may be matched with those shown in Figures A.2 – A.6 via their  $x_0$  values. It is valuable to be able to visibly compare the orbits' relative Jacobi constants when constructing free transfers in Section 3.10.2. Figure A.8 similarly compares the periods of these orbits, which may prove useful when designing certain transfer trajectories.

The orbits in each of the families will now be examined in more detail.

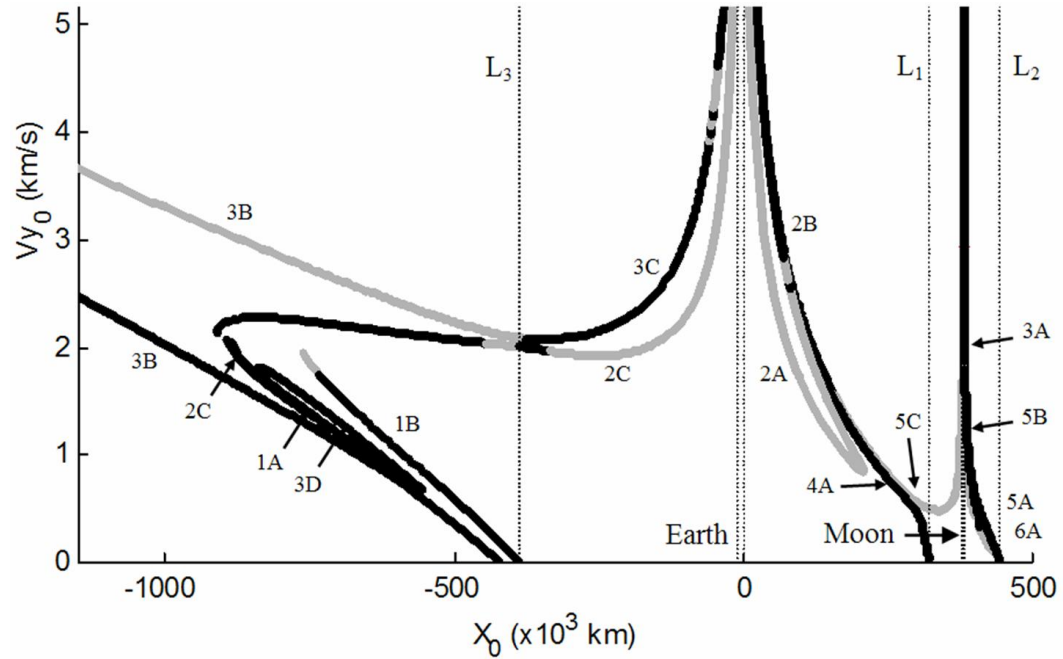


Figure A.2: A plot of  $x_0$  vs.  $y_0$  for the families of periodic orbits presented in this study. Orbits plotted in black are unstable; orbits plotted in gray are neutrally stable.

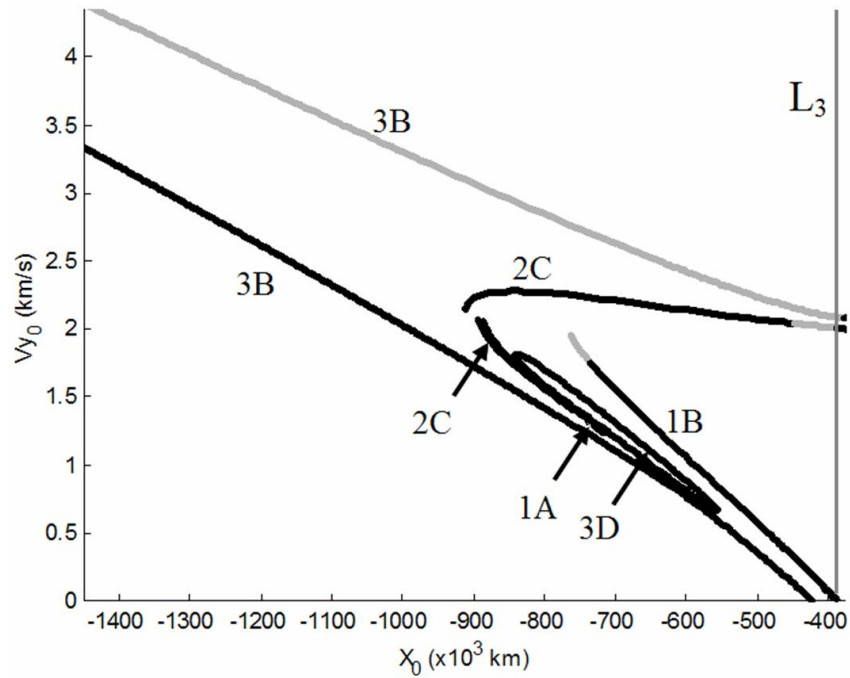


Figure A.3: A plot of  $x_0$  vs.  $y_0$  for the families of periodic orbits on the far side of  $L_3$ .

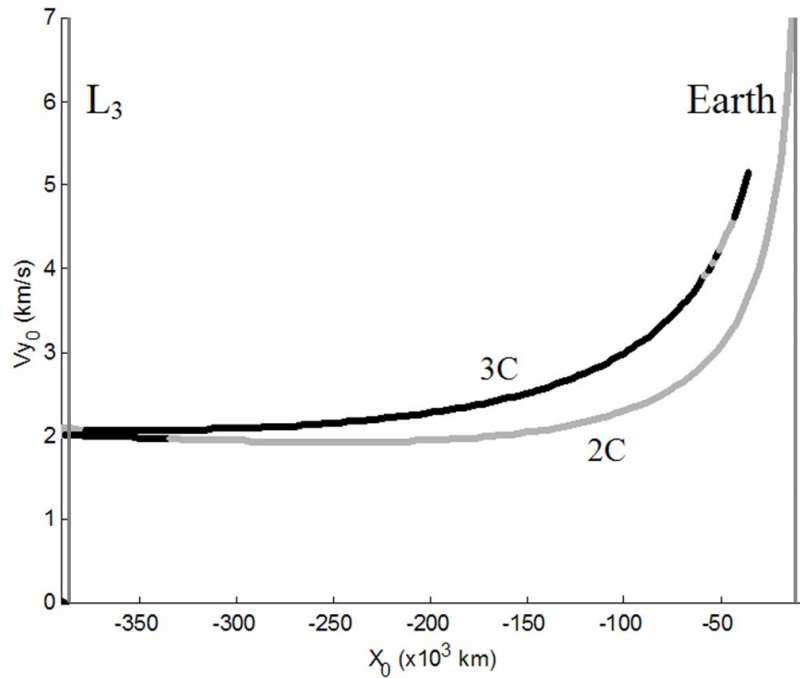


Figure A.4: A plot of  $x_0$  vs.  $y_0$  for the families of periodic orbits between  $L_3$  and the Earth.

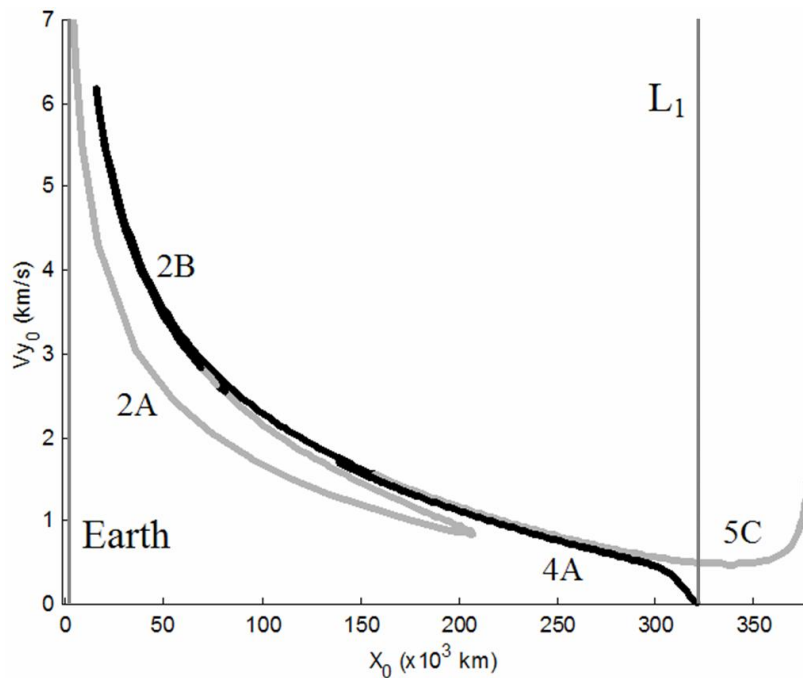


Figure A.5: A plot of  $x_0$  vs.  $y_0$  for the families of periodic orbits between the Earth and the Moon.

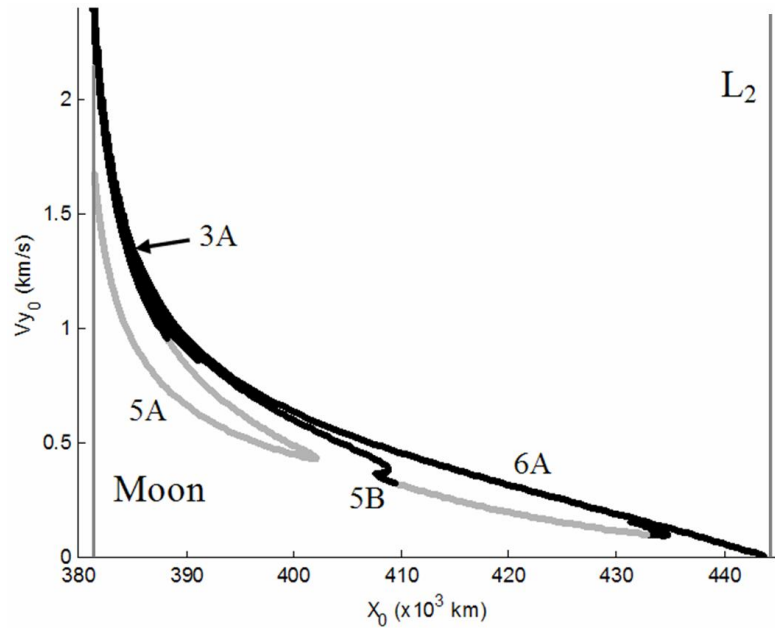


Figure A.6: A plot of  $x_0$  vs.  $y_0$  for the families of periodic orbits between the Moon and  $L_2$ .

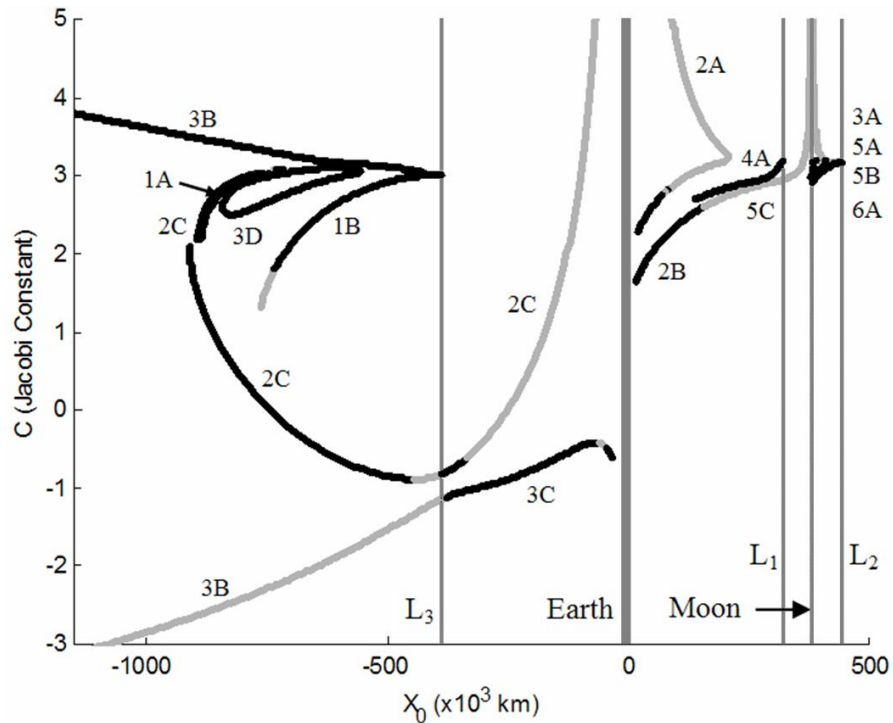


Figure A.7: A plot of  $x_0$  vs.  $C$  for the families of periodic orbits presented in this study. Orbits plotted in black are unstable; orbits plotted in gray are neutrally stable.

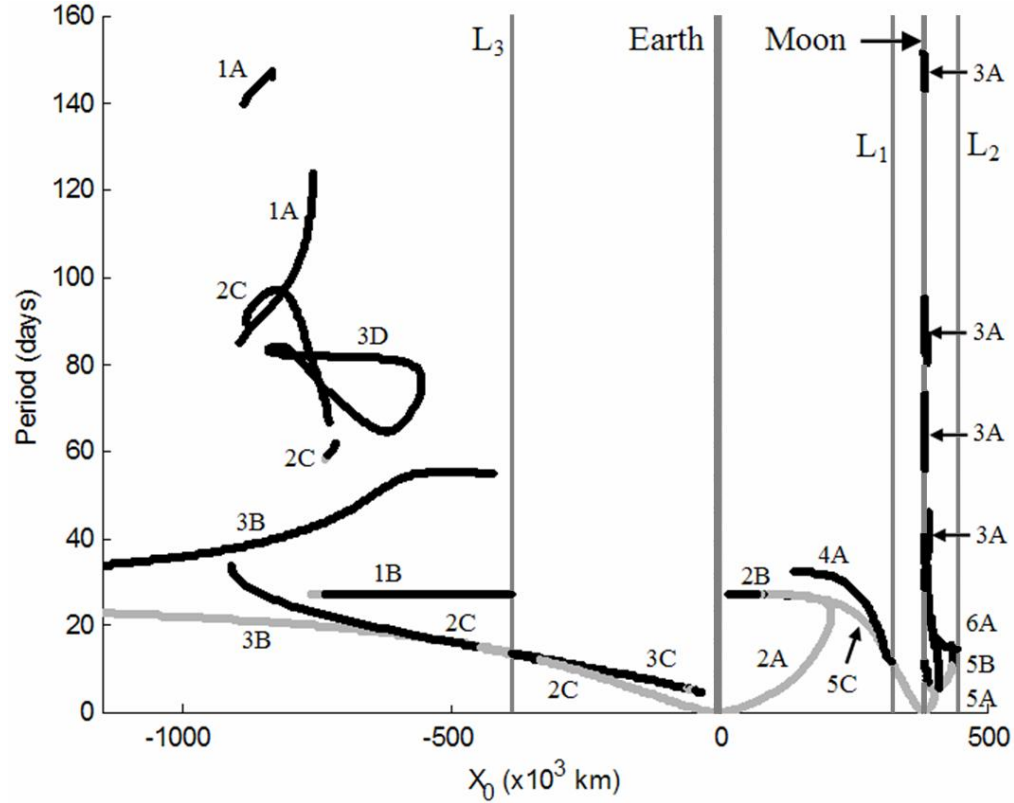


Figure A.8: A plot of  $x_0$  vs.  $P$ , the orbital period, for the families of periodic orbits presented in this study. Orbits plotted in black are unstable; orbits plotted in gray are neutrally stable.

### A.1 Class 1: Orbits Centered about $L_3$

Class 1 orbits include all simple periodic symmetric orbits that pierce the  $x$ -axis twice on the far side of the Earth. Several families have such characteristics, including the family of Lyapunov orbits centered about  $L_3$  as well as a large group of horseshoe-shaped families.

Figure A.9 presents three plots describing the Lyapunov family of orbits, including a plot of several trajectories showing the shape of the orbits (top), a plot of the initial conditions used to produce the orbits (bottom-left), and the family's orbital period compared with other nearby families (bottom-right). The plots are each colored

according to the stability of the orbit, where red represents unstable orbits and green represents neutrally stable orbits. The two plots on the bottom of the figure include the other families shown in Figures A.2 – A.8 for reference.

Figure A.10 includes several plots of families that trace out a horseshoe-like shape, including  $n$  loops in both the upper and lower sections of the plot, where  $n$  may be any positive integer. Because of the unrestricted value of  $n$  there are an infinite number of these families of orbits; as  $n$  grows the orbits approach periodic orbits that exist about  $L_4$  /  $L_5$ . Figure A.10 includes plots of orbits that have between 1 and 11 loops per side.

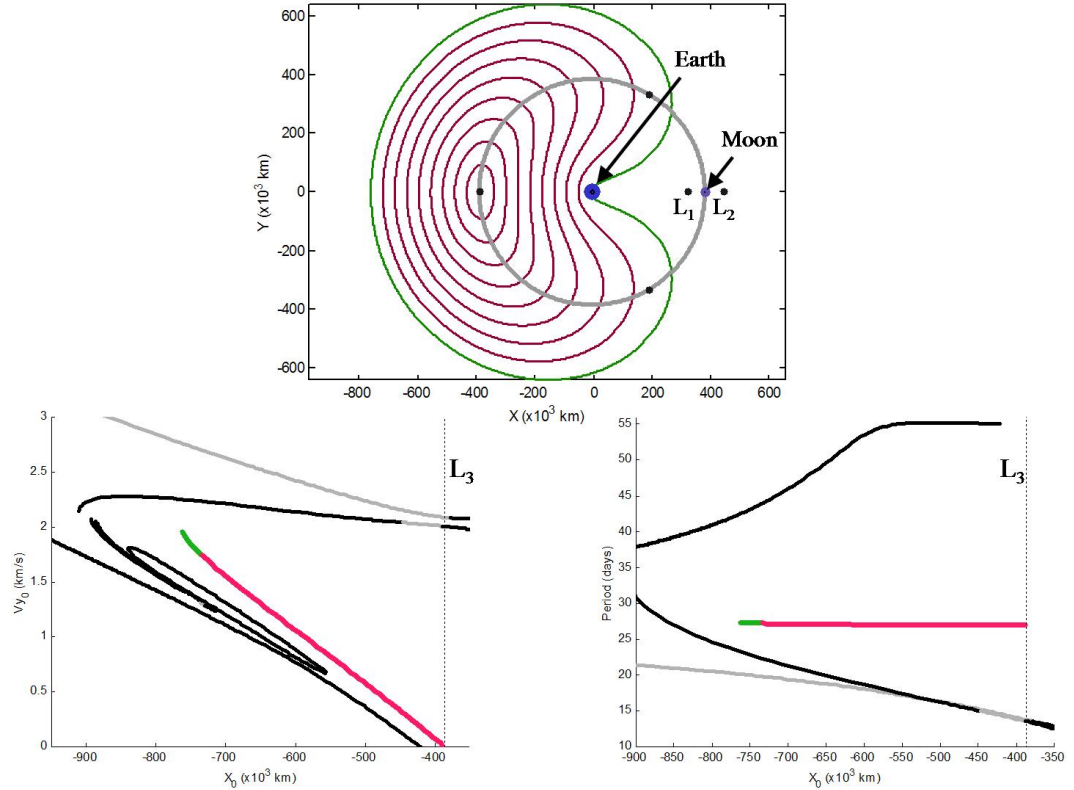


Figure A.9: Three plots describing the family of Lyapunov orbits centered about  $L_3$ , including a plot of several trajectories showing the shape of the orbits (top), a plot of  $x_0$  vs.  $v_{x0}$  (bottom-left), and a plot of  $x_0$  vs.  $P$  (bottom-right).

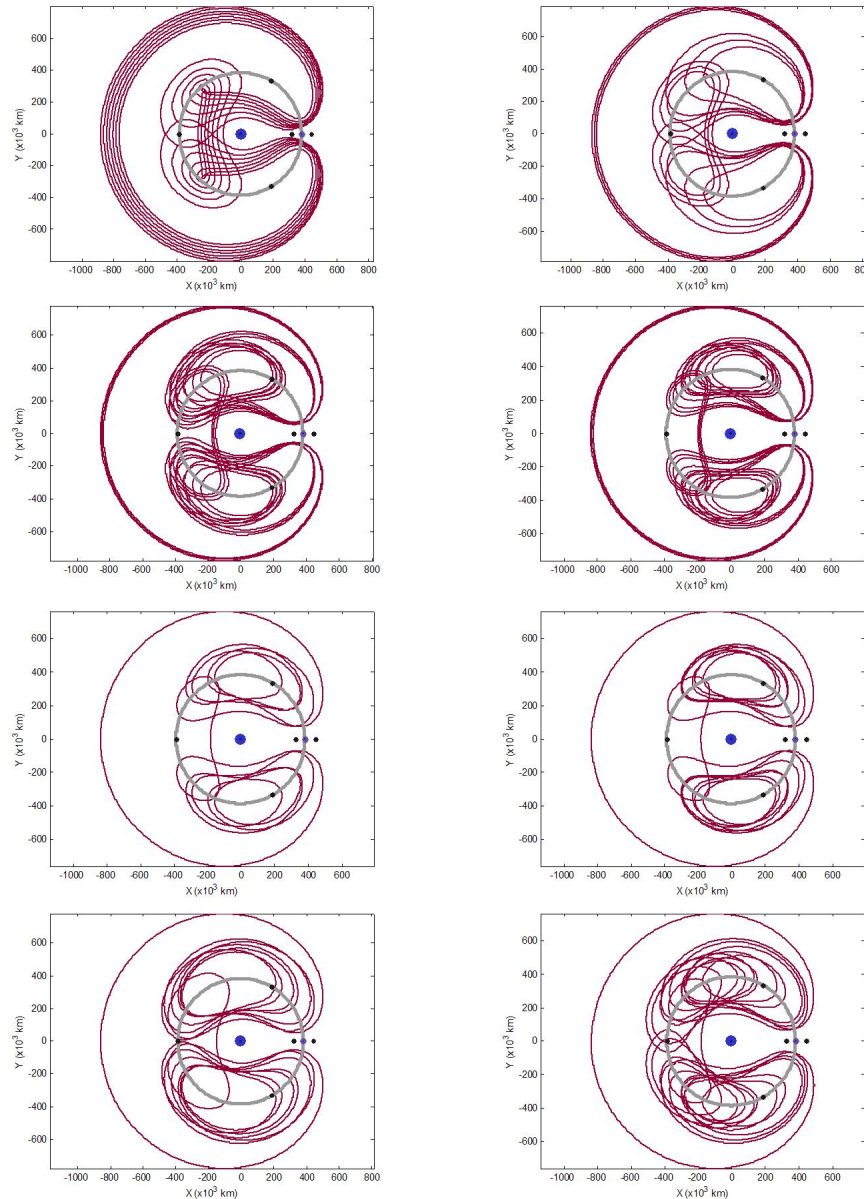


Figure A.10: Horseshoe-shaped orbits with varying numbers of upper and lower loops.

## A.2 Class 2: Orbits Centered about $M_1$

Class 2 orbits include all simple periodic symmetric orbits that pierce the  $x$ -axis on both sides of  $M_1$  (the Earth). There are several types of families that share this characteristic, including both prograde and retrograde orbits.

### A.2.1 Prograde Orbits about $M_1$

Only one family of prograde Class 2 orbits has been identified in this study. Figure A.11 includes four plots describing this family of orbits, including two plots of trajectories showing the shape of the orbits (top), a plot of the initial conditions used to produce the orbits (bottom-left), and the family's orbital period compared with other nearby families (bottom-right). The family approaches low Earth orbits on one side,

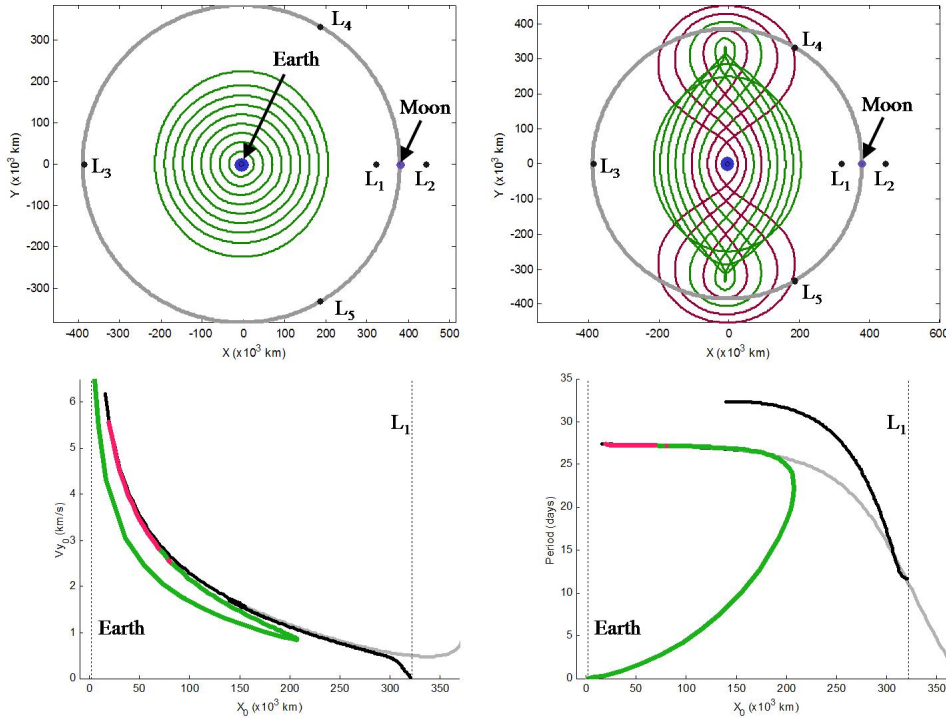


Figure A.11: Four plots describing the prograde Class 2 family centered about the Earth, including two plots of several trajectories showing the shape of the orbits (top), a plot of  $x_0$  vs.  $y_0$  (bottom-left), and a plot of  $x_0$  vs.  $P$  (bottom-right).

except that they require the Moon's presence to be periodic in this synodic frame. The other side of the family includes two Earth flybys, making them unstable.

### A.2.2 Retrograde Orbits about $M_1$

There are essentially two types of retrograde orbits in Class 2 that have been identified in this study. One type makes a smooth transition from low Earth retrograde to a point where it begins making periodic lunar flybys. The other type of family always makes periodic lunar flybys and includes  $n$  loops about the  $L_4$  /  $L_5$  vicinity, where  $n$  can be any integer greater than or equal to zero. Figure A.12 shows three plots describing the first family of retrograde orbits; Figure A.13 shows a few characteristic orbits of different families in the second type of retrograde orbits.

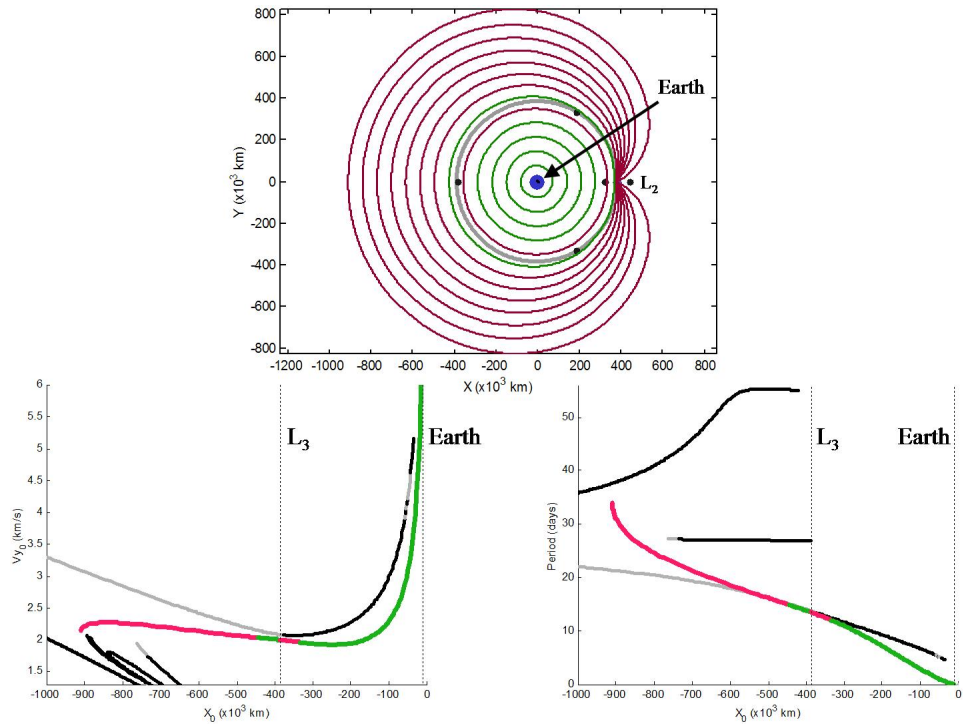


Figure A.12: Three plots describing the family of retrograde orbits centered about the Earth, including a plot of several trajectories showing the shape of the orbits (top), a plot of  $x_0$  vs.  $y_0$  (bottom-left), and a plot of  $x_0$  vs.  $P$  (bottom-right).

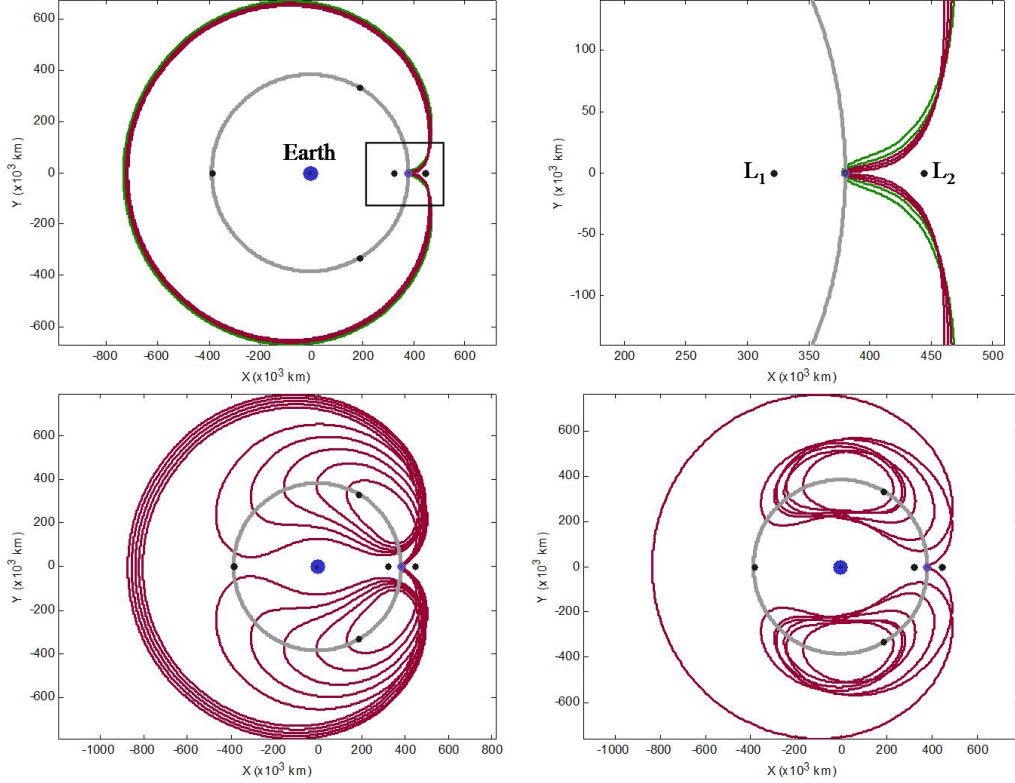


Figure A.13: A few characteristic orbits in the families that make periodic lunar flybys as well as  $n$  loops in the vicinity of  $L_4 / L_5$ . The top-right plot is a blow-up of the lunar flybys made by the orbits in the upper-left plot. The orbits in the lower-left plot make one loop in the  $L_4 / L_5$  vicinity; the orbits in the lower-right plot make six such loops.

### A.3 Class 3: Orbits Centered about $M_1+M_2$

The orbits in Class 3 pierce the  $x$ -axis on opposite sides of the two primaries, that is, they include both primaries within their “center”. Several families have been found in this class, including prograde and retrograde orbits.

#### A.3.1 Prograde Orbits about $M_1+M_2$

The only type of prograde orbits found in Class 3 in this study are contained in families of orbits that make periodic close flybys of the Moon while orbiting the Earth in nearly two-body motion. The lunar flybys occur at resonant times with the Moon’s

orbit about the Earth. Any resonance is theoretically possible, but most of them would strike the surface of the Moon. This study has explored four such families that fly by the Moon beyond its radius, theoretically safe for all missions designed in the PCRTBP. Figure A.14 shows a plot of the initial  $x$ -position that was used to produce three of these resonant orbits vs. the orbit's period, continued until the family began to impact the Moon's surface. It is useful to plot  $x_0$  vs. the orbit's period for these families because the resonances are then readily identified. The families constructed here have weak resonances near 3:1, 3:2, 5:1, and 5:2 with the Moon. Figure A.15 shows characteristic orbits of this resonant periodic type.

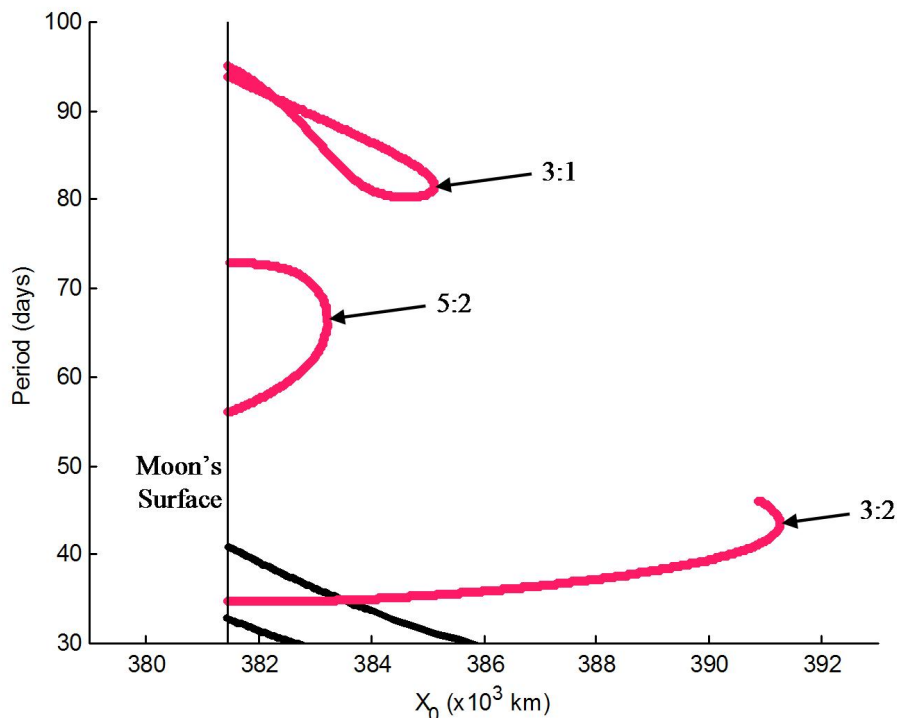


Figure A.14: Three curves showing how the orbital period depends on the initial condition of the orbit for orbits in three families of prograde Class 3 orbits. These orbits are all unstable and in resonance with the Moon.

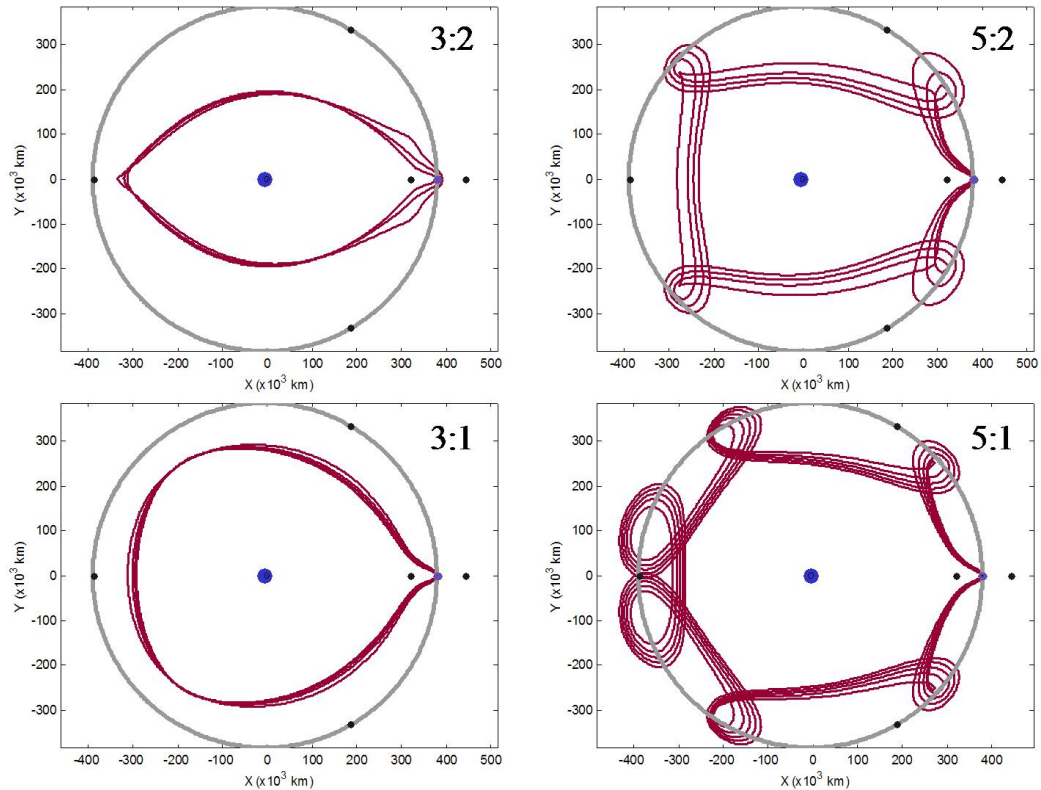


Figure A.15: Characteristic plots of four resonant prograde lunar flyby orbits. The resonances are: 3:2 (top-left), 5:2 (top-right), 3:1 (bottom-left), and 5:1 (bottom-right). All of these orbits are unstable.

### A.3.2 Retrograde Orbits about $\mathbf{M}_1 + \mathbf{M}_2$

Three interesting families of retrograde orbits in Class 3 have been identified in this study.

The first family includes all unstable distant periodic retrograde orbits, namely, those orbits that may generally be approximated as two-body orbits where both primaries are combined into one mass at their barycenter. These orbits, though, are unstable in their configuration. As the family approaches the primaries, it begins to pause at  $L_3$ , giving merit to its unstable nature, until the family ends at  $L_3$ . The family does actually continue, however the orbits in the continued curve no longer contain the structure of simple periodic symmetric orbits, so they will not be considered here. Figure A.16 displays the interesting characteristics of this family of orbits.

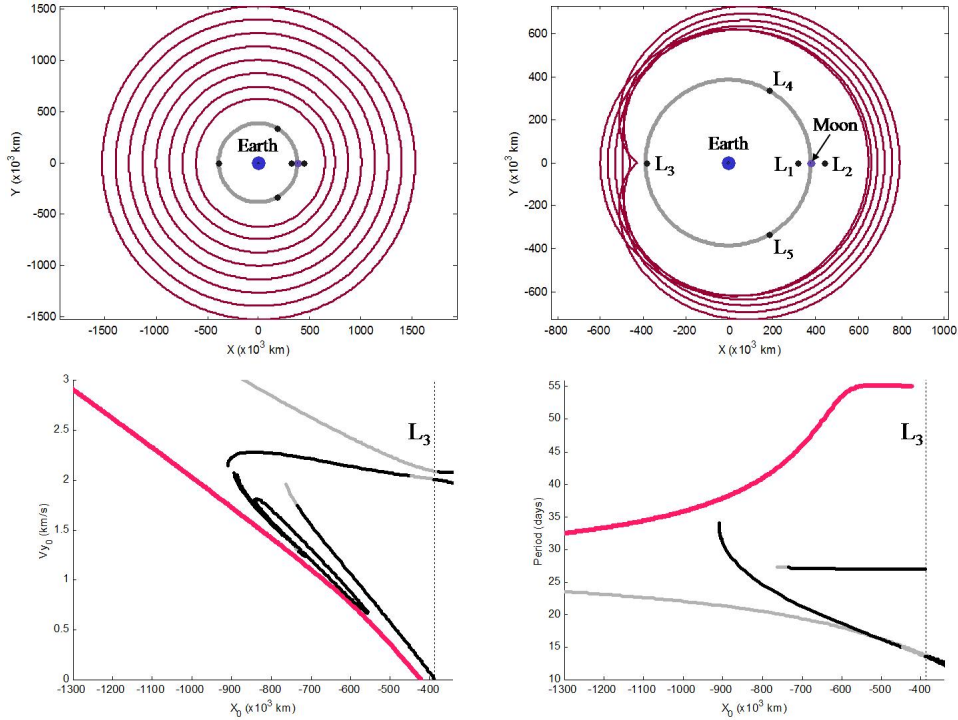


Figure A.16: Four plots describing the retrograde Class 3 family centered about the Earth+Moon, including two plots of several trajectories showing the shape of the orbits (top), a plot of  $x_0$  vs.  $y_0$  (bottom-left), and a plot of  $x_0$  vs.  $P$  (bottom-right).

The next family in this class includes orbits that appear very similar to the previous family: they orbit the system at such a distance that the two primaries may be approximated as a single mass at the barycenter. The difference, however, is that now the orbits are configured in a stable manner. As the family approaches the primaries, the orbits begin to make closer flybys of the Moon and the orbits become unstable. Gradually the orbits begin to take shape as Earth-Moon cyclers. Theoretically, this family would continue until it made close flybys of both the Earth and Moon, but by that time it will have been striking the surface of the Moon. Hence, the family is terminated, at least in this study. Figure A.17 displays the interesting characteristics of this family of orbits.

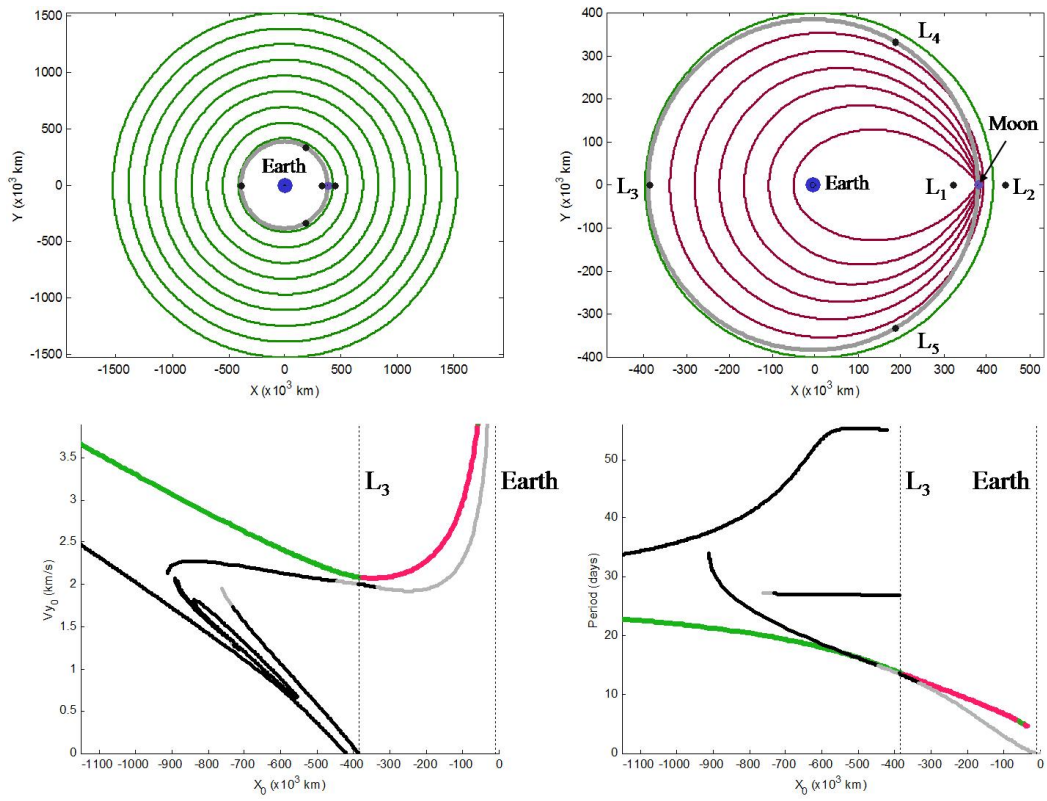


Figure A.17: Four plots describing the second retrograde Class 3 family centered about the Earth+Moon, including two plots of several trajectories showing the shape of the orbits (top), a plot of  $x_0$  vs.  $\dot{y}_0$  (bottom-left), and a plot of  $x_0$  vs.  $P$  (bottom-right).

The third family in this class includes orbits that make one loop in the vicinity of  $L_4$  /  $L_5$ . These orbits are all unstable. Figure A.18 displays the interesting characteristics of this family of orbits.

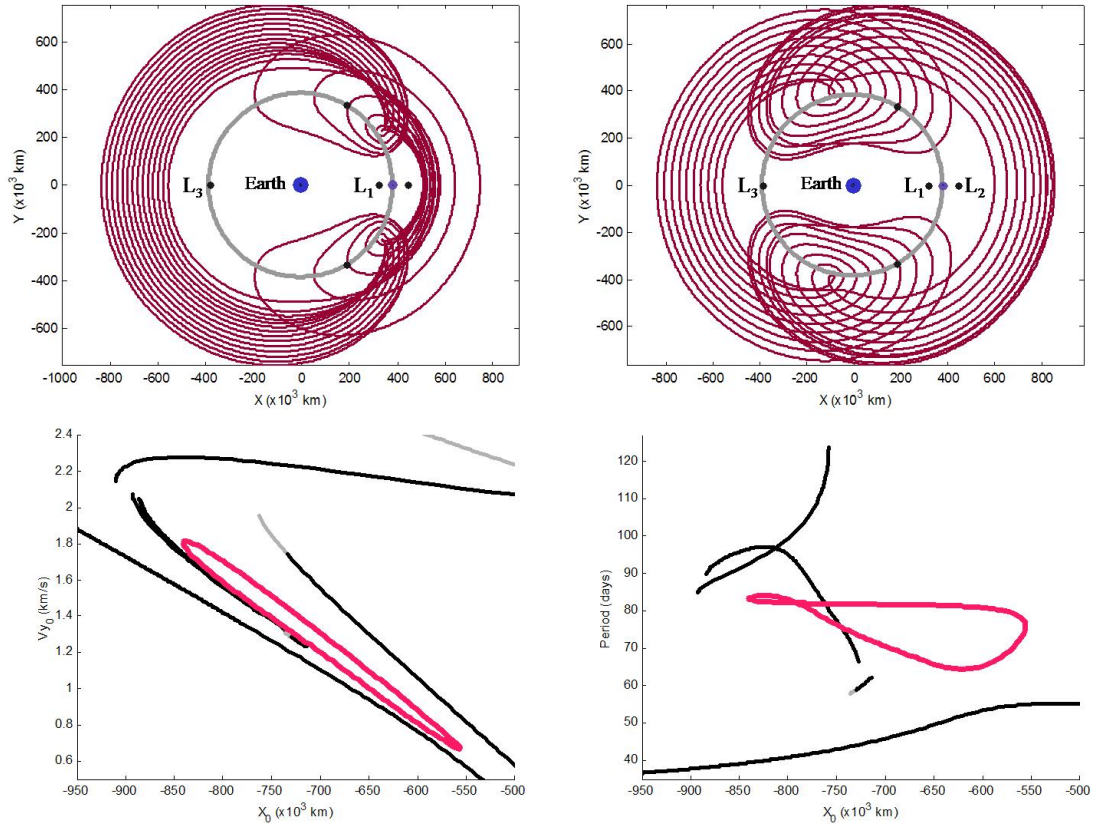


Figure A.18: Four plots describing the third retrograde Class 3 family centered about the Earth+Moon, including two plots of several trajectories showing the shape of the orbits (top), a plot of  $x_0$  vs.  $\dot{y}_0$  (bottom-left), and a plot of  $x_0$  vs.  $P$  (bottom-right).

#### A.4 Class 4: Orbits Centered about $L_1$

Class 4 orbits include all simple periodic symmetric orbits that pierce the  $x$ -axis twice between the primaries. Only one such family has been identified in the Earth-Moon system: the family of Lyapunov orbits centered about  $L_1$ . Figure A.19 includes three plots describing the Lyapunov family of orbits, including a plot of several trajectories showing the shape of the orbits (top), a plot of the initial conditions used to produce the orbits (bottom-left), and the family's orbital period compared with other nearby families (bottom-right).

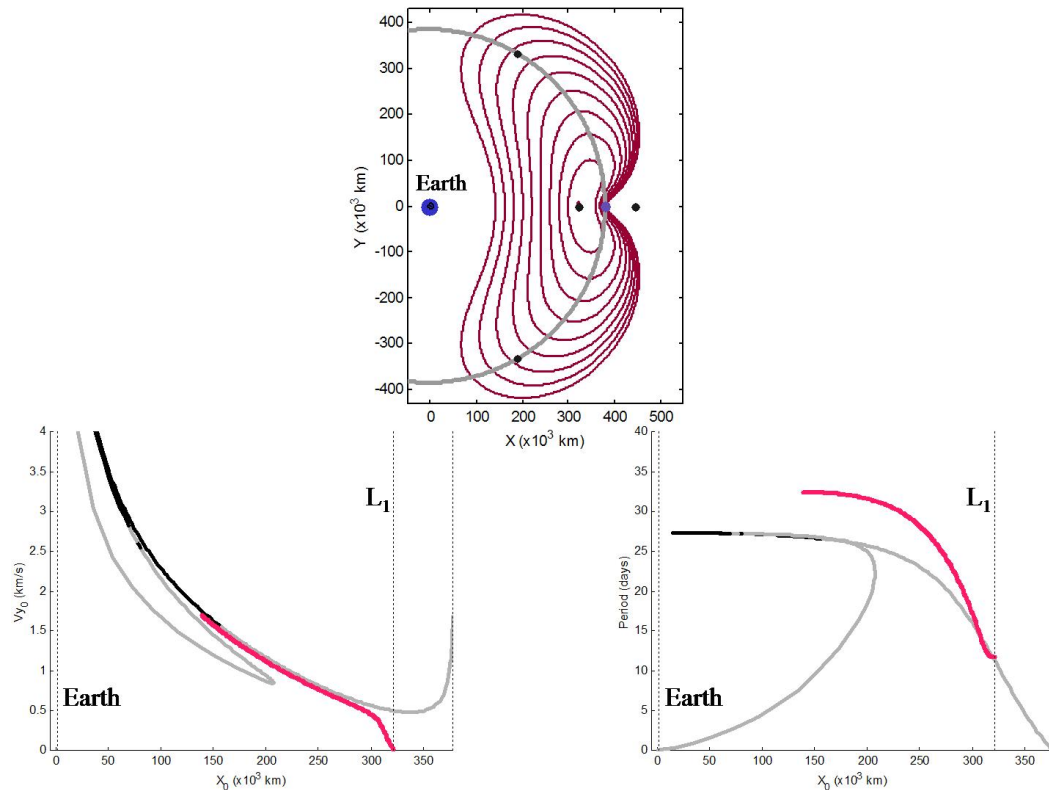


Figure A.19: Three plots describing the family of Lyapunov orbits centered about  $L_1$ , including a plot of several trajectories showing the shape of the orbits (top), a plot of  $x_0$  vs.  $y_0$  (bottom-left), and a plot of  $x_0$  vs.  $P$  (bottom-right).

## A.5 Class 5: Orbits Centered about $M_2$

All orbits in Class 5 include  $x$ -crossings on either side of  $M_2$  (the Moon). A total of three such families of orbits have been identified in this study, including two families of prograde orbits and one family of retrograde orbits.

### A.5.1 Prograde Orbits about $M_2$

The first family of prograde orbits presented here includes orbits that are low lunar orbits, periodic in the synodic frame. These orbits are neutrally stable. As the family is extended outward, it begins to drift toward  $L_1$ . While the family moves closer to  $L_1$  it also decreases its closest point to the Moon, which eventually causes the orbits

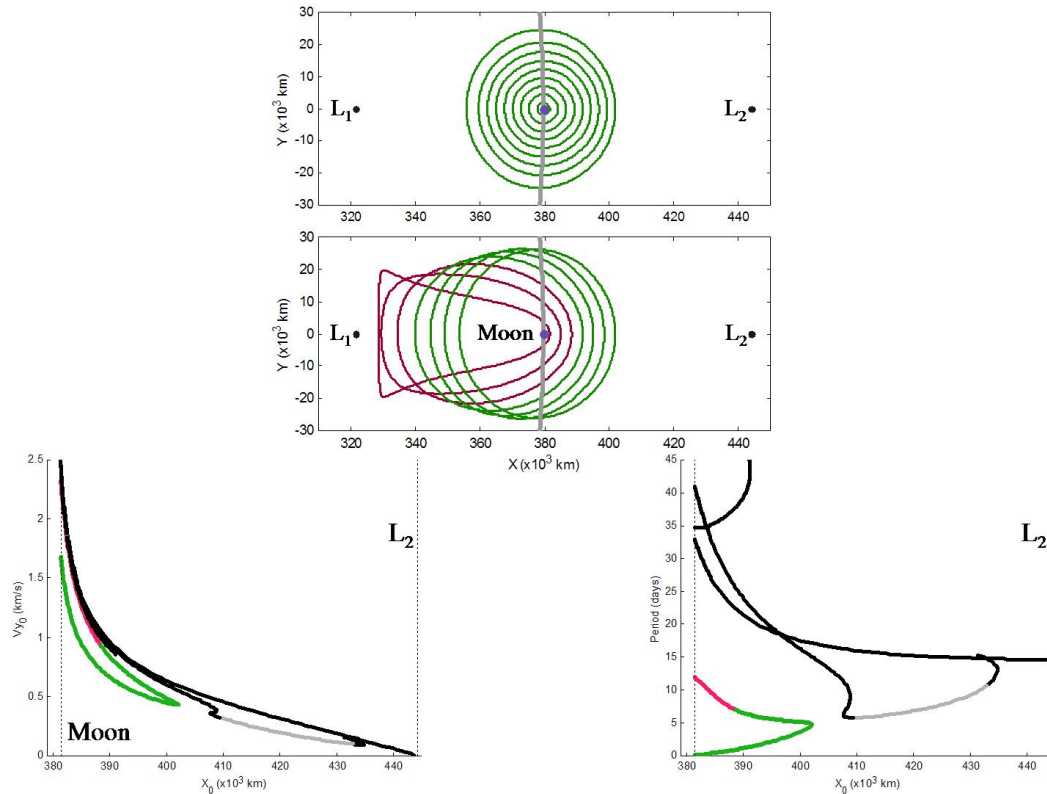


Figure A.20: Four plots describing the first prograde Class 5 family centered about the Moon, including two plots of several trajectories showing the shape of the orbits (top), a plot of  $x_0$  vs.  $y_0$  (bottom-left), and a plot of  $x_0$  vs.  $P$  (bottom-right).

to become unstable. Figure A.20 displays the interesting characteristics of this family of orbits.

The second family of prograde orbits presented here consists of some of the most interesting direct orbits about the Moon. The family includes a neutrally stable region that would have branched from the first prograde-orbit family in the case when  $\mu = 0$ . Continuing that region towards  $L_2$  one finds unstable orbits that are nearly symmetric to those found in the previous family; continuing towards the Moon's surface the shape of the orbits begins to bulge outward forming a lens; eventually the lens opens up into a double-lobe shape that includes two lunar flybys every orbit. Figure A.21 displays the interesting characteristics of this family of orbits.

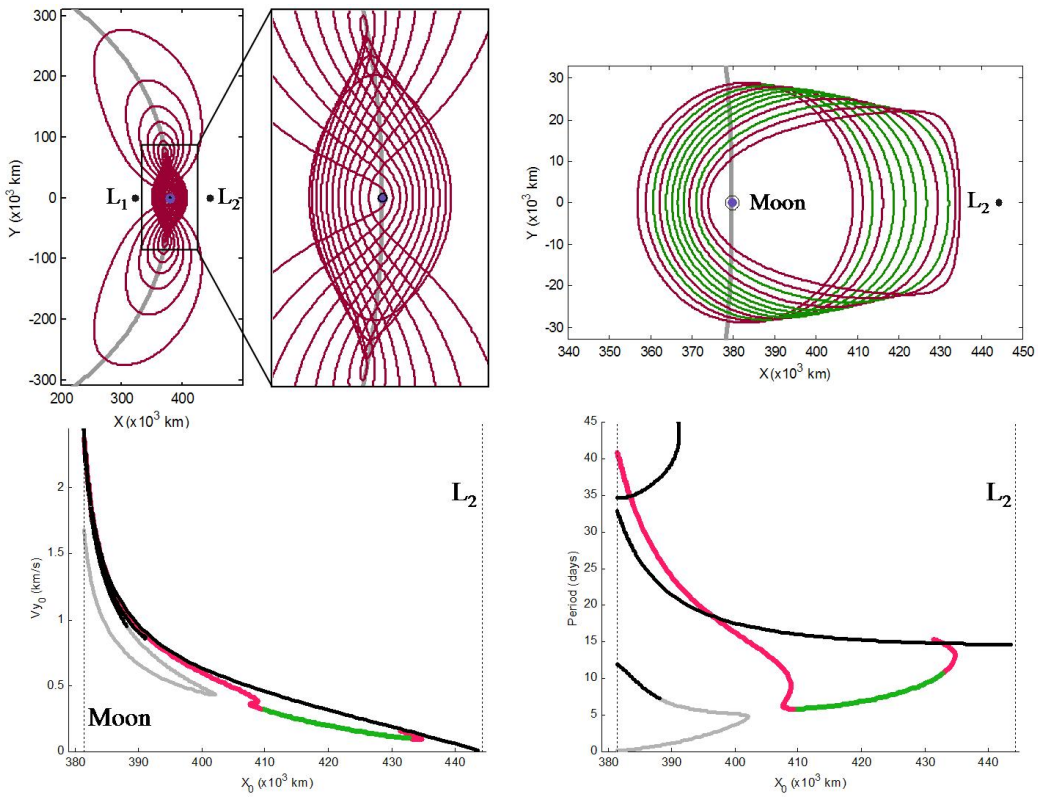


Figure A.21: Four plots describing the second prograde Class 5 family centered about the Moon, including two plots of several trajectories showing the shape of the orbits (top), a plot of  $x_0$  vs.  $v_{y0}$  (bottom-left), and a plot of  $x_0$  vs.  $P$  (bottom-right).

### A.5.2 Retrograde Orbits about $M_2$

The family of retrograde orbits centered about  $M_2$  includes low lunar retrograde orbits. As the family is extended away from the surface of the Moon, it gradually approaches the Earth and eventually performs Earth flybys every orbit. At that point the orbits in the family become unstable. Figure A.22 displays the interesting characteristics of this family of orbits.

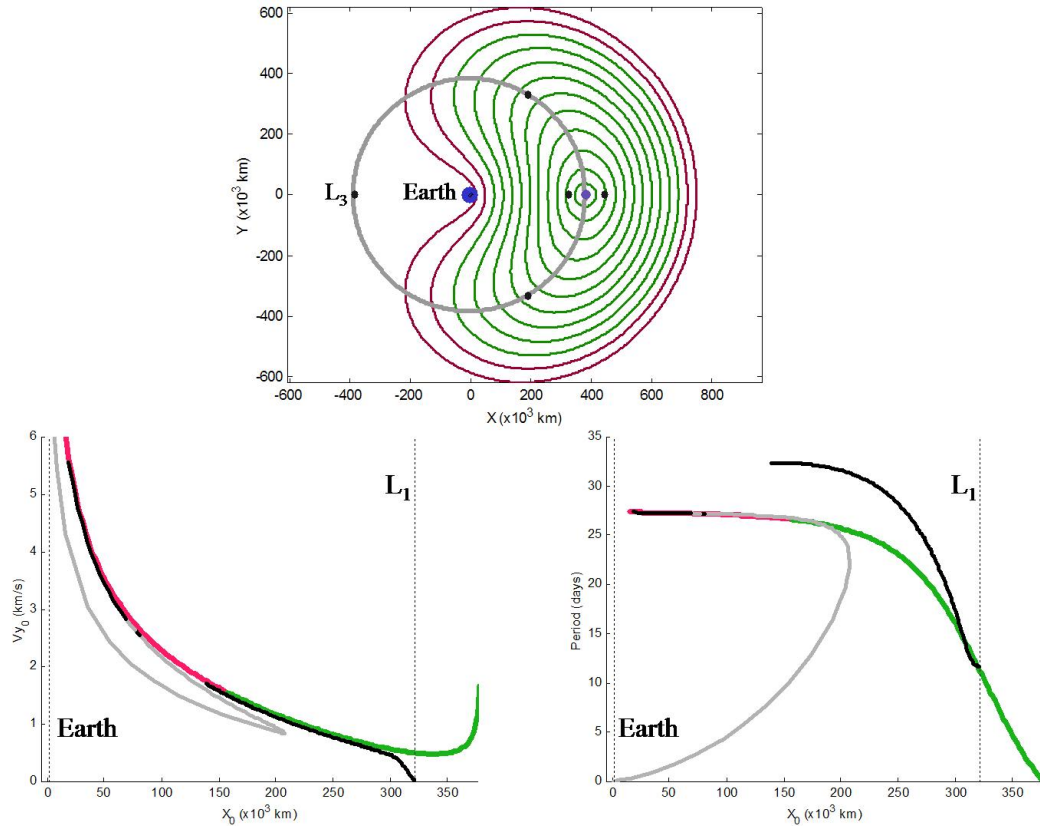


Figure A.22: Three plots describing the family of retrograde orbits centered about the Moon, including two plots of several trajectories showing the shape of the orbits (top), a plot of  $x_0$  vs.  $y_0$  (bottom-left), and a plot of  $x_0$  vs.  $P$  (bottom-right).

### A.6 Class 6: Orbits Centered about L<sub>2</sub>

The final class of simple periodic symmetric orbits in the Earth-Moon PCRTBP includes orbits that pierce the  $x$ -axis twice on the far side of the Moon. The only such family with this characteristic is the family of Lyapunov orbits centered about L<sub>2</sub>. Figure A.23 displays the interesting characteristics of this family of orbits.

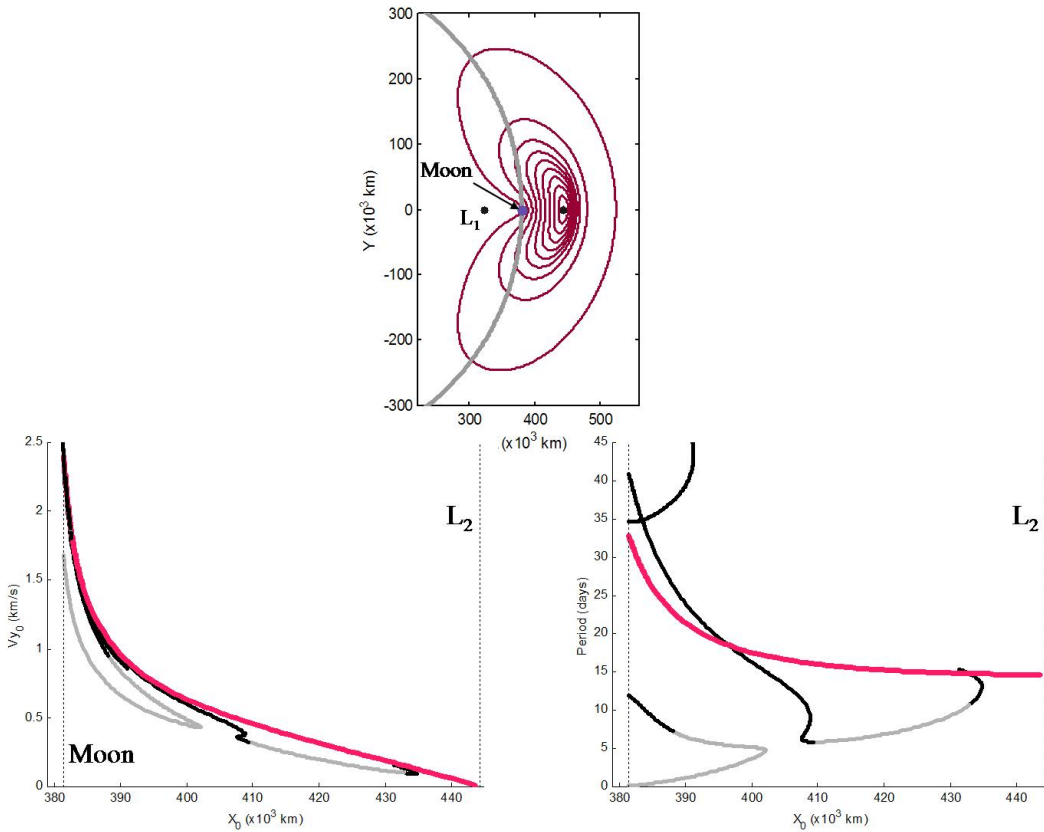


Figure A.23: Three plots describing the family of Lyapunov orbits centered about L<sub>2</sub>, including two plots of several trajectories showing the shape of the orbits (top), a plot of  $x_0$  vs.  $y_0$  (bottom-left), and a plot of  $x_0$  vs.  $P$  (bottom-right).

### A.7 Discussion

The orbits presented in this section represent a sample of the number of simple periodic symmetric orbits that exist in the CRTBP, which are in turn only a subset of the general periodic orbit solutions to the problem. Several families presented here include loops in the vicinity of  $L_4$  /  $L_5$  – in general, one may find a periodic orbit solution that makes an arbitrary number of loops in the vicinity of each Lagrange point; and in the more general case, one may choose to loop  $L_4$  a different number of times than  $L_5$ . However, in that case the orbit would no longer be symmetric. An alternative way of constructing these orbits would be to construct the stable and unstable invariant manifolds of unstable periodic orbits about  $L_4$  or  $L_5$  (not shown in this section because such orbits would not be classified as simple periodic symmetric orbits). Then one may find a trajectory that targets the vicinity of these manifolds, causing the orbit to approach the periodic orbit about  $L_4$  /  $L_5$  (making loops about that vicinity); if one does not perfectly arrive onto the stable manifold, then one's trajectory will fall off again. Finally, if it then pierces the  $x$ -axis orthogonally, it will have traced out a simple periodic symmetric orbit. This strategy uses the unstable dynamics in the system to freely transfer from one orbit – or the vicinity of one orbit – to another orbit. This type of free transfer is the subject of Section 3.10.

This chapter has hopefully demonstrated the variety of simple periodic orbits that exist in the CRTBP. These solutions may be used in practical mission designs in many ways. They may be used as science or communication orbits; they may be used as staging orbits for transfer between two other orbits; they may be used as quarantine orbits; etc.

## Appendix B

### Three-Dimensional Simple Periodic Symmetric Orbits

The purpose of this chapter is to supplement Appendix A by providing a taste of the variety of **three-dimensional** simple periodic symmetric orbits that exist in the CRTBP. The CRTBP permits an infinite number of families of three-dimensional orbits; this chapter presents only the simplest of those families. This collection provides examples of some of the most simple three-dimensional periodic orbits that may be useful to practical mission designs.

The orbits presented in this chapter are **simple periodic symmetric orbits** as defined in Appendix A. Many of the orbit families presented here bifurcate from families of planar orbits. In those instances, the three-dimensional families may be classified in the same way as their planar counterparts, although as the family diverts from its planar origin, the family's orbit characteristics may not appear to be in the same class of orbits. Other families of three-dimensional orbits do not bifurcate from any obvious family of planar orbits. It's certainly possible that those families bifurcate from families of planar orbits that are not **simple** periodic orbits. Since the subject of orbit-classification is not the focus of this dissertation, this subject will not be further explored, but left to the reader. This chapter does provide a large variety of simple three-dimensional periodic symmetric orbits and gives the impression of the wide variety of other periodic orbits that exist in the CRTBP.

It is important to point out that each and every orbit presented in this chap-

ter represents **two** orbits: a Northern and a Southern orbit. Due to the symmetry of the CRTBP about the  $x - y$  plane, each and every three-dimensional simple periodic symmetric orbit has a mirror-image orbit that also exists. The complimentary orbit is identical to the orbit presented here in every way, except that its  $z$ - and  $\dot{z}$ -components are of the opposite sign. Thus, for brevity purposes, the mirror-image of every orbit presented in this chapter is not shown. For consistency, the orbits presented in this chapter are each produced using a positive  $z_0$ -value.

Table B.1 summarizes the families of three-dimensional simple periodic symmetric orbits presented in this study. The labels indicated in parentheses are used to identify the families in Figures B.1 – B.5. Not every family identified here will be displayed graphically, but examples of each type of family will be included.

The initial conditions (the state of each orbit at its orthogonal  $x$ -axis crossing with positive  $y$ ) of the periodic orbits presented in this study are shown in Figures B.1 – B.5, below. Figure B.2 shows those orbits whose initial conditions lay on the far side of  $L_3$ , Figure B.3 shows the orbits between  $L_3$  and the Earth, Figure B.4 shows the orbits between the Earth and the Moon, and Figure B.5 shows the orbits between the Moon and  $L_2$ . In all of the plots, the gray orbits are neutrally stable and the black orbits are unstable; the labels indicate which type of family the orbits belong to, as defined in Table B.1 above. Some labels apply to more than one actual family of orbits, especially since some families bifurcate endlessly, preventing clear labels.

Figure B.6 shows two additional useful plots. The plot on the left is a plot that compares the Jacobi constant  $C$  for all of these periodic orbits. The orbits may be matched with those shown in Figures B.1 – B.5 via their  $x_0$  values. It is valuable to be able to visibly compare the orbits' relative Jacobi constants when constructing free transfers, such as those described in Section 3.10. The plot on the right in Figure B.6 similarly compares the periods of these orbits, which may prove useful when designing certain transfer trajectories or practical missions (any orbits with periods greater

than 100 days are not shown).

The orbits in each of the families will now be examined in more detail.

Table B.1: A summary of the families of simple periodic symmetric three-dimensional orbits presented in this study. The labels in parentheses are used to locate the family-types in Figures B.1 – B.6.

<b>Obvious Bifurcations of Planar Families</b>			
<b>Orbit Class</b>	<b>Center</b>	<b>Family Types</b>	
Class 1	$L_3$	Prograde	Horseshoe Families (1A)
		Retrograde	Halo $L_3$ (1B)
Class 2	$M_1$	Prograde	Two-Lobed Distant Flybys (2A)
		Retrograde	Retrograde Lunar Flybys (2B), Retrograde Lunar Flybys with $L_4/L_5$ Loops (2C)
Class 3	$M_1+M_2$	Prograde	N/A (None Identified)
		Retrograde	Distant High-Altitude (3A), Distant High-Altitude Orbits with $L_4/L_5$ loops (3B)
Class 4	$L_1$	Prograde	N/A
		Retrograde	Halo $L_1$ (4A)
Class 5	$M_2$	Prograde	Two-Lobed Distant Lunar Orbits (5A)
		Retrograde	Distant Retrograde Orbits (5B)
Class 6	$L_2$	Prograde	N/A
		Retrograde	Halo $L_2$ (6A)
<b>Additional Families of Orbits</b>			
<b>Orbit Class</b>	<b>Center</b>	<b>Family Types</b>	
Class M1	$M_1$	Prograde	Resonant Oscillating Orbits (M1A)
		Retrograde	High-Altitude Horseshoe Orbits (M1B)
Class M2	$M_2$	Prograde	Resonant Oscillating Orbits (M2A)
		Retrograde	N/A

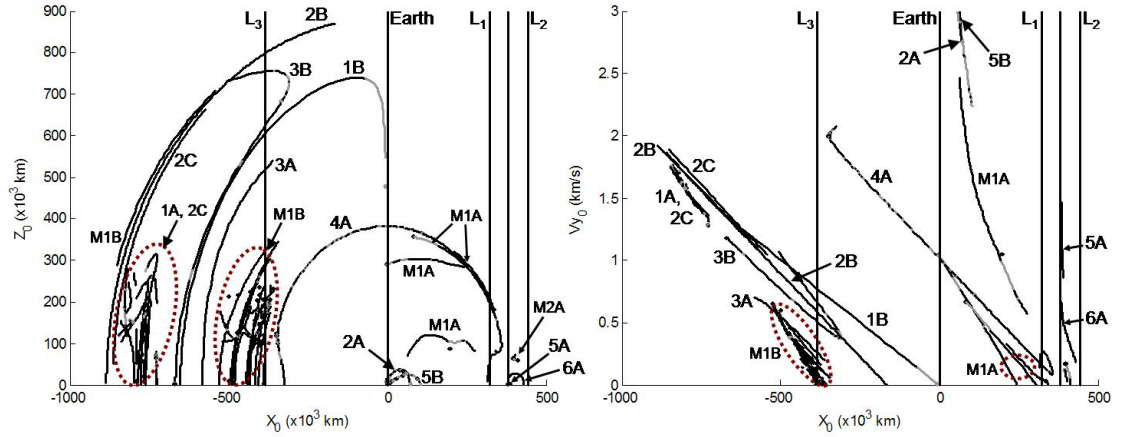


Figure B.1: Plots of  $x_0$  vs.  $z_0$  and  $x_0$  vs.  $y_0$  for the families of three-dimensional periodic orbits presented in this study. Orbits plotted in black are unstable; orbits plotted in gray are neutrally stable.

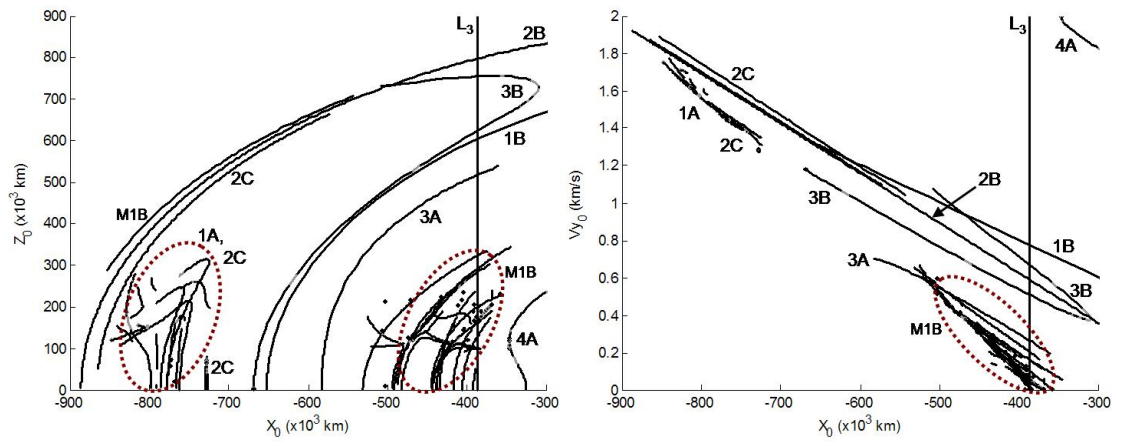


Figure B.2: Plots of  $x_0$  vs.  $z_0$  and  $x_0$  vs.  $y_0$  for the families of three-dimensional periodic orbits on the far side of  $L_3$ .

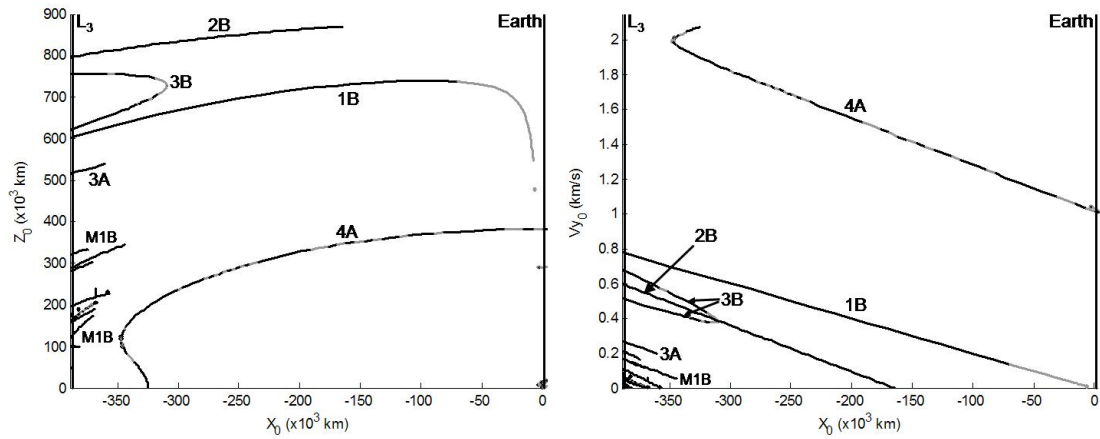


Figure B.3: Plots of  $x_0$  vs.  $z_0$  and  $x_0$  vs.  $y_0$  for the families of three-dimensional periodic orbits between  $L_3$  and the Earth.

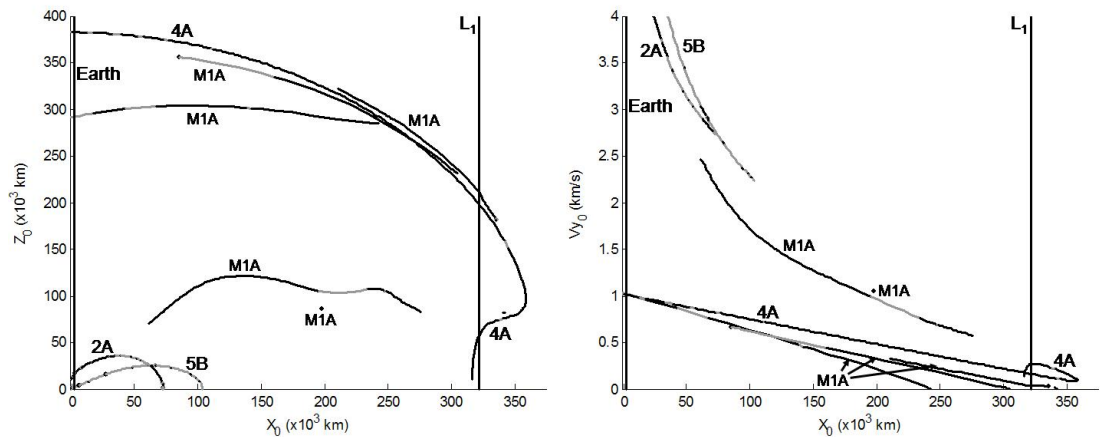


Figure B.4: Plots of  $x_0$  vs.  $z_0$  and  $x_0$  vs.  $y_0$  for the families of three-dimensional periodic orbits between the Earth and the Moon.

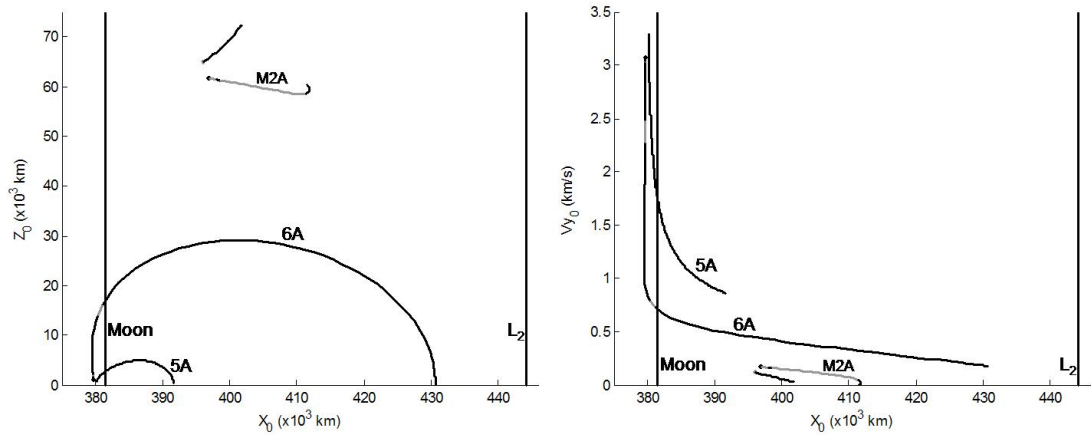


Figure B.5: Plots of  $x_0$  vs.  $z_0$  and  $x_0$  vs.  $\dot{y}_0$  for the families of three-dimensional periodic orbits between the Moon and  $L_2$ .

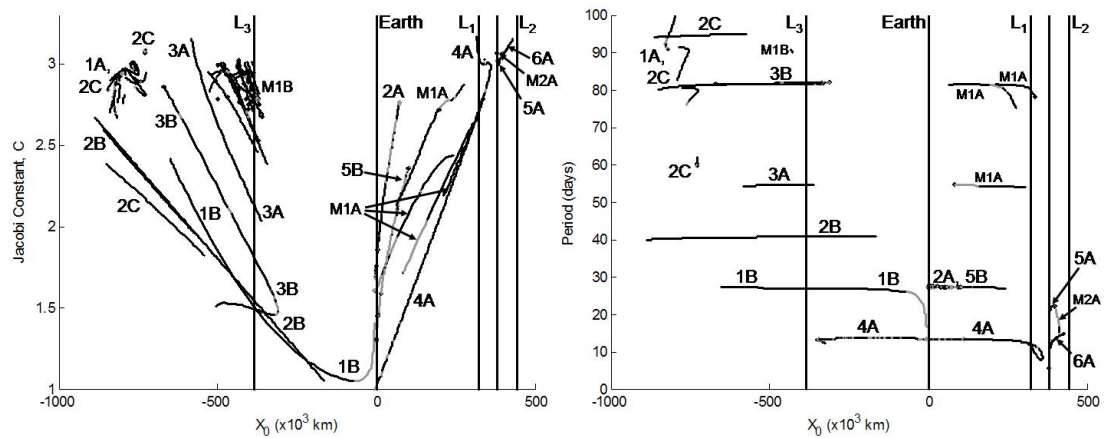


Figure B.6: Left: A plot of  $x_0$  vs.  $C$  for the families of three-dimensional periodic orbits presented in this study. Right: A plot of  $x_0$  vs.  $P$ , the orbital period. Orbits plotted in black are unstable; orbits plotted in gray are neutrally stable.

### B.1 Class 1: Orbits Centered about L<sub>3</sub>

Three-dimensional Class 1 orbits include all families of 3D simple periodic symmetric orbits that bifurcate from planar Class 1 families of orbits, namely, those planar orbits that pierce the  $x$ -axis twice on the far side of the Earth. Several three-dimensional families may thus be classified as Class 1 families, including the family of Halo orbits centered about L<sub>3</sub> as well as a large group of horseshoe-shaped families.

The family of Halo orbits centered about L<sub>3</sub> bifurcates from the family of Lyapunov orbits centered about L<sub>3</sub>. Figure B.7 shows four plots describing the Halo family of orbits. One can see that as the orbits in the family approach the  $x - y$  plane, the orbits begin to take on the same shape as the orbits in the family of Lyapunov orbits. Figure B.8 shows two plots of the Halo family's initial conditions: a plot of  $x_0$  vs.  $z_0$  and a plot of  $x_0$  vs.  $y_0$ . The plots include the other nearby families shown in Figures B.1 – B.6 for reference. The highlighted curves indicate the family of Halo orbits; they are colored according to the stability of the orbit, where red represents unstable orbits and green represents neutrally stable orbits.

Figure B.9 includes several plots of families that trace out a horseshoe-like shape in three-dimensions. These families appear to each bifurcate from the horseshoe-shaped families of planar Class 1 orbits. The horseshoe shape includes  $n$  loops in both the upper and lower sections of the plot, where  $n$  may be any positive integer. Because of the unrestricted value of  $n$  there are an infinite number of these families of orbits; as  $n$  grows the orbits approach periodic orbits that exist about L<sub>4</sub> / L<sub>5</sub>. Figure B.9 includes plots of orbits that have between 1 and 9 loops per side.

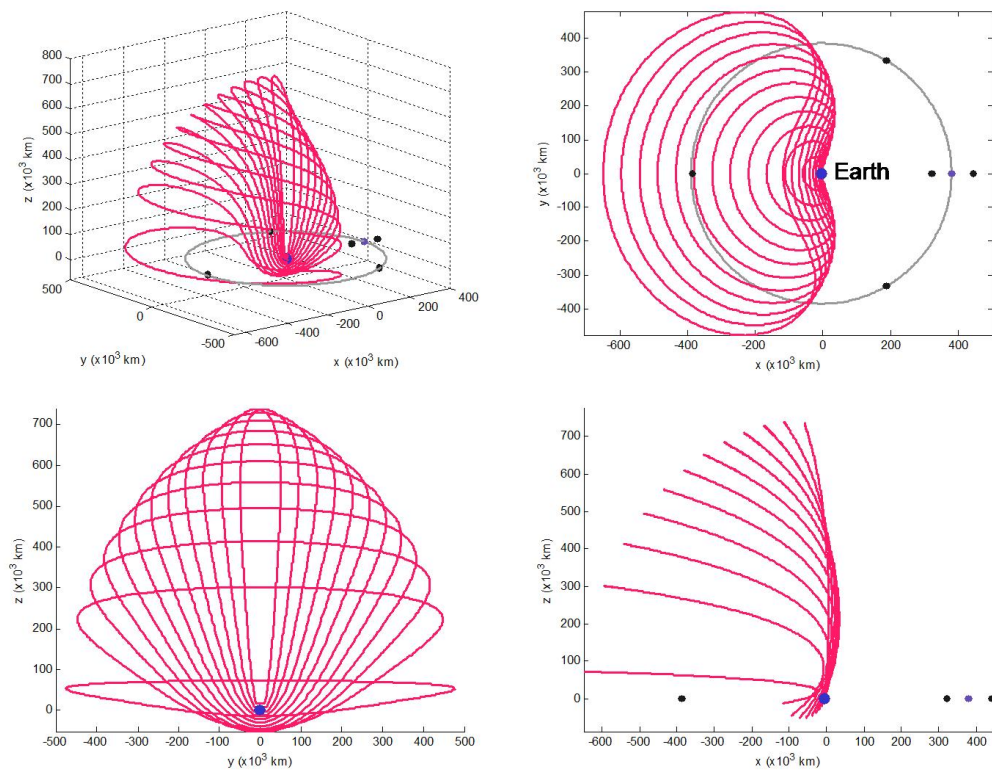


Figure B.7: Four perspectives of the family of Halo orbits centered about  $L_3$ .

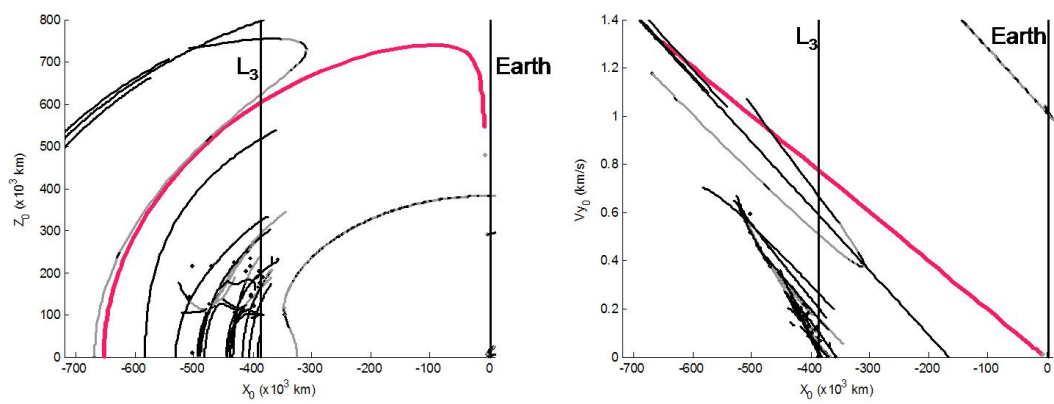


Figure B.8: Two plots showing the initial conditions yielding the family of Halo orbits centered about  $L_3$ . Left: the family's  $x_0$ -values vs. the family's  $z_0$ -values; Right:  $x_0$  vs.  $y_0$ .

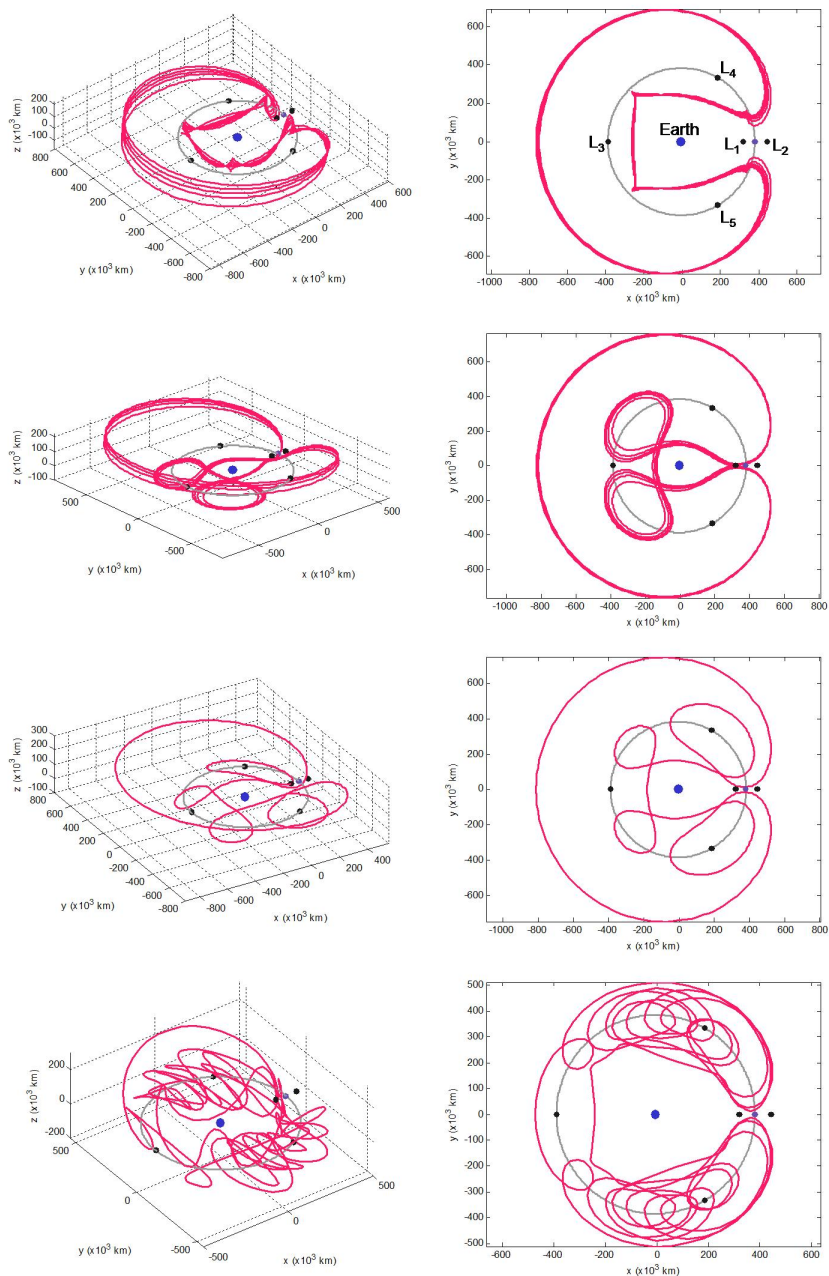


Figure B.9: Horseshoe-shaped orbits with varying numbers of upper and lower loops. The left column of plots shows the orbits viewed from an angle in three-dimensions; the right column of plots shows the same orbits viewed from above the ecliptic.

## B.2 Class 2: Orbits Centered about $M_1$

Three-dimensional Class 2 orbits include all families of 3D simple periodic symmetric orbits that bifurcate from planar Class 2 families of orbits, namely, those planar orbits that pierce the  $x$ -axis on both sides of  $M_1$  (the Earth). There are several types of families that share this characteristic, including both prograde and retrograde orbits.

### B.2.1 Prograde Orbits about $M_1$

Only one family of prograde three-dimensional Class 2 orbits has been identified in this study. Figure B.10 shows four perspectives of the orbits in this family. The orbits in this family show two large lobes that vary in the extent to which they traverse out of the  $x - y$  plane; the orbits that extend only slightly out of plane are very similar to the planar orbits from which this orbital family bifurcated. The orbits in this family vary in their stability, mostly as a function of how close they get to the Earth during each perigee passage. Figure B.11 shows two plots of this family's initial conditions: a plot of  $x_0$  vs.  $z_0$  and a plot of  $x_0$  vs.  $y_0$ . The plots include the other nearby families shown in Figures B.1 – B.6 for reference. The highlighted curves, indicating this family of orbits, are colored according to the stability of the orbit, where red represents unstable orbits and green represents neutrally stable orbits.

### B.2.2 Retrograde Orbits about $M_1$

The families of retrograde three-dimensional Class 2 orbits identified in this study all include low lunar flybys. It appears that many types of families may be constructed, including families that make  $n$  loops about the  $L_4$  /  $L_5$  vicinity, where  $n$  may be any non-negative integer. Figures B.12 and B.13 describe a family of retrograde three-dimensional Class 2 orbits that do not contain any loops about  $L_4$  /  $L_5$ . Figure B.14 shows a few characteristic families of orbits that do contain loops.

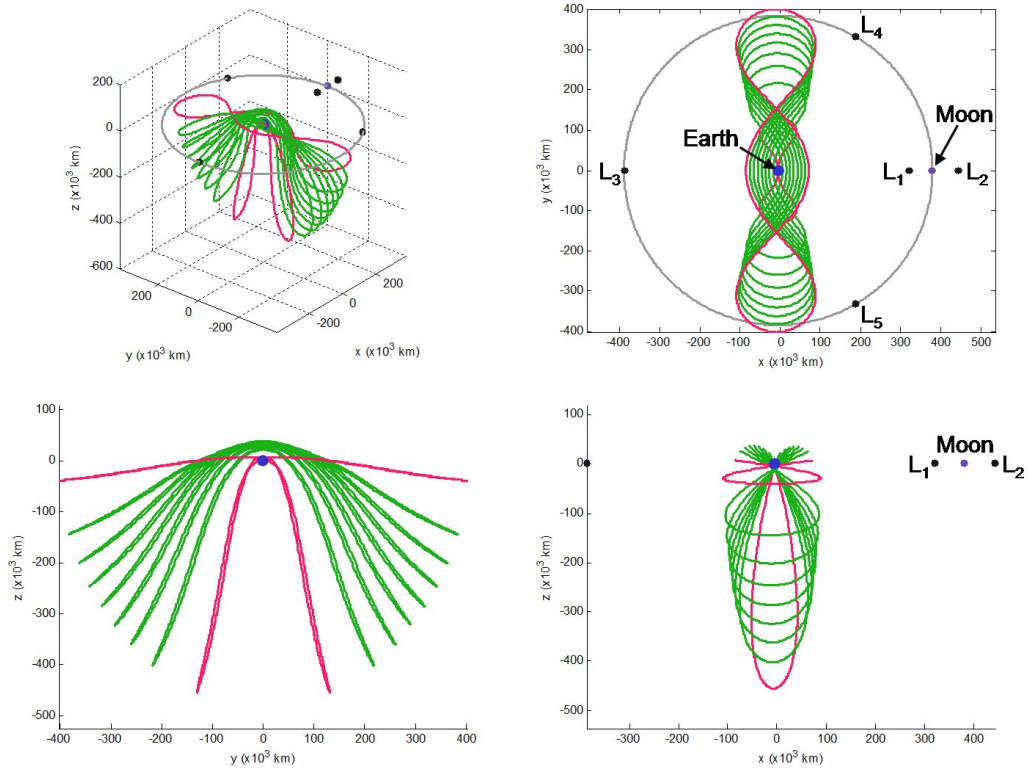


Figure B.10: Four perspectives of the family of prograde three-dimensional Class 2 orbits.

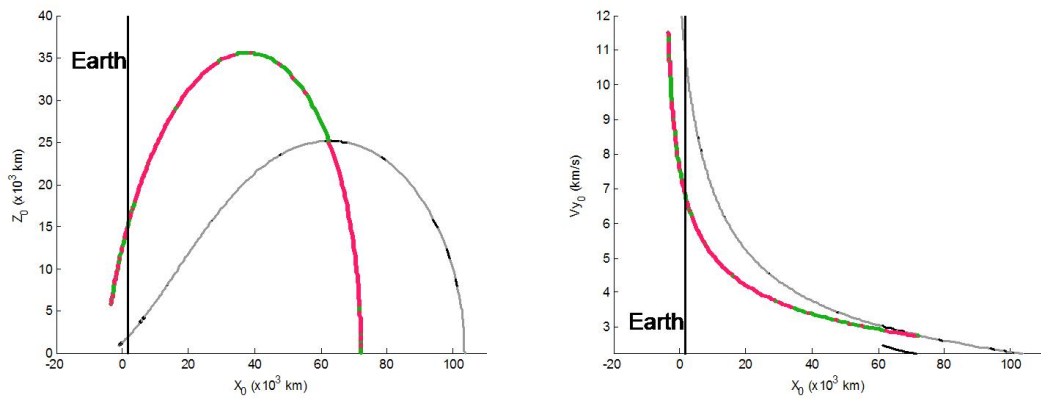


Figure B.11: Two plots showing the initial conditions yielding the family of prograde three-dimensional Class 2 orbits. Left: the family's  $x_0$ -values vs. the family's  $z_0$ -values; Right:  $x_0$  vs.  $\dot{y}_0$ .

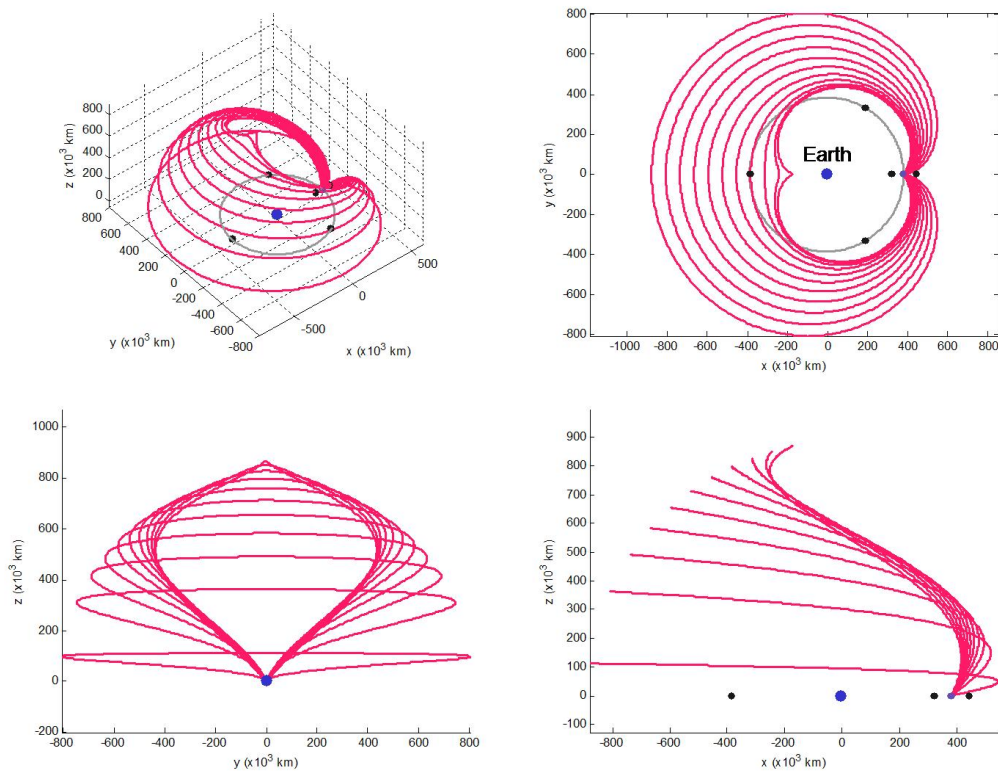


Figure B.12: Four perspectives of the family of retrograde three-dimensional Class 2 orbits that contain no  $L_4$  /  $L_5$  loops.

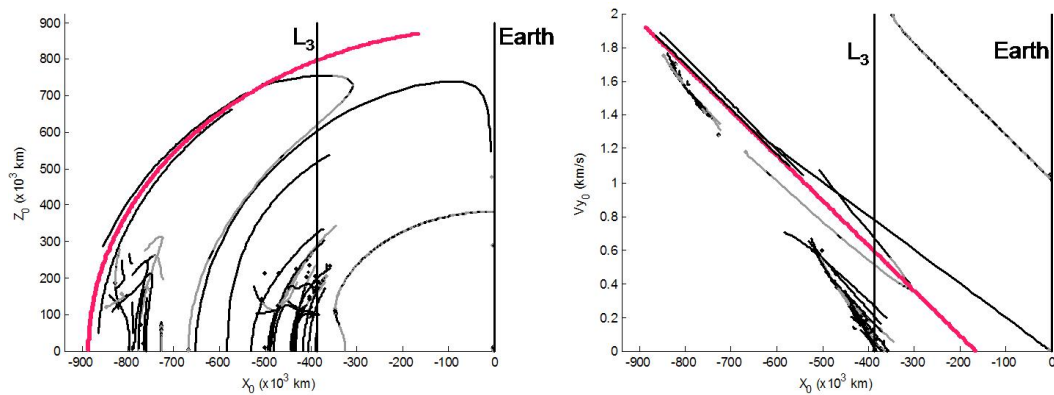


Figure B.13: Two plots showing the initial conditions yielding the family of retrograde three-dimensional Class 2 orbits shown in Figure B.12. Left: the family's  $x_0$ -values vs. the family's  $z_0$ -values; Right:  $x_0$  vs.  $v_{y0}$ .

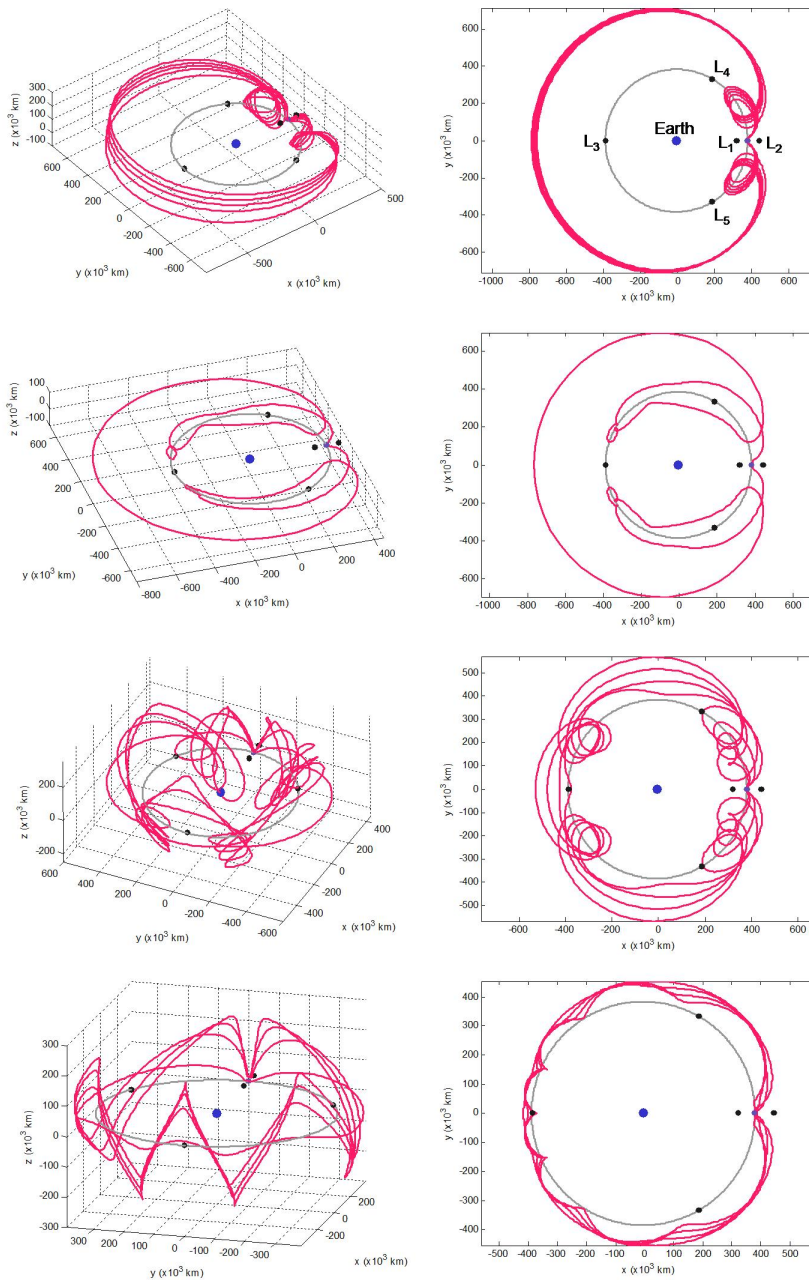


Figure B.14: A few characteristic orbits in the families that make periodic lunar flybys as well as  $n$  loops in the vicinity of L<sub>4</sub> / L<sub>5</sub>. The left column of plots shows the orbits viewed from an angle in three-dimensions; the right column of plots shows the same orbits viewed from above the ecliptic.

### B.3 Class 3: Orbits Centered about $M_1+M_2$

Three-dimensional Class 3 orbits include all families of 3D simple periodic symmetric orbits that bifurcate from planar Class 3 families of orbits, namely, those planar orbits that pierce the  $x$ -axis on opposite sides of the two primaries. That is, they include both primaries within their “center”. Several types of families were identified in this study that share this characteristic.

#### B.3.1 Prograde Orbits about $M_1+M_2$

The families of prograde planar Class 3 orbits identified in Appendix A include orbits that perform resonant lunar flybys. The flybys occur at any resonance, although only a few have been identified that do not impact the surface of the Moon. It is suspected that these orbits also exist in three-dimensions, but they have not yet been identified in this study. It is possible that the three-dimensional families of orbits that behave in a similar manner are not simple periodic symmetric orbits. If this conjecture is true, it would explain why no orbits were identified in this study with the same characteristics as planar Class 3 orbits.

#### B.3.2 Retrograde Orbits about $M_1+M_2$

Three interesting families of retrograde three-dimensional Class 3 orbits have been identified in this study.

The first family bifurcates from the family of distant retrograde planar orbits. As the orbits in the three-dimensional family diverge from the plane, they extend further out of the plane, eventually reaching a peak where a satellite following such an orbit would pause above or below the Moon, coming to a temporary rest before completing the orbit. Figure B.15 shows four perspectives of this family of orbits; Figure B.16 shows two plots of the initial conditions used to produce this family of orbits.

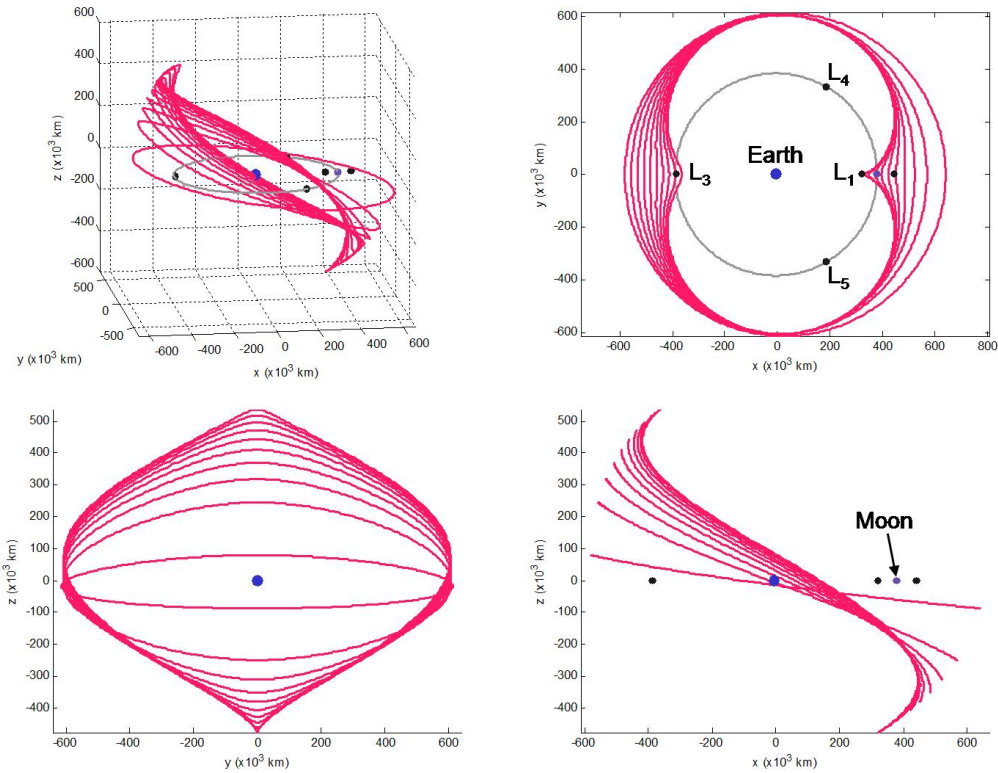


Figure B.15: Four perspectives of the first family of retrograde three-dimensional Class 3 orbits.

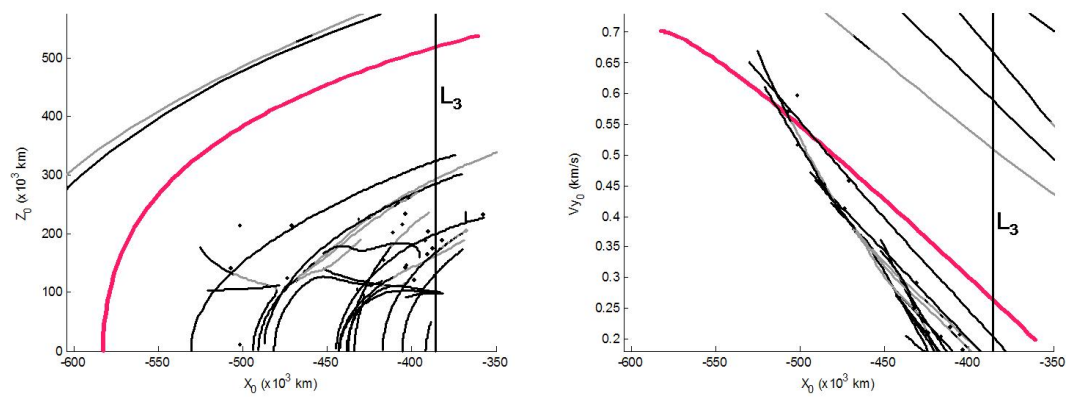


Figure B.16: Two plots showing the initial conditions yielding the first family of retrograde three-dimensional Class 3 orbits shown in Figure B.15. Left: the family's  $x_0$ -values vs. the family's  $z_0$ -values; Right:  $x_0$  vs.  $v_{y0}$ .

The second family bifurcates from the family of retrograde planar orbits that contain a single large loop about the vicinity of L<sub>4</sub> / L<sub>5</sub>. As the orbits in the three-dimensional family diverge from the plane, they extend further out of the plane, eventually coming to a point where they make two Earth flybys during each orbit. Figure B.17 shows four perspectives of this family of orbits; Figure B.18 shows two plots of the initial conditions used to produce this family of orbits. The highlighted orbits colored red are unstable orbits, the orbits colored green are neutrally stable orbits.

The third family bifurcates from the family of retrograde planar orbits that contain a single small loop very near the vicinity of L<sub>4</sub> / L<sub>5</sub>. As the orbits in the three-dimensional family diverge from the plane, they extend further out of the plane, eventually making a small trip near one of the poles of the Moon. Figure B.19 shows four perspectives of this family of orbits; Figure B.20 shows two plots of the initial conditions used to produce this family of orbits. The highlighted orbits colored red are unstable orbits, the orbits colored green are neutrally stable orbits.

#### B.4 Class 4: Orbits Centered about L<sub>1</sub>

Three-dimensional Class 4 orbits include all families of 3D simple periodic symmetric orbits that bifurcate from planar Class 4 families of orbits, namely, those planar orbits that pierce the *x*-axis twice between the primaries. Only one such family has been identified in the Earth-Moon system: the family of Halo orbits centered about L<sub>1</sub>. The family of Halo orbits centered about L<sub>1</sub> bifurcates from the family of planar Lyapunov orbits centered about L<sub>1</sub>. Figure B.21 shows four perspectives of this family of orbits. The orbits in the family that remain in the region of space near the Moon and the L<sub>1</sub> point are very different than the larger orbits in the family, hence, they are plotted separately. Figure B.22 shows two plots of the initial conditions used to produce this family of orbits. The highlighted orbits colored red are unstable orbits, the orbits colored green are neutrally stable orbits.

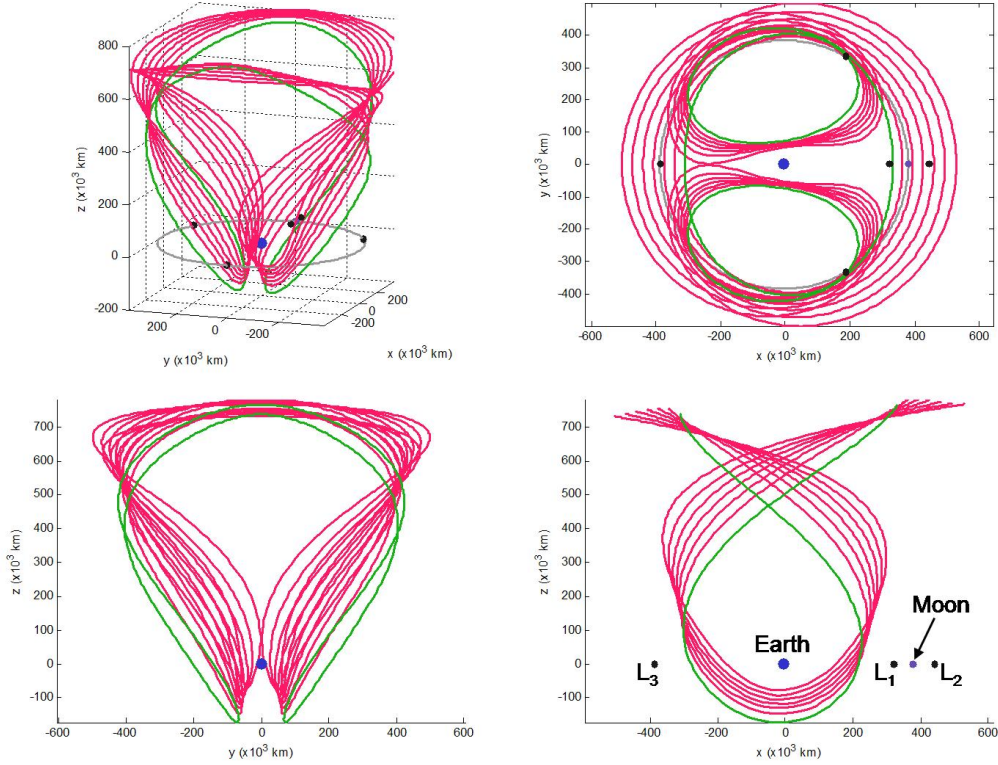


Figure B.17: Four perspectives of the second family of retrograde three-dimensional Class 3 orbits.

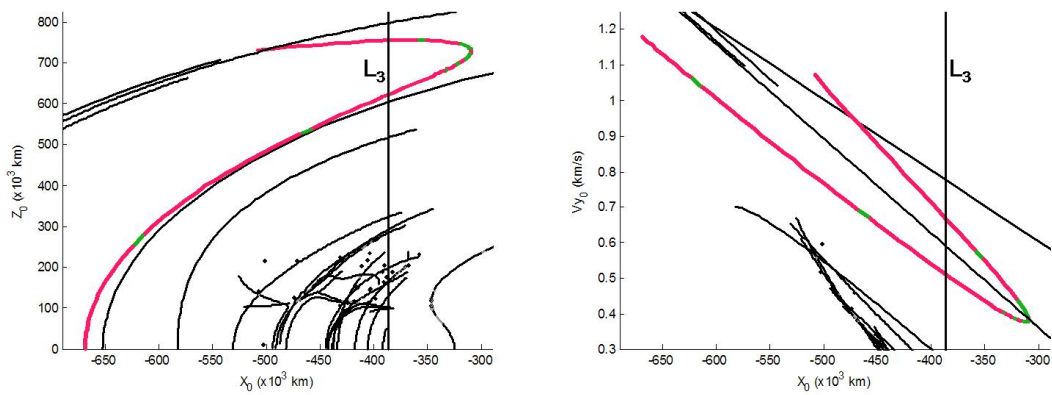


Figure B.18: Two plots showing the initial conditions yielding the second family of retrograde three-dimensional Class 3 orbits shown in Figure B.17. Left: the family's  $x_0$ -values vs. the family's  $z_0$ -values; Right:  $x_0$  vs.  $v_{y0}$ .

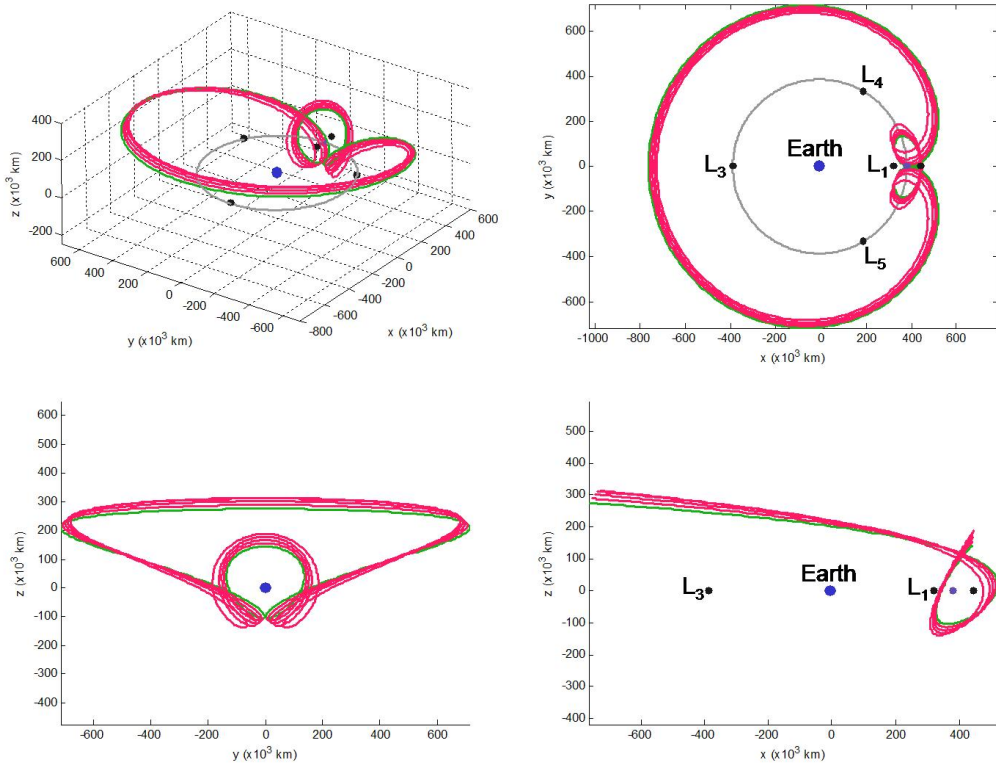


Figure B.19: Four perspectives of the third family of retrograde three-dimensional Class 3 orbits.

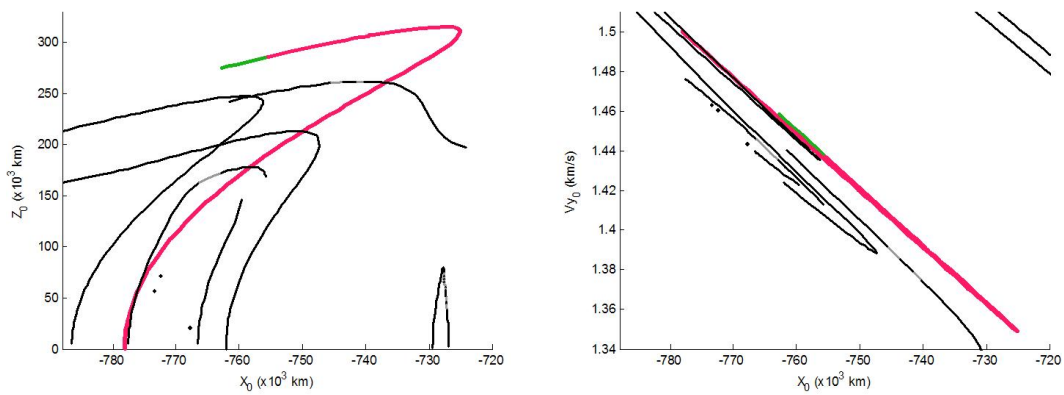


Figure B.20: Two plots showing the initial conditions yielding the third family of retrograde three-dimensional Class 3 orbits shown in Figure B.19. Left: the family's  $x_0$ -values vs. the family's  $z_0$ -values; Right:  $x_0$  vs.  $y_0$ .

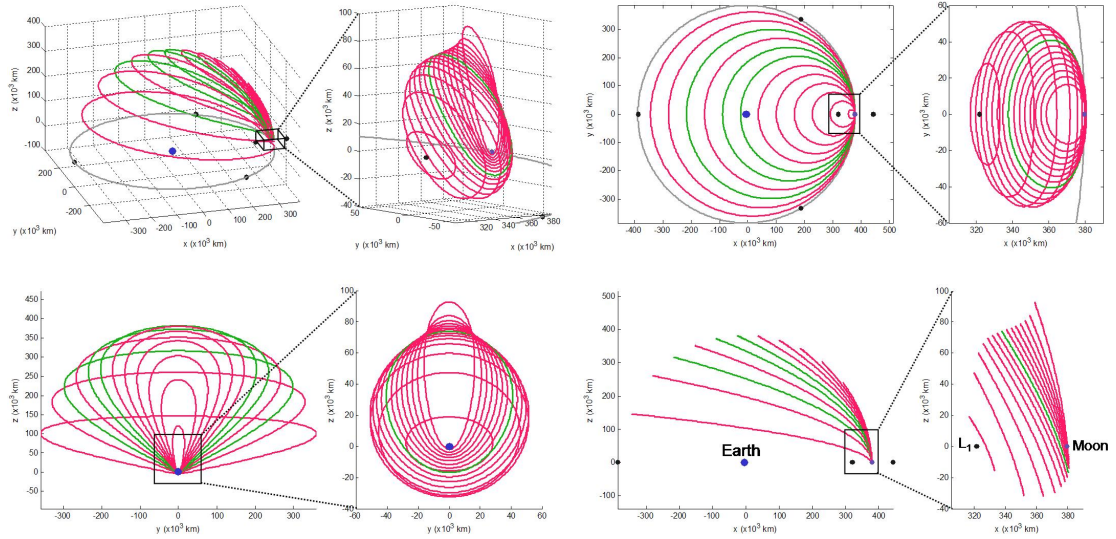


Figure B.21: Four perspectives of the family of Halo orbits centered about  $L_1$ .

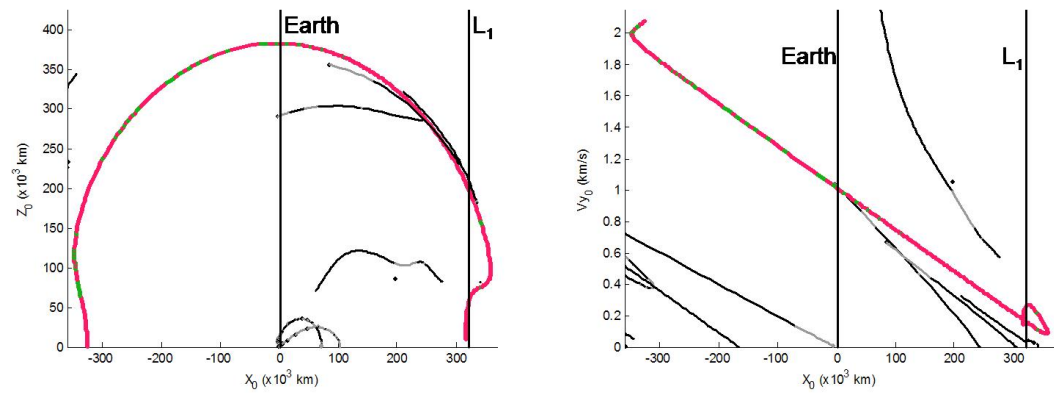


Figure B.22: Two plots showing the initial conditions yielding the family of Halo orbits centered about  $L_1$ . Left: the family's  $x_0$ -values vs. the family's  $z_0$ -values; Right:  $x_0$  vs.  $\dot{y}_0$ .

## B.5 Class 5: Orbits Centered about $M_2$

Three-dimensional Class 5 orbits include all families of 3D simple periodic symmetric orbits that bifurcate from planar Class 5 families of orbits, namely, those planar orbits that pierce the  $x$ -axis on either side of  $M_2$  (the Moon). Two such families of orbits have been identified in this study, including one family of prograde orbits and one family of retrograde orbits.

### B.5.1 Prograde Orbits about $M_2$

The family of prograde orbits presented here includes orbits that fly by the Moon twice per period, producing large lobes on either side of the Moon. As the orbits diverge from those in the corresponding planar family, the lobes gradually extend further out of the  $x - y$  plane and each perilune passage gets closer to the surface of the Moon. Figure B.23 shows four perspectives of this family of orbits; Figure B.24 shows two plots of the initial conditions used to produce this family of orbits. The highlighted orbits colored red are unstable orbits, the orbits colored green are neutrally stable orbits.

### B.5.2 Retrograde Orbits about $M_2$

The family of retrograde orbits centered about  $M_2$  bifurcates from the planar family of distant retrograde orbits. As the orbits in the family extend out of the plane, their perigee passages get closer to the Earth. Eventually the orbits in the family impact the surface of the Earth. Figure B.25 shows four perspectives of this family of orbits; Figure B.26 shows two plots of the initial conditions used to produce this family of orbits. The highlighted orbits colored red are unstable orbits, the orbits colored green are neutrally stable orbits.

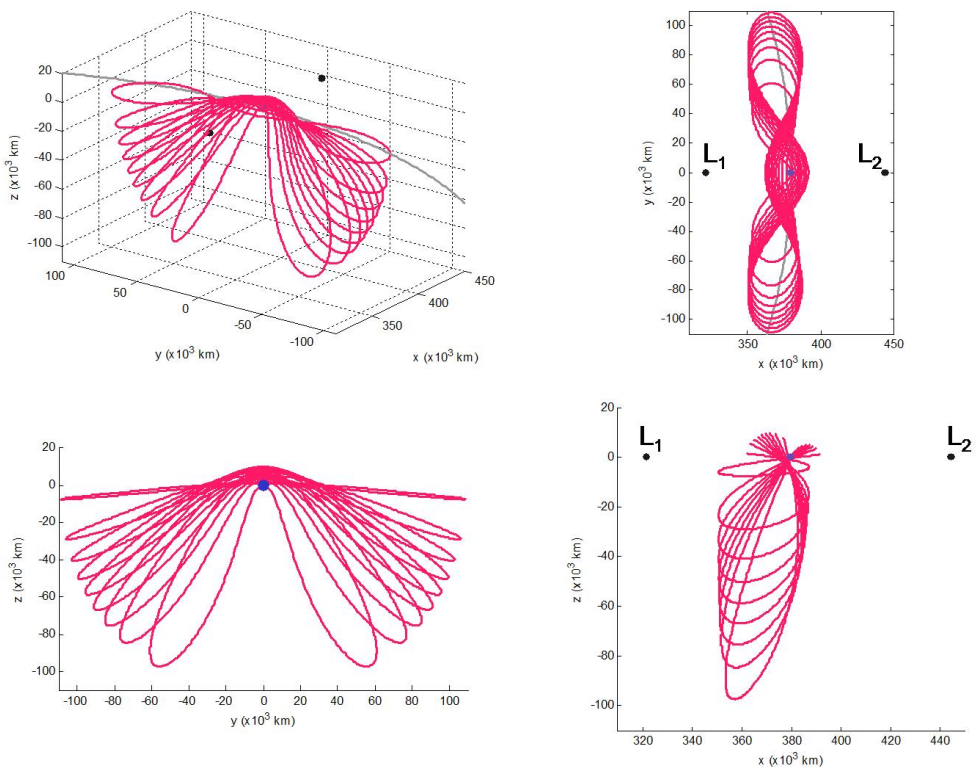


Figure B.23: Four perspectives of the family of prograde three-dimensional Class 5 orbits.

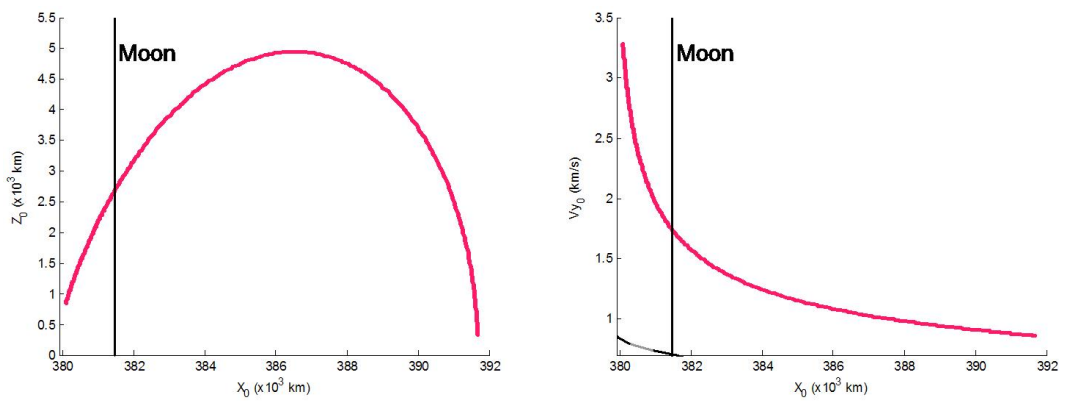


Figure B.24: Two plots showing the initial conditions yielding the family of prograde three-dimensional Class 5 orbits shown in Figure B.23. Left: the family's  $x_0$ -values vs. the family's  $z_0$ -values; Right:  $x_0$  vs.  $y_0$ .

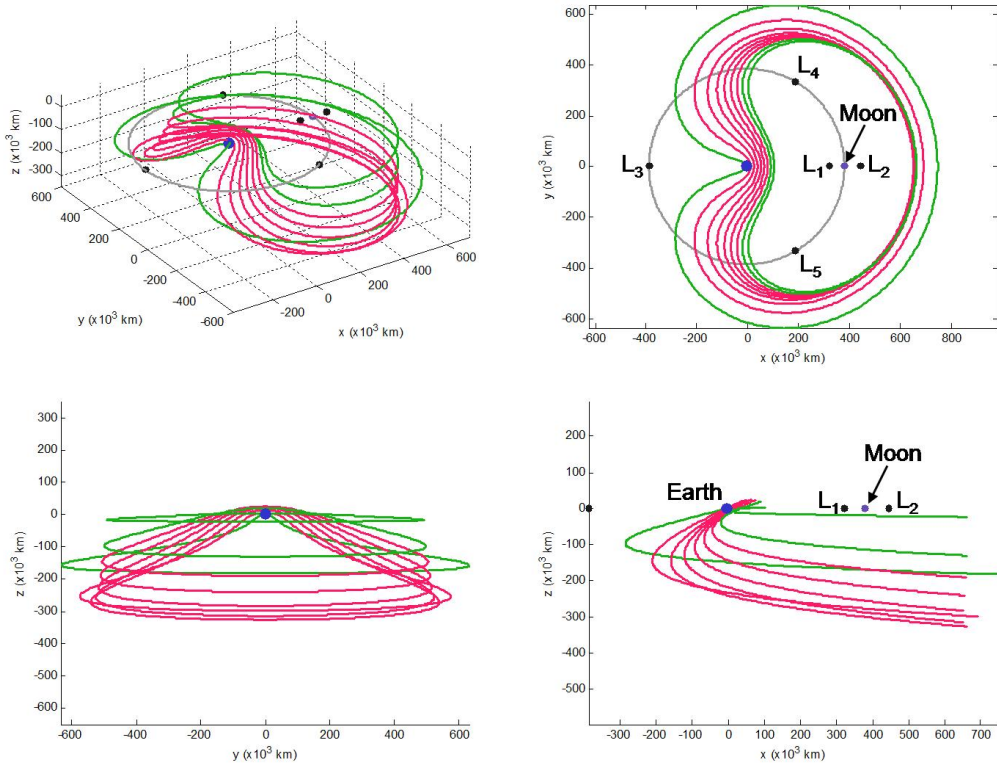


Figure B.25: Four perspectives of the family of retrograde three-dimensional Class 5 orbits.

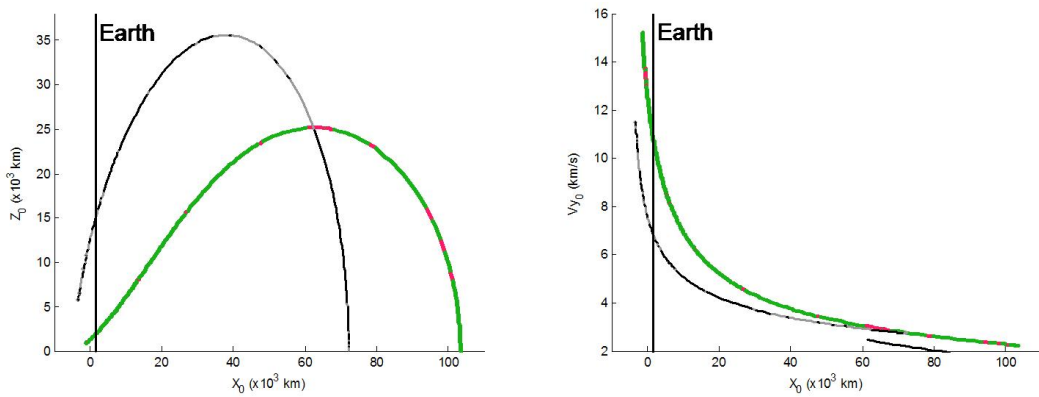


Figure B.26: Two plots showing the initial conditions yielding the family of retrograde three-dimensional Class 5 orbits shown in Figure B.25. Left: the family's  $x_0$ -values vs. the family's  $z_0$ -values; Right:  $x_0$  vs.  $y_0$ .

### B.6 Class 6: Orbits Centered about $L_2$

The final class of three-dimensional simple periodic symmetric orbits in the Earth-Moon CRTBP that bifurcates from planar families includes orbits that pierce the  $x$ -axis twice on the far side of the Moon. The only such family with this characteristic is the family of Halo orbits centered about  $L_2$ . This family bifurcates from the family of planar Lyapunov orbits centered about  $L_2$ . Figure B.27 shows four perspectives of this family of orbits; Figure B.28 shows two plots of the initial conditions used to produce this family of orbits. The highlighted orbits colored red are unstable orbits, the orbits colored green are neutrally stable orbits.

### B.7 Class M1: Miscellaneous Orbits Centered about $M_1$

Classes 1 – 6 contain each family of three-dimensional simple periodic symmetric orbits that obviously bifurcates from a planar family of simple periodic symmetric orbits. Several other families of orbits have also been identified in this study that do not obviously bifurcate from planar families of simple periodic symmetric orbits. These families may bifurcate from other planar orbits, but not simple symmetric orbits. Alternatively, these families may terminate before reaching a bifurcation with a planar family. That is, these families were each continued until an orbit was produced that was not a simple periodic symmetric orbit. It is possible that if the family were further continued, the orbits in the family may eventually revert back to being simple periodic symmetric orbits. Since this subject is not the focus of this dissertation, it was not pursued any further but left to the reader.

Class M1 contains families that do not obviously bifurcate from planar families and whose “center” is the larger primary, i.e., the Earth. Many such families exist, including both families of prograde and retrograde orbits.

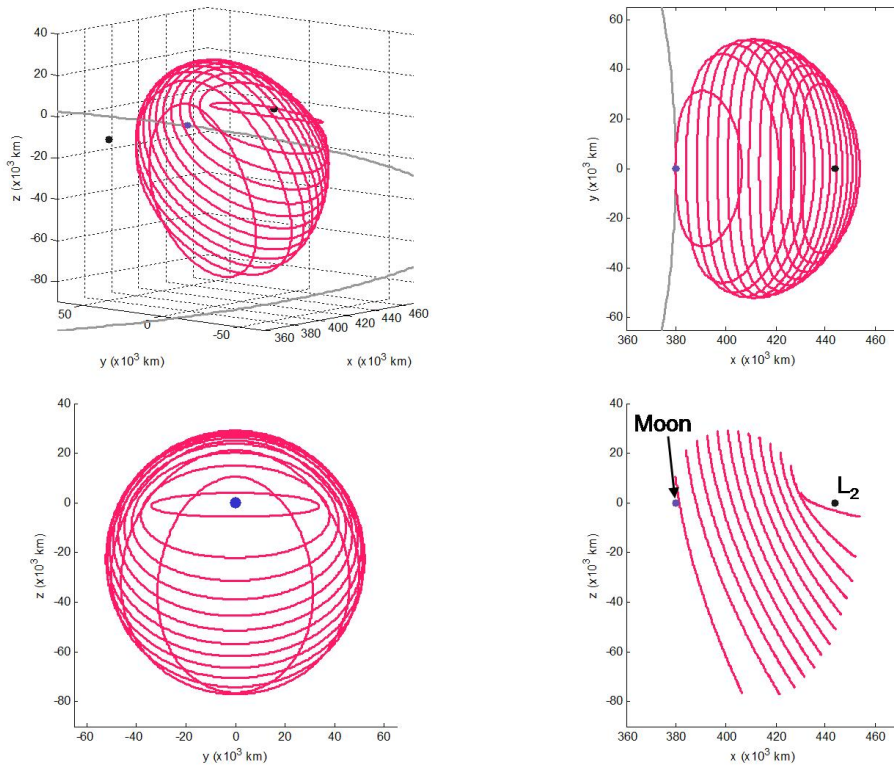


Figure B.27: Four perspectives of the family of Halo orbits centered about  $L_2$ .

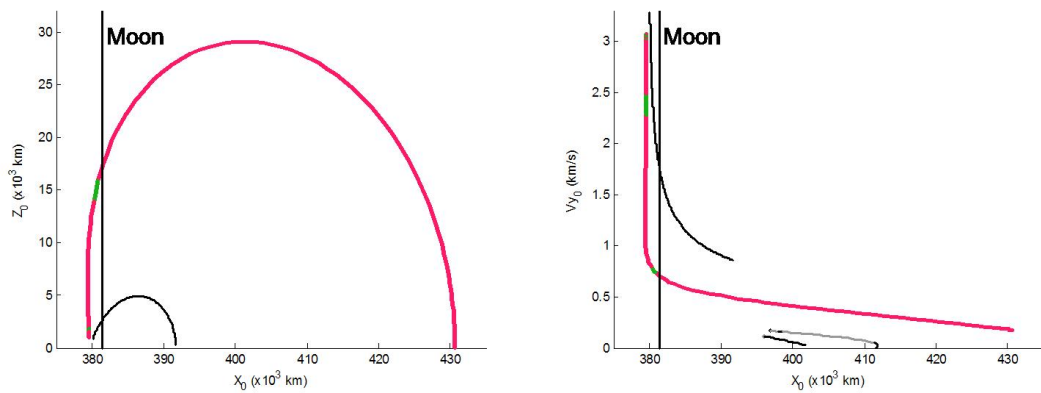


Figure B.28: Two plots showing the initial conditions yielding the family of Halo orbits centered about  $L_2$ . Left: the family's  $x_0$ -values vs. the family's  $z_0$ -values; Right:  $x_0$  vs.  $\dot{y}_0$ .

### B.7.1 Prograde Class M1 Orbits

The main class of prograde Class M1 orbits that has been identified in this study includes orbits that oscillate about the  $x - y$  plane an integer number of times per orbit. These oscillations extend far out of plane. Figures B.29 – B.33 show example orbits in the families that make between 2 and 6 oscillations per orbit. Each figure shows these orbits in four perspectives to provide a clear view of the shape of these orbits.

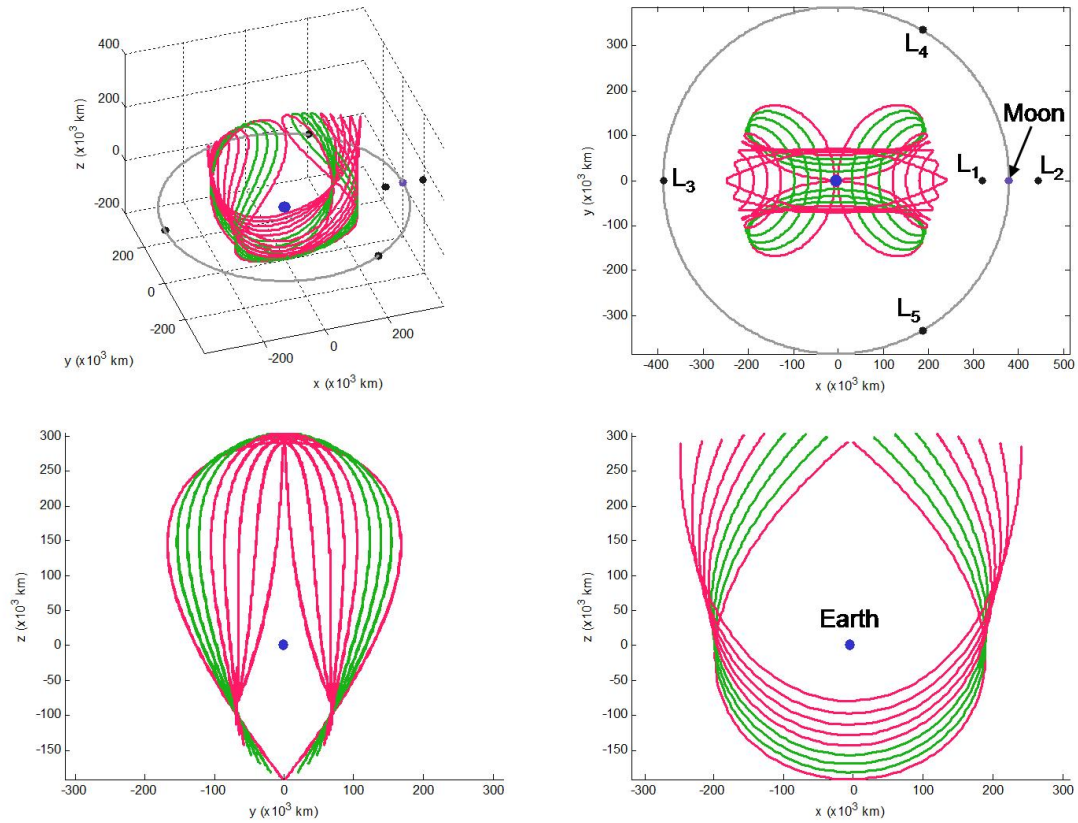


Figure B.29: Four perspectives of a family of prograde M1 orbits, each of which makes two oscillations per orbit.

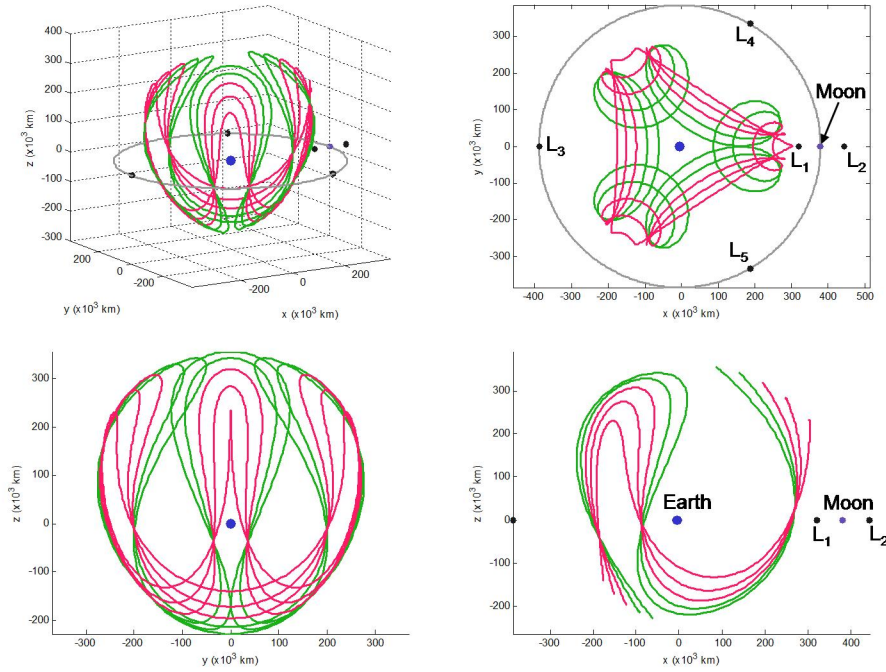


Figure B.30: Four perspectives of a family of prograde M1 orbits, each of which makes three oscillations per orbit.

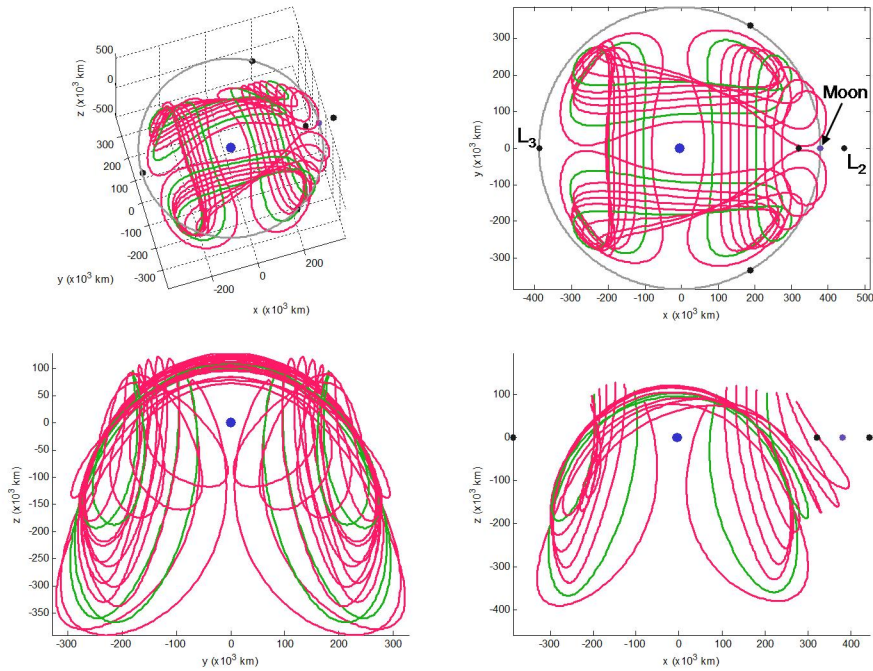


Figure B.31: Four perspectives of a family of prograde M1 orbits, each of which makes four oscillations per orbit.

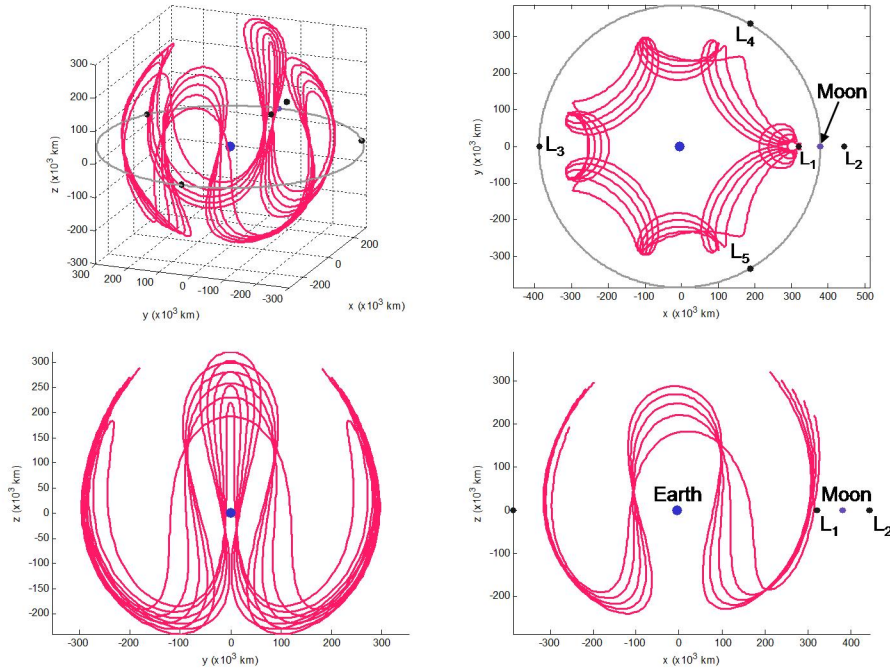


Figure B.32: Four perspectives of a family of prograde M1 orbits, each of which makes four oscillations per orbit.

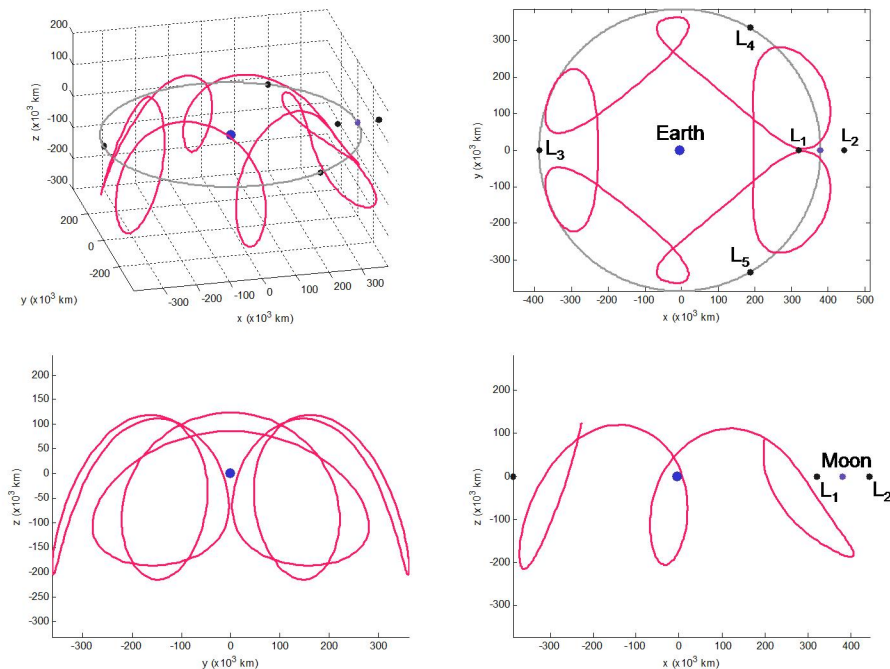


Figure B.33: Four perspectives of a family of prograde M1 orbits, each of which makes six oscillations per orbit.

### B.7.2 Retrograde Class M1 Orbits

The main class of retrograde Class M1 orbits that has been identified in this study includes orbits that resemble horseshoe orbits, such as those in Class 1, above. The main difference is that the orbits in these families oscillate a great deal out of the plane, preventing these families from bifurcating directly from planar families of simple symmetric horseshoe orbits. Four perspectives of an example orbit in one of these families is shown in Figure B.34.

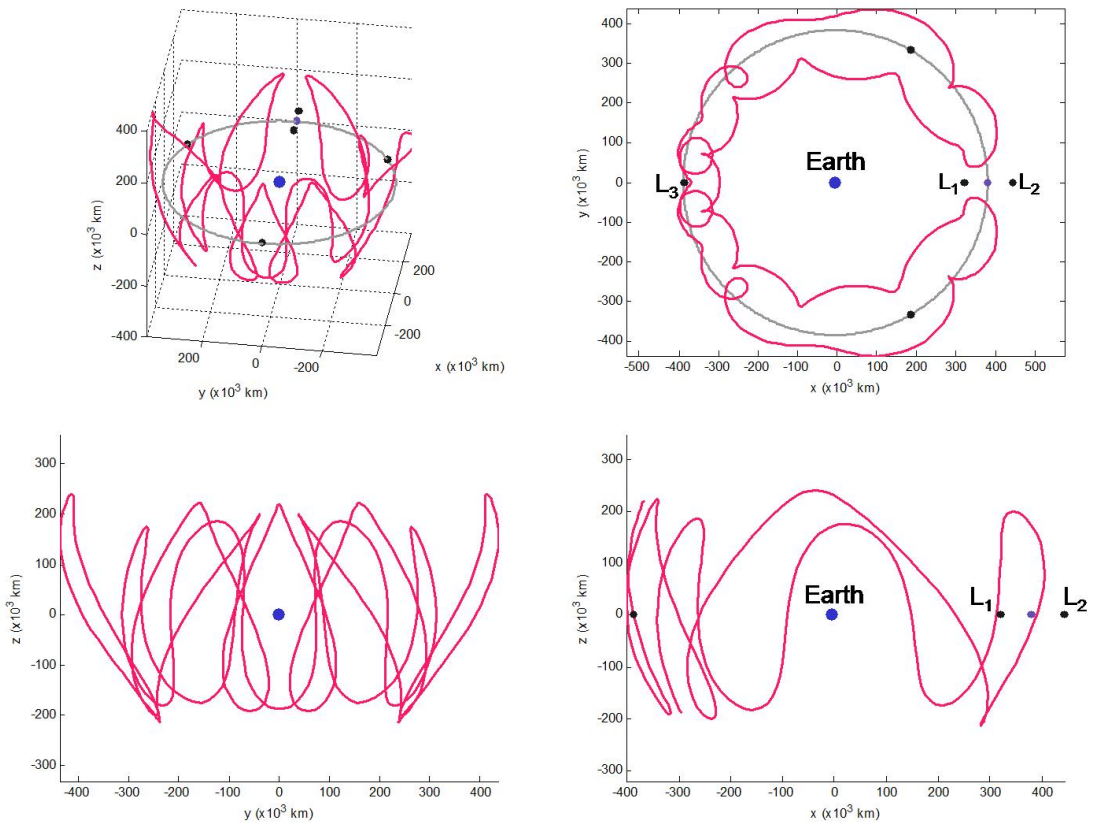


Figure B.34: Four perspectives of an example orbit in a family of retrograde M1 orbits that resemble horseshoe orbits.

### B.8 Class M2: Miscellaneous Orbits Centered about $M_2$

Class M2 contains families that do not obviously bifurcate from planar families and whose “center” is the smaller primary, i.e., the Moon. One such family was identified in this study, but others surely exist. The family that was identified in this study includes orbits that oscillate far out of the plane while orbiting the Moon in a prograde fashion. The orbits in this family each make two oscillations about the  $x - y$  axis per orbit. Figure B.35 shows four perspectives of this family of orbits.

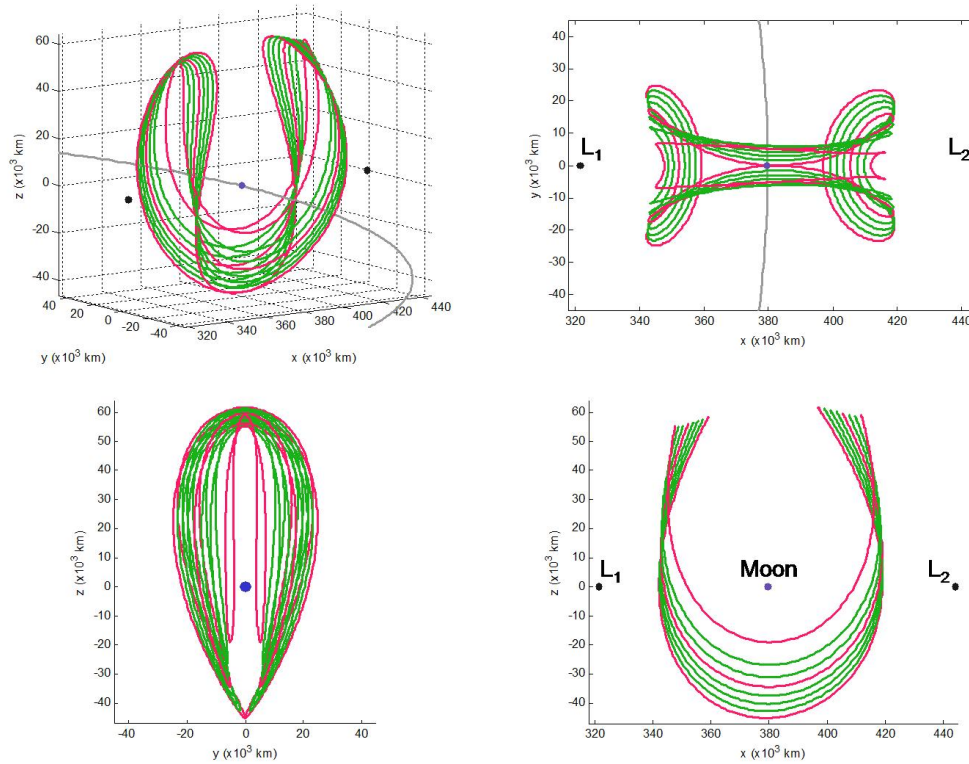


Figure B.35: Four perspectives of a family of retrograde M2 orbits, each of which makes two oscillations per orbit.

### B.9 Discussion

The families of orbits presented in this chapter supplement the families of planar orbits presented in Appendix A. These three-dimensional orbits help to paint a more complete picture of the variety of orbits that exist in the Earth-Moon CRTBP. However, this collection of orbits is still only a very small subset of the collection of all periodic orbit solutions that exist in the CRTBP.

Many of the orbits presented in this chapter may be used in practical missions in the Earth-Moon system. The Halo orbits that exist about the  $L_1$  and  $L_2$  points are implemented in Chapters 5 and 6 as staging orbits for ballistic lunar transfers. Other orbits may be implemented in very similar ways. The Halo orbits are also useful because a satellite in such an orbit always remains on one side of the Moon. Many of the orbits presented linger for many weeks in regions of space far from the Moon. Many of these orbits are stable in such regions, providing useful orbits to quarantine satellites that are returning from interplanetary missions. After a nominal check-out, the quarantined satellite may make an arbitrarily-small maneuver to transfer off of the quarantine orbit and return to the Earth. Other missions may use these orbits as staging orbits prior to injection to another planet or to deep space. These orbits may also be used for various communication, tracking, or science needs.

## Appendix C

### Analytical Expressions for the Lagrange Points

#### C.1 Introduction

The discussion given here is devoted to deriving analytical expressions for the Lagrange points in the CRTBP. Szebehely provides more details and a clear description of this derivation (Szebehely, 1967). Other derivations may be found in Moulton (1920) and Broucke et al. (1981).

#### C.2 Setting Up the System

Let us begin with a system of two masses,  $m_1$  and  $m_2$ , such that  $m_1 \geq m_2$ . Furthermore, each of these masses is orbiting the center of mass of the system in a circle. Then there exist cases where a third body,  $m_3$ , of negligible mass can be placed in the system in such a way that the force of gravity from both bodies and the centrifugal force in the system balance to produce a configuration that does not change in time with respect to the rotating system. That is, each body rotates about the center of mass at exactly the same rate and is seemingly fixed in the rotating frame of reference. Euler and Lagrange located five of these cases and those locations have henceforth been known as the five Lagrange points in a three-body system.

To locate the Lagrange points, we begin with the three bodies stationary in the

corotating frame of reference. That is,

$$\dot{\theta}_1 = \dot{\theta}_2 = \dot{\theta}_3 = \dot{\theta}(t) \quad (\text{C.1})$$

where  $\dot{\theta}_i$  is the angular velocity of the body of mass  $m_i$  about the center of mass. Furthermore, if the shape of the configuration does not alter over time, the relative distances  $r_{12}(t)$ ,  $r_{23}(t)$ , and  $r_{31}(t)$  are given by:

$$\frac{r_{12}(t)}{r_{12}(t_0)} = \frac{r_{23}(t)}{r_{23}(t_0)} = \frac{r_{31}(t)}{r_{31}(t_0)} = f(t). \quad (\text{C.2})$$

So far, there are no constraints on the relative size of the configuration, only on the angular velocity and the shape of the configuration.

Next, we move the origin to the center of mass of the configuration. Then  $\vec{R}_i$  describes the vector position of the  $i^{\text{th}}$  mass, satisfying the constraint:

$$\sum_{i=1}^3 m_i \vec{R}_i = 0. \quad (\text{C.3})$$

Equation C.3 may be written:

$$(m_1 + m_2 + m_3) \vec{R}_1 + m_2(\vec{R}_2 - \vec{R}_1) + m_3(\vec{R}_3 - \vec{R}_1) = 0, \quad \text{or}$$

$$M \vec{R}_1 = -m_2 \vec{r}_{12} - m_3 \vec{r}_{13}, \quad (\text{C.4})$$

where  $M$  is equal to the sum of the masses in the system. Squaring this relationship produces:

$$M^2 R_1^2 = m_2^2 r_{12}^2 + m_3^2 r_{13}^2 + 2m_2 m_3 \vec{r}_{12} \bullet \vec{r}_{13}, \quad (\text{C.5})$$

where  $R_i$  and  $r_i$  denote the magnitudes of the vectors  $\vec{R}_i$  and  $\vec{r}_i$ , respectively. Since we know that the relative shape of the configuration does not change, as seen above, we may substitute in the relationships for the relative angles and distances (Equations C.1 and C.2) into Equation C.5 to find that, in general:

$$R_i(t) = R_i(t_0) f(t). \quad (\text{C.6})$$

If  $F_i$  is the magnitude of the force per unit mass acting on the mass  $m_i$ , then the total force acting on  $m_i$  is  $m_i F_i$  and the equation of motion of that mass along the direction of the force satisfies:

$$m_i F_i = m_i (\ddot{R}_i - R_i \dot{\theta}_i^2). \quad (\text{C.7})$$

Since all of the particles are rotating at the same rate, we can reduce this relationship to the following:

$$m_i F_i = m_i [R_i(t_0) \ddot{f}(t) - R_i \dot{\theta}^2],$$

or equivalently

$$m_i F_i = R_i m_i [\ddot{f}(t)/f(t) - \dot{\theta}^2]. \quad (\text{C.8})$$

Hence, we have the proportionality relationship:

$$F_1 : F_2 : F_3 = R_1 : R_2 : R_3. \quad (\text{C.9})$$

There are two cases that will satisfy the conditions given in Equations C.8 and C.9. The two cases are:

$$\vec{R}_i \times \vec{F}_i = 0 \quad \text{or} \quad \vec{R}_i \times \ddot{\vec{R}}_i = 0. \quad (\text{C.10})$$

When we set  $i = 1$  and look at the first particle, we have the following force function:

$$m_1 \ddot{\vec{R}}_1 = G \left( \frac{m_1 m_2}{r_{12}^3} \vec{r}_{12} + \frac{m_1 m_3}{r_{13}^3} \vec{r}_{13} \right) \quad (\text{C.11})$$

When we take the cross product of  $\vec{R}_1$  with each side of Equation C.11, we obtain the following expression:

$$\vec{R}_1 \times \left( \frac{m_2}{r_{12}^3} \vec{R}_2 + \frac{m_3}{r_{13}^3} \vec{R}_3 \right) = 0. \quad (\text{C.12})$$

Using the center of mass relationship given in Equation C.3, this can be simplified to:

$$m_2 \vec{R}_1 \times \vec{R}_2 \left( \frac{1}{r_{12}^3} - \frac{1}{r_{13}^3} \right) = 0. \quad (\text{C.13})$$

Once, again, there are two similar equations for the other two particles. For Equation C.13 to hold, either of the following expressions must be true:

$$r_{12} = r_{23} = r_{31} = r \quad (\text{C.14})$$

(the equilateral triangle solution), or

$$\vec{R}_1 \times \vec{R}_2 = \vec{R}_2 \times \vec{R}_3 = \vec{R}_3 \times \vec{R}_1 = 0 \quad (\text{C.15})$$

(the collinear solution).

The triangular and collinear cases will be addressed separately in the next sections.

### C.3 Triangular Points

In the equilateral triangle case given in Equation C.14, we arrive at the following relationship for the first particle:

$$\ddot{\vec{R}}_1 + GM_1 \frac{\vec{R}_1}{R_1^3} = 0 \quad (\text{C.16})$$

where

$$M_1 = \frac{(m_2^2 + m_3^2 + m_2 m_3)^{3/2}}{(m_1 + m_2 + m_3)^2}. \quad (\text{C.17})$$

This result is the familiar two-body equation of motion. In this case, the first particle moves about the center of mass of the system in any conic orbit as if it had unit mass and a mass of  $M_1$  were placed at the center of mass of the system. Each particle moves in a corresponding trajectory and the figure remains in an equilateral triangle configuration (although its size may oscillate or grow indefinitely).

### C.4 Collinear Points

In the collinear case given in Equation C.15, we can also first show that each particle's orbit is a conic section. Beginning with the first particle, we can take the

collinear axis to be the  $x$  axis; the force acting on  $m_1$  is then:

$$F_1 = m_2 \frac{(x_2 - x_1)}{x_{12}^3} + m_3 \frac{(x_3 - x_1)}{x_{13}^3}. \quad (\text{C.18})$$

But we also know from Equation C.6 that

$$x_i(t) = x_i(t_0)f(t)$$

so that

$$F_1 = \frac{1}{f^2} \left[ m_2 \frac{(x_2 - x_1)}{x_{12}^3} + m_3 \frac{(x_3 - x_1)}{x_{13}^3} \right]_0 = \frac{\text{constant}}{f^2}. \quad (\text{C.19})$$

Since  $f$  is proportional to distance,  $m_1$  is acted upon by an inverse-square-law central force. Hence, the particle's orbit is a conic section.

Now we will impose the condition from Equation C.9 that

$$F_1 : F_2 : F_3 = x_1 : x_2 : x_3.$$

This condition will introduce the proportionality constant  $A$ , such that:

$$\begin{aligned} F_1 &= Ax_1 \\ F_2 &= Ax_2 \\ F_3 &= Ax_3 \end{aligned} \quad (\text{C.20})$$

or equally:

$$\begin{aligned} Ax_1 &= m_2 \frac{x_2 - x_1}{x_{12}^3} + m_3 \frac{x_3 - x_1}{x_{13}^3} \\ Ax_2 &= m_3 \frac{x_3 - x_2}{x_{23}^3} + m_1 \frac{x_1 - x_2}{x_{21}^3} \\ Ax_3 &= m_1 \frac{x_1 - x_3}{x_{31}^3} + m_2 \frac{x_2 - x_3}{x_{32}^3} \end{aligned} \quad (\text{C.21})$$

We are looking for the placement of the particle of mass  $m_3$  with respect to the other two particles such that the relative positions are constant in the rotating frame. The equilibrium positions possible for  $m_3$  are in the arrangements  $m_1 - m_3 - m_2$  (case 132),  $m_1 - m_2 - m_3$  (case 123), and  $m_3 - m_1 - m_2$  (case 312). Each case will be observed separately.

### C.4.1 Case 132: Identifying the L<sub>1</sub> point

For case 132, we are looking for a positive value of X such that

$$\left. \begin{aligned} X &= \frac{x_2 - x_3}{x_3 - x_1} = \frac{x_{32}}{x_{13}} \\ X + 1 &= \frac{x_2 - x_1}{x_3 - x_1} = \frac{x_{12}}{x_{13}} \end{aligned} \right\} \quad (\text{C.22})$$

We identify X using a series of steps. We first subtract  $Ax_1$  from  $Ax_3$  and  $Ax_3$  from  $Ax_2$  from Equation C.21 to arrive at  $Ax_{13}$  and  $Ax_{32}$ :

$$\begin{aligned} Ax_{13} &= -\frac{m_1 + m_3}{x_{13}^2} + m_2 \left( \frac{1}{x_{32}^2} - \frac{1}{x_{12}^2} \right) \\ Ax_{32} &= -\frac{m_2 + m_3}{x_{32}^2} + m_1 \left( \frac{1}{x_{13}^2} - \frac{1}{x_{12}^2} \right) \end{aligned} \quad (\text{C.23})$$

Using Equation C.22, we know that  $x_{32} = Xx_{13}$  and  $x_{12} = (X + 1)x_{13}$ . When we substitute these relationships into Equation C.23, we find two different relationships for the quantity  $Ax_{13}^3$ . When we set them equal and arrange in powers of X, we arrive at Lagrange's quintic equation:

$$\begin{aligned} (m_1 + m_3)X^5 + (3m_1 + 2m_3)X^4 + (3m_1 + m_3)X^3 \\ - (3m_2 + m_3)X^2 - (3m_2 + 2m_3)X - (m_2 + m_3) = 0 \end{aligned} \quad (\text{C.24})$$

We can use a quintic solver to solve for X (see Section C.5). Since the coefficients of (C.24) change sign only once, there can be only one positive real root. We can then use that value for X to determine the relative location of the massless particle, i.e., the location of L<sub>1</sub>, with respect to the other two particles by solving for  $x_3$  in Equation C.22:

$$X = \frac{x_2 - x_3}{x_3 - x_1} \quad \Rightarrow \quad x_3 = x_1 + \frac{x_2 - x_1}{X + 1} \quad (\text{C.25})$$

### C.4.2 Case 123: Identifying the L<sub>2</sub> point

For case 123, we are looking for a positive value of X such that

$$\left. \begin{aligned} X &= \frac{x_3 - x_2}{x_2 - x_1} = \frac{x_{23}}{x_{12}} \\ X + 1 &= \frac{x_3 - x_1}{x_2 - x_1} = \frac{x_{13}}{x_{12}} \end{aligned} \right\} \quad (\text{C.26})$$

In order to identify  $X$ , we follow a similar derivation as in case 132. We first subtract  $Ax_2$  from  $Ax_3$  and  $Ax_1$  from  $Ax_2$  from Equation C.21 to arrive at  $Ax_{23}$  and  $Ax_{12}$ :

$$\begin{aligned} Ax_{23} &= -\frac{m_2 + m_3}{x_{23}^2} + m_1 \left( \frac{1}{x_{12}^2} - \frac{1}{x_{13}^2} \right) \\ Ax_{12} &= -\frac{m_1 + m_2}{x_{12}^2} + m_3 \left( \frac{1}{x_{23}^2} - \frac{1}{x_{13}^2} \right) \end{aligned} \quad (\text{C.27})$$

We then substitute in  $X$  and  $(X + 1)$  from Equation C.26 as before, eliminate  $Ax_{12}^3$  between the resulting equations and arrange in powers of  $X$  to produce Lagrange's quintic equation:

$$\begin{aligned} (m_1 + m_2)X^5 + (3m_1 + 2m_2)X^4 + (3m_1 + m_2)X^3 \\ - (m_2 + 3m_3)X^2 - (2m_2 + 3m_3)X - (m_2 + m_3) = 0 \end{aligned} \quad (\text{C.28})$$

Once again, we can use a quintic solver to solve for  $X$  (see Section C.5), knowing that again there is only one real positive root. We can then use that value for  $X$  to determine the relative location of the massless particle, i.e., the location of  $L_2$ , with respect to the other two particles by solving for  $x_3$  in Equation C.26:

$$X = \frac{x_3 - x_2}{x_2 - x_1} \quad \Rightarrow \quad x_3 = x_2 + X(x_2 - x_1) \quad (\text{C.29})$$

#### C.4.3 Case 312: Identifying the $L_3$ point

For case 312, we are looking for a positive value of  $X$  such that

$$\left. \begin{aligned} X &= \frac{x_2 - x_1}{x_1 - x_3} = \frac{x_{12}}{x_{31}} \\ X + 1 &= \frac{x_2 - x_3}{x_1 - x_3} = \frac{x_{32}}{x_{31}} \end{aligned} \right\} \quad (\text{C.30})$$

In order to identify  $X$ , we follow a similar derivation as in case 132. We first subtract  $Ax_1$  from  $Ax_2$  and  $Ax_3$  from  $Ax_1$  from Equation C.21 to arrive at  $Ax_{12}$  and  $Ax_{31}$ :

$$\begin{aligned} Ax_{31} &= -\frac{m_1 + m_3}{x_{31}^2} + m_2 \left( \frac{1}{x_{12}^2} - \frac{1}{x_{32}^2} \right) \\ Ax_{12} &= -\frac{m_1 + m_2}{x_{12}^2} + m_3 \left( \frac{1}{x_{31}^2} - \frac{1}{x_{32}^2} \right) \end{aligned} \quad (\text{C.31})$$

We then substitute in  $X$  and  $(X + 1)$  from Equation C.30 as before, eliminate  $Ax_{31}^3$  between the resulting equations and arrange in powers of  $X$  to produce Lagrange's quintic equation:

$$(m_1 + m_3)X^5 + (2m_1 + 3m_3)X^4 + (m_1 + 3m_3)X^3 \\ - (m_1 + 3m_2)X^2 - (2m_1 + 3m_2)X - (m_1 + m_2) = 0 \quad (\text{C.32})$$

Once again, we can use a quintic solver to solve for  $X$  (see Section C.5), knowing that again there is only one real positive root. We can then use that value for  $X$  to determine the relative location of the massless particle, i.e., the location of  $L_3$ , with respect to the other two particles by solving for  $x_3$  in Equation C.30:

$$X = \frac{x_2 - x_1}{x_1 - x_3} \quad \Rightarrow \quad x_3 = x_1 - \frac{x_2 - x_1}{X} \quad (\text{C.33})$$

## C.5 Algorithms

The quintics given in Equations C.25, C.29, and C.33 provide analytic determinations of the locations of the first, second, and third Lagrange points, respectively, in the circular restricted three-body system. Szebehely outlines a fixed-point iterative scheme that may be implemented to identify the single positive real root of each of the quintic equations (Szebehely, 1967). The fourth and fifth Lagrange points make equilateral triangles with the primaries; hence, their locations are easily determined using geometry.

Sections C.5.1 – C.5.3 provide pseudo-code that may be used to implement a fixed-point iterative scheme to find the  $x$ -coordinate of  $L_1$  –  $L_3$ , respectively. The coordinate axis and the definition of  $\mu$  are defined in Section 2.3.1.

### C.5.1 Numerical Determination of L<sub>1</sub>

$$\gamma_0 = \left( \frac{\mu(1-\mu)}{3} \right)^{1/3}$$

$$\gamma = \gamma_0 + 1$$

while  $|\gamma - \gamma_0| > \text{tol}$

$$\gamma_0 = \gamma$$

$$\gamma = \left( \frac{\mu(\gamma_0 - 1)^2}{3 - 2\mu - \gamma_0(3 - \mu - \gamma_0)} \right)^{1/3}$$

endwhile

$$x_{L_1} = 1 - \mu - \gamma$$

### C.5.2 Numerical Determination of L<sub>2</sub>

$$\gamma_0 = \left( \frac{\mu(1-\mu)}{3} \right)^{1/3}$$

$$\gamma = \gamma_0 + 1$$

while  $|\gamma - \gamma_0| > \text{tol}$

$$\gamma_0 = \gamma$$

$$\gamma = \left( \frac{\mu(\gamma_0 + 1)^2}{3 - 2\mu + \gamma_0(3 - \mu + \gamma_0)} \right)^{1/3}$$

endwhile

$$x_{L_2} = 1 - \mu + \gamma$$

### C.5.3 Numerical Determination of $L_3$

$$\gamma_0 = \left( \frac{\mu(1-\mu)}{3} \right)^{1/3}$$

$$\gamma = \gamma_0 + 1$$

while  $|\gamma - \gamma_0| > \text{tol}$

$$\gamma_0 = \gamma$$

$$\gamma = \left( \frac{(1-\mu)(\gamma_0+1)^2}{1+2\mu+\gamma_0(2+\mu+\gamma_0)} \right)^{1/3}$$

endwhile

$$x_{L_3} = -\mu - \gamma$$

## Appendix D

### Conversions Between Reference Frames

#### D.1 Introduction

The discussion here is devoted to providing formulae to convert from one reference frame to another. The following reference frames are used in this dissertation:

- The standard inertial reference frame. This reference frame is centered at the barycenter of the system, unless otherwise noted, and does not rotate with the motion of any body.
- The standard synodic reference frame. This reference frame is centered at the barycenter of the system, unless otherwise noted, and rotates at a constant rate equal to the mean rotation rate of the two massive bodies about their barycenter. The  $x$ -axis of the system goes from the origin through the smaller massive body; the  $z$ -axis coincides with the angular momentum vector of the system; the  $y$ -axis completes the right-hand coordinate system. This reference frame is usually used when representing three-body trajectories.
- The Earth-Moon synodic reference frame. Most times, the Earth-Moon synodic frame is represented by the standard synodic reference frame. However, when the Sun, Earth, and Moon are all being included in a model, the Earth-Moon synodic frame is defined slightly differently. The Earth-Moon synodic frame is centered at the barycenter of the Earth and Moon and rotates at a constant rate

equal to the sum of the mean rotation rate of the Moon about the Earth and the mean rotation rate of the Earth about the Sun. In this way, the frame's origin follows the motion of the Earth about the Sun while rotating with the Moon's motion about the Earth.

- The JPL Ephemeris reference frame. This reference frame is centered at the barycenter of the solar system and is oriented with respect to the Earth's mean equatorial orientation at the J2000 epoch. It is a quasi-inertial reference frame, based on the locations of 212 extragalactic sources distributed across the sky (Ma et al., 1998). The reference frame is non-inertial only since those sources move slightly with respect to each other over time.

To move from one reference frame to another, several conversions are necessary. Sections D.2 and D.3 describe the conversions from a rotating reference frame to an inertial reference frame and vice versa. Sections D.4 and D.5 describe the conversions from the Earth-Moon synodic frame to the Sun-Earth synodic frame and vice versa. Finally, Sections D.6 and D.7 describe the conversions from the standard synodic reference frame to the JPL Ephemeris inertial reference frame and vice versa. In each case, the standard synodic and standard inertial reference frames assume that the massive bodies orbit their barycenter in circular orbits. Sections D.6 and D.7 may be used to convert between the JPL Ephemeris inertial reference frame and either the Sun-Earth/Moon synodic frame or the Earth-Moon synodic frame. Both sets of conversions are frequently used in this dissertation.

## D.2 Standard Synodic to Inertial

We begin with a state in the standard synodic frame of the CRTBP:

$$\mathbf{X}_r = [x_r, y_r, z_r, \dot{x}_r, \dot{y}_r, \dot{z}_r]^T.$$

We wish to convert  $X_r$  to the state  $X_i$  in the standard inertial coordinate frame:

$$X_i = [x_i, y_i, z_i, \dot{x}_i, \dot{y}_i, \dot{z}_i]^T.$$

The conversion assumes that the massive bodies orbit their barycenter in circular orbits in the inertial frame of reference. At the time of the conversion, the synodic frame is rotated by an angle  $\theta$  with respect to the inertial frame. That is, the smaller mass of the CRTBP has revolved about the barycenter of the system by an angle  $\theta$  in a counter-clockwise direction from the  $x$ -axis of the inertial reference frame. Then we may define the transformation  $T$ :

$$T = \begin{bmatrix} \cos \theta & -\sin \theta & 0 \\ \sin \theta & \cos \theta & 0 \\ 0 & 0 & 1 \end{bmatrix} \quad (\text{D.1})$$

Finally, we will use the notation that there are  $N_D$  kilometers per three-body distance unit  $d_{3B}$  and  $N_T$  seconds per three-body time unit  $t_{3B}$ . Then we may convert the state from the standard synodic reference frame to the standard inertial reference frame using the following expressions:

$$R_i = \begin{bmatrix} x_i \\ y_i \\ z_i \end{bmatrix} = T \begin{bmatrix} x_r \\ y_r \\ z_r \end{bmatrix} \left( \frac{N_D \text{ km}}{1 d_{3B}} \right) \quad (\text{D.2})$$

$$V_i = \begin{bmatrix} \dot{x}_i \\ \dot{y}_i \\ \dot{z}_i \end{bmatrix} = T \begin{bmatrix} \dot{x}_r - y_r \\ \dot{y}_r + x_r \\ \dot{z}_r \end{bmatrix} \left( \frac{N_D \text{ km}}{1 d_{3B}} \right) \left( \frac{1 t_{3B}}{N_T \text{ sec}} \right) \quad (\text{D.3})$$

### D.3 Inertial to Standard Synodic

We wish to convert the state  $X_i$  in the standard inertial reference frame to the state  $X_r$  in the standard synodic reference frame using the same angle  $\theta$  as defined

above in Section D.2. This conversion assumes that the massive bodies orbit their barycenter in circular orbits in the inertial frame.

We may define the transformation  $\hat{T}$  such that  $\hat{T}\hat{T} = I$ :

$$\hat{T} = \begin{bmatrix} \cos(-\theta) & -\sin(-\theta) & 0 \\ \sin(-\theta) & \cos(-\theta) & 0 \\ 0 & 0 & 1 \end{bmatrix} = \begin{bmatrix} \cos \theta & \sin \theta & 0 \\ -\sin \theta & \cos \theta & 0 \\ 0 & 0 & 1 \end{bmatrix} \quad (\text{D.4})$$

Then we may convert the state from the standard inertial reference frame to the standard synodic reference frame using the following expressions:

$$R_r = \begin{bmatrix} x_r \\ y_r \\ z_r \end{bmatrix} = \hat{T} \begin{bmatrix} x_i \\ y_i \\ z_i \end{bmatrix} \left( \frac{1 d_{3B}}{N_D \text{ km}} \right) \quad (\text{D.5})$$

$$V_r = \begin{bmatrix} \dot{x}_r \\ \dot{y}_r \\ \dot{z}_r \end{bmatrix} = \hat{T} \begin{bmatrix} \dot{x}_i \\ \dot{y}_i \\ \dot{z}_i \end{bmatrix} \left( \frac{1 d_{3B}}{N_D \text{ km}} \right) \left( \frac{N_T \text{ sec}}{1 t_{3B}} \right) + \begin{bmatrix} y_r \\ -x_r \\ 0 \end{bmatrix} \quad (\text{D.6})$$

#### D.4 Earth-Moon to Sun-Earth

The conversion from the Earth-Moon synodic frame to the Sun-Earth synodic frame involves several conversions. We begin with the state of a satellite in the Earth-Moon rotating frame  $X_{r-EM}^{Sat}$  and the angle  $\theta$ , defined to be the angle that the Moon has revolved in a counter-clockwise fashion since it last crossed the Sun-Earth line. We assume that the Earth and Moon orbit their barycenter in circular orbits and that the Earth-Moon system and the Sun orbit the barycenter of the entire system in circular orbits.

The first intermediate step is to use the conversion given in Section D.2 to produce the state  $X_{i-EM}^{Sat}$ , namely, the state of the satellite in the inertial frame centered at the Earth-Moon barycenter.

The next step is to determine the state of the Earth-Moon barycenter,  $X_{i-SE}^{EMB}$ , in the inertial frame centered at the Sun-Earth barycenter. A simple way to do that is to use the conversion given in Section D.2 on the state  $X_E = [1 - \mu_{SE}, 0, 0, 0, 0, 0]^T$  using an angle of zero.

Next, we transfer the state of the satellite into the inertial frame centered at the Sun-Earth barycenter using the simple translation:  $X_{i-SE}^{Sat} = X_{i-EM}^{Sat} + X_{i-SE}^{EMB}$ .

Finally, we transfer the state of the satellite into the Sun-Earth synodic frame using the conversion given in Section D.3 with an angle of zero (since the Earth is on the  $x$ -axis), producing the desired state  $X_{r-SE}^{Sat}$ .

## D.5 Sun-Earth to Earth-Moon

The conversion from the Sun-Earth synodic frame to the Earth-Moon synodic frame involves the conversions given in Section D.4 in the reverse order. Once again, we assume that the Earth and Moon orbit their barycenter in circular orbits and that the Earth-Moon system and the Sun orbit the barycenter of the entire system in circular orbits. We begin with the state of a satellite in the Sun-Earth rotating frame  $X_{r-SE}^{Sat}$ .

The first intermediate step is to use the conversion given in Section D.2 with an angle of zero to produce the state  $X_{i-SE}^{Sat}$ , namely, the state of the satellite in the inertial frame centered at the Sun-Earth barycenter. Since an angle of zero was used in the conversion, the Earth is on the  $x$ -axis in this frame.

The next step is to determine the state of the Earth-Moon barycenter,  $X_{i-SE}^{EMB}$ , in the inertial frame centered at the Sun-Earth barycenter. A simple way to do that is to use the conversion given in Section D.2 on the state  $X_E = [1 - \mu_{SE}, 0, 0, 0, 0, 0]^T$  using an angle of zero.

Next, we transfer the state of the satellite into the inertial frame centered at the Earth-Moon barycenter using the simple translation:  $X_{i-EM}^{Sat} = X_{i-SE}^{Sat} - X_{i-SE}^{EMB}$ .

Finally, we transfer the state of the satellite into the Earth-Moon synodic frame

using the conversion given in Section D.3 with an angle of  $\theta$ , producing the desired state  $X_{r-EM}^{Sat}$ .

## D.6 Standard Synodic to JPL Ephemeris

There are several significant differences between converting a state from the standard synodic reference frame to the standard inertial reference frame and converting a state to the JPL Ephemeris reference frame. The first trivial, but important difference is that the JPL Ephemeris model uses km and km/day as units of position and velocity, respectively. The second significant difference is the orientation of the coordinate axes. The JPL Ephemeris model uses the International Celestial Reference Frame (ICRF) for its orientation, which is a reference frame consistent with the FK5 J2000.0 optical reference frame, within the limits of the link accuracy (Ma et al., 1998). Hence, the axes are oriented with respect to the Earth's mean equatorial orientation at noon on January 1st, 2000 terrestrial time. The third significant difference is that in the JPL Ephemeris model, the planetary bodies do not move in circular coplanar orbits. Consequently, perturbations in the system are not perfectly periodic nor symmetric. The locations of the Lagrange points are not constant, but pulse inward and outward as the massive bodies follow their eccentric orbits. Since the motion of a satellite in the standard CRTBP is based on the relative location of the satellite with respect to each of the primary masses, the conversion to the JPL Ephemeris is not clearly defined. The conversions given here work well when the satellite is near the smaller primary in the three-body system.

We begin with the state of a satellite in the standard synodic reference frame,  $X_r^{Sat}$ , at an epoch time,  $JD$ . Let us say that the synodic frame that we are transferring from is the Sun-Earth/Moon three-body synodic frame. Then, we may use the JPL Ephemeris to determine the state of the Sun and Earth/Moon Barycenter at the epoch time to be  $X_{JPL}^{Sun}$  and  $X_{JPL}^{EM}$ , respectively.

We define the position and velocity vectors of the secondary mass (i.e., the Earth-Moon Barycenter) with respect to the primary mass (i.e., the Sun) in the JPL reference frame to be  $R_S = [x_S, y_S, z_S]^T$  and  $V_S = [\dot{x}_S, \dot{y}_S, \dot{z}_S]^T$ , such that they are constructed using the equation:

$$X_S = [x_S, y_S, z_S, \dot{x}_S, \dot{y}_S, \dot{z}_S]^T = X_{JPL}^{EM} - X_{JPL}^{Sun}.$$

Then we may define the following angles:

$$\theta = \tan^{-1} \left( \frac{y_S}{x_S} \right) \quad (D.7)$$

$$\phi = \tan^{-1} \left( \frac{z_S}{\sqrt{x_S^2 + y_S^2}} \right) \quad (D.8)$$

$$\beta = \tan^{-1} \left( \frac{\dot{z}_S}{\sqrt{\dot{x}_S^2 + \dot{y}_S^2}} \right) \quad (D.9)$$

The transformations  $T$  and  $\hat{T}$  are constructed by a combination of three rotations such that  $T\hat{T} = I$ :

$$T = \begin{bmatrix} \cos \theta & -\sin \theta & 0 \\ \sin \theta & \cos \theta & 0 \\ 0 & 0 & 1 \end{bmatrix} \begin{bmatrix} \cos \phi & 0 & -\sin \phi \\ 0 & 1 & 0 \\ \sin \phi & 0 & \cos \phi \end{bmatrix} \begin{bmatrix} 1 & 0 & 0 \\ 0 & \cos \beta & -\sin \beta \\ 0 & \sin \beta & \cos \beta \end{bmatrix} \quad (D.10)$$

$$\hat{T} = \begin{bmatrix} 1 & 0 & 0 \\ 0 & \cos \beta & \sin \beta \\ 0 & -\sin \beta & \cos \beta \end{bmatrix} \begin{bmatrix} \cos \phi & 0 & \sin \phi \\ 0 & 1 & 0 \\ -\sin \phi & 0 & \cos \phi \end{bmatrix} \begin{bmatrix} \cos \theta & \sin \theta & 0 \\ -\sin \theta & \cos \theta & 0 \\ 0 & 0 & 1 \end{bmatrix} \quad (D.11)$$

The number of kilometers,  $N_D$ , between the two primary bodies at the epoch is equal to:

$$N_D = \sqrt{x_S^2 + y_S^2 + z_S^2} \quad (D.12)$$

The number of **days**,  $N_T$ , in one normalized three-body time unit at the epoch is equal to:

$$N_T = \sqrt{\frac{N_D^3}{G(M_{Sun} + M_{Earth} + M_{Moon})}} \left( \frac{1 \text{ day}}{86400 \text{ sec}} \right), \quad (D.13)$$

assuming that  $G$  is in SI units. We emphasize that  $N_T$  is the number of days per time-unit because the JPL Ephemeris model uses days as its unit of time.

We now have the tools necessary to convert the satellite's state into the International Celestial Reference Frame. The position of the satellite in ICRF coordinates,  $R_{JPL}^{Sat}$ , is equal to:

$$R_{JPL}^{Sat} = TR_r^{Sat} \left( \frac{N_D \text{ km}}{1 d_{3B}} \right) + R_{JPL}^B, \quad (\text{D.14})$$

where  $R_{JPL}^B$  is the position vector of the barycenter of the original three-body system with respect to the ICRF's origin. Thus, if the satellite's state originated from the Earth-Moon three-body system, then  $R_{JPL}^B = R_{JPL}^{EM}$ .

The conversion of the satellite's velocity into ICRF coordinates is not trivial since the standard three-body system assumes circular orbits. The satellite's velocity must be rotated into the correct frame and transferred out of a rotating frame. The satellite's motion must also be scaled proportional to the location of the secondary body on its elliptical orbit. The following steps produce a result that is satisfactory for most purposes, e.g., as an initial guess for a differential-correction algorithm.

First, we require the velocity of the secondary body in the inertial frame rotated into the synodic axes at the epoch  $JD$ :

$$V_S^* = \hat{T}V_S \quad (\text{D.15})$$

This velocity acts as a scale when transferring from a CRTBP frame to the inertial frame. The velocity of the spacecraft in the inertial frame at the epoch due to the rotation rate of the synodic frame is then proportional to  $V_S^*$ . More precisely, it is equal to:

$$V_{frame}^{Sat} = T_{SC} \left[ V_S^* \left( \frac{\sqrt{(x_r^{Sat})^2 + (y_r^{Sat})^2}}{1 - \mu} \right) \right], \quad (\text{D.16})$$

where  $T_{SC}$  is the rotation transformation of the satellite's position in the synodic frame,

equal to:

$$T_{SC} = \begin{bmatrix} \cos \alpha & -\sin \alpha & 0 \\ \sin \alpha & \cos \alpha & 0 \\ 0 & 0 & 1 \end{bmatrix} \quad (\text{D.17})$$

where  $\alpha = \tan^{-1}(y_r^{Sat} / x_r^{Sat})$ .

Finally, we add the rotation rate of the synodic frame, scaled to the position of the secondary mass on its elliptical orbit, to the velocity of the satellite in the synodic frame, rotate it to the proper orientation of the ICRF, and add the velocity of the barycenter of the three-body system to produce  $V_{JPL}^{Sat}$ , the velocity of the satellite in the JPL Ephemeris model:

$$V_{JPL}^{Sat} = T \left[ V_r^{Sat} \left( \frac{N_D \text{ km}}{1 d_{3B}} \right) \left( \frac{1 t_{3B}}{N_T \text{ days}} \right) + V_{frame}^{Sat} \right] + V_{JPL}^B, \quad (\text{D.18})$$

where  $V_{JPL}^B$  is the velocity of the barycenter of the three-body system that the satellite's state originated from. Thus, if the satellite's state originated from the Earth-Moon three-body system, then  $V_{JPL}^B = V_{JPL}^{EM}$ .

Once again, the state of the satellite converted into the JPL Ephemeris model is an approximation since the conversions between the circular orbits of the CRTBP and the ephemerides of the planets are not well-defined.

## D.7 JPL Ephemeris to Standard Synodic

The conversion from the JPL Ephemeris model's reference frame to the standard synodic reference frame involves the conversions given in Section D.6 in the reverse order. See Section D.6 for a description about the reference frame and for the definitions of each variable.

We begin with the state of the satellite in the JPL Ephemeris model,  $X_{JPL}^{Sat}$ , at an epoch time  $JD$ . We wish to convert this state to the standard synodic reference frame, e.g., the Sun-Earth/Moon synodic reference frame.

We may use the JPL Ephemeris to determine the state of the Sun and Earth/Moon Barycenter at the epoch time to be  $X_{JPL}^{Sun}$  and  $X_{JPL}^{EM}$ , respectively. The vectors  $R_S$ ,  $V_S$ ,  $V_S^*$ ,  $R_{JPL}^B$ , and  $V_{JPL}^B$ , the angles  $\theta$ ,  $\phi$ , and  $\beta$ , the transformations  $T$  and  $\hat{T}$ , and the unit-conversion values  $N_D$  and  $N_T$  are all computed exactly as in Section D.6.

The position of the satellite in the synodic frame of reference,  $R_r^{Sat}$ , is equal to:

$$R_r^{Sat} = \hat{T} \left[ R_{JPL}^{Sat} - R_{JPL}^B \right] \left( \frac{1 d_{3B}}{N_D \text{ km}} \right). \quad (\text{D.19})$$

The velocity of the satellite in the synodic frame of reference,  $V_r^{Sat}$ , requires a few intermediate steps to compute. In the first few steps, we use the newly-converted position of the satellite in the synodic frame, computed in Equation D.19, to compute the velocity of the satellite due to the rotation of the synodic frame:

$$V_{frame}^{Sat} = T_{SC} \left[ V_S^* \left( \frac{\sqrt{(x_r^{Sat})^2 + (y_r^{Sat})^2}}{1 - \mu} \right) \right], \quad (\text{D.20})$$

where  $T_{SC}$  is the rotation transformation of the satellite's converted position in the synodic frame, equal to:

$$T_{SC} = \begin{bmatrix} \cos \alpha & -\sin \alpha & 0 \\ \sin \alpha & \cos \alpha & 0 \\ 0 & 0 & 1 \end{bmatrix} \quad (\text{D.21})$$

where  $\alpha = \tan^{-1}(y_r^{Sat} / x_r^{Sat})$ .

We compute the velocity of the satellite in the synodic frame of reference by subtracting the velocity of the barycenter of the three-body system from the velocity of the satellite in the JPL Ephemeris model, rotating the resulting relative velocity into the synodic coordinate frame, subtracting off the velocity of the satellite due to the rotating frame itself, and normalizing the velocity into nondimensional three-body units:

$$V_r^{Sat} = \left( \hat{T} \left[ V_{JPL}^{Sat} - V_{JPL}^B \right] - V_{frame}^{Sat} \right) \left( \frac{1 d_{3B}}{N_D \text{ km}} \right) \left( \frac{N_T \text{ days}}{1 t_{3B}} \right). \quad (\text{D.22})$$

The state of the satellite in the synodic frame of reference is an approximation since the conversions between the ephemerides of the planets in the JPL Ephemeris

model and the circular orbits of the CRTBP are not well-defined. However, the result of these conversions has been satisfactory in this dissertation for most purposes, e.g., as an initial guess for a differential-correction algorithm.

## Appendix E

### Computational Considerations

#### E.1 Introduction

This dissertation studies many trajectories that have been produced in the Circular Restricted Three-Body model, the Patched Three-Body model, and the JPL Ephemeris model (see Chapter 2 for more information about each of these models). These models do not have closed-form general solutions; hence, the trajectories must be numerically integrated. The purpose of this appendix is to provide some description about how the author has produced each trajectory in this dissertation, and to discuss some of the computational demands of each algorithm.

#### E.2 Development

The majority of the algorithms produced in this dissertation have been developed using MATLAB<sup>®</sup> 7.0 (R14) and the C programming language. In general, the high-level development has been conducted using MATLAB<sup>®</sup>, but all numerical integration routines have been coded in C and called from within MATLAB<sup>®</sup> using **mex**-functions. In this way, the development of each algorithm has been simplified without significantly increasing the computational time requirement of that algorithm, since the majority of the computational demand of the algorithm has been processed by executables compiled from C.

The comparisons produced in this appendix have been performed on a Toshiba Satellite Notebook 2415-S205 running Microsoft Windows XP, Version 2002 with Service Pack 2 installed. The Mobile Intel® Pentium® 4-M CPU runs at 2.00 GHz and has 1.00 GB of RAM accessible to it. Apart from the operating system MATLAB®, and the required executables in each comparison, no additional programs are executed during a simulation in order to produce the most comparable environment possible.

### E.3 Numerical Integration

In general, all numerical integration conducted in this dissertation has been performed using a variable time-step eighth-order Runge-Kutta integration method (Wilson and Turcotte, 1997), with an integration tolerance of  $10^{-12}$ . Many authors have performed surveys of the relative performances of different numerical integration algorithms, including Anderson (2005); we will not repeat their work here. However, this section provides a discussion that compares the relative speed of integrating arbitrary trajectories in the CRTBP using MATLAB® vs. using executables produced from C. In addition, this section compares the relative speed of integrating similar trajectories in the CRTBP vs. the JPL Ephemeris model using executables produced from C.

We have compared the computational requirements for propagating a given trajectory using four methods. These methods are outlined as follows:

- **Method 1:** The trajectory is propagated in the Earth-Moon CRTBP using an integrator written in MATLAB®.
- **Method 2:** The trajectory is propagated in the Earth-Moon CRTBP using an integrator written in C and called via a **mex**-function from MATLAB®.
- **Method 3:** The trajectory is propagated in a simple version of the JPL Ephemeris using an integrator written in C and called via a **mex**-function from MATLAB®.

The particle's motion is only affected by the gravity of the Sun, Earth, and Moon in this model.

- **Method 4:** The trajectory is propagated in a complex version of the JPL Ephemeris using an integrator written in C and called via a **mex**-function from MATLAB®.

The particle's motion is affected by the gravity of the Sun, Earth, and Moon, as well as the gravity of Mercury, Venus, Mars, Jupiter, Saturn, Uranus, and Neptune.

Each of these methods varies in complexity. The first method calls an integration function, which then calls a derivative function numerous times. Each function in Method 1 is written and executed in MATLAB®. The second method calls a single **mex**-function that sets up the call to a binary executable that had already been compiled from C source code. The C code calls its corresponding derivative function the same number of times as Method 1, but each of these function calls requires less overhead time. Once the integration is complete, the binary executable returns its data back to the **mex**-function, which then hands it back to MATLAB®. The two methods that involve the JPL Ephemeris model operate using the same sort of **mex**-functions. Integrating in the JPL Ephemeris model is more complex than the CRTBP, however, because the equations of motion vary as a function of the Julian Date. The JPL Ephemeris integrator must open up a set of Tchebyshev coefficients for each body that is included in the model. Hence, the simple JPL Ephemeris model (Method 3) requires that the Tchebyshev coefficients for the Sun, Earth, and Moon are loaded into memory, whereas the complex JPL Ephemeris model (Method 4) requires that the set of coefficients for each planet in the solar system be loaded into memory. Each of these four propagation methods requires a different amount of overhead time, as well as a different amount of computation time for the actual integration.

In order to determine the overhead time for each method, we have executed

each method using an integration tolerance of  $10^{12}$  and have requested that only a single state be outputted at a time of  $10^{-9}$  seconds after the initial time. In this way, the integration process is fully set up, but the integrator performs a very minimal amount of work. We have performed this integration overhead test 1000 times for each method in order to average out any slight variations in each execution. The results are shown in Table E.1. One can see that the overhead cost of the second method is the smallest, demonstrating that the computational overhead of setting up the **mex**-function is small, compared with performing the integration solely in MATLAB<sup>®</sup>. One can also see that the overhead cost of setting up the JPL Ephemeris integrator is significantly more demanding than setting up the CRTBP integrator. However, there is little difference between setting up the JPL Ephemeris integrator to process three gravitating bodies compared with ten.

Table E.1: The overhead computational time requirements for each of the four propagation methods tested.

Propagation Method	Overhead Cost
Method 1	0.0044934 sec
Method 2	0.0001512 sec
Method 3	0.0136997 sec
Method 4	0.0137547 sec

We have tested out each method of integration on a sample set of different trajectories in the Earth-Moon system. Since the bodies in the solar system move differently in the Circular Restricted Three-Body and JPL Ephemeris models, these trajectories are not identical in both models. However, they are heuristically very similar. Each trajectory has been propagated for thirty days using a tolerance of  $10^{-12}$ , and states have been outputted in each method at 0.1-day intervals. The sample trajectories, along with their initial conditions in the Earth-Moon CRTBP are shown in Figure E.1.

Each trajectory has been integrated using each propagation method a total of 100 times and an average computation time has been recorded. The results of these

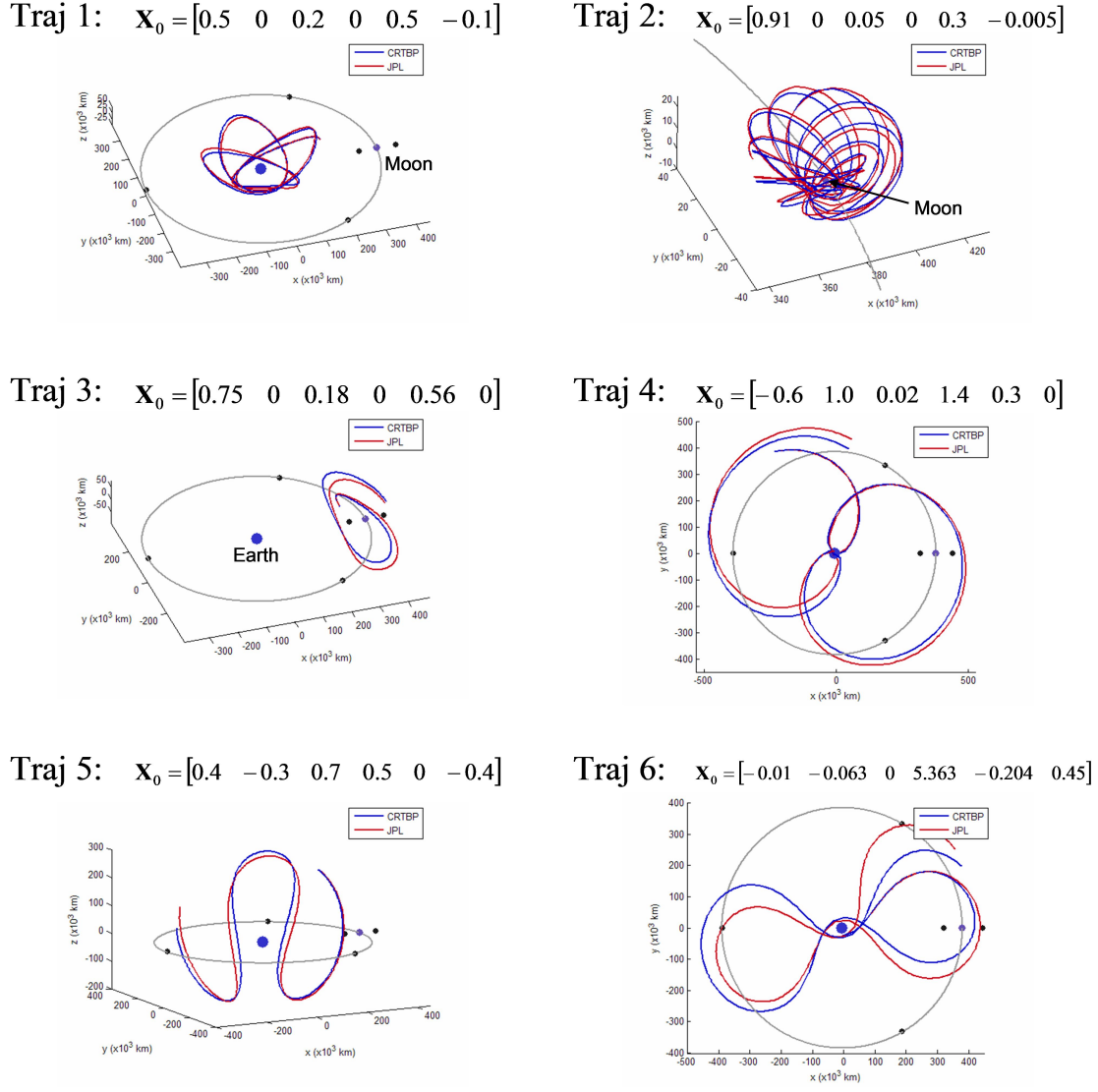


Figure E.1: Six sample trajectories that have been produced using each of the four propagation methods. The curves shown in blue have been propagated in the CRTBP; the curves shown in red have been propagated in the JPL Ephemeris model. Each trajectory is displayed in the Earth-Moon synodic reference frame from above.

tests are shown in Table E.2. One can see that Method 2 out-performs Method 1 by a factor of approximately 25. It requires about three times more computation time to propagate a trajectory in the simple JPL Ephemeris model as in the Earth-Moon CRTBP. Finally, it requires about twice as much computation time to propagate a trajectory in the full, complex JPL Ephemeris model (Method 4) as it does in the simple JPL Ephemeris model (Method 3).

Table E.2: The average computation time required by each of the four propagation methods for each of the six sample trajectories shown in Figure E.1.

Trajectory	Method 1	Method 2	Method 3	Method 4
Traj. 1	0.51965 sec	0.02133 sec	0.06079 sec	0.13529 sec
Traj. 2	0.87565 sec	0.03465 sec	0.07230 sec	0.16554 sec
Traj. 3	0.34339 sec	0.01252 sec	0.05769 sec	0.12458 sec
Traj. 4	0.54308 sec	0.01943 sec	0.06890 sec	0.15302 sec
Traj. 5	0.33027 sec	0.01312 sec	0.05638 sec	0.12138 sec
Traj. 6	0.55700 sec	0.02334 sec	0.06910 sec	0.15102 sec

#### E.4 Producing BLTs in the Patched Three-Body Model

When propagating a particle's trajectory in the Patched Three-Body model, one must pay attention to where the particle travels: if the particle pierces the Three-Body Sphere of Influence (3BSOI), then the model must switch coordinate frames from the Earth-Moon CRTBP to the Sun-Earth CRTBP or vice versa. In this way, the particle is propagated through a simplified four-body system. It is normally computationally inefficient to propagate the particle for the entire duration of the simulation in one reference frame before checking to see if the particle ever pierced the 3BSOI. In this dissertation, the particle is propagated for approximately two weeks before checking its state. If the particle did indeed pierce the 3BSOI during that time, then the propagation is returned to that state and the integration process switches three-body systems. The two-week duration was found to be a computational compromise between check-

ing continuously and checking after a full simulation time span. The computational requirements of producing BLTs vary depending on the geometry of the BLT. However, in order to provide a quantitative idea about the computational requirements, it was found that it required approximately  $0.32493 \pm 0.04010$  seconds to produce each of 100 sample exterior BLTs and approximately  $0.33041 \pm 0.04033$  seconds to produce each of 100 sample interior BLTs.

### **E.5 Producing BLTs in the JPL Ephemeris Model**

The computational requirements needed to integrate a particle's trajectory in the JPL Ephemeris model are much higher than those required by the CRTBP and Patched Three-Body models. Furthermore, in order to produce a BLT in the JPL Ephemeris model, one must first produce the target three-body orbit. This process requires several iterations of a multiple-shooting differential corrector, a time-consuming process that is discussed in more detail in Section 3.6.3. This process can take between several seconds and several minutes to complete, depending on the specified tolerance levels. Once the target orbit has been produced, it takes less than a second to produce each trajectory in that orbit's stable manifold, leading to potential BLTs.

### **E.6 Producing BLT Maps**

BLT Maps are constructed by integrating trajectories at each point in the grid. Each integration may be performed independently of each other; hence, the construction of a BLT Map is trivially parallelizable. In the Patched Three-Body model, the target three-body orbit, e.g., the target L<sub>2</sub> Halo orbit, may be produced once prior to integrating each trajectory in that orbit's stable manifold. The target three-body orbit doesn't change as the parameter  $\theta$  is varied. In the JPL Ephemeris model, however, a different three-body orbit must be produced for each reference Julian Date. Thus, in

the JPL Ephemeris model, it is more computationally efficient to produce a target orbit for a given reference Julian Date once and then produce that orbit's stable manifold before moving on to the next reference Julian Date.

The computational requirement of building a BLT Map varies depending on the target three-body orbit and the geometry of the particular stable manifold that is being produced. For instance, the interior BLT Map of a Halo orbit about L<sub>2</sub> requires more computational time than the exterior BLT Map of the same Halo orbit. The exterior stable manifold of that Halo orbit immediately departs the vicinity of the Moon and will encounter a massive body fewer times on average than the interior stable manifold that immediately approaches the Moon. Of course, the computational requirements also increase as the manifold-propagation duration,  $\Delta t_m$ , is increased.

To provide some quantitative comparison, we have measured the amount of time required to produce each trajectory within two different Patched Three-Body BLT Maps: the exterior BLT Map presented in Figure 6.3 on page 230 and the interior BLT Map presented in Figure 6.5 on page 233. The parameters of these two BLT Maps are given in Table E.3. These two BLT Maps are shown in Figure E.2. It required an average of approximately 0.13550 seconds to produce each of 60,000 points within the exterior BLT Map. Similarly, it required an average of approximately 0.13818 seconds to produce each of 60,000 points within the interior BLT Map. One can see that it does require more time to produce points within the interior BLT Map, however, the difference is only approximately 0.00268 seconds per point on average.

Table E.3: The parameters used to produce the BLT Maps shown in Section 6.2.3 and in Figure E.2.

Parameter	Value
$F$	The family of Earth-Moon L <sub>2</sub> Halo Orbits
$C$	3.05
$\theta$	$0^\circ \leq \theta \leq 360^\circ$
$\tau$	$0 \leq \tau \leq 1$
$p$	$\begin{cases} \text{"Exterior"} : \text{ Figures 6.3 and 6.4} \\ \text{"Interior"} : \text{ Figures 6.5 and 6.6} \end{cases}$
$\Delta t_m$	195.4 days (45 Earth-Moon time units)

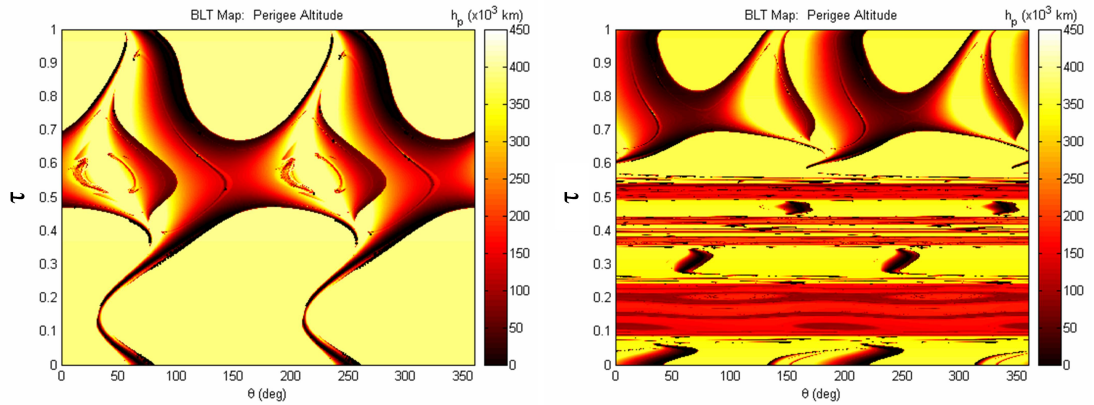


Figure E.2: Example exterior (left) and interior (right) BLT Maps produced in the Patched Three-Body model using the parameters shown in Table 6.2. The shading indicates the lowest perigee altitude that each trajectory encounters, such that points shaded darkest approach the closest to the Earth.